

Dissertation zur Erlangung des Doktorgrades
der Fakultät für Chemie und Pharmazie
der Ludwig-Maximilians-Universität München

**Genetic and chemical perturbation of amino acid sensing
by the GCN1-GCN2 pathway**



Johanna Barbara Brüggenthies

aus

Essen, Deutschland

2021

Erklärung

Diese Dissertation wurde im Sinne von § 7 der Promotionsordnung vom 01. Juni 2017 von Herrn Prof. Dr. Veit Hornung betreut.

Eidesstattliche Versicherung

Diese Dissertation wurde eigenständig und ohne unerlaubte Hilfe erarbeitet.

München, den 24.06.2021

Johanna B. Brüggenthies

Dissertation eingereicht am:

24.06.2021

1. Gutachter:

Prof. Dr. Veit Hornung

2. Gutachter:

Prof. Dr. Peter J. Murray

Mündliche Prüfung am:

01.09.2021

Summary

Amino acid stress activates the GCN2-regulated branch of the integrated stress response (ISR). This ancient pro-survival signaling network is conserved across eukaryotes to react to cellular stress by controlling proteostasis. Mechanistically, GCN2 blocks translation by phosphorylating the initiation factor eIF2 α and simultaneously activating an ATF4-dependent transcriptional program for stress adaptation. The amino acid response was initially discovered in *Saccharomyces cerevisiae*, where the HEAT-repeat protein GCN1 was suggested to regulate the GCN2 activation at the ribosomal machinery. The master regulator of cell growth, mTORC1, is another amino acid sensing hub, which also modulates translation. However, the molecular and mechanistic events that lead to the mammalian GCN2-ISR activation, its connection to the mTORC1 pathway and the outcomes in terms of cell state adaptation remain elusive.

In this PhD thesis, I investigated the GCN2-ISR by genetic and chemical perturbation in diverse murine cell systems. My major focus was to dissect the interplay of GCN1, GCN2 and mTORC1 upon amino acid stress. Using CRISPR/Cas9-genetically modified cell lines, I found that GCN1 acts upstream of GCN2 to regulate its autophosphorylation and ultimately the ATF4-induced transcriptional response in an eIF2 α independent way. Using a multi-omics approach, I show that GCN1 and GCN2 are isogenic in regulating the ISR in response to leucine stress by controlling transcriptome and proteome changes over time. Processes involved in mitochondrial 1C- metabolism, amino acid uptake, tRNA synthetases and glutamine metabolism are modulated at the gene and protein level in a GCN1 and/or GCN2 dependent way. Furthermore, I provide evidence that both proteins have a distinct bioenergetic profile – already at steady-state. I also show that GCN1 can be involved in the DNA damage response by physically interacting with the MRN complex in a transient way. I also highlight that the ISR can play a role in ferroptosis regulation in an ATF4-SLC7A11-dependent manner. Moreover, this thesis suggests that a direct interaction of GCN1 with GCN2 and the ribosome is unlikely. In a 3,876 compound GCN2 inhibitor screen, I discovered that dual mTOR inhibitors concurrently block the mTORC1 and the GCN2 branches of amino acid sensing upon amino acid stress. This effect was not mediated by direct GCN2-binding and independent of PERK and eIF2 α . Instead, these results suggest a role of mTOR in modulating the activation of GCN2 upon prolonged leucine stress. Finally, I provide new insights on the involvement of GCN1 in the mammalian ISR and potential GCN2- and amino acid stress-independent functions. Moreover, I discovered an unexpected interplay of the GCN1-GCN2 and the mTORC1 amino acid sensing pathways, which is of high importance for understanding how these complex multiprotein kinases integrate nutrient sensing. This finding paves a new frontier for mTOR and GCN2 anti-neoplastic drug development for the selective targeting of amino acid-dependent cell protection pathways in cancer.

Table of Contents

1. Introduction	1
1.1. Regulation of protein homeostasis upon cellular stress	1
1.1.1. Overview of the amino acid metabolism.....	1
1.1.2. Cellular protein quality control networks.....	2
1.1.3. Amino acid sensing and signaling pathways.....	4
1.2. The integrated stress response network.....	7
1.2.1. Sensors of the integrated stress response	7
1.2.2. Mechanism of the integrated stress response.....	8
1.2.2.1. eIF2-dependent regulation of the ternary complex formation.....	9
1.2.2.2. ATF4-dependent regulation of the stress-transcriptional response	11
1.2.3. GCN2-mediated integrated stress response	13
1.2.3.1. Discovery of GCN2, GCN1 and GCN20	13
1.2.3.2. Structural architectures of GCN2, GCN1 and GCN20	14
1.2.3.3. Molecular function of GCN1 in yeast and mammals	20
1.2.3.4. Current models of the amino acid response in yeast and mammals	23
1.2.3.5. Amino acid response in health and disease	27
1.2.3.5.1. Amino acid response in immunity.....	27
1.2.3.5.2. Amino acid response in cancer	29
1.2.3.5.3. Amino acid response in stem cell integrity, tissue remodeling and neurodegenerative disorders	30
1.2.3.5.4. GCN2 inhibition as therapeutic strategy.....	31
1.3. The mTORC1 pathway.....	33
1.3.1. Discovery of mTOR	33
1.3.2. Structural architectures of mTORC1 and mTORC2	33
1.3.3. Molecular functions of the mTORC1 signaling pathway	36
1.3.3.1. Biological role of mTORC1	36
1.3.3.2. Regulation of protein synthesis by mTORC1	37
1.3.3.3. Regulation of lipid and nucleotide synthesis by mTORC1.....	41
1.3.3.4. Regulation of autophagy and bioenergetics by mTORC1	42
1.3.4. Regulators of mTORC1 function	42
1.3.5. mTORC1 signaling upon amino acid stress	46
1.3.6. Interplay of mTORC1 and GCN2	49
1.3.7. mTOR in physiology and pathophysiology	52
2. Aims of the thesis.....	54

3. Materials and Methods.....	55
3.1. Mice	55
3.2. <i>In Vitro</i> Cell Culture	55
3.2.1. Cell systems	55
3.2.1.1. Cell culture of murine fibroblasts	55
3.2.1.2. Cell culture of murine bone marrow derived macrophages.....	56
3.2.1.3. Cell culture of murine embryonic stem cells	56
3.2.1.4. Cell culture of human cells	57
3.2.2. Differentiation of murine embryonic stem cells.....	57
3.2.3. Generation and validation of genetically modified cell lines	58
3.2.3.1. Generation of single-cell-based biallelic gene-deficient cell lines using CRISPR/Cas9 engineering	58
3.2.3.2. Generation of bulk cell-based biallelic gene-deficient cell lines using lentivirus- mediated CRISPR/Cas9 engineering	59
3.2.3.3. Generation of single-cell-based biallelic point mutated cell lines using CRISPR/Cas9 engineering	60
3.2.3.4. Generation of single-cell-based biallelic insertion-modified cell lines using CRISPR/Cas9 engineering	65
3.2.4. Transfection of cell lines	68
3.2.4.1. Transient transfection.....	68
3.2.4.2. Stable transfection	69
3.3. Nutrient deprivation	69
3.3.1. Fetal bovine serum dialysis	69
3.3.2. Amino acid starvation	70
3.3.3. Asparaginase treatment.....	70
3.3.4. Drug treatment	71
3.4. Cell biology-based methods.....	71
3.4.1. Cell death analysis using CellTox staining	71
3.4.2. Amino acid starvation-based <i>Ddit3</i> induction assay	72
3.4.3. Mitochondrial respiratory and glycolysis flux assay	72
3.4.4. Single-cell-dilution	73
3.4.5. Immunofluorescence assay	73
3.4.6. Nascent protein synthesis detection assay	74
3.4.7. Phospho-Flow cytometry analysis	74
3.4.8. Fluorescence activated cell sorting and analysis	75
3.5. Nucleic acid-based methods	75
3.5.1. Allelic discrimination-based Polymerase Chain Reaction.....	75

3.5.2. RNA isolation, cDNA synthesis and quantitative real-time PCR	76
3.5.3. CRISPR/Cas9 genome engineering plasmid preparation.....	78
3.5.4. Polysome profiling	79
3.6. Protein-based methods	79
3.6.1. Protein lysis and protein amount determination.....	79
3.6.2. Immunoblotting	80
3.6.3. Immunoprecipitation for native protein	81
3.6.4. <i>In vitro</i> immunoprecipitation-based GCN2 kinase assay	82
3.6.5. Radioactivity-based mTOR kinase activity assay	83
3.7. Multi-omics techniques.....	83
3.7.1. Transcriptomics	83
3.7.2. Proteomics and phosphoproteomics	84
3.7.3. Interactomics	86
3.8. Additional software.....	90
4. Results	91
4.1. Genetic characterization of genetically modified murine cell lines.....	91
4.1.1. Overview.....	91
4.1.2. Genetic characterization of <i>Eif2ak4</i> and <i>Gcn1</i> loss-of-function alleles	93
4.1.3. Genetic characterization of <i>Eif2ak4</i> and <i>Eif2s1</i> point mutations	96
4.1.4. Genetic characterization of <i>Atf4</i> loss-of-function alleles	100
4.1.5. Genetic characterization of GCN2-dependent amino acid stress reporter cell systems	101
4.2. Multi-omics analysis of GCN1 and GCN2 deficiency	105
4.2.1. Overview.....	105
4.2.2. Investigation of the optimal amino acid starvation conditions	105
4.2.3. Transcriptomics study of GCN1 and GCN2 deficiency	119
4.2.4. Full proteomics and phosphoproteomics studies of GCN1 and GCN2 deficiency... 143	
4.2.4.1. Full proteome analysis	144
4.2.4.2. Phosphoproteome analysis	157
4.2.5. Interactomics of endogenous GCN1	161
4.3. Functional analysis of GCN1 and GCN2 deficiency.....	168
4.3.1. Overview.....	168
4.3.2. Sub-cellular localization of GCN1 and GCN2.....	168
4.3.3. Interaction studies of GCN1 and GCN2	172
4.3.4. Ferroptosis regulation by GCN1 and GCN2	177
4.3.5. Bioenergetics regulation by GCN1 and GCN2	192

4.4. Mechanistic analysis of the mammalian amino acid response.....	199
4.4.1. Overview	199
4.4.2. GCN2 activation is regulated by GCN1.....	201
4.4.3. ATF4-dependent transcriptional response is regulated by GCN1	202
4.4.4. eIF2 α phosphorylation is regulated by GCN1	206
4.4.5. Translation is regulated by GCN1	212
4.5. Mechanistic analysis of the amino acid stress-regulated mTORC1 signaling	215
4.5.1. Overview	215
4.5.2. Interplay of the mTORC1 and the GCN2 amino acid sensing networks	215
4.6. Molecular verification of genetically modified cell lines in biological context	221
4.6.1. Overview	221
4.6.2. GCN1 and GCN2 deficiency in different clonal and murine cell systems	221
4.6.3. Reconstitution of the GCN1 and GCN2 phenotype	224
4.7. Chemical large-scale bioactive kinase compound screen for GCN2 inhibition.....	225
4.7.1. Overview	225
4.7.2. Primary GCN2 compound library screen: Class-IV-PI3K inhibitors prevent the GCN2-ISR upon leucine stress.....	226
4.7.3. Class-IV-PI3K inhibitors prevent the GCN2-ISR dose-dependently and GCN2-independently	234
4.7.4. GCN2-ISR is prevented by Torins but not rapamycin	243
4.7.5. Dual mTORi-mediated GCN2-ISR inhibition is indirect	252
4.7.6. Dual mTORi-mediated GCN2-ISR inhibition is regulated independently of eIF2 α ..	259
4.7.7. Dual mTORi-mediated GCN2-ISR inhibition is regulated independently of PERK..	260
4.7.8. GCN2 inhibition does not affect mTORC2 activity upon leucine stress	264
4.7.9. Dual mTORi-mediated GCN2-ISR inhibition is time-dependent	267
4.7.10. Translation is regulated by GCN2 and mTOR inhibition.....	269
4.7.11. Energy sensing is regulated by GCN2 and mTOR inhibition	272
4.7.12. Ferroptosis is regulated by GCN2 and mTOR inhibition.....	275
5. Discussion	281
5.1. Our model of the mammalian amino acid response	283
5.2. Global transcriptome and proteome changes upon leucine stress.....	284
5.3. Cell state adaptation upon amino acid stress	285
5.4. Unexpected functions of murine GCN1	286
5.5. Time-dependency of the mTORC1-GCN2 interplay upon amino acid stress	287
5.6. Concurrent suppression of the mTOR and the GCN2 pathways upon amino acid stress	289

5.7. Outlook.....	291
6. References.....	293
7. Supplementary material.....	319
7.1. Sequence alignments of the CRISPR/Cas9 genetically modified cell lines	319
7.1.1. Sequence alignments of <i>Eif2ak4</i> and <i>Gcn1</i> loss-of-function alleles.....	319
7.1.2. Sequence alignments of <i>Eif2ak4</i> and <i>Eif2s1</i> point mutations	325
7.1.3. Sequence alignments of <i>Atf4</i> loss-of-function alleles	328
7.1.4. Sequence alignments of the GCN2-dependent amino acid stress reporter cell systems	329

List of abbreviations

4EBP1	4E-binding protein 1
5' TOP	5' terminal oligopyrimidine tract
AAR	amino acid response
ABC	ATP-binding cassette
ALL	acute lymphoblastic leukemia
AML	acute myeloid leukemia
AMPK	AMP-activated protein kinase
Arg1	arginase 1
ASNase	asparaginase
ASNS	asparagine synthetase
ATF4	activating transcription factor 4
ATF5	activating transcription factor 5
ATF6	activating transcription factor 6
ATG13	autophagy-related protein 13
ATM	ataxia-telangiectasia-mutated
ATP	adenosine triphosphate
ATR	ataxia telangiectasia and Rad3-related
BiP	binding immunoglobulin protein
C/EBP β	CCAAT enhancer-binding protein-beta
CDK1	cyclin-dependent kinase 1
CHO	chinese hamster ovary
cGAS	cyclic GMP-AMP synthase
CHOP	C/EBP-homologous protein
CML	chronic myelogenous leukemia
CRISPR	clustered regularly interspaced short palindromic repeats
CSNK2A2	casein kinase II subunit alpha
CTD	C-terminal domain
DELE1	DAP3 binding cell death enhancer 1
DEPTOR	DEP-domain-containing mTOR-interacting protein
DNA-PK	DNA-dependent protein kinase
ECAR	extracellular acidification rate
eEF1A	eukaryotic translation elongation factor 1A
eEF3	eukaryotic translation elongation factor 3
eIF2	eukaryotic translation initiation factor 2
Eif2ak4	eukaryotic translation initiation factor 2 alpha kinase 4
eIF2B	eukaryotic translation initiation factor 2B
eIF4E/F/G	eukaryotic translation initiation factor 4E/F/G
EPRS	glutamyl-prolyl-tRNA synthetase
ER	endoplasmic reticulum
ERAD	ER-associated protein degradation
FDR	false discovery rate
FKBP12	FK506-binding protein 12; prolyl-isomerase 12
FLCN-FNIP2	Folliculin–folliculin interacting protein 2
FLS	fibroblast-like synoviocytes
GAAC	general amino acid control
GADD34	growth arrest and DNA damage-inducible protein
GAP	GTPase-activating proteins

GATOR1/2	GAP activity towards the Rag proteins 1/2
GCN1L1	general control of amino-acid synthesis 1-like 1
GCN2	general control non-derepressible 2
GCN20	ATP binding cassette subfamily F
GDP	guanosine 5'-diphosphate
GEF	GTP exchange factor
GIR2	genetically interacts with ribosomal genes 2
gRNA	guide RNA
GSH	glutathione
GTP	guanosine 5'-triphosphate
HEAT	huntingtin, eEF3, protein phosphatase 2 A, and mTor
HF	halofuginone
HIF1 α	hypoxia inducible factor 1 alpha
HisRS	class II histidyl tRNA synthetase-related
HRI	heme-regulated inhibitor kinase
HSC	hematopoietic stem cell
HSF1	heat shock factor 1
Hsp90	heat shock protein 90
HSR	heat shock response
IDO1/ 2	indoleamine dioxygenases 1/2
IFN γ	interferon gamma
IGF-1	insulin-like growth factor 1
IL-10	interleukin-10
IL-1 β	interleukin-1 beta
IMPACT	imprinted gene with ancient domain
INDELs	insertions and deletions
iNOS	nitric oxide synthase in macrophages
IP	immunoprecipitation
IRE1	inositol requiring enzyme 1
IRS-1	insulin receptor substrate 1
ISR	integrated stress response
LARP1	La-related protein 1
m ⁷ G-cap	7-methylguanosine-cap
MAPK	mitogen-activated protein kinase
MDSCs	myeloid-derived suppressor cells
MEF	mouse embryonic fibroblast
Met-tRNA ⁱ	methionyl-initiator tRNA
mLST8	mammalian lethal with SEC13 protein 8, also known as G β L
mSIN1	MAPK-interacting protein 1
MTHFD2	methylene- tetrahydrofolate dehydrogenase 2
mTOR	mechanistic target of rapamycin
mTORC1	mechanistic target of rapamycin complex 1
mTORC2	mechanistic target of rapamycin complex 2
MYC	myelocytomatose
NAD	nicotinamide adenine dinucleotide
NUFIP1	retardation-interacting protein 1
OAA	oxaloacetic acid
OCR	oxygen consumption rate
OMA1	overlapping with the M-AAA protease 1

ORF	open reading frame
OXPPOS	oxidative phosphorylation
p70S6K	ribosomal protein S6 kinase B1
PDCD4	programmed cell death 4
PDK1	phosphoinositide-dependent kinase 1
PD-L2	programmed cell death 1 ligand 2
PEP	phosphoenolpyruvate
PERK	protein kinase RNA (PKR)-like ER kinase
PI	protein-protein interaction
PI3K	phosphoinositid-3 kinase
PIKK	PI3K-related protein kinase family
PIP3	phosphatidylinositol (3,4,5)-trisphosphate
PKR	double-stranded RNA-dependent protein kinase
PPAR γ	peroxisome proliferator-activated receptor gamma
PRAS40	proline-rich Akt substrate of 40 kDa
PROTOR1/2	protein associated with rictor 1/2
PTEN	phosphatase and tensin homolog
RA	rheumatoid arthritis
RAPTOR	regulatory associated protein of mTOR
RAS	rat sarcoma
RBG2	ribosome interacting GTPase
RICTOR	rapamycin-insensitive companion of mTOR
RT	room temperature
RTK	receptor tyrosine kinase
RWD	RING finger proteins, WD-repeat-containing proteins, and yeast DEAD-like helicases
SAM	S-adenosylmethionine
SLC	solute carrier
SREBP1/2	sterol regulatory element binding protein 1/2
SSPCs	skeletal stem/progenitor cells
TAM	tumor-associated macrophage
TC	ternary complex
TCA	tricarboxylic acid
TFE3	transcription factor binding to IGHM enhancer 3
TFEB	transcription factor EB
TGF β	transforming growth factor beta
TNF α	tumor necrosis factor alpha
TORKinibs	ATP-competitive dual mTOR small molecules
Trib3	NF- κ B-regulator tribbles homolog 3
tRNA	transfer ribonucleic acid
TRS	threonyl-tRNA synthetase
TSC	tuberous sclerosis complex
UBC	ubiquitin-conjugating enzymes
ULK1	un-51-like autophagy-activating kinase 1
UPR	unfolded protein response
UTR	untranslated region
UV	ultraviolet
VCAM1	vascular cell adhesion molecule 1
XBP1	X-box binding protein 1
YIH1	yeast IMPACT homologue

1. Introduction

1.1. Regulation of protein homeostasis upon cellular stress

1.1.1. Overview of the amino acid metabolism

Proteins comprise more than 60 % of the cellular macronutrient mass in mammalian cells and control cell fate as well as cellular activity¹. The protein quantity and quality is constantly fine-tuned by protein biosynthesis and protein degradation². Protein biosynthesis is the most energy- and resource-intensive process in growing cells³. In contrast to other macronutrients like fatty acids or carbohydrates, a dedicated protein storage depot does not exist⁴. Instead, the protein pool is dynamically and compartment-wide rewired, which maintains cellular proteome integrity and fidelity and ultimately homeostasis. This is especially relevant when cells have to adjust to environmental challenges resulting in cellular stress, which is most likely induced by nutrient deficiency or withdrawal that affects various traits in cellular physiology and pathophysiology^{2,4,5}. In mammals, the 20 proteinogenic amino acids (21 with L-selenocysteine) are the building blocks of the cellular machinery. As proteins and protein complexes, they provide (i) architectural support for the cytoskeleton (e.g. actin), (ii) catalytic active enzymes for metabolic reactions (e.g. caspases for apoptotic cell death), (iii) intra- and intercellular signaling molecules or transport (e.g. hormone and cytokines) and (iv) energy supply (e.g. ATPase)⁶. Controlled by the equilibrium of anabolism and catabolism, proteins are degraded to ketogenic and glucogenic amino acids by deamination. This process supplies energy as adenosine triphosphate (ATP) by oxidative phosphorylation (OXPHOS) in mitochondria. Here, glucogenic amino acids (e.g. L-arginine) provide glucose via gluconeogenesis and ketogenic amino acids (e.g. L-Leucine) supply acetyl-CoA used for ketogenesis and lipid biosynthesis⁷. Anaplerotic reactions replenish intermediates in the TCA (tricarboxylic acid) cycle that are catabolized to serve as biosynthetic precursors such as the entry of L-glutamine into the TCA cycle as α -ketoglutarate⁸. Humans and most mammals are auxotrophic for 9 of 20 amino acids (L-histidine, L-leucine, L-lysine, L-isoleucine, L-phenylalanine, L-methionine, L-valine, L-threonine and L-tryptophan) and conditionally auxotrophic for L-arginine, which manifests an exogenous supply dependency of essential amino acids⁹. Those are internalized by dedicated amino acid transporters such as solute carriers^{10,11}. Amino acid auxotrophy has evolved as key immunoregulatory control checkpoint in myeloid cells to shape the immune response upon L-tryptophan or L-arginine depletion in the tumor microenvironment as discussed below in more detail (Section 1.2.3.5.1.)⁹.

1.1.2. Cellular protein quality control networks

Protein homeostasis, or proteostasis, is a multi-compartmental and coordinated system that regulates cellular fate towards death or life¹². A physiological and healthy environment is maintained by tightly controlling protein synthesis, assembly, folding, localization and degradation. Extrinsic (e.g. amino acid deprivation) and intrinsic (e.g. protein aggregation) stress stimuli disrupt the cellular proteostasis equilibrium. The mechanistic and molecular consequence is the activation of a plethora of intracellular sensing and signaling networks to reestablish and restore the cellular balance or to ultimately eliminate the malfunctioned cell¹³. Numerous overlapping and interacting proteotoxic stress-regulating pathways operate in the cytosol and/or the endoplasmic reticulum (ER) to adapt to stress and protect the cell by reprogramming gene expression (Figure 1): (i) The heat shock response (HSR) triggers the chaperone-mediated protein folding and degradation capacity in the cytosol¹⁴; (ii) The unfolded protein response (UPR) is fundamental to ensure that protein-folding capacity meets the load of client proteins in the ER. Misfolded proteins fail the ER-quality control check and become degraded by the ubiquitin-proteasome system (ER-associated protein degradation, ERAD)^{5,12,13}; (iii) The integrated stress response (ISR) inhibits protein synthesis in response to stress in both the ER and cytosol and can be coupled to the UPR and HSR in a collaborative manner^{15–17}.

Proteotoxic ER stress such as the accumulation of un- and misfolded proteins activates the UPR by the three ER-localized transmembrane stress sensors IRE1 (inositol requiring enzyme 1), ATF6 (activating transcription factor 6) and PERK (protein kinase RNA (PKR)-like ER kinase) (Figure 1)¹³. PERK is a component of the ISR, which mediates the ER stress adaptation response via the activating transcription factor 4, ATF4 (yeast: GCN4)¹⁵. Severe forms of proteotoxic stress increase the accumulation of cytoplasmic misfolded proteins, inducing the HSR that controls the activation of chaperones (mainly heat-shock proteins, HSPs) relevant for UPR activation: HSPs switch to interactions with denatured proteins by releasing the heat shock transcription factors, HSF (most-studied: heat shock factor 1, HSF1)¹⁴. Collectively, eukaryotic cells combat proteotoxicity by the HSR and UPR cross-talking with the ISR for stress adaptation or irreversible protein degradation via the proteasome^{15–20}. Mechanistically, multiple conserved transcription factors (ISR: ATF4; UPR: ATF6, XBP1 (X-box binding protein 1) and HSR: HSF1) direct the transcriptional stress response to control the expression of chaperones (UPR: BiP (binding immunoglobulin protein); HSR: HSP90; heat shock protein 90 and ISR: mainly HSP90) and other stress-protective proteins to regulate proteostasis. When proteostasis fails, a cytotoxic rather than cytoprotective program induces apoptotic cell death^{13,21}.

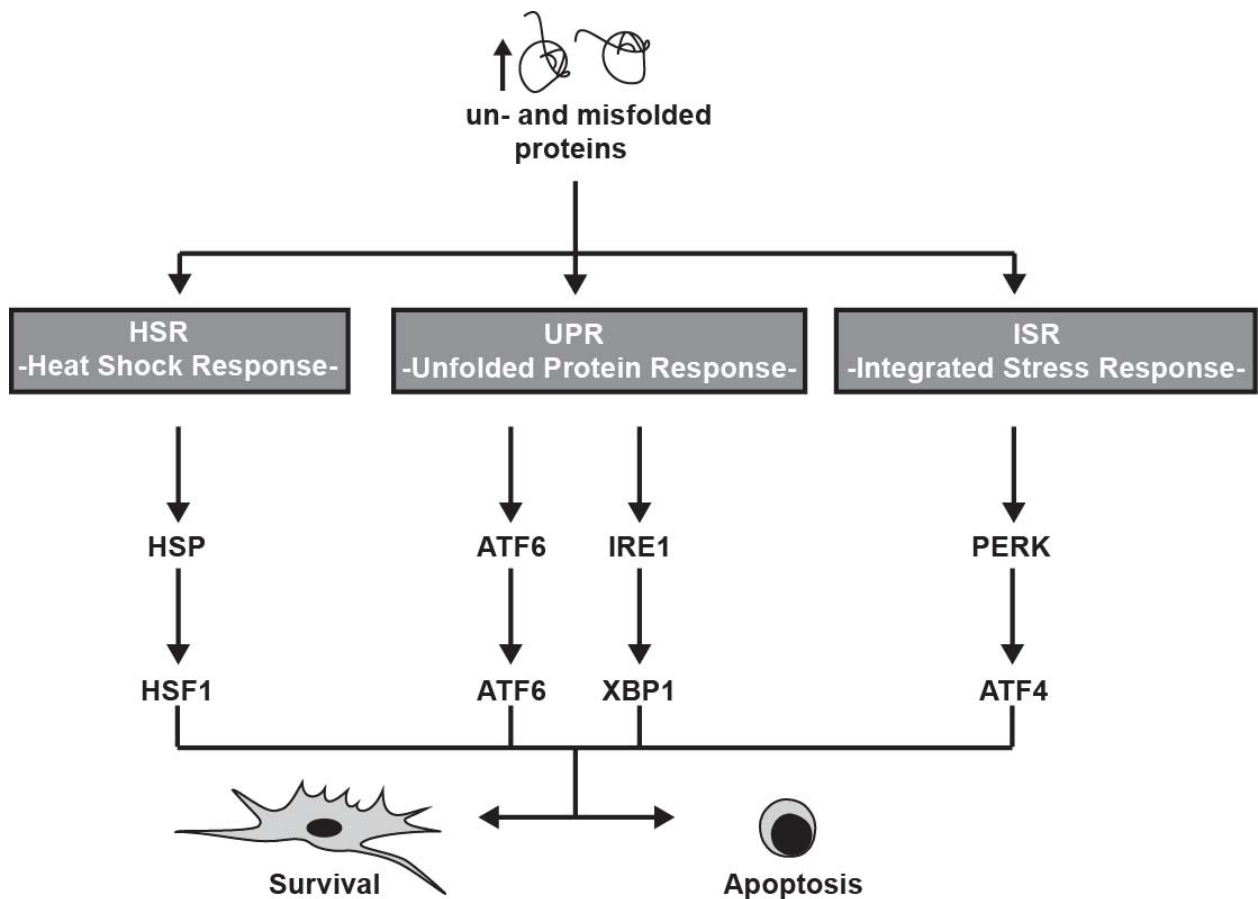


Figure 1. Schematic overview of the core elements of the main proteotoxic stress-regulating pathways. Un- and misfolded protein accumulation triggers three major proteotoxic stress-regulating pathways: the heat shock response (HSR), the unfolded protein response (UPR) and the integrated stress response (ISR) in the cytosol and/or the endoplasmic reticulum to regulate protein homeostasis in a specific and parallel way^{15,17–20}. Mechanistically, all branches operate by activating stress sensors (HSP, ATF6, IRE1 or PERK), which induce specific transcription factors (HSF1, ATF6, XBP1 or ATF4) ensuring the expression of stress-protective proteins (mostly chaperones) relevant for inducing protein homeostasis. When protein homeostasis cannot be reestablished, prolonged and unmitigated ER stress leads to cellular apoptosis^{5,12,13}.

Overall, the three described proteotoxic stress-regulating pathways are activated in a parallel spatio-, temporal- and cell-specific way in response to stress^{15,17–20}. While proteostasis is an active area of research and is strongly associated with health and disease²², our knowledge about how these pathways work remains rudimentary. This is especially the case for the ISR, a pathway controlled by multiple stress stimuli that regulate pro-survival stress adaptation²³. To this end, this thesis will focus on one branch of the ISR modulated by amino acid stress.

1.1.3. Amino acid sensing and signaling pathways

An intact amino acid metabolic system is essential to provide the building blocks for any protein machinery regulating for example cellular division, secretion and migration. Intrinsic complex cellular sensing and signaling networks respond to intracellular amino acid levels¹³. As soon as a single or more amino acids become limiting, two major amino acid stress sensing and signaling networks are affected: (i) The mTORC1 pathway²⁴; (ii) The GCN2-induced ISR (GCN2-ISR)²⁵ (Figure 2).

The GCN2-ISR is one branch of the ISR, which is induced by the universal stress kinase GCN2 (general control non-derepressible 2) that regulates translation in response to amino acid limitation²⁵. By contrast, the mechanistic target of rapamycin complex 1, mTORC1, is another amino acid sensing hub responding to amino acid availability promoting anabolic metabolism, translation and cell growth²⁴. By now, both amino acid stress responsive pathways work in a diametrically opposite way: cell preservation (by GCN2) versus anabolic metabolism (by mTORC1). However, crosstalk between the GCN2-ISR and mTORC1 cascade accumulate more evident by multiple recent studies²⁶⁻²⁹. For example, both pathways regulate their metabolic reprogramming such as protein synthesis mediated by the transcription factor ATF4²⁶ (Figure 2). Still, the interplay of their mechanistic *modi operandi*, especially upon amino acid stress, is yet unsolved. Another unsolved question is the exact nature of information transfer between amino acids, mTORC1 and GCN2, as well as how they regulate protein synthesis and finally cell fate decisions upon amino acid stress. The investigation of this mechanism is part of my PhD thesis.

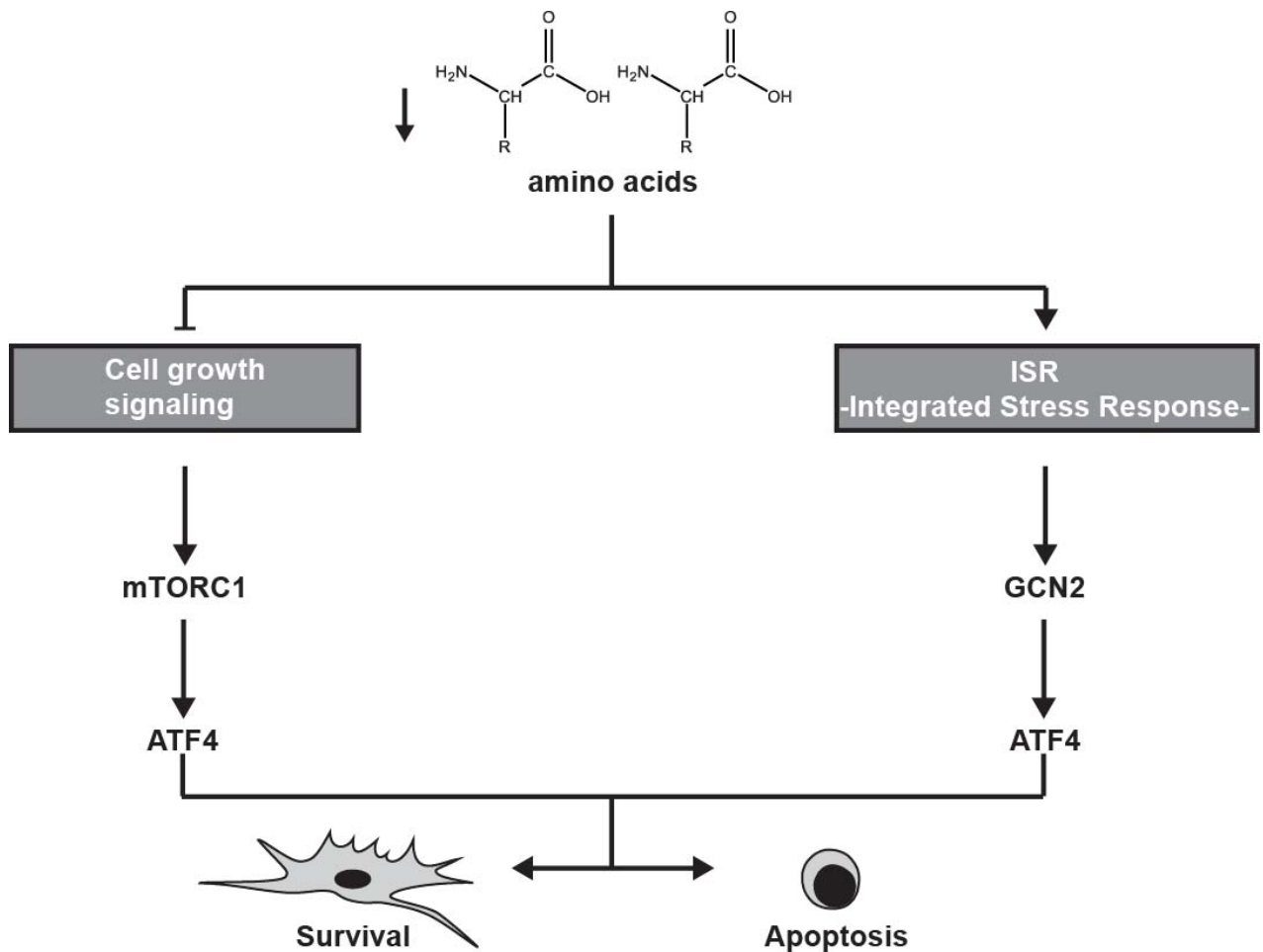


Figure 2. Schematic overview of the two major amino acid sensing and signaling pathways. Amino acid deprivation inhibits cell growth signaling and activates the integrated stress response, which is sensed by mTORC1 and GCN2, respectively. Both branches of the amino acid response work in a diametrically opposite way, but mediate the regulation of protein translation to reestablish cellular homeostasis by the transcription factor ATF4^{24,25}. When stress adaptation is not successful, cells undergo apoptotic cell death⁵⁶.

At the cellular level, stress adaptation by mTORC1 and GCN2 is linked to (macro-) autophagy³⁰. Autophagy is a lysosome-dependent intracellular and evolutionary conserved degradation process that involves the sequestration of damaged organelles and intracellular proteins as cargo in autophagosomes followed by their degradation in lysosomes^{31,32}. In addition, DNA damage-induced and infection-associated DNA is also degraded by this fundamental process³³. During amino acid starvation autophagy supplies amino acids as precursors for anaplerotic reactions in the TCA cycle and for protein biosynthesis of metabolic enzymes and transporters, which mitigate the metabolic stress^{34,35}. When the cell cannot adapt to the stress situation, apoptotic cell death is induced. The caspase (cysteine-aspartic proteases) driven active apoptotic cell death is an evolutionary conserved pathway relevant for proper development, maintenance of tissue homeostasis and tumor prevention^{36,37}. The mitochondria-mediated (intrinsic; BCL-2 proteins)

branch of apoptosis leads to the daily demise of more than 60 billion cells in the human body and is also modulated by the GCN2 and mTORC1 pathways^{38,39}. Recently, ferroptosis, the iron-dependent non-apoptotic cell death, was linked to the mTORC1 and GCN2 signaling networks as well. Conlon *et al.*⁴⁰ suggested that arginine stress correlates with ferroptosis-protection in a mTORC1- and GCN2-independent manner. However, the molecular link between apoptosis, ferroptosis and autophagy in both pathways upon amino acid stress remains elusive and will be in part addressed in this PhD thesis.

Currently, the three amino acids, L-glutamine, L-leucine and L-arginine (glutamine, leucine and arginine, hereafter) represent established 'workhorses' in the investigation of mTORC1- and GCN2-driven amino acid response⁴¹⁻⁴⁷. Glutamine is a non-essential amino acid that is the most abundant one in the human body accounting for more than 60 % of the free amino acid pool in tissues⁴⁸. Due to its ketogenic property, the carbon skeleton is degraded to α -ketoglutarate for anaplerotic reactions in the TCA cycle and the two nitrogen groups are used for non-essential amino acid synthesis as well as purine and pyrimidine biosynthesis⁴⁹. For example, the function of glutamine in amino acid response was linked to autophagy and mTORC1 function⁵⁰. Arginine, the precursor for polyamines and proline, is the substrate for nitric oxide synthesis and plays a major role in fighting pathogenic infections⁵¹. The branched-chain and ketogenic amino acid leucine was found to be a major contributor in ketogenic amino acid rich diets, possible treatment for non-alcoholic fatty liver disease and regulator of insulin secretion in diabetes⁵²⁻⁵⁴. Comparing prenatal and neonatal offspring mortality rates in GCN2^{-/-} mice upon diet-induced amino acid starvation revealed that leucine deprivation had a much higher effect than tryptophan or glycine removal⁵⁵. In addition, leucine and arginine are the two most effective prototypic stimulators⁴¹ of mTORC1 signaling detected by upstream sensors of the mTORC1 hub (Section 1.3.4.)⁵⁶⁻⁵⁸. However, at this point, the precise nature of how the mTORC1 sensors work in a normal cellular setting and how they interact with the GCN2 sensor, remains unknown. Moreover, leucine and arginine deprivation was linked to the mTORC1 and the GCN2 pathway in the context of ribosomal codon-pausing: only when GCN2 and mTORC1 do not sufficiently sense arginine deprivation, ribosome pausing by reducing protein synthesis rates and premature translation termination, was detected in mammalian cells⁵⁹. However, while mTORC1 is sensitive to concentration levels of the three mentioned amino acids, the contribution of other essential amino acids is entirely unclear. Also, the exact amino acid sensitivity code of GCN2 is still an unresolved question that will be investigated in this PhD thesis.

Overall, the regulation networks of amino acid response are fundamental to prevent detrimental cellular behavior such as cellular proteotoxicity that leads to pathophysiologic adaptations

(Section 1.2.3.5.). However, cellular adaptation to stress has proven to be a promising therapeutic target for pharmacological interventions (Section 1.2.3.5.4.).

1.2. The integrated stress response network

1.2.1. Sensors of the integrated stress response

The ISR is an evolutionary ancient survival pathway that senses non-cell-beneficial environmental alterations. A variety of extrinsic and intrinsic stress stimuli activate the ISR, which is sensed by four serine/threonine kinases⁶⁰. The ancestral kinase GCN2 (encoded by *Eif2ak4*) is the only known stress sensor in budding yeast detecting the accumulation of uncharged tRNAs (amino acid unloaded tRNAs)⁶¹. In mammals, GCN2 senses predominantly amino acid starvation, but is also activated during UV irradiation, glucose starvation or proteasome inhibition^{62,63}. The other three mammalian stress kinases were originally found to be activated as followed (Figure 3)⁶⁰: the PKR-like ER kinase PERK (encoded by *Eif2ak3*) is activated by ER stress, the heme-regulated inhibitor kinase HRI (encoded by *Eif2ak1*) is triggered by heme deprivation and the double-stranded RNA-dependent protein kinase PKR (encoded by *Eif2ak2*) is activated by viral infection²³. Today, the repertoire of stress stimuli activating PKR, HRI and PERK has evolved. For example, HRI activity is not only linked to hemoglobin synthesis, but can be induced by multiple other forms of stress, such as oxidative and mitochondrial stress^{64,65}. Recently, the mechanism how HRI senses mitochondrial perturbations in the cytosol was in part elucidated: the mitochondrial protease OMA1 (overlapping with the M-AAA protease 1) causes DELE1 (DAP3 binding cell death enhancer 1) cleavage whose short form accumulates in the cytosol, where it directly activates HRI^{65,66}. Structurally, all four kinases contain divergent regulatory domains, but share a conserved catalytic kinase domain that is relevant for their activation by dimerization and (trans)-autophosphorylation in response to stress signals^{63,67}. A further common feature of these stress kinases is their only known target, the eukaryotic translation initiation factor eIF2(α), underlining the categorization of PERK, PKR, HRI and GCN2 to the eIF2 α kinase family^{23,60}. Together, this explains the terminology of 'integrated stress response', which was first framed by Prof. Dr. David Ron in 2002, who mapped all four kinases in one pathway by their convergent eIF2 α signaling.

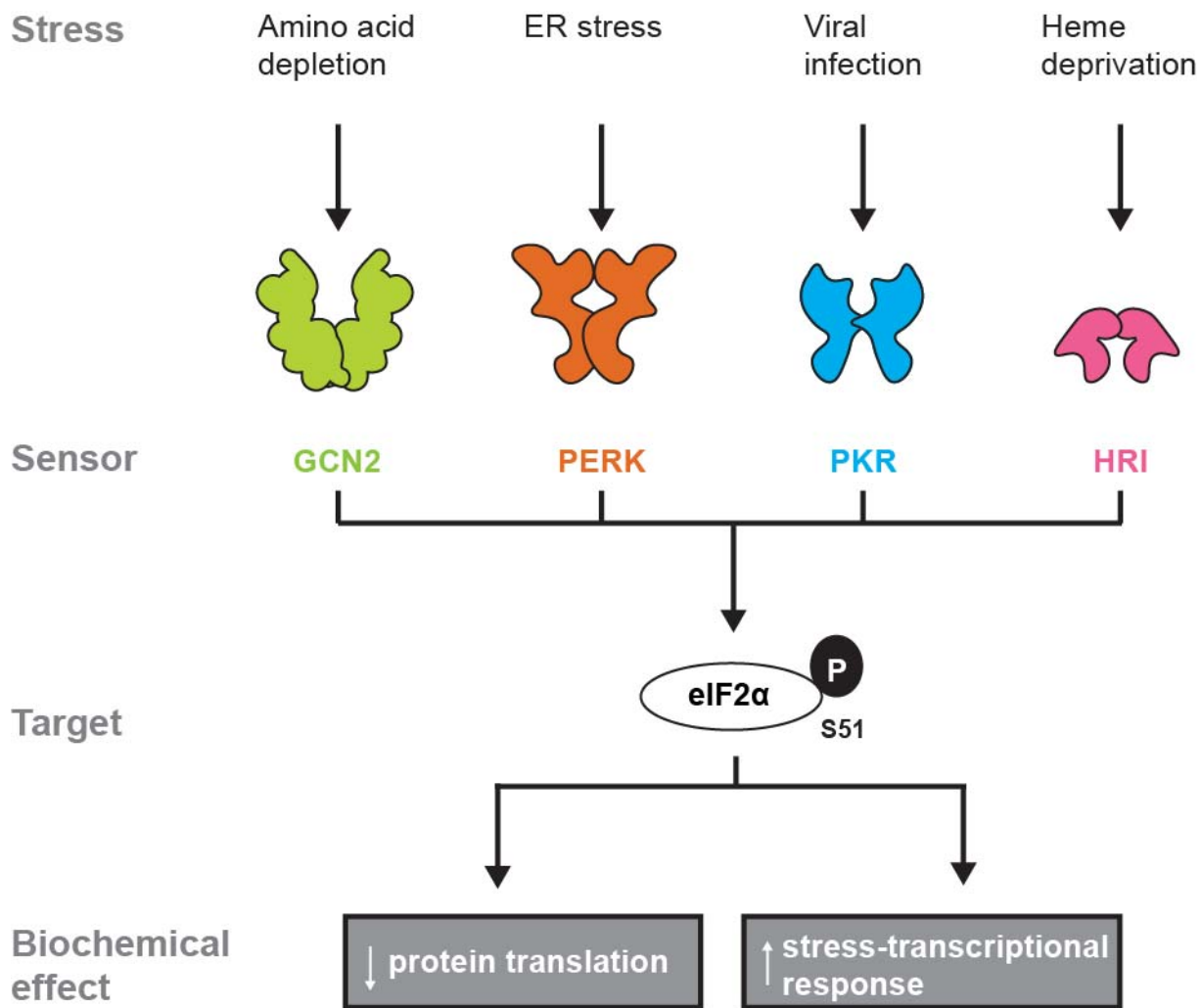


Figure 3. Schematic overview of the core elements of the integrated stress response. In mammals, distinct types of cellular stress (e.g. amino acid depletion, ER stress, viral infection or heme deprivation) are sensed by four different serine/threonine kinases (GCN2, PERK, PKR or HRI), which phosphorylate their common target – the eukaryotic translation initiation factor eIF2 – at serine 51 (mouse: serine 52) in the α -subunit⁶⁰. This phosphorylation event triggers the global shut-down of protein synthesis but simultaneously activates a stress-transcriptional program for stress adaptation²³. Depicted in color are the structural models of the dimerized kinase domains.

1.2.2. Mechanism of the integrated stress response

Initially found in *Saccharomyces cerevisiae* (budding yeast)⁶⁸, the ISR is an evolutionary conserved, cell-specific and central pathway that leads to two central outcomes in protein quality control: (i) The shut-down of overall protein synthesis by repressing translation initiation via eIF2 α phosphorylation; (ii) The increase in a specific repertoire of messenger ribonucleic acids (mRNAs) coding for proteins relevant for stress adaptation (Figure 3). Therefore, paradoxically, translation initiation inhibition parallels with the selective translation of specific mRNAs^{23,69}.

At the molecular level, 7-methylguanosine-cap (m^7G -cap) dependent translation initiation is regulated by the ternary complex (TC) formation, in which non-phosphorylated eIF2 α is a central component. TC formation initiates the translation at the AUG codon of open reading frames (ORFs) in the cellular transcriptome⁷⁰. However, some mRNA contain short inhibitory upstream ORFs (uORFs) in their 5' untranslated regions (UTRs) that normally prevent the initiation at the canonical AUG codon, but are scan through in stress situations^{71,72}. These inhibitory ORFs are well described for transcription factors, which activate or repress the promoter region for RNA-polymerase guided transcription⁷³. A key transcription factor involved in the ISR is ATF4, whose mRNA is also subjected to selective translation during stress^{61,71}. Therefore, conceptually, the two main ISR 'rheostats' of the translation initiation control are (i) the translation initiation factor eIF2 and (ii) the transcription factor ATF4.

1.2.2.1. eIF2-dependent regulation of the ternary complex formation

The TC consists of the heterotrimeric translation initiation factor eIF2 $\alpha\beta\gamma$, the charged methionyl-initiator tRNA (Met-tRNA_i) and the guanosine 5'-triphosphate (GTP) (Figure 4). Mechanistically, GTP hydrolysis is activated by AUG codon recognition that leads to the release of Met-tRNA_i to the ribosomal P-site and the dissociation of eIF2. Finally, this allows the ribosomal assembly to start translation elongation²³. eIF2 is exchanged to its active state (eIF2-GTP) by the five subunits (α to ϵ) consisting GTP exchange factor (GEF) eIF2B that catalyzes the condensation reaction of guanosine 5'-diphosphate (GDP) to GTP⁷⁴. At the structural level, eIF2 γ interacts with the eIF2B ϵ subunits of the decamer eIF2B stabilizing the GDP/GTP binding pocket in an open state for (re)-loading. Consequently, cap-dependent translation initiation is restricted by the TC concentration and rate-limited by the nucleotide exchange reaction²³.

Upon stress, the ISR kinases phosphorylate the α -subunit of eIF2 at the single serine 51 (mouse: serine 52). This leads to a structural rearrangement of the α -subunit, sterically interfering with the strong affinity of eIF2 γ -eIF2B ϵ bipartite interaction to induce a potent non-competitive inhibition of eIF2B⁷⁵⁻⁷⁸ (Figure 4). This means that the phosphorylation of eIF2 α effectively inhibits the translation initiation by increasing the complex formation of inactive eIF2B \cdot eIF2 α -P and replenishes the decameric assembly of free eIF2B^{75-77,79-83}. Due to the well-known structural interaction of eIF2 with eIF2B, a small molecule activator of the latter, named ISRIB (integrated stress response inhibitor)⁸⁴⁻⁸⁶, was developed by Prof. Dr. Peter Walter that binds in a deep pocket bridging across the eIF2B tetramer-tetramer symmetry to facilitate the assembly of more active eIF2B rescuing translation in the presence of phospho-eIF2 α . This drug is under investigation for neurodegenerative diseases due to the reduction in phospho-eIF2 α triggered stress granule formation⁸⁷⁻⁹⁰. Moreover, the eIF2 α phosphorylation event is tightly controlled by two phosphatase

complexes (GADD34•PP1 and CReP•PP1), which dephosphorylate eIF2 α based on the expression level of the regulatory subunits GADD34 (encoded by *PPP1R15A*) or CReP (encoded by *PPP1R15B*). Notably, GADD34 expression is also induced in an ATF4-dependent transcriptional manner and CReP expression is constitutively based on the steady state-rate of dephosphorylating eIF2 α ^{91,92}.

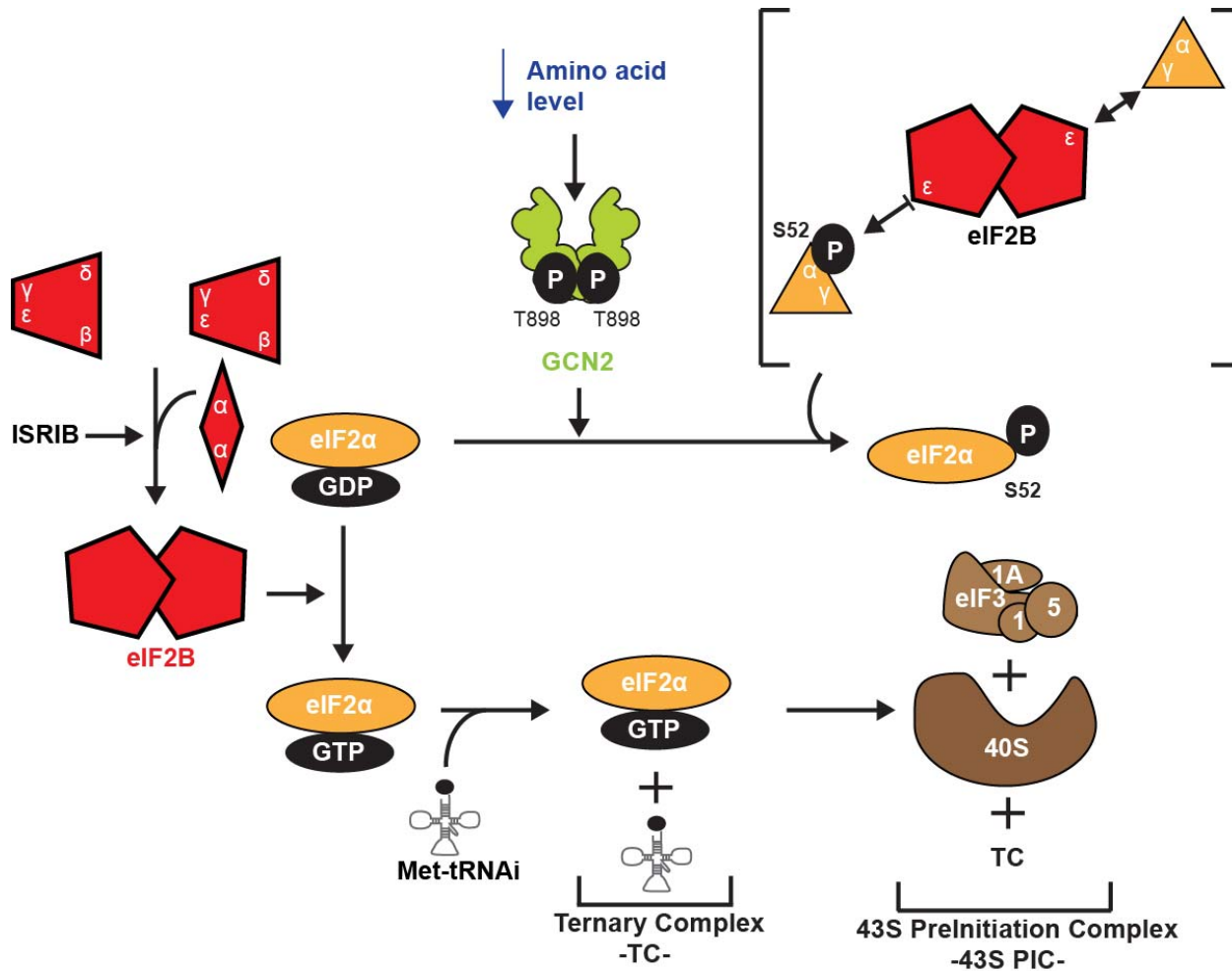


Figure 4. Schematic overview of the eIF2-dependent regulation of ternary complex formation by GCN2. Amino acid deprivation (blue arrow down) triggers the dimerization and autophosphorylation at threonine 898 (mouse site) of GCN2 (in green kinase domain)⁶⁷. Active GCN2 phosphorylates eIF2 α (orange) at serine 52 (mouse site) leading to a structural rearrangement of the α -subunit, sterically interfering with the strong affinity of the eIF2 γ -eIF2B ϵ bipartite interaction (bracket) to induce a potent non-competitive inhibition of the GEF eIF2B (red)^{75–78}. This action replenishes the decameric assembly of free eIF2B, which is antagonized by the integrated stress response inhibitor ISRIB^{84–86}, increases inactive eIF2B•eIF2 α -P complex formation and prevents the GTP-GDP exchange (black) of eIF2 α , which is relevant for ternary complex (TC) formation^{79–82}. Therefore, cap-dependent translation initiation is restricted by a low concentration of the TC complex (consisting of GTP bound eIF2 α and Met-tRNA_i), the relevant component of the 43S preinitiation complex (43S PIC; brown; 40S, eIF3/1A/1/5).

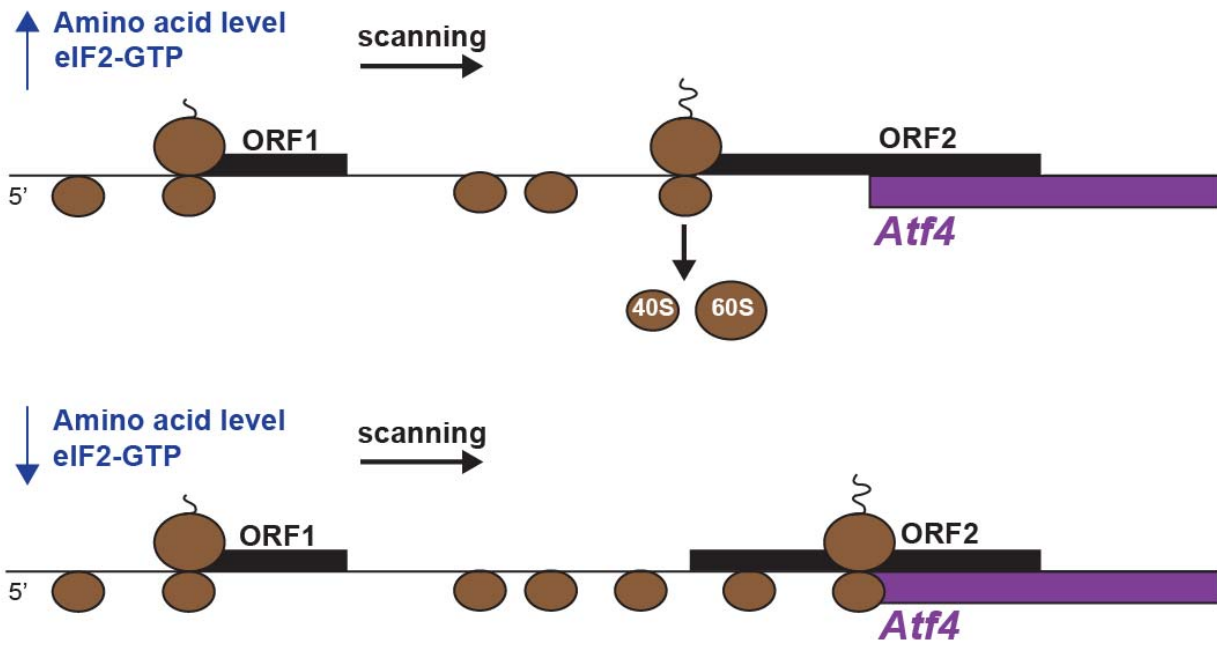
Combined, stress-activated eIF2 α kinases (PERK, PKR, HRI or GCN2) repress the final step in translation initiation by preventing TC formation by phosphorylating eIF2 α . In other words, the ISR kinases target the 'weakest link' in the chain of events necessary to begin protein synthesis. However, as we will see in this thesis, the ISR-mediated control of the TC is not absolute and subject to further complicated control pathways.

1.2.2.2. ATF4-dependent regulation of the stress-transcriptional response

At the same time, when the TC is blocked and translation declines upon stress exposure, the ISR begins to initiate physiological proteostasis by reprogramming gene expression. This process is mediated by transcription factors with short inhibitory uORFs that trigger mRNA translation of a specific set of proteins relevant for stress adaptation⁹³⁻⁹⁵.

The yeast stress transcription factor GCN4 (general control transcription factor) and its mammalian ortholog ATF4 (also known as: cAMP-response element binding protein 2 CREB-2; encoded by *Atf4*) bind to the DNA via their leucine zipper motifs (bZIP)^{15,61,96}. Besides the positive-regulatory uORF1, GCN4 contains three and ATF4 one inhibitory uORFs in their mRNA leader sequence^{71,96,97}, which are bypassed by the scanning ribosomes in presence of reduced TC formation based on the 'delayed reinitiation model' (Figure 5A)^{61,71,97}. In mammalian cells, ATF4 mediates selective translation of specific mRNAs, which make up the stress-transcriptional program. This includes the pro-apoptotic transcription factor CHOP (C/EBP-homologous protein; encoded by *Ddit3*), the pro-survival transcription factor ATF5 (activating transcription factor 5), the growth arrest and DNA damage-inducible protein GADD34, and the pro-apoptotic plus NF- κ B-regulator tribbles homolog 3 Trib3⁹⁸⁻¹⁰⁰. Thereby, for example, ATF4-induced CHOP expression is mediated by the 'ribosomal bypass model' meaning that the inhibitory uORF is bypassed due to poor start codon content and moderate Kozak consensus sequence when eIF2-GTP levels are low (Figure 5B)¹⁰¹. Overall, the components of the ISR-stress-protective transcriptional program perform a myriad of interconnected tasks for stress adaptation controlling survival and death induction (e.g. CHOP or ATF5) in addition to autophagy and protein synthesis (e.g. GADD34)¹⁰². For example, GADD34, the regulatory subunit of the PP1 complex (dephosphorylates eIF2 α), is highly expressed to antagonize the relative strength of eIF2 α phosphorylation, which correlates with the involvement of actin polymerization (PP1 complexes associate with G-ACTIN)^{92,97}. In contrast, ATF4 induction can also be induced independently of eIF2 α phosphorylation^{26,29,95}.

A
Delayed reinitiation model



B
Bypass model

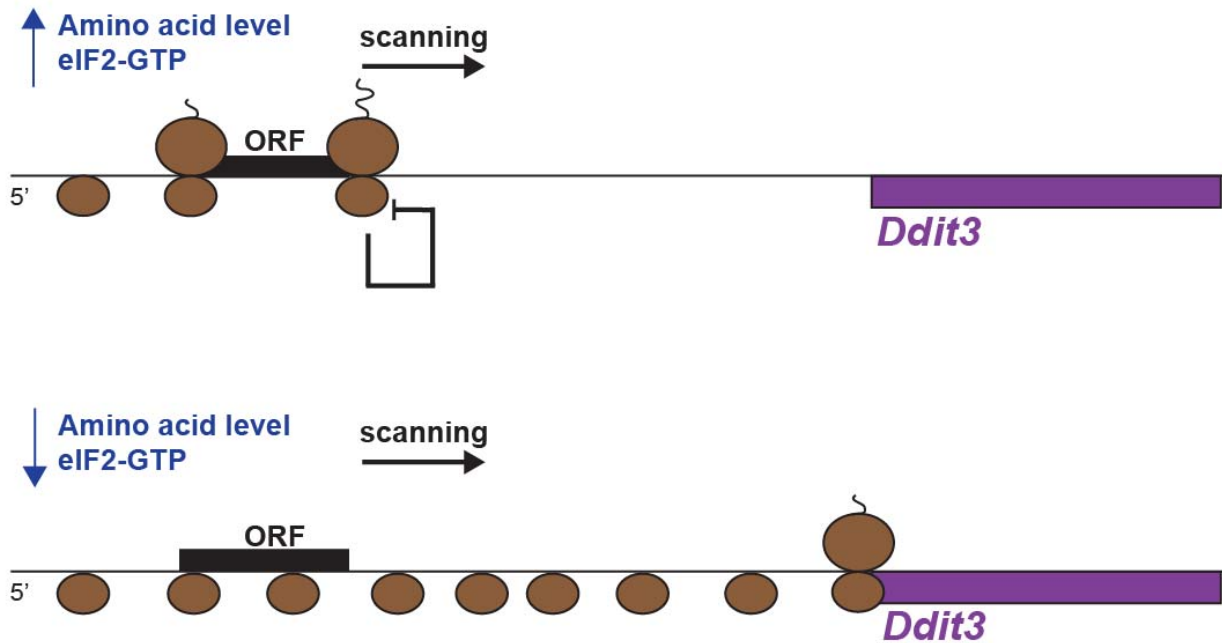


Figure 5. Schematic overview of the mechanistic basis for stress-transcriptional regulation of ATF4 and CHOP inductions upon amino acid stress. Translation of the transcription factors CHOP (encoded by *Ddit3*) and ATF4 (encoded by *Atf4*) (purple) is regulated by amino acid stress based on the level of eIF2-GTP (for ternary complex formation; blue). (A) *Atf4* overlaps out of frame with the coding sequence (black) and is transcribed based on the 'delayed reinitiation model': when amino acid levels are high (blue arrow up), the ribosome (brown) scans upstream ORF1 (positive element) and sequentially the downstream ORF2 (inhibitory element) by reacquisition of the 40S ribosome (brown). When amino acid levels are low (blue arrow down), the levels of eIF2-GTP are decreased, leading to continuous scanning after the translation of upstream ORF1 and inducing a delay time for reinitiation by limited eIF2-GTP levels. This delay allows the 40S ribosome to bypass ORF2 and reinitiate downstream at *Atf4*. (B) *Ddit3* is transcribed based on the bypass model: when amino acid levels are high (blue arrow up), translation of *Ddit3* mRNA is inhibited by the presence of a single inhibitory ORF (inhibitory arrow). When amino acid levels are low (blue arrow down), leaky ribosomes scan through the inhibitory ORF, which is suggested to result from the poor Kozak context of the start codon. Adapted from Ref.¹⁰¹.

Taken together, the ATF4 dependent stress-protective transcription program functions as a 'rheostat' in the ISR upon diverse stress stimuli tuning protein translation of a primed set of proteins relevant for stress adaptation.

1.2.3. GCN2-mediated integrated stress response

1.2.3.1. Discovery of GCN2, GCN1 and GCN20

In all eukaryotes, GCN2 is the sentinel kinase of the ISR induced by amino acid stress. This branch of the ISR is also known as amino acid response (AAR) in mammals, general amino acid control (GAAC) in yeast or cross pathway control (CPC) in fungi, such as *Neurospora* and *Aspergillus*^{61,101,103}. GCN2 (eukaryotic translation initiation factor 2 alpha kinase 4; encoded by *Eif2ak4*) stands for General Control Non-derepressible 2. This designation is based on its discovery in a genetic mutagenesis study for 'general control of amino acid synthesis' in yeast, performed in the laboratory of Dr. Alan Hinnebusch in 1983⁶⁸. In the same year, Penn *et al.*¹⁰⁴ manifested the identification of GCN2 as an AAS (amino acid analog-sensitive; *AAS1*) gene and its regulatory role in general control of amino acid biosynthesis in yeast. GCN1 (encoded by *Gcn1*; earlier named *Gcn111* for general control of amino-acid synthesis 1-like 1)^{105,106} and GCN20 (encoded by *ABCF*; ATP binding cassette subfamily F)^{107,108} were identified as positive regulators of *GCN4* (*AAS3*)^{68,104} expression in yeast. Follow-up yeast two-hybrid studies reported a physical interaction between GCN1 and GCN20 in the GCN2-regulated amino acid response¹⁰⁹. The relevance and ubiquitously conserved expression of these three proteins is highlighted as well in other model organisms: in *Caenorhabditis elegans*, GCN1 and GCN2 are involved in hypertonic stress response and dietary restrictions affecting the worm's life span and morphogenesis^{110,111}.

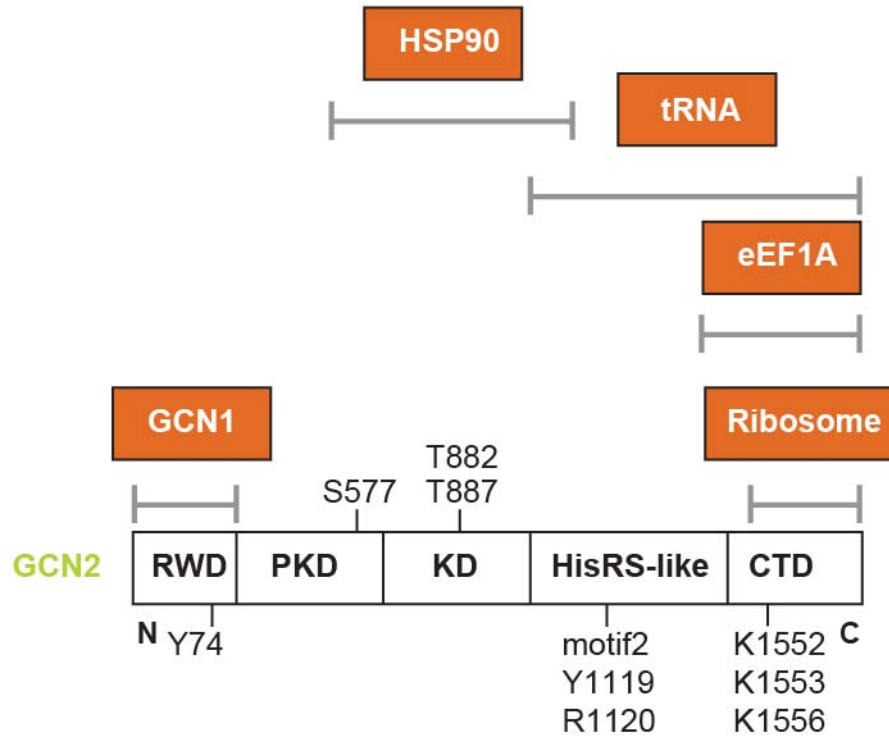
In addition, GCN1 and GCN20 promote apoptosis in a GCN2-independent manner¹¹². Most importantly, mice lacking GCN2 are viable and overtly normal, but have a decreased probability of completing development under conditions of amino acids deprivation⁵⁵. In contrast to GCN2, mice lacking a regulatory domain of GCN1 die perinatally – independent of the stress exposure¹¹³. Although yeast GCN1 and GCN2 were identified as regulators in the GAAC, the phenotypic difference of loss-of-function alleles in higher organisms (mouse) suggest that the two proteins may have distinct functions. This assumption was investigated in the course of this thesis.

1.2.3.2. Structural architectures of GCN2, GCN1 and GCN20

Studies in yeast yielded information about the structural domain arrangements and thereby interaction of GCN2, GCN1 and GCN20^{61,109}. However, the transfer of this information in the mammalian system as well as solving the atomic structure of all proteins in complex are subject of recent investigations¹¹⁴.

From the N- to C-terminus, GCN2 (mouse:186 kDa, yeast: 190 kDa) is a multi-domain protein that consists of five core domains⁶¹ (Figure 6A): the RWD-domain (RING finger proteins, WD-repeat-containing proteins, and yeast DEAD-like helicases), the pseudokinase domain, the kinase domain (KD), the HisRS-like domain (class II histidyl tRNA synthetase-related domain) and the C-terminal domain (CTD). Conservation of the protein kinase and HisRS-like domain are reported in *Mus musculus* and *Drosophila melanogaster*¹¹⁵. In contrast to the other three eIF2 α kinases, GCN2 contains a pseudokinase domain, which may assist the catalytic domain, but has no intrinsic catalytic activity²⁵. Unique for GCN2 is the RWD domain that is related to the ubiquitin-conjugating enzymes (UBC) domain, but lacks the catalytic cysteine, which is critical for ubiquitin-conjugating activity^{62,94,116}. The HisRS-like domain was considered the ‘trigger factor’ for studying tRNA aminoacylation in the context of GCN2 function. The motif2 was found by sequential residue substitutions (m2 mutation; Y1119L and R1120L), which is the binding motif of uncharged tRNAs (deacylated tRNAs) in the HisRS-like domain that leads to no, or hardly any *in vitro* eIF2 α phosphorylation shown in yeast^{117,118}. Moreover, three further residues (K1552, K1553 and K1556) in the CTD were found to play a role in uncharged tRNA binding. It is not yet known if these residues function as a second binding motif or are relevant for GCN2 dimerization^{118–120}. In this context, a bipartite binding mode of uncharged tRNAs could neutralize the autoinhibitory interaction between the catalytic domain and the CTD^{119,121}. Dimerization of GCN2 per se is mediated by the CTD that was also found to be the ribosome-binding domain. The crystal structure of yeast GCN2 CTD revealed a back-to-back GCN2 dimer^{122,123}.

A



B

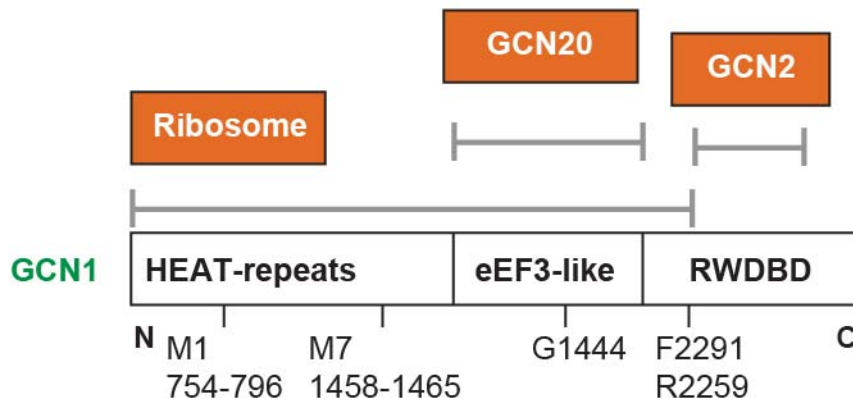


Figure 6. Schematic representation of yeast GCN1 and GCN2 domain arrangements. Schematic representation of GCN1 (dark green) and GCN2 (light green) domain arrangements in *Saccharomyces cerevisiae*. (A) From the N- to the C- terminus GCN2 is composed of the RWD (RING finger proteins, WD-repeat-containing proteins, and yeast DEAD-like helicases domain), the PKD (pseudokinase domain), the KD (kinase domain), the HisRS-like domain (class II histidyl tRNA synthetase-related domain) and the CTD (C-terminal domain)⁶¹. Areas indicated in gray double arrows display the association with GCN1 (Ref.¹²⁴), HSP90 (Ref.¹²⁵), tRNA¹²¹, eEF1A¹²⁶ and the ribosome¹²⁷ (orange). The respective amino acids with known biological function relevant for described interactions are indicated in black: Y74 (GCN1 binding site), Y1119 plus R1120 (termed motif2; tRNA binding sites), K1552 plus K1553 plus K1556 (ribosome association and some extent for deacyl-tRNA-binding)^{121,127}. In addition, S577, phosphorylated most likely by TOR, reduces GCN2 affinity to deacyl-tRNA^{128,129}. T882 plus T887 (mouse: T898 plus T903) are the autophosphorylation

sites of GCN2 (Ref.⁶⁷). (B) From N- to C-terminus, yeast GCN1 is composed almost entirely of about 20 HEAT-repeats, has an eEF3-like and RWD binding domain (RWDBD)¹⁰⁵. Areas indicated in gray double arrows display the association with the ribosomal machinery¹³⁰, GCN20 (Ref.¹³¹) or GCN2 (Ref.¹³⁰) (orange). Respective amino acids with known biological function relevant for described interactions are indicated in black: G1444 (GCN20 binding site)¹³¹, F2291 plus R2259 (GCN2 binding site)^{124,130} and M1 (12 basic residues) and M7 (motif ExxWRTKR) areas (ribosome binding)¹³⁰.

Further biochemical evidence about the mechanism of GCN2 was provided by crystal structure analysis of the human PKR kinase domain in complex with eIF2 α , yeast GCN2 kinase domain in the hyperactive and native form, and human PERK kinase domain¹³²⁻¹³⁴. The PKR kinase domain in complex with its target was used to infer that an induced-fit mechanism leads to the unfolding of the α -subunit that exposes the buried single serine 51 and allows this phospho-acceptor to sufficiently project into the kinase active site^{132,135,136}. However, PKR is organized as a parallel dimer whereas yeast GCN2 is an antiparallel dimer both organized by N-lobe interactions¹³⁷. In the yeast GCN2 kinase domain, a gatekeeper flap (N793) within the catalytic site consists of a hinge combining N-C terminal lobes to keep GCN2 in a close state to sterically restrict its access. In contrast to PKR, the catalytic salt bridge is broken and the C-helix is displaced from its presumably active position¹³⁴. ATP entering the catalytic site allows autophosphorylation of GCN2 locking it in its open active state. Therefore, GCN2 was postulated to be organized as an inherently latent antiparallel dimer activated by allosteric rearrangements of all domains upon uncharged tRNA binding¹²³. In 2020, the crystal structure of the human catalytic GCN2 domain in complex with two compounds was solved and contributed to the model of GCN2 forming an antiparallel inactive dimer until its activation to trigger conformational rearrangements into a parallel dimer¹³⁸ (Figure 7). An essential electrostatic interaction involves arginine 585 with glutamate 589, which is relevant for increasing the activity of GCN2. These residues are positioned at 10 Å distance in the antiparallel dimer as proposed for yeast kinase domain¹³⁸. Together, these findings suggest a different structural organization of human and yeast GCN2 kinase domains.

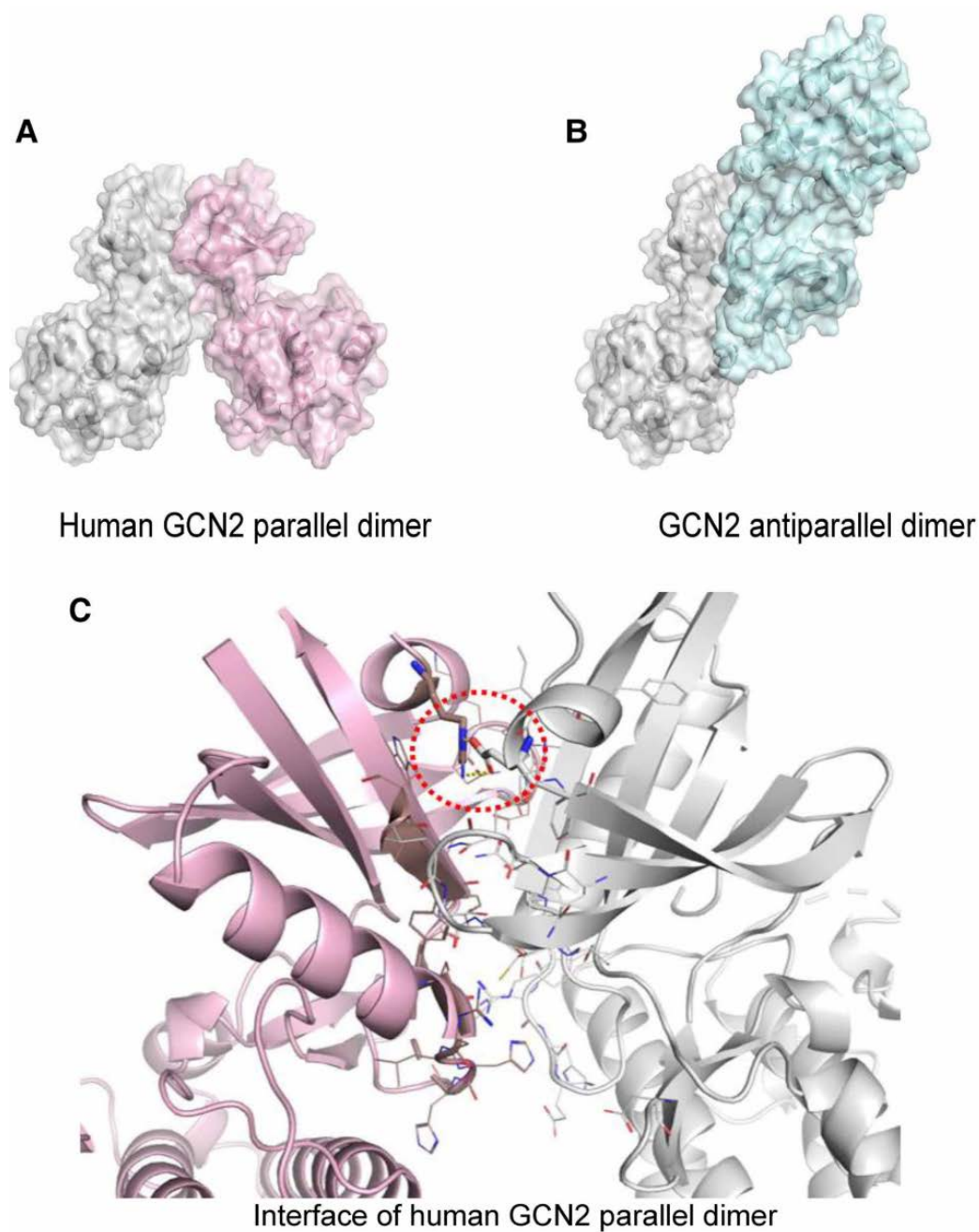


Figure 7. The crystal structure of the human GCN2 kinase domain. Crystal structure of the human GCN2 kinase domain found in complex with two compounds (GCN2:aminoquinazoline at 2.3 Å resolution and GCN2:dovinitib at 2.8 Å resolution). The compounds are not displayed. Graphic adapted from Ref.¹³⁸. (A) The electron density map of the human dimeric GCN2 kinase domain (pink, grey) is organized in a parallel orientation. (B) The electron density map of yeast dimeric GCN2 kinase domain (PBD ID: 1ZYD (Ref.¹³⁴)) is dimerized via a partially overlapping interface, thereby the monomers (turquoise, grey) are organized in antiparallel way. (C) The interface of the human back-to-back GCN2 dimer with the relevant electrostatic interaction between R585 and E589 (red dotted circle).

Like PKR, GCN2 contains two conserved threonine autophosphorylation sites in the activation loop of the catalytic domain (yeast: T882 and T887; mouse: T898 and T903) (Figure 6A). Both residues are at the exact same position relative to the residues in PKR⁶⁷. Consistent with the threonine sites for yeast PKR (T446 and T451), one site is the key site (GCN2: T898), which is crucial to abolish autophosphorylation shown by mutagenesis studies⁶⁷. Another phosphorylation site of GCN2 was found in yeast at serine 577 (S577), which was proposed to be a negative regulatory site for tRNA binding and GCN2 activity. Based on serine to alanine substitution studies, a model was proposed, in which an unknown kinase regulates the phosphorylation of this site upon amino acid stress¹²⁹. In this context, the TOR (target of rapamycin) kinase was assumed because the TOR inhibitor rapamycin was found to stimulate eIF2 α phosphorylation by GCN2 while reducing the phosphorylation of S577 in non-starved cells¹²⁸. Evidence that GCN2 interacts with the eukaryotic translation elongation factor 1A (eEF1A)¹²⁶ and the chaperone heat shock protein 90 (Hsp90)¹²⁵ was reported in yeast as well. Even though great strides have been made in compositional elucidation of GCN2 domains, the structure of any GCN2 is so far elusive. An even more important knowledge gap is the GCN2 activation mechanism upon low amino acid levels and how this affects the structural level.

Yeast GCN1 is a 296 kDa (mouse: 293 kDa) protein consisting almost entirely of about 20 HEAT-repeats (also found in Huntingtin, eEF3, protein phosphatase 2 A, and mTOR) with multiple segments sufficiently hydrophobic to function as membrane-spanning domains¹³⁰ (Figure 6B). Biochemical and genetic studies suggest that the C-terminal region (residues 2052–2428) of yeast GCN1 binds to the RWD domain (residues 1-125) at the N-terminus of yeast GCN2¹²⁴. Residue mutations of either GCN1 (F2291L, R2259A) or GCN2 (Y74A) disrupt their interaction, which is relevant for GCN2 activation^{124,130}. These residues seem irrelevant for the interaction of GCN1 with other binding partners such as the ribosome and GCN20 (Ref.¹³⁰). At its N-terminus, GCN1 contains a fungal (eukaryotic) translation elongation factor 3 (eEF3; residue 1330–1617) like region, which binds GCN20 (G1444 is essential for GCN20 binding activity) with its N-terminal segment (residues 4-118)^{107,131}. In yeast, overexpression of eEF3 represses GCN2 activity, arguing that GCN1 and eEF3 have overlapping binding sites on the ribosome¹³⁹. The N-terminal part of GCN1 (residues 1-2052) is relevant for the tight binding to ribosomes *in vivo*¹³⁰. Two structural segments were found for ribosome binding: M1 (12 basic residues) and M7 (motif ExxWRTRK)¹³⁰. In addition, yeast GCN1 has ribosomal binding affinity and co-sedimented with 80S ribosomes in ultracentrifugation experiments¹⁰⁹. Further, Wu *et al.*¹⁴⁰ showed in human non-tumorigenic epithelial cell lysates (MCF10A) that GCN1 was detected with 80S polysomes in a small portion (~10 % fraction) using polysome profiling. Recently, the Cryo-EM structure of native yeast GCN1 bound to a 80S colliding and stalling disome was solved in steady-state by GCN20 immunoprecipitation¹¹⁴ (Figure 8). This constitution shows the expected solenoid structure of the

HEAT-repeats laying like a serpent on the two ribosomes. However, this structure was captured from particles isolated from yeast without amino acid starvation and GCN2 was not detected at all, which most likely points towards a conditional interaction. Thus, further detailed structural investigations will be essential to uncover the mechanics of the GCN1-GCN2 interplay upon amino acid stress.

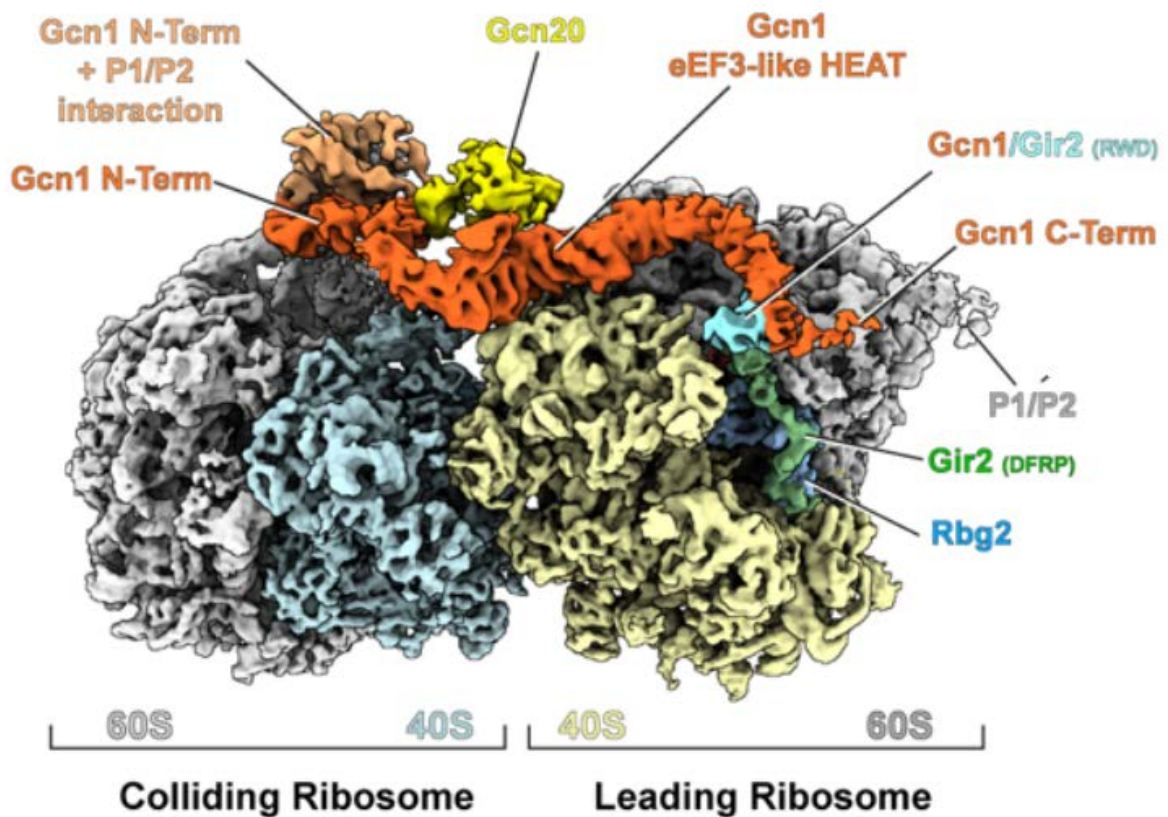


Figure 8. Cryo-EM structure of yeast native GCN1 bound to the 80S collided and stalled disome. Cryo-EM reconstitution of yeast GCN1-disome complex (PDB ID: 7NRC (Ref.¹¹⁴)) with an average resolution of 3.9 Å for the leading ribosome and 4.4 Å for the colliding ribosome in steady-state. In *Saccharomyces cerevisiae*, GCN1 binds directly with its N-terminus to GCN20 and interacts with its RWD binding domain with GIR2/RBG2^{111,137}. Evidence that GCN1 regulates P-stalk-mediated GCN2 activity has been shown as well¹¹¹. Segmented densities are color-coded: GCN1 (orange), GCN20 (yellow), 40S (cyan, pale yellow), 60S (grey), RBG2 (light blue), GIR2 (green), P1/P2-stalk tails (salmon). Graphic adapted from Ref.¹¹⁴.

Yeast GCN20 is a 85 kDa member of the ATP-binding cassette (ABC) family represented by its two putative ATP-binding domains with high homology to the C-terminal eEF3 region¹⁰⁷. The ABC family consists of members that are mostly working as membrane-bound transporters, which

couple energy obtained from ATP hydrolysis to the transport of substrates against a concentration gradient. GCN20 belongs to a subfamily of the ABC proteins that harbor twin ABC cassettes, but unlike the others it lacks the ATP transporting transmembrane domain¹⁴³. Importantly, GCN20 is a binding partner of GCN1, but does not interact with the ribosomal machinery or GCN2 suggesting its role as stimulatory and stabilizing effector of GCN1 (Refs.^{107,144,145}). In contrast to GCN1 and GCN2, functional homologues of GCN20 in mammals are not specific defined. However, the mammalian ABC-containing protein ABCF1 is described to participate in translation initiation and has a high sequence similarity with GCN20 - interestingly, it could not substitute the function of yeast GCN20¹⁴⁶. Recently, ABCF3 was identified as another GCN20 sequence isoform¹⁴⁰.

Overall, in yeast, GCN2 directly interacts at its N-terminus with GCN1, which binds GCN20 at its N-terminus¹⁰⁹. Even though data hint towards a clear role in direct translation, ribosomal interactions are only known for GCN1 and GCN2 so far¹⁰⁹.

1.2.3.3. Molecular function of GCN1 in yeast and mammals

Yeast GCN1 has been generally defined in conjunction with GCN2 by monitoring uncharged tRNA levels. This 'function' was linked to GCN1 by its sequence similarity with the eukaryotic translation elongation factor 3, whose eEF3-like region encoded 88 kDa of the total 297 kDa large GCN1 (Ref.¹⁰⁵). Further studies using yeast two-hybrid interaction experiments and residue substitution techniques, showed that GCN1 physically interacts with GCN2 at its C-terminus and with GCN20, an ABC domain containing protein, at its N-terminus¹³¹. Due to the structural organization of GCN1 and GCN20 containing membrane-spanning domains and ABC-domains, respectively, one hypothesis was framed that the GCN1/20 complex might constitute a transmembrane transporter to transfer amino acids from the cytoplasm to the vacuole where large pools of amino acids are stored to provide nutrient information transfer to GCN2 (Ref.¹³¹). This hypothesis was discarded because GCN1 showed no obvious membrane association and GCN20 ABC domains are dispensable for GCN2 activity¹³¹. GCN1 (and GCN20) *per se* does not affect the expression of GCN2, but is highly relevant for activation of GCN2 upon amino acid stress¹³¹. This was suggested by Kubota *et al.*¹²⁴, who showed that a point mutation in the C-terminal region (F2291L) of GCN1 prevented the induction of GCN4 and eIF2 α phosphorylation upon amino acid stress. The same deficiency was shown when mutating GCN2 in the N-terminal RWD domain (Y74A)¹²⁴. In detail, substitution of the amino acid arginine at position 2259 prevented the GCN1-GCN2 interaction completely, which correlates with abolished GCN1 regulatory function¹³⁰. Moreover, deletions of GCN1 impaired GCN2 activity more than GCN20 activity *in vivo*: in total, 15 to 25 % of the full-length GCN20 were scored as essential for their ability to cooperate with GCN1 in mediating

activation of GCN2 in amino acid starved cells. In contrast, at least 90 % of full-length GCN1 is required for its ability to activate GCN2¹²⁴. Consistent with budding yeast, fission yeast (*Schizosaccharomyces pombe*) also requires GCN1 for GCN2 activation, which was shown upon different type of stress stimuli (UV irradiation, hydrogen peroxide and amino acid stress)¹⁴⁷.

Direct interactors of GCN1 were also discovered in yeast. The protein IMPACT (imprinted gene with ancient domain) and its yeast homologue YIH1 (yeast IMPACT homologue) share sequence similarity with the GCN2 N-terminus and bind to GCN1 via the GI domain (GCN2 and IMPACT domain; also known as RWD domain)^{62,148–150}. YIH1 is a negative regulator of GCN2 by competing directly with the GCN1 interaction followed by its induced inhibition of GCN2 and eIF2 α phosphorylation upon diverse stress stimuli. Thereby, YIH1 binds independently of GCN1 to the ribosome¹⁵¹. In this context, G-ACTIN stimulates YIH1 function, but the overall involvement of actin polymerization is not yet understood¹⁵². Yeast GIR2 (genetically interacts with ribosomal genes 2) is another protein that interacts with GCN1 via arginine 2259 in complex with the small GTP-binding protein RBG2 (ribosome interacting GTPase)¹⁵³. Like YIH1, GIR2 overexpression prevents GCN2 and eIF2 α phosphorylation under starvation conditions, but the lack of GIR2 does not increase GCN2 activity arguing that GIR2 is not a general/continuous GCN2 inhibitor in contrast to YIH1 (Ref.¹⁵⁴). Moreover, the RBG2/GIR2 binary complex was found to enable cell growth under severe amino acid starvation conditions¹⁵⁵. In summary, several interactors of GCN1 have been uncovered, mainly by using yeast genetics. However, their exact roles in regulating the amino acid ISR remain unclear and will likely be elucidated best through detailed structural studies.

In contrast to yeast, the role of GCN1 in mammalian physiology and pathophysiology has been rarely studied and explored. One reason is that *Gcn1* is essential for embryonic development - in contrast to *Eif2ak4* (coding for GCN2)⁵⁵. Mice lacking *Gcn1* die at the intermediate stage of embryonic development due to severe growth retardation, while *Gcn1*^{ARWDBD} embryos (RWD binding domain is the GI binding domain) display mild growth retardation, but die soon after birth mainly due to respiratory failure¹¹³. Addition of progesterone during pregnancy prevented the embryonic lethality, which enabled studying the role of GCN1 in mouse embryonic fibroblasts. In this study, Yamazaki *et al.*¹¹³ found that the loss of GCN1 (but not GCN2) reduces cell proliferation and G2/M cell cycle arrest as shown by a decrease in cyclin-dependent kinase 1 (CDK1) and CYCLIN B1 gene expression levels. Therefore, GCN1 was proposed to play a role not only in the ISR, but also in the GCN2-independent cell cycle regulation¹¹³. Kim *et al.*¹⁵⁶, who analyzed cytokine-stimulated fibroblast-like synoviocytes with a knockdown in GCN1, highlighted the role of GCN1 in pro-inflammatory responses and tissue remodeling in a GCN2-independent manner. Treatment with halofuginone, a drug that inhibits the glutamyl-prolyl-tRNA synthetase mimicking amino acid stress, suppresses the inflammatory response. This effect was circumvented by

GCN1, but not GCN2 depletion¹⁵⁶. Recent studies in *Arabidopsis thaliana* also indicated that GCN1 regulates the innate immune response in plants in a GCN20-dependent, but GCN2-independent manner¹⁵⁷. In addition, Kim *et al.* and Yamazaki *et al.*^{113,156} showed the relevance of GCN1 for GCN2 autophosphorylation and thereby the induction of ATF4 expression and phosphorylation of eIF2 α upon UV irradiation and amino acid starvation in mammals. In this context, GCN1 was proposed to be dispensable for the other specifically stimulated eIF2 α kinases PERK, PKR and HRI¹⁰⁵.

In addition, interaction studies of GCN1 in mammals were performed. Consistent with the findings in yeast, IMPACT binds GCN1 to inhibit GCN2 activity in mouse neuronal cells⁶². Reference maps of human protein-protein interactome networks were provided from the Center for Cancer Systems Biology of the Dana-Faber Cancer Institute (HuRI database). In a large-scale study, more than 53,000 protein-protein interactions (PIs) were found by mapping binary PIs using yeast two-hybrid assays followed by orthogonal validation with alternative binary assays^{158,159}. GCN1 (average node factor 1.65) interacts with VCAM1 (vascular cell adhesion molecule 1), that plays a role in cell-cell recognition, leukocyte-endothelial cell adhesion and interacts with integrins for immune responses and leukocyte migration¹⁶⁰. A further interactor was proposed to be the transcription factor and proto-oncogene MYC that is well-known for its role in cell cycle progression, apoptosis and cellular transformation¹⁶¹. Additionally, the OpenCell atlas from the Chan Zuckerberg BioHub in collaboration with the Prof. Dr. Matthias Mann group provides a mass spectrometry and imaging-based map of human protein localization and interaction¹⁶². Here, GCN1 was found as a bait not as a prey protein (relative enrichment: 1.61; p-value(-log10) = 2.25) interacting with CSNK2A2 (casein kinase II subunit alpha), which is a serine/threonine kinase with functions in cell cycle progression (maintaining CYCLIN B-CDK1 activity and G2 arrest in response to spindle damage), apoptosis and transcription (via MYC)^{163,164}. However, IMPACT/YIH1 or GIR2, the known yeast GCN1 interactors, were not detected so far. Also, these large-scale protein-protein interaction studies have yet to be illuminated key elements of GCN1 biology, especially in the context of amino acid perturbation. This is an aspect I address in the course of this PhD thesis.

Overall, recent mammalian studies about the molecular and mechanistic role of GCN1 accumulate. Evidence was provided that GCN1 is involved in the ISR by regulating GCN2 activation on the ribosomal machinery¹⁰⁹, but might have additional intrinsic GCN2- and amino acid stress-independent functions, such as the regulation of the cell cycle and the inflammatory response^{113,156}.

1.2.3.4. Current models of the amino acid response in yeast and mammals

The earliest and still prevailing model of the general amino acid control in budding yeast is proposed to work as follows²⁵ (Figure 9): starvation of any key amino acid or the presence of a defective aminoacyl-tRNA synthetase, leads to the accumulation of free uncharged tRNAs (deacylated tRNAs), which bind to the HisRS-like domain of GCN2. Then, GCN2 undergoes a conformational rearrangement (antiparallel dimerization and autophosphorylation at T882 and T887) and becomes an active kinase, subsequently phosphorylating eIF2 α and increasing the expression level of a GCN4-dependent pathway leading to the transcription of over 40 genes (in budding yeast). These genes encode biosynthetic enzymes and transporters involved in amino acid biosynthesis and uptake to restore amino acid pools and tRNA synthetase function. In this context, GCN1 assists like a 'chaperone' by its direct involvement in the transfer of the starvation signal to GCN2. GCN1 in complex with GCN20 binds GCN2 RWD domain and the ribosomal machinery with its N-terminus. One suggestion is that GCN1 transfers, just like an eEF3, uncharged tRNAs into the HisRS binding cavity of GCN2 from the ribosomal A-site. Finally, YIH1 or the GIR2-RBG2 complex compete with GCN2 for binding GCN1 triggering prevention of the starvation signal to GCN2 and finally the phosphorylation of eIF2 α to block translation initiation. By now, in mammals, the GCN1-GCN2-eIF2 α -ATF4 axis represents the corresponding pathway⁹⁶. Therefore, we designed our working model of the mammalian ISR based on the described notions in budding yeast and refined it throughout this thesis (Figure 10A).

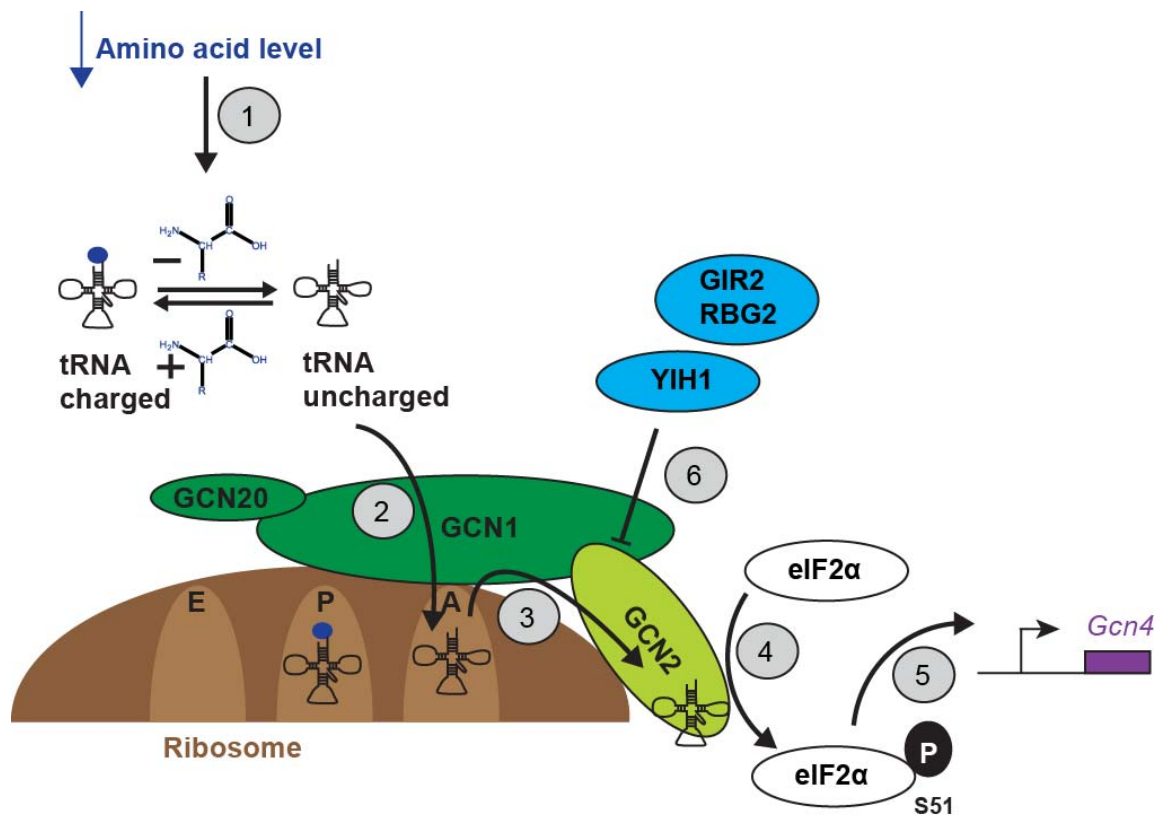


Figure 9. The classic dogma of the amino acid response in budding yeast. GCN20 is bound to the N-terminus of GCN1 (dark green) and GCN2 (light green) is bound to the C-terminus of GCN1 with its RWD domain. GCN1 and GCN2 interact with the ribosome (brown). GCN1 is proposed to be directly involved in the transfer of the starvation signal to GCN2^{130,131,165}. (1) Amino acid (blue dot) deprivation (blue arrow) increases the levels of uncharged tRNAs (deacyl-tRNA; no blue dot). (2) The deacyl-tRNA enters the ribosomal A-site in a codon specific manner. (3) The uncharged tRNA is then transferred to the HisRS-like domain of GCN2. (4) This action leads to the stimulation of GCN2 (autophosphorylation) phosphorylating its target, the eukaryotic translation initiation factor eIF2 α , at serine 51 (S51; mouse: S52) to shut down translation. (5) EIF2 α phosphorylation leads to an increase in GCN4 (mouse: ATF4)-mediated expression of more than 40 genes relevant for stress adaptation (e.g. amino acid transporters for amino acid uptake). (6) YIH1 (mouse: IMPACT) and GIR2/RBG2 are known interaction partners of GCN1 competing with GCN2 on the RWD binding domain, preventing the transfer of the starvation signal and activation of GCN2. Adapted from on Ref.¹⁵⁴.

Importantly, no detailed structural information is available for any of the proposed steps of GCN2 activation. Today, the classical ISR dogma of GCN2 activation, as outlined above, has evolved toward structural and functional studies investigating the interplay of GCN1-GCN2 signaling and the ribosomal machinery. It was shown by several studies that GCN2 activity also relies on a direct or indirect interaction with ribosomes or ribosome-associated proteins arguing for further activator-ligands other than uncharged tRNAs^{131,166–169}. In 2016 and 2019, parallel emerging links

between the ISR activation and ribosome stalling were shown by independent groups. Ishimura *et al.*¹⁷⁰ discovered that in mice lacking an abundant neuron-specific isoacceptor arginyl-tRNA, the levels of GCN2 activity increased in brain tissues compared to its wild-type counterpart. Strikingly, this increase in GCN2 activity was not associated with accumulated uncharged tRNAs, but with mutations in genes necessary to recycle stalled ribosomes¹⁷⁰. In line with this finding, Harding *et al.*¹⁷¹ performed a mammalian CRISPR/Cas9 screen to identify genes that compromise GCN2 activity. They found that GCN2 in CHO-cells (chinese hamster ovary) is also activated by ribosomal components, such as P-stalk, uL10 and P1 upon amino acid stress¹⁷¹. The P-stalk is a pentameric complex (uL10/P1/P2), which is part of the ribosomal GTPase-associated center: uL10 constitutes the helical spine of the P-stalk that protruded from the ribosome surface and the linker P1 and P2 connecting it to the ribosome core¹⁷¹. Thus, the prevailing yeast model was extended by the fact that amino acid stress leads to ribosomal stalling, while a lack of cognate charged tRNA exposes a latent capacity of the ribosomal P-stalk to activate GCN2 (Figure 10B). Inglis *et al.*¹⁶⁶ showed that intact ribosomes, or their isolated purified recombinant P-stalk, can stimulate GCN2-mediated phosphorylation of eIF2 α *in vitro*. Also, the uL10 domain was identified as the component that together with the 14-residues large C-terminal tails of P1 and P2 stimulate human recombinant GCN2 activity more potent than uncharged tRNAs¹⁶⁶. Interestingly, the autophosphorylation activation step of GCN2 was not affected by P-stalk lesions. In contrast, in budding yeast, only P1/P2 proteins sufficiently stimulate GCN2 autophosphorylation and eIF2 α phosphorylation *in vitro* and *in vivo*¹⁶⁹. Overall, this raises more questions about the free (not ribosome-associated) pool of GCN2 and its activation in mammals. Another study bridging ribosomal interaction with GCN2 activation was recently reported by Pochopien *et al.*¹¹⁴, who reported GCN1 in complex with GCN20. They suggest that GCN1 works as a sensor for disome formation, a structure consisting of 80S stalled and collided ribosomes, which evolve mainly due to defects arising during mRNA translation. The Cryo-EM structure of GCN1 (Figure 8) shows how GCN1 HEAT-repeats span from the P-stalk on the colliding ribosome to the P-stalk and the A-site of the lead ribosome. They argued that amino acid stress leads to increased binding of uncharged tRNAs in the ribosomal A-site inducing a stalling/collision of ribosomes, which is recognized by the GCN1/20 complex to activate GCN2 and prevented by the GIR2/RBG2 complex¹¹⁴. Ribosomal collision determines cell fate by triggering a series of quality control events, such as the ISR, the ribotoxic stress response and ribosome-associated quality control. GCN1, GCN20 and GCN2 associations with ribosomal collision was reported as well in a currently published human cell-based study from Wu *et al.*¹⁴⁰. Here, the MAPKKK family member ZAK α senses the gauge of collision by the signaling ISR activation for survival or SAPK (p38/JNK) signaling for apoptosis¹⁴⁰.

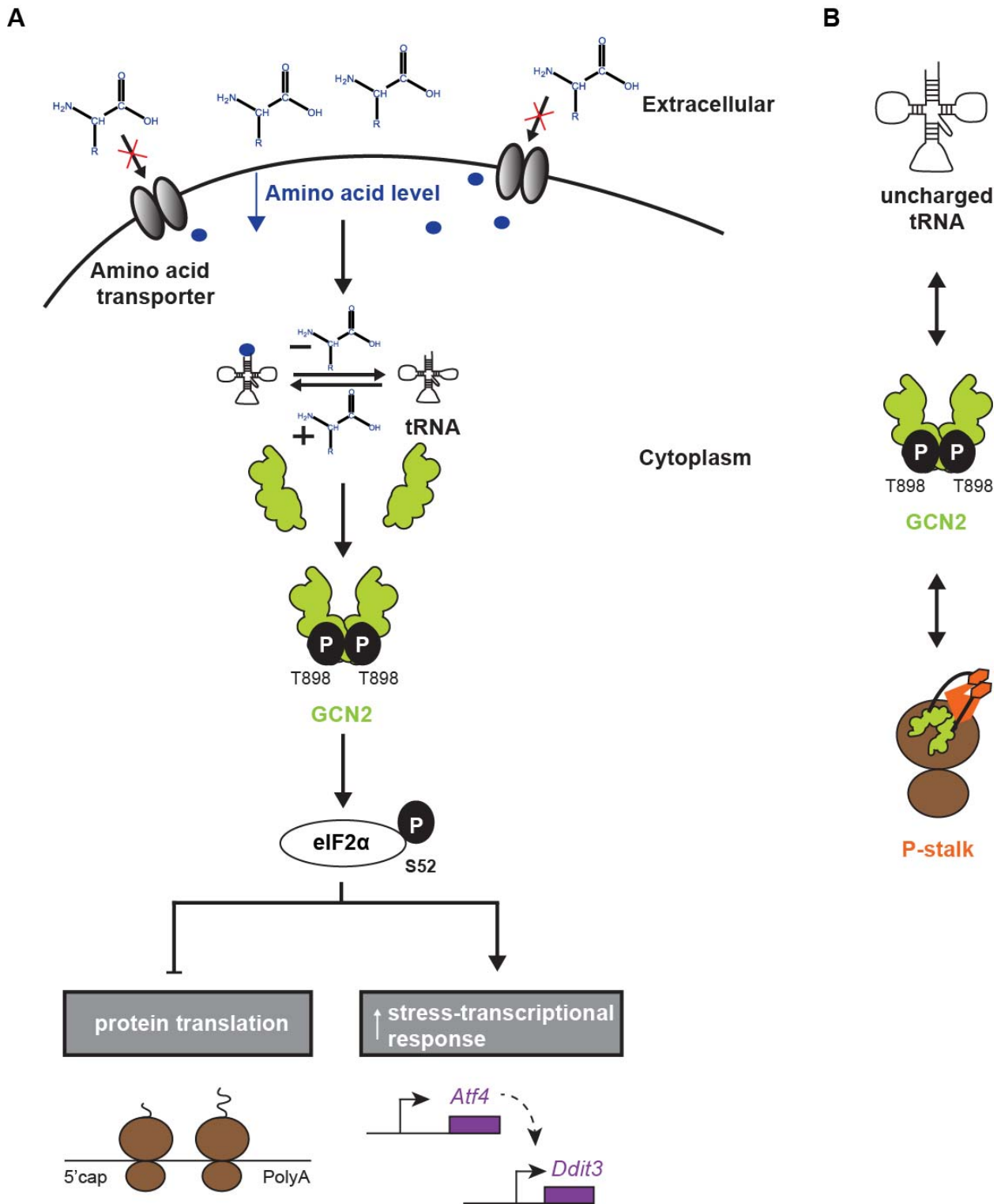


Figure 10. Our working model of the amino acid response in mammals. (A) Our working model of the murine ISR is based on the classical dogma (Figure 9) and will be refined in this thesis. The demand in exogenous amino acid supply via amino acid transport leads to amino acid stress. Subsequently, amino acid (blue dot) deprivation (blue arrow) leads to the accumulation of uncharged tRNAs in the cytoplasm triggering the dimerization and autophosphorylation of GCN2 (light green) at threonine 898 (T898). Then, active GCN2 phosphorylates eIF2 α at serine 52 (S52). This leads to a decrease in protein translation and

simultaneously to an increase in the stress transcriptional response in which transcription factors such as *Atf4* and *Ddit3* (purple) regulate the stress adaptation⁶¹. (B) Different currently known agonistic ligand binders activate GCN2 via autophosphorylation such as uncharged tRNAs^{117–119,172,173} and the heteropentameric ribosomal (brown) P-stalk (orange; P1 and P2 tails in black)^{166,171}.

In summary, the link between ISR activation and ribosome stalling extended the prevailing model by further assumptions: on the surface of the ribosome, the P-stalk is located adjacent to the A-site and works by recruiting elongation factors to the ribosome and by stimulating their GTPase activity^{174–176}. Therefore, the P-stalk might regulate translation elongation by detecting the need to activate GCN2 if it senses uncharged tRNAs via the P1 and P2 tails: elongation factors might mediate steric blocking of the interaction between GCN2 and uL10 or induce a conformational rearrangement by blocking the P1/P2 binding to GCN2. A lack of charged tRNAs may disrupt the elongation leading to a stalled and paused ribosome to activate GCN2 via P-stalk interaction¹⁷¹. Overall, the tightly regulated mechanism how GCN2 is activated upon amino acid stress in mammalian cells is not fully understood. Evidence that GCN1 and GCN20 regulate the activation of GCN2 by ligand binding at the ribosomal machinery is provided¹¹⁴. However, the spatio-, cell- and temporal regulation coupled with the relevance for both stimuli (uncharged tRNAs and ribosomal P-stalk) to activate GCN2 is still under investigation.

1.2.3.5. Amino acid response in health and disease

1.2.3.5.1. Amino acid response in immunity

Tissue homeostasis is fundamental for organ integrity and is monitored and regulated through vital roles of immune cells, which control productive and resolving inflammation¹⁴². Thus, inflammatory responses are modulated by a balance between pro- and anti-inflammatory secretion of cytokines, which activate and recruit cellular and humoral components of the immune system. Immune cells represent only about 1 % of the total cell population in the human body and often operate in nutrient-rich and nutrient-restricted niches, like the gut, the lymph nodes, the hypoxic injury sites and the tumor microenvironments¹⁷⁷. Importantly, immune cells are auxotrophic for all essential and most non-essential amino acids (e.g. glutamine)⁹. Consequently, immune cells depend on extracellular amino acid supply by amino acid transporters¹¹. Therefore, amino acid limitation, as a form of metabolic stress, directly affects immune cell function.

Multiple immunoregulatory processes exist to suppress self-reactivity and tissue destruction by activated lymphoid and myeloid cells. In the absence of immunoregulatory control, chronic and acute autoimmune syndromes form and can be amplified to life-threatening diseases. Many factors that control activated and potentially immunopathologic responses are mediated by myeloid cells^{178–182}. Thus, myeloid cells have a central dual role in activating (e.g. antigen

presentation by dendritic cells) and suppressing immune responses (e.g. immunosuppressive regulatory macrophages). The molecular mechanisms of immunoregulation include the expression of suppressive cell surface molecules like PD-L2 (programmed cell death 1 ligand 2), secretion of anti-inflammatory cytokines like interleukin-10 (IL-10) and the activation of amino acid metabolizing pathways¹⁷⁸. In the context of immunoregulation, amino acid catabolizing enzymes work as immunomodulatory checkpoints. For example, myeloid cells express the tryptophan catabolizing enzymes indoleamine dioxygenases (IDO1 and IDO2) that locally degrade tryptophan to kynurenines and their downstream metabolites¹⁸³. The depletion of the essential amino acid tryptophan was hypothesized to be detected by the stress kinase GCN2 and causes T-cell proliferative arrest. Here, cell cycle arrest of T-cells is mainly induced as a safeguard mechanism controlling the production of daughter cells that are important for fighting pathogenic infections¹⁷⁸. The regulation of arginine metabolism by immunoregulatory myeloid cells represents an additional immunomodulatory checkpoint. In M1-like macrophages, activated by bacterial products and interferons, the inducible nitric oxide synthase iNOS produces nitric oxide as product of the oxidation reaction of arginine¹⁸⁴. Nitric oxide accumulation can be immunoregulatory, suppressing microbial and pathogenic infections^{185,186}, such as *Helicobacter pylori*¹⁸⁷. Another immunomodulatory checkpoint for T-cell regulation is the arginine catabolizing enzyme Arginase 1 (Arg1), which converts arginine to ornithine and urea, and is highly expressed in activated myeloid cells. These cells locally degrade arginine and activate the GCN2 pathway sensed by T-cells, which respond by reducing T-cell receptor signal transduction and inhibiting cell cycle progression by Cyclin D3 downregulation¹⁸⁸. Most of the knowledge about the role of myeloid cells, Arg1 and arginine depletion resulted from genetic studies of the immune response to schistosome eggs deposited in the liver parenchyma in mice, where Arg1 was selectively depleted only in macrophages^{189–191}. In these animals, a lethal T-cell-mediated immune response occurred, highlighting the vital immunosuppressive role of a single amino acid metabolizing enzyme in a pathophysiological context. Here, macrophage-mediated arginine deprivation followed by T-cell immunosuppression is partly regulated by RICTOR/mTORC2 signaling pathway¹⁹². However, the direct connection between the GCN2 amino acid response and the regulation of cell cycle progression is controversial^{183,192,193}. In addition, the mechanistic outcome of amino acid response of the overall T-cell population seems highly specific. For example, GCN2 signaling represses activated CD8+ T-cells in entering the cell cycle, but this effect is independent of the amino acid ISR pathway¹⁹². *In vivo*, GCN2 controls the intrinsic proliferative fitness and lymphoid organ trafficking of CD8+, but not CD4+ T-cells¹⁹². In T-cells, amino acid depletion that leads to cell cycle arrest is completely independent of GCN2¹⁹⁴.

GCN2 affects the intrinsic functions of myeloid cells, too. In autoimmune disease, active GCN2 signaling modifies the immune response of macrophages and dendritic cells towards an

IL-10+TGF β phenotype¹⁹⁵. Also, effective dendritic cell activation and antigen presentation is linked to GCN2 activity¹⁹⁶. Collectively, GCN2 regulates and controls immunity in the lymphoid as well as myeloid lineage by modulating the immune responses in different and cell-type specific manner.

1.2.3.5.2. Amino acid response in cancer

Superficially, cancer evolves due to an imbalance between cell death and cell survival, both processes are regulated directly and indirectly by the ISR machinery^{197,198}. Tumors with a deficiency in GCN2 or ATF4 grow slower^{199,200}. Therefore, in cancers where amino acids are scarce, targeting the GCN2 cascade may be beneficial.

ATF4 activation is regulated by intrinsic stress like oncogene activation. Cancer cells need to rewire their metabolism to cope with oncogene-driven proliferation, which is a key motivation for the development of ISR-based therapeutics^{201–203}. MYC is a prominent proto-oncogene amplified or overexpressed in many human malignancies and functions as intrinsic stressor by upregulating components of the translation apparatus inducing ribosomes, tRNAs and translation factors as well as causing metabolic changes^{204–206}. A connection between MYC and ATF4 was recently proposed²⁰⁷: ATF4 and MYC have overlapping DNA binding sites on common target genes like 4EBP1. ATF4 cooperates with MYC to fine-tune the stress-protective transcription program as an anti-proteotoxic strategy for tumor cell survival²⁰⁵. Removing the ATF4 arm results in an increase in ER stress and consequently PERK signaling. This perturbation culminates in a cytotoxic effect for tumor cells. Combined, ATF4 fulfills a pro-tumorigenic role in MYC-driven malignancies. Together with GCN2 inhibition, the ATF4-induced feedback effect could be repressed as a new strategy for MYC-regulated cancers²⁰⁷.

In the field of immuno-oncology, immunosuppression is a determinant that protects a tumor from pro-inflammatory T-cell attack^{208,209}. The intra-tumoral CD8+ T-cell infiltration and activation is opposed by different negative regulatory factors including the myeloid lineage response in the tumor microenvironment. In T-cells, activation of the GCN2 network comes along with naïve T-cell suppression, T-cell receptor signal transduction blockage and Foxp3+regulatory functional T-cell (Treg) promotion²¹⁰. On the myeloid side, the integrity and activation of the GCN2-ATF4 cascade was found *in vivo* as a mechanism for maturation and polarization of tumor-associated macrophages (TAMs) and myeloid-derived suppressor cells (MDSCs)^{211–214}. The loss of GCN2 affects the ATF4-induced inflammatory gene expression and shifts the metabolic phenotype of the myeloid lineage. In detail, GCN2 deficient mice showed characteristic reduction in immunosuppressive IL-10, but an increase in pro-inflammatory cytokine expression levels (IFN γ , IL-1 β or TNF α)²¹⁰. Transcriptional data showed that the GCN2-ATF4 axis changed the

bioenergetic profile of alternatively activated regulatory macrophages by having an effect on OXPHOS, but not glycolysis gene expression levels²¹⁰. Collectively, myeloid GCN2 function is required for tumor growth and T-cell exhaustion. Therefore, especially in myeloma, GCN2 inhibitors could serve in dual ways as suitable anti-cancer and immuno-oncologic agents by shaping the tumor-immune landscape. In addition, GCN2 inhibition might function as a useful tool to pinpoint which cell (T-cell, tumor cell or myeloid cell) has a greater dependency on GCN2.

1.2.3.5.3. Amino acid response in stem cell integrity, tissue remodeling and neurodegenerative disorders

Hematopoiesis is fundamental in immunity for maintenance and restoration of the lymphoid and myeloid lineage pools^{215,216}. Severe metabolic perturbations of the cellular homeostasis in the blood system lead to a rapid hematopoietic stem cell (HSC) loss^{217–219}. However, how HSCs survive low-level stress like amino acid deprivation remains elusive. A connection between the ISR and HSC survival was underlined by Van Galen *et al.*²²⁰, who found that translation dynamics prime hematopoietic and leukemia stem cells to activate the GCN2 stress response. Therefore, the ATF4-induced stress- transcriptional program combined with the eIF2 α scarcity enables the longevity and integrity of the stem cell pool. This finding is relevant for therapeutic strategies such as promoting HSC survival for transplantation or targeting anti-tumorigenic survival in acute lymphoblastic and myeloid leukemia (ALL and AML)^{221–224}. Moreover, amino acid sensing through the GCN2-ATF4 cascade is fundamental for bone homeostasis. Here, GCN2 is indispensable for skeletal stem/progenitor cells (SSPCs) proliferation to provide continuous supply of osteoblasts that are the key determinants for collagen production for bone integrity²²⁵. Overall, the ISR is relevant for protecting the correct stem cell development in blood and bones.

Aminoacyl-tRNA synthetase inhibitors were used to treat autoimmune disease^{226–228}, but also function in suppressing TGF- β -stimulated fibrotic tissue remodeling^{229,230}. As previously described, tRNA synthetase inhibition leads to the accumulation of uncharged tRNAs that are the classical activators of the GCN2 pathway. Kim *et al.*¹⁵⁶ aimed to dissect the mechanistic basis for suppressing inflammation response and tissue remodeling by halofuginone (HF) treatment in (TNF α)-stimulated fibroblast-like synoviocytes (FLS) that are resident mesenchymal cells in the lining of synovial joints, relevant in rheumatoid arthritis (RA)^{231,232}. Interestingly, they found that the inhibitory function of HF is only sensitive to the removal of GCN1 – independent of GCN2 and mTORC1 signaling. Collectively, aminoacyl-tRNA synthetase inhibition activates a pathway that branches for the canonical ISR that might underline an ISR-independent function of GCN1.

The brain is affected by dysregulation of the integrated stress response¹⁸⁰. Mainly misfolded proteins and oxidative stress lead to chronic ISR activation that is a phenotypic trait found in

neurodegenerative diseases and in conditions exhibiting memory consolidation defects such as traumatic brain injury^{81,89,90}. Mechanistically, chronic stress granule formation is associated with persistent eIF2 α phosphorylation²³³. Therefore, the small molecule ISRIB and ISRIB-like molecules (2BAct)²³⁴ serve as primary pharmacological agents to treat phospho-eIF2 α -dependent stress granules in restoring translation. In Alzheimer's disease, GCN2 and PERK play a fundamental role in alleviating the Alzheimer's disease-related long-lasting synaptic plasticity^{235,236}. Recently, the ISR was linked to cholinergic neuronal functions independent of cell stress showing that ISR inhibition changes dopamine neuromodulation and enhanced performance of learning in mice²³⁷. Taken together, the GCN2 cascade has been linked to cognitive and neurodegenerative diseases, but amino acid stress was not yet reported to be the primary cause for severe neurological pathologies in contrast to misfolded protein aggregation²³⁷.

1.2.3.5.4. GCN2 inhibition as therapeutic strategy

The GCN2 pathway is used in certain tumor types as a metabolic defense pathway^{207,238–240}. Pharmaceutical intervention of GCN2 inhibition may be promising because GCN2 is per se not essential, but regulates a survival-stress-adaptation pathway triggered by a specific set of nutrient stimuli^{200,241}. Cancer cells may therefore have a GCN2-dependent vulnerability because they need the protein to cope with chronic amino acid stress¹⁹⁸. ISRIB, the first known small molecule inhibitor of the ISR, shows good pharmacokinetics *in vivo* since it is bioavailable, blood-brain barrier penetrant, highly potent and not toxic⁹⁰. However, ISRIB has no activity in abolishing the ISR cytotoxic effects, which accumulate when the ISR is strongly activated by severe stress^{84,86,87}. Mechanistically, ISRIB cannot increase the decameric assembly of eIF2B when the equilibrium is shifted to eIF2B•eIF2-P complex state caused by an increase in phosphorylated eIF2 α concentration^{85,88}. Other small-molecule inhibitors that intersect with the ISR like salubrinal, Sal003, guanabenz, sephin1 or raphin1 inhibit either both or one of the two phosphatase complexes (GADD34•PP1 and CReP•PP1) regulating the dephosphorylation of eIF2 α ^{242–244} – although their pharmacokinetic profiles and their off-target mode of action limits their use for therapeutic purposes by now^{245,246}.

In 2013, the first commercially available allosteric GCN2 inhibitor GCN2-IN-1(A-92) was isolated by Takeda Pharmaceutical Company, licensed and patented by the MERCK GmbH, Germany²⁴⁷. This triazolo [4,5-d] pyrimidine derivative reduces tumor viability in APC-deleted colon rectal cancer (CRC) cell lines²⁴⁸. Further compounds were developed based on the initial GCN2-IN-1, from which GCN2-IN-6 showed the best enhancement in potency and a good pharmacokinetic profile in mouse xenograft models²⁴⁸. The non-competitive inhibitor GCN2-IN-6 (IC₅₀ 1.8 nM) binds GCN2 with its triazolo [4,5-d] pyrimidine core while burying the allosteric pocket adjacent to

the kinase α C-helix. However, this inhibitor has off-target activity towards PERK (IC_{50} 0.26 nM)²⁴⁸. Recently, a novel ATP-competitive inhibitor GCN2iB with an IC_{50} of 1.8 nM was detected in a radioactivity ATP-based 27 compound kinase screen and selectivity determined using a panel of 468 kinases in a KINOMEscan²³⁹. In this study, GCN2iB was tested in drug co-treatment with asparaginase (ASNase) in diverse acute lymphoblastic leukemia and pancreatic cell lines. The therapeutic strategy targets two arms of amino acid response to induce apoptosis: (i) ASNase depletes asparagine inducing MAPK signaling; (ii) Asparagine depletion in combination with GCN2 inhibition prevents the ATF4-induced upregulation of the asparagine synthetase (ASNS)²³⁹. In addition, GCN2-IN-6 demonstrated suppression of the GCN2 pathway activation with asparaginase treatment in ALL (CCRF-CEM cells)²⁴⁸. Therefore, GCN2 inhibition plays a relevant role for low-ASNS ALL sensitivity to ASNase treatment that has been clinically used or is under evaluation in clinical trials for other tumor types, such as ovarian neoplasms²⁴⁹. Further, GCN2iB was efficiently used in a study where microcystin-leucine-arginine inhibits testosterone synthesis via oxidative stress activated GCN2 cascade in mouse testes²⁵⁰. Moreover, GCN2iB was utilized in a screen for iron-dependent non-apoptotic cell death regulators⁴⁰. Recently, GZD824 (a pan-BCR-ABL inhibitor) was reported to be a novel direct GCN2 inhibitor tested in human fibrosarcoma and non-small cell lung cancer cells, mainly used in Bcr-Abl^{T315I} mutation-induced imatinib resistance in chronic myelogenous leukemia (CML)²³⁸. However, GZD824 suppresses activation of the GCN2 amino acid response, while it paradoxically stimulates this stress signaling pathway at lower non-suppressive concentrations^{238,251}. Collectively, two allosteric (GCN2-IN-1 and GCN2-IN-6) and one ATP-competitive GCN2 inhibitor (GCN2iB) are commercially available, but not reported in clinical trials by now and rarely investigated in pathologies. The use of these inhibitors forms a key part of one chapter of this PhD thesis that describes the creation of a novel cell-based system to screen for GCN2 inhibitors.

Summarized, the ISR is implicated in the pathogenesis of a plethora of inflammatory and non-inflammatory diseases, including cancer, diabetes, neurodegeneration and metabolic disorders²³. Thereby, perturbing the translational quality control has emerged as a promising therapeutic avenue for treating the variety of diseases¹⁹⁸. Manipulating the GCN2-ISR network was reported to be especially beneficial in combination treatment with ASNase in ALL²³⁹. Further therapeutic strategies in an immuno-oncological context aim for the targeting of GCN2 with its close connectors like MYC, ATF4, PERK and mTORC1^{207,240,252}. First, the role of GCN1 in regulating inflammatory responses independent of GCN2 was highlighted in a study by Kim *et al.*¹⁵⁶.

1.3. The mTORC1 pathway

1.3.1. Discovery of mTOR

The mTOR, mechanistic (originally mammalian) Target Of Rapamycin, kinase is also termed previously FRAP by Prof. Dr. Stuart L. Schreiber²⁵³ and RAFT1 by Prof. Dr. David M. Sabatini²⁵⁴. mTOR was discovered by several research groups, who demonstrated biochemically the direct inhibitory binding of the natural macrolide cyclic peptide rapamycin with FKBP12 (FK506-binding protein 12; prolyl-isomerase 12) by partially occluding the substrate entry into the kinase active site^{255,256}. At the cellular level, this allosteric intercalation represses cell growth and proliferation^{254,257–259}. In addition, the same function and mode of action of rapamycin was verified for the mTOR homolog in yeast (TOR/DRR proteins) and in other model organisms^{255,256,260}. Rapamycin, termed by its place of origin in the island of Rapa Nui (also called Easter Island), produced by *Streptomyces hygroscopicus* and has immunosuppressive, anti-mitotic, anti-fungal, neuroprotective and anti-tumoral properties^{261–264}. Accordingly, rapamycin served as a platform to develop a range of related drugs collectively termed rapalogs, all of which target the FRB domain (FKBP12–rapamycin binding) of mTOR. Interestingly, mTOR was found approximately 30 years later, mainly from the initial work of Prof. Dr. Michael Hall and colleagues²⁶⁵.

1.3.2. Structural architectures of mTORC1 and mTORC2

In mammals, the serine/threonine kinase mTOR (289 kDa; encoded by *Mtor*), belongs to the class-IV of PI3K related protein kinase family (PIKK) and is the core catalytic subunit of the mTOR complex 1 (mTORC1) and the mTOR complex 2 (mTORC2)²⁵³. From the N- to the C-terminus mTOR contains of HEAT-repeats, a FAT (FRAP, ATM, TRRAP) domain, the FRB (FKBP12–rapamycin binding) domain, the kinase domain and the FATC (FRAP, ATM, TRRAP C-terminal) domain (Figure 11).

mTORC1 consists of three core proteins (Figure 11A): mTOR, mLST8 (mammalian lethal with SEC13 protein 8, also known as GβL) and regulatory associated protein of mTOR (RAPTOR)^{266–268}. On the RAPTOR scaffold, two accessory proteins are present: proline-rich AKT substrate 40 kDa (PRAS40) that acts as an endogenous inhibitor of mTORC1 activity alongside DEP-domain-containing mTOR-interacting protein (DEPTOR)^{269–271}. Cryo-EM and X-ray structural analyses showed that PRAS40 binds with FKBP12 in the same allosteric pocket of mTOR as rapamycin. Moreover, RAPTOR provides a scaffold for PRAS40 and DEPTOR, which is essential for proper subcellular localization of mTORC1 and can recruit mTORC1 substrates by binding the TOR signaling motifs (5' terminal oligopyrimidine tract (5' TOP))^{272,273}. mLST8 stabilizes mTOR but is not relevant for its catalytic activity^{256,274}. Just like GCN1, mTOR contains many HEAT-repeats. Similar to GCN2, mTOR is latent and becomes activated by autophosphorylation at serine 2481

and dimerizes along the HEAT-repeats and the mTOR-RAPTOR interface when the small GTPase Rheb is bound^{255,275,276}. Importantly, the autophosphorylation site at serine 2481 is rapamycin-insensitive in contrast to the ‘substrate’ phosphorylation site at serine 2448 (Refs.^{277,278}).

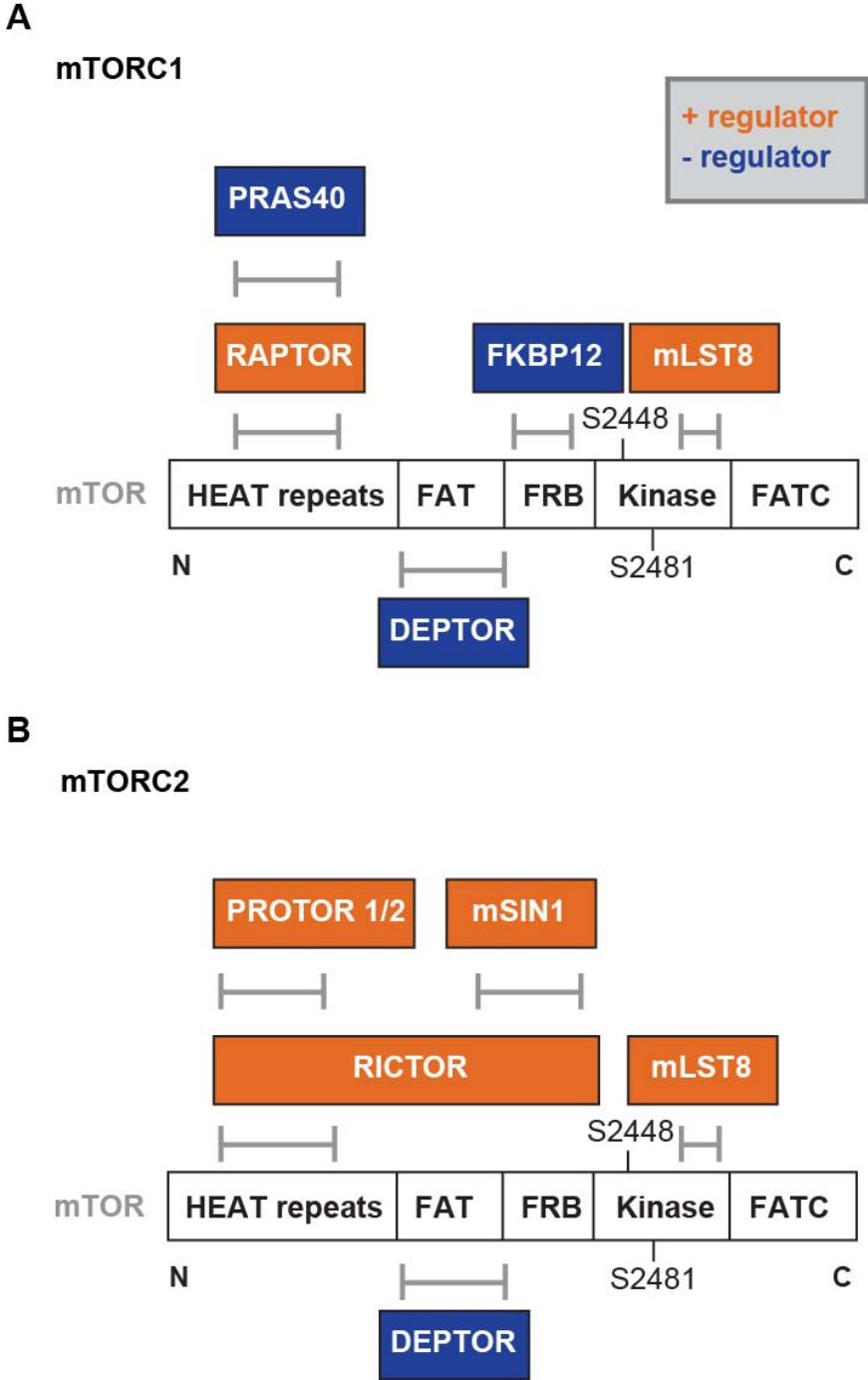


Figure 11. Schematic representation of mTOR domain arrangements. (A) From the N- to the C-terminus mTOR contains of HEAT-repeats, a FAT (FRAP, ATM, TRRAP) domain, the FRB (FKBP12–rapamycin binding) domain, the kinase domain and the FATC (FRAP, ATM, TRRAP C-terminal) domain.

Several positive (+; orange) and negative (-; blue) regulators bind mTOR (grey double arrows): mLST8 (core component), RAPTOR (core component), DEPTOR (endogenous inhibitor), FKBP12 (rapamycin binding partner) and PRAS40 (insulin-regulated inhibitor)²⁴. (B) mTORC2 is arranged similarly to mTORC1 and contains next to mLST8, DEPTOR and its defined core component RICTOR that recruits PROTOR1/2 along with mSIN1 (Ref.²⁴). (A+B) The PI3K-AKT signaling pathway phosphorylates mTOR at S2448 and mTOR is autophosphorylated at S2481 (Refs.^{277,278}).

mTORC2 consists of three core proteins (Figure 11B): mTOR, mLST8 and the scaffold protein RICTOR (rapamycin-insensitive companion of mTOR protein)^{132,279,280}. On the RICTOR scaffold, two accessory proteins are present: MAPK-interacting protein 1 (mSIN1), protein associated with rictor 1 or 2 (PROTOR1/2) and DEPTOR^{253,281-285}. Like mTORC1, mLST8 is relevant for mTORC2 stability and function^{256,280}. mSIN1 was found to help mTORC2 to assemble on the plasma membrane via its phospholipid-binding pleckstrin homology domain²⁸⁶. Just like mTORC1, mTORC2 dimerizes to be active and has the same autophosphorylation site^{287,288}. Moreover, both complexes are structurally similar adopting the same 'lozenge' shape (Figure 12).

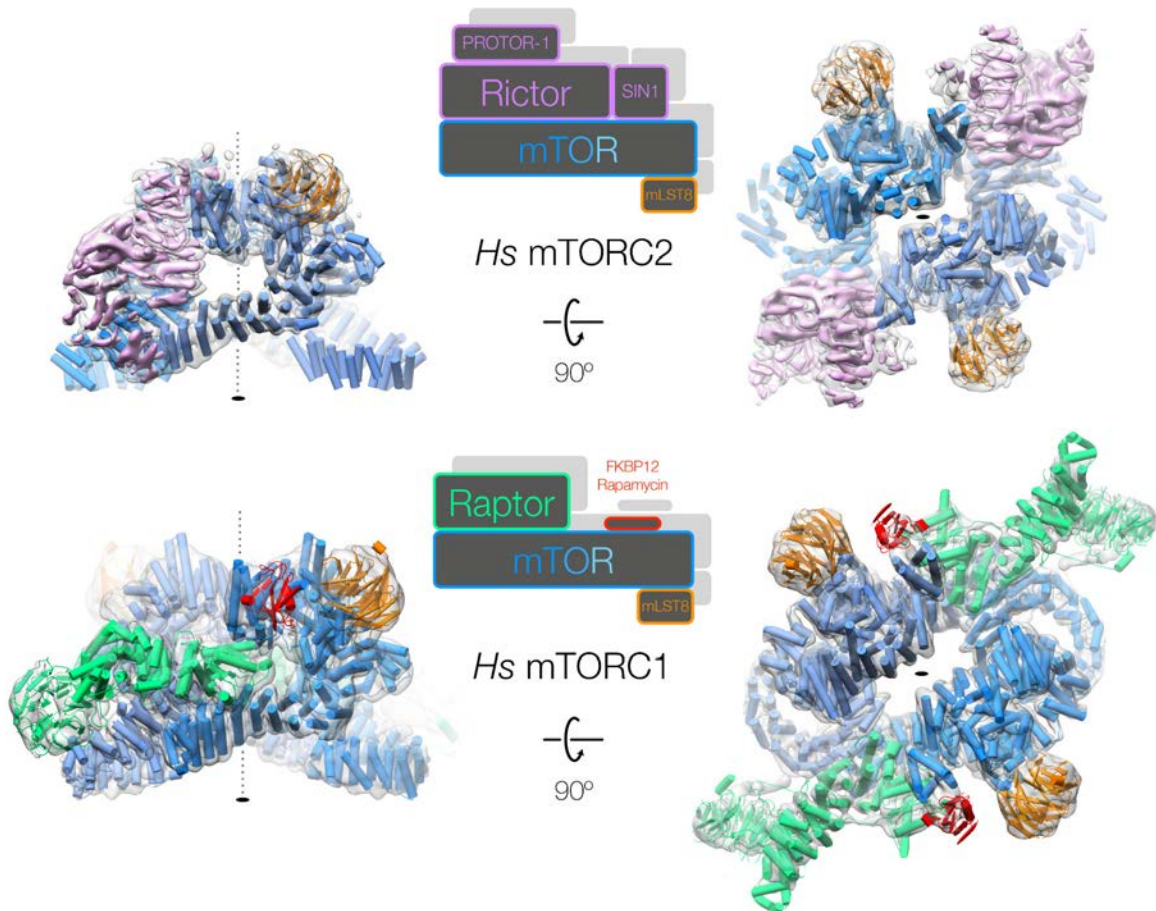


Figure 12. The structural architecture of the human mTORC1 and mTORC2. (Top) A 4.9 Å cryo-EM density of human mTORC2 (without DEPTOR) is shown as a surface representation (PDB ID: 5ZCS (Ref.²⁸⁷)). (Bottom) A 5.9 Å cryo-EM of human mTORC1 (without PRAS40 and DEPTOR) in complex with FKBP12–rapamycin is shown as a surface representation (PDB ID: 5FLC (Ref.²⁷⁵)). The structures are shown rotated that is indicated by the arrows across the panels. The resolutions are based on Refs.^{275,287}. Graphic adapted from Ref.¹³⁸.

1.3.3. Molecular functions of the mTORC1 signaling pathway

1.3.3.1. Biological role of mTORC1

Nutrient and energy availability is sensed at the molecular and cellular level by mTOR, which lies at the nexus of multiple signaling pathways coordinating the cellular and organismal (patho-) physiology of all eukaryotic species. In contrast to GCN2, the molecular role of mTOR in mammalian cells is overall reasonably well studied. The mTOR complex 1, mTORC1, integrates information about nutritional abundance and environmental status to enable a cellular homeostasis in anabolism and catabolism for cellular growth (increase in cell number and size). In a complex architecture with other fundamental accessory and core proteins (Section 1.3.4.), mTORC1 modulates critical cellular processes including protein-, lipid-, nucleotide biosynthesis, ribosome translation and generation, glucose metabolism and suppression of autophagy (Figure 13). Metabolic perturbations, like amino acid stress, disrupt the cellular homeostasis of mTORC1 leading to pathological consequences such as cancer, ageing and metabolic disease (Section 1.3.7.)²⁴.

In contrast to mTORC1, mTORC2, regulates cytoskeletal arrangement and activates several pro-survival pathways (Figure 13). Both complexes are functioning in glucose metabolism and responding to growth signals. Because of the mTORC2 role in actin-cytoskeleton reorganization and cell migration, it is an appealing target for metastasis spreading in cancer research^{289–291}. The major molecular difference between mTORC1 and mTORC2 is the rapamycin insensitivity of mTORC2²⁹². In other words, FKBP12-rapamycin only actively blocks mTORC1 function. Although, prolonged rapamycin treatment blocks also mTORC2 signaling which is proposed to be a consequence of nucleated mTOR in a rapamycin bound state preventing mTOR incorporation into mTORC2^{279,293}. Another suggestion for mTORC2 rapamycin insensitivity comes from its structural composition, where RICTOR sterically blocks the FKBP12-rapamycin binding site, shown in human and yeast system^{288,294}.

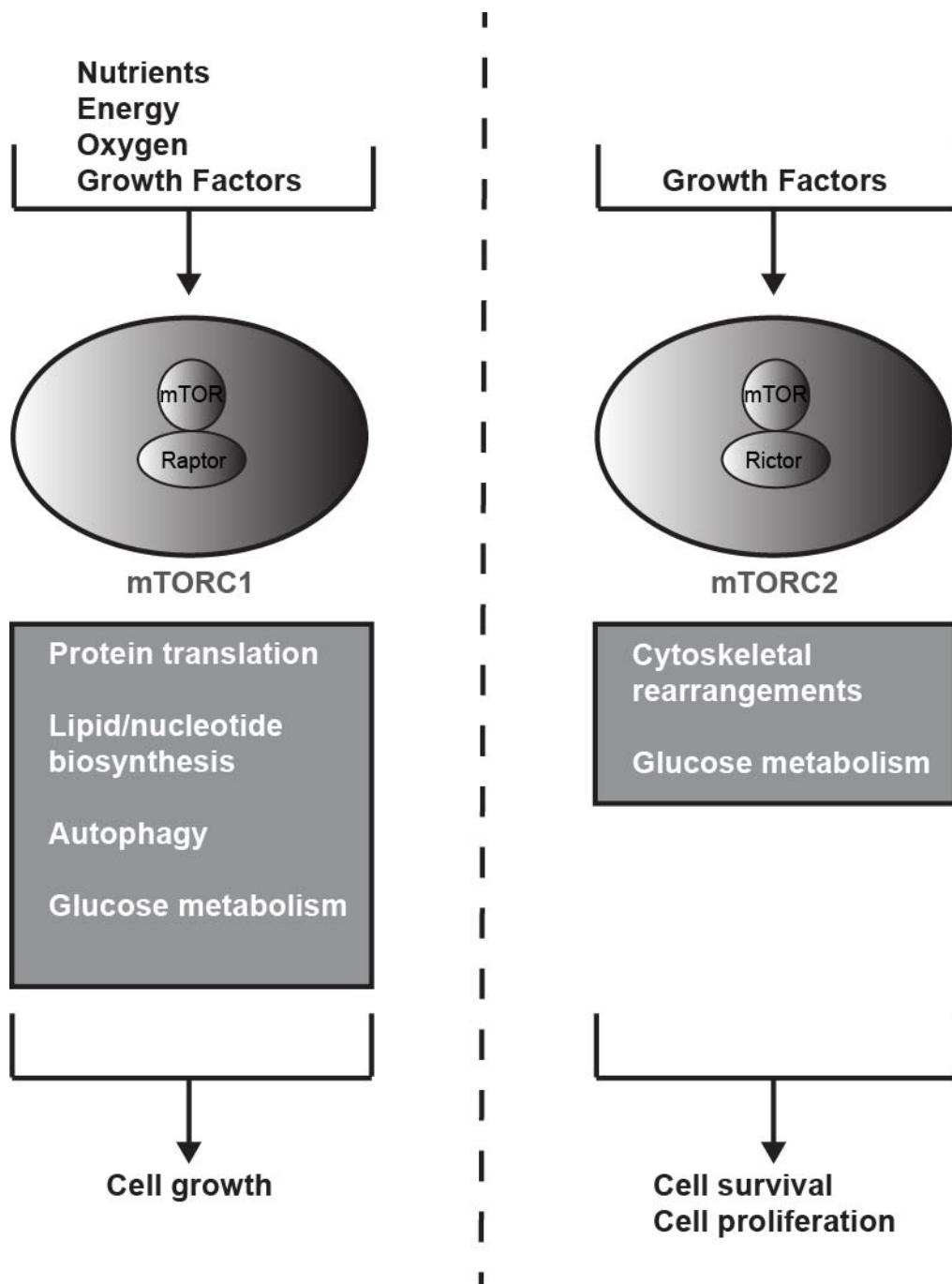


Figure 13. Schematic representation of the distinct roles of mTORC1 and mTORC2. mTORC1 and mTORC2 have distinct cell signaling roles: mTORC1 integrates information about environmental status and nutritional abundance to control balance between catabolism and anabolism for cellular growth. In contrast, mTORC2 regulates cytoskeletal behavior and triggers pro-survival. However, mTORC1 and mTORC2 are both stimulated by growth factors and regulate glucose metabolism²⁴.

1.3.3.2. Regulation of protein synthesis by mTORC1

mTORC1 regulates protein synthesis by phosphorylating substrates that signal downstream to increase anabolic reactions while reducing autophagy of cellular components. The core known

and well-understood mTORC1 substrates are the eukaryotic initiation factor 4E-binding proteins (4EBPs) and the ribosomal protein S6 kinase beta-1 (p70 S6 kinase 1, known as well as S6K1)⁴¹. The most important difference of the proteins is their relative sensitivity to rapamycin treatment: Rapamycin potently inhibits S6K1 activity throughout the duration of treatment in contrast to 4EBPs^{295,296}. Thereby, the mechanism is still not fully understood, but recently linked to FKBP12-rapamycin-induced structural occlusion at mTOR preventing the hyperphosphorylation of all 4EBP1 phosphorylation sites²⁹⁵.

The 4EBP family contains three isoforms (4EBP1-4EBP2-4EBP3; encoded by *Eif4ebp1-2-3*) of which 4EBP3 lacks a conserved N-terminal regulatory motif (RAIP) relevant for mTOR responsiveness^{297,298}. 4EBP1 and 4EBP2 are well-studied in the mTORC1 field and behave the 'same' even if they vary in their abundance across tissues and cell types (e.g. 4EBP2 is mostly expressed in the brain)^{299,300}. All isoforms contain a N-terminal regulatory motif Y(X)4L ϕ (X: variable, ϕ : hydrophobic) by which they bind the eukaryotic translation initiation factor 4E (eIF4E)³⁰¹. The translation repressor 4EBP1 in its de- or hypophosphorylated state suppresses translation initiation competitively by binding and sequestering the eIF4E that is relevant to bind the eukaryotic translation initiation factor 4G (eIF4G) to form the eukaryotic translation initiation factor 4F complex (eIF4F complex) for cap-dependent mRNA translation. In other words, the phosphorylation of 4EBP1 at threonine 37 and threonine 46 (further referred to the mouse equivalents: T36/45) induced by mTOR-RAPTOR primes for subsequent phosphorylation at serine 65 and threonine 70, triggers the formation of eIF4F at the cap and thereby the recruitment of the 40S ribosomal subunit to the 5' end of mRNA^{298,302}. In brief, mTORC1 controls translation initiation by modulating 4EBP1 role in the eIF4F complex formation.

S6K1 (encoded by *Rps6kb1*) and its homolog S6K2 (p85S6K) are 80 % identical in their amino acid sequence. S6K2 has an additional nuclear localization signal proposing its phosphorylation of the free, chromatin-bound nuclear form of S6 (Ref.³⁰³). Like 4EBP1, S6K1 has multiple phosphorylation sites located within the catalytic (T229 phosphorylated by PDK1), linker (T389 phosphorylated by mTOR) and pseudo-substrate domains (S411, T421 and S424 phosphorylated by PI3K) that control the activity of S6K1 (Ref.³⁰⁴). Rapamycin blocks all these phospho-events that leads to the repression of the cell cycle progression³⁰⁴. In this context, overexpression of eIF4E partially rescues rapamycin-inhibited G1 phase progression highlighting how 4EBP1 and S6K1 substrate arms couple cell growth with cell cycle progression in a rate-limiting way³⁰⁵. S6K1 in its dephosphorylated state prevents the phosphorylation of the 40S component, ribosomal protein S6, which leads to no activation of eIF4B, a positive regulator of cap-dependent translation, and no degradation of the eIF4A inhibitor programmed cell death 4 (PDCD4)^{306,307}.

In detail, translation is thought to be regulated by 4EBP1 and S6K1 as follows (Figure 14): Upon mitogen stimulation or amino acid availability, mTOR-RAPTOR is active, is recruited to the eIF3 (eukaryotic translation initiation factor 3; binding via eIF3c) and phosphorylates S6K1 (bound via eIF3b at eIF3 complex) at threonine 389 and 4EBP1 at threonine 36 and 45. This leads to the dissociation of phospho-S6K1 from eIF3 and following phosphorylation at threonine 229 by phosphoinositide-dependent kinase-1, PDK1. Then, phospho-S6K1 can phosphorylate S6 at multiple sites and eIF4B at serine 422 promoting the association with the 43S preinitiation complex³⁰⁸. Concurrently, phospho-4EBP1 dissociates from the cap and triggers the recruitment of the eIF4G scaffold (with PABP1; polyadenylate-binding protein 1) to the cap binding eIF4E as part of eIF4F complex³⁰⁷. Then, translation of many 5' TOP motifs containing mRNAs is induced³⁰⁹. In mammals, 20 - 30 % of the total cellular mRNAs contain TOP motifs that encode for components of the translational apparatus, including ribosomal proteins and translational elongation factors³⁰². In this context, the La-related protein 1 (LARP1), an RNA-binding protein and mTORC1 effector, was found to repress TOP mRNA translation in its dephosphorylated state by binding the mRNA cap and 5' TOP motifs³¹⁰.

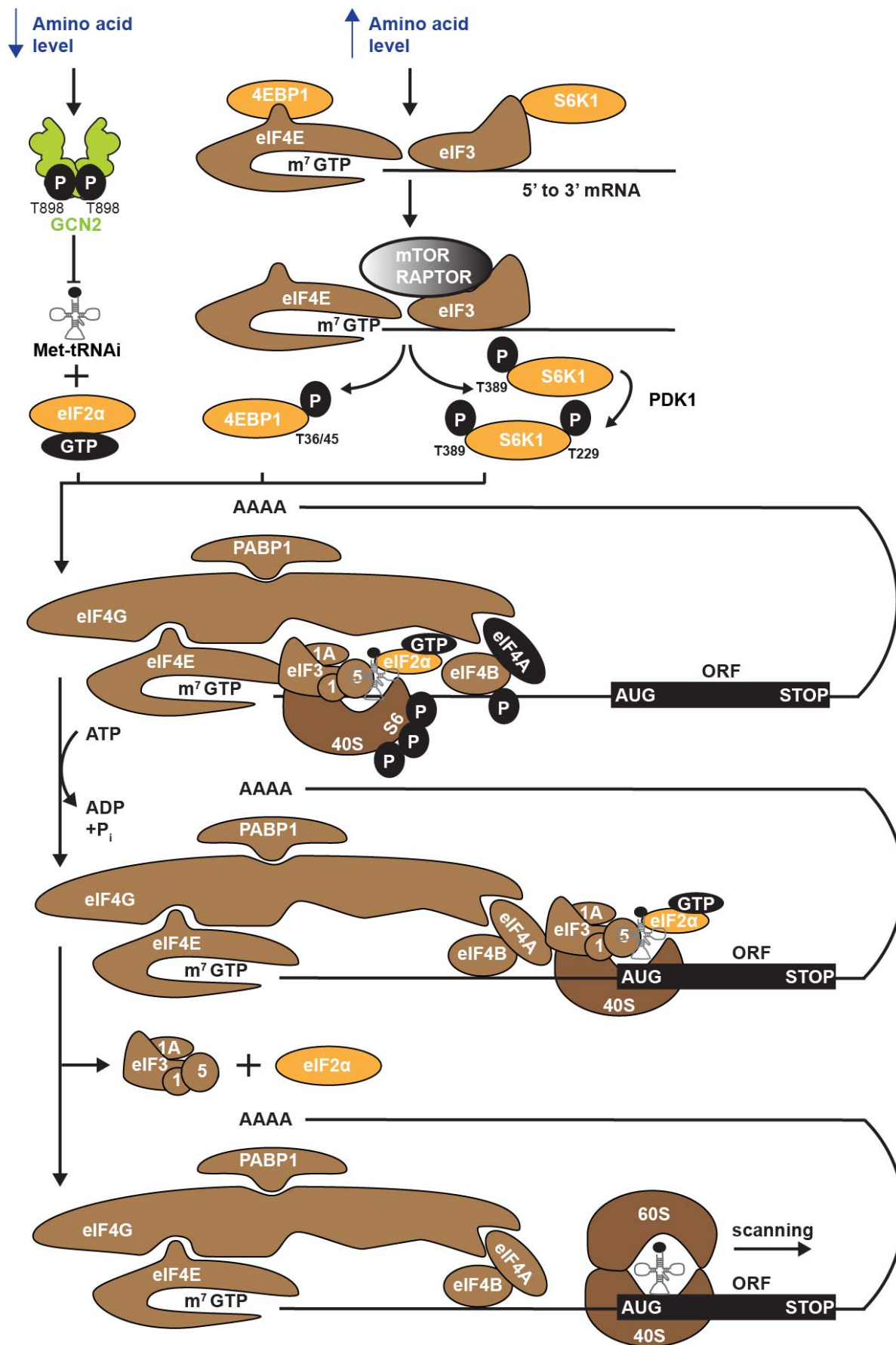


Figure 14. Schematic representation of the canonical eukaryotic translation initiation mechanism regulated by GCN2 and mTORC1. Eukaryotic translation initiation is regulated by mTORC1 (grey) and GCN2 (light green) affected by amino acid availability (blue arrow). Upon amino acid deprivation (blue arrow down), GCN2 phosphorylates the translation initiation factor eIF2 α (orange) preventing the ternary complex formation (TC; consisting of eIF2 α , GTP and Met-tRNAⁱ) and consequently blocking protein synthesis⁷⁴. Detailed information is provided in figure 4. By contrast, under normal growth conditions (blue arrow up), activated mTOR-RAPTOR binds to eIF3 (brown) to phosphorylate S6K1 at T389 (Ref.³⁰⁷). This leads to the dissociation of S6K1 from eIF3 followed by phosphorylation at T229 by PDK1 to trigger the (hyper-)phosphorylation of S6 at 40S and eIF4B at S422 (Ref.³⁰⁸). In addition, mTOR-RAPTOR hyperphosphorylates the translation repressor 4EBP1 at T36/45 (mouse sites) promoting its dissociation from the 5' cap leading to the recruitment of the eIF4G scaffold (with PABP1) to the 5' cap (m⁷ GTP) binding of eIF4E as part of eIF4F complex (brown)³⁰⁷. This overall action is relevant to form the 48S initiation complex and to initiate translation by ATP hydrolysis for scanning the first ORF towards the AUG start codon (black)⁷⁴. Thereby scanning starts upon recognition of the initiation codon, 60S subunit recruitment, and release of the eukaryotic translation initiation factors eIFs (3, 1A, 1 and 5) and eIF2 α (Ref.¹⁹⁷).

Together, active mTORC1 triggers the (hyper-) phosphorylation of 4EBP1 (T36/45; mouse sites) and S6K1 (T389; mouse site) that induces the downstream regulation of the translation factor repertoire relevant to boost protein synthesis^{311,312}. In this context, the activity of mTORC1 to modulate translation initiation is controlled by amino acid availability. In other words, amino acid stress activates GCN2 but prevents mTORC1 signaling to shut down protein translation (Figure 14).

1.3.3.3. Regulation of lipid and nucleotide synthesis by mTORC1

Active mTORC1 also controls lipid- and nucleotide biogenesis²⁴. Lipid production is mediated by two 'master' transcription factors, sterol regulatory element binding protein 1/2 (SREBP1/2) and peroxisome proliferator-activated receptor γ (PPAR γ), which regulate lipid and cholesterol expression dependent on mTORC1 activity²⁴. For example, SREBP translocates from the ER to the nucleus to upregulate a gene expression program that is mediated by the mTORC1 regulated inhibition of SREBP inhibitor lipin1 (Ref.³¹³).

mTORC1 regulates the one-carbon metabolism (1C-metabolism) that provides the building blocks for DNA and rRNA (further ribosomes) synthesis²⁶. This is mediated by the transcription factor ATF4 followed by activation of a transcriptional cascade in which exemplary mitochondrial tetrahydrofolate cycle enzyme methylene- tetrahydrofolate dehydrogenase 2 (MTHFD2) drives *de novo* purine synthesis²⁹. Phosphorylated S6K1 promotes the activation of the carbamoyl-phosphate synthetase 2, aspartate transcarbamoylase, dihydroorotase (CAD), which is a trifunctional multi-domain and rate-limiting enzyme in the pyrimidine biosynthesis^{314,315}. In this

PhD thesis, we provide a link between *de novo* purine synthesis and the GCN1-GCN2 pathway upon amino acid stress.

1.3.3.4. Regulation of autophagy and bioenergetics by mTORC1

In parallel to anabolic reactions, active mTORC1 directly represses autophagy via inhibitory phosphorylation of un-51-like autophagy-activating kinase 1 (ULK1) and autophagy-related protein 13 (ATG13)^{316–318}. These two proteins cause the origin of the autophagosome, whose arrangement is repressed by mTORC1 that also prevents the conversion of endosomes into lysosomes³¹⁹. Bioenergetics are modulated by mTORC1 as well to generate energy and carbon units. mTORC1 upregulates the transcription factor hypoxia inducible factor 1 α (HIF1 α) that regulates glycolysis over OXPHOS by increasing glycolytic enzyme expression^{317,320}. SREBP also affects the bioenergetic flux of NADPH and carbon-precursors for lipogenesis and nucleotide biosynthesis via the pentose phosphate pathway³²⁰. mTORC1 also regulates the translation of nuclear encoded mitochondrial transcripts via the ATF4-4EBP1 axis to increase the ATP production rate^{321,322}. In contrast to mTORC1, the role of mammalian GCN2 in autophagy, and bioenergetics remains not fully understood, which is in part addressed in this PhD thesis.

1.3.4. Regulators of mTORC1 function

Growth factor signals and nutrient status affect the nucleotide-loading state of two sets of small G proteins, Rheb and Rag GTPases, which modulate mTOR kinase activity and its intracellular localization. In normal growth state, GTP-Rag and GTP-Rheb are bound to the lysosome in their active state. Here, GTP-Rag recruits mTORC1 from the cytoplasm to the lysosome, where GTP-Rheb stimulates mTOR activation^{286,323–325}. Thus, Rag and Rheb proteins define the two independent arms, which converge to control the mTORC1 pathway in normal growth state and under stress condition (Figure 15).

Growth factors activate the PI3K-AKT or RAS-driven MAPK pathways to signal to the tuberous sclerosis complex (TSC; consisting of TSC1, TSC2 and TBC1D7). The TSC acts as GTPase-activating protein (GAP) to hydrolyse GTP and thereby regulates the nucleotide loading state of Rheb and consequently mTORC1 activation^{323,326} (Figure 15). For example, insulin stimulates the insulin-like growth factor 1 (IGF-1), which binds to its receptor (IGFR) and activates the serine/threonine kinase AKT (also known as PKB; protein kinase B) that phosphorylates TSC2 to dissociate TSC from the lysosome and finally relieves inhibition of Rheb and mTORC1 (Refs.^{327–330}). To balance mTORC1 activation and TSC restoration, the mTORC1 substrate S6K1 directly phosphorylates the insulin receptor substrate 1 (IRS-1) as part of a negative feedback loop blocking PI3K–AKT signaling to TSC^{331,332}. Insulin also plays a role in blocking the function of the

endogenous inhibitor of mTORC1, PRAS40, which associates with RAPTOR to abolish Rheb-driven mTORC1 activation^{271,325}. Insulin stimulates AKT and consequently the phosphorylation and sequestration of PRAS40. Upon energy or oxygen scarcity, several factors work together to activate the TSC axis and prevent mTORC1 signaling. Metabolic stress leads to ATP depletion triggering the AMP-activated protein kinase (AMPK) complex, which then antagonizes mTORC1 activity by phosphorylating RAPTOR directly and TSC2 indirectly^{333,334}.

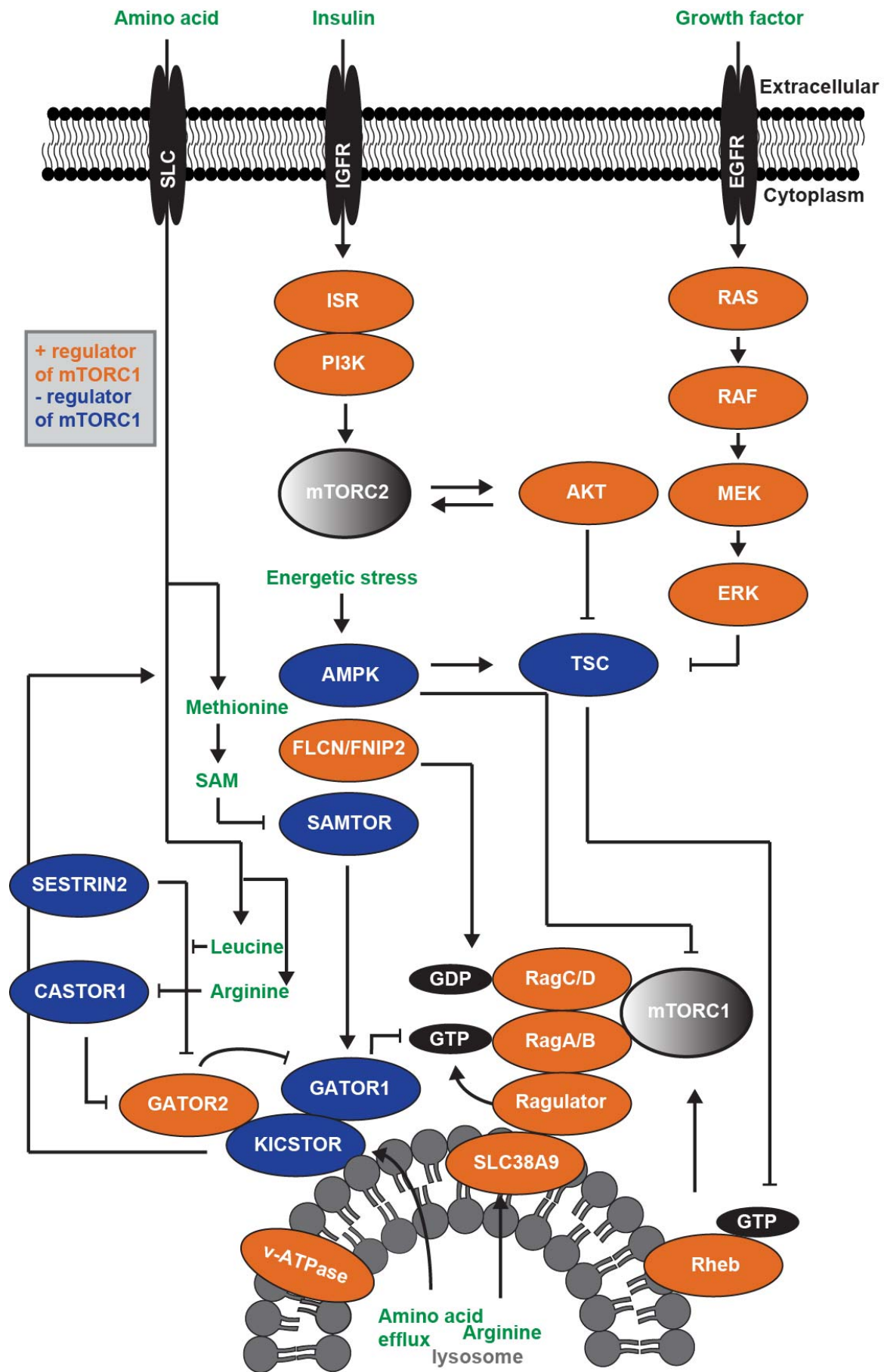


Figure 15. Schematic representation of the negative and positive regulators of mTORC1. mTORC1 is only activated when sufficient growth resources are available (amino acids, insulin/growth factors, ATP and oxygen) that are transported partially by SLC transporters or receptors such as IGFR and EGFR. Simplistically, when amino acids are available Rag GTPases (A/B/C/D) translocate mTORC1 to the lysosome where mTORC1 becomes activated by the small GTPase Rheb in its GTP (black)-bound state. mTORC2 is primarily activated by growth factors and has by now no specific known cellular localization spot²⁴. Stimulation signals are highlighted in green. Positive regulators are shown in orange, while negative regulators are displayed in blue. Action of the regulators is shown by activating and inhibitory arrows.

In addition to growth factor activity and energy status, amino acids play a dominant role in regulating the mTORC1 pathway. Hara *et al.*⁴¹ discovered that the amino acids leucine and arginine are required for mTORC1 activity in mammals, which is modulated by the function of Rag-GTPases^{286,325}. The heterodimeric Rag-GTPases connect to the lysosome via the pentameric Ragulator complex (RagA/B, RagC/D and Ragulator: p18, p14, MP1, C7orf59 and HBXIP, otherwise known as LAMTOR1–LAMTOR5)^{325,335,336} and are regulated by upstream ‘nutrient sensing complexes’ with GAP or GEF activity. Sensing cytosolic and lysosomal amino acid concentrations, these upstream protein complexes affect the conformation and thereby activation status of Rags: RagA or RagB is bound to RagC or RagD. An ‘on-state’ is represented when RagA/B is bound to GTP and RagC/D to GDP. In normal growth state, RAPTOR triggers the ‘on-state’, leading to the recruitment of mTORC1 to the lysosome, where its activity is stimulated by Rheb^{335,337}. Upon nutrient withdrawal, the GATOR1 complex (GAP activity towards the Rag proteins; consists of DEP domain-containing 5 (DEPDC5), nitrogen permease related-like 2 (NPRL2) and NPRL3) hydrolyses GTP on RagA and Rag B, thereby preventing the activation of mTORC1 (Refs.^{336,338}). In this context, the KICSTOR complex (KPTN, ITFG2, C12orf66 and SZT2) sequesters GATOR1 at the lysosome and is required for cellular sensitivity to amino acid deprivation³³⁹. In addition, GATOR1 physically interacts with GATOR2 (pentameric complex of WDR59, WDR24, MIOS, SEH1L and SEC13)³⁴⁰, which is a positive regulator of mTORC1 and an antagonist of GATOR1. In contrast to GATOR1, the folliculin (FLCN)–FNIP2 complex acts as a GAP for RagC and RagD by sustaining mTORC1 activation in the presence of amino acids^{341,342}.

The leucine sensor SESTRIN2 binds and inhibits GATOR2 and blocks mTORC1 localization to the lysosome in the absence of leucine^{57,343}. When leucine is present, direct binding of leucine to SESTRIN2 (K_d of 20 μ M) reverses the effect^{57,343}. The binding affinities of SESTRIN1 and SESTRIN2 are similar compared to the human leucyl–transfer RNA synthetase (LRS) for leucine (40 μ M)- this is in stark contrast to the weak affinity of SESTRIN3 (Refs.^{57,343}). In *in vitro* experiments, SESTRIN2 overexpression alone is sufficient to block mTORC1 signaling, which is

transcriptionally upregulated by ATF4 upon amino acid starvation^{344,345}. The arginine sensor CASTOR1 responds to cytosolic arginine alone, exists as a homodimer or heterodimer with CASTOR2 and inhibits mTORC1 in the same mode of action as SESTRIN2^{56,346-348}. Arginine binds to CASTOR1 with a dissociation constant of approximately 30 μ M (Ref.⁵⁶). Another putative arginine sensor is SLC38A9, which is a solute carrier transporter residing at the lysosome. Its function is to sense arginine levels inside the lysosomal lumen and to transport essential amino acids in an arginine-regulated fashion into the cytoplasm³⁴⁹. The v-ATPase, which regulates a proton gradient via ATP hydrolysis, was found to be closely localized to SLC38A9^{58,349,350}. Moreover, mTORC1 also senses metabolic byproducts such as S-adenosylmethionine (SAM) from the methionine metabolism via SAMTOR³⁵¹. SAMTOR negatively regulates mTORC1 by binding KICSTOR and GATOR1 under SAM and methionine deprivation³⁵¹.

Growth factors like phosphatidylinositol (3,4,5)-trisphosphate (PIP3), a product of insulin stimulation and a component of the PI3K pathway, relieve the autoinhibitory function of mSIN1 (Refs.^{352,353}). Consequently, mSIN1 may recruit mTORC2 to the plasma membrane, where it interacts with AKT by reciprocal phosphorylation to modulate their activity and localization status³⁵⁴. Moreover, AMPK positively regulates mTORC2 signaling under energy stress and mTORC1 negatively regulates mTORC2 by downregulating the insulin-PI3K-AKT axis³⁵⁵.

Overall, mTOR activity is modulated by a plethora of positive and negative regulatory proteins and protein complexes. However, the intrinsic role of GCN2, which senses amino acid depletion and its connection to the mTORC1 and mTORC2 signaling nodes remains an area of active research.

1.3.5. mTORC1 signaling upon amino acid stress

Upon fluctuations in amino acid availability, the mTORC1 pathway responds with a stress adaptive signaling that mimics a metabolic switch/feedback reaction. In detail, amino acid stress circumvents the process of autophagy repression and biomass production by triggering the inhibition of mTORC1 and corresponding activation of autophagy²⁴. Most importantly, this process happens in a narrow time window. After prolonged amino acid stress (more than 1 h), mTORC1 becomes active again by a so far unknown mechanism, but was shown to be linked to glutamine metabolism³⁵⁶.

In the context of the GCN2 cascade, mTORC1 is initially inhibited by amino acid stress when GCN2 is active (Figure 16). The mechanism how mTORC1 senses arginine, leucine and methionine deprivation was found to be mediated by the amino acid specific sensors CASTOR1^{56,348} or SLC38A9³⁴⁹, SESTRIN2⁵⁷ and SAMTOR³⁵¹, respectively. At short-term amino acid stress, mTORC1 function is inhibited, which can be measured by the non-phosphorylation of

the key targets S6K1 (at T389) and 4EBP1 (at T36/45), inducing translation shut-down. Consequently, mTORC1 does not phosphorylate ULK1 at serine 757 anymore leading to an intact interaction between ULK1 and AMPK³⁵⁷. This is one way how mTORC1 inhibition activates autophagy. After prolonged amino acid stress, mTORC1 is reactivated and this process is highly connected to autophagy²⁴. Autophagy triggers the processing and lysosomal recycling of damaged organelles or proteins that is followed by restoration of protein translation³⁰. In interphase cells, autophagosome construction is increased and nuclear translocation of the transcription factor EB (TFEB) and the related transcription factor E3 (TFE3) is induced to increase lysosomal biogenesis that is also linked to the ISR^{358,359}. Early lysosomes release peptides to the cytoplasm –via SLC38A9³⁵⁰- to regenerate the pool of cellular amino acids in order to reactivate mTORC1³⁰.

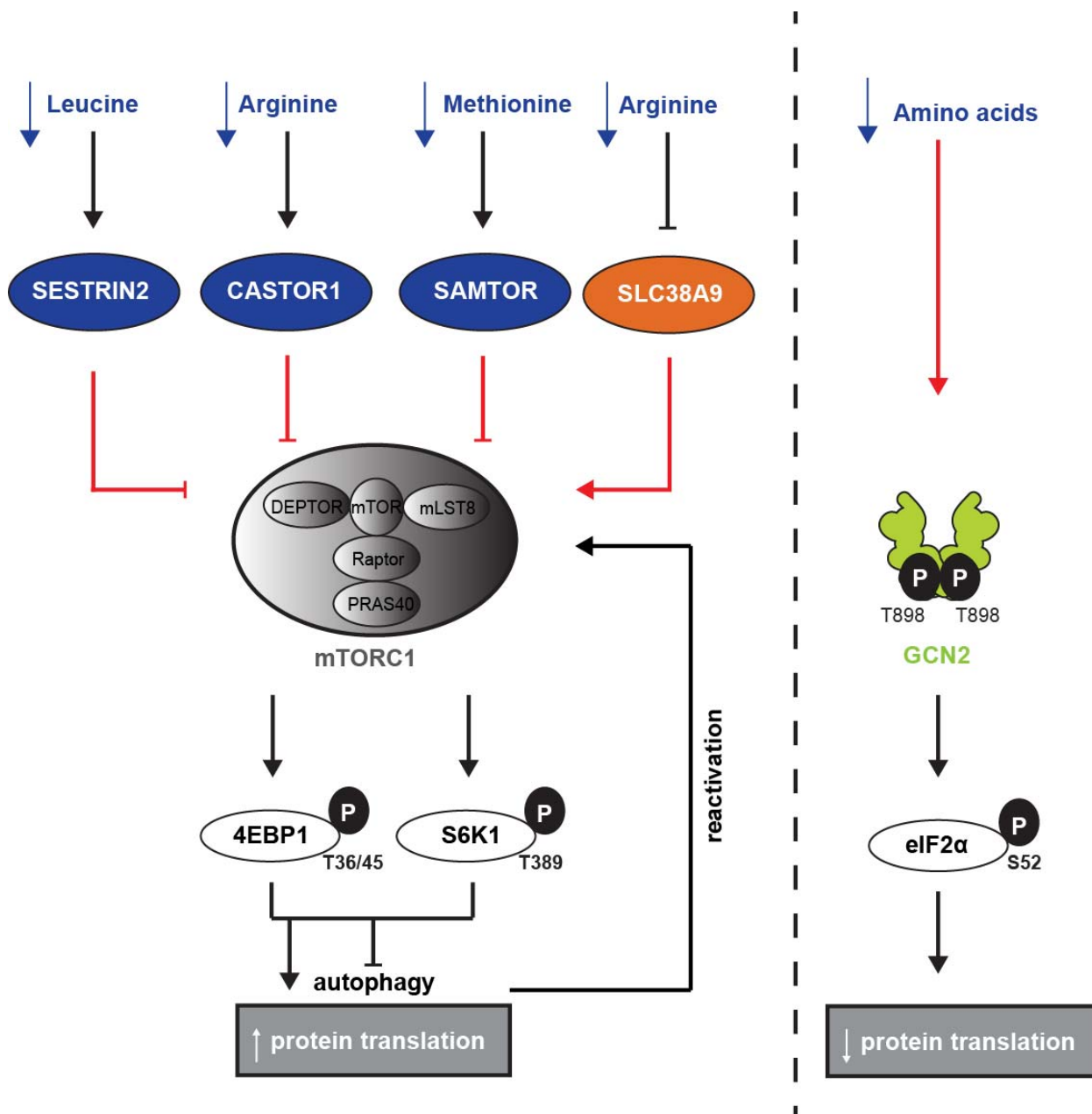


Figure 16. Schematic representation of mTORC1 and GCN2 signaling upon amino acid stress. (Left) In a simplistic way, specific amino acid deprivation (arginine, leucine and methionine) is sensed by the respective sensors CASTOR^{156,348}, SLC38A9³⁴⁹, SESTRIN2⁵⁷ and SAMTOR³⁵¹ (blue (negative regulator) and orange (positive regulator)). This leads to the inactivation (red) of mTORC1 (grey) blocking the phosphorylation of the downstream targets S6K1 (at T389; mouse site) and 4EBP1 (at T36/45; mouse sites). This action prevents protein translation and removes the repression of autophagy. The activation of autophagy is a proposed crucial step to reactivate mTORC1: autophagy triggers processing and lysosomal recycling of damaged organelles or proteins followed by restoration of protein translation^{30,350,360}. (Right) Amino acid stress triggers in parallel the activation (red) of GCN2 (light green; at T898; mouse site) to phosphorylate eIF2 α (at S52; mouse site) and to block protein translation⁶¹.

Another mTORC1-lysosomal feedback loop is provided by the ribophagy, which is the autophagy and destruction of ribosomes. This process seems to require the autophagy receptor nuclear fragile X mental retardation-interacting protein 1 (NUFIP1)^{361–363}; although this model is discussed controversially³⁶⁴. However, lysosome activity only partially restores the amino acid pool by autophagy, suggesting a more specific driven process of mTORC1 reactivation^{365,366}. In this context, the single amino acid glutamine can restore mTORC1 activity during prolonged amino acid starvation in an autophagy-dependent way, which is impaired when glutaminolysis or transamination processes, to generate glutamate, are repressed³⁶⁷. Interestingly, protein translation in a ‘low amino acid pool’ cellular environment is limited by tRNA^{Gln} charging compared to all other tRNAs being retained charged with their cognate amino acid. This process happens in a manner that is dependent on intact lysosomal function³⁶⁸.

Overall, amino acid deprivation suppresses mTORC1 activation and thereby activates autophagy that restores mTORC1 activation as a feedback effect. However, the kinetics, the role of GCN2 and the mechanism behind the time-dependent and subsequent mTORC1 reactivation and the lysosome-autophagy axis is not fully understood.

1.3.6. Interplay of mTORC1 and GCN2

Amino acid demand is sensed by the GCN2 and mTORC1 signaling nodes²⁸. Both pathways control opposite networks via cell preservation (by GCN2) versus anabolic metabolism (by mTORC1)^{13,24}. However, both pathways couple amino acid sensing to protein translation (Figures 14+16). By now, the knowledge accumulates that the GCN2 and the mTORC1 pathways do not operate independently and both pathways are linked through multiple layers of crosstalk, most of which are still poorly understood.

Mechanistically, an intercalation of both pathways was first described by Averous *et al.*¹⁷⁹ in mouse embryonic fibroblasts (MEFs). They found that GCN2 contributes to mTORC1 inhibition upon leucine and arginine deprivation and proposed that phosphorylation of eIF2 α is necessary, but not sufficient for the mechanistic mTORC1 inhibition. In MEFs and budding yeast, GCN2 was proposed as an upstream regulator of mTORC1 upon leucine and histidine starvation³⁶⁹. Furthermore, a time-resolved analysis of hepatic mTORC1 activity upon asparaginase treatment (globally reducing intracellular asparagine levels) was performed by Nikonorova *et al.*³⁷⁰. They found that eIF2 α phosphorylation blocks mTORC1 induction within 15 minutes, but the ATF4-stress transcriptional program increased after more than 3 h proposing a non-essential role of ATF4 in the early GCN2 driven mTORC1 suppression. In their model, eIF2 α phosphorylation happened upstream of mTORC1 regulation, but independent of ATF4. This ATF4 independence of mTORC1 suppression upon starvation was reported as well by Averous *et al.*¹⁷⁹. The role of eIF2 α was also analyzed in the context of mTORC1-mediated autophagy repression: Wengrod *et*

*al.*³⁷¹ proposed that upon amino acid withdrawal mTORC1 inhibition activates the phosphatase PP6C (protein phosphatase 6, catalytic subunit) that associates with GCN2 to promote the phosphorylation of eIF2 α leading to autophagy induction. Collectively, GCN2 seems to contribute to mTORC1 inhibition by regulating the phosphorylation of eIF2 α and finally translation initiation upon short-term amino acid stress. However, the longitudinal signaling cascade position of the main players relative to each other, and across time of amino acid stress, remains unsolved. It seems likely that the GCN2-eIF2 α -mTORC1 network is far more complex than originally proposed by the studies noted above and addressed throughout this thesis.

Another layer of complexity between GCN2 and mTORC1 is the expression and function of the stress-transcriptional program for stress adaptation mediated by ATF4 (Figure 2). As first shown by Harding *et al.*¹⁵ the ISR regulates amino acid metabolism and resistance to oxidative stress in an ATF4-dependent manner. Ye *et al.*³⁴⁴ highlighted that GCN2 activates ATF4-mediated SESTRIN2 (specific leucine sensor of mTORC1 signaling^{57,348}) induction that was linked to sustained repression of mTORC1 by blocking its lysosomal trafficking upon prolonged amino acid stress (Figure 17). In this context, Saveljeva *et al.*³⁴⁵ found that SESTRIN2 induction leads to mTORC1 inactivation and autophagy activation upon ER stress-mediated PERK-ISR. SESTRIN2 is also a critical regulator of cancer cell survival upon glutamine deprivation regulating an mTORC1-mTORC2 feedback effect to restore homeostasis³⁷². Transcriptomics studies by Park *et al.* and Torrence *et al.*^{26,95} indicated that ATF4-mediated SESTRIN2 induction is regulated by mTORC1 (via insulin) and PERK (via tunicamycin) stimulated networks – independent of eIF2 α phosphorylation. Recently, translation regulation was also linked to ATF4 showing that the translation repressor 4EBP1 is highly expressed upon induction of ATF4^{26,207,373}.

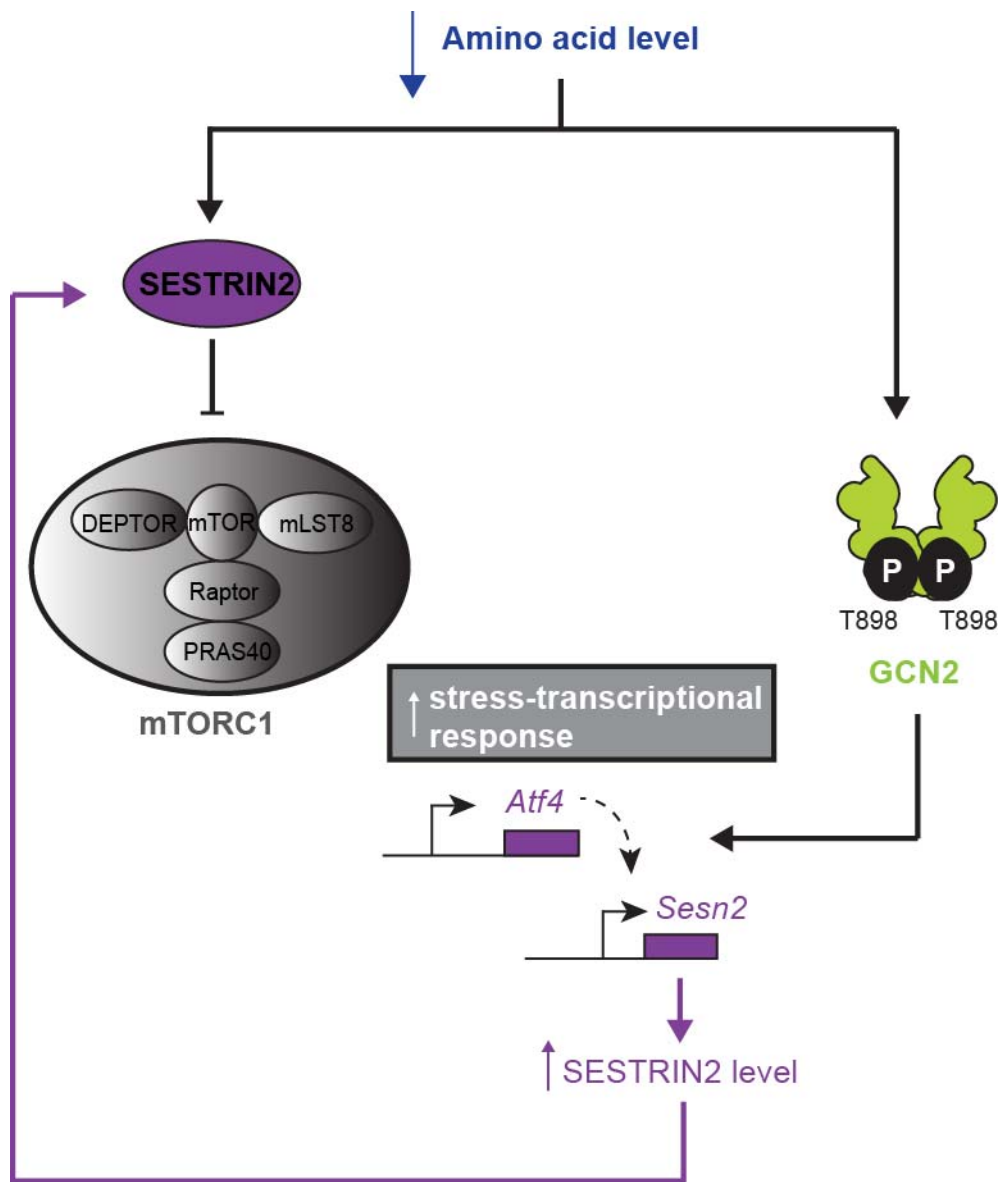


Figure 17. Schematic representation of a proposed interplay of mTORC1 and GCN2 induced by the ATF4-SESTRIN2 axis. Depicted is one model how the mTORC1 pathway is regulated by the GCN2 cascade³⁴⁴: upon amino acid stress (blue), GCN2 (light green) is activated (autophosphorylation at T898; mouse site) and induces the stress-transcriptional response. Thereby, ATF4 (purple; encoded by *Atf4*) mediates the expression of *Sesn2*. SESTRIN2 (encoded by *Sesn2*) is the leucine sensor of mTORC1 that sustains suppression of mTORC1 upon amino acid stress³⁴⁴. Principle based on Ye *et al.*³⁴⁴.

At present, the mechanistic interplay of mTORC1 and GCN2 is most likely a time-dependent phenomenon, but how GCN2 controls mTORC1 and vice-versa is so far not fully understood. Especially, the role of ATF4 and the function of the stress-transcriptional program (e.g. SESTRIN2, 4EBP1 or amino acid transporters)^{26,95} in regulating mTORC1 activity in amino acid starved cells is in the focus of many research groups and is connected to GCN2 in this PhD thesis.

1.3.7. mTOR in physiology and pathophysiology

Like GCN2, aberrant mTOR signaling leads to physiological pathogenesis including cancer, diabetes and metabolic disorders²⁴. mTORC1 and mTORC2 regulate glucose metabolism and have an impact on metabolic disorders like diabetes and obesity. For example, glucose reduction in mice lacking SESTRIN proteins show fatal hypoglycaemia, which leads to perinatal lethality due to their repression in autophagy^{374,375}. RAPTOR and RICTOR lacking mice have impaired hepatic lipogenesis that are partially rescuable by AKT activation^{376–378}. In addition, these mice display microcephaly phenotypes, a reduction in neuron size and number^{379,380}. A further well-studied disease arising from constitutive mTORC1 activity is the neurodevelopmental disorder of tuberous sclerosis complex (lack of TSC1/harmatin or TSC2/tuberin), which is a rare multisystem autosomal dominant genetic disease-causing non-cancerous tumors³⁸¹. mTOR modulates learning and memory by promoting translation at synapses through S6K1 and 4EBP2 dependent on neuronal activity³⁸². Moreover, mTORC1 inhibition was associated with slowing ageing by reversing molecular changes involved with cellular deterioration^{383,384}. Senescent cells arrest in G0-phase are characterized by synthesizing and secreting pro-inflammatory cytokines, which exacerbate aging related tissue decline^{385,386}. Therefore, mTORC1 inhibition is a strategy to block senescent cells-induced gaining phenotype.

In cancer, hyperactivation of mTORC2 and/or mTORC1 supports cancer cells to evade metabolic checkpoints of anabolism and proliferation. Intrinsically, mTOR is rarely mutated, but upstream nodes of mTOR signaling are highly mutated, such as RAS-MAPK or PI3K-AKT signaling, which underlines why mTOR is hyperactivated in 80 % of human cancers³⁸⁷. Therefore, a growing interest is the pharmacological intervention of mTOR. The macrolide rapamycin (sirolimus) and its analogues (e.g. everolimus or temsirolimus) belong to the class of rapalogs, which are the first generation of allosteric mTORC1 inhibitors³⁸⁸. However, rapamycin-dependent mTORC1 inhibition suppresses a negative feedback loop that normally diminishes growth factor signaling to PI3K, therefore causing pro-tumorigenic hyperactivation of PI3K and mTORC2 (Ref.³⁸⁹). Moreover, rapamycin-mediated inhibition of mTORC2 and mTORC1 signaling is highly dose- and cell-tissue-specific and only long exposure of rapamycin can suppress mTORC2^{279,390–392}. mTORC2 inhibition in PI3K/PTEN (phosphatase and tensin homolog) driven tumors is beneficial because mTORC2 regulates hyperactivation and not basal PI3K activity in solely tumorigenic tissues^{389,393}. Consequently, the second-generation of dual mTOR kinase inhibitors, termed TORKinibs are of highest interest. TORKinibs are small molecule ATP-competitive inhibitors of mTORC1 and mTORC2. Mainly driven by the group of Prof. Dr. Roger Williams, their development based on a similar mode of action known for PI3K inhibitors: the first PI3K inhibitor PI-103 (Ref.³⁹⁴) inhibits mTOR in an ATP-competitive manner and was used as lead compound

for the development of many mTOR targeting small molecules. The most prominent selective ATP-competitive mTOR inhibitor is the pyridinonequinoline compound Torin-1 that inhibits both mTOR complexes, mTORC1 and mTORC2, equally with IC_{50} of 2–10 nM, respectively and has better pharmacological profiles as rapalogs³⁹⁰. A further related potent selective mTOR inhibitor is sapanisertib (INK-128, TAK-228; IC_{50} 1 nM) that displays a more than 100 fold selectivity to PI3K kinases and is currently undergoing preclinical evaluation^{395,396}, highlighted by the recently started clinical phase 2 for non-small cell lung cancer³⁹⁷. However, mTOR inhibitory agents have ‘double edged sword’ characteristics meaning that beneficial effects (e.g. low nephrotoxicity, lower incidences of viral infection^{398–400}) need to be balanced against immunological side effect, such as immunostimulation paired with limited immunosuppressive potency^{401–404}. In addition, preliminary investigations advocate the combination instead of single agent treatment of mTOR inhibitors with standard chemotherapies, such as receptor tyrosine kinase (RTK) and angiogenesis inhibitors^{405–407}. Moreover, dose-toxicity as well as drug resistance are still under investigation^{408–410}. Therefore, refinements of mTOR inhibition strategies are essential for the use of these agents in clinical implications for cancer therapies⁴¹¹.

Overall, mTOR and GCN2 are both relevant for cellular survival upon amino acid stress making them attractable for pharmaceutical interventions, especially in cancer. The chemical perturbation of mTOR and GCN2 in an amino acid starved cellular environment is one aim of this thesis.

2. Aims of the thesis

The integrated stress response (ISR) is a multi-component stress- and cell-specific protection pathway²³. Across eukaryotic species, the ISR is a conserved and ancient survival pathway for coping with cellular stress by controlling proteostasis^{23,60}. Upon cellular stress, cancer cells can potentially become dependent on components of this metabolic defense pathway for cellular fitness and survival¹⁹⁸. Therefore, non-essential components of the ISR are appealing drug targets for a metabolic vulnerability of cancer cells^{239,412}. First found in *Saccharomyces cerevisiae*, amino acid availability is sensed by the non-essential kinase GCN2, which is activated by amino acid deprivation⁴¹³. In mammals, GCN2 is one of the four ISR stress kinases (along with PKR, PERK, HRI; activated by other distinct stresses)⁶⁰ that phosphorylates the common target, the eukaryotic translation initiation factor eIF2 α ⁷⁷. Mechanistically, GCN2 phosphorylates eIF2 α to block translation, but simultaneously induces a transcriptional program for stress adaptation mediated by the transcription factor ATF4^{61,71,77}. mTORC1 is another amino acid sensing hub that responds to amino acid availability by promoting anabolic metabolism, translation and growth²⁴. Thus, GCN2 and mTORC1 work in a diametrically opposite way: cell preservation versus anabolic metabolism, respectively. Recently, extensive crosstalk between the mTORC1 and GCN2 pathways has been uncovered²⁶⁻²⁹, although the precise mechanism remains unclear. Unlike the other eIF2 α kinases (HRI, PERK and PKR), GCN2 interacts with a large HEAT-repeat protein named GCN1 that regulates the activity of GCN2 via an unknown mechanism that may involve ribosomal association via a heteropentameric P-stalk induced by ribosomal collision^{114,166,171}.

In this PhD thesis, I aimed to understand the underlying molecular and mechanistic ISR induced by amino acid stress in mammals. To break new ground in dissecting the GCN1 and GCN2 biology, I generated single-cell-based CRISPR/Cas9 biallelic GCN1 and/or GCN2 deficient cell lines in three different mouse systems to further study the major effects induced at the protein and gene level using global multi-omics approaches. Moreover, I developed novel GCN2-dependent and amino acid stress-sensitive reporter systems to perform a large-scale GCN2 inhibitor screen and applied the findings in different cellular contexts. In addition, I investigated the involvement of GCN1 in the ISR, GCN1 and GCN2 roles in bioenergetics and the iron dependent non-apoptotic death pathway, termed ferroptosis. Moreover, I dissected and then linked the GCN2 and mTORC1 amino acid sensing and signaling networks. Overall, this PhD thesis sets the first steps in mechanistically decipher the mammalian amino acid response: the regulation by GCN1 and the manipulation by specific GCN2 and mTOR inhibitors upon amino acid stress.

3. Materials and Methods

3.1. Mice

All animal experimentations described in this thesis were performed at the animal facility of the Max-Planck-Institute of Biochemistry in accordance with the approval from the 'Regierung von Oberbayern'. The animal facility covers the housing and the breeding of mice (Animal Welfare Officer, Dr. Eva Hesse) that is additionally approved by the European Union. Euthanasia was conducted by cervical dislocation following training by Dr. Corinna Mörth. All animals were documented using the 'Max-Planck-Gesellschaft-PyRat system', which is used for reporting animal usage yearly to government entities. Animal breeding was performed behind a barrier system that permits restricted access to approved users and incorporates a specific pathogen free hygiene system. Mice were maintained in humidity- and temperature-controlled rooms on a 14-10 h light-dark cycle and maintained Helicobacter-free.

C57BL/6 (B6) mice bearing a loss-of-function of *Eif2ak4* in exon 12 (B6.129S6-*Eif2ak4*^{tm1.2Dron}/J; termed GCN2^{-/-}) were originally obtained from the Jackson Laboratory (Stock No: 008240) that were bred with C57BL/6 wild-type mice from the common breeding colony of the animal facility. GCN2^{-/-} mice were generated from heterozygous intercrosses to improve breeding performance. Progeny were genotyped using the primers described on the Jackson Laboratory web page for this strain.

3.2. *In Vitro* Cell Culture

3.2.1. Cell systems

3.2.1.1. Cell culture of murine fibroblasts

NIH-3T3 cell line (3T3, hereafter) was established, characterized and provided by Prof. Dr. Andreas Pichlmair (Technical University Munich, Munich, Germany). NIH-3T3-Cas9-hyg stable cell line (3T3-Cas9, hereafter) was purchased from GeneCopoeia (Rockville, MD, USA). Murine embryonic fibroblasts (MEFs, hereafter) and littermate derived GCN2^{-/-} counterparts were obtained by Prof. Dr. Peter J. Murray (Max-Planck-Institute of Biochemistry, Munich, Germany). All adherent cells were cultured in Dulbecco's modified Eagle's medium (DMEM; 41966-029, Thermo Fisher) supplemented with 10 % fetal bovine serum (FBS; 10270, Life Technologies) and 1 % penicillin-streptomycin (P/S; 09-757F, Lonza) in humidified tissue culture incubators at 37 °C with 5 % CO₂. The FBS was filtered before using (0.22 µM; 833.941.001, Sarstedt). Cells were not used for any experiment above passage 5 and the medium was changed every other day. All cells were tested for mycoplasma infection by PCR screening (LookOut mycoplasma PCR detection kit, MP0035-1KT, Sigma-Aldrich). At 60–70 % confluency, fibroblasts were washed

once with PBS (1x PBS; 10010015, Life Technologies) detached using 1 mL 0.25 % trypsin-EDTA (trypsin; 25200-056, Gibco) for 5 min at 37 °C with 5 % CO₂, neutralized in sufficient cell culture medium, harvested at 1400 rpm for 5 min and seeded in tissue culture plates (10 cm dish; 353003, Falcon) for cultivation or counted and plated according to experimental need. Cells were frozen in 10 % DMSO (12611S, CST) in FBS.

3.2.1.2. Cell culture of murine bone marrow derived macrophages

Murine bone marrow derived macrophages (WT BMDMs, hereafter) and littermate derived GCN2^{-/-} counterparts (GCN2^{-/-} BMDMs, hereafter) were cultured in DMEM as previously described for murine fibroblasts. For the preparation of BMDMs, bone marrow cells (BMs) were flushed from femur and tibia bones of C57BL/6 (B6) WT and GCN2^{-/-} mice and filtered using a 70 µM cell strainer (352350, Falcon). The collected cells were centrifuged at 1300 rpm for 5 min and lysed in 1x Red Blood Cell lysis buffer (RBC lysis buffer; 0.25 M EDTA (E9884, Sigma-Aldrich), 1.5 mM ammonium chloride (A9434, Sigma-Aldrich), 10.9 mM potassium bicarbonate (237205, Sigma-Aldrich)) for 2 min at room temperature (RT) before neutralization with PBS. After two PBS washing steps, the BMs were seeded in 15 cm tissue culture plates (430599, Corning) and cultured in DMEM supplemented with 1:10000 recombinant human colony stimulating factor-1 (0.87 mg/mL CSF-1, MPIB Core Facility) as previously described. Per mouse, the BMs (about 40-80x10⁶ cells) were plated on total four 15 cm tissue plates (430599, Corning). Every other day, 3 mL fresh DMEM containing CSF-1 (1:10000) was added in each plate for approximately 7 days. Expanded and differentiated BMDMs were detached in PBS using a cell scraper (833951, Sarstedt), neutralized in sufficient cell culture medium, harvested at 1300 rpm for 5 min, counted and seeded in tissue culture plates according to the experimental need.

3.2.1.3. Cell culture of murine embryonic stem cells

ES-E14TG2a cell line (E14, hereafter) was established, characterized and provided by Prof. Dr. Danny Nedialkova (Max-Planck-Institute of Biochemistry, Munich, Germany) and maintained under feeder-free conditions. Embryonic stem cells (ES) were cultivated on 0.1 % coated gelatin (G1393, Sigma-Aldrich) tissue culture plates in DMEM GlutaMAX (61965-059, Life Technologies) comprising of 15 % fetal bovine serum (FBS; 10270, Life Technologies), 0.1 mM β-mercaptoethanol (55 µmol/L; 41010-026, Life Technologies) and 1 % penicillin-streptomycin (P/S; 09-757F, Lonza) in humidified tissue culture incubators at 37 °C with 5 % CO₂. The FBS was filtered before using (0.22 µM; 833.941.001, Sarstedt). Additionally, fresh recombinant murine leukemia inhibitory factor (LIF; 10-20 ng/mL, MPIB Core Facility) was supplemented to the medium, which was changed daily to prevent the differentiation of ES cells. As previously

described for murine fibroblasts, the cells were not used for any experiment above passage 5 and tested for mycoplasma contamination, routinely. At 60 – 70 % confluency, ES cells were detached using 3 mL of 0.1 % Accutase (A1110501, Thermo Fisher) for 3 min at RT, neutralized in sufficient PBS, harvested at 1300 rpm for 5 min and seeded in tissue culture plates according cultivation (10 cm dish; 353003, Falcon) or experimental need. Cells were frozen in 10 % DMSO (12611S, CST) in FBS.

3.2.1.4. Cell culture of human cells

HeLa (CCL-2), HEK293T (CRL-3216), RS4;11 (CRL-1873) cells were purchased from the American Type Culture Collection (ATCC), cultured and maintained as described above with the exception of RSA4;11, which was cultured in RPMI media (21875034, Gibco) supplemented with 10 % FBS as described in Zeitler *et al.*⁴¹⁴.

3.2.2. Differentiation of murine embryonic stem cells

Embryoid body (EB) formation and murine ES-derived macrophage (ESDM) differentiation were performed according to the protocol published by Zhuang *et al.*⁴¹⁵ with minor adaptations. E14 cells (0.1×10^6 cells/well) were seeded in EB medium (10 % FBS (10270, Life Technologies), 1 % non-essential amino acids (11140050, Life Technologies), 1 % P/S (09-757F, Lonza), 0.5 % GlutaMAX (35050-061, Life Technologies), 1 mM sodium pyruvate (11360-070, Gibco), 0.1 mM β -mercaptoethanol (41010-026, Life Technologies) in Glasgow Modified Essential Medium (GMEM; 21710025, Life Technologies)), supplemented with 10 ng/mL recombinant murine interleukin 3 (IL-3, MPIB Core Facility) and 1:10000 CSF-1 (0.87 mg/mL; MPIB Core Facility) in a 6-well bacteriological plate (657185, Greiner) and incubated at 37 °C, 5 % CO₂ on an orbital shaker at 60 rpm (35929, Inotech) to form EBs. After 6 days, the medium was replaced. At day 8, the EBs were collected and per 6 well (around 15 EBs) seeded in EB medium in a 0.1 % gelatin (G1393, Sigma-Aldrich) coated plate (10 cm dish; 353003, Falcon). Three days later, the first batch of non-adherent macrophage progenitors were collected by washing with PBS and centrifugation at 1300 rpm for 5 min and seeded in ESDM differentiation medium (10 % FBS (10270, Life Technologies), 1 % P/S (09-757F, Lonza), 0.1 mM β -mercaptoethanol (41010-026, Life Technologies) in Roswell Park Memorial Institute (RPMI 1640, GlutaMAX 61870-010, Life Technologies)) supplemented with CSF-1 (1:10000) in a non-tissue culture 10 cm dish (633181, Greiner). Progenitors were harvested 4 times every 2-3 days. For following 8-10 days, macrophages were cultured in ESDM differentiation medium, thereby changing the medium every 4 days feeding additional CSF-1 (1:10000). Macrophages were harvested by scraping them in cold PBS. Each cell state was visualized by brightfield microscopy (Leica DM IL LED, Leica).

3.2.3. Generation and validation of genetically modified cell lines

3.2.3.1. Generation of single-cell-based biallelic gene-deficient cell lines using CRISPR/Cas9 engineering

The CRISPR/Cas9-mediated genome engineering technique was used to establish single-cell clones bearing biallelic loss-of-function of *Eif2ak4* or *Gcn1* in 3T3 and E14 cells. First, guide RNAs (gRNAs, hereafter) predicted to introduce high-score out of frame insertions and deletions (INDELS, hereafter) at the targeted locus were designed using the CRISPR Design tool (MIT, Prof. Dr. Feng Zhang) and correlated to references in literature. Then, the gRNAs individually cloned into a GFP-marked Cas9 containing vector (pSpCas9(BB)-2A-GFP (PX458); #48138, Addgene) and transiently transfected into 3T3 cells using Lipofectamine 3000 (L3000015, Thermo Fisher) or into E14 cells using nucleofection (P2 Primary Cell 4D-Nucleofector X Kit S; V4XP-2032, Lonza) (Section 3.2.4.). Next, GFP⁺ cells were sorted using the FACSaria III cytometer (Becton Dickinson) and expanded in culture. The bulk cell population was screened by Sanger sequencing (Mix2Seq, Eurofins) for out of frame INDELS in the engineered locus. Therefore, screening primers spanning the gRNAs were used to amplify the respective region and TOPO TA-cloned (pCR 2.1 TOPO TA vector; 451641, Thermo Fisher). Afterwards, the cells were manually single-cell-diluted in a 96-well tissue culture plate format (Section 3.4.4.; 655180, Greiner). By visual scoring, single clones were detected after about 10 days in culture, expanded and lysed for detecting the loss-of-function by immunoblotting (Section 3.6.2.). Finally, the *Eif2ak4* and *Gcn1* deficiency in each cell system was additionally confirmed by Sanger sequencing (Mix2Seq, Eurofins). Overall, the respective targeted coding locus, the used gRNAs and the screening primers for genetic validation are summarized in tables 1-4. The gRNAs were cloned as described in section 3.5.3.

Table 1: Mouse *Gcn1* locus modification: guides to target the 5' end of the *Gcn1* coding sequence

5' to 3' sequence	Nomenclature
CACCGGTGCAGGAGGTTCTTGGCGG	Oligo_F_gRNA1_mGcn1_exon4
AAACCCGCCAAGAACCTCCTGCACC	Oligo_R_gRNA1_mGcn1_exon4
CACCGAGGTTCTTGGCGGTGGCCTC	Oligo_F_gRNA2_mGcn1_exon4
AAACGAGGCCACCGCCAAGAACCTC	Oligo_R_gRNA2_mGcn1_exon4
CACCGGAGAGGCTGCGTCTCTAAAG	Oligo_F_gRNA3_mGcn1_exon4
AAACCTTTAGAGACGCAGCCTCTCC	Oligo_R_gRNA3_mGcn1_exon4

Table 2: Mouse *Gcn1* locus modification: sequencing primers to amplify the insertion site from 5' to 3'

5' to 3' sequence	Nomenclature
TAGATTCTGCCCTTCTTGTC	S_ <i>Gcn1</i> _exon4_F
GCAGTAAGAGACTCATTAC	S_ <i>Gcn1</i> _exon4_R

Table 3: Mouse *Eif2ak4* locus modification: guides to target the 5' end of the *Eif2ak4* coding sequence

5' to 3' sequence	Nomenclature
CACCGGCAAAGTAGCGGACGATATT	Oligo_F_gRNA1_m <i>Eif2ak4</i> _exon9
AAACAATATCGTCCGCTACTTTGCC	Oligo_R_gRNA1_m <i>Eif2ak4</i> _exon9
CACCGAGTAGCGGACGATATTTGGA	Oligo_F_gRNA2_m <i>Eif2ak4</i> _exon9
AAACTCCAAATATCGTCCGCTACTC	Oligo_R_gRNA2_m <i>Eif2ak4</i> _exon9
CACCGCTCCATTGTGATCGACATTC	Oligo_F_gRNA3_m <i>Eif2ak4</i> _exon9
AAACGAATGTGCATCACAATGGAGC	Oligo_R_gRNA3_m <i>Eif2ak4</i> _exon9

Table 4: Mouse *Eif2ak4* locus modification: sequencing primers to amplify the insertion site from 5' to 3'

5' to 3' sequence	Nomenclature
TGAAACACCAGCTAATGTCA	S_ <i>Eif2ak4</i> _exon9_F
GGAGTTGCTGTGTAGGTAAT	S_ <i>Eif2ak4</i> _exon9_R

3.2.3.2. Generation of bulk cell-based biallelic gene-deficient cell lines using lentivirus-mediated CRISPR/Cas9 engineering

The CRISPR/Cas9-mediated genome engineering technique was used to establish bulk cell populations bearing biallelic loss-of-function of *Atf4* and *Gcn1* in 3T3 cells. First, gRNAs were designed as previously described and cloned into pLentiGuide-Puro (#52963 Addgene). Next, high-titer lentivirus particles (Section 3.2.4.) were produced in HEK293T cells which were seeded in tissue culture plates (10 cm dish; 353003, Falcon) until 80 % confluency. In general, per transfected gRNA-construct one full 10 cm dish was needed. After transient transfection using Lipofectamine 3000 (L3000015, Thermo Fisher) and medium change 6 h later, the supernatant was centrifuged at 1200 rpm for 5 min on the next day, aliquoted into 500 μ L/tube and immediately frozen at - 80 °C. The second supernatant was collected 48 h later. 3T3-Cas9 cells (1.5×10^6 cells/well) were seeded in 12-well tissue culture plates (3513, Corning), infected in duplicates with 150 μ L first supernatant plus 8 μ g/mL polybrene (TR-1003-G, Sigma-Aldrich) and centrifuged at 1000xg for 2 h. On the next day, the cells were washed once with PBS (10010015, Life Technologies) detached with 0.25 % trypsin-EDTA (25200-056, Gibco) and seeded in 10 cm

tissue culture plates (353003, Falcon) kept for 7 days in culture under puromycin selection (1µg/mL, A1113802, Gibco). The ATF4 and GCN1 deficiency was screened by immunoblotting and additionally by Sanger Sequencing (Mix2Seq, Eurofins) as previously described. Overall, the respective targeted coding locus, the used gRNAs and the screening primers for genetic validation are summarized in tables 5-6. The gRNAs were cloned as described in section 3.5.3.

Table 5: Mouse *Atf4* locus modification: guides to target the 5' end of the *Atf4* coding sequence

5' to 3' sequence	Nomenclature
CACCGAGCATAGCCCCTCCACCTCC	Oligo_F_gRNA1_mAtf4_exon3
AAACGGAGGTGGAGGGGCTATGCTC	Oligo_R_gRNA1_mAtf4_exon3
CACCGGACAATCTGCCTTCTCCAGG	Oligo_F_gRNA2_mAtf4_exon3
AAACCCTGGAGAAGGCAGATTGTCC	Oligo_R_gRNA2_mAtf4_exon3

Table 6: Mouse *Atf4* locus modification: sequencing primers to amplify the insertion site from 5' to 3'

5' to 3' sequence	Nomenclature
GTAAAGGAGGAAGACACT	S_At4_exon3_F
CTTAACTCGCCAGTGAG	S_At4_exon3_R

3.2.3.3. Generation of single-cell-based biallelic point mutated cell lines using CRISPR/Cas9 engineering

The CRISPR/Cas9-mediated genome engineering technique (Section 3.5.3.) was used to establish single-cell clones bearing biallelic point mutations of *Eif2ak4* and *Eif2s1* in 3T3 cells. First, gRNAs targeting the respective coding region were designed, cloned and transfected in 3T3 cells as described above for the single-cell-based *Eif2ak4* and *Gcn1* deficient background. To mutate the autophosphorylation site of *Eif2ak4* (threonine 898/903 to alanine; mouse sites), a key residue in the catalytic site of *Eif2ak4* (aspartate 849 to asparagine; mouse site) and the inactivating phosphorylation site of *Eif2s1* (serine 52 to alanine; mouse site), a respective circular repair construct (made by complete gene synthesis in a minimal ampicillin-resistant vector) was co-transfected in a 1:1 ratio with the gRNA-construct (Section 3.2.4.). The inserted mutations are equivalent to the budding yeast ones reported in Scheuner *et al.* and Romano *et al.*^{67,416}. The following procedure of GFP⁺- cell sorting and single-cell-dilution were performed as already highlighted. Next, the expanded clones were screened by an allelic discrimination-based PCR mutation detection assay (Section 3.5.1.) and send for confirmation to Sanger sequencing (Mix2Seq, Eurofins). Overall, the respective targeted coding locus, the used gRNAs, the repair

construct sequence and the screening primers for genetic validation are summarized in table 7-15.

Table 7: Mouse *Eif2ak4* T898/903A locus modification: guides to target the 5' end of the *Eif2ak4* coding sequence

5' to 3' sequence	Nomenclature
CACCG CATGCCAGTCAAATGGCCTA	Oligo_F_gRNA1_mEif2ak4_exon18
AAACTAGGCCATTTGACTGGCATGC	Oligo_R_gRNA1_mEif2ak4_exon18
CACCG TCCTCCATAGGCCATTTGAC	Oligo_F_gRNA2_mEif2ak4_exon18
AAACGTCAAATGGCCTATGGAGGAC	Oligo_R_gRNA2_mEif2ak4_exon18
CACCGTATGTAAGCCCTGAGGTCCA	Oligo_F_gRNA3_mEif2ak4_exon18
AAACTGGACCTCAGGGCTTACATAC	Oligo_R_gRNA3_mEif2ak4_exon18
CACCGTGCTCTGTATGTAAGCCCTG	Oligo_F_gRNA4_mEif2ak4_exon18
AAACCAGGGCTTACATACAGAGCAC	Oligo_R_gRNA4_mEif2ak4_exon18

Table 8: Mouse *Eif2ak4* T898/903A locus modification: sequencing primers to amplify the insertion site from 5' to 3'

5' to 3' sequence	Nomenclature
TGAAACAGCAACACCAGGAA	S_Eif2ak4_exon18_F
TGGTTGTATGCAGACTTGGTG	S_Eif2ak4_exon18_R
HEX- CATTTGACTGGCATGGTTGG –ZEN	WT hybridization probe
FAM- CACCTAGCAGGTATGGTAGG –ZEN	Mutant hybridization probe

Table 9: Mouse *Eif2ak4* T898/903 locus modification: repair construct (generated by complete gene synthesis, IDT). Mutations to suppress further Cas9 activity are lower case within the upper case part of the sequence. The introduced point mutations (T898A; T903A) are shown in red.

5' to 3' sequence
CTCTTGAGCCACAGAGTGGAAGGAGACAATGAACTCCCACAAGTTGTCCTCTGACTCCCACATA CATGCCACAGCGTCCACACATCCACACAAATAAATAAATACTAGGAGTTAGGAGGAAGCCCTT TGGTTTTAAGTTTACTCTATCTGGAGCTAGGGGTGTAGCTCACTGCCCTCACCGGCATGCACAA GGCCCTGGGTTTCAGTACTGAGCACTGTGAAACAGCAACACCAGGAATAACTTAGTCCCTGGCTGA AATGCTTCCCTCCTTTCCTCCATAGGCCAccta gca GGtATGGTaGGT gca GCTTAcGTgtccCCaGAaGT CCAgGGAAGCACCAAGTCTGCATACAACCAGGTACAGTGTGTGTGTGTGTGTGTGTGTGTGTGTG TGTGTGTGTGTGGTGGGGTCTCAGAGTAAGTGACAAGTGTGACCATCAGGACTGTACCATGTA GGGTTTAGTGACCAGCTGAAGTAGGAACAGTCATTCTAGGCAGAGCATGCAGCAGTGCCCCAGG GCAGCAACGGAAGCTGGCATCGTTGCTGCAGAAGTTGGCAGTTCCTCTATCCATTAGGACTATGG GAGCTAGCCTCTATGCTGTTCCCTCCCCGTCAGGTACATAGGGAACAAGGCAGCCACCGGAG TAACAGCTGTGTACAGGAGGTCAGAGAGCTGACCCAGTGATGGCGAAACCCATGTTGAGCAGGA AGCAATGGAAGAGAAATGCCCTAAATTAGGATGAGGCCTGTGAAGAATGGAAGTGAAGTGAAGG CAGTAGTGGGGCCTGGCAGGCATTGAGAATTGCTTCTTCTGCTCTGGGCATTCAACTCTAAGGG CCTTGACATTCTAGGCGGTAAGTCCACCATC

Table 10: Mouse *Eif2ak4* D849N locus modification: guides to target the 5' end of the *Eif2ak4* coding sequence

5' to 3' sequence	Nomenclature
CACCGCAAAGTCACCTATTTTCACA	Oligo_F_gRNA1_mEif2ak4_exon16
AAACTGTGAAAATAGGTGACTTTGC	Oligo_R_gRNA1_mEif2ak4_exon16
CACCGGAATCCAAAAAATATTGAC	Oligo_F_gRNA2_mEif2ak4_exon16
AAACGTCAATATTTTTTTGGATTCC	Oligo_R_gRNA2_mEif2ak4_exon16
CACCGCGGTGTATCATCCCCTGT	Oligo_F_gRNA3_mEif2ak4_exon16
AAACACAGGGAATGATTCATCGCGC	Oligo_R_gRNA3_mEif2ak4_exon16

Table 11: Mouse *Eif2ak4* D849N locus modification: sequencing primers to amplify the insertion site from 5' to 3'

5' to 3' sequence	Nomenclature
CTGTGTGGGAAGAAGCAGTG	S_ Eif2ak4_exon16_F
CTCACAGTGAAGGCCAGATG	S_ Eif2ak4_exon16_R
HEX- CATCGCGACTTGAAGCCTG-ZEN	WT hybridization probe
FAM-CACCGAAACTTAAAACCAG-ZEN	Mutant hybridization probe

Table 12: Mouse *Eif2ak4* D849N locus modification: repair construct (generated by complete gene synthesis, IDT. Only the homologous region is shown). Mutations to suppress further Cas9 activity are lower case within the upper case part of the sequence. The introduced point mutation (D849N) is shown in red.

5' to 3' sequence
AGGCAAAACAGGGAGATGTCGGTGCAGCTGGAATGAGAGGACAAGTCCAGGAGTGTGGCAGGC AGAAGTAGTGCAAAGGAAAACGGCAGAGGAAGGAGAGTAGGGCCTGAGCAGAGCACAGGGAAA GCCAGCAGGAGTCTCTGGGGAGCCAGGGAGCAGAGCCTGGGGTTGCCCTGCTCAGGACCAC CAGCAGAGAGGTCAGAGGTCACAGGACGGACATTCCAGAGACCAGGAAGTCCATGGGAGAAGAC TCATCCAGTGGTCATCACAACCCTCTTCTTTAAAGTCGGGAAACAGAGTGCTGAGTTCTGTGTGG GAAGAAGCAGTGGATGGACTCTTCATTGTCTTCCAACAGGGgATGATaCAcCGaaACTTaAAaCCaG TaAAcATcTTcctaGAcagcGATGATCAcGTcAAtATcGGgGAtTTcGGCCTGGCAACAGACCATCTGGCCT TCACTGTGAGTTGTTTGTGGTTTGTGGTTTGTGGTTTGTGGTTTATTTAAATTAGGCTATGCCTGTAAAT GACTTGGGTACCTTAATAACCCTGGAAACACAGAGATGGGATAATGATCTCCTGTTCTCCTTCCAT GTCTTCCTCTACTGTGAGGCAAGCCTGAAGGGACAGTCTGCAAGTGTGTCTTAGGTTCTGAATCTT AGGGATGTAAAGTTATTGGTTTATGAACAATGTTTAGGTAAGGCATATGATGCTTTATGAAATAA TTTGGCAGTTGGGTCTCCTTACTGGGCATTTGACAAGCTCTTGCATCTGAGGAACTTTCCACTGGC TTGCAAAAAGTAAGTCTCAGTCCTGGACAAACACTGGCTCTGACACTACTGATTAGTTTAGCATACA GAGCTAATTAATGTGAGGGGTAAGAAACAGTGAGATGAGAGTA

Table 13: Mouse *Eif2s1* S52A locus modification: guides to target the 5' end of the *Eif2s1* coding sequence

5' to 3' sequence	Nomenclature
CACCGTATAGAACGGATACGTCGTC	Oligo_F_gRNA1_mEif2s1_exon2
AAACGACGACGTATCCGTTCTATAC	Oligo_R_gRNA1_mEif2s1_exon2
CACCGTTGGAATATAATAACATTGA	Oligo_F_gRNA2_mEif2s1_exon2
AAACTCAATGTTATTATATTCCAAC	Oligo_R_gRNA2_mEif2s1_exon2

Table 14: Mouse *Eif2s1* S52A locus modification: sequencing primers to amplify the insertion site from 5' to 3'

5' to 3' sequence	Nomenclature
GGGCCTATGTCAGCTTGTTG	S_Eif2s1_exon2_F
CTGCCAATTCGGATCAGTTT	S_Eif2s1_exon2_R
HEX-CGACGTATCCGTTCTATAAAC-ZEN	WT hybridization probe
FAM-CGCCGCATTCGATCCATTAAC-ZEN	Mutant hybridization probe

Table 15: Mouse *Eif2s1* S52A locus modification: repair construct (generated by complete gene synthesis, IDT). Mutations to suppress further Cas9 activity are lower case within the upper case part of the sequence. The introduced point mutation (S52A) is shown in red.

5' to 3' sequence
cgggctgttttcaaactcataatcctctgggtaagcctctagagtggtgatgtacatatatacacctagatgccctacttaagtggtaatattcaaatag tgtttaaccttgacatgttccttaaccttaggcctcacgtcactttatagatagtcattatTTTTAatagtttctctaaaagtgattgcctaagcatcaca aaaatatggagcatataaaaaactaaagttgagtcctgggtatccattttctgacttgtaagagatgagactaatatcaatgttactttgttctgttccttc attgtcagggtctacaacattgattatTTtagcttaacactttatTTTgtttgtaaattcagAATGCCGGGGCTAAGTTGTAGATTTT ATCAACACAAATTTCTGAGGTGGAAGATGTAGTGATGGTGAATGTAAGATCCATTGCTGAAATGG GGGCCTATGTCAGCTTGTGGAgTAcAAcAAATcGAgGGCATGATTCTTCTTAGTGAATTA gCC cgaC GcCGcATiCGaTcCAtAACAAACTGATCCGAATTGGCAGAAATGAATGTGTTGTTGTCATTAGAGTG GATAAAGAAAAAGgtaagtgaggaaaaatagttaagaaataaaactataaaaactaaagaatttctattttaaattgtttatttttaaagta tatattataaaaatacacctaataaaactactatactttgttagtttctgagctcaagagacaattaaagaaagaaggctcactcaaggatgagacttt actcacagggaaatctagcctctgaactgaatatcaaaaagaccctctaaagcatatttattaattgttcacaaaagttatTTTTggcttagtttctcat actaaaagaccctaataatgttctgaaggacatccctccttgcaactcagtcctattgggtactgtttggactgtttgcagtactcaataattcaa gatattcaggtgtgccagaactgactctgtgaccaaaagttacgcaaaagctgtaaagctccttcagacagacaactctgtagtaacagaaaa cactgttttctacaatgacttctcaagatcagagtactctagaaaactatttcattctactattacgtagatataatgattctactagaattctgtctaca taagttctttacatacaaaaatgtagagaagcacgtgggggctgaggacataaccagtcattaaatgcttgattacaagctggaagaggtga gtcaatccctgaaccatataaaaaggccaagtgtgatagcataggctgtagtcccgacaactctgggaaaggtggaaatctgggattccag ccagccagcctccta

3.2.3.4. Generation of single-cell-based biallelic insertion-modified cell lines using CRISPR/Cas9 engineering

The CRISPR/Cas9-mediated genome engineering technique was used to establish single-cell clones bearing biallelic insertion of mCherry or NanoLuc-PEST next to the first coding region of *Ddit3* (exon 3) in 3T3 cells. As described already above, the approach started with designing gRNAs targeting the coding locus of *Ddit3*, cloning the gRNAs in the GFP-marked Cas9 containing vector (pSpCas9(BB)-2A-GFP (PX458); #42230 Addgene) and transfecting the 3T3 cells with the gRNA-construct plus the repair construct coding for NanoLuc-PEST or mCherry using Lipofectamine 3000 (L3000015, Thermo Fisher). Next, the GFP⁺-cells were sorted and expanded in culture. Based on the theoretical principle that *Ddit3* is an amino acid starvation-induced gene, the *Ddit3*::mCherry bulk cells were leucine starved for 24 h and afterwards mCherry positive sorted by Flow cytometry. After cell-expansion, the cells were single-cell-diluted (Section 3.4.4.) and positive clones validated by Sanger sequencing (Mix2Seq, Eurofins). In case of the *Ddit3*::NanoLuc-PEST version, the bulk population was first single-cell-diluted and then leucine starved to read out positive clones by chemiluminescence (Section 3.4.2.). Overall, the respective targeted coding locus, the used gRNAs, the repair construct sequences and screening primers

for genetic validation are summarized in tables 16-19. The gRNAs were cloned as described in section 3.5.3.

Table 16: Mouse *Ddit3* modifications: guides to target the 5' end of the *Ddit3* coding sequence

5' to 3' sequence	Nomenclature
CACCgGCCATGACTGCACGTGGACC	Oligo_F_gRNA1_mDdit3_exon3
AAACGGTCCACGTGCAGTCATGGCC	Oligo_R_gRNA1_mDdit3_exon3
CACCgACCTGGTCCACGTGCAGTCA	Oligo_F_gRNA2_mDdit3_exon3
AAACTGACTGCACGTGGACCAGGTC	Oligo_R_gRNA2_mDdit3_exon3
CACCgTCAGCTGCCATGACTGCACG	Oligo_F_gRNA3_mDdit3_exon3
AAACCGTGCAGTCAGTGCAGCTAGC	Oligo_R_gRNA3_mDdit3_exon3

Table 17: Mouse *Ddit3* modifications: sequencing primers to amplify the insertion site from 5' to 3'

5' to 3' sequence	Nomenclature
TGGAATGTATGTCCTTTCCA	S_Ddit3_exon3_F
CTCTTGCCTATACTTGACAA	S_Ddit3_exon3_R

Table 18: Mouse *Ddit3* modifications: mCherry repair construct (generated by Gibson assembly). The mCherry coding region is indicated in red and the SV40 PolyA sequence is underlined.

5' to 3' sequence
<p> CCCGGAGAAAGCCTATCAGTTCACACCCATGCTGCCTGTGTGCCGTACCTGAGTCAGGTTTCCA GCAGCCACAGAAGGTGGCTCACATGGCCTGGACCTCCAGCTCCAGGAGAGCCAATGAATGCTGC TGGCCCCCAGACACTGAATTACATCCGTTTCAGGGTCTGGCCATGGTGTGCATGTGATCATCTG GACAACTTTTGAGAGTTGGATCTGGCAGGGTCAAAGTCAAGGCTGCTAGGCTTGAGAGGCAGCCA TCTCCCCATCCCGACACACCATCATTAGTGTGTGTGCAGGTCAGAGAACAACCTTGTGCGAGTTGA CTCTTCACCTCCACCCTCTGCCAATGTAGCCTTCAAGGAGTGACAACCCATGCCCTTACCTATCGT GCAAGACCAGTAAATTTTAAATTCTACGTGTTAGAAAAGGGACAAGGTCAGCTCACCGACTGTGGT GAATGGAATGTATGTCCTTTCCAGAACCTGGTCCACGTGCAGTCAATGGTGAGCAAGGGCGAGGA GGATAACATGGCCATCATCAAGGAGTTCATGCGCTTCAAGGTGCACATGGAGGGCTCCGTGAACG GCCACGAGTTCGAGATCGAGGGCGAGGGCGAGGGCCGCCCTACGAGGGCACCCAGACCGCCA AGCTGAAGGTGACCAAGGGTGGCCCCCTGCCCTTCGCCTGGGACATCCTGTCCCCTCAGTTCAT GTACGGCTCCAAGGCCTACGTGAAGCACCCCGCCGACATCCCCGACTACTTGAAGCTGTCCTTCC CCGAGGGCTTCAAGTGGGAGCGCGTGATGAACTTCGAGGACGGCGGCGTGGTGACCGTGACCC AGGACTCCTCCCTGCAGGACGGCGAGTTCATCTACAAGGTGAAGCTGCGCGGCACCAACTTCCC CTCCGACGGCCCCGTAATGCAGAAGAAGACCATGGGCTGGGAGGCCTCCTCCGAGCGGATGTAC CCCGAGGACGGCGCCCTGAAGGGCGAGATCAAGCAGAGGCTGAAGCTGAAGGACGGCGGCCAC TACGACGCTGAGGTCAAGACCACCTACAAGGCCAAGAAGCCCGTGCAGCTGCCCGGCGCCTACA ACGTCAACATCAAGTTGGACATCACCTCCACAACGAGGACTACACCATCGTGGAACAGTACGAA CGCGCCGAGGGCCGCCACTCCACCGGCGGCATGGACGAGCTGTACAAGTAA<u>TTGTTTATTGCAG</u> <u>CTTATAATGGTTACAAATAAAGCAATAGCATCACAAATTTACAAATAAAGCATT</u><u>TTTTTCACTGCAT</u> <u>TCTAGTTGTGGTTTGTCCAAACTCATCAATGTATCTTAGTGAGTGAGAATGCTGGTCTTAGGATGG</u> GCGAGCAGAGTGATGGTGTGGGTGCCTATAGCCCCAGTGCTTGTCAAGTATAGGCAAGAGGCTC AGTTCATGGCCAGCCTAAGCTAGAGTTTGAATGTAGCCTATACAAGACCCTGTCTCAAAAACCAAG CAAAAGTAAAACCCAGGAACTGGGGGTTTGTATGCCTCTCCTGAACTAATTAATATCTATCTCC CTTCTTCATTTCTTAAAGGAAGAATCAAAAACCTTCACTACTCTTGACCCTGCGTCCCTAGCTTG GCTGACAGAGGAGCCAGGGCCAACAGAGGTCACACGCACATCCCAAAGCCCTCGCTCTCCAGAT TCCAGTCAGAGTTCTATGGCCCAGGAGGAAGAGGAGGAAGAGCAAGGAAGAAGTAAAGGAAACGGA AACAGAGTGGTCAGTGCCAGCCCGGCCTGGGAAGCAACGCATGAAGGAGAAGGAGCAGGAGA ACGAGCGGAAAGTGGCACAGCTAGCTGAAGAGAACGAGCGG </p>

Table 19: Mouse *Ddit3* modifications: NanoLuc-PEST repair construct (generated by complete gene synthesis, IDT). The NanoLuc-PEST coding region is indicated in blue and the SV40 PolyA sequence is underlined.

5' to 3' sequence
<p>GAGCCCGGAGAAAGCCTATCAGTTCCACACCCATGCTGCCTGTGTGCCGTACCTGAGTCAGGTTT CCAGCAGCCACAGAAGGTGGCTCACATGGCCTGGACCTCCAGCTCCAGGAGAGCCAATGAATGC TGCTGGCCCCCAGACACTGAATTACATCCGTTTCAGGGTCCCTGGCCATGGTGTGCATGTGATCAT CTGGACAACTTTTGAGAGTTGGATCTGGCAGGGTCAAAGTCAAGGCTGCTAGGCTTGAGAGGCAG CCATCTCCCATCCCGACACACCATCATTAGTGTGTGTGCAGGTCAGAGAACAACCTTGTGCGAGT TGACTCTTCACCTCCACCCTCTGCCAATGTAGCCTTCAAGGAGTGACAACCCATGCCCTTACCTAT CGTGCAAGACCAGTAAATTTTAAATTCTACGTGTTAGAAAAGGGACAAGGTCAGCTCACCGACTGT GGTGAATGGAATGTATGTCCTTTCCAGAACCTGGTCCACGTGCAGTCATGGTCTTTCACACTCGAA GATTCGTTGGGGACTGGCGACAGACAGCCGGCTACAACCTGGACCAAGTCCTTGAACAGGGAG GTGTGTCCAGTTTGTTCAGAATCTCGGGGTGTCCGTAACCTCCGATCCAAAGGATTGTCCTGAGC GGTAAAATGGGCTGAAGATCGACATCCATGTCATCATCCCGTATGAAGGTCTGAGCGGCGACCA AATGGGCCAGATCGAAAAATTTTTAAGGTGGTGTACCCTGTGGATGATCATCACTTTAAGGTGAT CCTGCACTATGGCACACTGGTAATCGACGGGGTTACGCCGAACATGATCGACTATTTCCGACGGC CGTATGAAGGCATCGCCGTGTTTCGACGGCAAAAAGATCACTGTAACAGGGACCCTGTGGAACGG CAACAAAATTATCGACGAGCGCCTGATCAACCCCGACGGCTCCCTGCTGTTCCGAGTAACCATCA ACGGAGTGACCGGCTGGCGGCTGTGCGAACGCATTCTGGCGAATTCTCACGGCTTTCGCTGA GGTTGAAGAGCAAGCCGCGGTACATTGCCTATGTCCTGCGCACAAGAAAGCGGTATGGACCGG CACCCAGCCGCTTGTGCTTCAGCTCGCATCAACGTCTAA<u>TTGTTTATTGCAGCTTATAATGGTTAC</u> <u>AAATAAAGCAATAGCATCACAAATTTACAAATAAAGCATTTTTTTCACTGCATTCTAGTTGTGGTTT</u> <u>GTCCAAACTCATCAATGTATCTTAGTGAGTGAGAATGCTGGTCCTAGGATGGGCGAGCAGAGTGA</u> TGGTGTGGGTGCCTATAGCCCCAGTGCTTGTCAAGTATAGGCAAGAGGCTCAGTTCATGGCCAGC CTAAGCTAGAGTTTGAATGTAGCCTATACAAGACCCTGTCTCAAAAACCAAGCAAAAAGTAAAACCC CAGGAACTGGGGGTTTGTATGCCTCTCCTGAACATAATTAATATCTATCTCCCCTTCTTCATTTCT TAAAGGAAGAATCAAAAACCTTCACTACTCTTGACCCTGCGTCCCTAGCTTGGCTGACAGAGGAG CCAGGGCCAACAGAGGTCACACGCACATCCCAAAGCCCTCGCTCTCCAGATTCCAGTCAGAGTTC TATGGCCCAGGAGGAAGAGGAGGAAGAGCAAGGAAGAAGGAAACGGAACAGAGTGGTCAG TGCCCAGCCCGCCTGGGAAGCAACGCATGAAGGAGAAGGAGCAGGAGAACGAGCGGAAAGTG GCACAGCTAGCTG</p>

3.2.4. Transfection of cell lines

3.2.4.1. Transient transfection

3T3 cells were seeded to approximately 60 % confluency and transfected using Lipofectamine 3000 (L3000015, Thermo Fisher) according to the manufacturer's instructions. Different plasmid amounts were used to enable the highest transfection efficiency: 1 µg for a single construct

transfection or 1 µg in a ratio of 1:1 for a double construct transfection. For the Twin-Strep tagged GCN1 (provided by Dr. Fabien Boneau) the PiggyBac transposon system was used (Refs^{417,418}): 1.5 µg Twin-Strep-GCN1 and 0.3 µg PB-RN. Expression was induced by adding 1 µg/mL doxycycline (24390-14-5, Sigma-Aldrich) 4 h after transfection. Positive transfected cells were validated by Flow cytometry analysis, immunoblotting or immunofluorescence (Sections 3.4.5., 3.4.8 and 3.6.2). E14 cells were kept in culture for 2-3 passages in 0.22 µM sterile-filtered N2B27 medium (1 % N2 (17502048, Thermo Fisher), 1 % B27 (A3582801, Thermo Fisher), 0.5 % GlutaMAX (35050-061, Life Technologies), 0.1 mM β-mercaptoethanol (55 µmol/L; 41010-026, Life Technologies), 1 % penicillin-streptomycin (09-757F, Lonza) in 50 % DMEM/F12 (11320033, Thermo Fisher) and neurobasal medium (21103049, Thermo Fisher)) supplemented with LIF (2.2 µg/µL, MPIB Core Facility), 3 µM CHIR99021 (HY-10182, MCE) and 1 µM PD0325901 (HY-10254, MCE). The day before nucleofection, the cells were seeded (2x10⁶ cells/plate) in 10 cm tissue culture plates (353003, Falcon). Next, the Amaxa 40 –Nucleofector instructions for a single reaction in a 100 µL single nucleocuvette was conducted (AAF-1002B, Lonza): 1 µg gRNA-construct, 82 µL nucleofector solution and 18 µL supplement. After 48 h, the cells were processed for further validation by Flow cytometry (Section 3.4.8.).

3.2.4.2. Stable transfection

3T3 stable transfected cells were achieved by puromycin selection for about 7-10 days in culture until control cells were dead. The doses of puromycin (A113802, Gibco) varied based on the experimental setup: 1 µg/mL was used for lentivirus infected 3T3-Cas9 cells and 2-4 µg/mL for the Twin-Strep-GCN1 expressing cells. The gRNA construct range for lentiviral transfected 3T3-Cas9 cells was 1:2:4 (pLentiGuide-Puro+gRNA; pMD2.G (#12259, Addgene); psPax2 (#12260, Addgene). For the Twin-Strep-GCN1 expressing cells, the stable integration was achieved following the protocol in Yusa *et al.*⁴¹⁷ using the pCMV-hyPBBase system.

3.3. Nutrient deprivation

3.3.1. Fetal bovine serum dialysis

Fetal bovine serum (FBS; 10270, Life Technologies) was thawed and transferred into a 3.5 kDa cut-off thin dialysis membrane (D9527, Sigma-Aldrich). Therefore, one membrane was filled with about 300 mL FBS and surrounded by 2 L of 1x PBS (PBS; 10010015, Life Technologies) at 4°C while stirring. For three days in total, the PBS was exchanged daily. Dialyzed serum was filtered (0.22 µM; 833.941.001, Sarstedt), aliquoted and stored at - 80 °C. The performance of the dialyzed serum was monitored in *Ddit3::mCherry* cells (Section 3.4.2.) determining the mCherry intensity in the IncuCyte S3 system (EssenBioscience).

3.3.2. Amino acid starvation

The SILAC labeling version of Dulbecco's modified Eagle's medium (DMEM 9443, Sigma-Aldrich, lacking arginine, leucine and lysine) was supplemented with 5 % in-house prepared dialysed FBS (Section 3.3.1.), 3.5 g/L glucose (A2494001, Gibco) and 1 % penicillin-streptomycin (P/S; 09-757F, Lonza). Depending on the induced amino acid depletion (leucine, arginine or lysine) the medium was comprised of additional L-arginine HCl (0.084 g/L; 1689.3, Roth), L-Leucine (0.105 g/L; 1699.1, Roth) and/or L-Lysine HCl (0.146 g/L; 1700.1, Roth). Amino acid stocks were made up in 1 x PBS (10010015, Life Technologies). For E14 cells the starvation medium contained additional LIF (2.2 µg/µL, MPIB Core Facility), 0.5 % GlutaMAX (35050-061, Life Technologies) and 0.1 mM β-mercaptoethanol (55 µmol/L; 41010-026, Life Technologies). For depleting L-glutamine, the DMEM low glucose without amino acid powder from Usbio (D980013) was made up as manufacturer's instructions. In addition, 5 % in-house prepared dialysed FBS, 3.5 g/L glucose (A2494001, Gibco) and 1 % penicillin-streptomycin (P/S; 09-757F, Lonza) were supplemented as well. The following amino acids were added: L-arginine HCl (0.084 g/L), L-cystine 2HCl (0.063 g/L), glycine (0.03 g/L), L-histidine HCl H₂O (0.042 g/L), L-isoleucine (0.105 g/L), L-Leucine (0.105 g/L), L-Lysine HCl (0.146 g/L), L-methionine (0.03 g/L), L-phenylalanine (0.066 g/L), L-serine (0.042 g/L), L-threonine (0.095 g/L), L-tryptophan (0.016 g/L), L-tyrosine (0.072 g/L) and L-valine (0.094 g/L). Amino acid stocks were made in 1 x PBS, except glutamate, which was prepared in 1 M HCl. After aspirating the cell culture medium, the 60-70 % confluent seeded adherent cells were washed three times with 1x PBS (10010015, Life Technologies) and amino acid starvation medium was added according to the appropriate volume indicated by the used tissue culture plate format. Depending on the experimental purpose amino acid starvation was performed for different timeframes and with drug addition (Section 3.3.4.). In case of 'adding back' amino acid(s) to the deprived cells, the used starvation medium was aspirated, the cells twice washed in PBS and the respective cell culture medium (containing the supplemented amino acid(s)) incubated for 1 h at 37 °C with 5 % CO₂ before proceeding.

3.3.3. Asparaginase treatment

Asparagine depletion was induced by recombinant bacterial asparaginase (Elspar, for injection, obtained originally from the St. Jude Children's Research Hospital pharmacy, aliquoted in 5 µL and frozen at -80 °C) treatment (1.5 U/mL) in RS4;11 cells. The cells were cultivated and prepared as indicated in sections 3.2.1.4. and 3.3.2.

3.3.4. Drug treatment

If not further mentioned, drug treatment was performed at the same time as starvation was applied to the cells. All used drugs in this thesis were made in DMSO (12611S, CST) (Table 20). The used drug concentrations are indicated in the respective figure legend. The compounds for the inhibitor screen were provided by the Max-Planck-Gesellschaft Lead Discovery Center in Dortmund and are listed in table 32.

Table 20: Used drugs in combination with amino acid starvation

Drug	Supplier
Anisomycin	A9789, Sigma-Aldrich
BSO	B2515, Sigma-Aldrich
Cycloheximide	C7698, Sigma-Aldrich
Erastin	S7242, Selleckchem
Ferrostatin-1	S7243, Selleckchem
Insulin solution human	I9278, Sigma-Aldrich
ISRIB	SML0843, Sigma-Aldrich
JR-AB2-011	HY-122022, MedChemExpress
Puromycin	P8833, Sigma-Aldrich
Rapamycin	553210, Calbiochem
RSL3	S8155, Selleckchem
Sodium meta arsenite	S7400, Sigma-Aldrich
Thapsigargin	586005, Merck
Torin-1	14379S, CST
Torin-2	SML1224, Sigma-Aldrich

3.4. Cell biology-based methods

3.4.1. Cell death analysis using CellTox staining

Cell death was monitored by live-cell phase-contrast microscopy (IncuCyte S3, EssenBioscience) over time by reading out the green fluorometric channel (green object intensity/image). 3T3 cells were seeded to 60 % confluency in tissue culture plates (96-, 48- or 12-well format) and treated with CellTox™ Green reagent (1:2000, G8741, Promega) the next day. For tracking ferroptosis, 5 µM erastin (S7242, Selleckchem), 1 µM RSL3 (S8155, Selleckchem) and/or 5 µM Ferrostatin-1 (S7243, Selleckchem) were used. Several technical and experimental replicates were conducted every time. Images were taken at 10 x objective and the following mask was applied to each image using a not stained one as control: filter area 40 (min, max), mean intensity 45 (min, max), radius 100 µM and edge split on.

3.4.2. Amino acid starvation-based *Ddit3* induction assay

mCherry induction was monitored by live-cell phase-contrast microscopy (IncuCyte S3, EssenBioscience) over time by reading out the red fluorometric channel (red object intensity/image). The *Ddit3*:mCherry cells and/or their *GCN2*^{-/-} counterpart were seeded in 96-well (92696TPP, TPP), 48-well (3548, Corning) or 12-well tissue culture plate format (3513, Corning) to reach a 60% confluency on the next day. The cells were treated according to their experimental purpose. Wild-type 3T3 cells were used as negative control. Several technical and experimental replicates were conducted every time. Images were taken at 10 x objective and the following mask was applied to each image overlaying mCherry⁺ to mCherry⁻ intensity: 0.1 RCU. Nano-Luciferase induction was tracked by measuring the luminescence with an integration time of 1 s in a Tecan plate reader (Infinite 200 PRO, Tecan). The assay procedure is based on the manufacturer's instructions using the Nano-Glo Dual Luciferase reporter assay kit (REF N1610 Promega). The cellular luminescence intensity was monitored in white opaque 96 flat bottom tissue culture plates (353296; Falcon). The 3T3 *Ddit3*:NanoLuc-PEST cells were seeded in triplicates per treatment condition in a 96-well tissue culture format (92696TPP, TPP) to reach a 60 % confluency on the next day. The cells were treated according to their experimental purpose. 3T3 cells functioned as negative control.

3.4.3. Mitochondrial respiratory and glycolysis flux assay

To determine the cellular mitochondrial respiratory and glycolysis capacity the oxygen consumption rates and extracellular acidification rates were measured in a Seahorse XF8 Analyzer (Agilent). The performed assay based on the manufacturer's instructions following the protocol for the Seahorse XFp Cell Mito Stress Test Kit (103010-100, Agilent). The used XF Assay medium was supplemented with provided reagents of XF 100 mM pyruvate (1 mM), XF 200 mM glutamine (2 mM) and XF 1.0 M glucose solutions (10 mM). For 3T3 cells, 0.01x10⁶ cells/well in triplicates were seeded in XF8 cell culture microplates (103022-100, Agilent). For BMDMs, 0.04x10⁶ cells/well in triplicates were used. The FCCP was adjusted based on the assayed cell type: 1 μM FCCP for 3T3 and 2 μM FCCP for BMDMs. Two wells on each XF8 cell culture microplate functioned as background controls. Data were normalized to protein amount. Therefore, the assayed XF8 cell culture microplate (medium was aspirated) was stored at - 80 °C immediately after the Seahorse run was performed and thawed on ice for 30 min prior to protein lysis (RIPA buffer 10 μL/well). The protein amount/well was determined performing a BCA assay (Section 3.6.1.). BMDMs were generated from 20-30 week old mice (WT and *GCN2*^{-/-}) and maintained in the presence of 1:10000 CSF-1 (0.87 mg/mL, MPIB Core Facility). In a 6-well-format, 2x10⁶ cells/well were seeded and treated on the next day with 10 ng/mL IL4 and IL13

(MPIB Core Facility) or 5 ng/mL LPS (L439, Sigma-Aldrich) for a 48 h stimulation duration. Before seeding onto the XF8 cell culture microplates, the LPS was removed via several PBS washes.

3.4.4. Single-cell-dilution

Single clones were grown in their respective growth medium supplemented with 20 % FBS (10270, Life Technologies). In total, 0.01×10^6 cells in 1 mL medium were diluted separately in 10 mL medium as followed: 6 μ L (dilution 1), 12 μ L (dilution 2) and 18 μ L (dilution 3). Each dilution was prepared three times and 100 μ L/well distributed in a 96-well flat bottom tissue cell culture plate (92696TPP, TPP). Additional, 100 μ L medium were added and the cells grown for about 7-10 days at 37 °C, 5 % CO₂. Single clones were visually scored by brightfield microscopy (Leica DM IL LED, Leica) or in the live-cell imager (IncuCyteS3, EssenBioscience). For 3T3 cells, the single-cell-dilution was performed manually as described. For E14 cells, 1 cell/96-well was sorted by Flow cytometry directly in the tissue culture plate (coated with 0.1 % gelatin (G1393, Sigma-Aldrich) in PBS) using the FACSAriaIII cell sorter (Becton Dickinson).

3.4.5. Immunofluorescence assay

3T3 cells (0.02×10^6 cells/well) were cultured on 8-chamber glass bottom slides (80827, IBIDI) for 24 h and treated in quadruplicates based on their experimental purpose on the next day. In case, an overexpressed protein was analyzed, the cells were transiently transfected in a 6-well tissue culture format (657160, Corning), as previously described in section 3.2.4. The cells were fixed in 37 °C preheated 4 % PFA (P6148, Sigma-Aldrich) in PBS (10010015; Life Technologies) for 10 min at RT, washed gently three times in PBS and permeabilized in 3 % BSA (A2059; Sigma-Aldrich), 0.2 % Triton X-100 (9002-93-1, Sigma-Aldrich) in PBS for 2 h at RT. After several PBS washes, the added primary antibody was diluted 1:500 in 3 % BSA in PBS and incubated overnight at 4 °C. On the next day, the cells were washed again three times in PBS and secondary antibody (1:1000) in 3 % BSA in PBS was added for 2 h at RT. Afterwards, the cells were washed again (3x PBS wash) and nuclei stained with 0.1 μ g/mL DAPI in PBS (1:20000; 10236276001, Sigma-Aldrich) for 15 min at RT. After PBS wash, the cells were mounted using VECTASHIELD Antifade Mounting medium (H-1200-10, Vector laboratories) or covered with PBS before imaging on a Zeiss confocal microscope (CF1 Zeiss LSM 780) with a 20 x / 63 x immersion objective (Zeiss). Images were analyzed using ImageJ version 1.46. The following primary antibodies were used: Nanog (#ab80892, abcam), Oct-3/4 (#sc-5279, Santa Cruz), FLAG (#F1804, Sigma-Aldrich), StrepMAB-classic (#0043, iba), GCN1L1 (#LS-C288620, LSBio). The following secondary antibodies were used: Alexa Fluor 488 goat anti-mouse IgG (H+L) (#A11029, Thermo

Fisher Scientific) and Alexa Fluor 633 goat anti-rabbit IgG (H+L) (#A21071, Thermo Fisher Scientific).

3.4.6. Nascent protein synthesis detection assay

The Click.iT Plus OPP Protein Synthesis assay (C1045, Life Technologies) was used to quantify newly synthesized protein levels. This method is based on detecting protein synthesis by a fluorimetric click reaction between a translation inhibitor OPP (alkyne moiety) and an Alexa Fluor 488 dye (picolyl azide moiety). The manufacturer's instructions were followed with minor adaptations: 0.01×10^6 cells/well were seeded in a 96-well tissue culture plate (92696, TPP) the day before the assay and 2 μ M OPP was used. The fluorescence read-out (λ_{ex} 495 nm, λ_{em} 519 nm, 1 nm stepwidth) was performed in a CLARIOstar Plus microplate reader (BMG Labtech). DNA was stained using a HCS NuclearMask Blue dye (λ_{ex} 350 nm, λ_{em} 451 nm, 1 nm stepwidth) for normalization. The translation elongation inhibitor cycloheximide (1 μ M CHX; 39765, Sigma- Aldrich) was used as control. Protein synthesis was also screened by immunoblotting. Therefore, 1 μ g/mL puromycin (P8833, Sigma-Aldrich) was added 10 min before cell lysis. The membrane was imaged using anti-puromycin clone12D10 (#MABE 343, Millipore) as primary antibody.

3.4.7. Phospho-Flow cytometry analysis

3T3 cells were seeded in duplicates onto 6-well tissue culture (657160, Greiner) plates at a density of 0.5×10^6 cells/well. On the next day, the cells were treated with the indicated starvation medium for a certain time, washed once with 1x PBS (10010015, Life Technologies), removed from the plates using 0.25 % trypsin (25200-056, Gibco) and neutralized in the indicated starvation medium. Afterwards, the cells were pelleted at 300xg for 5 min, permeabilized at 37 °C for 10 min in prewarmed fresh 4 % paraformaldehyde (PFA; P6148, Sigma-Aldrich) in PBS, washed once with 1x PBS and fixed in 100 % methanol (34860, Sigma-Aldrich) overnight at - 20 °C. Then, methanol was removed by several washing steps in 1x PBS and 1 % FBS (10270, Life Technologies) in PBS at 450xg for 5 min. Finally, the pelleted cells were stained with isotype control (100 μ g/mL) and phospho-antibody (50 μ g/mL) in a volume of 100 μ L and kept for 1h at RT in the dark before proceeding to Flow cytometry analysis. The phospho-specific antibodies were purchased from CST and were used single-stained: phospho-S6 ribosomal protein (Ser235/236) (D57.2.2E) XP® rabbit mAb (PE conjugate) #5316; phospho-4EBP1 (Thr37/46) (236B4) rabbit mAb (Alexa Fluor® 647 conjugate) #5123; rabbit (DA1E) mAb IgG XP® isotype control (PE conjugate) #5742; rabbit (DA1E) mAb IgG XP® isotype control (Alexa Fluor® 647 conjugate) #2985. If necessary, cells were passed through an appropriate filter (50 μ M CellTrics,

04-0042-2317, Sysmex) to remove cell aggregates. Flow cytometry analysis was performed using 'singlets' by reading out the PE and APC intensity (566 nm and 651 nm laser excitation) (Section 3.4.8.).

3.4.8. Fluorescence activated cell sorting and analysis

A FACSAriaIII cell sorter (Becton Dickinson) was used for bulk and single-cell population sorting at a flowrate of 1 event/second. The neutral density (ND) filter and nozzle size was the same for fibroblasts and ES cells: 100 μ M nozzle and 1.5 FSC ND filter. For phospho-specific antibody, or mCherry-based flow cytometric analyses, a LSR Fortessa cell analyzer (Becton Dickinson) was utilized. If not further indicated, cells were filtered (50 μ M CellTrics, 04-0042-23-17, Sysmex) and kept in 1 % FBS (10270, Life Technologies) in 1x PBS (10010015, Life Technologies). GFP, FITC, CFSE, Alexa Fluor 488 and PI were detected using the blue laser (λ_{ex} 488 nm). The fluorochrome mCherry and PE was excited at 561 nm. APC-stained cells were analyzed at 660 nm (λ_{ex} 651 nm). Flow Cytometry data were analyzed using FlowJo version 10.4.2 (Becton Dickinson).

3.5. Nucleic acid-based methods

3.5.1. Allelic discrimination-based Polymerase Chain Reaction

To quantify the copy of specific alleles a TaqMan-based PCR approach was used which enabled the detection of point mutations. First, PCR across the mutated region (about 150-200 bp) was optimized using SYBR Green qPCR (1725150, Biorad) in a CFX96 Touch Deep Well Real-Time PCR System (Biorad). Specific screening primers for the amplification of the mutated locus were used (Tables 8, 11, and 14). Second, probe-labeled TaqMan probes flanking the mutation region were designed to bind to the wild-type (control) or mutant DNA at the same site and labeled with FAM or HEX, respectively, at the 5' end, and ZEN at the 3' end (synthesized by IDT, Tables 8, 11, and 14). Genomic DNA (gDNA) was isolated from wild-type cells, the bulk population and each single clone. To perform allelic discrimination-based PCR, gDNA was amplified with the screening primers in the presence of an equimolar amount of each FAM and HEX labeled TaqMan primers diluted in addition with the SsoAdvanced™ Universal Probes Supermix (dNTPs, Sso7d fusion polymerase, MgCl₂, stabilizers, ROX normalization dyes 172-5280, Biorad) (Table 21). Controls included each probe alone, repair plasmid, bulk population, water and wild-type gDNA with the FAM and HEX labeled probes (of which only the FAM primer will elicit signal upon 5' dye cleavage). After amplification of triplicate gDNAs (10 ng and 25 ng), the FAM or HEX signal was independently analyzed to determine wild-type (FAM), heterozygosity (FAM and HEX) or biallelic mutation (HEX, HEX). To confirm the mutations of interest, the targeted region was TOPO TA-cloned (pCR 2.1 TOPO TA vector; 451641, Thermo Fisher) and Sanger sequenced (Mix2Seq,

Eurofins). The PCR was run in a CFX96 Touch Deep Well Real-Time PCR System (Biorad) (Table 22).

Table 21: Allelic discrimination-based PCR: reaction setup

Component	Volume/reaction	Final concentration or amount
Distilled MilliQ water	up to 10 μ L	-
Forward primer*	0.25 μ L	2.5 μ M
Reverse primer*	0.25 μ L	2.5 μ M
WT hybridization probe	0.06 μ L	0.6 μ M
Mutant hybridization probe	0.06 μ L	0.6 μ M
SsoAdvanced™ Universal Probes Supermix	5 μ L	2x
gDNA	X	10 or 25 ng

*Primers indicated in tables 8, 11 and 14.

Table 22: Allelic discrimination-based PCR: Cycling protocol

Step	Time	Temperature
PCR initial activation	2 min	50 °C
Denaturation	10 min	95 °C
	15 s	95 °C
Annealing/Extension	1 min	60 °C
Number of Cycles: 39	-	-

3.5.2. RNA isolation, cDNA synthesis and quantitative real-time PCR

Total RNA was isolated using TriFast peqGold reagent (30-2010, VWR). Cells (0.5×10^6 cells/well) were plated in triplicates per treatment condition in a 12-well cell culture format (3513, Corning) the day before. After treating the cells for their experimental purpose, the cells were dissolved in 1 mL/well TriFast peqGold reagent (30-2010, VWR) on ice and transferred in a precooled tube. In total, 200 μ L 100 % chloroform (C2432, Sigma-Aldrich) was added to the tube, mixed and centrifuged for 10 min, 4 °C at maximal speed. The RNA (400 μ L) was separated (upper phase) from the organic phase, added to a new precooled tube containing 500 μ L 100 % isopropanol (W292907, Sigma-Aldrich), mixed, incubated 10 min on ice and centrifuged again for 10 min, 4°C at maximal speed. After decanting the isopropanol, the RNA was washed once with 200 μ L 70 % ethanol (32205-M, Sigma-Aldrich) and air-dried for 3 min. At last, 25 μ L distilled MilliQ water was added and the tube stored overnight at - 80 °C to ensure optimal solubility. The RNA concentration was determined using a NanoPhotometer® P330 (IMPLEN). In total, 500 ng RNA was reverse transcribed to cDNA. Therefore, 0.4 μ L Oligo(dT)₁₂₋₁₈ (0.5 μ g/ μ L, 18418012, Thermo Fisher) and

0.06 μL random hexamer (50 μM , N8080127, Thermo Fisher) were added to the template, filled up with distilled MilliQ water to 11 μL total and heated for 10 min at 65 $^{\circ}\text{C}$. After 10 min at 4 $^{\circ}\text{C}$, 4 μL 5x buffer (250 mM Tris-HCl pH8.3, 375 mM KCl, 15 mM MgCl_2), 2 μL DTT (100 mM), 0.5 μL dNTP (10 mM) and 0.25 μL SuperScript II reverse transcriptase (200 U/ μL ; 18064022, Thermo Fisher) were supplied and incubated for 2 h at 42 $^{\circ}\text{C}$. Gene expression was analyzed by real-time quantitative PCR (RT-qPCR). Therefore, 100 ng of synthesized cDNA was used as template. GAPDH functioned as control which contained a TaqMan probe labelled with FAM at the 5' end (4333764F, Applied Biosystem). The respective genes were tagged with a SYBR Green probe. Except for mCherry (Table 27), all genes were set up in a SYBR Green-based RT-qPCR QuantiTect primer assay (Qiagen): Mm_Ddit3_2_SG (QT01749748); Mm_ATF4_1_SG (QT00096033) and Mm_eif2ak4_1_SG (QT00138677). The reaction setups and the cycling protocols are summarized in tables 23-26, 28 and 29. The relative gene expression was calculated by the $\Delta\Delta\text{C}_q$ method⁴¹⁹. Data were normalized to the untreated control.

Table 23: *Atf4*, *Eif2ak4* and *Ddit3* expression: Reaction setup

Component	Volume/reaction	Final concentration or amount
Distilled MilliQ water	up to 10 μL	-
SYBR Green	5 μL	1 μM
10x QuantiTect primer	1.25 μL	10 μM
cDNA	x	100 ng

Table 24: *Atf4*, *Eif2ak4* and *Ddit3* expression: Cycling protocol

Step	Time	Temperature
PCR initial activation	30 s	95 $^{\circ}\text{C}$
Denaturation	10 s	95 $^{\circ}\text{C}$
Annealing/Extension	30 s	60 $^{\circ}\text{C}$
Number of Cycles: 40	-	-

Table 25: *GAPDH* expression: Reaction setup

Component	Volume/reaction	Final concentration or amount
Distilled MilliQ water	up to 10 μL	-
TaqMan	5 μL	1 μM
Primer	0.5 μL	10 μM
cDNA	x	100 ng

Table 26: GAPDH expression: Cycling protocol

Step	Time	Temperature
PCR initial activation	2 min	50 °C
	2 min	95 °C
Denaturation	3 s	95 °C
Annealing/Extension	30 s	60 °C
Number of Cycles: 39	-	-

Table 27: mCherry expression: Primers to amplify the mCherry locus

5' to 3' sequence	Nomenclature
AAGCTGAAGGTGACCAAGGG	mCherryQuant_F
CAAGTAGTCGGGGATGTCGG	mCherryQuant_R
FAM-GGCCTACGTGAAGCACCCCG-TAMRA	mCherry Quant_INT

Table 28: mCherry expression: Reaction setup

Component	Volume/reaction	Final concentration or amount
Distilled MilliQ water	up to 20 µL	-
TaqMan	12.5 µL	1 µM
mCherryQuant_F	0.2 µL	10 µM
mCherryQuant_R	0.2 µL	10 µM
mCherryQuant_INT	0.1 µL	1:200
cDNA	x	100 ng

Table 29: mCherry expression: Cycling protocol

Step	Time	Temperature
PCR initial activation	10 min	95 °C
Denaturation	15 s	95 °C
Annealing/Extension	1 min	60 °C
Number of Cycles: 39	-	-

3.5.3. CRISPR/Cas9 genome engineering plasmid preparation

The designed oligonucleotides (Tables 1, 3, 5, 7, 10, 13 and 16) were annealed and phosphorylated using the following program parameters in a CFX96 Touch Deep Well Real-Time PCR System (Biorad): Step1: 37°C 30 min; Step2: 95 °C 5 min ramp down to 25 °C at 5 °C/min. This was conducted in a total volume of 10 µL containing 1 µL of each oligonucleotide (100 µM), 1 µL 10x T4 ligation buffer (M0202S, NEB) and 0.5 µL T4 polynucleotide kinase (10 U/µL; M0201S, NEB). Next, 50 ng of the respective linearized vector (pSpCas9(BB)-2A-GFP (PX458)

#42230 Addgene; BbsI or pLentiGuide-Puro #52963 Addgene; BstBI) was ligated with the annealed and phosphorylated oligonucleotides (2 μ L) in a 20 μ L total reaction using 1 μ L T4 Ligase (400 U/ μ L; M0202S, NEB) in 10x T4 ligase buffer (M0202S, NEB) for 10 min at RT followed by 10 min at 65 °C. Finally, the ligated construct was transformed into chemically competent *E. coli* cells (Mach1; C862003, Thermo Fisher) and Sanger sequenced (Mix2Seq, Eurofins).

3.5.4. Polysome profiling

Cells (2×10^6 cells/mL) were seeded in 15 cm tissue culture plates (430599, Corning) to 80 % confluency. Next, the medium was changed and the cells treated with leucine depletion (Section 3.3.2.) for 8 h and/or normal growth medium before adding 100 μ g/mL cycloheximide (1 μ M CHX; 39765, Sigma-Aldrich) for 20 min. At 4 °C, the cells were rinsed once with 1 x PBS (PBS; 10010015, Life Technologies), scraped in PBS, centrifuged for 2 min at 800xg and the cell pellet lysed in 250 μ l lysis buffer (10 mM HEPES (15630106; Sigma-Aldrich) pH 7.9; 10 mM KCl (P9541; Sigma-Aldrich), 1.5 mM MgCl₂ (M8266; Sigma-Aldrich)). After incubation for 10 min, the lysate was centrifuged for 5 min at 250xg, resuspended again in lysis buffer and mechanically lysed in a glass homogenizer (T2690; Sigma-Aldrich). Next, the lysate was centrifuged for 10 min at 1000xg and 10 μ l 4 M KCl (P9541; Sigma-Aldrich) plus 10 μ l EDTA-free protease inhibitor cocktail (5056489001, Roche Diagnostics) was added. In total, 200 mg of total RNA were run through 10 % (w/v) - 40% (w/v) sucrose gradients (20 mM HEPES (15630106; Sigma-Aldrich), 100 mM NaCl (S9888, Sigma-Aldrich) and 10 mM MgOAc (M5661, Sigma-Aldrich); in 12 mL Seton tubes; 7031) using Beckman Coulter SW40 Ti rotor at 40000xg for 2 h at 4 °C (Beckman Optima XPN-80; A95765, Beckman). Finally, the gradients were fractionated using a Biocomp piston gradient fractionator (Biocomp gradient station with a TRiAX full spectrum flow cell, 4160373, Biocomp) and the absorbance was recorded at 260 nm. The fractions were run on 4–15 % Criterion TGX Stain-Free protein gels (5678084, Bio-Rad) for immunoblotting and the membrane blocked for the following primary antibodies: GCN2 (1:800; #3302, CST), GCN1L1 (1:2000; #LS-C288620, LSBio) and RPL8 (1:1000; #ab169538, abcam).

3.6. Protein-based methods

3.6.1. Protein lysis and protein amount determination

Cells (0.25×10^6 cells/well) were seeded the day before in a 12-well tissue culture plate format (3513, Corning) and treated according to their experimental purpose, unless indicated differently. After aspirating the cell culture medium, cells were washed quickly in ice-cold 1x PBS (10010015, Life Technologies) and lysed in 100 μ L/well 1x RIPA lysis buffer (50 mM Tris-HCl pH 8.0 (T1503; Sigma-Aldrich), 150 mM NaCl (7647-14-5, VWR), 1 % NP-40 (127087-87-0, Sigma-Aldrich),

0.5 % SDC (D6750, Sigma-Aldrich), 0.1 % SDS (CN30.1, Roth)). The lysis buffer was always prepared fresh with the addition of the protease + phosphatase inhibitor cocktail (supplied as a 100x stock; 78440, Thermo Scientific). After 1 min incubation on ice, the cells were scratched mechanically from the plate using the inner part of a luer syringe (303172; Becton Dickinson), the homogenate transferred quickly in a pre-cooled tube and centrifuged at 4 °C for 10 min at maximal speed (127500 rpm). The pellet was discarded and the supernatant (cytosolic fraction) was frozen at - 80 °C. Protein concentrations were quantified using Pierce BCA Protein Assay Kit (23225, Thermo Fisher Scientific) according to the manufacturer's instructions and the fluorescence was measured in a Tecan plate reader (Infinite 200 PRO, Tecan). In total, 10 µL of each protein extract was used to determine the protein amount and divided into two equal biological replicates. BSA was diluted in lysis buffer and used as the reference control. Adjustments towards the lysis procedure are separately described in the different methodical sections. In case of studying phosphoproteins, the cell lysates were always used once for their experimental purpose.

3.6.2. Immunoblotting

In total, 30 µg of each cell lysate was diluted with 6 x protein loading dye (375 mM Tris-HCl pH 6.8 (T1503, Sigma-Aldrich), 416.13 mM SDS (CN30.1, Roth), 60 % glycerol (G5516; Sigma-Aldrich), a tip of bromophenol blue (B0126; Sigma-Aldrich) in water; fresh 5 % β-mercaptoethanol (M7522; Sigma-Aldrich)) and heated for 5 min at 95 °C. Precision Plus Protein™ Dual Color Standard (1610374, Biorad) or Novex™ Sharp Pre-stained Protein Standard (LC5800, Thermo Scientific) was used as protein ladders. Proteins were separated on 4–15 % Criterion TGX Stain-Free protein gels (5678085 or 5678084, Bio-Rad) using Tris/glycine buffer (25 mM Tris (T1503, Sigma-Aldrich), 190 mM glycine (G8790, Sigma-Aldrich), 1 % SDS (CN30.1, Roth)) in a Criterion Vertical Electrophoresis Cell (Bio-Rad) at 130 V. Proteins were transferred to 0.2 µm nitrocellulose membrane (10600001, Amersham) using 1x transfer buffer (25 mM Tris (T1503, Sigma-Aldrich), 190 mM glycine (G8790, Sigma-Aldrich), 10 % methanol (34860, Sigma-Aldrich)) in a Criterion Blotter (Bio-Rad) for 2.5 h at 40 V. To confirm proper transfer, the membrane was incubated for 30 sec with Ponceau S Solution (09189, Sigma-Aldrich) and rinsed with distilled MilliQ water afterwards. Then, the membrane was blocked for 1 h in TBS (20 mM Tris pH 7.5 (T1503, Sigma-Aldrich), 150 mM NaCl (7647-14-5, VWR)) or PBS (10010015, Life Technologies) containing 0.01 % Tween 20 (TBST; P1379; Sigma-Aldrich) and milk (170-6404, Roth) or BSA (A2059; Sigma-Aldrich) based on the used primary antibody. Primary antibody was incubated overnight at 4 °C in blocking buffer. On the next day, the membrane was washed with 1x TBST and incubated for 1 h at RT in 3 % milk in TBST with secondary antibody (1:3000) against goat-anti-rabbit IgG peroxidase or goat-anti-mouse IgG peroxidase (#111-035-003 or #115-035-003,

Jackson ImmunoResearch). Subsequently, the membrane was washed with TBST and distilled MilliQ water and incubated for 5 min with ECL substrate (SuperSignal West Pico Substrate (34080; Pierce)). Visualization of the protein was monitored in the ChemiDoc Imager (Bio-Rad) and quantified using Image Lab (Bio-Rad). To re-probe the membrane with different primary antibodies, the membrane was incubated for 30 min at 65 °C while shaking in stripping buffer (62.5 mM Tris pH 6.8 (T1503, Sigma-Aldrich), 10 % SDS (CN30.1, Roth), 5 % β -mercaptoethanol (M7522; Sigma-Aldrich)) and re-blocked in milk or BSA after several 1x TBST washing steps. The following primary antibodies were used: PERK (C33E10) (1:2000; #3192, CST), p-PERK T980 (16F8) (1:300; #3179, CST), GCN2 (1:800; #3302, CST), p-GCN2 T899 (1:1000; #ab75836, abcam), eIF2 α (D7D3) XP (1:1000; #5324, CST), p-eIF2 α S51 (119A11) (1:1000; #3597, CST), p-p70 S6K T389 (108D2) (1:1000; #9234, CST), p70 S6K (49D7) (1:1000; #2708, CST), mTOR (7C10) (1:1000; #2983, CST), p-mTOR S2448 (D9C2) (1:1000; #5536, CST), p-mTOR S2481 (D9C2) (1:1000; #2974, CST), GCN1L1 (1:2000; #LS-C288620, LSBio), Grb2 (1:1000; #610112, Becton Dickinson), 4EBP1 (53H11) (1:1000; #9644, CST), p-4EBP1 T37/46 (236B4) (1:1000; #2855, CST), mCherry (1:2000; #ab167453, abcam), FLAG (1:1000; #F1804, Sigma-Aldrich), StrepMAB-classic (1:1000; #2-1507-001, iba), Akt (pan) (C67E7) (1:1000; #4691, CST), p-Akt S473 (1:1000; D9E9 XR) (#4060, CST), puromycin clone 12D10 (1:10000; #MABE343, Millipore), CREB-2 (b3) (1:1000; #sc-390063, Santa Cruz), p-PKR T446 (1:1000; #ab32036, abcam), PKR (B-10) (1:1000; #sc-6282, Santa Cruz), CHOP L63F7 (1:500; #2895, CST), Mre11 (1:1000; #4895, CST), p95/NBS1 D6J5I (1:1000; #14956, CST), Rad50 (1:1000; #ab124682, abcam), RPL8 (1:1000; #ab169538, abcam), SAPK/JNK (1:1000; #9252, CST), p-SAPK/JNK T183/Y185 (81E11) (1:1000; #4668, CST), AMPK α (1:1000; #2532, CST) and p-AMPK α T172 (1:1000; #2535, CST).

3.6.3. Immunoprecipitation for native protein

3T3 cells (1.0×10^6 cells/well) were seeded the day before lysis in 10 cm tissue culture plates (353003, Falcon) and treated according to their experimental purpose. Protein lysis was performed as previously described using 200 μ L/plate non-denaturing buffer (20 mM Tris-HCl pH8.0 (T1503; Sigma-Aldrich), 137 mM NaCl (7647-14-5, VWR), 2 mM EDTA (15575020, Thermo Scientific), 10 % glycerol (G5516; Sigma-Aldrich), 1 % NP-40 (127087-87-0, Sigma-Aldrich)) supplemented with fresh protease + phosphatase inhibitor cocktail (100x; 78440, Thermo Scientific). In total, 20 μ L protein A agarose beads (9863, CST) per cell lysate (600-800 μ g) were incubated for 3 h at 4 °C on a rotating wheel. After centrifugation for 10 min at 4 °C, the supernatant was transferred in a precooled fresh tube. In total, 1 μ g/ μ L of unconjugated primary antibody as added to the tube and incubated overnight at 4 °C with gentle rocking. Again, 20 μ L

of protein A beads per tube were incubated for 3 h at 4 °C on the wheeling device. After microcentrifugation for 1 min at 4 °C, the pellet was washed five times with 500 µL of 1x non-denaturing buffer and kept on ice between these steps. Further, the sample was analyzed by immunoblotting. Therefore, the beads were removed after the pellet was resuspended in 20 µL RIPA lysis buffer (50 mM Tris-HCl pH 8.0 (T1503; Sigma-Aldrich), 150 mM NaCl (7647-14-5, VWR), 1 % NP-40 (127087-87-0, Sigma-Aldrich), 0.5 % SDC (D6750, Sigma-Aldrich), 0.1 % SDS (CN30.1, Roth)) supplemented with fresh 100x protease + phosphatase inhibitor cocktail, centrifuged again for 1 min and heated in 6 x protein loading dye (375 mM Tris-HCl pH 6.8 (T1503, Sigma-Aldrich), 416.13 mM SDS (CN30.1, Roth), 60% glycerol (G5516; Sigma-Aldrich), a tip of bromophenol blue (B0126; Sigma-Aldrich) in water; fresh 5 % β-mercaptoethanol (M7522; Sigma-Aldrich)) for 5 min at 95 °C. As controls, lysate input and pulldown with just protein A beads were loaded. A normal isotype antibody (#2729, CST) was used to estimate non-specific binding of the primary used antibody. A conformation specific IgG antibody (#3678, CST) was used to remove the heavy and light chain background on the membranes. The following primary antibodies were used: GCN2 (#3302, CST), GCN1L1 (LS-C288620, LSBio), Rad50 (ab124682, abcam), Mre11 (#4895, CST), p95/NBS1 D6J5I (#14956, CST) and Grb2 (610112, Becton Dickinson). In case protein A magnetic beads were used (ab214286, abcam), the abcam IP-instructions were followed.

3.6.4. *In vitro* immunoprecipitation-based GCN2 kinase assay

3T3 cells were transiently transfected with GCN2-3xFLAG plasmid (Section 3.2.4.), leucine-starved (Section 3.3.2.) for indicated time, lysed in TritonX-100 (9002-93-1, Sigma-Aldrich) containing buffer (50 mM Tris pH7.4 (T1503; Sigma-Aldrich), 150 mM NaCl (7647-14-5, VWR), and 1 mM EDTA (15575020, Thermo Scientific); 200 µL/well) supplemented with protease + phosphatase inhibitors (100x; 78440, Thermo Scientific) and transferred to pre-chilled tubes. Then, anti-FLAG M2-affinity gel beads (A2220 Sigma; 8 µL/200 µL lysate) were added and incubated for 1 h at 4°C on a moving rotor. The supernatant was carefully removed after centrifugation at 12750 rpm for 1 min and washed with 1 mL lysis buffer without Triton-X 100. Then, 0.5 mg/mL 3x-FLAG peptide (MPIB Core Facility) was added per sample, incubated for 15 min with occasional agitation and eluted in wash buffer for a final volume of 10 µL. The ATP reaction was set up as in table 30, 10 µL of 2x reaction buffer (25 mM HEPES pH 7.4; 50 mM potassium acetate, 2.5 mM magnesium acetate) added to the 10 µL IP sample, transferred to BSA-coated (100 mg/mL BSA previously coated for 2h) tubes and incubated at 32 °C in a PCR cycler (Biorad) for 10 min. Finally, the reaction was quenched by adding 5 µL of 94 °C pre-warmed 6 x SDS SB and stored at -80 °C for further immunoblotting. Whole cell lysates and reactions

omitting ATP were used as internal control. In general, the GCN2 and mTOR inhibitors (Table 33 and figures for experiment-specific concentrations) were added either to the eluate or during the starvation period.

Table 30: ATP-reaction setup

Component	Volume/reaction	Final concentration
Distilled MilliQ water	fill up to 100 μ L	-
Reaction buffer	200 μ L	4x
BSA	100 μ L	0.5 mg/mL
DTT	4 μ L	1 M
Beta-gp	4 μ L	1 M
ATP	2 μ L	0.5 mM
MgCl ₂	7.5 μ L	1 M
Recombinant human eIF2 α	2 μ L	294 μ M

3.6.5. Radioactivity-based mTOR kinase activity assay

In vitro mTOR activity was assayed in 10 μ L reactions containing the kinase mTOR Δ N-LST8 (100 nM; provided by Julian Brötzmann) and the substrate GST-AKT1 450–480 (1 μ M; provided by Julian Brötzmann) in a specific reaction buffer (10 mM MgCl₂, 1 mM DTT in PBS; made by Julian Brötzmann). Before, the inhibitors (Torin-2, GCN2-IN-6, sapanisertib and rapamycin; Table 33) were added to the kinase in different concentrations (200 nM, 100 nM and 10 nM) and incubated for 10 min on ice. To start the reaction, radiolabeled ATP mix (0.5 mM ATP, 0.8 μ Ci [γ - 32P]-ATP; provided by Julian Brötzmann) was supplied for 30 min at 30 °C. Afterwards, the reaction was quenched by adding 2x SDS sample buffer for 2 min at 55 °C, phosphoproteins Coomassie-stained (12.5 % SDS gel; self-made by Julian Brötzmann) and detected by autoradiography using a Typhoon FLA7000 imager (GE Healthcare). As internal controls, the reaction was performed without the ATP mix with or without the addition of 3 % DMSO.

3.7. Multi-omics techniques

3.7.1. Transcriptomics

3T3 cells (0.2x 10⁶ cells/well; WT, GCN2^{-/-}, GCN1^{-/-} and GCN2^{-/-} + GCN1^{-/-}) were seeded in triplicates per treatment condition in 12-well tissue culture plates (3513, Corning). On the next day, four treatment conditions were applied to the cells: Leucine starvation for 1 h, 4 h, 8 h and no starvation (Section 3.3.2.). Total RNA was isolated as previously described in section 3.5.2. and the sequences analyzed in the MPIB Core Facility by Dr. Marja Driessen.

According to the manufacturer's protocol, mRNA libraries were prepared with 1 µg of total RNA per sample using the NEBNext Ultra II Directional RNA Library Prep Kit for Illumina (E7765, NEB) with NEBNext Poly(A) mRNA Magnetic Isolation Module (E7490, NEB). Total RNA and the final library quality controls were conducted using Qubit Flex Fluorometer (Q33327, Thermo Fisher Scientific) and 2100 Bioanalyzer Instrument (G2939BA, Agilent) before and after library preparation. The paired-end sequencing was performed on Illumina NextSeq 500 (2 × 43 bp reads). Moreover, the samples were multiplexed and sequenced on one High Output Kit v2.5. BCL raw data conversion to FASTQ data and demultiplexing was performed by bcl2fastq conversion software (Illumina). BAM and bigwig files were established by STAR alignment and file conversion scripts – bam2wig and wigToBigWig.

After quality-checking using the tool FastQC (v.0.11.8), the files were mapped to the mouse genome (Genome build *GRCm38*) downloaded from Ensembl using the star aligner (v. 2.6.1)⁴²⁰. The mapped files were then quantified on a gene level based on the ensembl annotations, using the featureCounts⁴²¹ tool from the SubRead package⁴²¹ (v. 1.6.3). Using the DESeq2 package (R 4.0.2, DESeq version 2.1.28)^{422,423} the count data was normalized by the size factor to estimate the effective library size. After calculating the gene dispersion across all samples, the comparison of each two different conditions resulted in a list of differentially expressed genes for each comparison. A filtering step for removing genes with no reads in at least three samples was used. Genes with an adjusted p-value of smaller than 0.05 were then considered to be differentially expressed for downstream analysis.

Using the Perseus computational platform⁴²⁴, the raw intensities of all 26,672 genes were log2-transformed and filtered on valid values (cut-off more than 50). The remaining 12,147 genes were genotype and replicates grouped and GO-annotated (*mus musculus* 32,406 entries). Statistical analysis was applied by ANOVA processing, whereby the coefficient of variation S0 was set to 0.2 and permutation-based FDR was set to 0.05. All values were Z-scored and hierarchical clustered (Euclidean distance, average linkage) for ANOVA significance.

3.7.2. Proteomics and phosphoproteomics

3T3 cells were seeded in 10 cm tissue culture plates (353003, Falcon) in quadruplicates per treatment condition to reach a 70-80 % confluency on the next day. Leucine depletion (Section 3.3.2.) was performed for 1 h, 4 h and 8 h in WT, GCN2^{-/-} and GCN1^{-/-} cells. As control, the cells were treated without starvation using the amino acid refeeding medium. On ice, the medium was aspirated, the cells were washed three times with precooled 1x TBS (50 mM Tris-HCl pH 7.5, (T6066; Sigma-Aldrich), 150 mM NaCl (7647-14-5, VWR)) and lysed in 4 % SDC (30970; Sigma-Aldrich) in 100 mM Tris-HCl pH 8.5 (500 µL/10 cm dish; T6066; Sigma-Aldrich) for 1 min. The

lysates were transferred immediately into a precooled tube and heated for 10 min at 95 °C. Afterwards, the extracts were shock frozen in liquid nitrogen and stored at - 80 °C. The protein concentration was determined by BCA protein assay and adjusted to 1 mg/sample.

Following the EasyPhos protocol^{425,426}, samples were prepared for phosphopeptide enrichment and proteome library preparation. Overnight, each sample was reduced with 10 mM TCEP (75259; Sigma-Aldrich), alkylated with 40 mM 2-chloroacetamide (C0267, Sigma-Aldrich) and digested with trypsin and LysC (1:100, enzyme/protein, w/w; MPIB Department Mann). In total, 20 µg of peptide was taken for full proteome and 800 µg of peptide for phosphoproteome measurement. Using SDB-RPS stage tips, the desalted peptides (500 ng) were resolubilized in 2 % ACN (34851; Sigma-Aldrich) and 0.1 % FA (T6508; Sigma-Aldrich) before injection into the mass spectrometer. For phosphopeptide enrichment, several additional steps were performed before desalting and injection into the mass spectrometer: The digested samples were probed with 6 % TFA (T6508; Sigma-Aldrich), 50 % isopropanol (I9516, Sigma-Aldrich) and 1 mM KH₂PO₄ (P5655; Merck), mixed and centrifuged for 3 min at 2000xg. Next, TiO₂ beads were added to the supernatants for 5 min at 40 °C (1:10; protein /beads w/w) and washed five times with isopropanol and 5 % TFA (T6508; Sigma-Aldrich). Phosphopeptides were eluted with 40 % ACN (34851; Sigma-Aldrich) and 15 % NH₄OH (431311, Sigma-Aldrich) from C8 stage tips and dried in a SpeedVac (20 min, 45 °C).

Peptides were loaded on 50 cm in-house columns packed with C18 1.9 µM ReproSil particles (Dr. Maisch GmbH) and separated with an EASY-nLC 1200 system (Thermo Fisher Scientific). Phosphopeptides were separated with a linear 70 min gradient ramped from 3 % buffer B to 19 % in 40 min, 41 % in 20 min, 90 % in 5 min and 95 % in 5 min (flow rate of 300 nl/min). Peptides for full proteome measurements were separated with a linear 120 min gradient ramped from 5 % buffer B to 30 % in 95 min, 60 % in 5 min, 95 % in 2 x 5 min and 5 % in 2 x 5 min (flow rate of 300 nl/min). Buffer A was composed of 99.9 % ddH₂O and 0.1 % FA, while buffer B was composed of 80 % ACN, 19.9 % ddH₂O and 0.1 % FA. The liquid chromatography system was coupled to an orbitrap mass spectrometer (Q Exactive HFX, Thermo Fisher Scientific) for spectral acquisition.

A data-independent acquisition MS method was used for the phosphoproteome analysis in which one full scan (300 to 1650 *m/z*, *R* = 60,000 at 200 *m/z*) at a target of 3 × 10⁶ ions was first performed, followed by 32 windows with a resolution of 30,000 where precursor ions were fragmented with higher-energy collisional dissociation (stepped collision energy 25%, 27.5%, 30%) and analyzed with an AGC target of 3 × 10⁶ ions and a maximum injection time at 54 ms in profile mode using positive polarity.

For full proteome measurements a data-dependent acquisition (TopN) MS method was used in which one full scan (300 to 1650 *m/z*, *R* = 60,000 at 200 *m/z*, maximum injection time 20 ms) at

a target of 3×10^6 ions was first performed, followed by 15 data-dependent MS/MS scans with higher-energy collisional dissociation (AGC target 10^5 ions, maximum injection time at 28 ms, isolation window 1.4 m/z , normalized collision energy 27 %, $R = 15,000$ at 200 m/z). A dynamic exclusion of 30 sec was enabled.

For the experiments measured in DDA mode, MS raw files were processed with the MaxQuant version 1.5.38 (Ref.⁴²⁷) and fragments lists were searched against the human UniProt FASTA database (21,039 entries, August 2015) with cysteine carbamidomethylation as a fixed modification and N-terminal acetylation and methionine oxidations as variable modifications. We set the false discovery rate (FDR) to less than 1 % at the PSM and protein levels and specified a minimum length of 7 amino acids for peptides. Enzyme specificity was set as C-terminal to arginine and lysine since we used trypsin and lysC as proteases and a maximum of two missed cleavages.

For experiments measured in DIA mode MS raw files were processed in a directDIA search with the Spectronaut software version 13 (Biognosys⁴²⁸). Against the mouse uniprot FASTA database (22,220 entries, 39,693 entries, 2015). Serine/Threonine/Tyrosine phosphorylation was added as variable modification to the default settings, which include cysteine carbamidomethylation as fixed modification and N-terminal acetylation and methionine oxidations as variable modifications. The variable modification and localization cutoffs were set to 0 and the maximum number of fragment ions per peptide was set to 15. The false discovery rate (FDR) was set to less than 1% at the peptide level at a minimum length of 7 amino acids for peptides. Enzyme specificity was set as C-terminal to Arginine and Lysine as expected using trypsin and LysC as proteases and a maximum of two missed cleavages.

Bioinformatics data analyses were performed with the Perseus software (version 1.6.2.2)⁴²⁴. Spectronaut output tables were collapsed to phosphosites and the localization cutoff was set to 0.75 using the peptide collapse plug-in tool for Perseus⁴²⁹. Raw intensities were log2-transformed, processed by valid values (cut-off 70 %), GO-annotated, z-scored and missing values imputed. Significant enriched proteins (q-value of 0.01) were determined by multiple-sample test (one-way analysis of variance (ANOVA), FDR 0.05) for genotype- comparison and Student's t-test (two-sided), (FDR 0.05) for genotype plus starvation comparison.

3.7.3. Interactomics

3T3 WT cells (0.25×10^6 cells/well) were seeded in quadruplicates per treatment condition in 12- well tissue culture plates (3513, Corning). Next day, two treatment conditions were applied to the cells: Leucine starvation for 4 h and no starvation (Section 3.3.2.). After 4 h, the cells were washed once in ice-cold 1x PBS (10010015, Life Technologies), lysed in lysis buffer (50 mM Tris-

HCl (1185-53-1, Sigma-Aldrich), pH 8; 150 mM NaCl (S8889, Sigma-Aldrich); 5 % glycerol (G5516, Sigma-Aldrich); 0.05 % IGEPAL CA-630 (I8896, Sigma-Aldrich); 0.1 % benzonase (E1014, Sigma-Aldrich)) supplemented with protease + phosphatase inhibitor cocktail (100x; 78440, Thermo Scientific) followed by centrifugation for 10 min at 4 °C and 14000xg to pellet cell debris. The supernatant was transferred into a fresh 1.5 mL Eppendorf tube and kept on ice. For the target protein pulldown GCN1 MagStrep type III beads (2-4090-002, IBA) or protein A magnetic beads (S1425S; NEB) were equilibrated and washed three times with 500 µL wash buffer 1 (50 mM Tris-HCl, pH 8; 150 mM NaCl; 5 % glycerol). 222 ng of anti-GCN1L1 (1:2000; #LS-C288620, LSBio) per sample were added to the beads in a total volume of 20 µL buffer 1 (5 % bead to wash buffer 1 suspension (v/v)) and incubated rotating for 30 min at 4 °C to foster antibody binding to the beads. The whole volume of antibody-conjugated beads (20 µL) was added to each pulldown sample and incubated for 1 h at 4 °C and 800 rpm. Subsequently, the bead-protein solution was washed twice with 300 µL wash buffer 2 (wash buffer 1, 0.05 % IGEPAL CA-630) followed by two washes with 300 µL wash buffer 1 using a magnetic rack. Afterwards, samples were subjected to on-bead digestion. Here, beads were resuspended in 100 µL master mix 1 (6 M Urea (U5379, Sigma-Aldrich); 100 mM Tris-HCl (1185-53-1, Sigma-Aldrich), pH 8; 10 mM dithiothreitol (DTT-RO, Sigma-Aldrich)) and incubated for 20 min at RT, 800 rpm, to reduce disulfide bridges. Then, 100 µL master mix 2 (6 M Urea; 100 mM Tris-HCl, pH 8; 20 mM chloroacetamide (C0267, Sigma-Aldrich)) were added followed by incubation for 20 min at RT, 800 rpm. Next, 50 ng LysC (324796, Sigma-Aldrich) and 50 ng trypsin (T4799, Sigma-Aldrich) were added and the sample was incubated overnight at RT, 800 rpm. Next day, the digestion was quenched at 5 % TFA (T6508, Sigma-Aldrich). Residual beads were pelleted with a magnetic rack and the peptide-containing supernatant was transferred into a clean 1.5 mL Eppendorf tube followed by purification by solid phase extraction. Here, samples were transferred into Stage-tips (self-made; MPIB Department Mann) containing styrenedivinylbenzene reverse-phase sulfonate (SDB-RPS; 6686U, Merck) sorbent and subjected to 'In-stageTip' cleanup. The StageTip containing the samples was spun at 2000xg until all liquid passed and peptides were bound to the SDB-RPS, followed by two washes with ddH₂O 1 % TFA into lprOH 1 % TFA (I9039, Sigma-Aldrich). Clean peptides were eluted with 80 % ACN, 5 % ammonia (431311, Sigma-Aldrich), 15 % ddH₂O and speedvaced until dryness. Peptides were then reconstituted in 2 % ACN (34851, Sigma-Aldrich), 0.1 % FA (F0507, Sigma-Aldrich), 97.9 % ddH₂O and injected into the mass spectrometer.

For separating peptides by hydrophobicity and eluting them into the tims-qTOF mass spectrometer, we used an EvoSep One liquid chromatography system (EvoSep, GmbH) and analyzed purified peptides with a standard 21 min method (60 samples per day). We used a 15 cm × 150 µm ID column with 1.9 µm C18 beads (PepSep) coupled to a 20 µm ID electrospray

emitter (Bruker Daltonics). Mobile phases A and B were 0.1 % FA in water and 0.1 % FA in ACN, respectively. The EvoSep system was coupled online to a trapped ion mobility spectrometry quadrupole time-of-flight mass spectrometer (timsTOF Pro, Bruker Daltonics) equipped with via a Captive nano-electrospray ion source. The column was kept at 40 °C by a sonation column toaster.

For separating peptides hydrophobicity and eluting them into a quadrupole Orbitrap mass spectrometer (Orbitrap Exploris, Thermo Fisher Scientific), we used an EASY nanoLC 1200 (Thermo Fisher Scientific). Peptides were loaded on a 45 cm in-house packed HPLC-column (75 µm inner diameter packed with 1.9 µm ReproSil-Pur C18-AQ silica beads (Dr. Maisch GmbH, Germany). Sample analytes were separated using a linear 60 min gradient from 5-30 % B in 45 min followed by an increase to 65 % for 2.5 min, an increase to 95 % for 2.5 min, a 5 min wash at 95 %, a decrease to 5 % B for 2.5 min, and a re-equilibration step at 5 % B for 2.5 min (Buffer A: 0.1 % FA, 99.9 % ddH₂O; Buffer B: 0.1 % FA, 80 % CAN, 19.9 % ddH₂O). Flow-rates were kept constant at 300 nl/min. The column temperature was kept at 60 °C by an in-house manufactured oven.

Mass spectrometric analysis on the tims-qTOF was performed in a data-dependent PASEF mode (ddaPASEF). For ddaPASEF, 1 MS1 survey TIMS-MS and 4 PASEF MS2 scans were acquired per acquisition cycle. The cycle overlap for precursor scheduling was set to 2. Ion accumulation and ramp time in the dual TIMS analyzer was set to 50 ms each and we analyzed the ion mobility range from $1/K_0 = 1.3 \text{ Vs cm}^{-2}$ to 0.8 Vs cm^{-2} . Precursor ions for MS2 analysis were isolated with a 2 m/z window for $m/z < 700$ and 3 m/z for $m/z > 700$ in a total m/z range of 100-1,700 by synchronizing quadrupole switching events with the precursor elution profile from the TIMS device. The collision energy was lowered linearly as a function of increasing mobility starting from 59 eV at $1/K_0 = 1.6 \text{ VS cm}^{-2}$ to 20 eV at $1/K_0 = 0.6 \text{ Vs cm}^{-2}$. Singly charged precursor ions were excluded with a polygon filter (otof control, Bruker Daltonics). Precursors for MS2 were picked at an intensity threshold of 2,000 arbitrary units (a.u.) and re-sequenced until reaching a 'target value' of 24,000 a.u. considering a dynamic exclusion of 40 s elution.

Mass spectrometric analysis on the Orbitrap was performed in (data-dependent acquisition) DDA mode. For full proteome measurements, MS1 spectra were acquired at 60,000 resolution and a m/z range of 300-1,650 with a normalized automatic gain control (AGC) target of 300 and a maximum injection time of 25 ms. The top 10 most intense ions with a charge of two to five from each MS1 scan were isolated with a width of 1.4 m/z, followed by higher-energy collisional dissociation (HCD) with a normalized collision energy of 30 %. MS/MS spectra were acquired at 15,000 resolution with a normalized AGC target of 300, and a maximum injection time of 80 ms. Dynamic exclusion of precursors was set to 40 s.

Tims-qTOF raw files were processed using MaxQuant (v1.6.7), which extracts features from a four-dimensional isotope patterns and associated MS2 spectra. Files were searched against the mouse Uniprot databases (UP000000589_10090.fa, UP000000589_10090_additional.fa). False-discovery rates were controlled at 1 % both on peptide spectral match (PSM) and protein levels. Peptides with a minimum length of seven amino acids were considered for the search including N-terminal acetylation and methionine oxidation as variable modifications and cysteine carbamido-methylation as fixed modification, while limiting the maximum peptide mass to 4,600 Da. Enzyme specificity was set to trypsin cleaving c-terminal to lysine and arginine. A maximum of two missed cleavages were allowed. Maximum precursor and fragment ion mass tolerance were searched as default for TIMS-DDA data and the main search tolerance was reduced to 20 ppm. Protein quantification was performed by label-free quantification using a minimum ratio count of 1. Peptide identifications by MS/MS were transferred by matching four-dimensional isotope patterns between the runs (MBR) with a 0.7-min retention-time match window and a 0.05 1/K0 ion mobility window. Orbitrap raw-files were searched just like the tims-qTOF data with the following modifications: Maximum precursor and fragment ion mass tolerance was set to 4.5 and 20 ppm. Peptide identifications by MS/MS were transferred by matching three-dimensional isotope patterns between the runs with a 0.7-min retention-time match window.

Bioinformatics analysis was performed in Perseus (version 1.6.7.0) and GraphPad Prism (version 8.2.1). For all analyses, reverse database, contaminant, and only by site modification identifications were removed from the dataset. Data were grouped by analytical replicates and filtered to at least two observations in triplicate measurements or three observations in case of quadruplicate measurements per group. Data were log₂-transformed and missing values were imputed from a normal distribution with a downshift of 1.8 and a width of 0.3. Different pulldowns were tested for differences in their mean by a two-sided Student's t-test with S_0 0.2 and a permutations-based FDR correction for multiple hypothesis testing at an FDR of 0.05 and 250 randomizations and presented as volcano plots. Profile plots for solute carrier transporters were visualized after log₂-transformation. The profile plot for GCN1 was visualized after log₁₀-transformation. Hierarchical clustering using Euclidean as the distance parameter for column- and row-wise clustering was performed after ANOVA significance testing with S_0 0.2 and permutation-based FDR control at 0.05 and 250 randomizations, filtering for significantly changed proteins across categories and Z-scoring. 1D gene ontology enrichments of clustered and systematically changed proteins were performed with regards to their biological process and molecular function assignment at the gene level with an FDR at 0.04. Z-scored data for each respective cluster were visualized for the top enriched terms in profile plots. Enrichment factors for each of the respective terms within the cluster were visualized as bar plots.

3.8. Additional software

If not indicated previously, softwares were used as followed: Graphs were generated by GraphPad Prism (version 7.03). Brightfield microscopic images were taken with a Leica DM IL LED (Leica) microscope including a SPOT Insight 2.0 Mp Firewire Monochrome Camera (Spotimaging, Burroughs Sterling Heights) and captured with VisiView version 2.0.1 (Visitron Systems). Figures were made using Adobe Illustrator (version 11). Omics data analyses were performed in the Perseus environment (version 1.6.7). FASTA sequence alignment were annotated in SnapGene (version 5.0.4) or geneious (version 10). Immunoblot images were processed in ImageJ (version 1.46). Gene expression analyses were conducted with the CFX Manager 3.1 (Biorad). Flow Cytometry data were analyzed using FlowJo version 10.4.2 (Becton Dickinson). The oligonucleotides for guide RNA design were designed using the CRISPR Design Tool (MIT, Prof. Feng Zhang) that was optimized to the new version CRISPick (Broad Institute; <https://portals.broadinstitute.org/gppx/crispick/public>). Chemical structures were made with ChemDraw (version 19).

4. Results

4.1. Genetic characterization of genetically modified murine cell lines

4.1.1. Overview

One aim for this thesis was the genetic dissection of the amino acid stress-induced ISR in three different murine cell systems (Figure 18A): mouse embryonic stem cells (E14 cells), mouse immortalized fibroblasts (3T3 cells) and primary embryonic fibroblasts (MEFs). Due to their experimental tractability⁴³⁰, the 3T3 system was used as the base model system for most experiments. Findings from the 3T3 system were extrapolated to the E14 cell system, which were chosen due to their differentiation potential to any cell type⁴³¹. To minimize the influence of immortalization and compensatory effects, 3T3 cells with genetic lesions in GCN2 were compared to their MEF counterpart derived from the embryos of GCN2 deficient mice.

The mechanistic focus of this thesis was to understand functional roles and connections between GCN2 (encoded by *Eif2ak4*) and GCN1 (encoded by *Gcn1*). This chapter describes the genetic manipulation of the components of the GCN2 cascade by CRISPR/Cas9-mediated genome engineering and how the cell lines were validated (Sections 4.1.2.-4.1.5.). Therefore, an important part essential for the entire thesis was to establish a set of highly-specific antibodies that recognize GCN2, GCN1 and other known ISR-key players (e.g. ATF4, CHOP or eIF2 α) summarized in section 3.6.2. As shown in figure 18B, GCN1 and GCN2 are detected specifically at 186 kDa (mouse GCN2) and 293 kDa (mouse GCN1) in all three murine cell systems. As loading control, the growth factor receptor-binding protein 2 (GRB2) was used, which is the conserved adaptor protein involved in receptor tyrosine kinase signal transduction⁴³² and routinely used in our laboratory as a reliable loading control. In human cells, GCN1 is about 10 to 20 times more abundant than GCN2 that was determined by a mass spectrometry-based estimation of the copy numbers of individual proteins per cell⁴³³ (Figure 18C). The stoichiometric difference between GCN1 and GCN2 in terms of their function in cell physiology and amino acid response will be explored in the subsequent sections 4.2.-4.7.

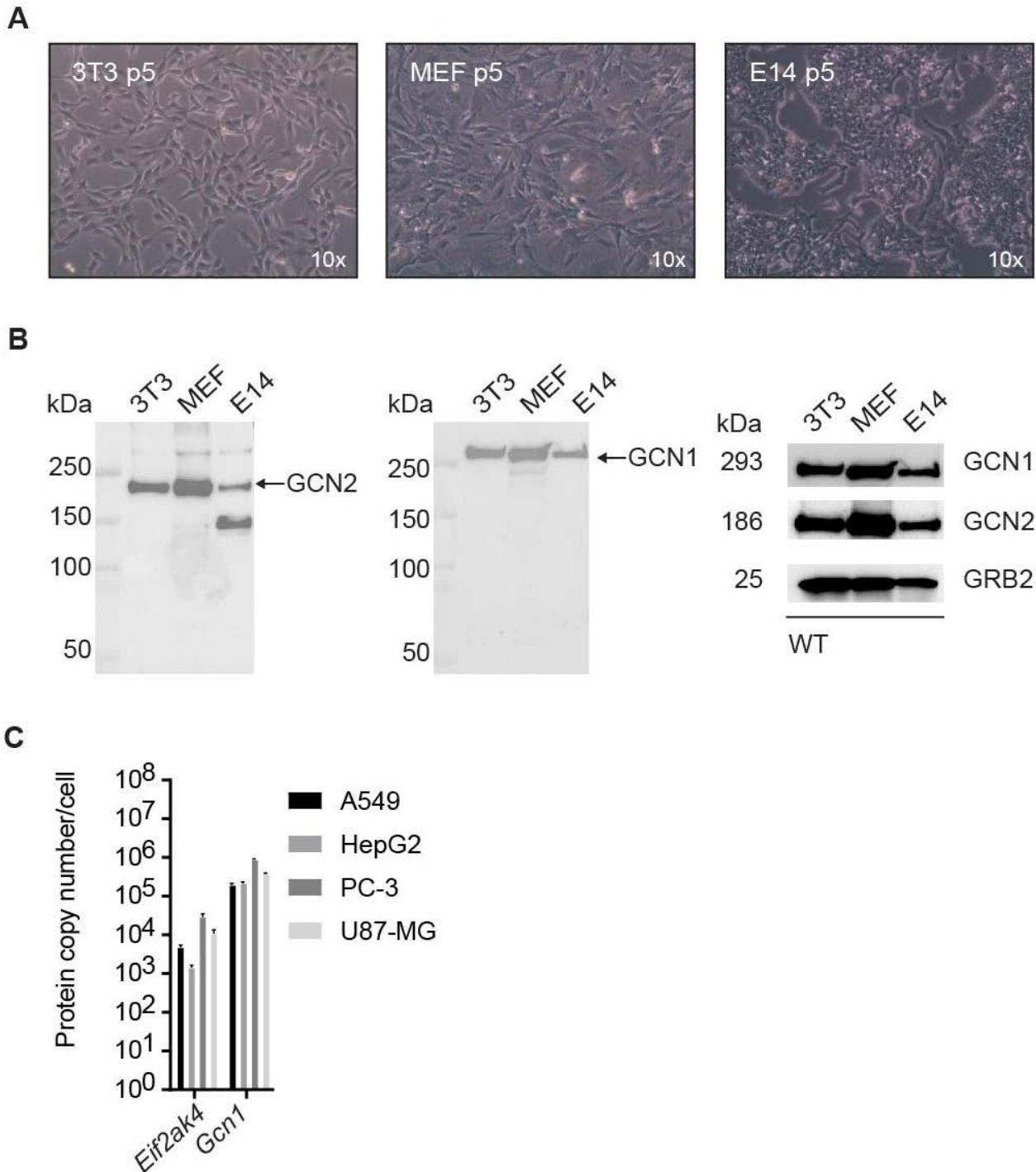


Figure 18. GCN1 and GCN2 are expressed and detectable in our murine cell systems. (A) Bright field microscope images of cultivated and viable mouse immortalized fibroblasts (3T3 cells), mouse embryonic fibroblasts (MEFs) and mouse embryonic stem cells (E14 cells) at passage 5. (B) GCN2 (186 kDa) and GCN1 (293 kDa) are detected at the protein level by immunoblotting. GRB2 (25 kDa) was used as loading control. The GCN2 antibody gives in contrast to the GCN1 antibody faint background bands. Data are depicted as one of two representative gels. (C) Estimation of the copy numbers of GCN1 and GCN2 per cell⁴³³ in diverse human cell lines (A549 (adenocarcinomic alveolar basal epithelial cell line); HepG2 (liver cancer cell line), PC-3 (prostate adenocarcinoma cell line), U87-MG (brain glioblastoma cell line)).

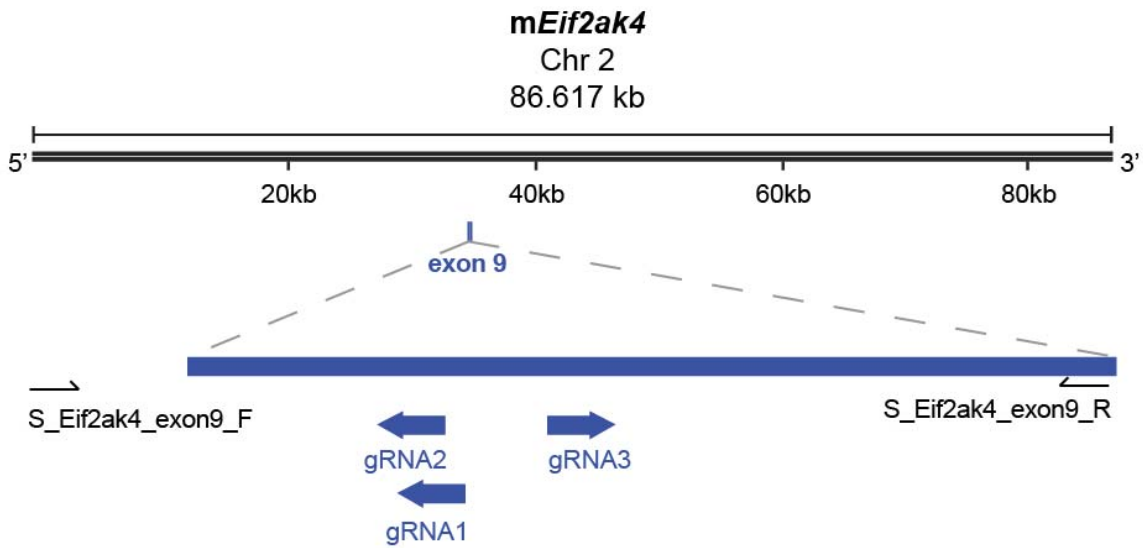
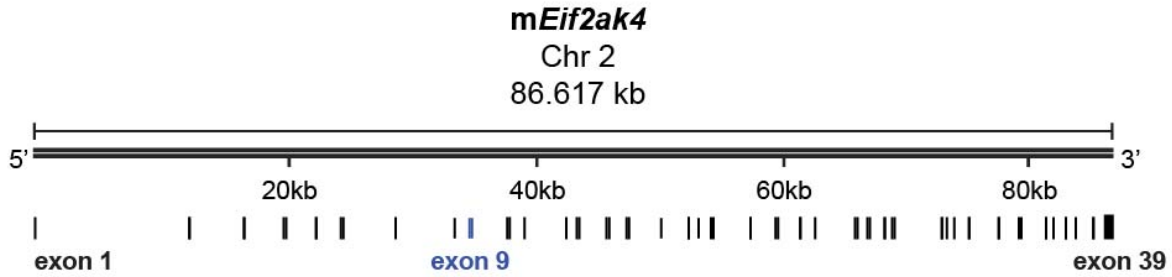
4.1.2. Genetic characterization of *Eif2ak4* and *Gcn1* loss-of-function alleles

The current dogma of the amino acid ISR argues that GCN2 activity is controlled by the direct interaction with the HEAT-repeat protein GCN1; first reported in yeast^{105,130,131}. To study the close interaction of GCN1 and GCN2 in mammals, genetic systems were established.

To generate clones bearing biallelic GCN1 or GCN2 deficiency in 3T3 and E14 cells, CRISPR/Cas9 -mediate genome engineering was used⁴³⁴. First, gRNAs predicted to introduce out of frame INDELS at the targeted locus were designed using the CRISPR Design tool (MIT, Prof. Dr. Feng Zhang). The gRNAs were chosen by their highest quality score that is a mean for the inverse likelihood of off-target binding of the respective gRNA. For *Eif2ak4*, located on chromosome 2, three partly overlapping gRNAs, which target coding exon 9 were already reported by Taniuchi *et al.*⁶⁰ and were also ranked as highest efficient ones in the CRISPR Design tool (MIT, Prof. Dr. Feng Zhang). In contrast to *Eif2ak4*, *Gcn1* is an essential gene in most cell types (DepMap portal, Broad Institute USA) consistent with the perinatal lethality of GCN1 deficient mice¹¹³. Using the CRISPR Design tool (MIT, Prof. Dr. Feng Zhang), gRNAs targeting coding exon 1 and 2 on chromosome 5 gave the highest scores. However, gRNAs targeting coding exon 4 in the end led to a successful *Gcn1* loss-of-function. Importantly, the engineered GCN1 locus is not the same one that was reported for the direct interaction with GCN2 at its RWD region in yeast¹⁵⁰ and mammals¹¹³. All used gRNA sequences for GCN1 and GCN2 engineering are summarized in tables 1 and 3.

Next, the gRNAs were individually cloned into a GFP-marked Cas9 containing vector (pSpCas9(BB)-2A-GFP (PX458); Section 3.2.4.) and selected by FACS. GFP⁺ cells were single-cell-diluted to generate overall single-cell-based lines deficient in GCN1 or GCN2 (Section 3.2.3.1.). Additionally, a *Gcn1* loss-of-function lentiviral approach in bulk cells was conducted as well that was relevant for the further functional understanding of GCN1 at the molecular level (Section 3.2.3.2.). To confirm the deficient background, each bulk or clone derived cell line was Sanger sequenced in the respective engineered locus. To do this, primers spanning the gRNAs (Tables 2 and 4) were used to amplify a region suspected of containing the introduced mutations (Figure 19). The consensus of the sequence alignments of wild-type (WT) with the loss-of-function in *Gcn1* or *Eif2ak4* are shown in red in figure 19A+B. The quality score and amino acid sequence of the respective alignment is summarized in section 7.1.1. In table 31, the number of positively sequenced clones of each genotype in 3T3 or E14 cells are listed.

A



Consensus: sequence alignment WT and *Eif2ak4*^{-/-} + *Gcn1*^{-/-} in 3T3

Consensus: sequence alignment WT and *Eif2ak4*^{-/-} in 3T3

Consensus: sequence alignment WT and *Eif2ak4*^{-/-} + *Ddit3*::mCherry in 3T3

Consensus: sequence alignment WT and *Eif2ak4*^{-/-} in E14

Table 31: Clone-derived gene-modified cell lines

Cell system	Cell line	Number of clones
3T3	<i>Ddit3::mCherry</i>	1
3T3	<i>GCN2^{-/-} Ddit3::mCherry</i>	1
E14	<i>Ddit3::mCherry</i>	1
3T3	<i>Ddit3::NanoLuc-PEST</i>	1
3T3	<i>Eif2s1 S52A</i>	1
3T3	<i>Eif2ak4 D849N</i>	1
3T3	<i>Eif2ak4 T898/903A</i>	5
3T3	<i>GCN2^{-/-}</i>	2
E14	<i>GCN2^{-/-}</i>	2
3T3	<i>GCN1^{-/-}</i>	1
E14	<i>GCN1^{-/-}</i>	1
3T3	<i>GCN2^{-/-} GCN1^{-/-}</i>	1

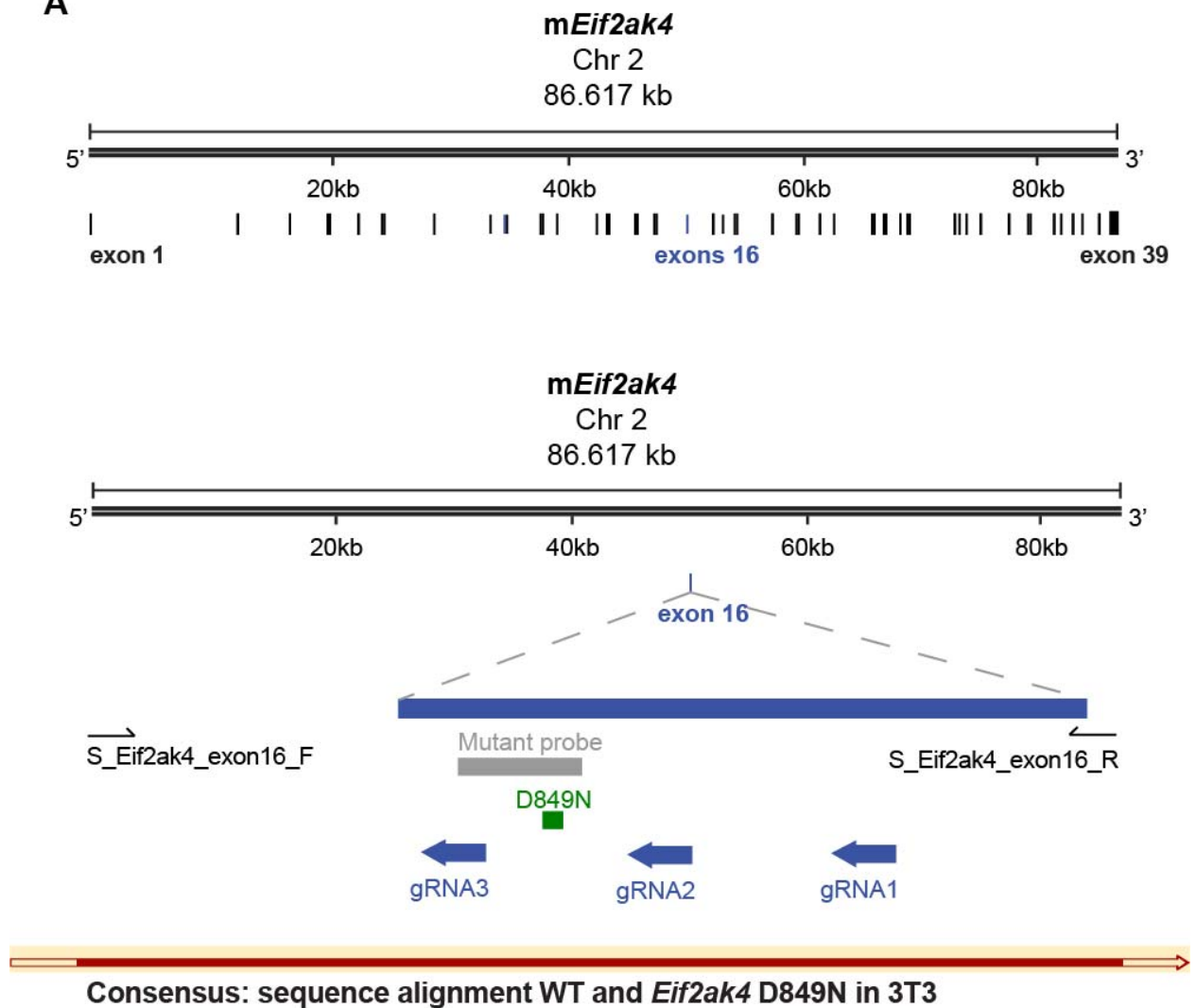
Overall, GCN1 (*GCN1^{-/-}*, hereafter), GCN2 (*GCN2^{-/-}*, hereafter) and GCN1 plus GCN2 (*GCN2^{-/-} + GCN1^{-/-}*, hereafter) single-cell-based biallelic loss-of-functions 3T3 cell lines were created. In E14 cells, *GCN1^{-/-}* and *GCN2^{-/-}* cell lines were established. Moreover, another GCN1 monoallelic deficient cell line (*GCN1^{+/-}*, hereafter) was created in 3T3 cells based on a lentiviral genome engineered approach. Further phenotypical and functional analyses with the established cell lines are reported in sections 4.3.-4.7.

4.1.3. Genetic characterization of *Eif2ak4* and *Eif2s1* point mutations

Genetic studies in yeast from Romano *et al.*⁶⁷ showed that GCN2 is activated by autophosphorylation at threonine 898 and 903 (mouse sites). The catalytically active GCN2 kinase phosphorylates the translation initiation factor eIF2 α at serine 52 (mouse site) to block cap-dependent protein translation⁷⁷. To investigate the connection between the catalytic and autophosphorylated GCN2 with its target eIF2 α in the mammalian ISR, we introduced kinase and target specific inactivating point mutations using the CRISPR/Cas9-mediated genome engineering technique⁴³⁴.

A 'catalytic-dead' version of GCN2 was created by introducing a point mutation in the codon encoding an aspartate to an asparagine (D849N) of *Eif2ak4* on coding exon 16 (*Eif2ak4* D849N, hereafter) (Figure 20A). Based on Romano *et al.*⁶⁷, codons encoding threonine 898 and 903 of *Eif2ak4* on coding exon 18 were modified to an alanine to induce an 'autophospho-dead' version of the active kinase domain (*Eif2ak4* T898/903A, hereafter) (Figure 20B). Thereby, threonine 898 is the site in the activation loop that is critical for complete inactivity of GCN2, a phenomenon consistent with the two autophosphorylation sites known for the eIF2 α kinase PKR⁶⁷. Reported by Scheuer *et al.*⁴¹⁶, the phosphorylation of eIF2 α is prevented by mutating the serine 52 to an alanine (S52A) on the first coding exon (exon 2) (*Eif2s1* S52A, hereafter) (Figure 20C).

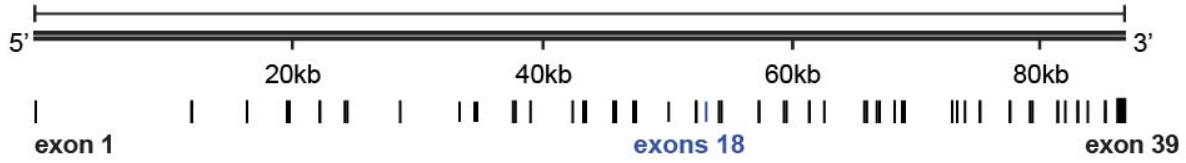
A



B

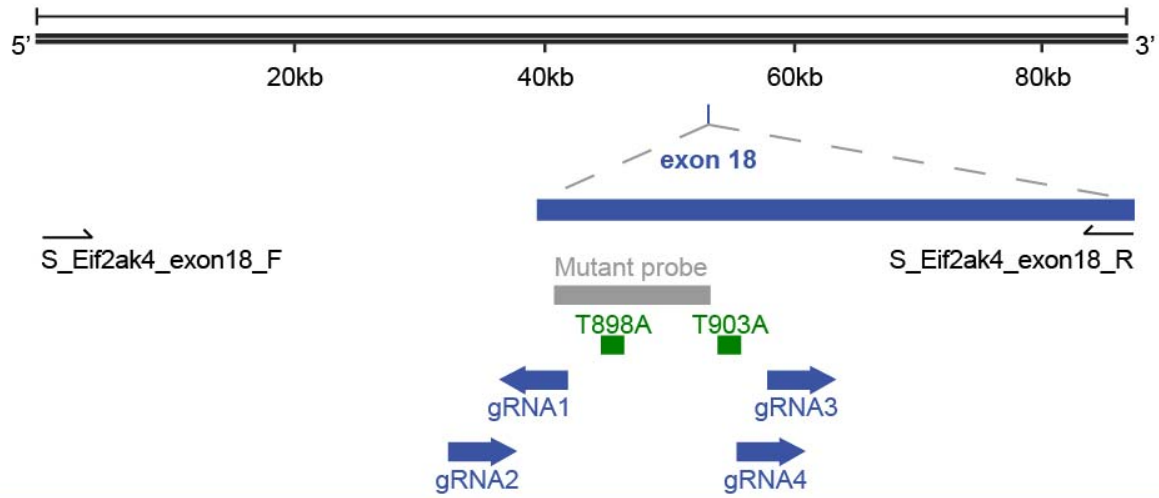
mEif2ak4

Chr 2
86.617 kb

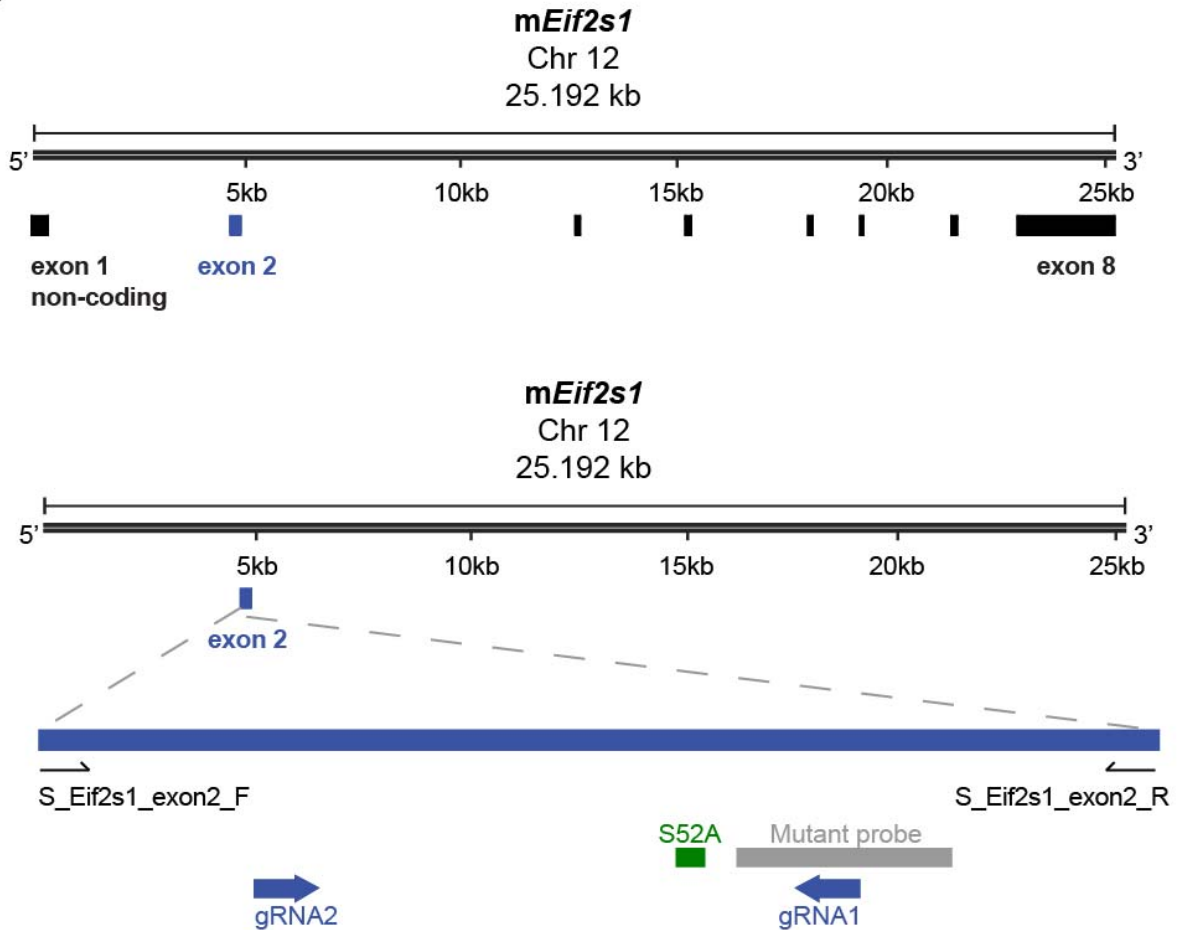


mEif2ak4

Chr 2
86.617 kb



Consensus: sequence alignment WT and *Eif2ak4* T898/903A in 3T3

C

Consensus: sequence alignment WT and *Eif2s1* S52A in 3T3

Figure 20. Schematic representation of the sequence-based characterization of GCN2 and eIF2 point mutations. (A) Schematic overview of the mouse *Eif2ak4* (coding for GCN2) locus on chromosome 2 (86.617 kb; 39 coding exons). Coding exon 16 (blue) was CRISPR/Cas9-genetically modified using gRNA 1, 2 and 3 (blue). Consensus sequence alignment (in red) with wild-type (WT) illustrates the point mutation of aspartate 849 to asparagine (D849N, green) in the generated 'catalytic-dead' (*Eif2ak4* D849N) 3T3 line. (B) Schematic overview of the mouse *Eif2ak4* (coding for GCN2) locus on chromosome 2 (86.617 kb; 39 coding exons). Coding exon 18 (blue) was CRISPR/Cas9-genetically modified using gRNA 1, 2, 3 and 4 (blue). Consensus sequence alignment (in red) with wild-type (WT) illustrates the point mutation of threonine 898 and 903 to alanine (T898/903A, green) in the generated 'autophospho-dead' (*Eif2ak4* T898/903) 3T3 line. (C) Schematic overview of the mouse *Eif2s1* (coding for eIF2) locus on chromosome 12 (25.192 kb; 7 coding exons). First coding exon (exon 2; blue) was CRISPR/Cas9-genetically modified using gRNA 1 and 2 (blue). Consensus sequence alignment (in red) with wild-type (WT) illustrates the point mutation of serine 52 to alanine (S52A, green) in the generated 'target-dead' (*Eif2s1* S52A) 3T3 line. Designed mutant probe is highlighted in grey. Detailed information is summarized in sections 3.2.3.3. and 7.1.2.

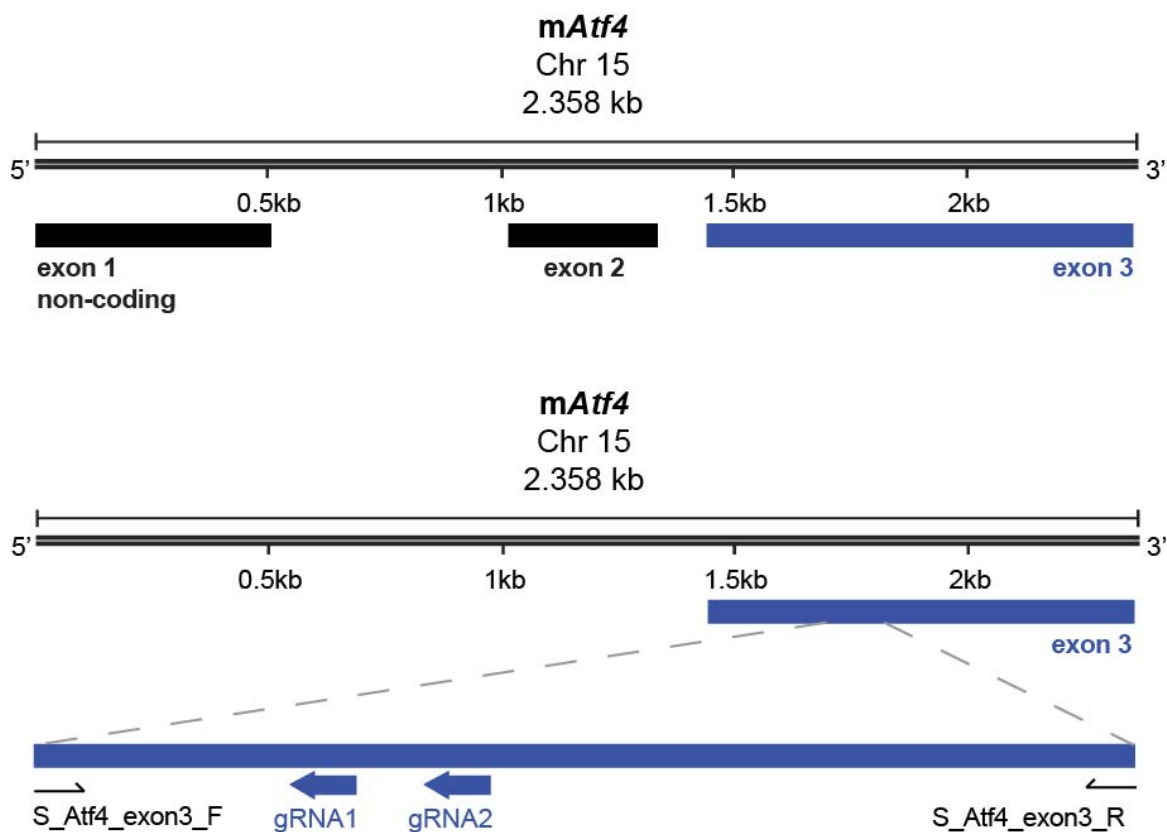
As described for other CRISPR/Cas9 derived cell lines above, gRNAs were designed (Table 7, 10 and 13), cloned into the GFP-marked Cas9 containing vector and co-transfected into 3T3 cells with a synthetic repair construct containing the targeted mutation and multiple mutations to ablate further Cas9 activity at the repaired locus (Section 3.2.3.3.; Tables 8, 9, 11, 12, 14 and 15). Following GFP⁺-FACS sorting and single-cell-dilution, positive clones were read out by a competitive allelic discrimination-based PCR assay (Section 3.5.1.) and confirmed by Sanger sequencing (Figure 20). The quality score and amino acid sequence of the respective alignment is summarized in section 7.1.2. As highlighted for the other CRISPR/Cas9-based approaches, the outcome of positive clones was low (Table 31), especially for the engineered target and the catalytic site of the kinase.

In summary, single-cell-based cell lines mutated in the autophosphorylation (T898/903A) and catalytic site (D849N) of GCN2 and the phosphorylation site of eIF2 α (S52A) were created in 3T3 cells (*Eif2ak4* T898/903A, *Eif2ak4* D849N and *Eif2s1* S52A). Further phenotypical and functional analyses are reported in sections 4.4.-4.7.

4.1.4. Genetic characterization of *Atf4* loss-of-function alleles

Amino acid deprivation activates a highly specific and conserved transcriptional response in which specific ISR-linked transcription factors are upregulated⁶¹. ATF4 is a central example of this, controlling the expression of a specific set of proteins for the ISR¹⁵. ATF4 is a member of the conserved bZIP transcription factor family, which further regulates the expression of *Ddit3* (Ref.⁹⁶), the target of our stress response reporter systems (Section 4.1.5.). To determine the relevance of ATF4 in our system, we studied its role by loss-of-function.

ATF4 deficiency was reported in Torrence *et al.*²⁶, which provided two functional gRNAs targeting the second coding exon (exon 3) located on chromosome 15 used for their CRISPR/Cas9 genome engineering approach (Table 5). We cloned the gRNAs individually into a puromycin-marked vector (pLentiGuide-Puro) and transfected the gRNA-construct separately in 3T3 Cas9 containing cells (Section 3.2.3.2.; Table 6). The out of frame loss-of-function was confirmed by Sanger sequencing (Section 7.1.3.) and highlighted in red in the consensus alignment in (Figure 21).



Consensus: sequence alignment WT and *Atf4*^{-/-} in 3T3

Figure 21. Schematic representation of the sequence-based characterization of ATF4 deficiency. Schematic overview of the mouse *Atf4* (coding for ATF4) locus on chromosome 15 (2.358 kb; two coding exons). The second coding exon (exon 3; blue) was CRISPR/Cas9-genetically modified using gRNA 1 and 2 (blue). Consensus sequence alignment (in red) with wild-type (WT) illustrates the gRNA-induced INDELS (insertions and deletions) in the bulk derived *Atf4*^{-/-} 3T3 line (further termed ATF4^{-/-}). Detailed information is summarized in sections 3.2.3.2. and 7.1.3.

In conclusion, a bulk derived ATF4 biallelic deficient 3T3 cell line (ATF4^{-/-}, hereafter) was established, which forms an important tool for the dissection of the GCN2-ISR described in later components of this thesis.

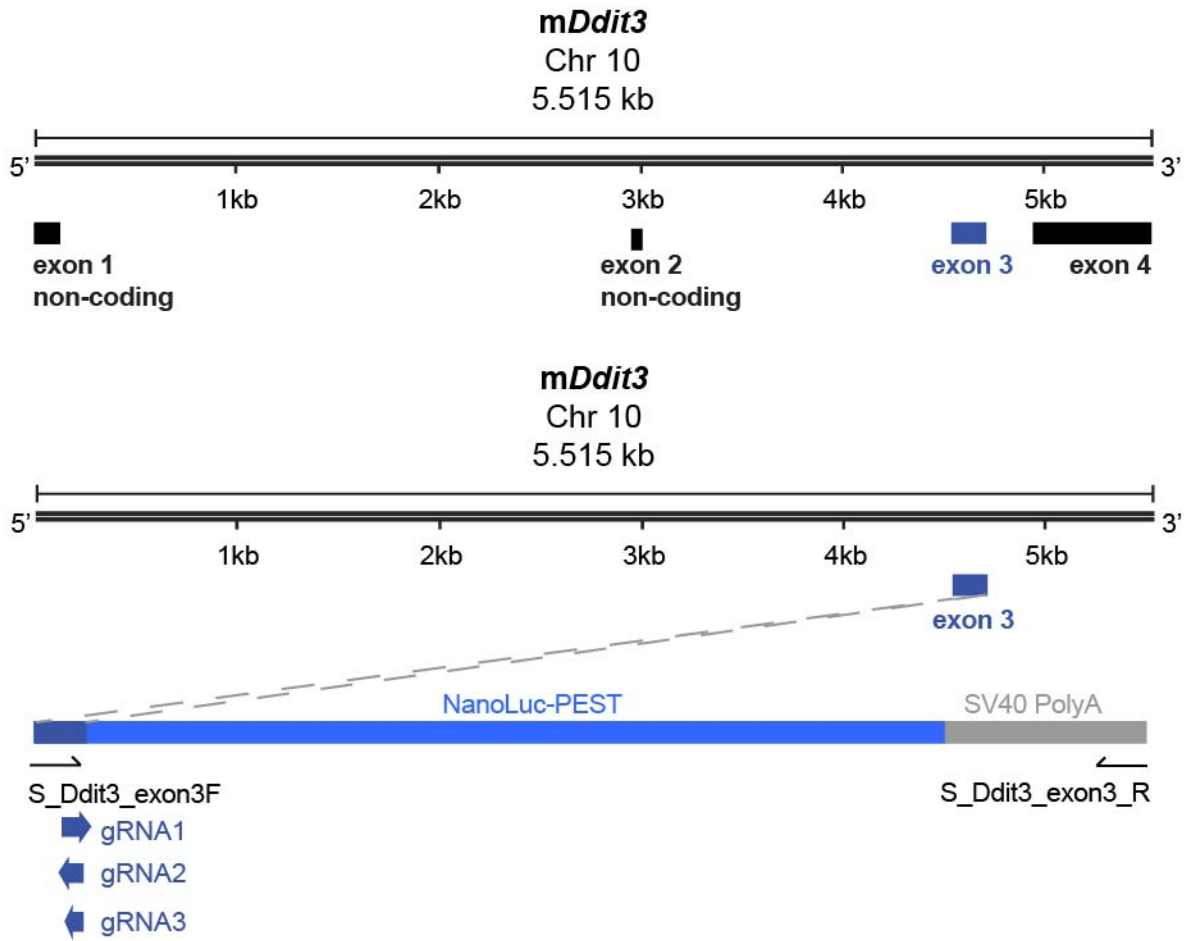
4.1.5. Genetic characterization of GCN2-dependent amino acid stress reporter cell systems

Previous studies indicate that the *Ddit3* expression (coding for CHOP) is tightly controlled by GCN2 under amino acid stress⁷². To enable the screening and analysis of changes dependent on GCN2 and the amino acid availability, we made use of this connection to establish two cellular

GCN2 amino acid stress reporter systems. The mCherry reporter system was used to study the GCN2 driven amino acid response as a proof of concept (Section 4.2.2.). The NanoLuc-PEST line was constructed for the GCN2 kinase inhibitor screen (Section 4.7.). We decided to use NanoLuc-PEST, because it is more sensitive and technical easier than mCherry for a large-scale robotic screen⁴³⁵. Also, the PEST-tag-induced degradation lowers the signal-to-noise ratio⁴³⁶.

First, we used the CRISPR/Cas9-mediated genome engineering technique to introduce out of frame INDELS in the first coding exon (exon 3) of the *Ddit3* locus on chromosome 10. Successful homologous recombination with synthetic repair plasmid replaced the entire coding exon of *Ddit3* with mCherry or NanoLuc-PEST translation beginning with the exact genomic and transcript context as *Ddit3*. Cells were transfected with three partly overlapping gRNAs, which were designed with the CRISPR Design tool (MIT, Prof. Dr. Feng Zhang) (Section 3.2.3.4.; Table 16). The CRISPR-induced INDELS were repaired with a mCherry or NanoLuc-PEST plasmid co-transfected with the gRNAs and consisting of mCherry or NanoLuc-PEST coupled to the SV40 polyadenylation signal at the 3' end (Section 3.2.3.4.; Tables 17, 18 and 19). The GFP⁺-sorted cells were then expanded and amino acid starved for 24 h. Amino acid starvation induced the expression of NanoLuc or mCherry, which enabled us to sort by Flow only mCherry⁺ cells or by chemiluminescence to read out only luciferase⁺ cells (Section 3.4.2.). Cells were single-cell-diluted and successful genome editing was confirmed by Sanger sequencing (Figure 22A+B; Section 7.1.4.). For both reporter systems one positive clone was verified (Table 31). To map the robust amino acid inducible reporter system to the GCN2 cascade, a loss-of-function deficiency in GCN2 was introduced in the positive mCherry line, as described above. The deficiency was confirmed by Sanger sequencing (Figure 19A; Section 7.1.1.). Additionally, the wild-type mCherry reporter cell line was also established in E14 cells (Figure 22B; Section 7.1.4.).

A



Consensus: sequence alignment WT and *Ddit3*::NanoLuc-PEST in 3T3

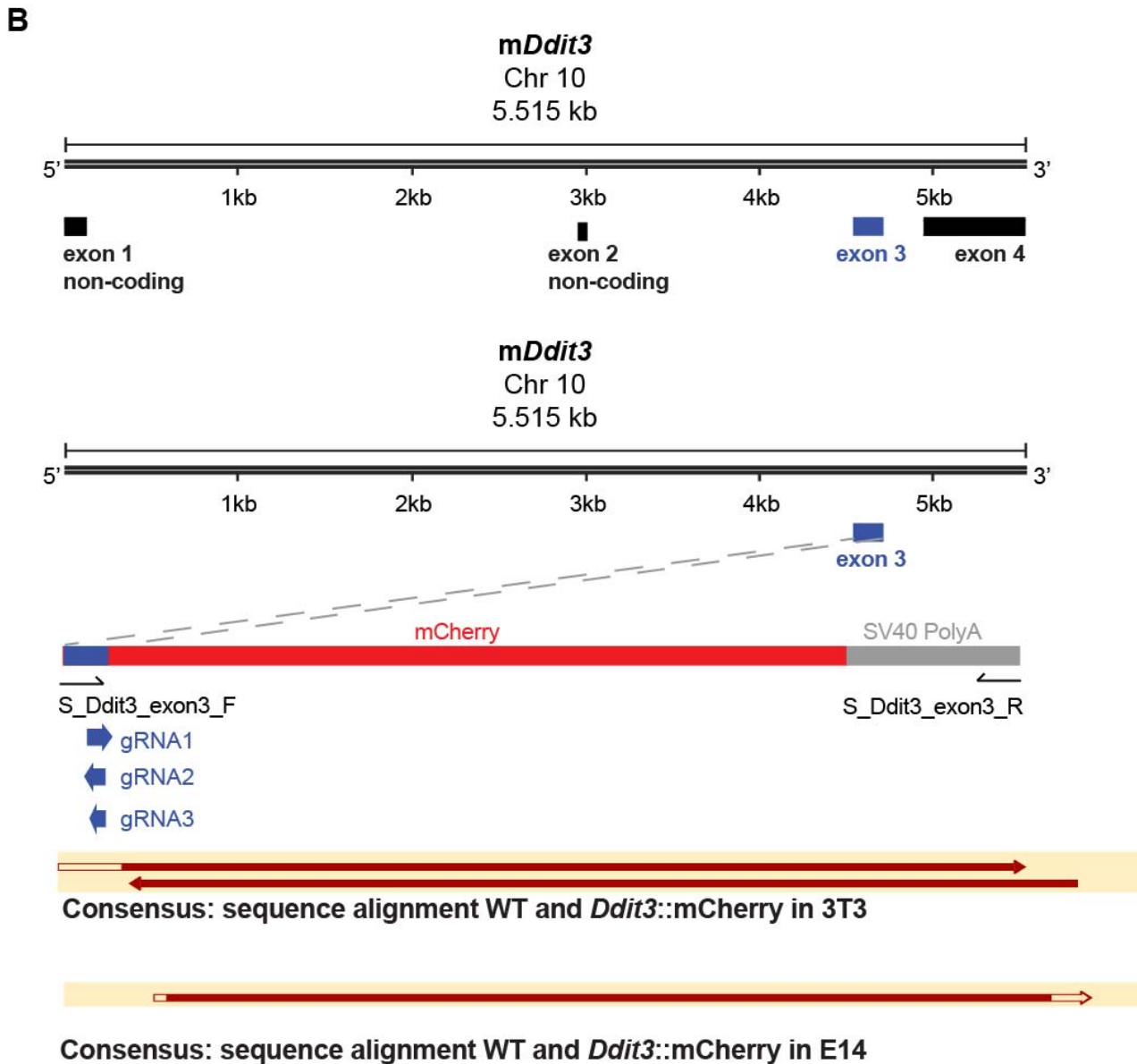


Figure 22. Schematic representation of the sequence-based characterization of mCherry and NanoLuc-PEST insertion into *Ddit3*. (A) Schematic overview of the mouse *Ddit3* (coding for CHOP) locus on chromosome 10 (5.515 kb; two coding exons). The first coding exon (exon 3; blue) was CRISPR/Cas9-genetically modified using gRNA 1, 2 and 3 (blue). Consensus sequence alignment (in red) with wild-type (WT) illustrates the NanoLuc-PEST insertion of the generated 3T3 *Ddit3*::NanoLuc-PEST cell line. (B) Schematic overview of the mouse *Ddit3* (coding for CHOP) locus on chromosome 10 (5.515 kb; two coding exons). The first coding exon (exon 3; blue) was CRISPR/Cas9-genetically modified using gRNA 1, 2 and 3 (blue). Consensus sequence alignments (in dark red) with wild-type (WT) illustrate the mCherry insertion of the generated *Ddit3*::mCherry cell lines in 3T3 and E14. Detailed information is summarized in sections 3.2.3.4. and 7.1.4.

In conclusion, two robust amino acid stress-induced reporter systems were established in murine cell lines (3T3 and E14), which enabled functional studies of amino acid response in a GCN2

dependent manner. The reporter systems can be read out fluorimetrically (*Ddit3::mcherry* cell line and GCN2^{-/-} + *Ddit3::mcherry*; hereafter) or by chemiluminescence (*Ddit3::NanoLuc-PEST* cell line, hereafter).

4.2. Multi-omics analysis of GCN1 and GCN2 deficiency

4.2.1. Overview

To gain a global insight into the ISR upon amino acid stress, we determined the optimal experimental conditions to quantify the stress response in our murine cell system(s). Therefore, we made use of the generated reporter cell lines (Section 4.1.5.) to track amino acid depletion over time determining the 'starvation cocktail' that was applied to broad omics analyses. We performed two matched large-scale omics studies at the transcriptome and proteome level (Section 4.2.3.-4.2.4.1.) in GCN1 and/or GCN2 pro- and deficient 3T3 cells to transfer findings to the cellular context (Section 4.3.). In addition, a phosphoproteomics approach was performed to identify specific GCN2 targets (Section 4.2.4.2.). Moreover, interaction proteomics was conducted to determine interactors of GCN1 in normal growth and under amino acid stress (Section 4.2.5.).

4.2.2. Investigation of the optimal amino acid starvation conditions

The transcription factor CHOP (encoded by *Ddit3*) is universally upregulated by the four mammalian eIF2 α stress kinases independent of the type of stress^{60,96}. Amino acid depletion triggers the activation of the GCN2-induced stress cascade that can be tracked by the induction of *Ddit3* expression (Figure 23A). As reported in section 4.1.5., we made use of this connection by inserting a reporter construct for either fluorescence or chemiluminescence read-out in the *Ddit3* coding locus (Figure 23B). Using our established GCN2-dependent reporter systems, we tested diverse stimuli in order to figure out the most potent activator(s) of the GCN2-regulated ISR in a time-dependent fashion. This enabled us to choose the optimal conditions to investigate the ISR in a GCN1 and/or GCN2 deficient context in the following global omics studies.

To start, we tracked GCN2 at the gene and protein level in the reporter lines (*Ddit3::mCherry* and *Ddit3::NanoLuc-PEST*) versus 3T3 cells in GCN2 pro- and deficient background. Both systems showed consistent GCN2 expression with the prevailing notion that GCN2 activity is not overtly regulated by protein amounts (Figure 23C+D).

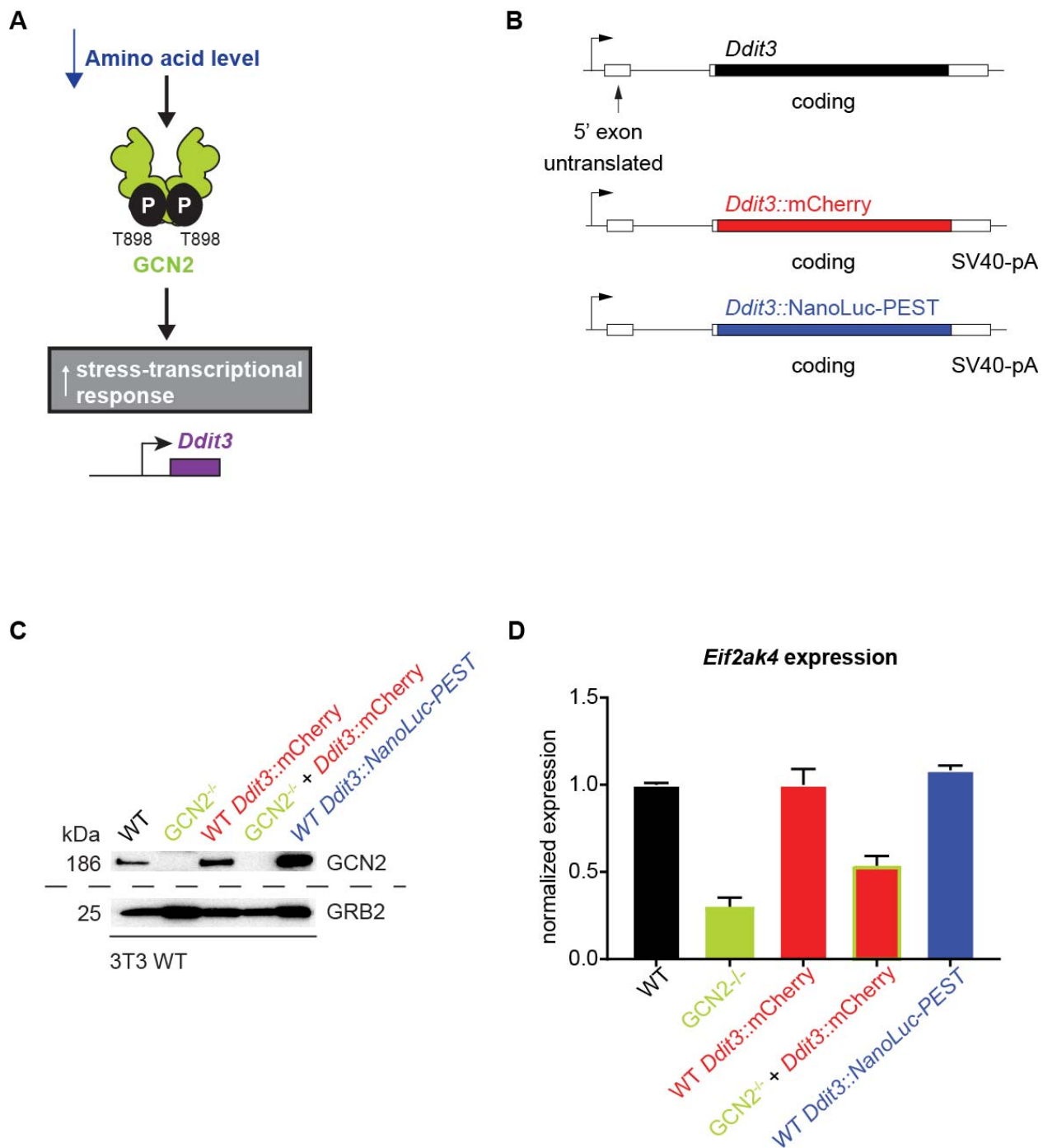
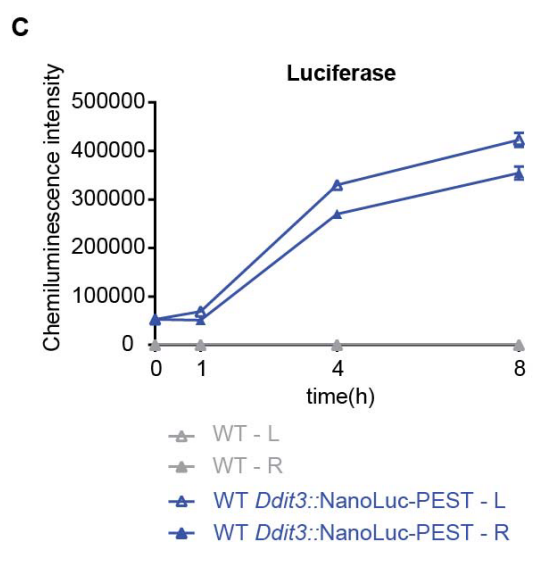
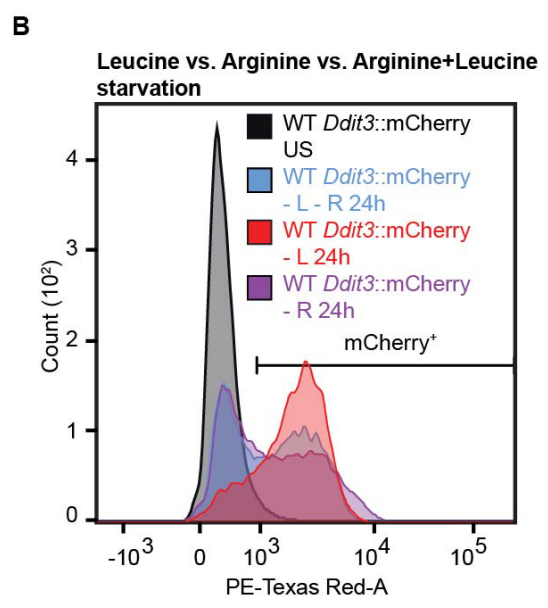
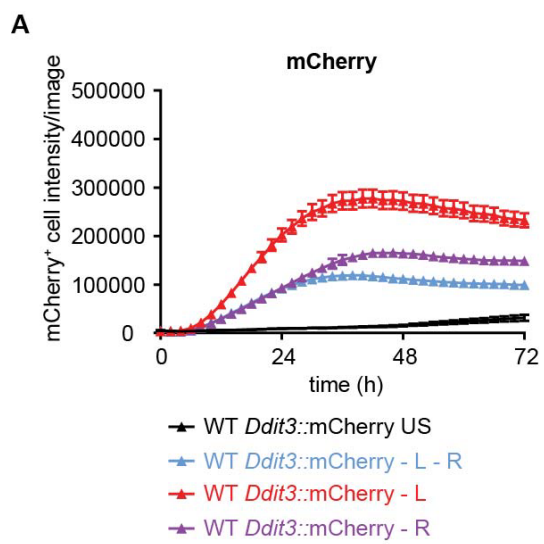


Figure 23. Genetic modification of the *Ddit3* locus does not affect the expression of GCN2 at the gene and protein level. (A) Overall principle of the stress-transcriptional program⁷²: amino acid depletion (blue) activates GCN2 by dimerization and autophosphorylation at T898 (green; encoded by *Eif2ak4*) that increases the induction of *Ddit3* (coding for CHOP). (B) Schematic representation of the reporter cloning strategy inserting into the first coding exon of *Ddit3* (black) either mCherry (red) or NanoLuc-PEST (blue). Detailed information is provided in the section 4.1.5. (C) Representative immunoblot of lysates from *Ddit3* modified (*Ddit3::mCherry* (red) and *Ddit3::NanoLucPEST* (blue)) versus non-*Ddit3* genetically engineered 3T3 cell lines under unstarved condition. The GCN2 deficient lines are indicated by GCN2^{-/-} (light green)

compared to the wild-type (WT) ones. GRB2 was used as loading control. (D) Normalized expression of *Eif2ak4* in the described *Ddit3* modified and non-modified cell lines from B. (C-D) Data are depicted as mean + SEM of three independent experiments or one of two representative gels.

Next, we applied depletion of a cocktail of essential amino acids to our *Ddit3*::mCherry reporter cell line and tracked the induction of mCherry over time by FACS analysis and live-cell imaging (IncuCyte). Therefore, the two amino acids leucine (L) and arginine (R) were chosen based on their involvement in the mTORC1 amino acid signaling⁴¹. Single and double depletion of leucine and/or arginine increased the mCherry response over time (Figure 24A+B). Interestingly, the deprivation of leucine induced the strongest activation of the GCN2 driven ISR in comparison to arginine or double depletion, which was shown in both assays and could be detected as well by eye over time (Figure 24D). Moreover, the time-dependent and leucine potent induction was also confirmed in the NanoLuc-PEST system (Figure 24C).



D

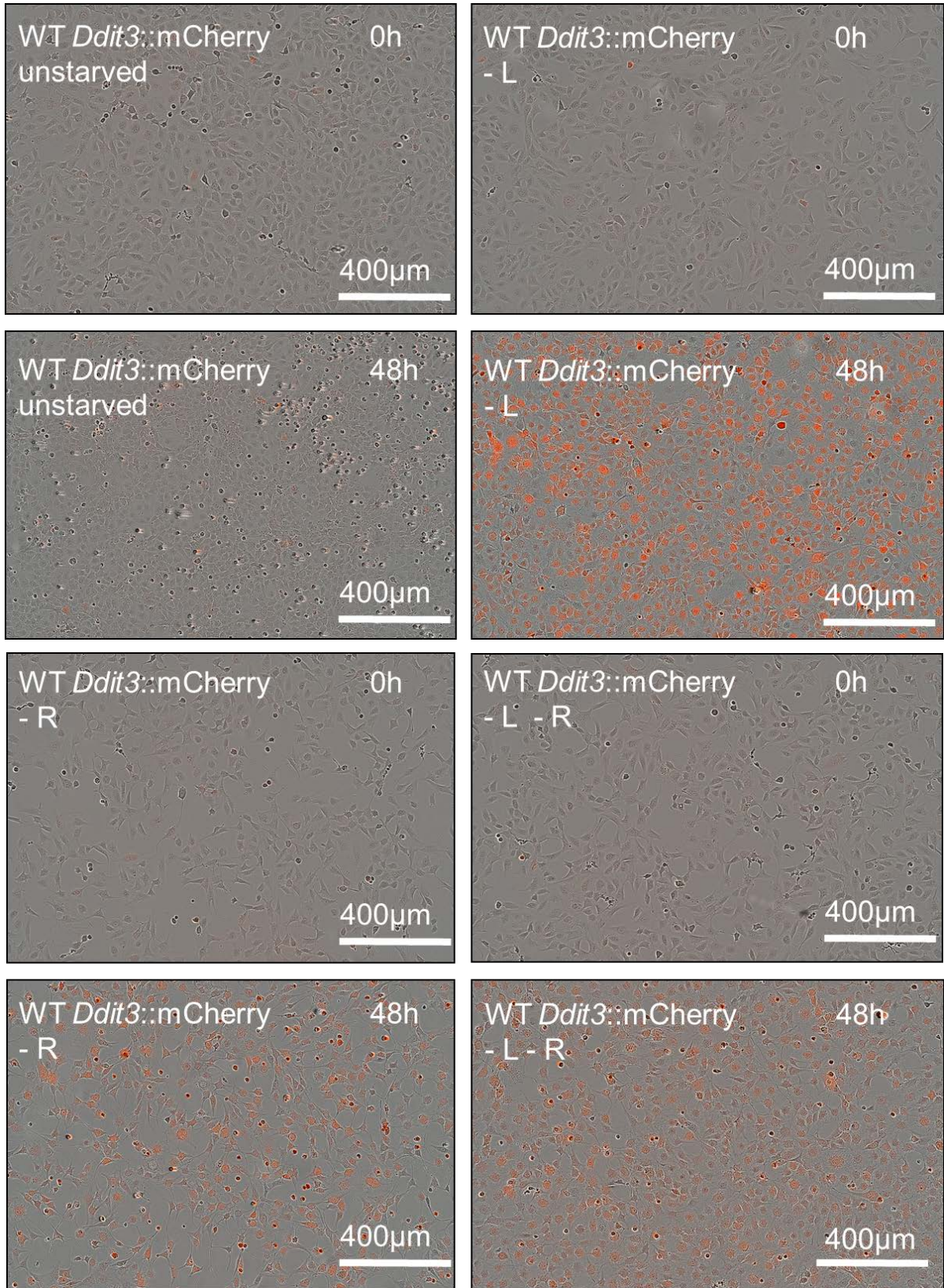
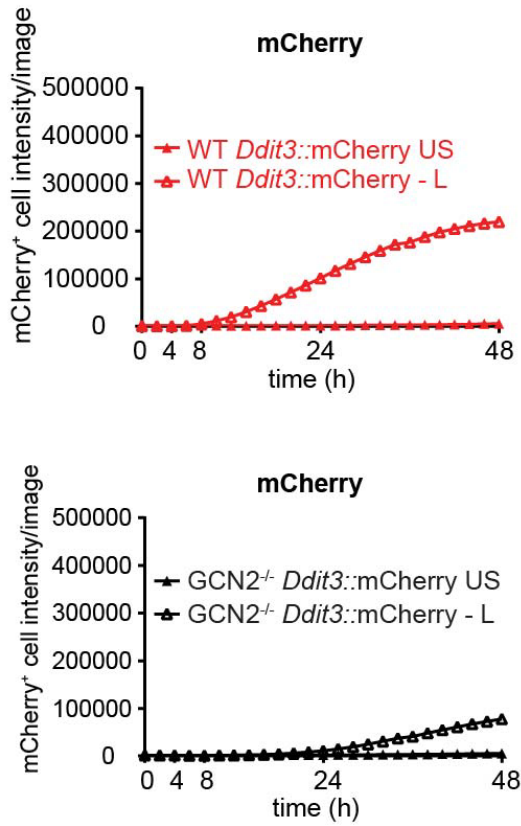
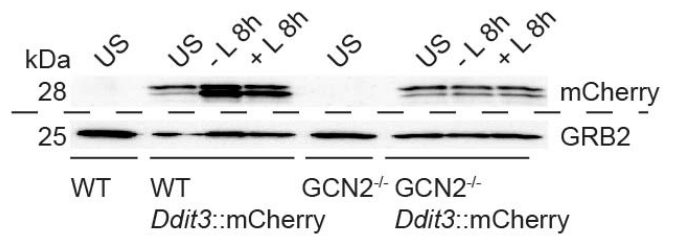
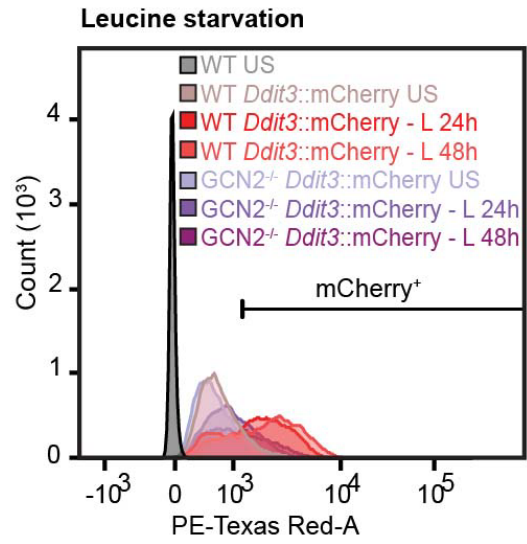


Figure 24. Amino acid stress-induced *Ddit3* reporter systems function as indirect read-out for the activation of the GCN2-ISR at the cellular level. (A) Quantification of the mCherry intensity of 3T3 wild-type (WT) *Ddit3*::mCherry cells stimulated with unstarved condition (US), leucine (- L; red), arginine (- R; purple) and leucine plus arginine (- L - R; blue) starvation for 72 h. (B) Same setup as described for B, except: the mCherry intensity was tracked by Flow in the PE-Texas Red channel for 24 h. (C) Quantification of the chemiluminescence intensity in 3T3 wild-type (WT; grey; control) and *Ddit3*::NanoLuc-PEST cells (blue) stimulated with leucine (- L) or arginine (- R) starvation for 0 h, 1 h, 4 h and 8 h. (D) Microscopic visualization of mCherry⁺ cells from B upon amino acid stress over time (comparison: 0 h versus 48 h). (A+C) Data are depicted as mean + SEM of three independent experiments.

To map the induction of the ISR to the GCN2 cascade, live-cell imaging analysis (IncuCyte) was applied to the GCN2 deficient *Ddit3*::mCherry reporter cells (GCN2^{-/-} + *Ddit3*::mCherry), which showed no potent increase in mCherry signal compared to the wild-type counterpart over time upon leucine stress (Figure 25A). This was confirmed at the protein level by the mCherry signal (Figure 25B). In case of long-term leucine starvation (more than 24 h), the GCN2 deficient cells induced a mCherry signal (Figure 25A+C). This can be explained by the eventual activities of other stress kinases regulating CHOP and consequently mCherry at prolonged stress exposure^{15,60}. Furthermore, the long-term starvation triggers cell death, as shown by the round dead mCherry positive cells at 48 h (Figure 25D). This effect eventual biases the readout of mCherry⁺ cells at 48 h. Therefore, we decided to investigate the molecular amino acid signaling network for further functional analyses choosing the timeframes from 1 h, 4 h, 8 h and 24 h.

A**B****C**

D

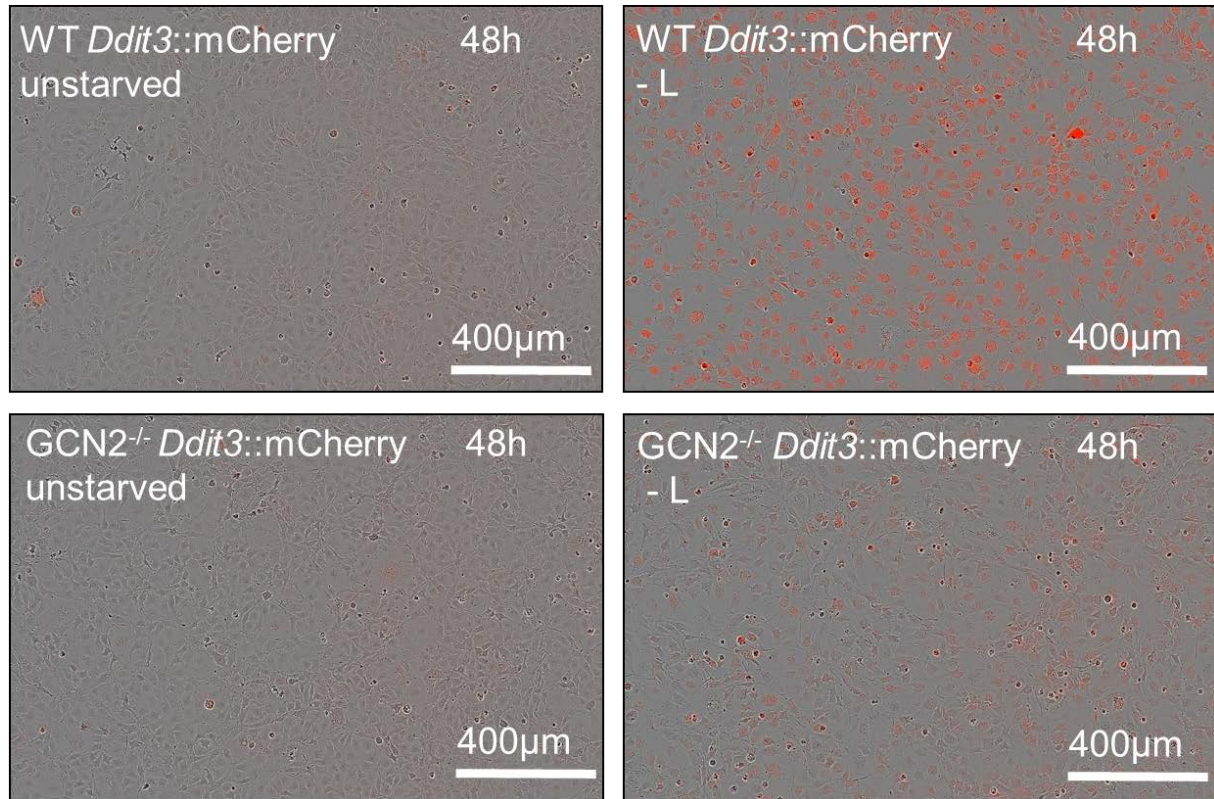


Figure 25. Amino acid stress-induced *Ddit3* reporter cells respond dependent on GCN2. (A) Quantification of mCherry intensity of 3T3 *Ddit3*::mCherry cells, de- and proficient in GCN2 (WT; GCN2^{-/-}) stimulated with leucine stress (- L) or unstarved condition (US) for 48 h. (B) Immunoblot of 3T3 *Ddit3* modified and non-modified, de- and proficient in GCN2 (WT; GCN2^{-/-}), cell lysates stimulated under unstarved condition (US), leucine- starvation (- L) or leucine-resupplementation (+ L) for 8 h. GRB2 was used as loading control. (C) Same setup as described for A, except: the mCherry intensity was tracked by Flow in the PE-Texas Red channel for 24 h and 48 h. The *Ddit3*-non modified wild-type (WT) cell line served as control. (D) Microscopic visualization of mCherry⁺ cells from A upon leucine stress or unstarved condition at 48 h. (A+B) Data are depicted as mean + SEM of three independent experiments or one of two representative gels.

To link the induction of mCherry with the induction of *Ddit3*, the mCherry cell lines were compared to their non-genetically-modified counterparts at the gene and protein level. Tracking the *Ddit3* versus *mCherry* gene expression, both cell systems responded to the same extent upon leucine and arginine depleted stimuli over time (Figure 26A). At the protein level, we detected the same phenomenon reading out CHOP versus mCherry expression levels: Both stimuli induce only the activation of the GCN2 driven ISR in wild-type, but not GCN2^{-/-} cells (Figure 26B). In this context, thapsigargin, an inhibitor of the sarco/endoplasmic reticulum Ca²⁺ ATPase, provided a key control as a PERK-activating reagent that induced mCherry and CHOP independent of GCN2 presence

or amino acid stress (Figure 26B). Importantly, ATF4, the upstream transcription factor of CHOP, was also not induced upon amino acid stress in a GCN2 deficient context that matches to reported literature data⁹⁶. However, a stronger induction of the ISR by leucine compared to arginine deprivation was not detected at the gene as well as at the protein level, as it was observed by live-cell imaging (Figure 24). Thus, we checked the codon usages of *Ddit3* and *mCherry* arguing that the potency of leucine towards arginine stress by live-cell imaging is maybe a consequence of codon usage (Figure 26C). Consequently, leucine and arginine depletion were mainly used for comparative experimental studies in this thesis, also keeping in mind that both amino acids are main driver of mTORC1-mediated amino acid signaling⁴¹⁻⁴⁶.

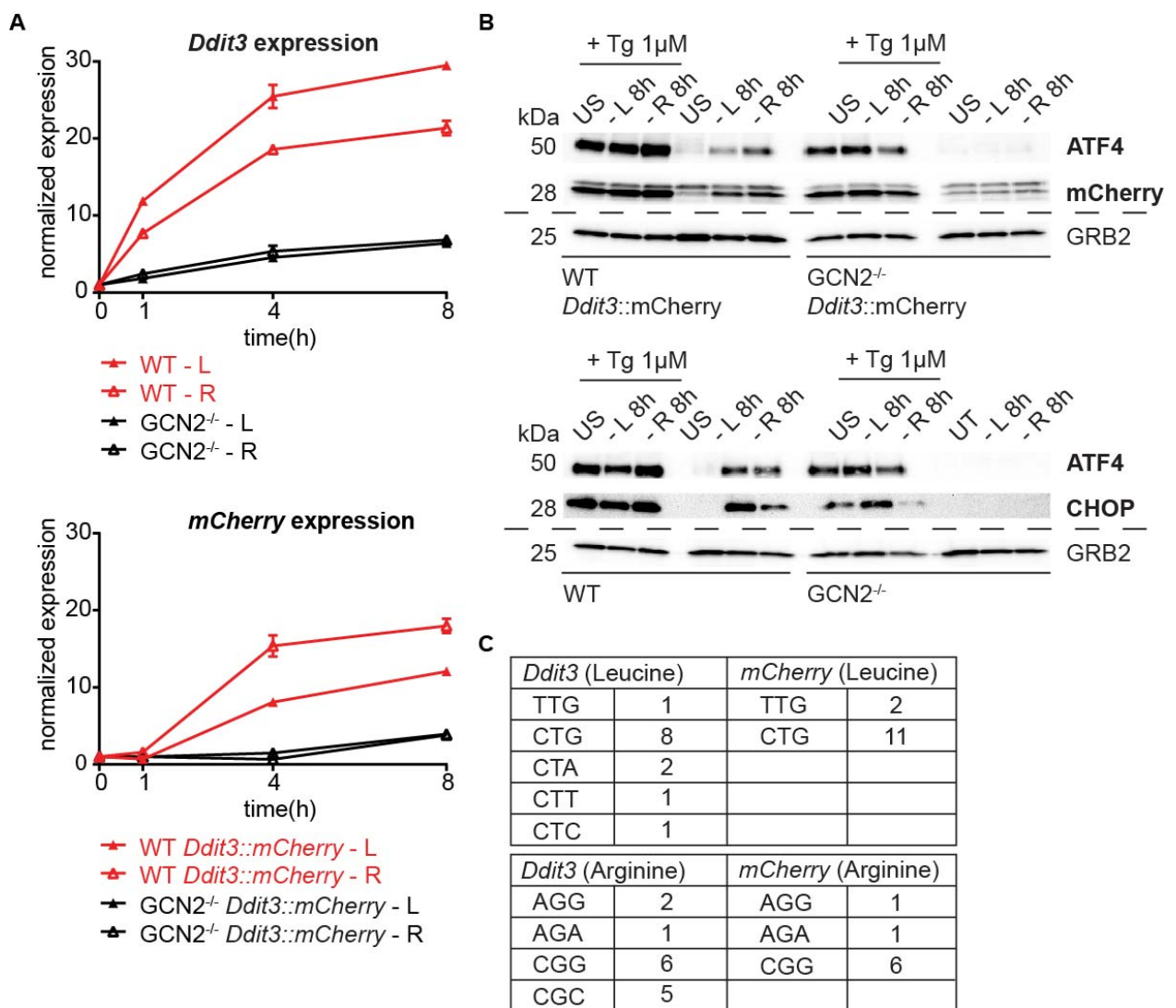
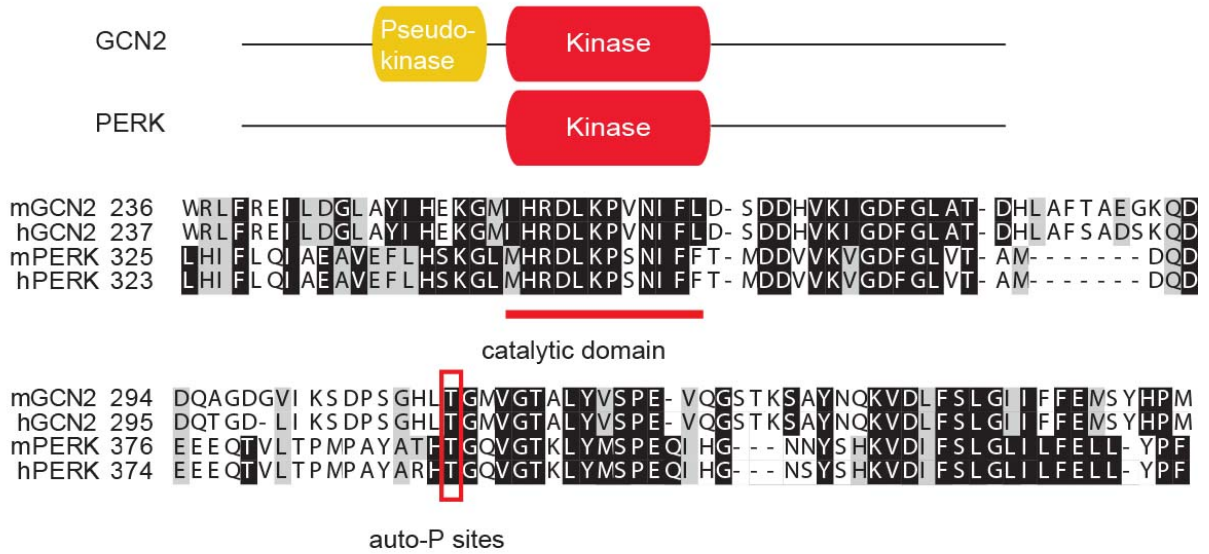


Figure 26. GCN2 driven amino acid response is trackable at the gene and protein level. (A) Normalized *mCherry* and *Ddit3* expression levels of *Ddit3* modified and not-modified cells (WT; GCN2^{-/-}) treated for 0 h, 1 h, 4 h, 8 h with leucine (- L) or arginine (- R) stress. (B) Immunoblot of 3T3, de- and

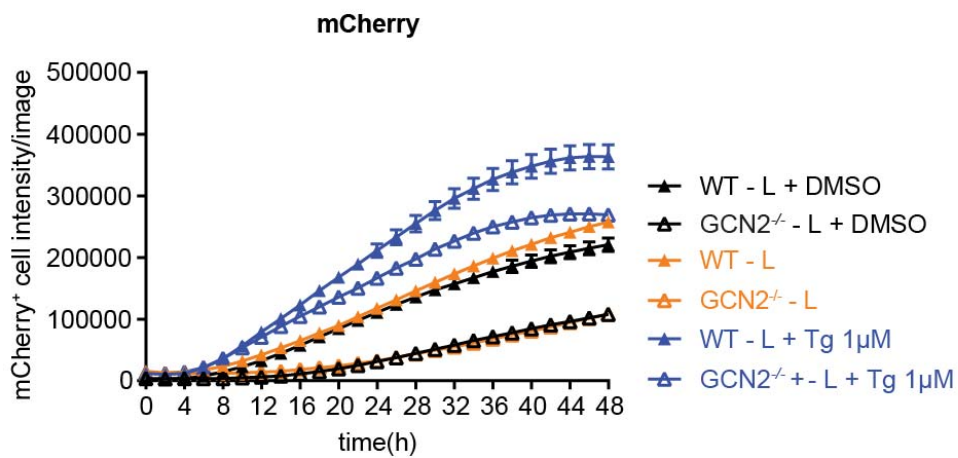
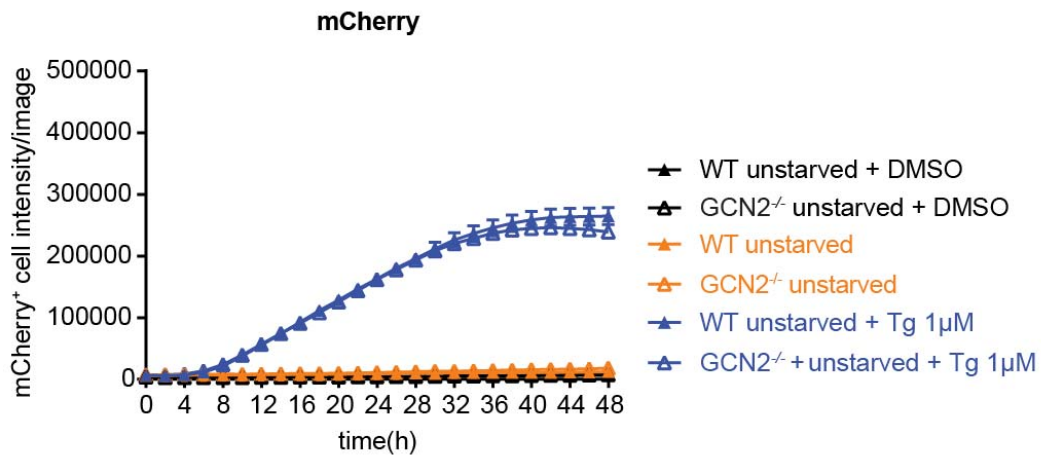
proficient in GCN2 (WT; GCN2^{-/-}) cell lysates stimulated under unstarved condition or leucine- (- L) or arginine (- R) starvation for 8 h in combination with thapsigargin (Tg; 1 μ M) treatment. Same was performed with the *Ddit3*:mCherry modified counterparts. GRB2 is the loading control. In bold, changes due to the genotype. (C) Codon usage of leucine and arginine of *mCherry* versus *Ddit3* genes. (A+B) Data are depicted as mean + SEM of three independent experiments or one of two representative gels.

Based on the findings (Figure 26B) that thapsigargin-mediated PERK signaling induces CHOP, ATF4 and mCherry independent of GCN2 presence upon amino acid stress, we decided to screen PERK activation in more detail. In mammals, the two eIF2 α kinase members PERK and GCN2 have intrinsically similar catalytic domains and autophosphorylation sites for kinase activation (PERK: T980; GCN2:T898) (Figure 27A). Therefore, we asked if PERK is activated over time upon amino acid stress or solely triggered by ER stress. We found that thapsigargin-induced ER stress upregulated mCherry expression more potently than amino acid stress at the cellular level, which may explain why mis- and unfolded proteins are more proteotoxic than amino acid deficiency in a cellular environment^{12,437}. This mCherry induction is independent of GCN2 or amino acid stress (Figure 27B). This was also shown for arginine and leucine stress at the protein level, where PERK was only activated (autophosphorylation at T980) when thapsigargin was added to the cells (Figure 27C+D). In this context, thapsigargin-stimulated PERK autophosphorylation did not stimulate the activation of GCN2 (autophosphorylation of T898) (Figure 27C). Combined, PERK signaling is not activated upon amino acid stress at time points below 24 h, which is an important consideration for our further time-resolved amino acid starvation studies (1 h, 4 h, 8 h and 24 h).

A



B



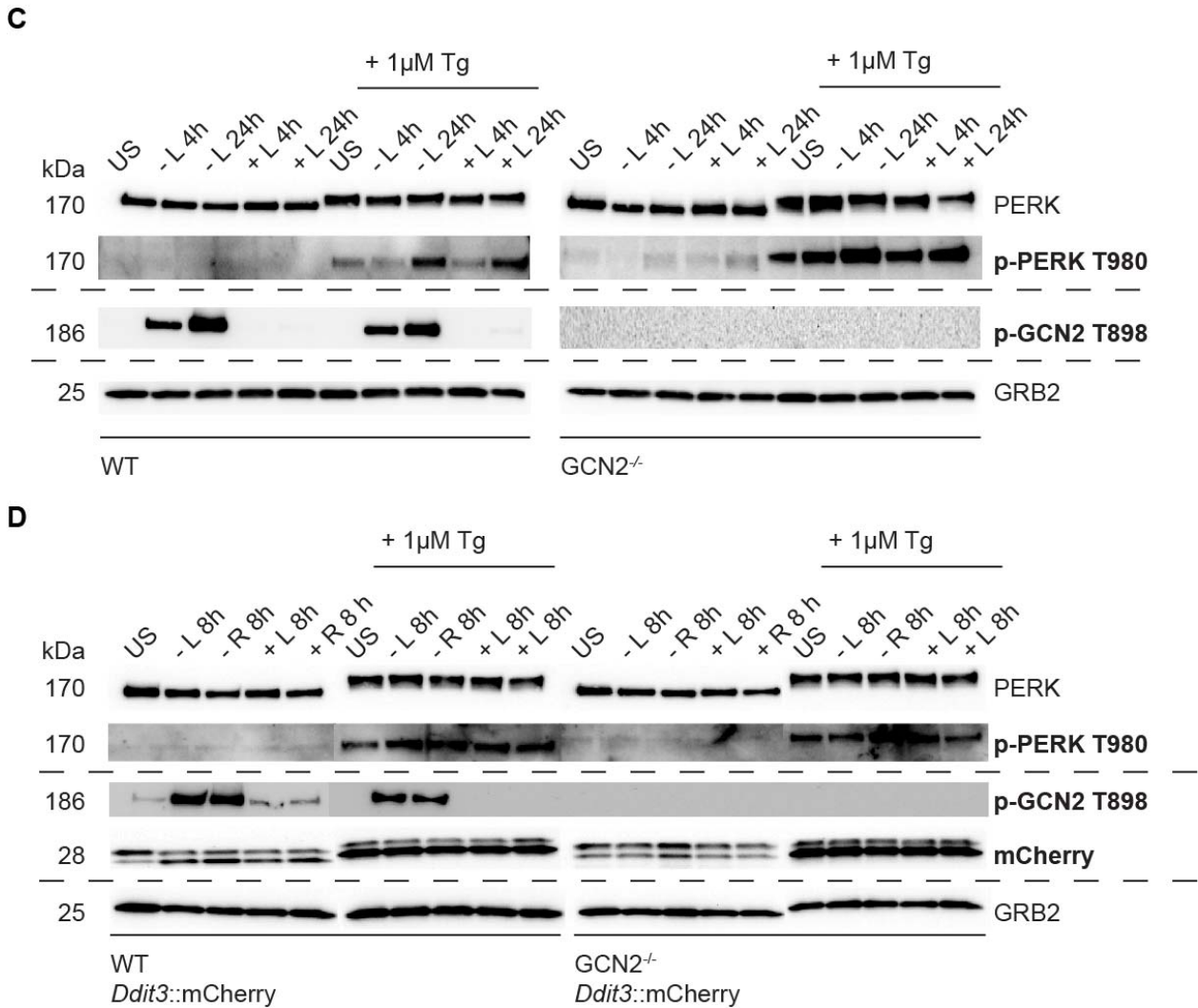


Figure 27. PERK signaling is not activated upon amino acid stress up to 24 h. (A) Scheme of the sequence similarities of the autophosphorylation sites and the catalytic domains of GCN2 and PERK (human and mouse). In contrast to PERK, GCN2 consists of an additional pseudokinase domain (yellow) next to its kinase domain (red). (B) Quantification of mCherry intensity of 3T3 *Ddit3::mCherry* cells, de- and proficient in GCN2 (WT; GCN2^{-/-}), treated with leucine (- L) starved or unstarved medium for 48 h in the presence of thapsigargin (Tg; 1 μM). Data are depicted as mean + SEM of three independent experiments. (C) Immunoblot of unstarved (US) and leucine-starved 3T3 wild-type (WT) and GCN2 deficient (GCN2^{-/-}) cell lysates treated with thapsigargin (Tg; 1 μM) upon leucine-starved (- L) or leucine-resupplemented (+ L) condition at 4 h and 24 h. GRB2 was used as loading control. (D) Immunoblot of 3T3 *Ddit3::mCherry* cells, de- and proficient in GCN2 (WT; GCN2^{-/-}), treated with thapsigargin (Tg; 1 μM) upon unstarved condition (US), leucine (- L) or arginine (- R) depletions or resupplementations (+ L or + R) for 8 h. GRB2 was used as loading control. (B-D) Data are depicted as mean + SEM of three independent experiments or one of two representative gels. (C-D) In bold, changes due to the compound treatment.

Moreover, we optimized our 'amino acid starvation medium' in further detail. We checked if dialyzed serum in different amounts affects the mCherry response. This was done, because our 'amino acid starvation medium' was prepared equivalently to the normal cell culture medium except using self-made dialyzed FBS (Section 3.3.1.). As shown by live-cell imaging, the use of 5 % dialyzed FBS instead of 10 % FBS did not affect the overall ISR induction for the indicated used timeframe (Figure 28A). Consequently, we continued with 5 % dialyzed FBS keeping in mind that our self-made dialyzed FBS might have residual tryptophan due to the molecular weight cutoff of the dialysis membrane. In addition, we also showed that our reporter system worked equally in two diverse cell culture media (RPMI versus DMEM), which is relevant when applying stress on differently cultured cell types (Figure 28B). In this thesis, the murine cells were cultured in DMEM. Thus, we decided to use DMEM instead of RPMI as the basis for our 'amino acid starvation medium'. In addition, the amino acid-induced stress response could also be tracked over time in the E14 cells (Figure 28C).

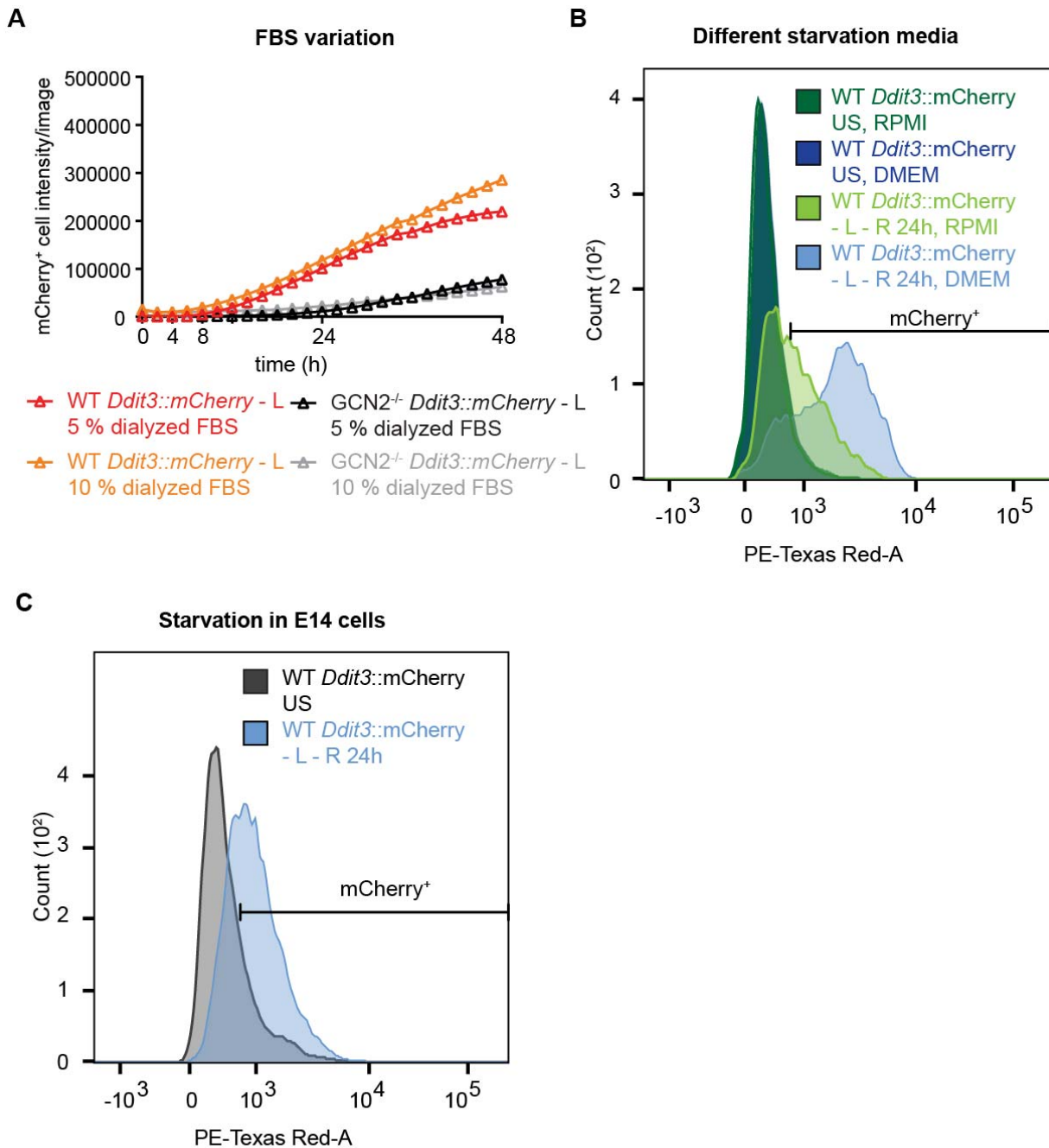


Figure 28. GCN2 dependent *Ddit3* reporter system is robust in sensing amino acid starvation. (A) Quantification of mCherry intensity of 3T3 *Ddit3::mCherry* cells, de- and proficient in GCN2 (WT; GCN2^{-/-}), stimulated with leucine (- L) starvation with varying amounts of dialyzed FBS up to 48 h. Data are depicted as mean + SEM of three independent experiments. (B) Quantification of mCherry intensity of 3T3 *Ddit3::mCherry* cells treated with leucine and arginine (- L - R) starvation in two different culture media (RPMI versus DMEM) for 24 h. Unstarved cells (US) were used as control. mCherry intensity was measured by Flow in the PE-Texas Red channel. (C) Same setup as described for B, except: E14 *Ddit3::mCherry* cells were used and starved with DMEM containing arginine and leucine depletion (- L - R) for 24 h.

In conclusion, the established amino acid stress reporter systems work efficiently to track any kind of amino acid depletion over time in a GCN2 dependent manner at the live-cell, the gene and the protein level. The best conditions to further study the GCN2-ISR at the molecular level were arginine and leucine depletion at 1 h, 4 h, 8 h and 24 h. These conditions were overall used in this thesis (i) to investigate the transcriptome and proteome changes upon amino acid stress, (ii) to dissect the mTORC1 and the GCN2 interplay at early and late amino acid stress stages and (iii) to chemically manipulate the GCN2-ISR upon amino acid starvation (Sections 4.2.-4.7).

4.2.3. Transcriptomics study of GCN1 and GCN2 deficiency

RNASeq is a powerful technique, which has the capability to quantify gene expression changes induced by loss-of-function mutagenesis⁴³⁸. Transcriptional changes induced by the ISR were highlighted in a study from Harding *et al.*¹⁵, who showed in mouse embryonic fibroblast that the ER stress-induced PERK-ATF4 axis mediates processes involved in amino acid biosynthesis, amino acid transport and resistance to oxidative stress. Studies focused more on ATF4 after its regulation of other bZIP transcription factors for cellular stress response was reported by Newman *et al.* and Wortel *et al.*^{73,102}. Next, Park *et al.*⁹⁵ showed that insulin-treated mTORC1 also fine-tunes mRNA levels of amino acid transporters, metabolic enzymes, and aminoacyl-tRNA synthetases expressions that were independent of eIF2 α phosphorylation, but dependent on ATF4-4EBP1. Recently, a broad transcriptional study comparing transcript level changes induced by insulin-activated mTORC1 versus tunicamycin-activated PERK-ISR signaling, highlighted that both pathways co-opt ATF4¹⁵. Furthermore, mTORC1 specifically activates additional ATF4-mediated transcripts involved in glutathione biosynthesis, 1C-metabolism or purine biosynthesis^{15,26,29}. Due to the highly cited findings that GCN2 contributes to mTORC1 inhibition through an ATF4-independent mechanism upon amino acid stress^{179,370}, the GCN2-ATF4 driven transcriptional changes were not brought into context until now. Even if, GCN2 was further found to sustain mTORC1 suppression via the ATF4-SESTRIN2 axis upon prolonged amino acid starvation (24 h)³⁴⁴. Given the complexity of these interactions in stress sensing and response, we aimed to elucidate transcriptional changes upon amino acid stress in a time-resolved manner. To this end, a transcriptomics study was performed in collaboration with Dr. Maja Driessen and Dr. Assa Yeroslaviz from the MPIB Core Facility.

We conducted a transcriptome analysis upon leucine stress over time in the wild-type and GCN1 and/or GCN2 deficient 3T3 cells to map global changes of the GCN1-GCN2 cascade in a time-dependent fashion. Cells were stimulated for 1 h, 4 h and 8 h with leucine-depletion medium (Figure 29A), while unstimulated cells in normal growth medium served as unstarved condition. In total, three biological replicates were provided to measure the gene expression signature of each genotype by Illumina sequencing (Section 3.7.1.). After statistical processing 12,147 from

26,672 genes were ANOVA significant and used for conditional analysis. All gene names listed in this chapter are referred to the terminology from the HUGO gene nomenclature committee (www.genenames.org).

Principal component analysis (PCA) was performed to determine the distribution of the genetic signatures of the GCN1 and/ or GCN2 deficient lines (GCN1^{-/-}, GCN2^{-/-} and GCN2^{-/-} + GCN1^{-/-}) in comparison to the wild-type (WT) across time (Figure 29B). Importantly, the biological replicates clustered tightly for each condition, indicating the reproducibility of the system. Interestingly, each cell line showed a distinct pattern in an unstarved context that is shifted over time by leucine stress. Long-term (4 h and 8 h) leucine stress changed the gene expression profile far more than early stress exposure (1 h). Therefore, we concluded that the loss of GCN1 and/or GCN2 leads to an adaptation of the cell to adjust its biological gene signature for intrinsic physiological survival. Moreover, we found that the pattern of the GCN2 deficient and the double deficient lines was more similar than to the GCN1 deficient line. This suggested that GCN2 dominates the overall transcriptional profile. Interestingly, the GCN1^{-/-} line regulated its own transcriptional make-up independently of GCN2 suggesting a distinct transcriptional regulatory function for GCN1. This observation is discussed further below.

Next, we checked the number of significant genes that were genotype and treatment-based dependently upregulated (Figure 29C). For the wild-type, more than 60 genes changed significantly upon leucine stress at 1 h and increased up to more than 1,600 genes at the 4 h time point and more than 2,800 genes at the 8 h time point. This is in stark contrast to the GCN2^{-/-} and the GCN1^{-/-} cell line, losing up to 49 % of the differentially expressed genes compared to the wild-type condition. Interestingly, independently of the single knockout, the number of differentially expressed genes was very similar, hinting that both genes play an important and presumably similar role in cellular adaptation to leucine deprivation. This effect amplified when both proteins were knocked out, decreasing the percentage of changed genes to 8 % at 8 h leucine stress only. These data underline that the GCN1-GCN2 axis plays an essential role in leucine stress adaptation.

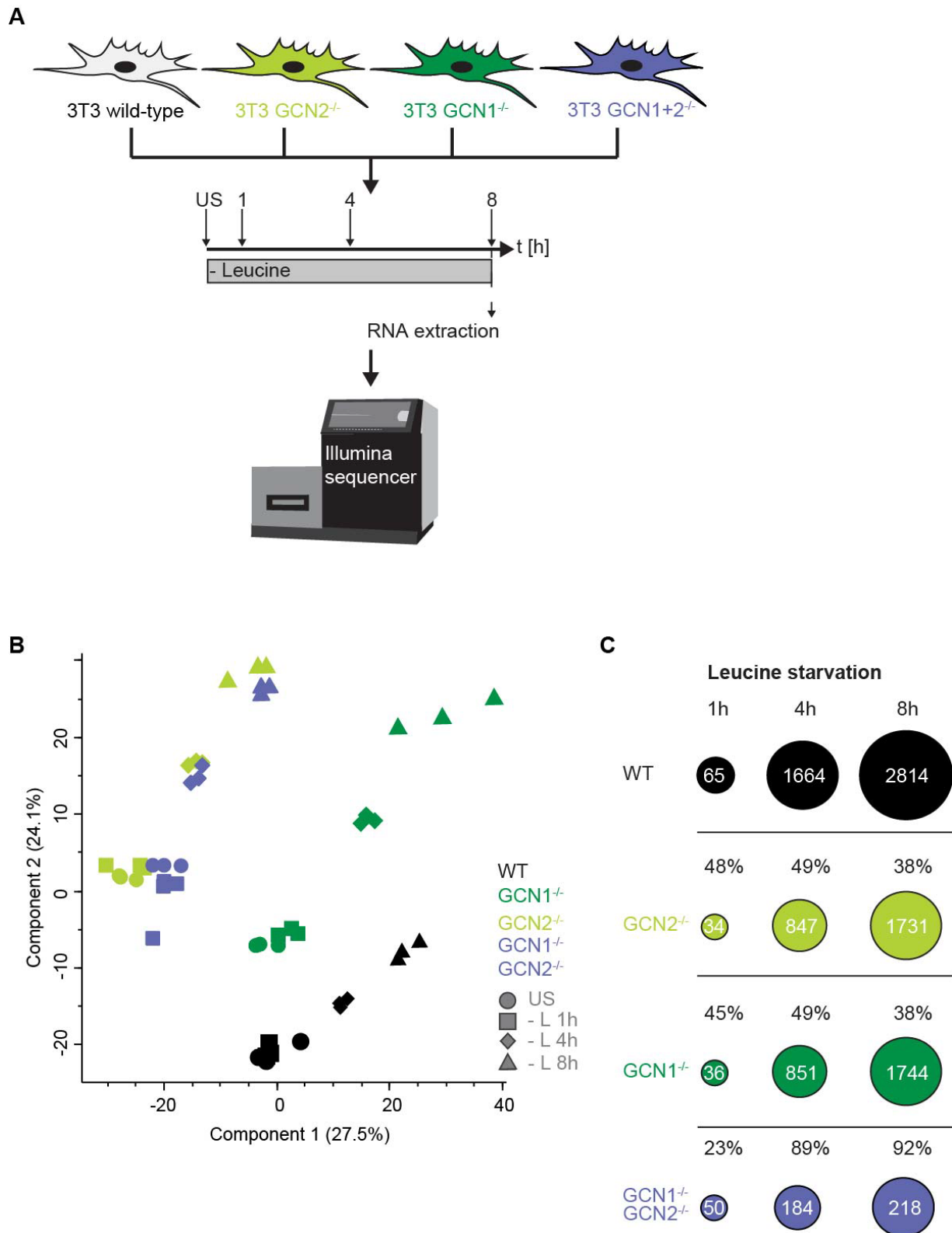


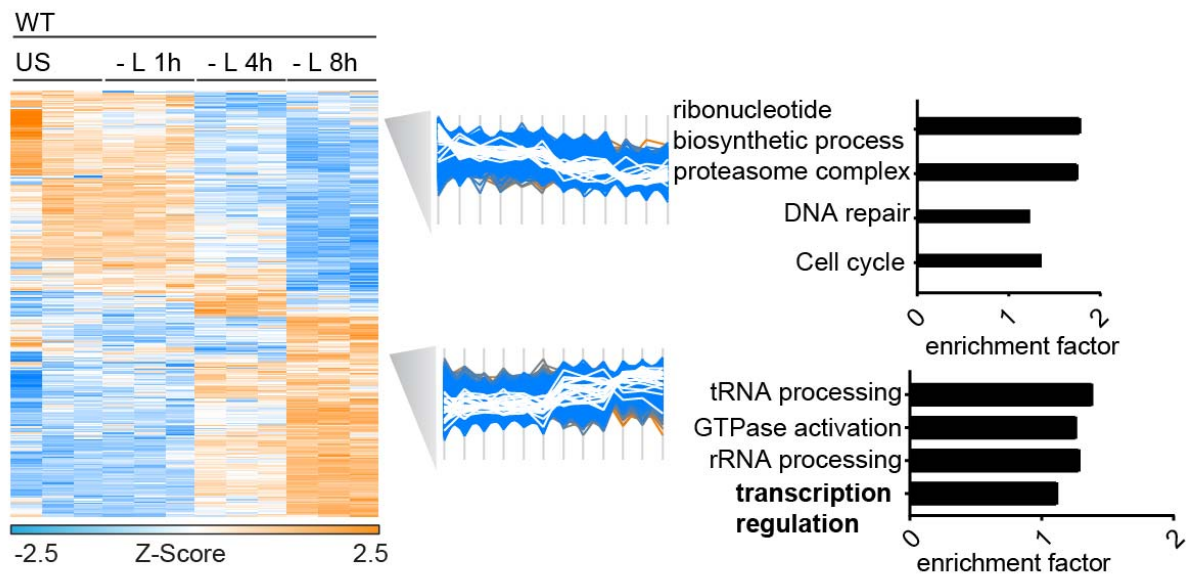
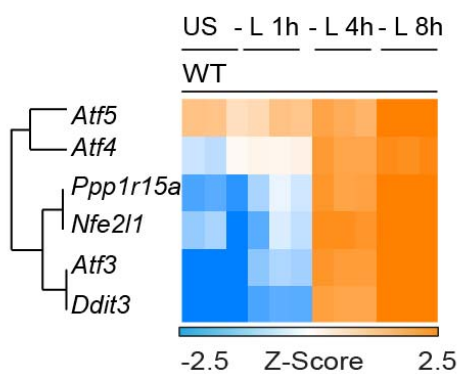
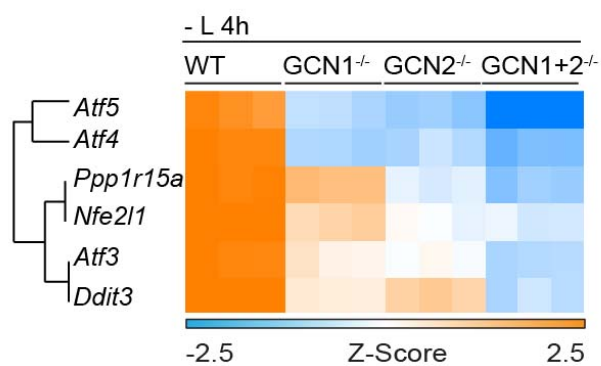
Figure 29. GCN1 and/or GCN2 deficient cells have an intrinsic transcriptional profile. (A) Scheme of the RNAseq setup: 3T3 cells, de- or proficient in GCN1, GCN2 or both (WT (black), GCN1^{-/-} (dark green), GCN2^{-/-} (light green) and GCN1^{-/-} + GCN2^{-/-} (purple)), were leucine starved for 1 h, 4 h, 8 h. Cells grown in normal medium were used as unstarved condition (US). After RNA extraction, the samples were read in an

Illumina Sequencer. (B) Principal component analysis (PCA) of the reads in all four genotypes (WT (black), GCN1^{-/-} (dark green), GCN2^{-/-} (light green) and GCN1^{-/-} + GCN2^{-/-} (purple)), leucine starved over time versus unstarved (US). (C) Differentially expressed transcripts significantly upregulated over time of leucine starvation in all four genotypes (WT (black), GCN1^{-/-} (dark green), GCN2^{-/-} (light green) and GCN1^{-/-} + GCN2^{-/-} (purple)). The percentage indicates the loss of differential upregulated genes at each timepoint towards the wild-type one (FDR < 0.05).

Next, we screened the biologic processes enriched in the wild-type, dependent on leucine deprivation using hierarchical clustering and gene ontology (GO) annotation. For example, we found a significant increase in GTPase activation (p-value ≤ 0.002), tRNA and rRNA processing (p-value ≤ 0.002; p-value ≤ 0.001) and transcriptional regulation (p-value ≤ 0.0001) upon leucine stress over time (Figure 30A). Genes assigned to the proteasome complex, ribonucleotide biosynthetic processes (p-value ≤ 0.00001), DNA repair (p-value ≤ 0.001) or cell cycle (p-value ≤ 0.001) are downregulated in sync. Interestingly, changes at the transcriptome level happen from 4 h leucine stress onwards, hinting a switch in gene expression profile at this stage. In general, the ISR is characterized by a specific stress-protective transcriptional program that is induced upon stress situations mediated by ATF4 (Refs.^{61,439}). Therefore, we moved on to evaluate the ‘transcriptional regulation’ cluster in more detail to screen for well-known stress bZIP transcription factors (Figure 30B+C)^{73,102}.

The wild-type cells induce the expression of the key ISR transcription factor *Atf4* (coding for ATF4), the growth arrest gene *Ppp1r15a* (coding for GADD34) and the pro-apoptotic gene *Ddit3* (coding for CHOP) over time (Figure 30B). Moreover, we detected other bZIP transcription factors, like *Atf3* (coding for ATF3) and *Nfe2l1* (coding for NRF2), which were regulated by leucine stress. In contrast, the bZIP transcription factor *Atf5* (coding for ATF5) is already highly expressed at the unstarved condition and gene expression levels were only marginally increased over time. bZIP transcription factors can homo- and heterodimerize to regulate gene expression⁷³. Since we detected multiple family members upon leucine stress, we assumed that these transcription factors are fundamental for a complex network of changes in cell state, necessary for cellular stress protection. Consistent with our finding, gene expression changes of transcription factors induced by ER stress-stimulated PERK-ISR activation were reported by Harding *et al.*¹⁵ and Torrence *et al.*²⁶. Most importantly, the patterns of transcription factor upregulation were clearest from 4 h leucine stress towards the unstarved control. This is consistent with the cluster in figure 30A and the PCA data in figure 29B in which the greatest shifts are found at 4 h leucine stress. Next, we compared the wild-type data to the three deficient backgrounds (GCN1^{-/-}, GCN2^{-/-} and GCN2^{-/-} + GCN1^{-/-}). Strikingly, we found that the knockouts have very similar expression levels of the bZIP transcription factors at the 4 h leucine stress time point, which is in stark contrast to the

increased levels in the wild-type condition (Figure 30C). Combining this finding with the data from figure 26B (Section 4.2.2.), GCN2 inactivity prevented the induction of ATF4 and CHOP upon amino acid starvation at the gene and protein level. Moreover, the detected loss of the transcriptional program in the GCN1 deficient background matched well to the published data where GCN1 regulates the GCN2 activity and finally GCN4/ATF4 induction in yeast¹⁰⁹ and mammalian cells^{113,156}. Thus, we assumed that the GCN1-induced loss of GCN2 activity affects its ATF4 dependent stress-protective transcriptional response as discussed in more detail in section 4.4. Moreover, *Atf4* and *Ddit3* expression levels in all knockouts increased at 8 h, but the net-values were always lower than in the wild-type system and highlighted a drastically delayed stress adaptation, most likely triggered by other complementary pathways (Figure 30D). This finding underlines the relevance of both transcription factors that are key targets of many nodes, such as PERK and mTORC1 signaling relevant for stress adaptation upon severe metabolic perturbation^{15,26}. In addition, ATF4 has common overlapping DNA-binding sites with MYC and can couple MYC dependent translation activity to bioenergetic demand in tumorigenic growth²⁰⁷. Therefore, we analyzed the *Myc* expression as well. As expected, *Myc* had very similar expression levels across the cell lines, which increased over stress duration (Figure 30D). Combined, we found that the leucine stress-induced transcription factor program was increased over time. The highest expression difference was found at 4 h leucine stress. Strikingly, GCN1 and/or GCN2 deficiency reverted the described phenomenon.

A**B****C**

D

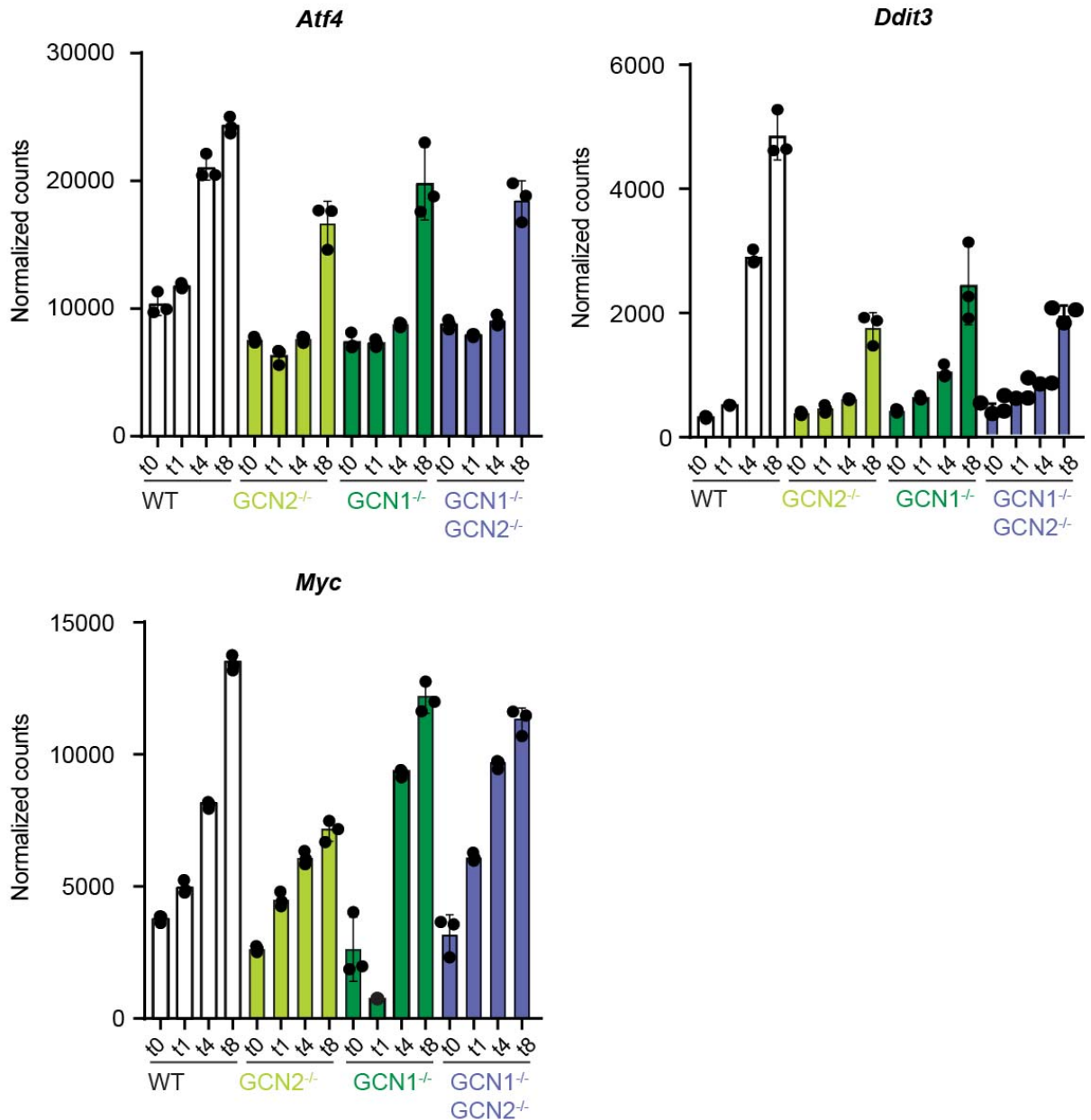


Figure 30. Leucine depletion induces expression of bZIP transcription factors over time dependent on *GCN1* and/or *GCN2* proficiency. (A) Heatmap of z-scored transcript intensity involved in processes ANOVA significantly regulated upon leucine stress (- L) over time in 3T3 wild-type (WT) cells (FDR < 0.05). Statistical significance was calculated using two-way ANOVA: ribonucleotide biosynthetic process (p-value ≤ 0.00001), proteasome complex (p-value ≤ 0.00001), DNA repair (p-value ≤ 0.001), cell cycle (p-value ≤ 0.001), tRNA processing (p-value ≤ 0.002), GTPase activation (p-value ≤ 0.002), rRNA processing (p-value ≤ 0.001) and transcription regulation (p-value ≤ 0.0001). (B) Heatmap of z-scored transcripts intensities of transcription factors (*Atf3*, *Atf4*, *Atf5*, *Ddit3*, *Nfe211* and *Ppp1r15a*) that are significantly ANOVA regulated over time of leucine starvation (1 h, 4 h and 8 h) in the wild-type (FDR < 0.05). (C) Heatmap of z-scored transcripts intensities of transcription factors (*Atf3*, *Atf4*, *Atf5*, *Ddit3*, *Nfe211* and *Ppp1r15a*) that are

significantly ANOVA-regulated at 4 h of leucine starvation in the studied genotypes (WT, GCN1^{-/-}, GCN2^{-/-} and GCN1^{-/-} + GCN2^{-/-}) (FDR < 0.05). (D) Normalized reads of *Myc*, *Ddit3* and *Atf4* expression in all studied genotypes (WT (black), GCN1^{-/-} (dark green), GCN2^{-/-} (light green) and GCN1^{-/-} + GCN2^{-/-} (purple)) over time of leucine starvation (- L; t: 0 h, 1 h, 4 h, 8 h). 0 h means unstarved condition. (A-C) The profiles are color coded according to their distance from the respective cluster center (orange is close to the center; blue is further away from the center).

As we found that the PERK-ISR and GCN2-ISR regulate the same set of bZIP transcription factors, we compared our data to the recent transcriptomics study from Torrence *et al.*²⁶, who found 61 ATF4 overlapping transcripts (8 % of ATF4 gene targets) induced by PERK via ER stress and mTORC1 via insulin stimulation. These transcripts are in part involved in amino acid uptake, 1C-metabolism and tRNA aminoacylation. We found that these processes were also systematically upregulated upon leucine stress in wild-type cells (Figure 31A). Moreover, we could also detect in our system the finding from Torrence *et al.*²⁶ that mitochondrial tRNA synthetases in contrast to the cytoplasmic ones did not follow the ATF4-regulated pattern. In other words, leucine starvation mediated the induction of cytoplasmic tRNA synthetases (e.g. *Yars*) over time in the wild-type and basal level in the knockouts while mitochondrial tRNA synthetases (e.g. *Yars2*) were not enriched upon leucine stress (Figure 31B+C). Interestingly, cytoplasmic glutamine-tRNA synthetase, QARS, was an exception of cytoplasmic tRNAs synthetases, which did not enrich upon leucine stress across time in the wild-type background (Figure 31C). A study from Nakazawa *et al.*⁴⁴⁰ highlighted the relevance of glutamine-specific tRNAs that selectively become uncharged upon amino acid limitation in contrast to all other tRNAs in a way that is dependent on intact lysosomal function.

Due to these parallels, we compared all reported 61 ATF4 overlapping transcripts²⁶ with our RNASeq data upon leucine stress over time in our genotypes. Strikingly, we could detect the same transcriptional changes in our wild-type background induced over time upon leucine deprivation and not in any GCN1 or GCN2 deficient background. The respective differential gene expressions in all genotypes are shown at 4 h leucine limitation (Figure 32A). To map this finding solely to the activation of the GCN2-ISR, we compared the induction of ATF4 upon leucine stress and unstarved condition towards stimulation with insulin or the loss of TSC2 that mimics the same phenotype as insulin treatment at the protein level⁴⁴¹. Interestingly, the GCN2-ATF4 axis was not activated in TSC2 deficient cells or by treatment with insulin in unstarved condition (Figure 32B). Leucine stress at 4 h activated GCN2 (autophosphorylation at T898) and ATF4 induction equally in all genotypes. PERK is also not activated upon leucine stress as shown already in figure 27 (Section 4.2.2.). Combined, we assume that the leucine depletion-induced GCN2-ISR co-opt as well the 61 ATF4 overlapping transcripts of PERK-induced ISR and insulin-stimulated mTORC1

(Ref.²⁶). This process is highly dependent on GCN1 and GCN2. Moreover, we show for the first time that the GCN1-GCN2 signaling is involved in regulating glycine/serine/threonine -, cysteine/methionine - and folate metabolism (1C-metabolism) upon leucine stress (Figures 31+32).

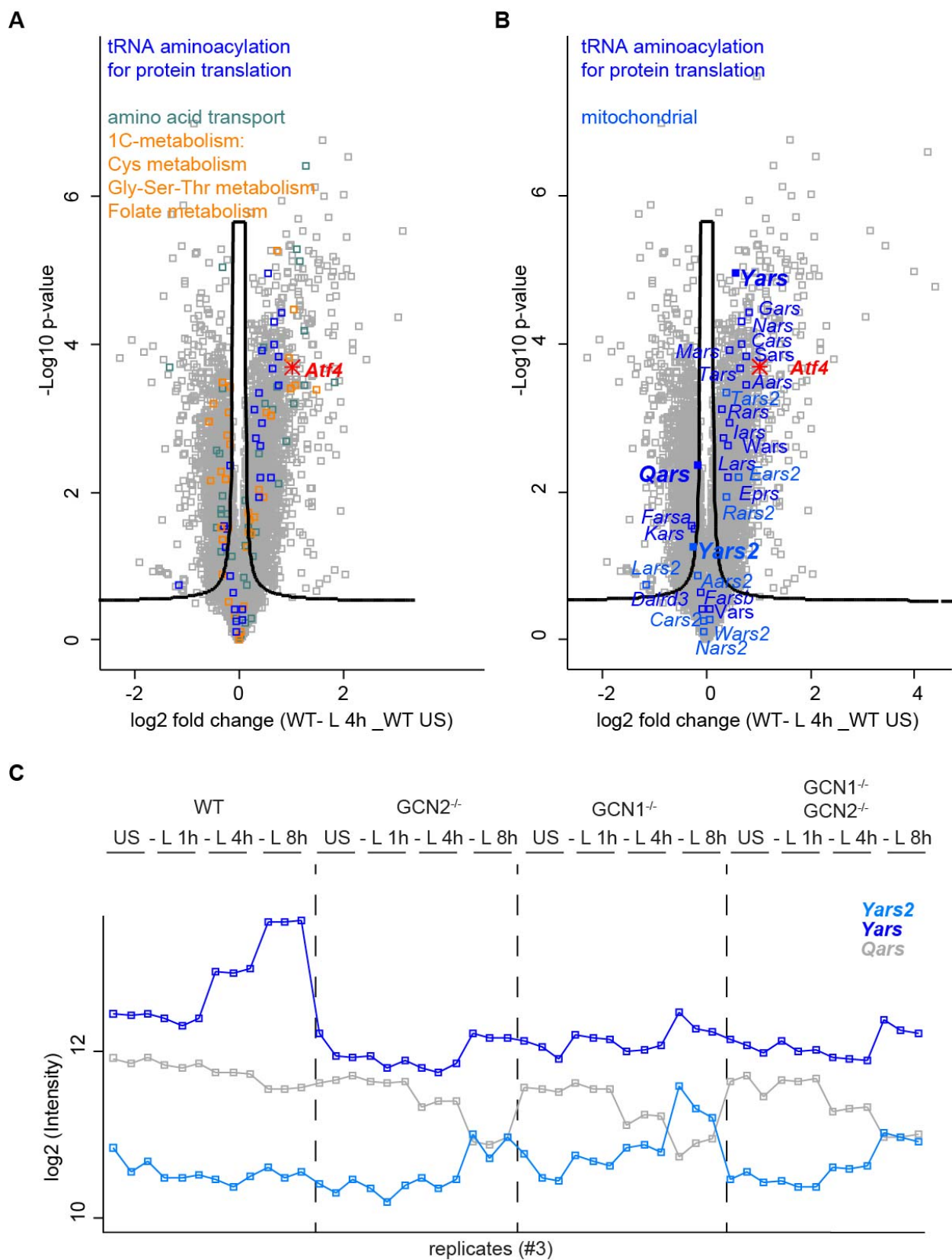
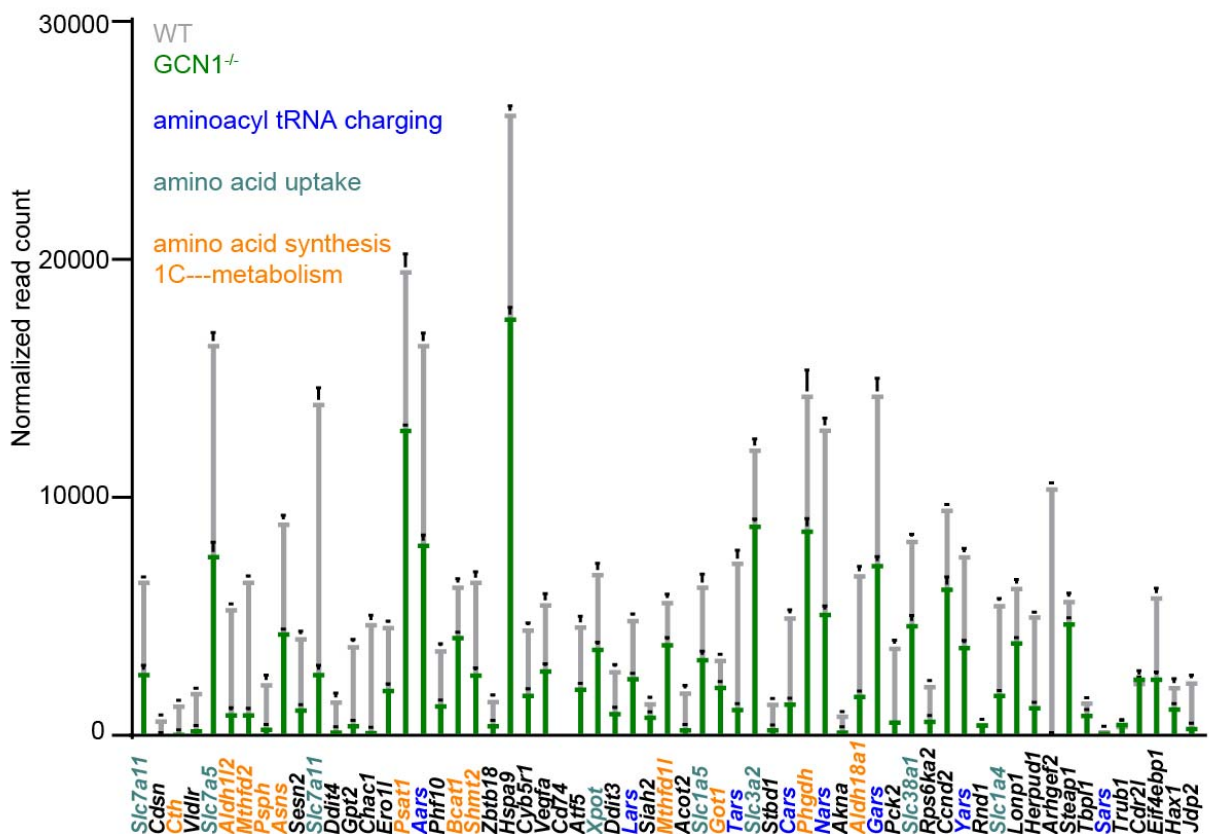
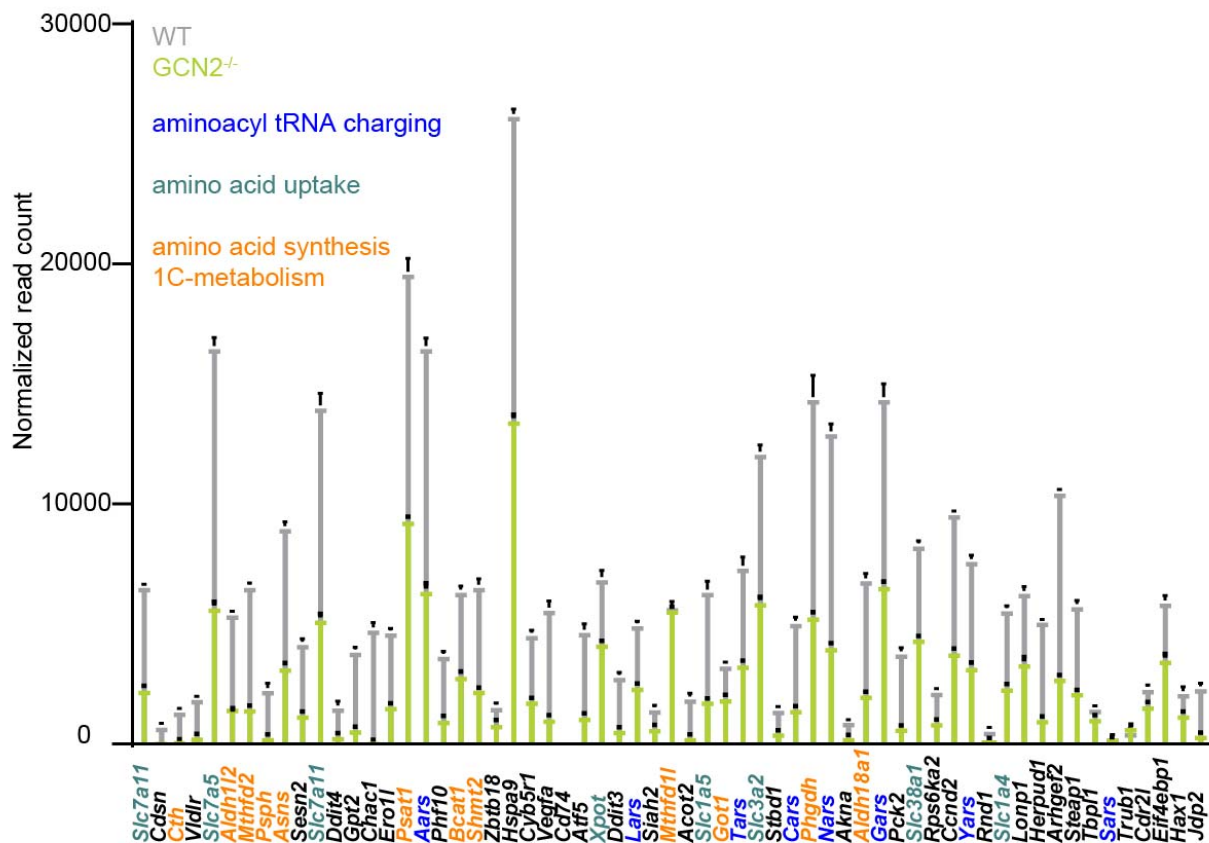
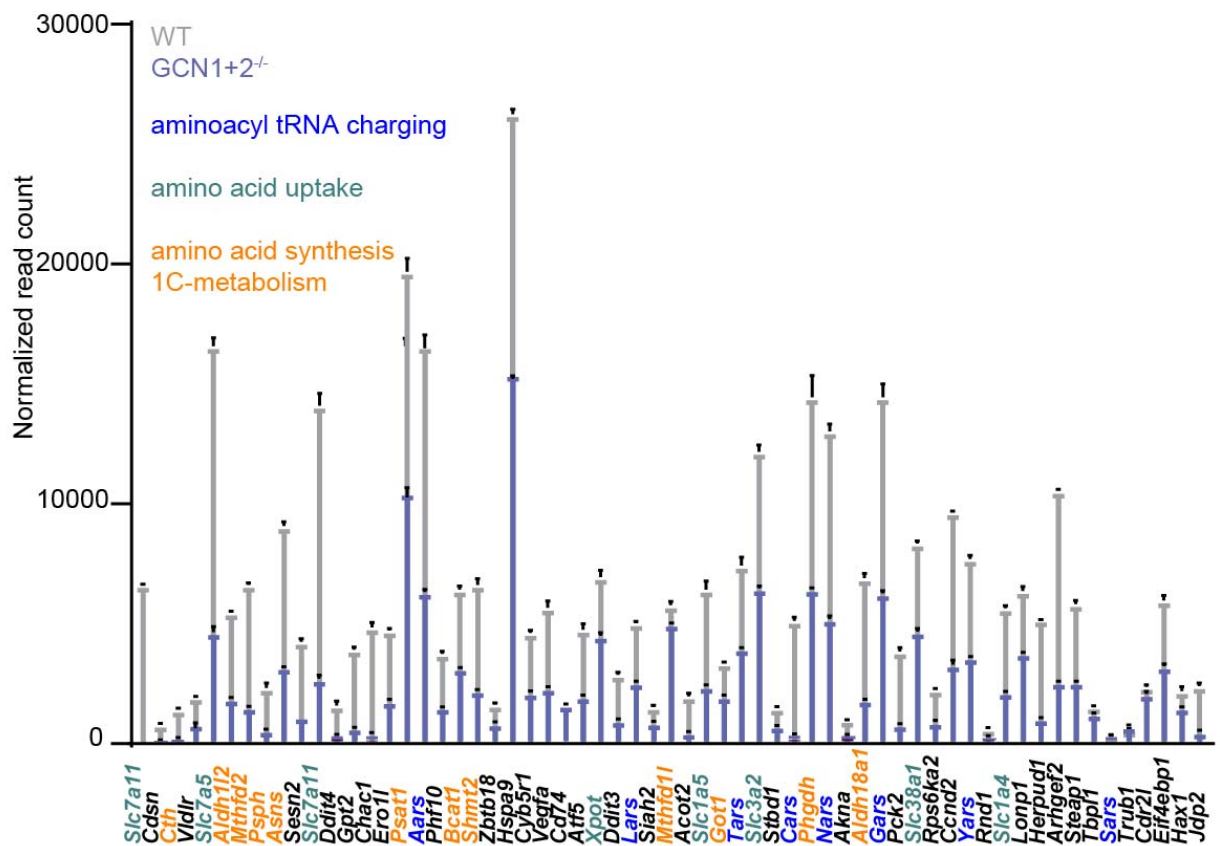


Figure 31. GCN1-GCN2 signaling induces genes involved in amino acid transport, cytoplasmic tRNA charging and mitochondrial 1C-metabolism upon leucine stress. (A) Volcano plot comparing p-value and log₂-fold changes of genes involved in tRNA aminoacylation (blue), amino acid transport (green) and

1C-metabolism (orange) between leucine stress (- L) at 4 h and unstarved condition (US) in 3T3 wild-type (WT) cells (FDR < 0.05). (B) Volcano plot comparing p-value and log₂-fold changes of genes involved in tRNA aminoacylation, cytoplasmic (dark blue) and mitochondrial tRNA synthetases (light blue), between leucine stress (- L) at 4 h and unstarved condition (US) in 3T3 wild-type (WT) cells (FDR < 0.05). (C) Single-plot of log₂ intensities of *Yars* (dark blue), *Yars2* (light blue) and *Qars* (grey) upon leucine stress for 1 h, 4 h and 8 h and unstarved condition in 3T3 wild-type (WT), GCN2 knockout (GCN2^{-/-}) and GCN1 knockout (GCN1^{-/-}) cells (FDR < 0.05). (A-B) *Atf4* (red) represents the internal starvation control.

A





B

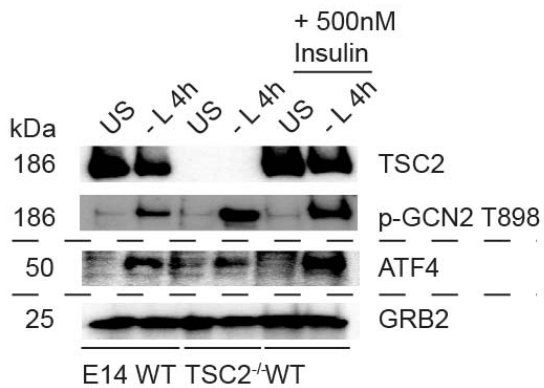


Figure 32. GCN1-GCN2 signaling activates upon leucine stress a subset of 61 ATF4 transcripts known to be regulated by stimulated PERK-ISR and mTORC1 signaling²⁶. (A) Normalized reads of differentially and significantly enriched transcripts in all genotypes (WT (grey), GCN1^{-/-} (dark green), GCN2^{-/-} (light green) and GCN1^{-/-} + GCN2^{-/-} (purple)) at 4 h of leucine starvation. Color coding of genes underlines the affiliation to GO-annotated processes. (B) Immunoblot of E14 cells (wild-type WT or TSC2^{-/-}) cell lysates stimulated with unstarved condition (US) or leucine-starvation (-L) for 4 h in combination with insulin (500 nM) treatment. GRB2 was used as loading control. Data are depicted as one of two representative gels.

The 1C-metabolism has important functions in maintenance of epigenetic modifications, antioxidant response, nucleotide biosynthesis and amino acid homeostasis^{442,443}. Reich *et al.*⁴⁴⁴ showed that genes (*Phgdh*, *Psat1*, *Psph*, *Shmt2*, *Aldh1l2* and *Mthfd2*) involved in transferring intermediary metabolites from glycolysis to the folate-mediated mitochondrial 1C-metabolism via serine biosynthesis were induced by the ER stress-induced ISR. These enzymes induce a metabolic rewiring dependent on the PERK-eIF2 α -ATF4 axis triggering stress-induced resistance to folate-based antimetabolites in human cancer cell lines⁴⁴⁴. We found that the same gene signature (*Phgdh*, *Psat1*, *Psph*, *Shmt2*, *Aldh1l2* and *Mthfd2*) is induced upon leucine stress only in the wild-type and not in the GCN1 and/or GCN2 knockouts (Figure 33). In other words, we discovered that GCN1-GCN2 signaling upon leucine limitation modulates mitochondrial 1C-metabolism and serine biosynthesis at the transcriptional level that is in stark agreement with data from the PERK-ISR study published by Reich *et al.*⁴⁴⁴. Recently, the relevance of controlling the serine and nucleotide metabolism for metabolic reprogramming in cancer was illustrated by the dependence of AML on the transcription factor ATF3 (Ref.⁴⁴⁵). In this context, we also highlighted that the ATF3 induction is regulated by GCN1-GCN2 signaling upon leucine stress (Figure 30B+C). Consequently, we provided evidence that the GCN1-GCN2 cascade is most likely involved in serine metabolism, purine biosynthesis and antioxidative response via the serine biosynthesis coupled to mitochondrial 1C-metabolism upon amino acid stress.

Mitochondrial 1C-metabolism and serine biosynthesis
Mthfd2 *Psat1* *Aldh1l2* *Phgdh* *Shmt2* *Psph*

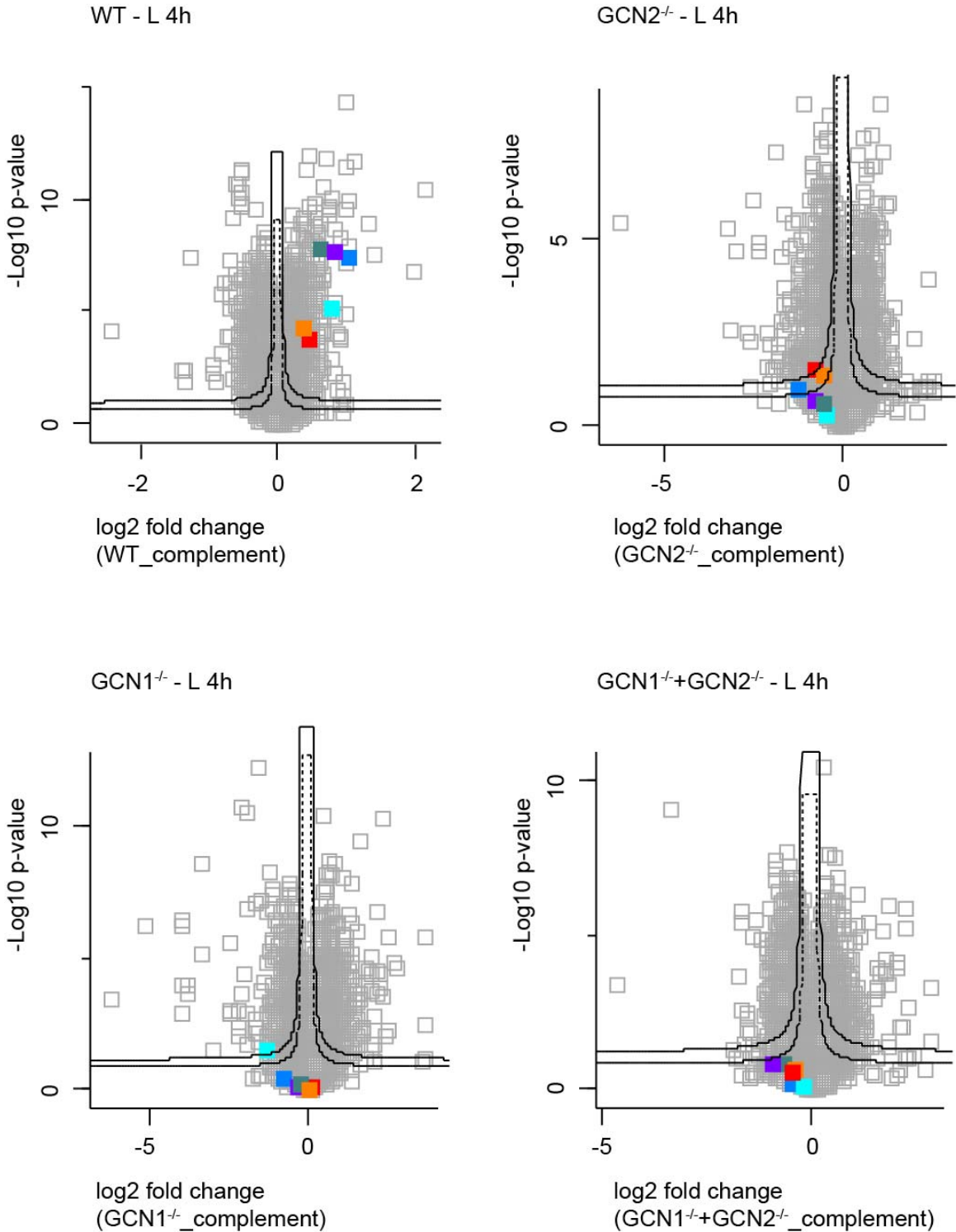


Figure 33. GCN1-GCN2 signaling regulates mitochondrial 1C-metabolism and serine biosynthesis upon leucine stress. Volcano plots comparing p-value and log2-fold changes of genes (black box) coding for enzymes, relevant in diverting metabolites from glycolysis to fuel mitochondrial 1C-metabolism via serine

biosynthesis, between all analyzed genotypes (WT, GCN2^{-/-}, GCN1^{-/-} and GCN2^{-/-} + GCN1^{-/-}) upon leucine stress (- L) at 4 h (FDR < 0.05).

In addition to the 61 ATF4 transcripts involved in part in amino acid uptake, 1C-metabolism and cytosolic aminoacyl-tRNA charging (Figure 32), we detected additional differentially expressed gene signatures, which were highly GCN1- and/or GCN2-dependent and upregulated over time upon leucine stress in wild-type cells, but not under knockout conditions. A collection of representative genes (black box) was shown for 4 h of leucine stress as volcano plots (Figure 34). For example, we detected transcriptional changes in glutamine metabolism (*Asns* and *Gpt2*) and transamination reactions (*Got1*) following the mentioned pattern, which were in line with the data by Torrence *et al.*²⁶. Interestingly, *Asns* expression is highly relevant in prospect of GCN2 inhibition in tumorigenic cells as described at a later stage (Section 4.7.). Nakamura *et al.*²³⁹ reported that GCN2 inhibition sensitizes low-*Asns* expressing AML cancer cells to asparaginase treatment by disrupting the amino acid response. Next, we detected several mTORC1 key players like *Eif4ebp1*, *Rheb*, *Sestrin2* and *Ddit4* arguing for a potential interaction between the mTORC1 and GCN2 pathway as discussed in detail below (Sections 4.5. and 4.7.). In addition to *Eif4ebp1*, the translation initiation factor 3, *Eif3c*, which is a binding partner of mTOR-RAPTOR to trigger translation initiation³⁰⁷ (Section 1.3.3.2.; Figure 14) was upregulated under wild-type condition at the 4 h time point (Figure 34). This also holds true for the *Mknk1* gene that encodes the MAPK interacting kinase, regulating transcription by phosphorylating the translation initiation factor eIF4E via interaction with the C-terminal region of the translation initiation factor eIF4G⁴⁴⁶. Besides translational control, we also found that the GCN1-GCN2 signaling regulates *Tfe3* expression relevant for lysosomal biogenesis to recycle peptides in the cytoplasm and regenerate the pool of cellular amino acids in order to reactivate mTORC1 (Refs.^{358,359}) (Section 1.3.5.). Interestingly, these discussed genes were not significantly changed under any single- or double-knockout condition. Taken together, our data hint that GCN1 and GCN2 are involved in an isogenic way to regulate the amino acid stress-induced ISR. Due to several parallels to the RNA Seq data from Torrence *et al.*²⁶, our initial assumption was again indirectly underlined that the loss of these changes in the GCN1 and/or GCN2 background is most likely a consequence of the loss in ATF4, but clearly, other factors are involved in the network of metabolic changes that occur downstream of the GCN1-GCN2 axis of amino acid stress sensing, too. The link between ATF4, GCN1 and GCN2 is described in more detail in Section 4.4.

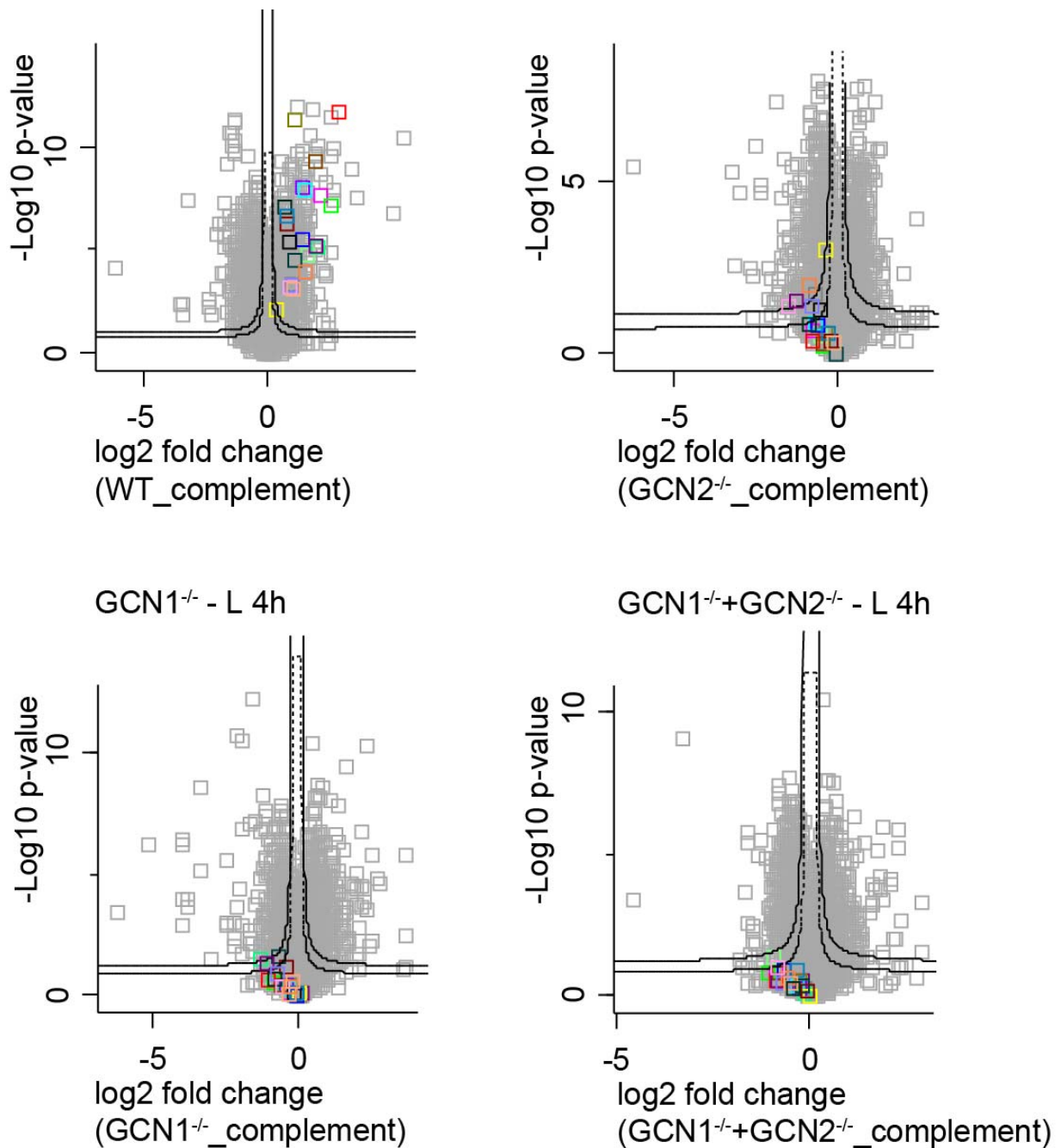


Figure 34. GCN1- and GCN2-dependent transcriptional changes are isogenic upon leucine depletion.

Volcano plots comparing p-value and log₂-fold changes of a subset of genes involved in different processes (black box) between the analyzed genotypes (WT, GCN2^{-/-}, GCN1^{-/-} and GCN2^{-/-} + GCN1^{-/-}) upon leucine stress (- L) at 4 h (FDR < 0.05).

Next, we screened for GCN1 and GCN2 specific transcriptional changes with the notion that GCN1 and GCN2, while connected via the ISR, may have intrinsic functions. This was assumed based on the intrinsic different transcriptional pattern illustrated by the PCA (Figure 29B) and

recent studies reported by Yamazaki *et al.* and Kim *et al.*^{113,156}. First, we compared all genotypes in normal growth state, because ATF4 (and other ISR-dependent changes) in this condition was not upregulated beyond baseline in the wild-type background (Figure 30B). We detected clusters in which processes regulating tRNA aminoacylation (p-value ≤ 0.002), DNA-dependent transcription (p-value ≤ 0.01) and translation initiation (p-value ≤ 0.0001) were downregulated in the knockouts compared to the wild-type background (Figure 35A). This finding is consistent with our previously described data that GCN1 and GCN2 are relevant for ISR dependent processes and cannot respond to leucine stress-induced changes as wild-type cells do - already at basal level. Interestingly, we detected in this cluster a 3- and 5-fold enrichment in glycolytic processes (glycolysis (p-value ≤ 0.002) and gluconeogenesis (p-value ≤ 0.001)), respectively. Only three genes mediated the transcriptional changes (*Gpi1*, *Tpi1* and *Pck2*) in gluconeogenesis. One of them, *Pck2*, coding for the mitochondrial phosphoenolpyruvate carboxykinase 2, was transcriptionally regulated by leucine stress across time as well (Figure 35B). PCK2 is involved in the rate-limiting step of the metabolic network that produces glucose from lactate and other precursors derived from the TCA cycle and was already linked to the ISR in tumor cell adaptation upon nutrient stress⁴⁴⁷. Referred to the changes in glycolysis, Torrence *et al.*²⁶ proposed that ATF4 and HIF1 (hypoxia-inducible factor 1) function as stress and nutrient sensing transcription factors that are independently co-opted by mTORC1 to drive the expression of nutrient transporters and metabolic enzymes. The heterodimer HIF1 (HIF1 $\alpha\beta$) is primarily regulated by oxygen depletion (hypoxia) to induce genes involved in glucose uptake, glycolysis and angiogenesis to hypoxia adaptation and decrease mitochondrial respiration⁴⁴⁰. However, in normoxia (no oxygen limitation), HIF1 α protein synthesis is increased by growth factor-stimulated mTORC1 leading to elevated expression of HIF1 gene targets for glucose uptake and glycolysis (aerobic glycolysis)³²⁰. In this context, we discovered that some of these HIF1 targets (*Ldha*, *Pdk1*, *Poglut1*, *Pfkfb* and *Hk2*) that were established to be regulated downstream of mTORC1^{320,448-452} were primarily GCN2-dependently modulated in unstarved condition as well (Figure 35C). Combined, this showed that the bioenergetic profile of GCN1 and GCN2 was already affected by the protein loss in a normal growth state; a phenomenon that is described in more detail in section 4.3.

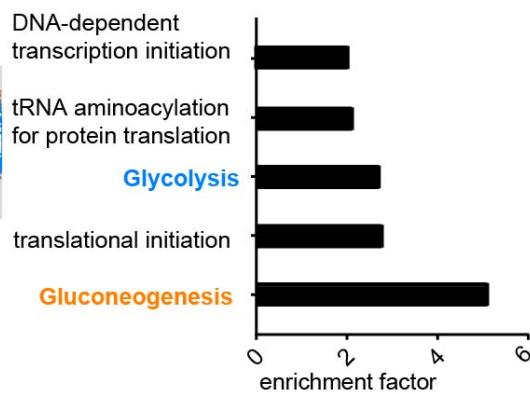
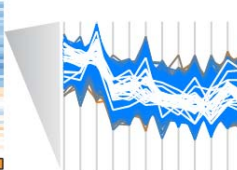
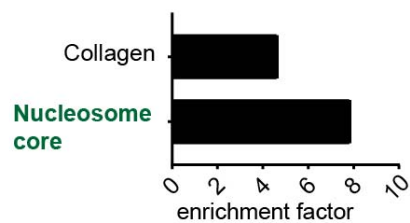
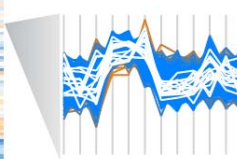
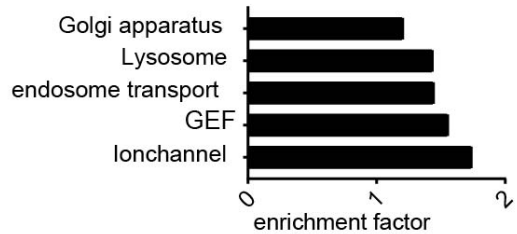
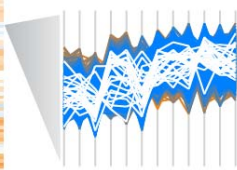
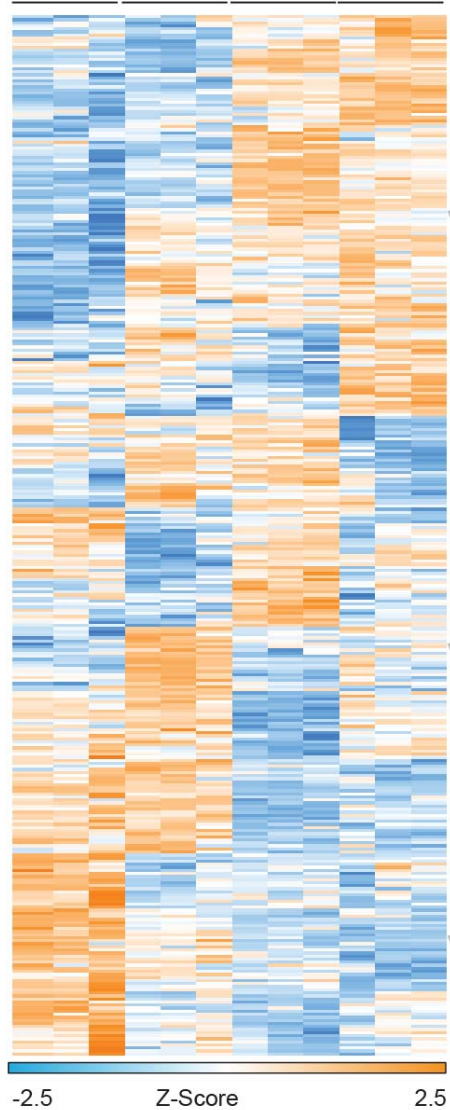
Further evidence that GCN1 and GCN2 loss regulate processes independently of the ISR are highlighted (Figure 35D): we detected two NF- κ B key players upregulated in all knockout lines in contrast to wild-type cells independent of leucine stress (*Nlrp4e* and *Tbk1*). Moreover, we found an 8-fold enrichment in nucleosome core transcripts (p-value ≤ 0.00001 ; Figure 35A) only in the GCN1 deficient context that was most likely driven by genes coding for histones H2A and H2B (Figure 35C). H2A and H2B are core elements of the nucleosome and crucial for transcriptional regulation, DNA repair, DNA replication and chromosomal stability⁴⁵³. Genes significantly

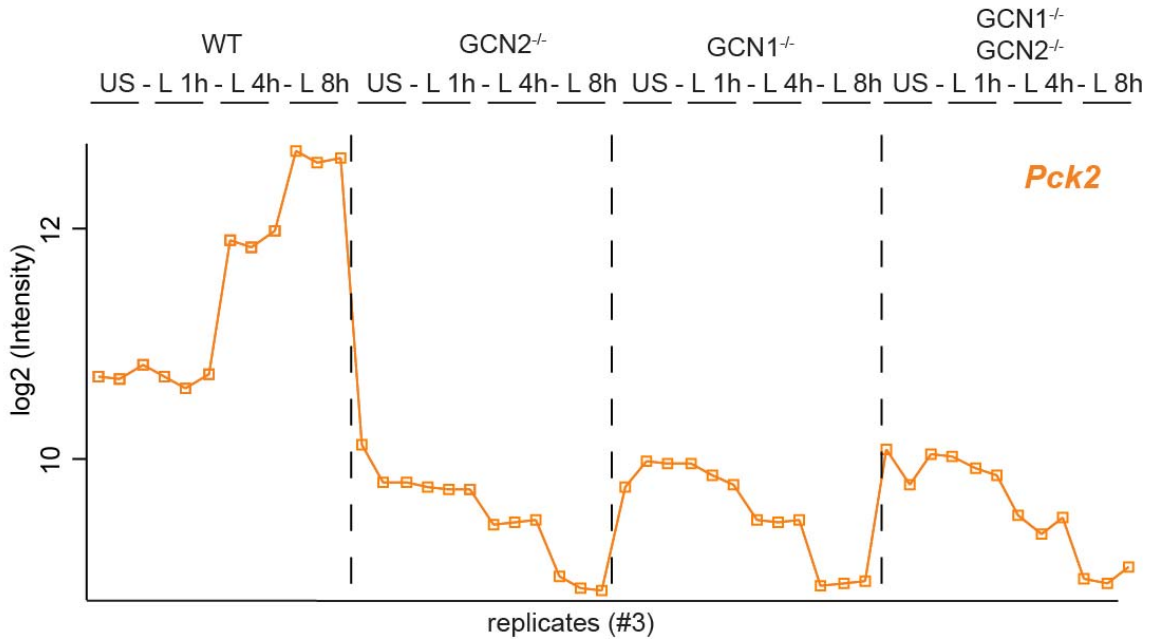
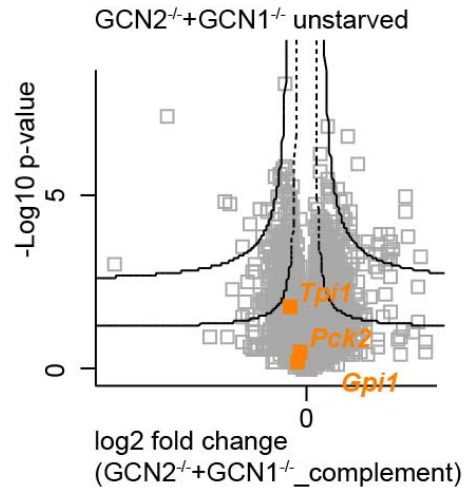
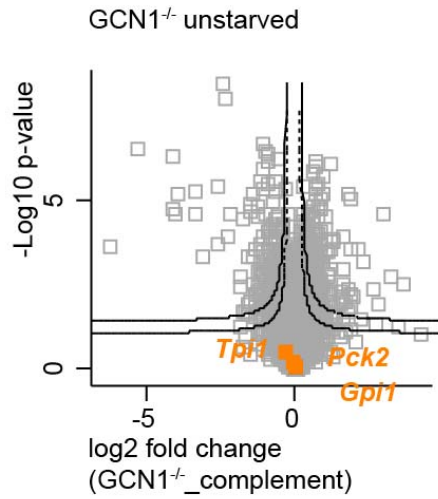
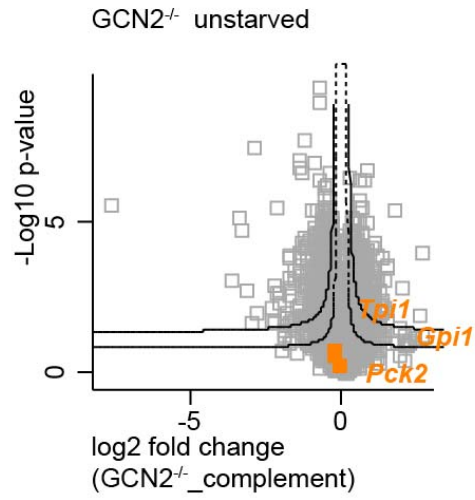
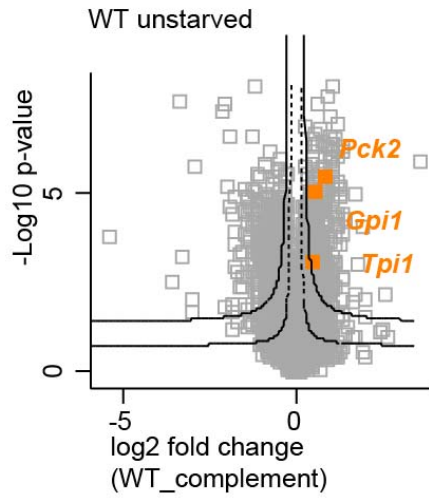
changed in DNA dependent processes (DNA replication initiation (p-value ≤ 0.00001), condensed chromosome outer kinetochore (p-value ≤ 0.00001), homologous recombination (p-value ≤ 0.00001), condensin complex (p-value ≤ 0.0001), and central spindlin complex (p-value ≤ 0.001) were affected primarily in the double GCN1 and GCN2 deficient cell line upon leucine stress (Figure 36). Thus, the loss of both proteins most likely affect DNA integrity and fidelity in normal growth state and leucine stress. Evidence that the ISR is relevant in DNA damage response and DNA replication were already provided by Clementi *et al.*⁴⁵⁴ and Choo *et al.*⁴⁵⁵ arguing that the stress response is fundamental to modulate DNA synthesis depending on nutrient availability. In addition to that, we detected genes coding for calreticulin and RAB20 involved in regulating phagocytic processes enriched in GCN1 deficient background at 4 h of leucine starvation in contrast to all other genotypes (Figure 36). This finding matches our data (Figure 35A), where processes relevant for supplying proteins in the cytoplasm mediated by lysosome (p-value ≤ 0.001), endosome transport (p-value ≤ 0.002) and golgi apparatus (p-value ≤ 0.001) cluster in the knockouts. Combined, the data argue that GCN1 mediates GCN2- and amino acid stress-independent transcriptional changes.

A

US

WT GCN1^{-/-} GCN2^{-/-} GCN1+2^{-/-}



B**Gluconeogenesis**

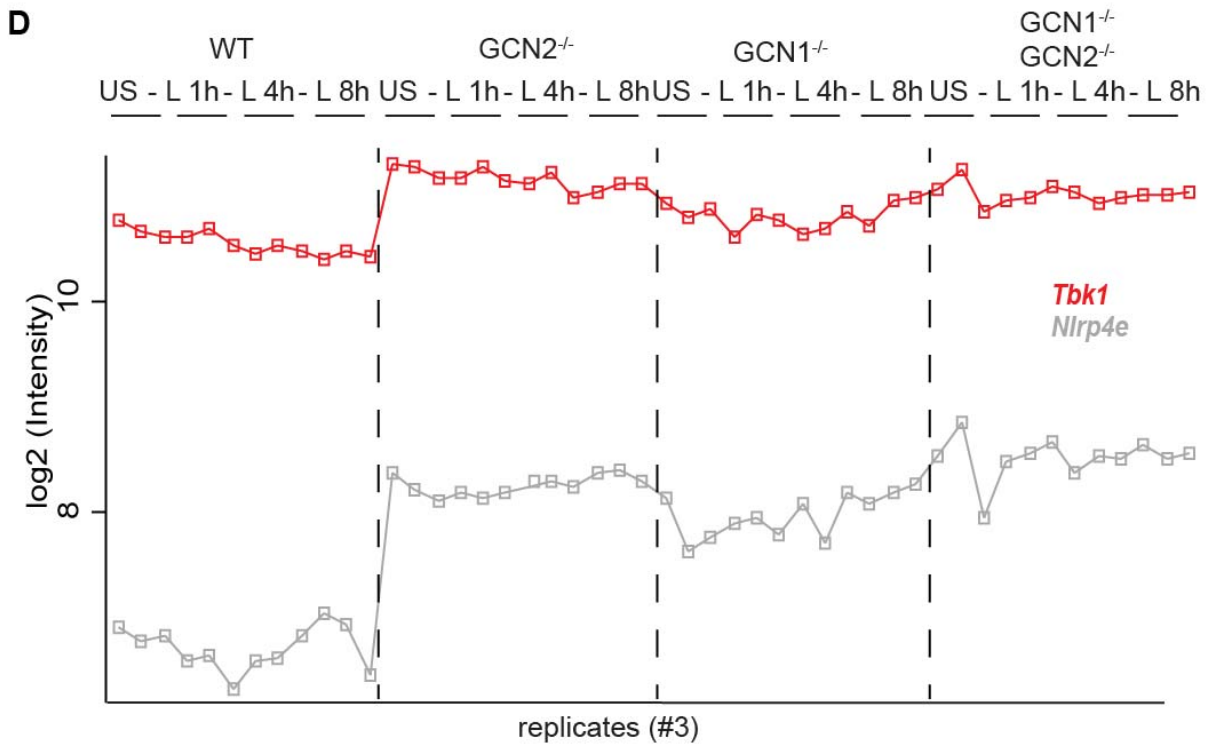
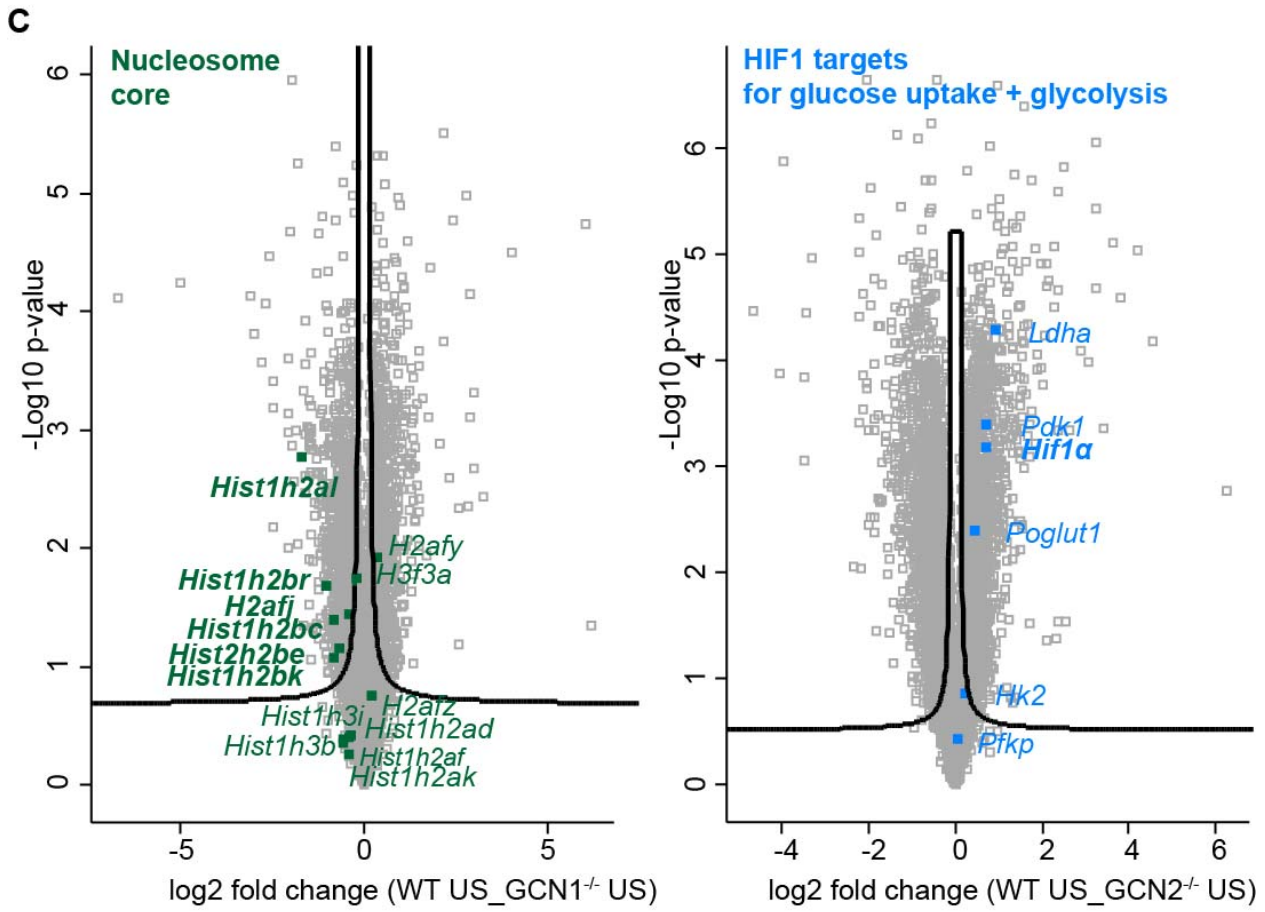


Figure 35. GCN1 and GCN2 regulate transcriptional changes independent of leucine stress. (A) Heatmap of z-scored transcript intensities involved in processes significantly ANOVA-regulated upon unstarved condition (US) in 3T3 wild-type (WT), GCN2 deficient (GCN2^{-/-}), GCN1 deficient (GCN1^{-/-}) and double knockout (GCN2^{-/-}+ GCN1^{-/-}) cells (FDR < 0.05). Statistical significance was calculated using two-way ANOVA: golgi apparatus (p-value ≤ 0.001), lysosome (p-value ≤ 0.001), endosome transport (p-value ≤ 0.002), guanine-nucleotide releasing factor (p-value ≤ 0.002), ion channel (p-value ≤ 0.001), DNA-dependent transcription regulation (p-value ≤ 0.01), tRNA aminoacylation for protein translation (p-value ≤ 0.002), glycolysis (p-value ≤ 0.002), translation initiation (p-value ≤ 0.0001), gluconeogenesis (p-value ≤ 0.001), nucleosome core (p-value ≤ 0.00001) and collagen (p-value ≤ 0.0001). The profiles are color coded according to their distance from the respective cluster center (orange is close to the center; blue is further away from the center). (B) Volcano plots comparing p-value and log₂-fold changes of *Pck2*, *Gpi1*, *Tpi1* (orange) between the analyzed genotypes (WT, GCN2^{-/-}, GCN1^{-/-} and GCN2^{-/-} + GCN1^{-/-}) in unstarved condition. Single-plot of log₂ intensity of *Pck2* in all genotypes (WT, GCN2^{-/-}, GCN1^{-/-} and GCN2^{-/-} + GCN1^{-/-}) upon leucine stress (- L) across time (1h, 4h and 8h) and unstarved condition (US) (FDR < 0.05). (C) Volcano plots comparing p-value and log₂-fold changes of transcripts belonging to nucleosome core (green) and HIF1 glycolytic targets (blue) between 3T3 wild-type (WT) and GCN2 knockout (GCN2^{-/-}) or GCN1 knockout (GCN1^{-/-}) in unstarved condition (FDR < 0.05). (D) Single-plot of log₂ intensity of *Tbk1* (red) and *Nlrp4e* (grey) in all genotypes (WT, GCN2^{-/-}, GCN1^{-/-} and GCN2^{-/-} + GCN1^{-/-}) upon leucine stress (- L) across time (1h, 4h and 8h) and unstarved condition (US) (FDR < 0.05).

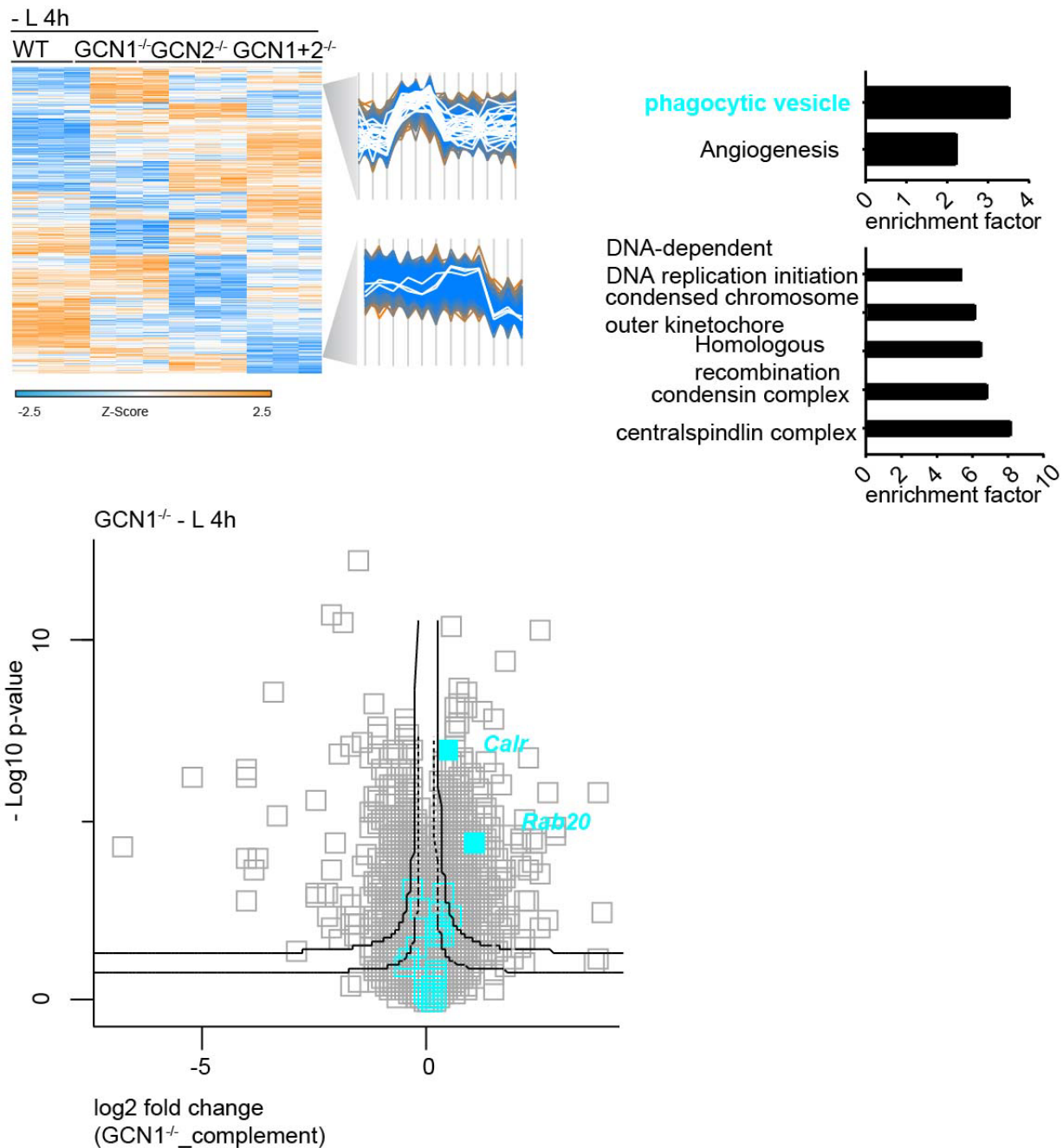


Figure 36. GCN1 might be involved in several processes induced by leucine stress. Heatmap of z-scored transcript intensity involved in processes significantly ANOVA-regulated upon leucine stress (- L) at 4 h in 3T3 wild-type (WT), GCN2 deficient (GCN2^{-/-}), GCN1 deficient (GCN1^{-/-}) and double knockout (GCN2^{-/-} + GCN1^{-/-}) cells (FDR < 0.05). Statistical significance was calculated using two-way ANOVA: phagocytic vesicle (p-value ≤ 0.0001), angiogenesis (p-value ≤ 0.001), DNA-dependent DNA replication initiation (p-value ≤ 0.00001), condensed chromosome outer kinetochore (p-value ≤ 0.00001), homologous recombination (p-value ≤ 0.00001), condensin complex (p-value ≤ 0.0001), and central spindlin complex (p-value ≤ 0.001). Volcano plot comparing p-value and log₂-fold changes of transcripts belonging to phagocytic vesicle (turquoise) between GCN1 knockout (GCN1^{-/-}) and all other genotypes (WT, GCN2^{-/-} and GCN2^{-/-} + GCN1^{-/-}) upon leucine stress for 4 h (FDR < 0.05). The profiles are color coded according to

their distance from the respective cluster center (orange is close to the center; blue is further away from the center).

In summary, transcriptional changes over time upon leucine stress were highly dependent on GCN1 and GCN2 highlighting the isogenic character of both proteins involved in the amino acid response. Thus, GCN1-GCN2 signaling modulates at the transcriptional level upon leucine stress across time processes involved in amino acid transport, tRNA charging, glutamine metabolism, translational initiation, mTOR signaling, serine biosynthesis and mitochondrial 1C-metabolism. These changes are consistent with findings reported by others^{15,26,29,95,444} who studied the transcriptome of ER stress-induced PERK-ISR and/or insulin-stimulated mTORC1 signaling. In line with Torrence *et al.*²⁶, we showed that the GCN2 driven cascade regulates the same 61 ATF4 transcripts that are modulated as well by the ER stress-induced PERK-ISR and the insulin-stimulated mTORC1 network. Based on the finding that GCN1 is relevant for GCN2 activity^{109,113,156}, we suggest that our detected transcriptome changes might also be mediated by ATF4 upon leucine stress (Section 4.4.). Furthermore, we provide evidence that the loss of both proteins – already in steady-state- affects bioenergetics and DNA-replication dependent processes.

4.2.4. Full proteomics and phosphoproteomics studies of GCN1 and GCN2 deficiency

Translational changes are commonly analyzed by two methodologies: (i) Ribosomal profiling (Ribo-Seq), based on sequencing of mRNA pieces protected by ribosomes; (ii) Quantitative mass spectrometry-based proteomics⁴⁵⁶. However, both techniques have challenges with regards to resolution, depth or technical bias especially when global and rapid protein dynamics are monitored, which is the case for the ISR and the mTORC1 pathway since they integrate cellular stress responses and are highly sensitive to experimental perturbations^{457,458}. The proteome dynamics of mTORC1 and the ISR have so far been rarely studied. A first multiplexed enhanced Protein Dynamics (mePROD) proteomics approach combined with pulsed-SILAC and tandem mass tag (TMT) multiplexing was performed by Klann *et al.*²⁷. They figured out that the ISR and the mTORC1 network use overlapping protein targets to enable translation attenuation upon environmental stress. However, GCN2 was not included in this study. Here, we aimed to address proteome level changes upon leucine stress in a time-dependent manner and to find complementary outcomes to the transcriptional changes reported in section 4.2.3. Additionally,

we performed phosphoproteome analysis from the same sample setup to identify GCN2 targets (Section 4.2.4.2.).

For these bottom-up mass spectrometry-based attempts, we used label-free quantification of all identified digested peptides using the DDA (data-dependent acquisition) mode for full proteome analysis and DIA (data-independent acquisition) mode for phosphoproteomics. DIA has the advantage to increase the dynamic range coverage and finally protein identifications, as well as quantitative accuracy compared to DDA^{429,459,460}. This was important to increase the identification of phosphosites of less abundant proteins. Both omics studies were performed in collaboration with Dr. Maria Tanzer from the Prof. Dr. Matthias Mann department.

4.2.4.1. Full proteome analysis

In line with the RNA-Seq approach, we used 3T3 wild-type cells and 3T3 cells deficient in GCN1 or GCN2, which were stimulated for 1 h, 4 h and 8 h with leucine-depletion medium (Figure 37A). Cells cultured in normal growth medium served as unstarved control condition. In total, four biological replicates per condition were used for full proteome measurement (Section 3.7.2.). We detected 6,455 proteins from which 1,966 proteins were 2D-ANOVA significant scored and used in our downstream analysis. The mentioned protein names in this section correspond to the gene names based on the terminology from the HUGO gene nomenclature committee (www.genenames.org).

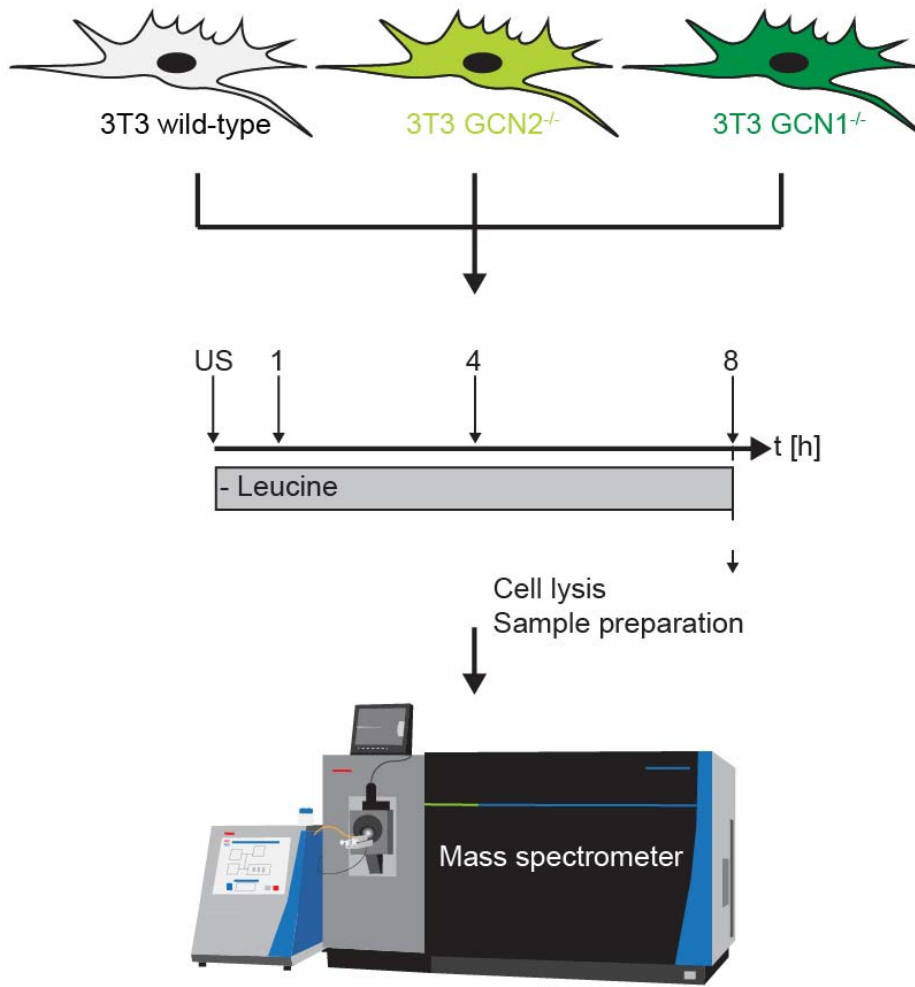
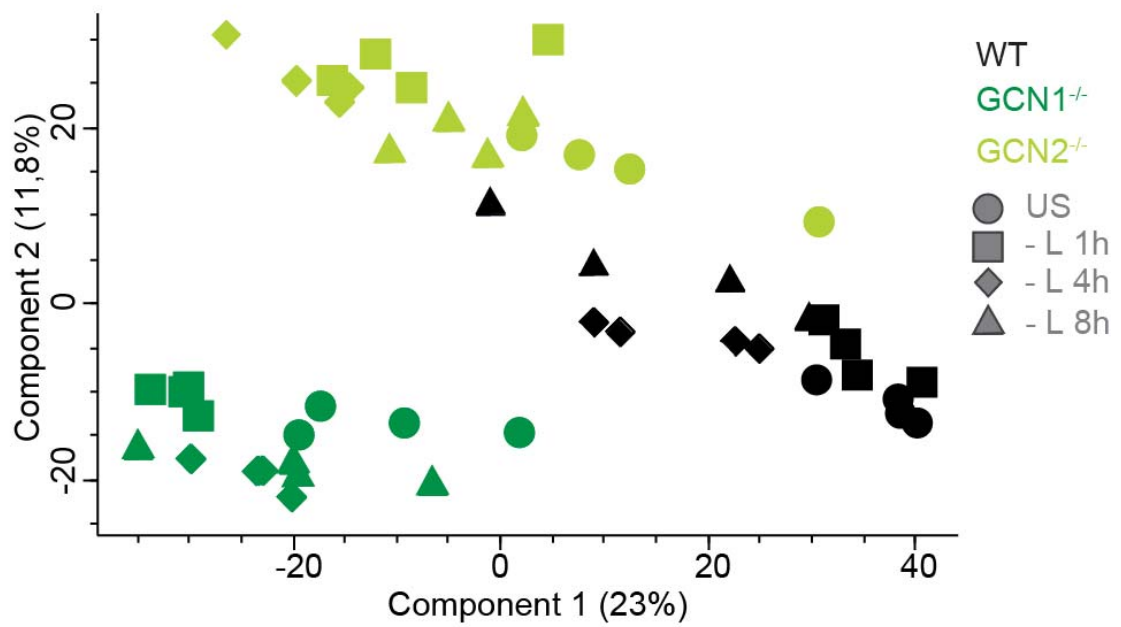
A**B**

Figure 37. GCN1 and GCN2 deficient cells have an intrinsic proteome profile. (A) Scheme of the proteomics setup: 3T3 cells, de- or proficient in GCN1 and GCN2 (WT (black), GCN1^{-/-} (dark green) and GCN2^{-/-} (light green)), were leucine starved for 1 h, 4 h and 8 h. Cells grown in normal medium were used as unstarved condition (US). After cell lysis and sample preparation, the samples were measured by liquid chromatography coupled to mass spectrometry. (B) Principal component analysis (PCA) of detected proteins in all three genotypes (WT (black), GCN1^{-/-} (dark green) and GCN2^{-/-} (light green)), leucine starved over time versus unstarved condition (US).

First, we evaluated the distribution of the proteins by PCA to analyze the genotypic and stress related proteome signatures. In line with the transcriptomics study (Figure 29B), the replicates clustered for each condition and the genotypes (GCN1^{-/-}, GCN2^{-/-} and WT) showed distinct patterns (Figure 37B). Interestingly, in contrast to the transcriptomics data, the proteomics profile of each genotype did not shift substantially over time of leucine stress. This hints that stronger transcriptional changes might be needed to adapt to the stress condition as compared to the proteome, or that changes at the overall proteome level simply do not need to drastically change their abundance levels to adapt to the stress situation.

Next, we addressed the profile of the ISR-related bZIP transcription factors, which are modulated upon leucine stress across time at the transcriptional level dependent on GCN1 and GCN2 (Figure 30). Unfortunately, we could not detect ATF4 and did not identify any other ISR linked transcription factor such as NRF2, GADD34 or ATF5. This could be explained by the systematic low abundance of transcription factors and the sensitivity and dynamic range coverage limitations of the mass spectrometry setup. In contrast, CHOP was significantly enriched in all genotypes over time compared to the time point zero control. Interestingly, CHOP protein abundance correlates well with the transcriptome level: it is significantly upregulated across time of stress exposure (from 4 h onwards) in the wild-type cells and reduced in the knockouts (Figures 30 and 38A). We verified the induction of CHOP by immunoblotting (Figure 38B).

To map more proteins to this 'CHOP cluster', we screened the proteins coding for genes belonging into the ISR-regulated stress program (e.g. *Lars*, *Slc7a5*, *Eif4ebp1*) illustrated in figures 32 and 34. Specifically, we aimed to understand if the components were quantitatively regulated like CHOP at the transcriptional and proteome level upon leucine depletion – dependent on GCN1 and GCN2. In total, we only detected a small number of proteins that were significantly changed between the genotypes upon leucine stress at 4 h (Figure 38C). However, we provided evidence that proteins involved in 1C-metabolism, amino acid transport and tRNA aminoacylation were only significantly changed in the wild-type in contrast to the knockout background upon leucine starvation at 4 h. For example, the glutamine-leucine transporter SLC7A5 matched into the described 'CHOP cluster' meaning that it was upregulated only in the wild-type background across

leucine stress time points (Figure 38C+D). Consequently, we showed that our proteome data matched with the transcriptional findings reported in section 4.2.3. However, we also realized that not all proteins matched into the 'CHOP cluster'. For example, the translation initiation factor eIF3c, which is a relevant binding partner of mTOR-RAPTOR to trigger translation initiation³⁰⁷, showed no significant change between the genotypes at 4 h leucine stress – even though this protein is highly regulated across leucine stress time points in the wild-type background (Figure 38C+E). This finding hints that eIF3c is significantly changed upon leucine stress, but this change is not mediated by the difference between the GCN1 or GCN2 deficient genotypes. In addition to that, we found the opposite scenario for the mTORC1 regulator Rheb. Rheb is significantly regulated between the genotypes, but showed no significant difference between unstarved to 4 h leucine starved condition in the wild-type (Figure 38C+E). Combined, this shows that the ATF4-mediated stress-transcription program does not exclusively regulate all components at the transcriptional and proteome level dependent on GCN1 and GCN2 over time. This hints that protein levels are rather stable and maintained independently of the GCN2-ISR.

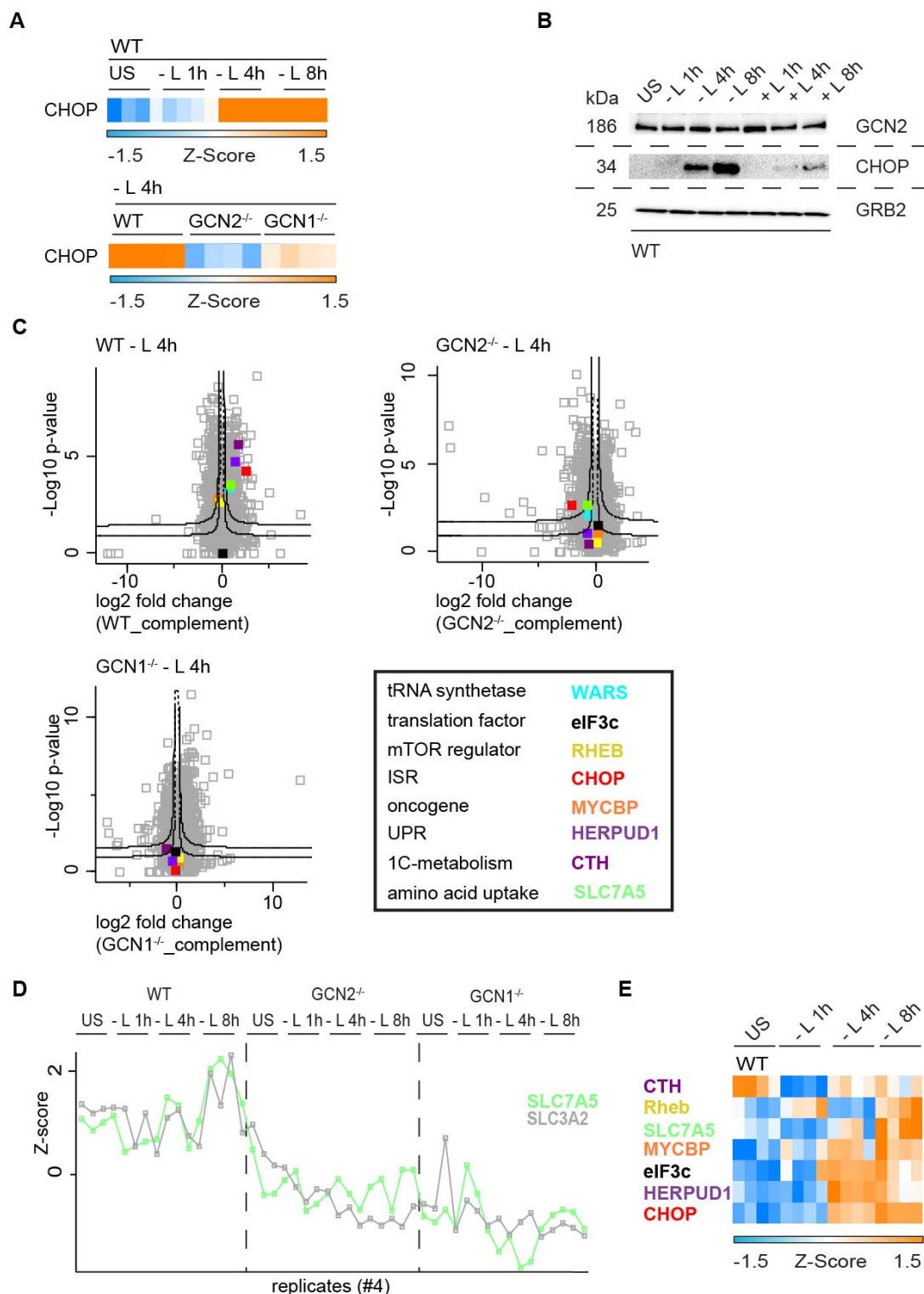


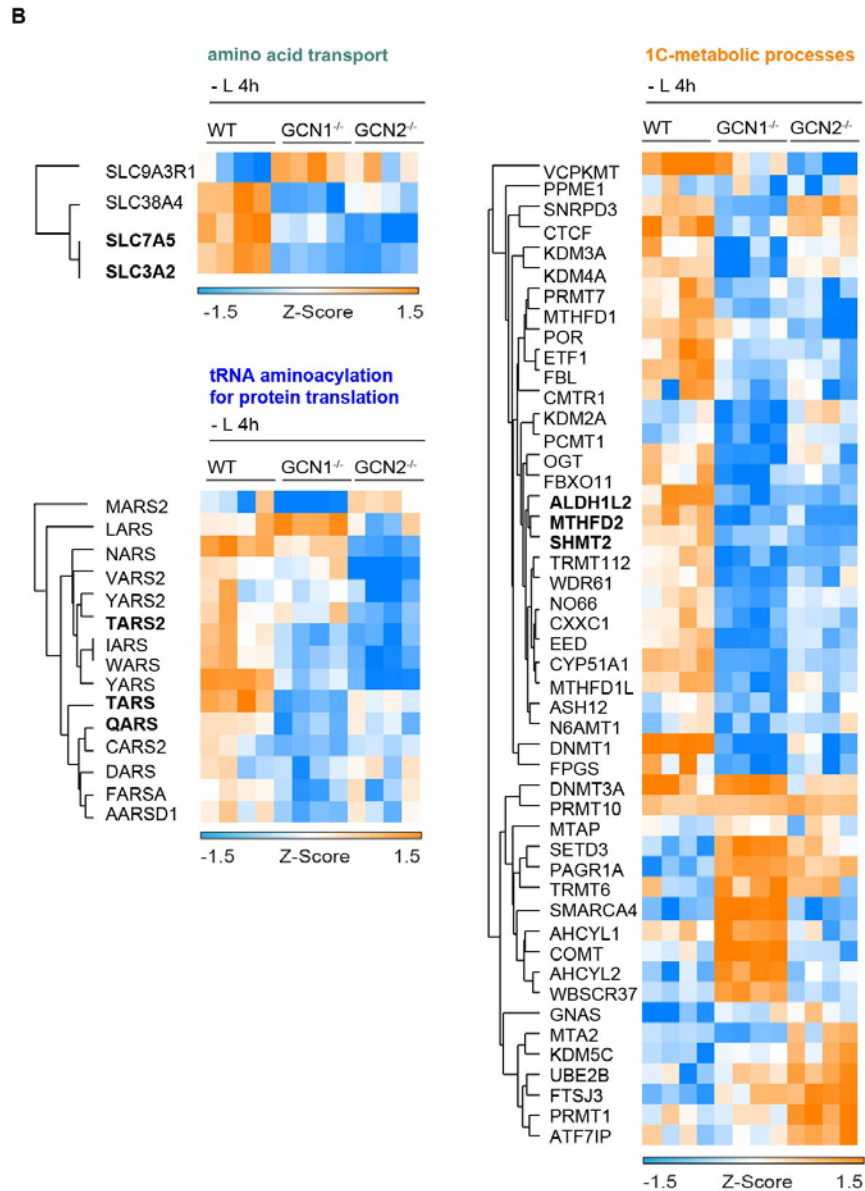
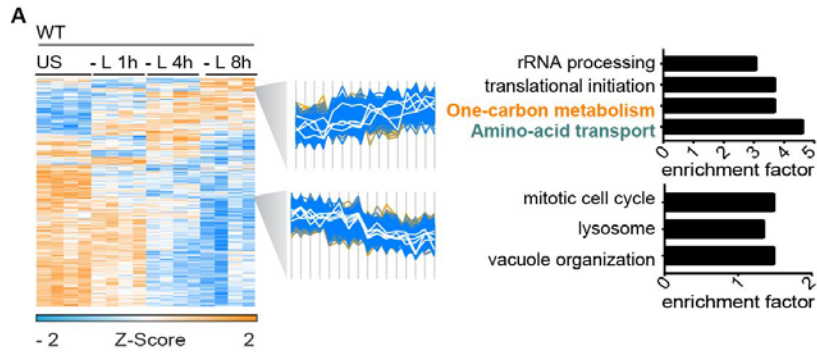
Figure 38. Proteome changes correlate with the transcriptional changes upon leucine stress. (A) Heatmap of z-scored protein intensity of CHOP that is significantly ANOVA-regulated upon leucine stress (- L) over time in 3T3 wild-type (WT), GCN2 deficient (GCN2^{-/-}) and GCN1 deficient (GCN1^{-/-}) background (FDR < 0.05). (B) Immunoblot of 3T3 wild-type (WT) cell lysate stimulated with leucine-starvation (- L), unstarved condition (US) or leucine-resupplementation (+ L) over time (1h, 4h and 8h). GRB2 was used as loading control. (C) Volcano plots comparing p-value and log₂-fold changes of proteins (black box) upon

leucine stress at 4 h (- L 4h) between 3T3 wild-type (WT), GCN2 deficient (GCN2^{-/-}) and GCN1 deficient (GCN1^{-/-}) background. (D) Single-plot of z-scored protein intensities of SLC7A5 (mint green) and SLC3A2 (grey) across time of leucine stress in 3T3 wild-type (WT), GCN2 deficient (GCN2^{-/-}) and GCN1 deficient (GCN1^{-/-}) cells. (E) Heatmap of z-scored protein intensities that are significantly ANOVA-regulated upon leucine stress (- L) over time in 3T3 wild-type (WT), GCN2 deficient (GCN2^{-/-}) and GCN1 deficient (GCN1^{-/-}) background (FDR < 0.05). (A+E) The profiles are color coded according to their distance from the respective cluster center (orange is close to the center; blue is further away from the center).

In figure 38, we highlighted that proteome changes affect many similar processes like found in the transcriptomics study (Figures 32 and 34). Consequently, we checked the GO-annotated processes significantly enriched over time of leucine starvation in wild-type cells. Consistent with the transcriptomics data (Figs 30 and 31), amino acid transport (p-value \leq 0.001), 1C-metabolism (p-value \leq 0.01), rRNA processing (p-value \leq 0.01) and translation initiation (p-value \leq 0.001) were upregulated upon amino acid stress (Figure 39A). In contrast, processes involved in vacuole organization (p-value \leq 0.001), lysosome (p-value \leq 0.03) and mitotic cell cycle (p-value \leq 0.1) were decreased (Figure 39A). Again, processes involved in 1C-metabolism, amino acid transport and tRNA aminoacylation were significantly enriched dependent on GCN1 and GCN2 upon leucine stress (Figure 39B) that matched with the proteins detected in figure 38C. Here, we found that the number of proteins mediating the difference were low in contrast to the transcriptional changes. For example, four amino acid transporters (SLC7A5, SLC3A2, SLC38A4 and SLC9A3R1) were significantly enriched upon leucine depletion at 4 h in wild-type in contrast to the 41 detected by RNASeq for the same term (Figure 31). Thus, we think that a distinct set of proteins mediate these phenotypic differences. However, technological limitations can also only yield a small part of the picture, which could be alleviated in the future with next generation approaches.

To get a deeper view, we checked the protein signatures in the mentioned three processes (1C-metabolism, amino acid transport and tRNA aminoacylation; Figure 39B bold). The leucine-glutamine shuttle (SLC7A5/SLC3A2) was not induced upon leucine depletion at 4 h in both knockout lines and matched the 'CHOP cluster' (Figure 38B). Further studies on this transporter shuttle that is known to connect the glutamine metabolism with the mTORC1 pathway^{50,461}, is highlighted in section 4.3. Moreover, we identified 14 tRNA synthetases, which were induced solely in the wild-type context upon leucine stress (Figure 39B). We detected QARS, the glutamine tRNA synthetase, which showed the same profile at the proteome level as described at the transcriptome level at 4 h of leucine stress in all three analyzed genotypes (Figures 39B and 31C). Interestingly, mitochondrial as well as cytoplasmic tRNAs were detected in the 'tRNA aminoacylation for protein translation' cluster. In this context, we realized that changes were

already mediated at the baseline condition, as shown for instance for TARS2 and TARS (Figure 39C). In addition, we found mitochondrial 1C- metabolism actors such as MTHFD2, ALDH2L1 and SHMT2 that were not induced in the GCN1 and GCN2 deficient knockouts in contrast to the wild-type at 4 h of leucine stress (Figure 39B). In this context, Reich *et al.*⁴⁴⁴ showed that thapsigargin/tunicamycin-induced PERK signaling controls the expression of enzymes that are involved in a pathway diverting intermediate metabolites from glycolysis to fuel mitochondrial 1C-metabolism. We highlighted at the transcriptional level that we detect the induction of the same enzymes upon leucine stress dependent on GCN1 and GCN2 presence (Figure 33). Strikingly, we discovered the same set of enzymes (PHGDH, PSAT1, PSPH, ALDH1L2, SHMT2 and MTHFD2) and their regulation upon leucine stress also at the proteome level (Figure 40). Combined, we showed that leucine stress triggers similar processes (tRNA aminoacylation, mitochondrial 1C-metabolism, serine biosynthesis and amino acid transport) at the transcriptional and proteome level, which are dependent on GCN1 and GCN2 upon leucine stress.



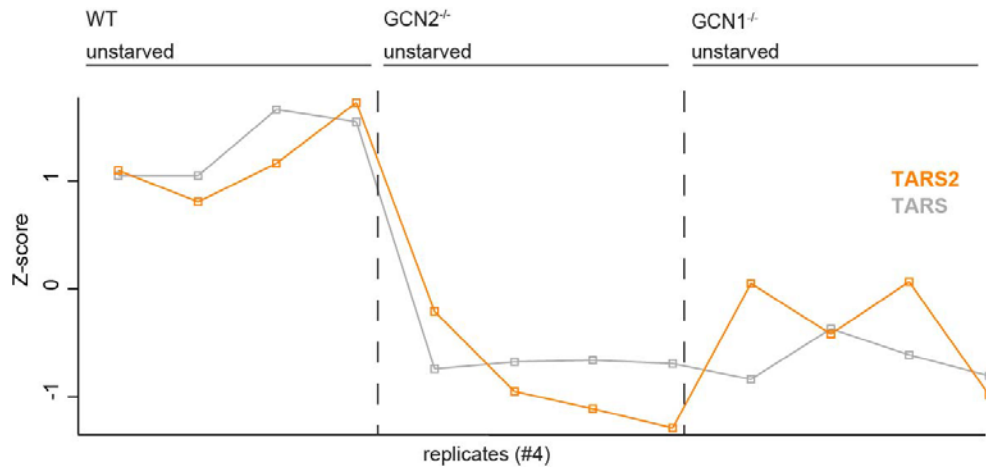
C

Figure 39. GCN1-GCN2 signaling regulates proteins involved in amino acid transport, tRNA aminoacylation and mitochondrial 1C-metabolism upon leucine stress. (A) Heatmap of z-scored protein intensities that are significantly ANOVA-regulated upon leucine stress (- L) over time (1h, 4h and 8h) in 3T3 wild-type (WT) cells (FDR < 0.05). Statistical significance was calculated using two-way ANOVA: amino acid transport (p-value ≤ 0.001), 1C-metabolism (p-value ≤ 0.01), rRNA processing (p-value ≤ 0.01) and translation initiation (p-value ≤ 0.001), vacuole organization (p-value ≤ 0.001), lysosome (p-value ≤ 0.03) and mitotic cell cycle (p-value ≤ 0.1). (B) Heatmap of z-scored protein intensities involved in amino acid transport, 1C-metabolism, tRNA aminoacylation for protein translation that are significantly ANOVA-regulated upon leucine stress (- L) at 4 h in 3T3 wild-type (WT), GCN2 deficient (GCN2^{-/-}) and GCN1 deficient (GCN1^{-/-}) backgrounds (FDR < 0.05). (D) Single-plots of z-scored protein intensities of TARS (grey) and TARS2 (orange). (A+B) The profiles are color coded according to their distance from the respective cluster center (orange is close to the center; blue is further away from the center).

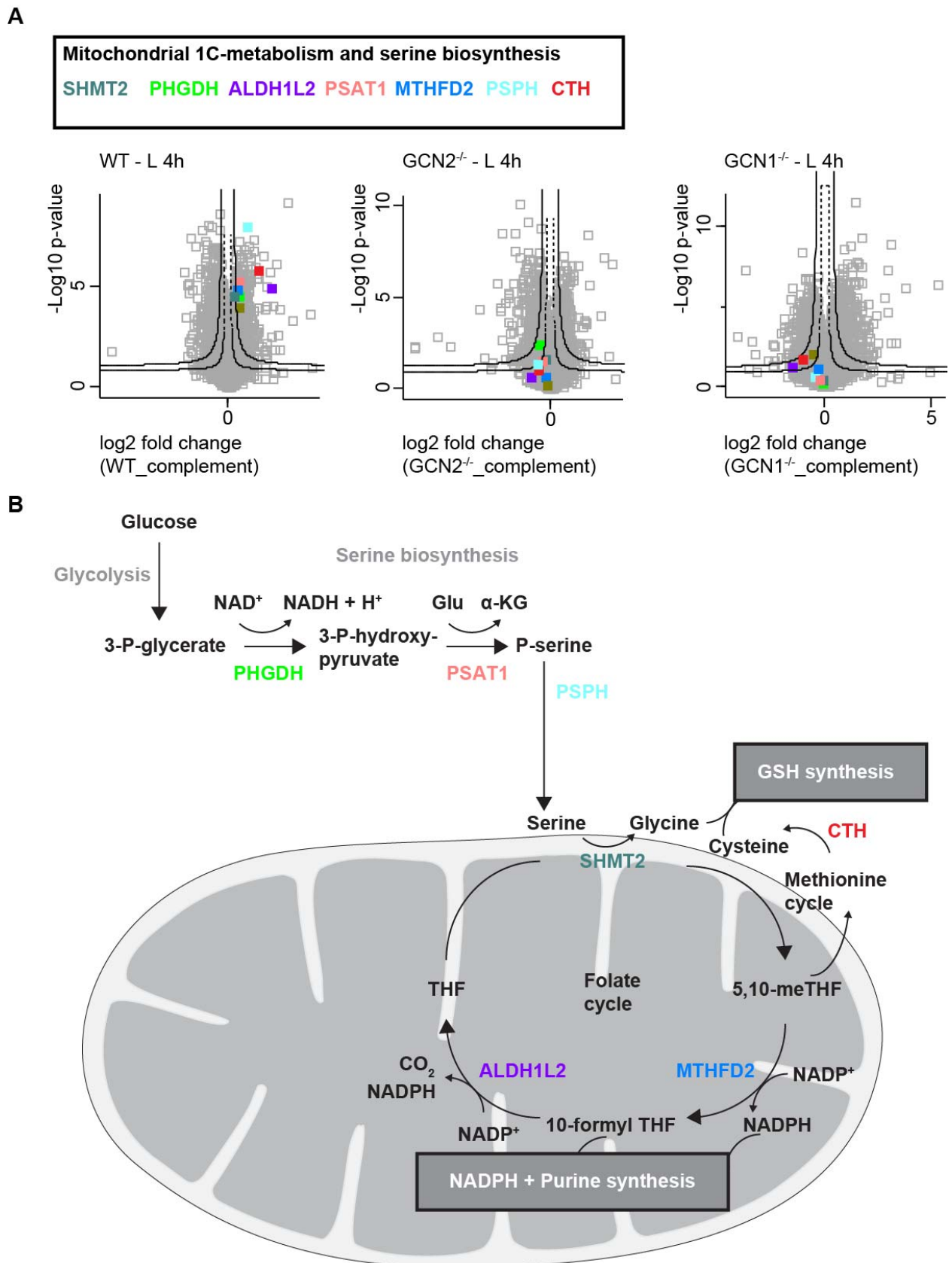
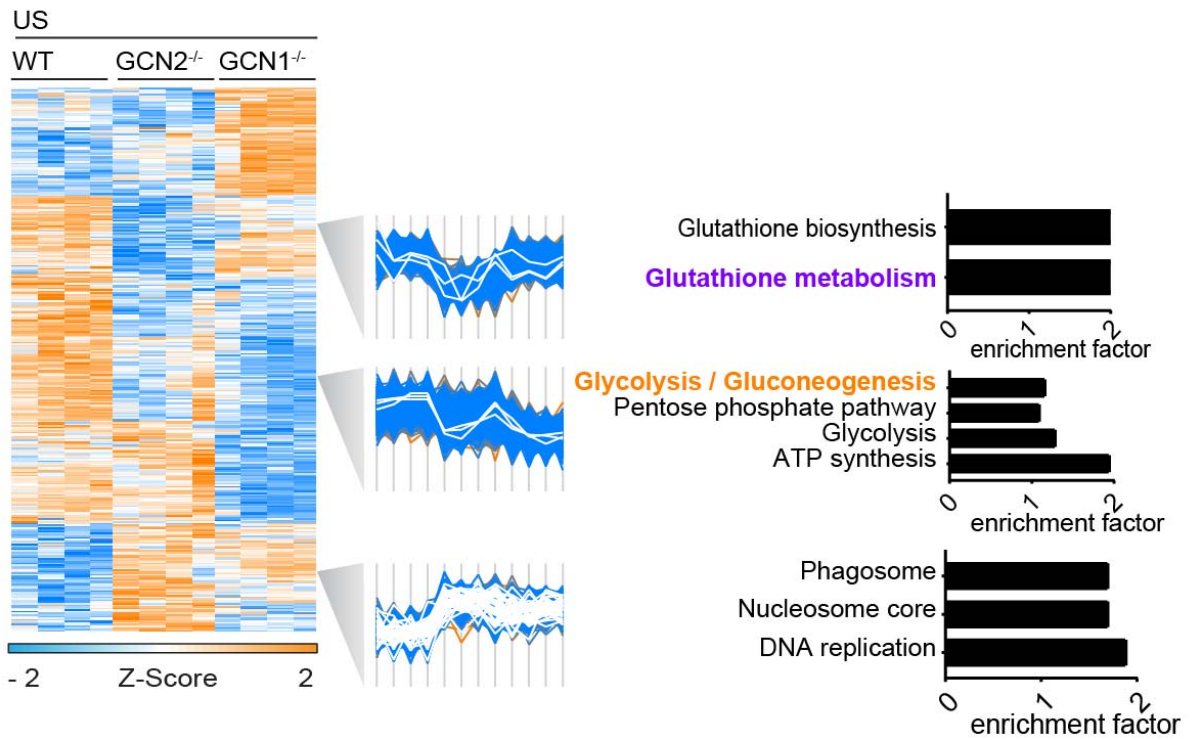


Figure 40. GCN1-GCN2 signaling regulates mitochondrial 1C-metabolism and serine biosynthesis upon leucine stress. (A) Volcano plots comparing p-value and log₂-fold changes of proteins (black box)

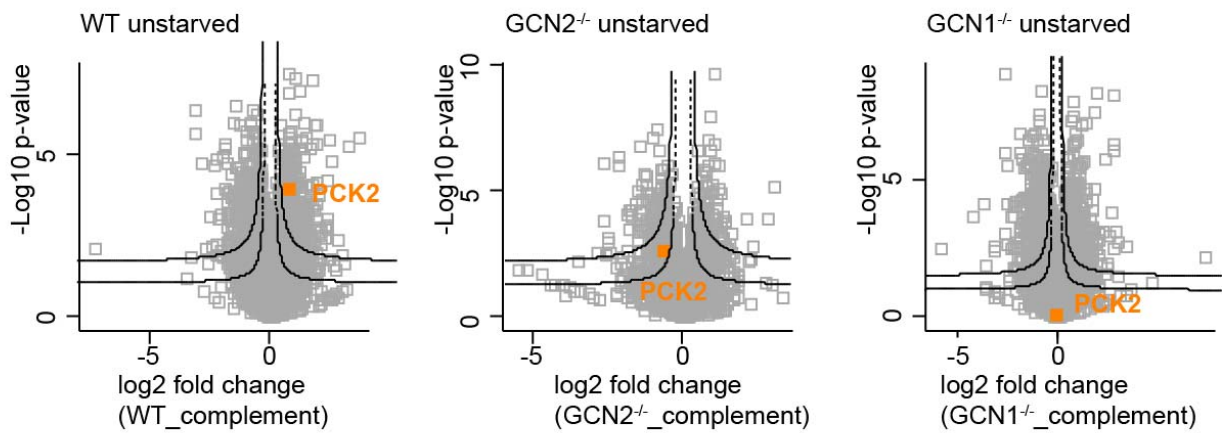
involved in mitochondrial 1C-metabolism and serine biosynthesis between 3T3 wild-type (WT), GCN2 deficient (GCN2^{-/-}) and GCN1 deficient (GCN1^{-/-}) backgrounds upon 4 h of leucine stress (- L 4h). (B) Simplified scheme of the serine biosynthesis, folate and methionine cycles (1C-metabolism) relevant for NADPH production, purine synthesis and GSH synthesis. Adapted from Ref.⁴⁴⁴. α -KG: alpha-ketoglutarate; THF: tetrahydrofolate; Glu: glutamate; GSH: glutathione.

Next, we tracked the ISR-independent functions of GCN1 and GCN2 comparing the significant enrichment of proteins in the unstarved condition. In harmony with our transcriptome data (Figure 35), we found that bioenergetic processes such as ATP synthesis (p-value ≤ 0.001), pentose phosphate pathway (p-value ≤ 0.1), glycolysis/gluconeogenesis (p-value ≤ 0.01) were induced only in the wild-type (Figure 41A). In line with our transcriptomics data (Figure 35B) and the study from Torrence *et al.*²⁶, we identified PCK2, the mitochondrial isoform of phosphoenolpyruvate carboxykinase (PEPCK-M), which catalyzes the GTP-dependent reaction of oxaloacetic acid (OAA) to phosphoenolpyruvate (PEP) to induce gluconeogenesis (Figure 41B). Mendez-Lucas *et al.*⁴⁴⁷ linked the GCN2/PERK-ATF4 mediated expression of *Pck2* to pro-tumorigenic stress adaptation. As recently reported, this gluconeogenic enzyme opposes the TCA cycle and maintains redox balance in glucose and serum-starved lung cancer cells^{462,463}. Redox balance is also mediated in the cell by sufficient glutathione levels. We detected a cluster diminished solely in the GCN2^{-/-} cells, which is clearly involved in glutathione metabolism (p-value ≤ 0.00001) (Figure 41A+C). Most interestingly, the NADH dehydrogenase complex, which is the complex I in the electron transport chain, was only downregulated in the GCN1^{-/-} background (Figure 41C). This suggests that the cellular bioenergetic profile regulated by GCN1 also affects the mitochondrial respiration. In addition, we provide further evidence that GCN1 and GCN2 modulate processes involved in DNA replication (p-value $p \leq 0.01$), phagosome formation (p-value ≤ 0.01) and nucleosome core regulation (p-value ≤ 0.02) (Figure 41A). Combined, these data suggest that GCN1 and GCN2 have distinct functions independent of the activation of the ISR upon amino acid stress. Thereby, GCN1 and/or GCN2 deficiency at the protein as well as at the gene level downregulates processes associated with mitochondrial function such as glutathione metabolism, gluconeogenesis or purine synthesis.

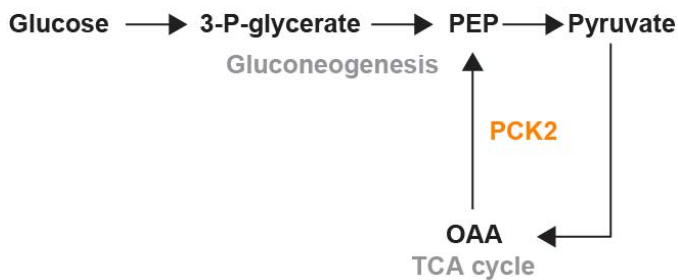
A



B



Glycolysis



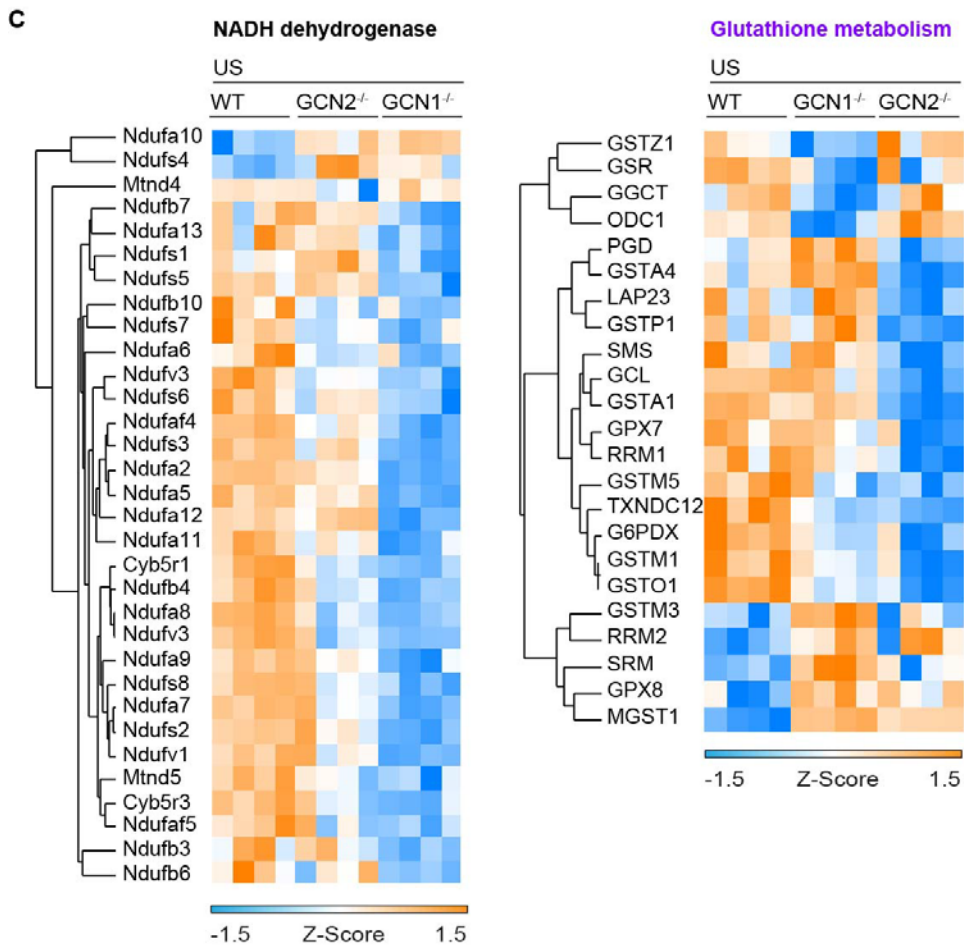


Figure 41. GCN1 and GCN2 have ISR-independent functions at the protein level. (A) Heatmap of z-scored protein intensities that are significantly ANOVA-regulated upon unstarved condition (US) in 3T3 wild-type (WT), GCN2 deficient (GCN2^{-/-}) and GCN1 deficient (GCN1^{-/-}) backgrounds (FDR < 0.05). Statistical significance was calculated using two-way ANOVA: glutathione metabolism (p-value ≤ 0.00001), glutathione biosynthesis (p-value ≤ 0.1), ATP synthesis (p-value ≤ 0.001), pentose phosphate pathway (p-value ≤ 0.1), glycolysis/gluconeogenesis (p-value ≤ 0.01), DNA replication (p-value p ≤ 0.01), phagosome (p-value ≤ 0.01) and nucleosome core (p-value ≤ 0.02). (B) Volcano plots comparing p-value and log₂-fold changes of PCK2 (orange) between 3T3 wild-type (WT), GCN2 deficient (GCN2^{-/-}) and GCN1 deficient (GCN1^{-/-}) background at basal condition (unstarved) (FDR < 0.05). Simplified scheme of PCK2 involved in gluconeogenesis. OAA: oxaloacetic acid; PEP: phosphoenolpyruvate. (C) Heatmap of z-scored protein intensities enriched in NADH dehydrogenase (black) or glutathione metabolism (purple) that are significantly ANOVA-regulated upon unstarved condition (US) in 3T3 wild-type (WT), GCN2 deficient (GCN2^{-/-}) and GCN1 deficient (GCN1^{-/-}) backgrounds (FDR < 0.05). (A+C) The profiles are color coded according to their distance from the respective cluster center (orange is close to the center; blue is further away from the center).

Overall, the leucine stress-induced ISR regulates the same processes at the transcriptional and proteome level that are highly dependent on the presence of GCN1 and GCN2. GCN1 and GCN2

are involved in pathways beyond the amino acid response. Interestingly, we found that the bioenergetics were modulated by the loss of both proteins already in normal growth state. Exclusively, GCN1 knockout cells showed a downregulation in the complex I of the ETC whereby GCN2 knockout cells in glutathione metabolism. We also showed that systematic protein changes of the mitochondrial 1C-metabolism, the amino acid transporter machinery and tRNA synthetases were affected in their enrichment by the genotype and the stress situation.

4.2.4.2. Phosphoproteome analysis

GCN2 has so far only one known target, which is the translation initiation factor eIF2 α (encoded by *Eif2s1*) that becomes phosphorylated at a single serine (S52) to shut-down protein translation in response to amino acid stress⁷⁷. Thus, a key question in the ISR field is if GCN2 is solely dedicated to eIF2 α or are other substrates involved in the ISR regulation. Here, we aimed to identify additional targets of the GCN2-driven amino acid response. We also focused on the mTORC1 signaling pathway in light of the poorly understood connection between the two amino acid sensing networks²⁴.

The phosphoproteomics analysis was conducted using the same conditions as described for the full proteome study and the samples came from the same lysate pool (Section 3.7.2.; Figure 37A). In total, we detected 34,091 phosphosites and more than 20,000 per sample. Within this dataset, 3,678 phosphopeptides were identified as significantly changed. First, we visualized the distribution of the phosphopeptide repertoire in a genotype and stress dependent manner (Figure 42). Replicates clustered together and the genotypes showed an intrinsic signature at steady-state, in agreement with the full proteome and transcriptome data analysis (Figures 29B and 37B). Interestingly, we detected a strong systematic change from the condition 'unstarved' to 1 h of leucine stress, especially in the wild-type and GCN2^{-/-} backgrounds. In contrast to that, the GCN1^{-/-} cells displayed a drastic change towards long-term starved conditions. Combined, this hints that the phosphosite changes upon leucine stress were most likely highly time-dependent. The drastic phosphorylation change at 1 h will be the major focus and analyzed in detail below.

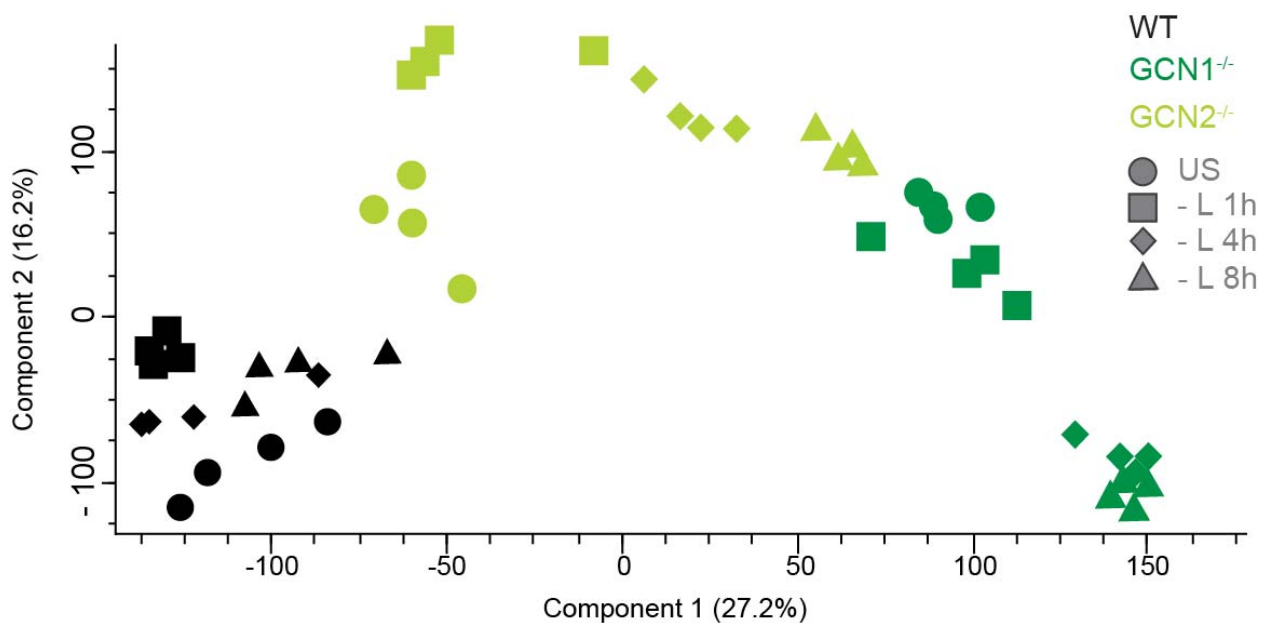


Figure 42. GCN1 and GCN2 deficient cells have a distinct phosphoproteome profile. Principal component analysis (PCA) of the peptides in all three genotypes (WT (black), GCN1^{-/-}(dark green) and GCN2^{-/-} (light green)), leucine starved over time versus unstarved condition (US).

First, we screened for the well-known key players of the amino acid response: GCN2, eIF2 α , ATF4 and CHOP. Unfortunately, the depth of analysis limited us to detect GCN2 phosphopeptides. Thus, the autophosphorylation of GCN2 was not possible to study, which is consistent with public data (PhosphoSitePlus) highlighting very low T898 phosphorylation level detection. Next, we screened for the known GCN2 target - the phosphorylation site of eIF2 α at serine 52. Again, this site was below the limit of detection. However, we detected ATF4 and CHOP specific phosphosites. We found that the phosphosites for ATF4 were already significantly upregulated at 1 h of leucine starvation, which is in contrast to the phosphosites for CHOP that were detected from 4 h onwards (Figure 43A). This pattern matches the expression kinetics of both proteins at the protein level analyzed by immunoblotting (Figure 43B). In the GCN1 and GCN2 deficient cells, the phosphosites for ATF4 and CHOP were downregulated compared to the wild-type, which is illustrated upon 4 h of leucine stress in figure 43C. Collectively, these data were consistent with the described transcriptome and full proteome pattern highlighted in figures 30 and 38. Strikingly, we could verify at the transcriptome, the full proteome and the phosphoproteome level that ATF4 and CHOP are induced upon leucine stress over time dependent on GCN1 and GCN2.

To provide further proof for the modulation of the GCN2-ISR, we screened for amino acid transporters, which are regulated by the PERK-ISR, mTORC1 pathway^{15,26,95} as well as the GCN1-GCN2-ISR (Figures 34 and 39). For example, the glutamate-cystine antiporter SLC7A11 is known to become phosphorylated by mTORC2 at serine 26 (S26), modulating its induction and

activity⁴⁶⁴. The upregulation of SLC7A11 upon leucine stress across time, dependent on GCN1 and GCN2, was shown at the transcriptional level (Figure 34). Interestingly, we discovered that the phosphosite at S26 was significantly upregulated in a time-dependent manner in the wild-type background (Figure 43D). In the GCN1 and GCN2 knockout lines, SLC7A11 phosphorylation was not significantly enriched at 4h leucine stress compared to the wild-type. Combined, we provided another example that manifests the modulation of the amino acid response across time of leucine deprivation, highly dependent on GCN1 and GCN2.

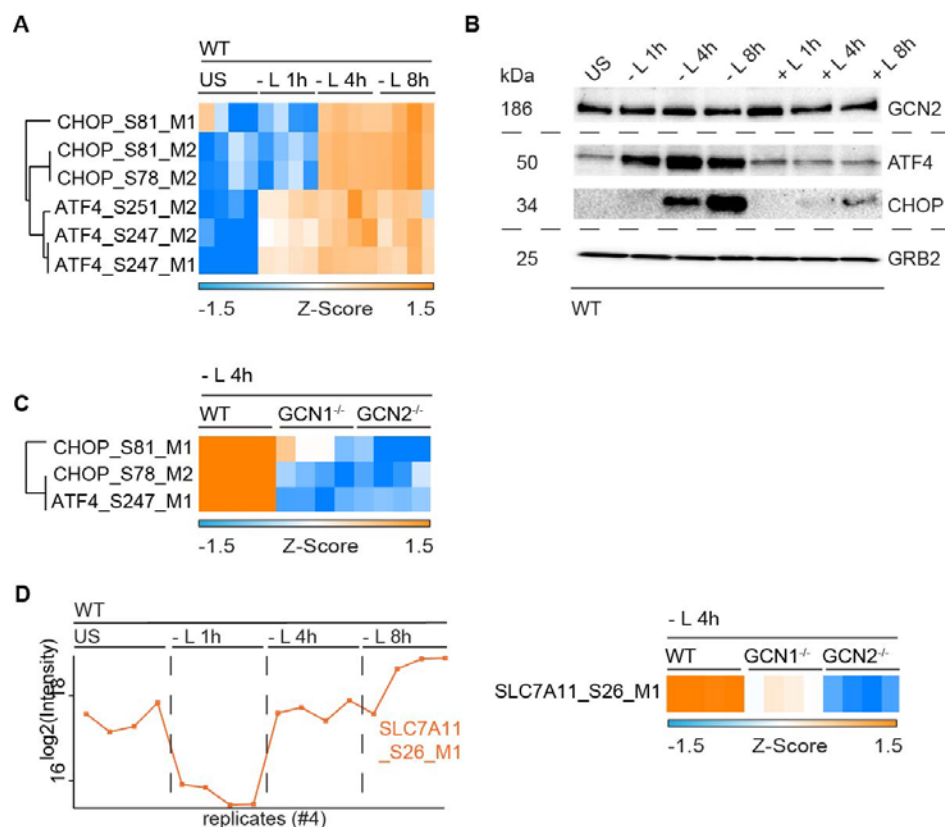


Figure 43. SLC7A11, ATF4 and CHOP phosphorylations are modulated across time upon leucine stress dependent on GCN1 and GCN2. (A) Heatmap of z-scored phosphosite intensities of CHOP and ATF4 that are significantly ANOVA-regulated upon leucine stress over time in 3T3 wild-type (WT) cells (FDR < 0.05). (B) Immunoblot of 3T3 wild-type (WT) cell lysates stimulated with leucine-starvation (- L), unstarved condition (US) or leucine-resupplementation (+ L). GRB2 was used as loading control. Data are depicted as one of two representative gels. (C) Heatmap of z-scored phosphosite intensity of CHOP that is significantly ANOVA-regulated at 4 h of leucine stress (- L 4h) in 3T3 wild-type (WT), GCN2 deficient (GCN2^{-/-}) and GCN1 deficient (GCN1^{-/-}) cells. (D) SLC7A11 phosphorylation at S26 in 3T3 wild-type (WT), GCN2 deficient (GCN2^{-/-}) and GCN1 deficient (GCN1^{-/-}) cells upon leucine stress (- L) illustrated as single plot (log₂ intensity) or heatmap (z-scored). (A+C+D) The profiles are color coded according to their distance from the respective cluster center (orange is close to the center; blue is further away from the center).

Next, we aimed for a deeper understanding of the phosphorylation changes induced by the timing of stress exposure. In line with the PCA (Figure 42), we determined one large cluster in which the shift in enrichment was mediated at 1 h of leucine stress. In this cluster, we detected 18 hits for proteins of the mTOR signaling pathway (Figure 44A). Interestingly, we detected both targets of mTORC1: 4EBP1 (encoded by *Eif4ebp1*) and S6K1 (encoded by *Rps6kb1*). For decades, the activation of mTORC1 is read out by the phosphorylation at threonine 37 and 46 of 4EBP1⁴¹. Strikingly, we found a significant downregulation of the phospho-4EBP1 at threonine 46 (mouse T47) at 1 h in contrast to prolonged stress exposure or normal growth state (Figure 44A). This finding is consistent with the literature highlighting the reactivation of mTORC1 upon long-term nutrient withdrawal³⁶⁷. This data will be described in further detail in section 4.5. For p70S6K (S6K1), we did not detect the characteristic mTORC1 phosphosite at threonine 389, but found hits on threonine 444 and serine 447 that are the isozyme sites of serine 424 and threonine 421, respectively (Figure 44B). S6K1 is phosphorylated in a sequential way on seven phosphosites (T229, T389, S404, S411, S418, T421 and S424), while serine 424 and threonine 421 reside within the putative autoinhibitory domain. Substitution of these both sites to an alanine suppresses activation of the S6K1 (Refs. ^{447,465–467}). Active S6K1 phosphorylates ribosomal protein S6 (RPS6), a component of the 40S, and eIF4B (at S422), a member of the translation initiation factor family to control protein translation³⁰². In line with this, we could identify hits for both downstream targets and show a phosphosite downregulation at 1 h of leucine stress followed by an upregulation at later time points (Figure 44A). Combined, we provide evidence that the phosphorylation status of proteins regulated downstream by mTORC1 to control translation, are modulated in a time-dependent manner upon leucine stress. Unfortunately, the mentioned phosphosites were not interpretable in the knockouts due to variation in the replicates.

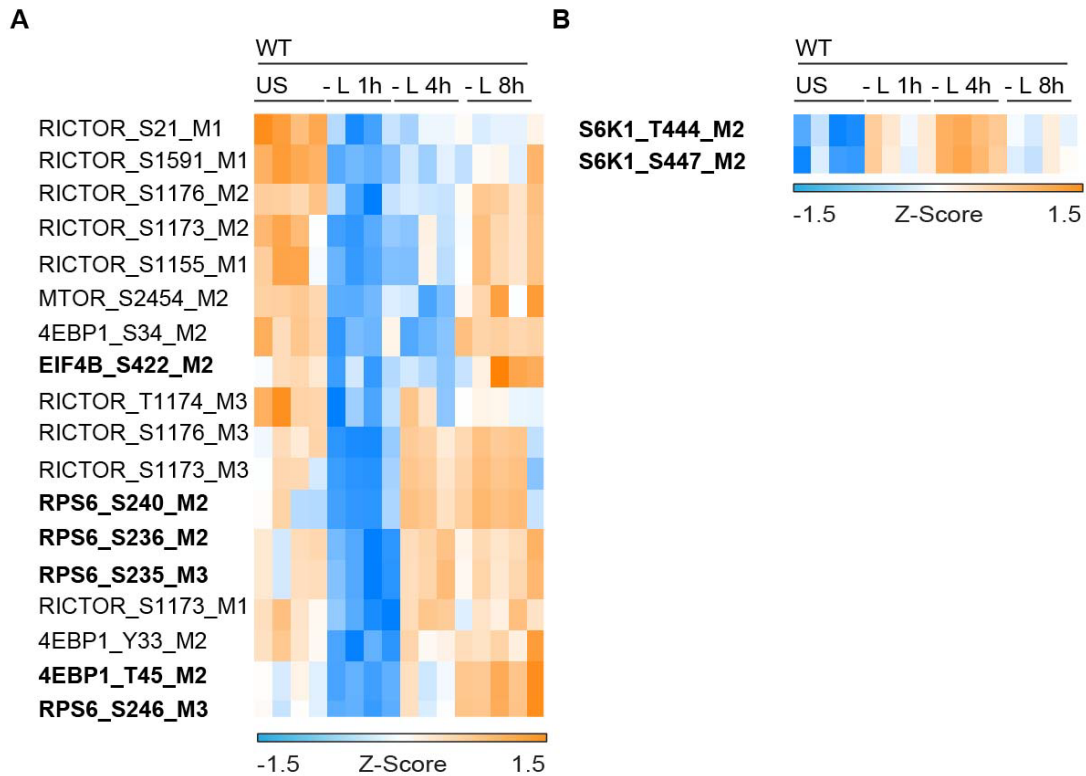


Figure 44. Leucine stress regulates the phosphorylation of mTOR signaling proteins relevant for translational control in a time-dependent manner. (A+B) Heatmap of z-scored phosphosite intensities of mTOR regulatory proteins (in bold) that are significantly ANOVA-regulated upon leucine stress over time in 3T3 wild-type (WT) cells (FDR < 0.05). The profiles are color coded according to their distance from the respective cluster center (orange is close to the center; blue is further away from the center).

In summary, major phosphorylation changes of mTOR signaling relevant for translational control were detected at early stress exposure and circumvented upon prolonged stress duration – a phenomenon in line with recent literature³⁶⁰. Moreover, we detected ATF4 dependent ISR targets, such as SLC7A11 and CHOP, which are modulated in a time- and genotype-specific way. Unfortunately, the methodological limit of detection prohibited the screening of the autophosphorylation of GCN2 at T898 and the phosphorylation of eIF2 α at S52. Therefore, other potential targets of GCN2 could not be postulated so far.

4.2.5. Interactomics of endogenous GCN1

Biochemical evidence was provided in yeast and mammals that the ribosomal P-stalk (uL10/P1/P2) activates GCN2 (Refs.^{166,169–171}). The P-stalk was also detected in the Cryo-EM structure of yeast GCN1 under steady-state condition¹¹⁴. In addition, yeast GCN1 directly interacts with GCN2, GCN20 and the ribosomal machinery as shown by genetic mutagenesis approaches^{124,131}. Moreover, YIH1 and GIR2/RBG2 compete with GCN2 for binding to GCN1 at

the GI domain^{153,154}. However, several open access human interactome projects (HuRI and OpenCell) did not report a GCN2 or ribosomal interaction of human GCN1^{158,159,162}.

Quantitative proteomics is a powerful and highly sensitive technique to distinguish true interactors from background binders⁴⁶⁸. To identify the main interaction partners of murine GCN1, which may give hints about GCN1 role in different biological processes, we performed label-free quantitative affinity enrichment mass spectrometry (AE-MS) analysis upon leucine stress and under normal growth state (Section 3.7.3.). This interaction proteomics study was performed in collaboration with Dr. Andreas-David Brunner from the Prof. Dr. Matthias Mann department. A priori, we expected to isolate a similar set of GCN1 interacting partners as reported in yeast in basal condition such as GCN20, GCN2 and ribosomal proteins^{124,131}.

We decided to use the quantitatively accurate affinity enrichment (AE) instead of the affinity purified (AP) MS approach to circumvent the need to purify GCN1 to homogeneity and retain rather weak and transient binders, which can otherwise be lost during harsh washing steps⁴⁶⁹. GCN1 was used as the bait protein in this analysis, which needed to be 'labeled' in order to verify it (bait protein) with its interaction partners (prey proteins) by LC-MS. Two strategies are commonly used to pull the bait and enrich it with its interaction partners, which is a simple antibody targeting approach against the protein or against a tag sequence, which is fused either to the N- or C-terminus of the protein of interest⁴⁶⁹. When the bait protein is very low abundant and no specific antibody exists, the tagging strategies are highly preferred. However, a tag can affect the properties and behavior of the bait protein at its physiological level⁴⁶⁹. Therefore, we aimed to compare both strategies to prevent any technical bias.

First, we performed the interactomics approach with overexpressed GCN1. Here, wild-type 3T3 cells were transiently transfected with Twin-Strep-tagged GCN1 and leucine starved for 4 h or cultivated in normal growth medium. Then, the overexpressed lysate was affinity purified, digested, enriched and quantified by LC-MS (Figure 45A). The untagged wild-type cell line was used as a control for unspecific enrichments by the means of background binders.

In a proof of concept experiment, we detected GCN1 to have 1000-fold increased expression levels in the overexpressed (OE) cell line, independent of leucine stress compared to the endogenous GCN1 in the baseline wild-type cell line (Figure 45B). Then, we checked the proteome profile of the overexpressed GCN1 to the endogenous GCN1: the overexpressed line highlighted many systematic GO-enrichments (amino acid transporter activity, translation and catabolic processes), which we also found in the full proteome analysis (Section 4.2.4.). However, we did not expect that the overexpression of GCN1 shifts the proteomic signature compared to the endogenous GCN1 independently of the leucine stress (Figure 45C). Interestingly, even SLC transporter expression levels were increase by 32-fold in response to GCN1 overexpression (Figure 45B). This means that the overexpression of GCN1 induces protein expression artefacts.

This observation forced us to abandon the overexpression construct and focus on the GCN1 interactome at endogenous expression level to retain its most likely native interactome.

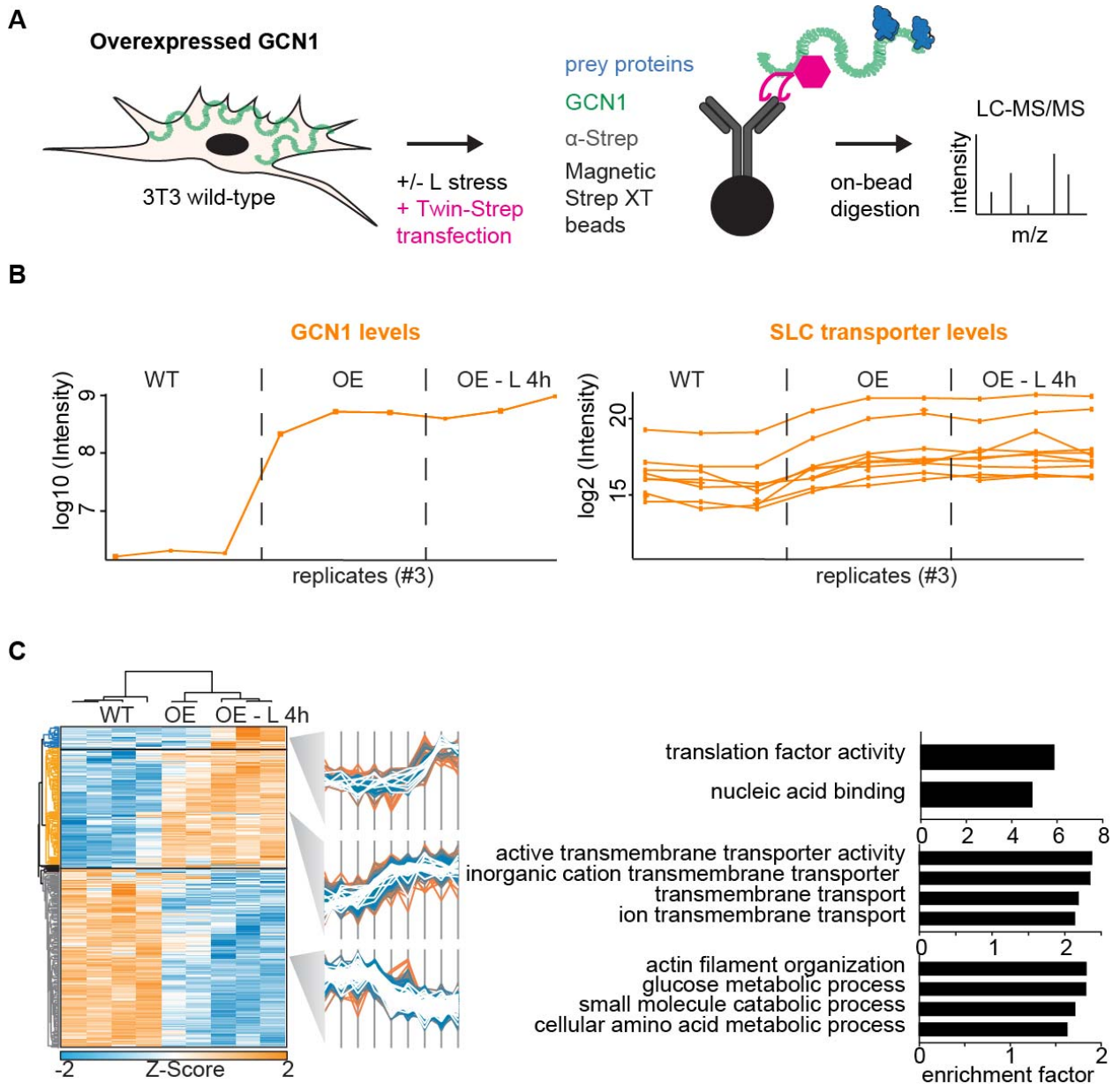


Figure 45. Overexpression of GCN1 shifts the proteomic signature. (A) Interaction-proteomic setup of overexpressed GCN1 (dark green): Twin-Strep-GCN1 (pink) transfected 3T3 wild-type cells were treated with or without leucine starvation (L stress for 4 h) prior to lysis, magnetic immunoprecipitation and on-bead digest. Prey proteins (blue) were analyzed by liquid chromatography coupled to mass spectrometry (LC-MS). (B) Representative single-plots of significantly enriched GCN1 (log₁₀ intensity) and SLC transporters (log₂ intensity) from the condition described in C. Data are measured in three different biological replicates. (C) Heatmap of z-scored protein intensities stimulated with 4 h leucine stress (- L 4h) or unstarved condition in 3T3 wild-type (WT) or Twin-Strep GCN1 overexpressed (OE) cells (FDR < 0.05). The profiles are color

coded according to their distance from the respective cluster center (orange is close to the center; blue is further away from the center).

In consequence, we changed the strategy and used a specific GCN1-targeting antibody for the pull-down experiments (Figure 46A). Wild-type cells without the addition of the GCN1-specific antibody served as internal controls. In total, six biological replicates per condition were used. Represented by a volcano plot (Figure 46B), GCN1 significantly enriched by more than 60-fold highlighting that the enrichment worked. Potential GCN1-interacting prey proteins showed an enrichment greater than 4-fold. However, we detected a rather heterogeneous interactor distribution across replicates. Thus, high confidence calling of direct GCN1 interactors was not possible in this series of experiments. In consequence, we repeated the experiment several times in order to verify the putative interactors. In the next series of GCN1 pull-down experiment, successful pull-down of the bait was proven by an enrichment of more than 200-fold (Figure 46C). Importantly, pull-down results were consistent across biological replicates and highlighted many interactors like the proteins RAD50 (double strand break repair protein), NBS1 (nijmegen breakage syndrome 1) and MRE11 (meiotic recombination 11 homolog), which assemble the MRN complex relevant for DNA double-strand break (DSB) repair⁴⁷⁰ (Figures 46B+C). Upon sensing DSBs, the class-IV member of PI3K serine/threonine kinase ATM (ataxia telangiectasia mutated) is activated, which requires the MRN complex in the early phase of DSBs detection in order to trigger various branches of the complex DNA damage response network for cell cycle arrest or apoptosis⁴⁷¹. In addition, we also detected an enrichment of MDC1 (mediator of DNA damage checkpoint protein 1), NUDT16L1 (nudix hydrolase 16 like 1) and USP10 (ubiquitin-specific-processing protease 10) as potential GCN1 interactors (Figure 46C). These proteins have distinct roles in DSBs induced ATM signaling⁴⁷²⁻⁴⁷⁴. Interestingly, the relevance of GCN1 in cell cycle regulation was previously reported by Yamazaki *et al.*¹¹³, which strengthen our identified GCN1 interaction partners. This finding matched our omics results as well (Sections 4.2.3. and 4.2.4.), where GCN1 was identified to be involved in DNA-replication dependent processes. Most importantly, RPLP0 was also identified as potential GCN1 interaction partner (Figure 46C), which is the uL10 component of the P-stalk, relevant for GCN2-P-stalk binding¹⁶⁶. This finding matches the detection of the P-stalk in the Cryo-EM structure of GCN1 in yeast and adds another piece to the puzzle how GCN1 might trigger GCN2 activation via ribosomal interaction in murine cells^{114,171}.

Next, we analyzed the interaction profile after 4 h of leucine deprivation. Again, we identified components of the MRN complex, RAD50 and MRE11, as well as the USP10 protein as interactors of GCN1 (Figure 46D). However, we did not detect an enrichment in RPLP0 at this

time point. Most importantly, GCN2, GCN20 or other ribosomal proteins were not identified as direct GCN1 interactors across all experimental setups (Figure 46).

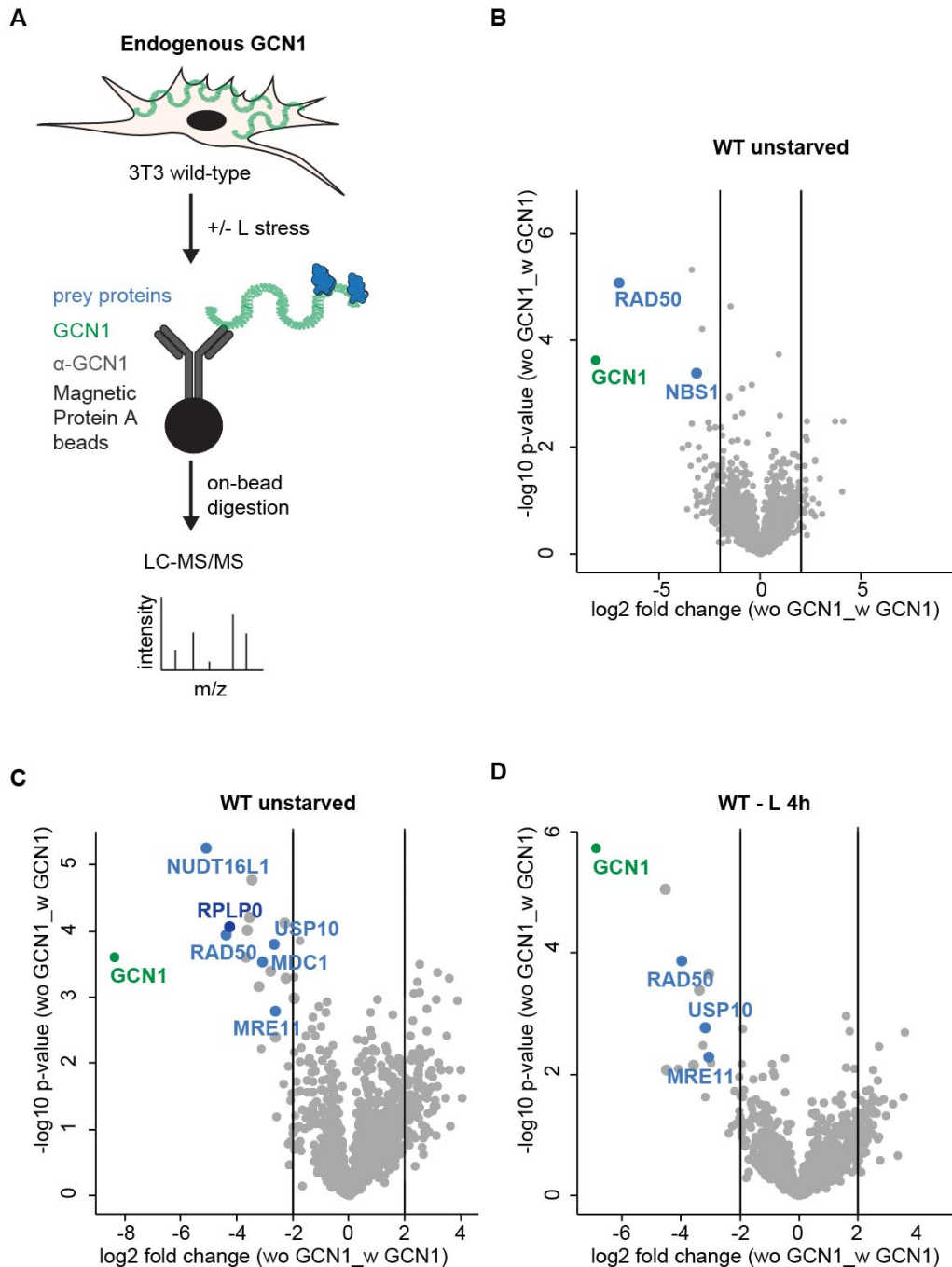


Figure 46. Endogenous GCN1 potentially interacts with the MRN complex independent of leucine stress. (A) Interaction-proteomic setup of endogenous GCN1: 3T3 wild-type cells were treated with or without leucine starvation (L stress for 4h) prior to lysis, magnetic immunoprecipitation and on-bead digest. Prey proteins (blue) were analyzed by liquid chromatography coupled to mass spectrometry (LC-MS). (B-D) Volcano plots comparing p-value and log₂-fold changes of GCN1 (dark green) and prey proteins (blue) between 3T3 wild-type (WT) cells pulled on GCN1 (w GCN1) or not (wo GCN1) upon unstarved and leucine-

starved (- L for 4h) conditions. (B+C) Data are based on two independent experiments with several biological replicates.

To verify the interaction partners RAD50, MRE11 and NBS1 identified by AE-MS, we performed affinity immunoprecipitation using protein A beads. The isotype control verified no unspecific antibody interactions. However, we detect all complex members (RAD50, MRE11 and NBS1) in the wild-type and the GCN1 deficient pulldown. In the latter, the signal was not as strong as in the wild-type indicating a very weak MRN abundance when GCN1 is lost (Figure 47A). We also pulled on MRE11 to cross-verify its GCN1 interaction, but did not detect GCN1 in the process of immunoblotting (Figure 47B). In contrast to immunoprecipitation, AE-MS is more specific with regards to protein identification since it analyzes protein sequences directly. Therefore, we would argue that the identified interaction partners are rather correct. However, we assume that GCN1 interaction partners are rather transient and in flux, which makes it challenging to identify them – especially with antibody-based immunoblotting approaches.

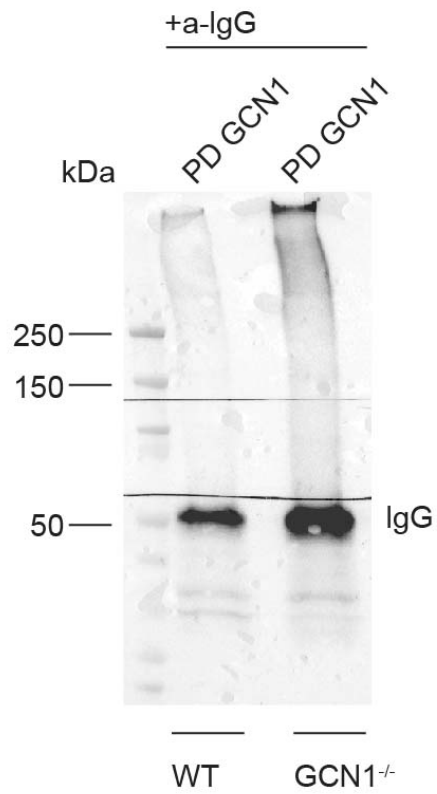
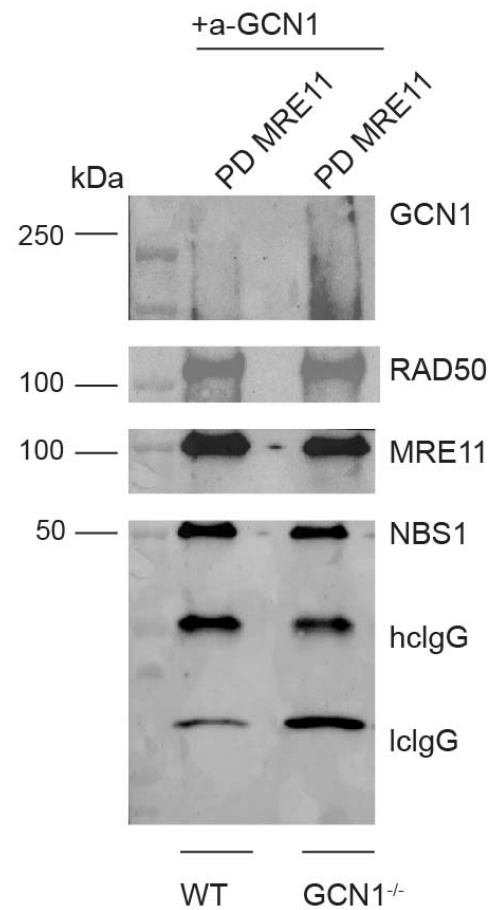
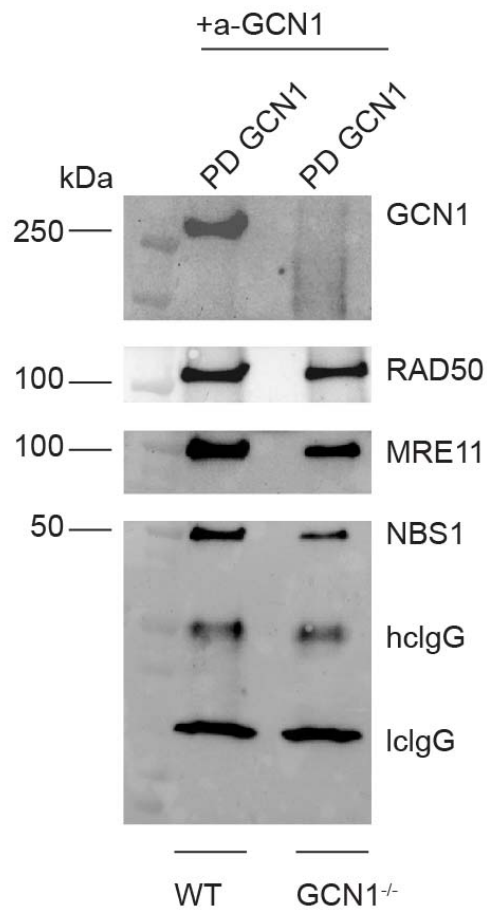
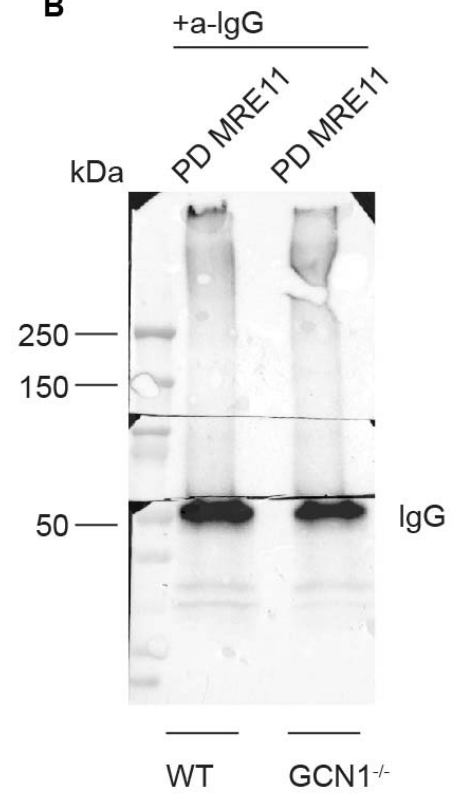
A**B**

Figure 47. GCN1 might transiently interact with the MRN complex. (A) Immunoprecipitation of GCN1 (PD GCN1) using protein A beads in wild-type (WT) and GCN1 knockout (GCN1^{-/-}) lysates. Specificity of the GCN1 antibody was verified by the IgG control. (B) Immunoprecipitation of MRE11 (PD MRE11) using protein A beads in wild-type (WT) and GCN1 knockout (GCN1^{-/-}) lysates. Specificity of the MRE11 antibody was verified by the IgG control.

In summary, we performed label-free quantitative affinity enrichment mass spectrometry analysis to determine interaction partners of GCN1 under normal growth and leucine deprived conditions. We showed that GCN1 interacts most likely in a condition-dependent and transient way with the DNA damage response complex MRN. Moreover, we presented evidence for the P-stalk interaction of GCN1 via the uL10 component, but no direct interaction with GCN2 or GCN20. However, based on these experiments, we will verify these interaction partners with crosslinking approaches to trap transient GCN1 interaction partners and also consider the use of split GFP systems for endogenous tagging of GCN1⁴⁷⁵.

4.3. Functional analysis of GCN1 and GCN2 deficiency

4.3.1. Overview

In chapter 4.2, three omics studies were conducted to get a broad overview about the distinct signatures of GCN1 and GCN2 in a murine cell system (3T3). In the interaction-proteomics study, we provided evidence that GCN1 interacts with the uL10 component of the ribosomal P-stalk, a heteropentameric complex activating GCN2 at the ribosomal machinery^{114,166,171}. Since GCN2 was not identified in the enriched prey proteins as direct interaction partner of GCN1 (Section 4.2.5.; Figure 46), this finding stands in direct contrast to the N to C terminal interaction of both proteins found by genetic mutagenesis in yeast¹³¹. Moreover, we discovered that GCN1 and GCN2 deficiency affect the bioenergetic profile of the cells already in normal growth state (Section 4.2.; Figures 35 and 41). In addition, the transcriptomics and (phospho)proteomics studies underlined that the GCN1-GCN2 signaling modulates the amino acid transporter machinery upon leucine stress relevant for amino acid uptake, such as SLC7A11 and SLC3A2 (Section 4.2.; Figures 34, 39 and 43). In this context, Torrence *et al.*²⁶ found that the mTORC1-ATF4-mediated expression of the SLC7A11/SLC3A2 transporter complex regulates cystine uptake relevant for glutathione biosynthesis and for controlling non-apoptotic iron-dependent cell death (ferroptosis)⁴⁷⁶. Here, we used this information about GCN1 and GCN2 to address our findings in further context.

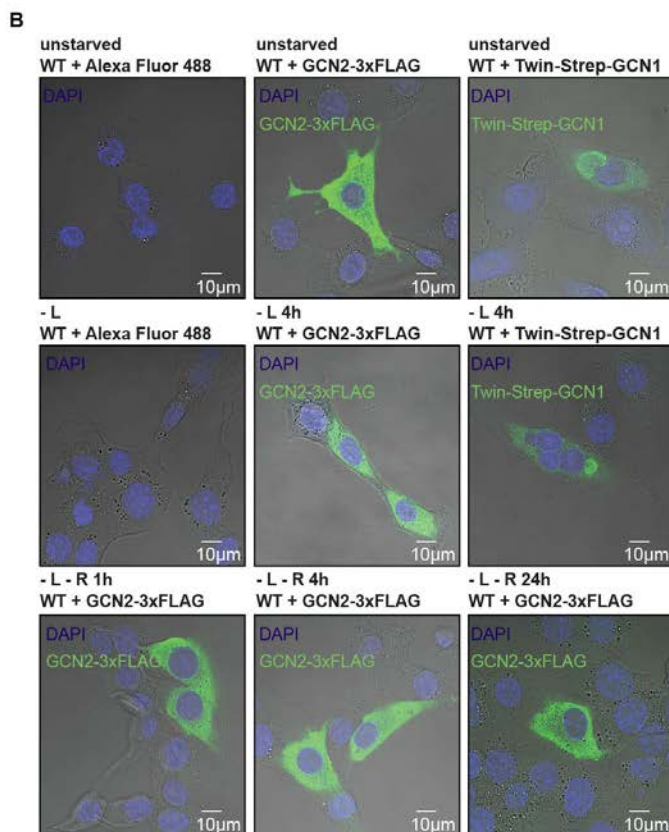
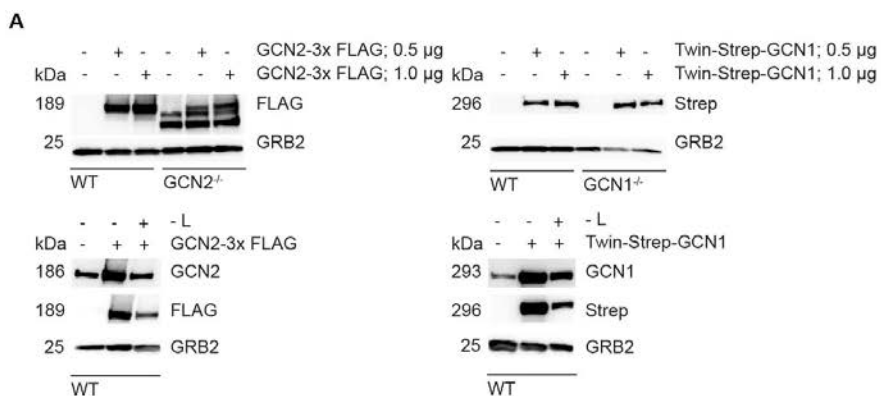
4.3.2. Sub-cellular localization of GCN1 and GCN2

The sub-cellular localization of GCN1 and GCN2 is generally characterized as cytoplasmic, which was reported in a small subset of human cell lines by the human protein atlas⁴⁷⁷. However, in-depth studies over time of amino acid stress and tracking both proteins together have not been performed so far. Consequently, we applied immunofluorescence microscopy to identify potential location changes of both proteins dependent on amino acid deprivation. This information could lay the groundwork for further attempts such as organelle interaction studies or Cryo-EM structure analyses.

To detect both proteins at sufficient signal by immunofluorescence, we overexpressed GCN1 and GCN2 in 3T3 cells. Therefore, we transiently transfected the cells with either GCN2-3xFLAG (provided by Prof. Dr. Seiichi Oyadomari) or Twin-Strep-GCN1 (provided by Dr. Fabien Bonneau) and verified the overexpression by immunoblotting (Figure 48A). In this context, the overexpression of both proteins was detected upon leucine stress and in the GCN2 or GCN1 reconstituted backgrounds as well (Figure 48A).

As shown in figure 48B, FLAG-tagged GCN2 localized in the cytoplasm under normal growth conditions and upon amino acid stress. Localization was not affected by different stress durations (1 h, 4 h or 24 h) or the type of depleted amino acid (leucine and arginine starvation) (Figure 48B). We made the same observation when the GCN2 deficient cells were phenotypically reconstituted (Figure 48C). As for GCN2, the Strep-tagged GCN1 was located cytoplasmically and was close to the nucleus forming a vesicle-like cluster under normal growth conditions (Figure 48B). This vesicle-like cluster was also found upon amino acid stress or in the GCN1-reconstituted cell line (Figure 48C). This means that GCN1 could be located next to the ER where protein biosynthesis takes place, which is in line with its ribosomal binding reported in yeast¹¹⁴ and leaves space for the possibility of having GCN1 as 'vacuolar nutrient storage place'¹³¹. At this stage, this idea is purely speculative and requires higher resolution approaches for proper definition. To check if the vesicle-like cluster is not a technical artefact of aggregated antibodies, we performed immunofluorescence microscopy using the specific GCN1 antibody, which was also utilized in the interactomics study (Section 4.2.5.). Independently of the used antibody, GCN1 was detected as vesicle-like cluster (Figure 48D). However, throughout all immunofluorescence approaches, the vesicle-like cluster was not found exclusively in all stained cells (Figure 48D). In addition, both proteins seemed to co-localize at the outer membrane (Figure 48D). For the ER stress kinase PERK, it is known that it can coordinate ER-plasma membrane formation through the interaction with filamin-A and F-actin⁴⁷⁸. Actin polymerization was also reported in yeast studies to be relevant for YIH1 and GIR2/RBG2 interactions with GCN2 (Refs.^{153,154}). Moreover, we discovered a multi-nuclear formation of some cells independent of the treatment conditions (Figure 48B). Dark dot-like structures in the images suggested stress granule formation induced by amino acid stress. Stress granules are assemblies of non-translating mRNPs (mRNA binding proteins) that form

from stalled mRNAs in translation initiation^{437,479}. To proceed with detailed analysis by immunofluorescence, Z-stacking implied high content imaging would be needed.



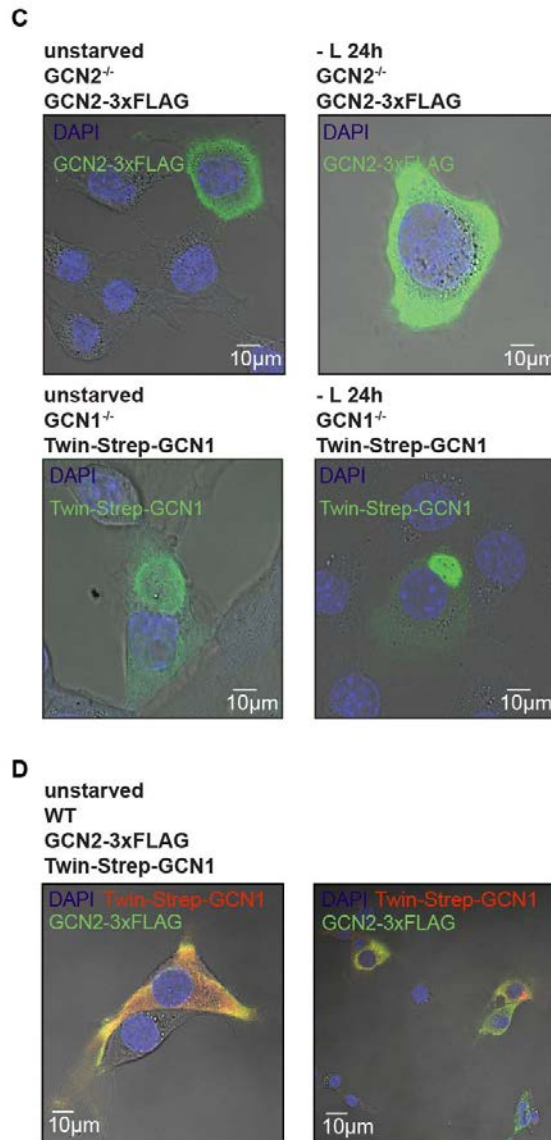


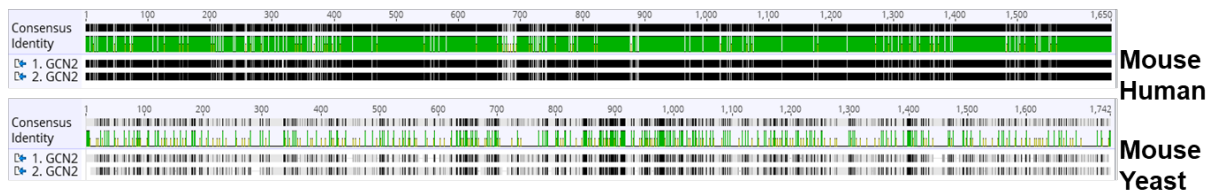
Figure 48. GCN1 and GCN2 localize in the cytoplasm. (A) Immunoblots of 3T3 wild-type (WT), GCN2 (GCN2^{-/-}) and GCN1 deficient (GCN1^{-/-}) cells transiently transfected with Twin-Strep-GCN1 or GCN2-3xFLAG (0.5 and 1.0 µg) at unstarved or leucine-starved (- L) condition. GRB2 was used as loading control. (B) Immunofluorescence images of GCN2-3xFLAG or Twin-Strep-GCN1 overexpressed 3T3 wild-type (WT) cells. DAPI staining for the nucleus (blue). Alexa Fluor 488 staining for GCN2-3xFLAG (green) or Twin-Strep-GCN1 (green). Cells were leucine starved (- L), arginine plus leucine starved (- L - R) and unstarved for 1 h or 4 h or 24 h prior to confocal imaging. Untransfected cells were stained with DAPI and Alexa Fluor 488 to serve as internal control. (C) Immunofluorescence images of GCN2-3xFLAG or Twin-Strep-GCN1 overexpressed in GCN2 (GCN2^{-/-}) and GCN1 (GCN1^{-/-}) deficient 3T3 cells, respectively. Cells were unstarved or leucine-starved for 24 h (- L 24h). Staining was performed as C. (D) Immunofluorescence images of 3T3 wild-type (WT) cells transiently transfected with GCN2-3xFLAG and Twin-Strep-GCN1 at unstarved condition. DAPI staining for the nucleus (blue). Alexa Fluor 488 staining for GCN2-3xFLAG (green) and Alexa Fluor 633 staining for Twin-Strep-GCN1 (red).

In conclusion, we made use of immunofluorescence microscopy to show that GCN1 and GCN2 localize in the cytoplasm under normal growth conditions and under amino acid starvation. Here, GCN1 was detected as vesicle-like cluster. Further studies will follow to address this phenomenon in detail.

4.3.3. Interaction studies of GCN1 and GCN2

In the prevailing budding yeast-based ISR-dogma, GCN1 and GCN2 directly interact to regulate translation at the ribosomal machinery (Section 1.2.3.4.; Figure 9)^{25,109}. However, structural studies of GCN2 bound to GCN1 remain elusive in yeast and mammals and the genetic conservation of both proteins is low between yeast and mammals (Figure 49). By now, interactions with stalled and collided ribosomes in the yeast and human systems were only investigated for GCN1 and solely addressed under non-starved conditions^{114,140}. In this context, we detected in our interaction proteomics approach no GCN2 when pulling on GCN1, but found the uL10 component of the P-stalk enriched – only in a non-starved condition (Section 4.2.5.; Figure 46). Here, the objective was to use different experimental strategies (immunoprecipitation and polysome profiling) to define the potential interaction of GCN1 and GCN2 under the influence of amino acid stress.

Gene sequences of GCN2 (*Eif2ak4*)



Gene sequences of GCN1 (*Gcn1*)

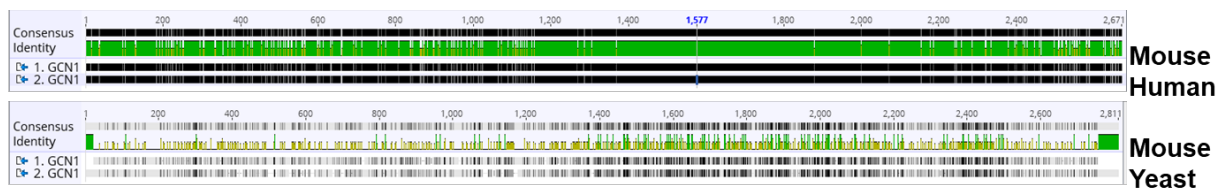


Figure 49. Respective *Eif2ak4* or *Gcn1* consensus identity is higher from mouse to human than to yeast. (Top) Sequence alignment of *Eif2ak4* from mouse (*Mus musculus*), human (*Homo sapiens*) and budding yeast (*Saccharomyces cerevisiae*). (Bottom) Sequence alignment of *Gcn1* from mouse (*Mus musculus*), human (*Homo sapiens*) and budding yeast (*Saccharomyces cerevisiae*). Consensus identity shown by the green bar.

In initial experiments, we isolated endogenous GCN1 by immunoprecipitation (IP) to determine if GCN2 associates with GCN1 under different conditions (Section 3.6.3.). As for the interactome studies (Section 4.2.5; Figure 47), we pulled on GCN1 instead of GCN2, because of the observed high background reactivity when using the GCN2 antibody (Section 4.1.; Figure 18). As shown in figure 50A, GCN1 was pulled down only in the wild-type lysate, however GCN2 was not detected. Upon leucine starvation, a direct interaction between GCN1 and GCN2 interaction was not found (Figure 50B). We also varied the used IP-method (protein A magnetic beads) resulting again in no detection of GCN2 (Figure 50C). In addition, GCN2 was also not identified in the GCN1 deficient lysate (Figure 50D). Overall, the data obtained from the IP approach matched well to the interactome study showing no obvious direct interaction of both proteins in normal growth state and under amino acid stress.

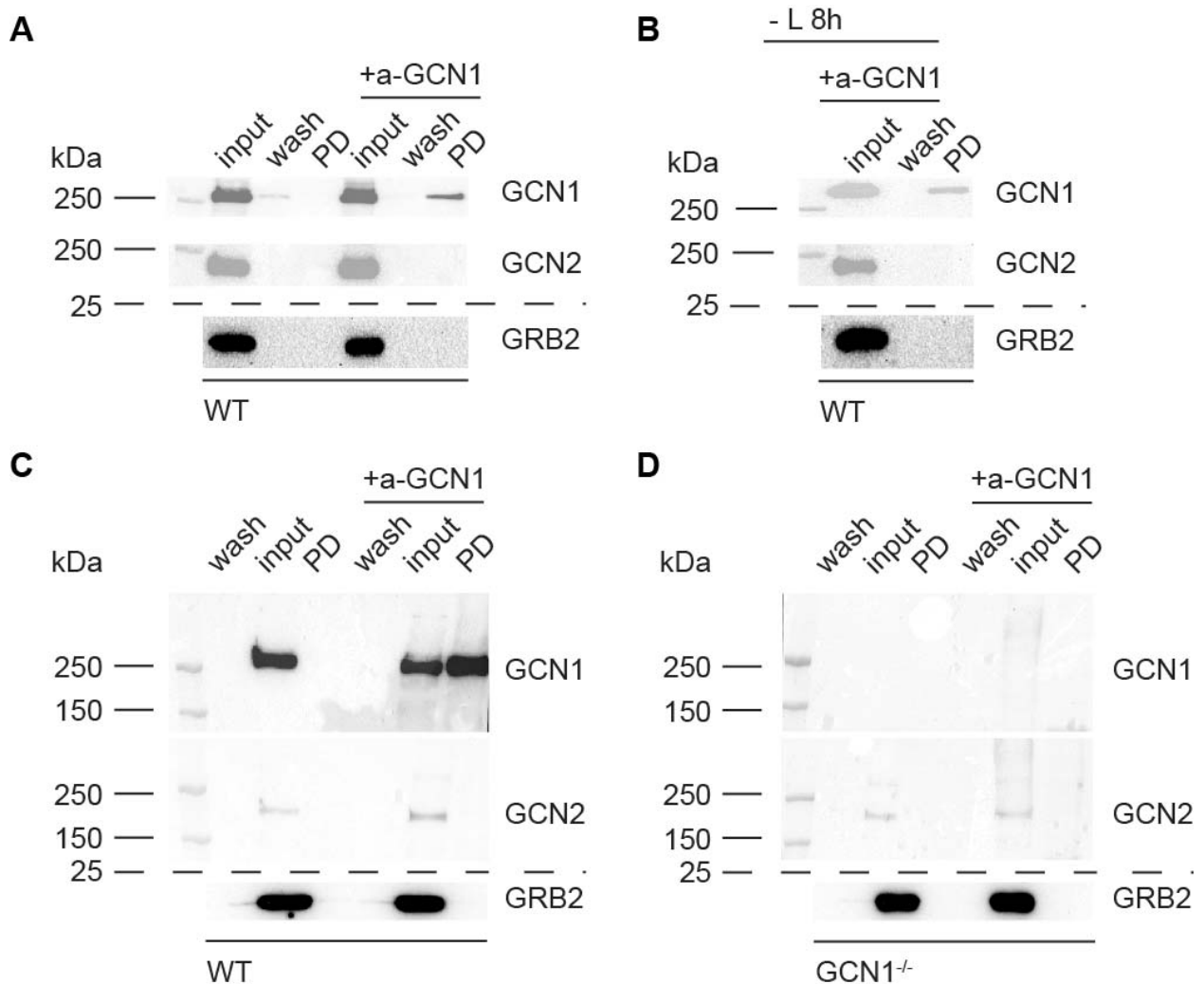
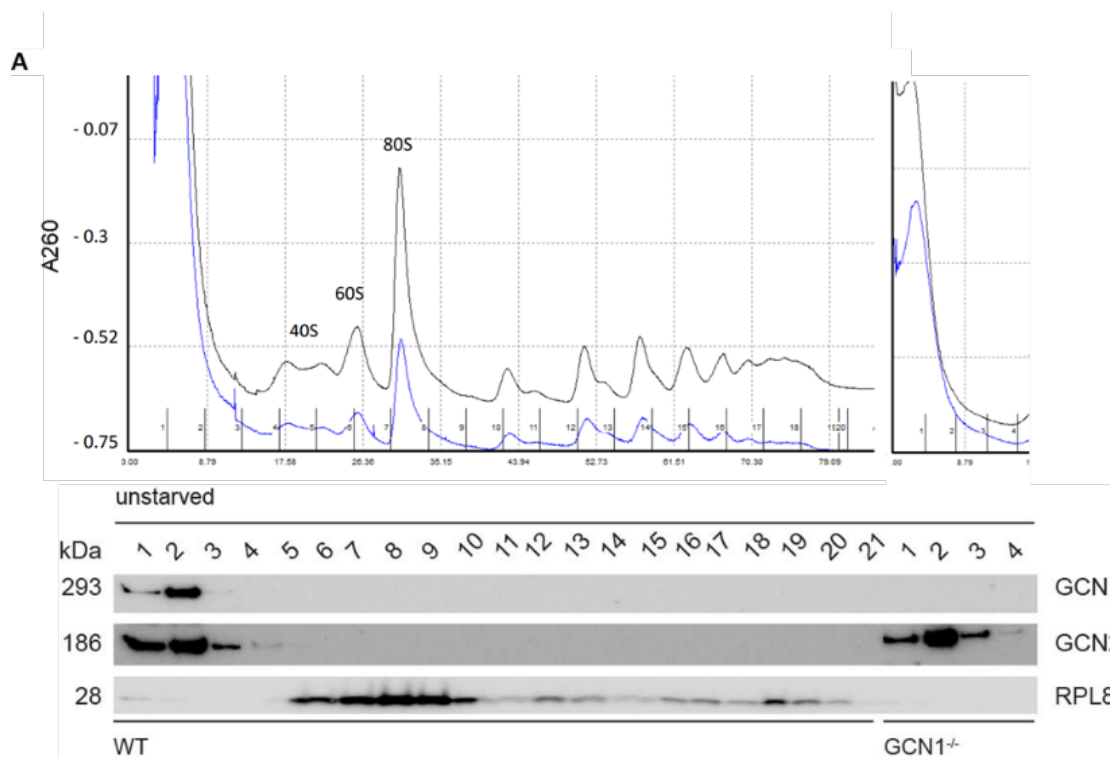


Figure 50. GCN2 does not directly interact with GCN1 independent of leucine stress. (A) Protein A agarose bead-immunoprecipitation of GCN1 from 3T3 wild-type (WT) lysate at unstarved condition. Input means not-pulled lysate. PD means pulled-lysate with anti-GCN1 (a-GCN1). Wash means first wash

fraction. (B) Same as A, except: cells were leucine-starved for 8 h (- L 8h) prior to lysis and immunoprecipitation. (C) Same as A, except: protein A magnetic bead-immunoprecipitation was performed. (D) Same as C, except: in GCN1 deficient (GCN1^{-/-}) background. (A-D) Data are depicted as one of two representative gels. GRB2 was used as loading control.

Next, in collaboration with Achim Keidel from Prof. Dr. Elena Conti's department, we tested the concept that, like in yeast, GCN1 would associate with stalled and trailing 80S ribosomes (ribosome collision) using polysome profiling. Recently, Wu *et al.*¹⁴⁰ showed that in a human cancer cell line (MCF10A) only GCN1 is associated in a small fraction (about 10 %) with colliding disomes in normal growth condition, but not GCN2. We repeated this type of experiment by using the 3T3 cells with or without leucine starvation. Neither GCN1 nor GCN2 co-sedimented in the 40S fractions and were not detected in the polysomal fractions (Figure 51A). Upon amino acid stress, no change in this pattern was observed (Figure 51B). The 60S ribosomal protein L8 (RPL8) was used as an internal control to detect polysomes.



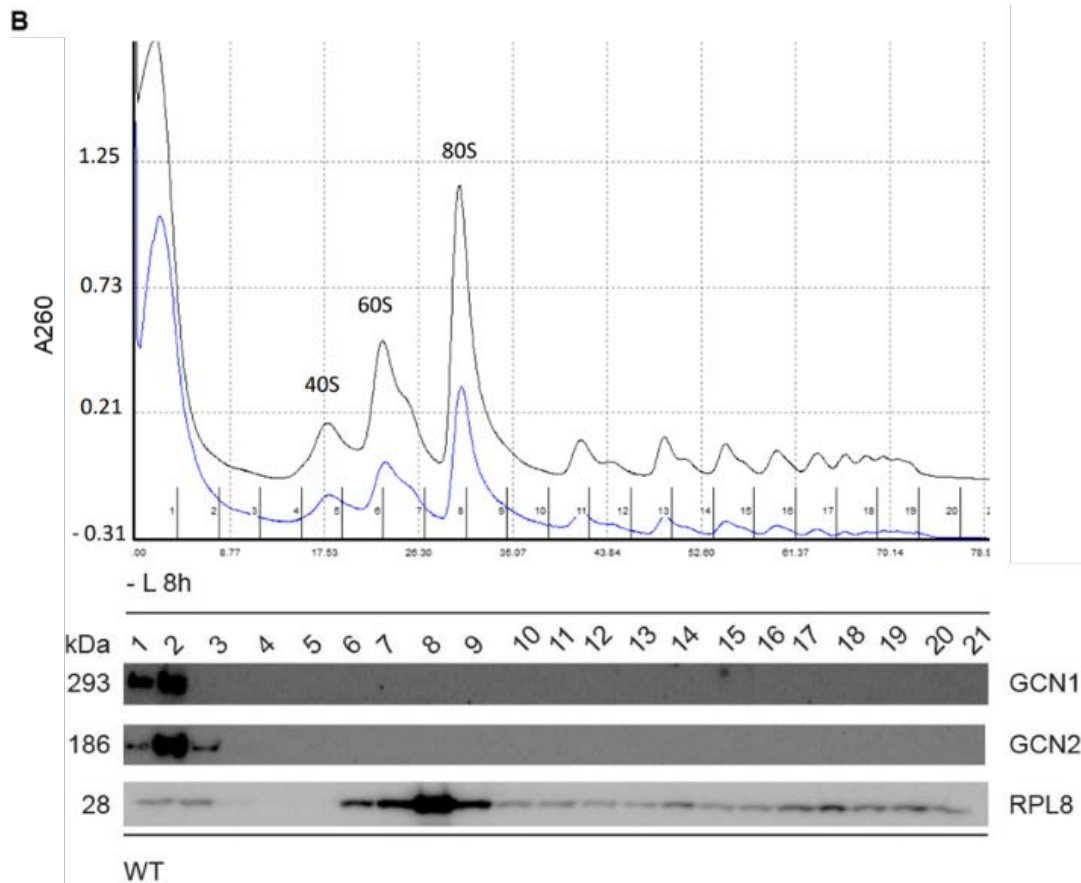


Figure 51. Polysome profiling of GCN1 and GCN2 revealed no disome formation. (A) Polysome profiles from unstarved 3T3 wild-type (WT) and GCN1 deficient (GCN1^{-/-}) cells. Fractions were analyzed by immunoblotting with indicated antibodies. (B) Same as A, except: 3T3 wild-type (WT) cells were leucine starved for 8 h (- L 8h). Data are depicted as one of two representative profiles.

In Wu *et al.*¹⁴⁰, the protein synthesis inhibitor anisomycin was used to induce ribosome stalling at high concentration (1 mg/mL), and ribosome collision (disome formation) at intermediate concentration (0.001 mg/mL) (Figure 52A). Anisomycin treatment regulates the level of ribosome collision leading to the activation of the MAPKKK ZAK α , which in turn triggers the activation of the SAPK (p38/JNK) pathway inducing apoptosis or the GCN2 pathway for survival¹⁴⁰. We compared leucine deprivation separately and in combination with anisomycin treatment in wild-type 3T3 cells reading out active JNK by immunoblotting. Leucine deprivation did not induce the SAPK pathway independently of short or long stress exposure (Figure 52B). In contrast, anisomycin at intermediate and high dosing activates JNK as reported¹⁴⁰. Interestingly, the GCN2 pathway was activated at intermediate doses of anisomycin treatment as shown by the autophosphorylation of GCN2 at T898 (Figure 52B). In contrast, GCN2 was inactivated at high doses of anisomycin. This phenomenon argues for a separate activation of both pathways for stress adaptation versus apoptosis, which is tightly regulated by protein synthesis inhibition. Further studies on disome

formation will follow by combining amino acid starvation and anisomycin treatment at early and late periods.

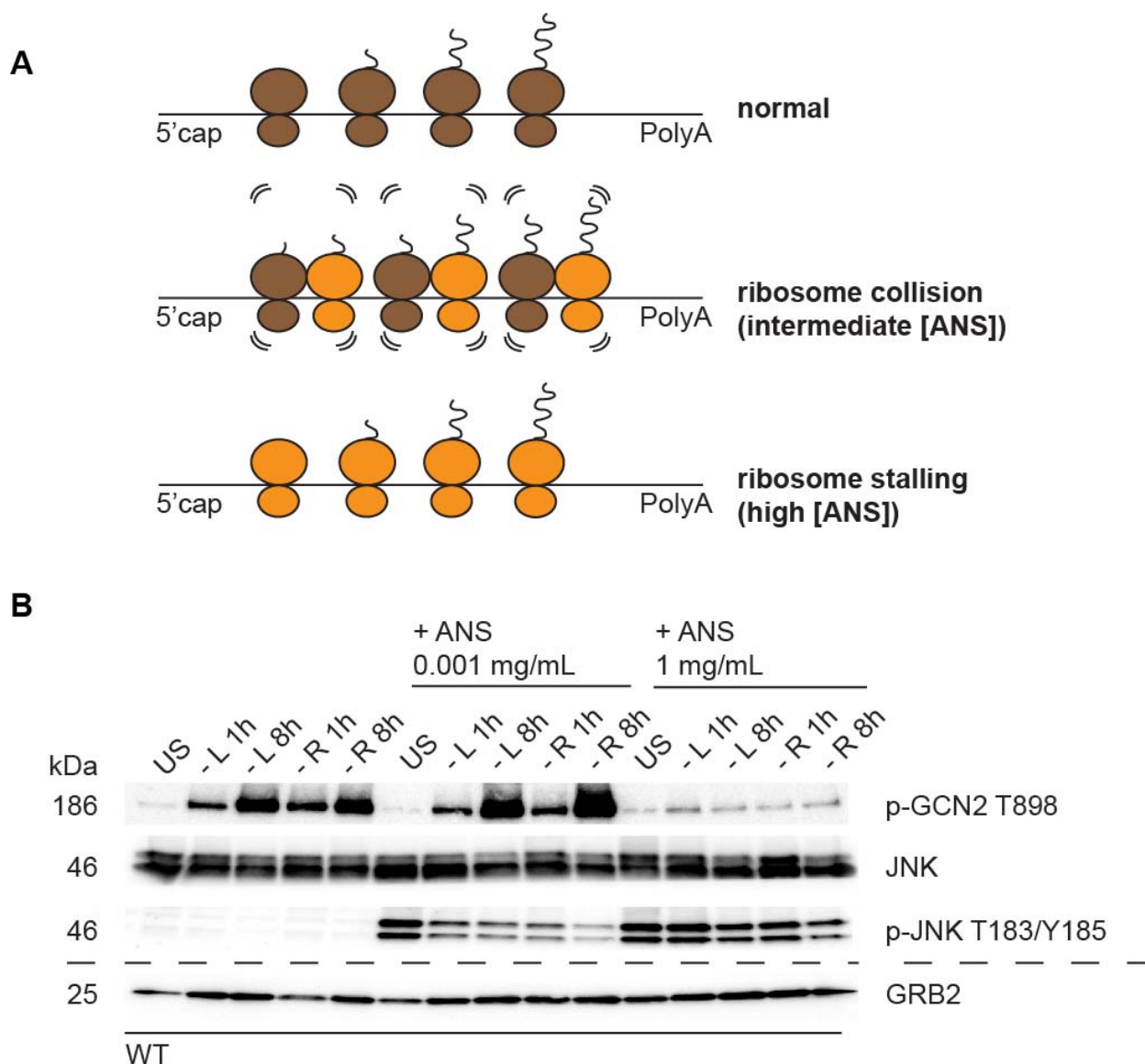


Figure 52. Leucine starvation does not activate JNK signaling over time. (A) Schematic representation of ribosome collisions (orange and brown) and ribosome stalling (orange) on treatment with varying concentrations of anisomycin (ANS; elongation inhibitor) at intermediate or high dose. (B) Immunoblot of 3T3 wild-type (WT) lysates treated with anisomycin (ANS) at intermediate (0.001 mg/mL) or high (1 mg/mL) dose. Simultaneously, cells were leucine (- L) or arginine (- R) starved or unstarved (US). Concentrations are based on Wu *et al.*¹⁴⁰. GRB2 was used as loading control. Data are depicted as one of two representative gels.

In summary, in 3T3 cells, we could not detect a physical association of GCN1 with ribosomal disomes as well as a direct interaction with GCN2 upon leucine stress or normal growth condition.

4.3.4. Ferroptosis regulation by GCN1 and GCN2

In our multi-omics study (Section 4.2.), we discovered that the GCN1-GCN2 signaling regulates the induction of several amino acid transporters at the gene and protein level, such as the sodium-independent anionic amino acid heterodimeric complex SLC7A11 and SLC3A2 upon leucine stress across time. SLC7A11/SLC3A2 expression was linked to oncogene (RAS and MYC) driven malignancies⁴⁸⁰⁻⁴⁸², for example in regulating ROS levels via the p62-KEAP1-NRF2 pathway^{483,484}. In addition, this transporter system was connected in recent studies to ferroptosis⁴⁸⁵ via modulating amino acid metabolism (via IL4i1⁴¹⁴), the T-cell tumor response (via INF γ -SLC7A11/3A2 axis⁴⁸⁶), the mTORC1 pathway (via ATF4-SLC7A11/3A2-GSH axis^{26,40,487}) or the role of mitochondria (via TCA and ETC integrity⁴⁸⁸). Further, a compendium of kinetic modulatory profiling identified that arginine stress can suppress ferroptosis⁴⁰. Collectively, we used this information to study ferroptotic cell death under normal growth state and under amino acid stress to connect it to the function of GCN1 and GCN2.

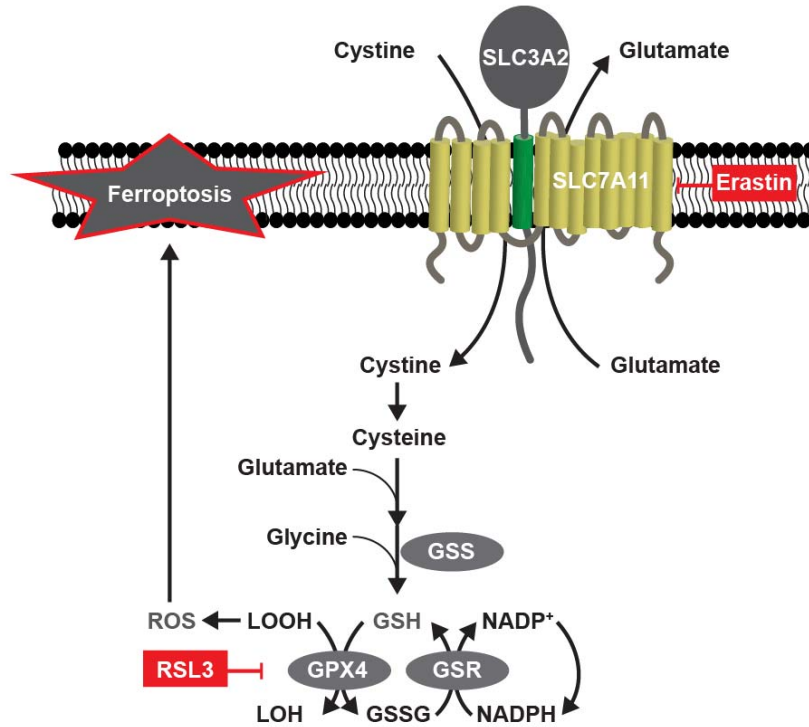
Ferroptosis is an iron-dependent, non-apoptotic, caspase-independent form of cell death that is genetically, morphologically and biochemically distinct from necrosis, apoptosis and autophagy⁴⁸⁹. Ferroptosis is triggered by the accumulation of reactive oxygen species (ROS) in the cellular environment^{480,490-492} (Figure 53A). This oxidative stress is ultimately protected by the glutathione peroxidase 4 (GPX4), which directly and indirectly catalyzes the reduction of lipid peroxides at the expense of reduced glutathione (GSH)⁴⁹³. The heterodimeric transporter complex (system x_c⁻) consisting of SLC7A11 and SLC3A2 exchanges the anionic form of cysteine for glutamate^{365,481}. This reaction is required to build up GSH via glutamate-cysteine ligase (GCL) and glutathione synthetase (GSS), which then links the system to GPX4. Ferroptosis induction can be achieved in several ways by either inhibiting GPX4 by RSL3 or by inhibiting the SLC7A11 transporter by erastin^{494,495} (Figure 53A). The ferroptosis inhibitor ferrostatin-1 reverts the RSL3 and erastin effect via a reductive mechanism to prevent damage to membrane lipids and finally inhibits cell death^{496,497}.

First, we aimed to understand if ferroptosis induction blocking SLC7A11 (erastin treatment) differs from GPX4 inhibition (RSL3 treatment) upon amino acid stress. Therefore, we treated wild-type (WT), GCN1 (GCN1^{-/-}) and GCN2 (GCN2^{-/-}) deficient 3T3 cells with the two mentioned reagents and read out cell death using a green fluorescent dye (CellTox) at the live-cell level.

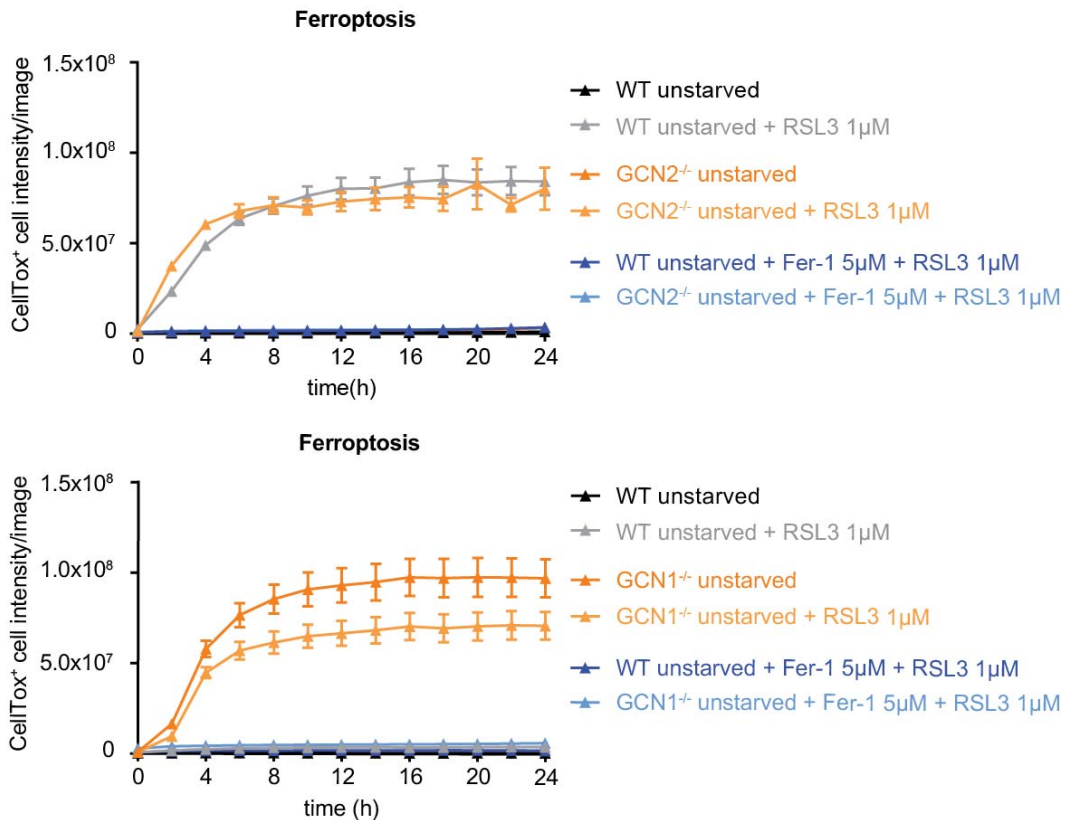
In the normal growth state, RSL3 treatment increases cell death after 2 h, which was blocked with ferrostatin-1 (Figure 53B). This effect was independent of GCN1 or GCN2 presence. Upon amino acid stress, we detected the same phenomenon (Figure 53C+D): RSL3 activated ferroptosis fast and independent of the type of stress (arginine versus leucine depletion) in all three genotypes

(WT, GCN1^{-/-} and GCN2^{-/-} cells). Combined, we showed that GPX4 inhibition via RSL3 treatment induced potent ferroptosis – independent of amino acid stress, GCN1 or GCN2 presence.

A



B



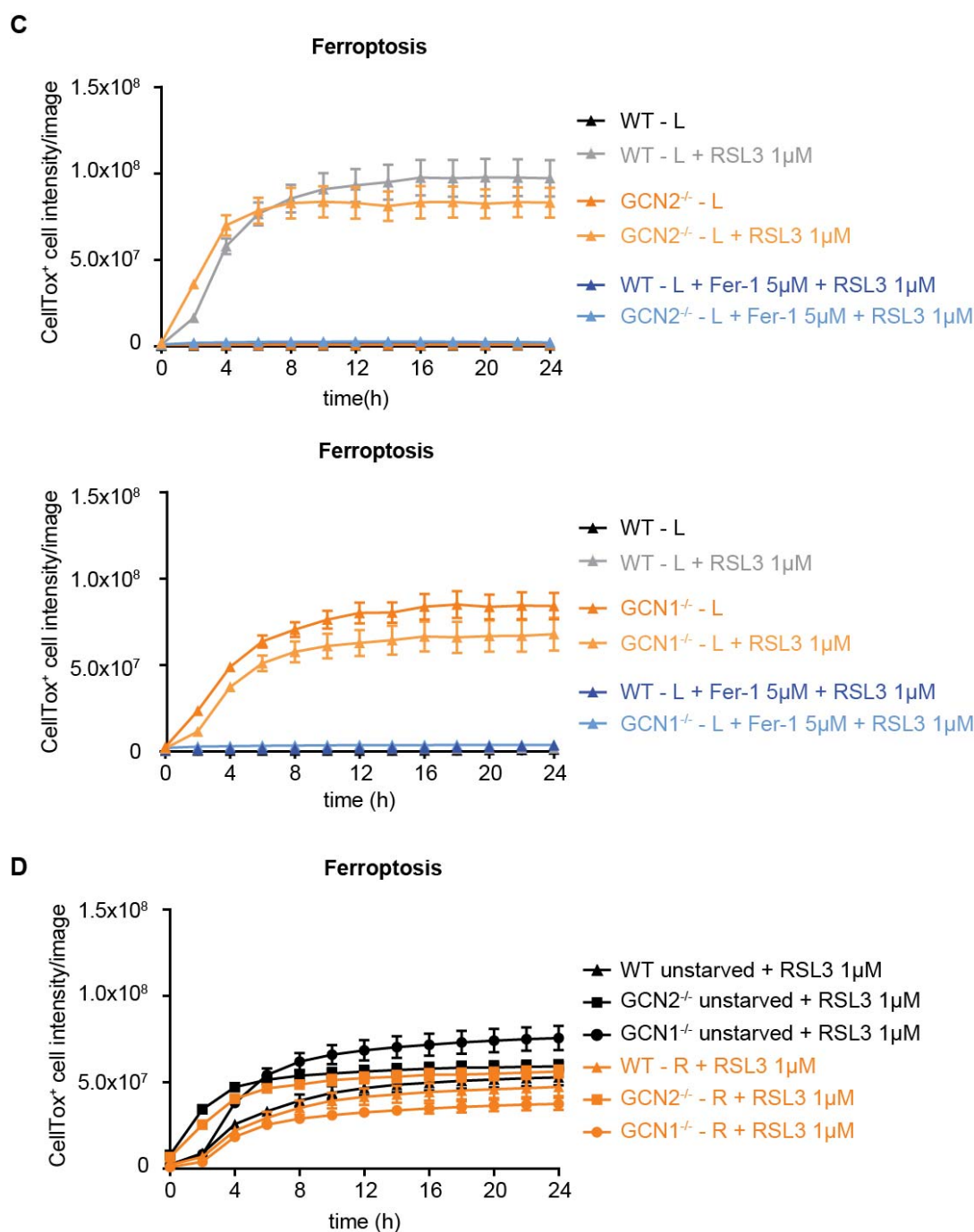
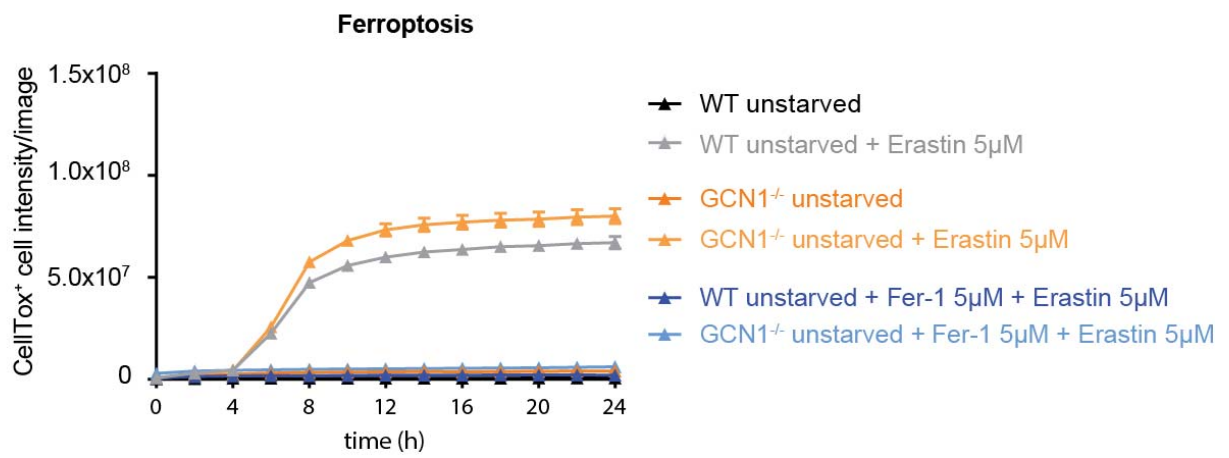
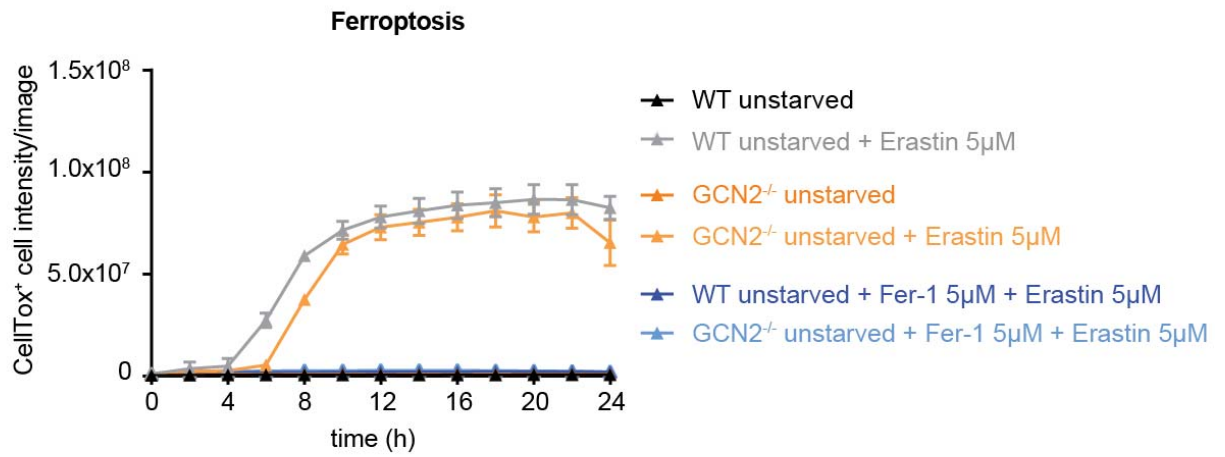
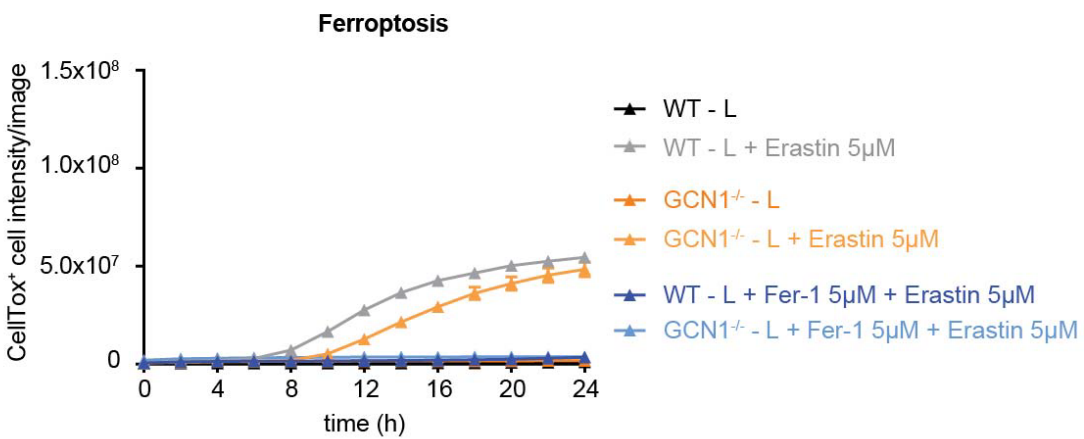
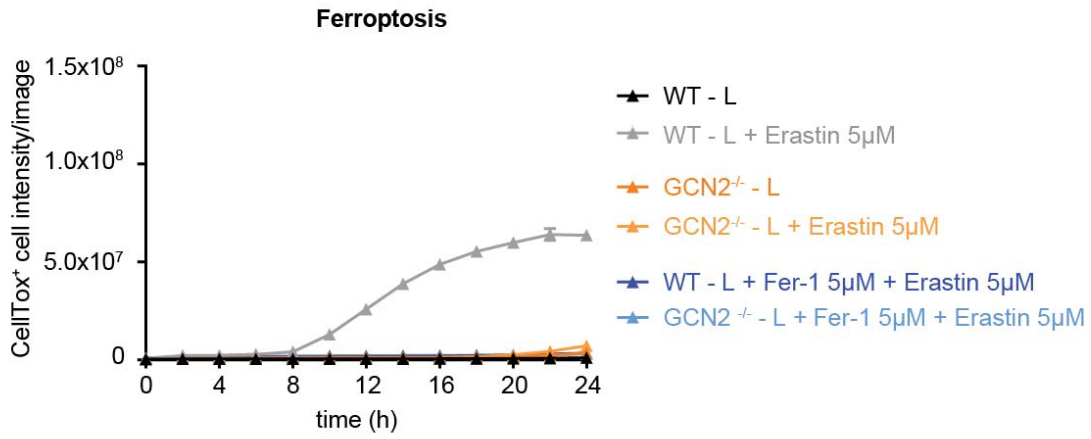
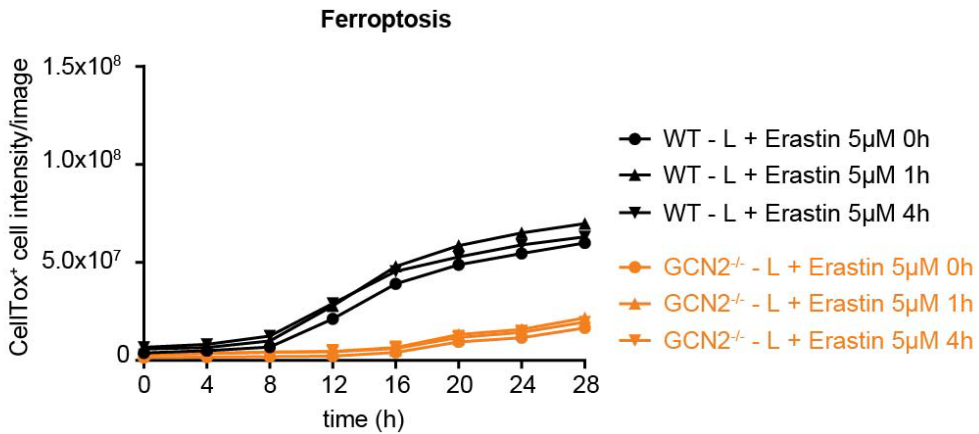


Figure 53. GPX4-induced ferroptosis is regulated independently of GCN1-GCN2 signaling. (A) Simplified scheme of ferroptosis control: chemical perturbations by erastin (blocks SLC7A11; red) or RSL3 (blocks GPX4; red) induce ferroptosis (star). Details are provided in the respective text paragraph. (B-D) Quantification of ferroptosis of 3T3 cells treated with the ferroptosis inducer RSL3 (1 μ M) in the presence of leucine (- L) or arginine (- R) starvations or unstarved condition by live-cell imaging using CellTox green staining. Ferrostatin-1 (Fer-1; 5 μ M) was added as control to block RSL3-induced death. Ferroptosis was analyzed in the three genotypes: 3T3 wild-type (WT), GCN2 knockout (GCN2^{-/-}) and GCN1 knockout (GCN1^{-/-}) cells. (B-D) Data are depicted as mean + SEM of three independent experiments.

Next, we transferred the same experimental setup in the context of erastin treatment that blocks the SLC7A11 transporter. In contrast to RSL3 treatment, ferroptosis increased after 4 h of erastin treatment in wild-type cells under normal growth condition (Figure 54A). Interestingly, the GCN2^{-/-} cells had a delayed cell death compared to GCN1^{-/-} or wild-type cells. This observed time-regulated 'shift' in ferroptosis induction also happened in wild-type cells when removing leucine from the cellular environment (Figure 54B). Most surprisingly, the GCN2 deficient cells did not die upon erastin treatment under leucine stress over time (up to 24 h) (Figure 54B+D). The GCN1 deficient cells died, but not as quickly as the wild-type cells (Figure 54B). To prevent the possibility that the co-treatment of erastin and starvation affected the described protection of GCN2 deficient cells under leucine stress, we conducted a titration experiment 'spiking' in erastin at different time points (0 h, 1 h and 4 h). Again, this did not change the outcome in wild-type or GCN2 deficient cells (Figure 54C). Recently reported by Conlon *et al.*⁴⁰, U2OS cells (human bone osteosarcoma epithelial cells) were ferroptosis-protected only upon arginine and not leucine depletion that was regulated independently of the GCN2-ISR. Therefore, we compared the induction of ferroptotic cell death under arginine starvation for all genotypes as well (Figure 55). Interestingly, all the cell types died independently of their genotype with altered kinetics in response to arginine starvation. This finding argues that ferroptosis regulation might be cell-specific and differ in oncogenic background.

A



B**C**

D

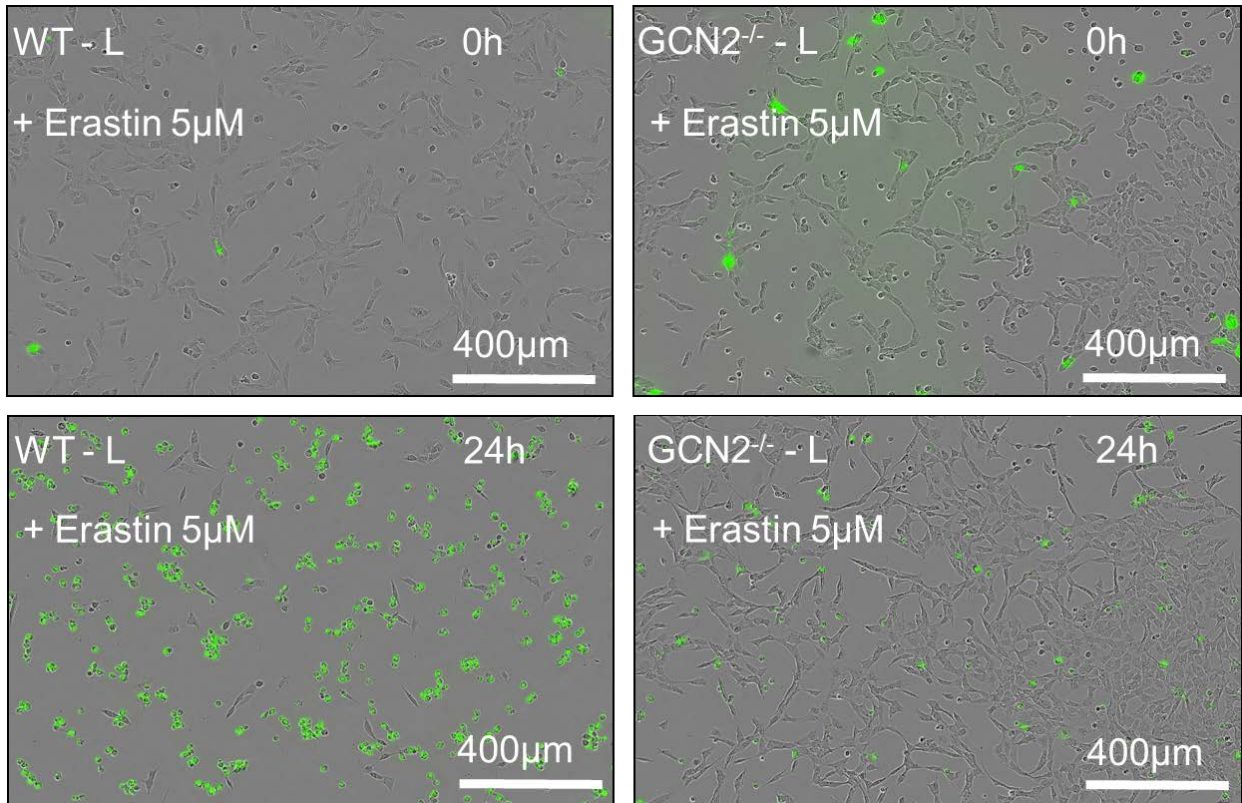


Figure 54. GCN2^{-/-} cells are protected from erastin-induced ferroptosis upon leucine stress. (A-B) Quantification of ferroptosis of 3T3 cells treated with the ferroptosis inducer erastin (5 µM) in the presence of leucine (- L) starvation or unstarved condition by live-cell imaging using CellTox green staining. Ferrostatin-1 (Fer-1; 5 µM) was added as control to block erastin-induced death. Ferroptosis was analyzed in the three genotypes: 3T3 wild-type (WT), GCN2 knockout (GCN2^{-/-}) and GCN1 knockout (GCN1^{-/-}). (C) Same as B, except: time-points (0 h, 1 h and 4 h) indicate the addition of erastin to the cells. Quantification of cell death started for all conditions at the same time. (D) Microscopic visualization of dead cells (green) at 0 h to 24 h from experiments in A+B. (A+B) Data are depicted as mean + SEM of three independent experiments.

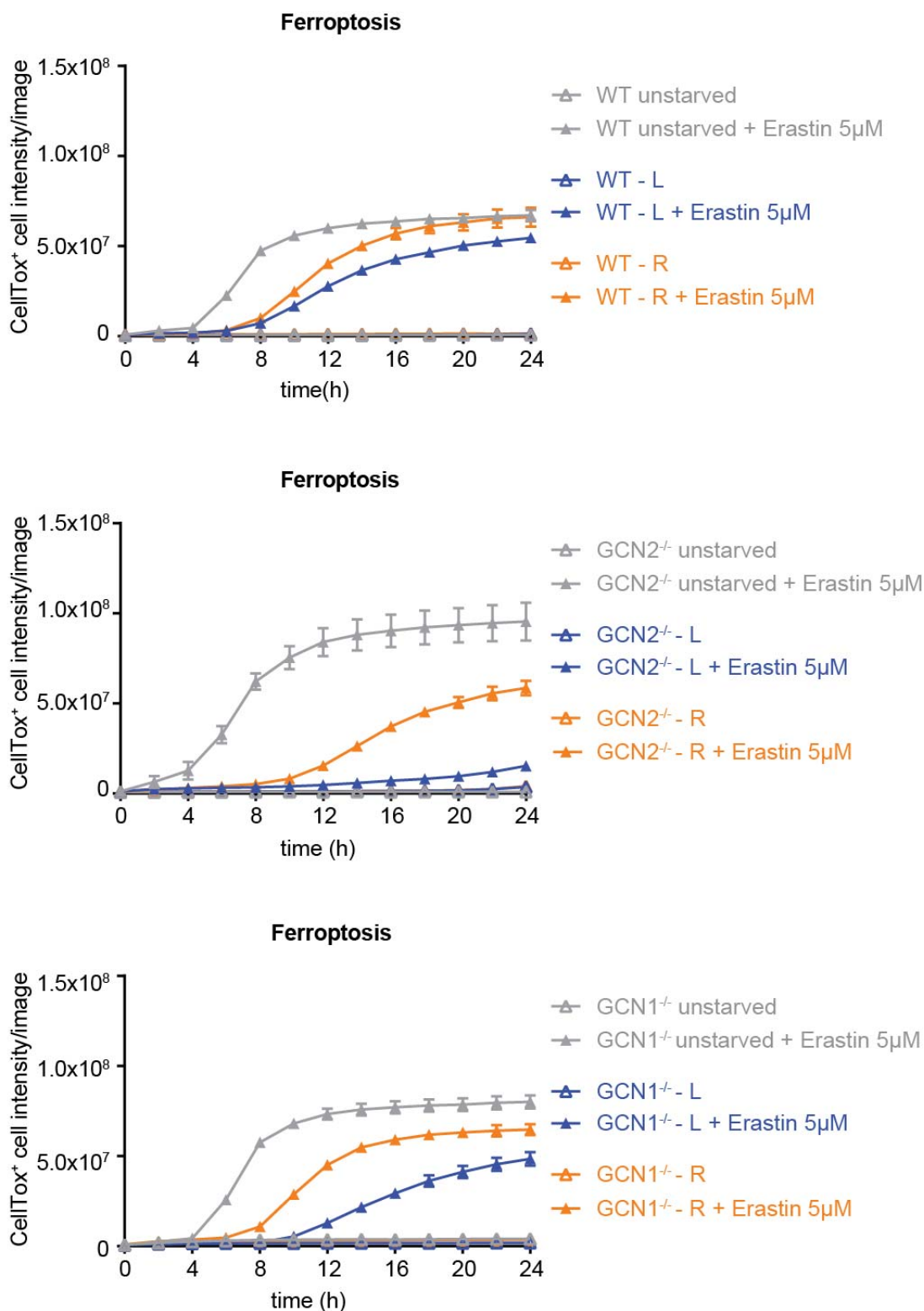


Figure 55. Erastin-induced ferroptosis is diminished upon amino acid stress. Quantification of ferroptosis of 3T3 cells treated with the ferroptosis inducer erastin (5 μ M) in the presence of leucine (- L) and arginine (- R) starvations or unstarved condition by live-cell imaging using CellTox green staining. Ferroptosis was analyzed in the three genotypes: 3T3 wild-type (WT), GCN2 knockout (GCN2^{-/-}) and GCN1 knockout (GCN1^{-/-}) cells. Data are depicted as mean + SEM of three independent experiments.

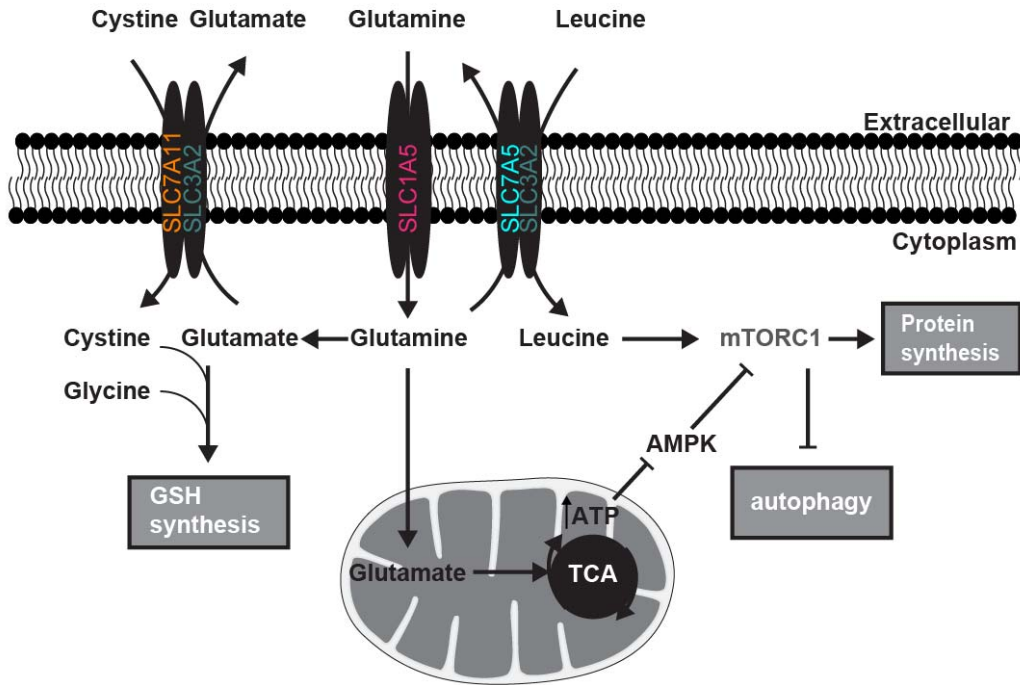
We concluded that amino acid stress can regulate erastin-induced ferroptosis in a GCN2 dependent manner. Leucine and arginine depletion controlled ferroptotic death in a time- and genotype-specific way. In detail, GCN2 deficient cells are only ferroptosis-protected upon leucine stress. Preventing the GPX4 function using RSL3 treatment did not affect the iron-dependent non-apoptotic cell death regulated by amino acid stress or the GCN2 cascade. Overall, our data argued that ferroptosis regulation by the GCN2-ISR upon leucine stress is related to the modulation of SLC7A11 induction.

Based on our omics analyses (Section 4.2.), GCN1-GCN2 signaling controlled the induction of amino acid transporters, such as SLC1A5 (glutamine import) and SLC7A5 (leucine-glutamine antiporter) upon leucine stress. Next to SLC7A11/SLC3A2, both transporters were enriched at the transcriptome and proteome level dependent on GCN2 (Figure 56B) and are known to be involved in glutamine metabolism (Figure 56A). The relevance of glutamine (Q) in the cellular environment can be encapsulated by three important roles¹²⁹: (i) Besides glucose, glutamine is the second carbon source relevant for supplying metabolic intermediates for nucleotide- and nitrogen for amino acid-biosynthesis; (ii) Glutamine regulates the mitochondrial TCA integrity by anaplerotic reactions; (iii) Glutamine has an antioxidative function by providing glutamate for GSH biosynthesis. In this context, mTORC1 activation is connected to the efflux of glutamine versus leucine via SLC transporters SLC7A5/3A2 upon amino acid stress⁴⁶¹. In addition, supplementation of glutamine is sufficient to restore mTORC1 activity during prolonged amino acid starvation⁵⁰. Consistent with this finding, we could also detect a reactivation of mTORC1 at 1 h of amino acid stress when adding more glutamine to the cells (Figure 56C). Moreover, Torrence *et al.*²⁶ showed that the mTORC1-mediated activation of ATF4 regulates processes involved in glutathione biosynthesis, transamination reaction (deamination of essential amino acids (alanine and aspartate) to glutamate) and glutaminolysis. These processes were also found to be enriched in our transcriptomics study dependent on GCN1-GCN2 signaling (Section 4.2.3.; Figure 34). Collectively, we address if glutamine depletion affects the regulation of the GCN2-ATF4-SLC7A11 interplay and thereby modulating ferroptosis sensitivity.

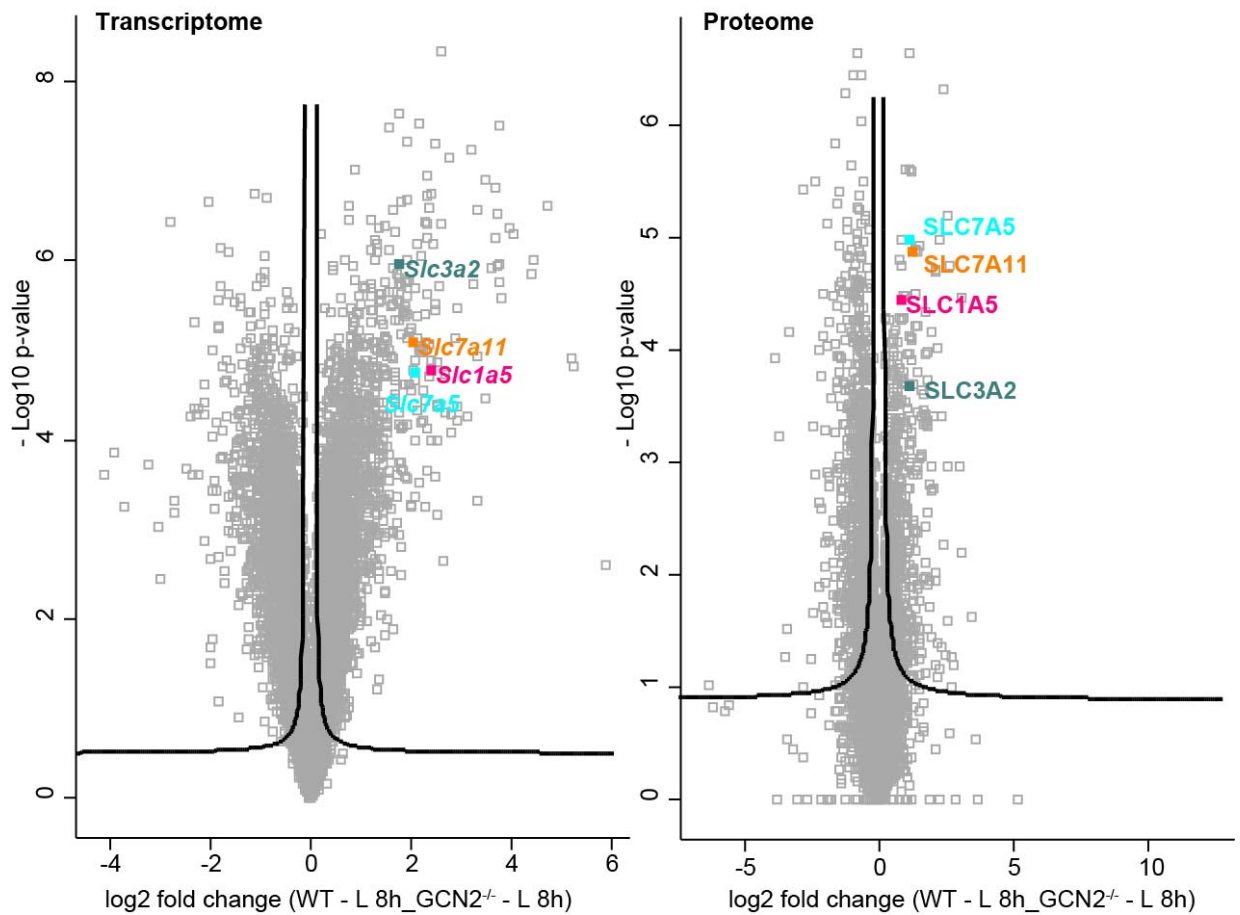
Therefore, we treated the 3T3 wild-type and GCN2 deficient cells with glutamine and/or leucine starvation in combination with erastin. Strikingly, we found that glutamine deprivation (and in combination with leucine deprivation) protected the wild-type cells for erastin-induced ferroptosis in contrast to leucine starvation on its own (Figure 56D+E). GCN2 deficient cells were protected up to 24 h for ferroptosis-induced death when depleting leucine, glutamine, or both amino acids. We assume that the GCN2-ATF4-regulated transcriptional response is required for the amino acid transport systems (SLC1A5, SLC7A11/3A2 and SLC7A5/3A2) preserving the glutamine

metabolism to maintain glutamate in the TCA cycle for mitochondrial respiration (Figure 56A). In this context, Gao *et al.*⁴⁸⁸ proposed that mitochondria play an important role in ferroptosis regulation: GPX4-induced ferroptosis is independent of mitochondrial function in contrast to erastin-induced ferroptosis. This means that glutaminolysis and the TCA cycle are essential for ferroptosis-associated mitochondrial membrane potential hyperpolarization and lipid peroxide accumulation upon erastin-treatment. Consistent with our finding, in the absence of glutamine the effect is reverted and the cells are protected against ferroptosis⁴⁸⁸.

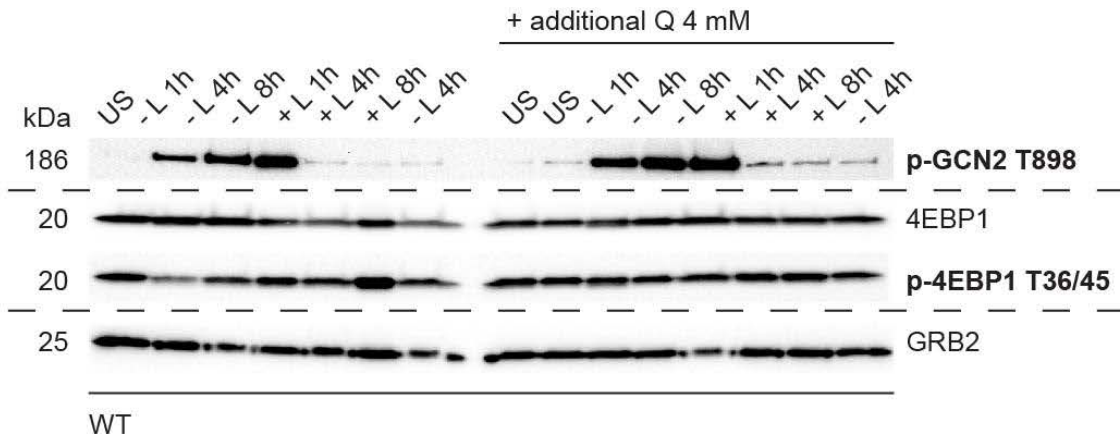
A



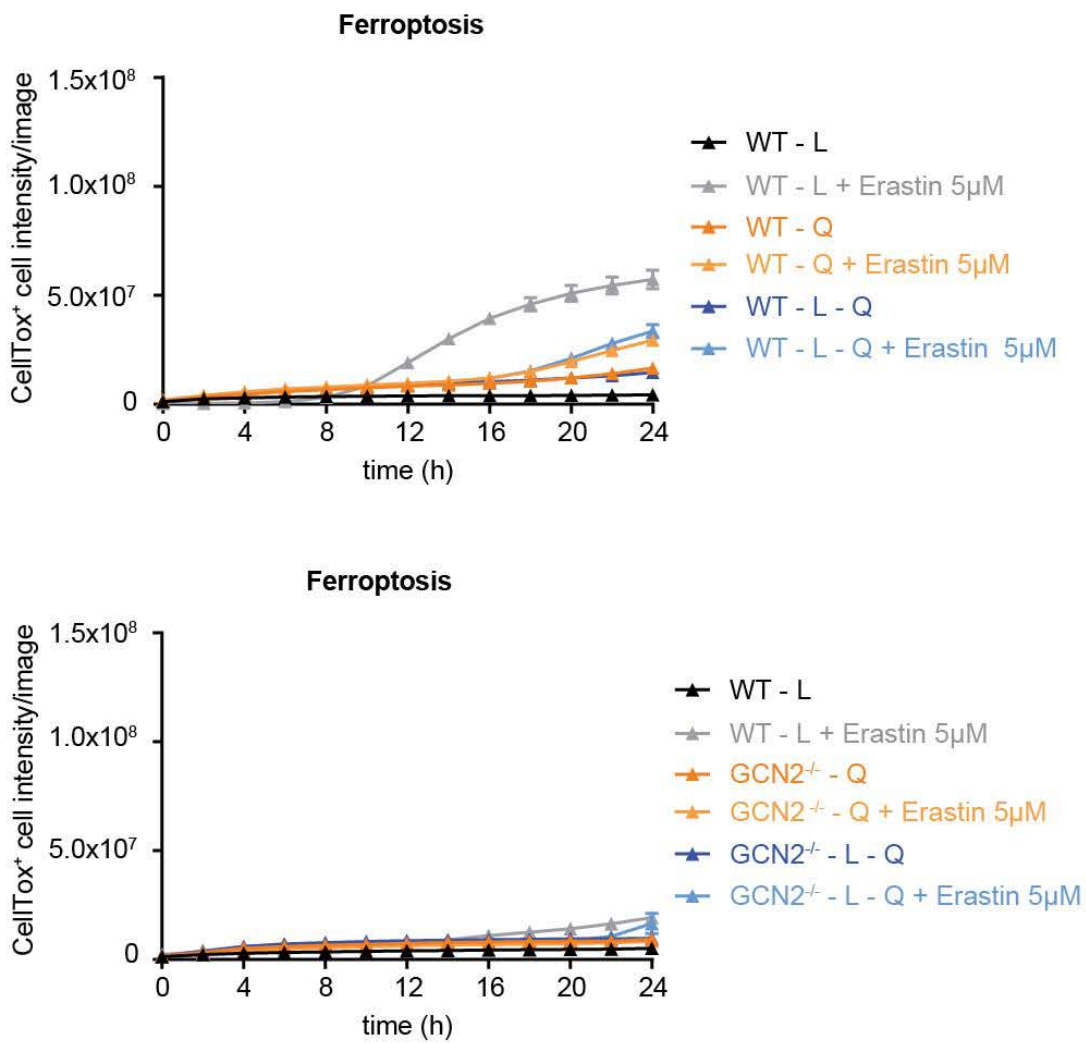
B



C



D



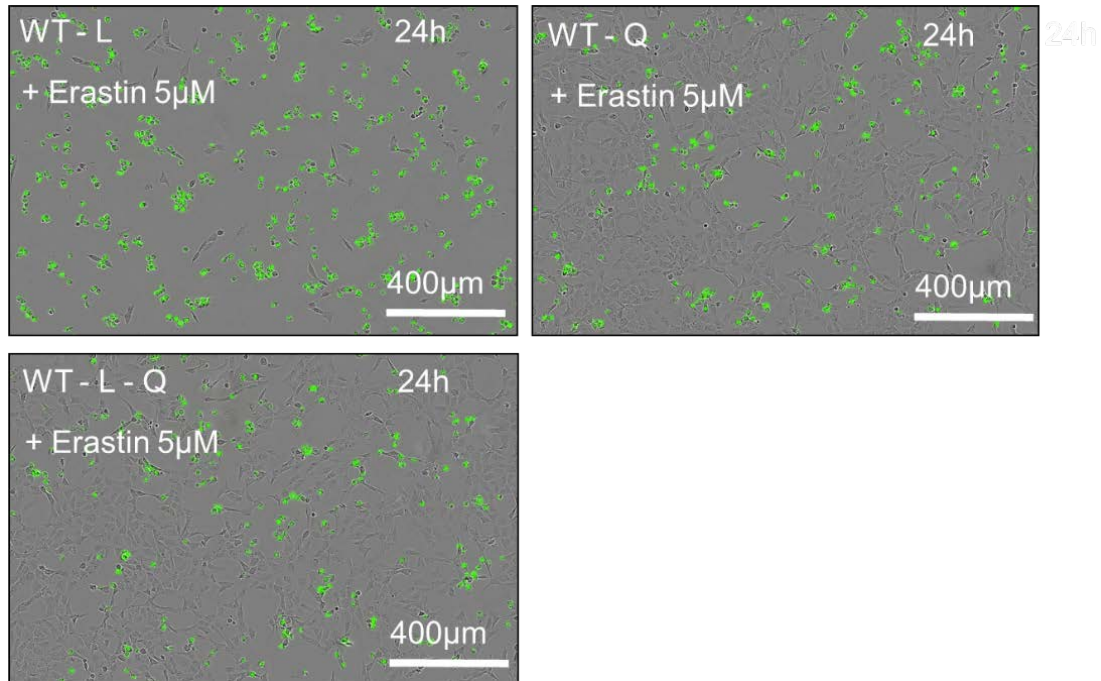
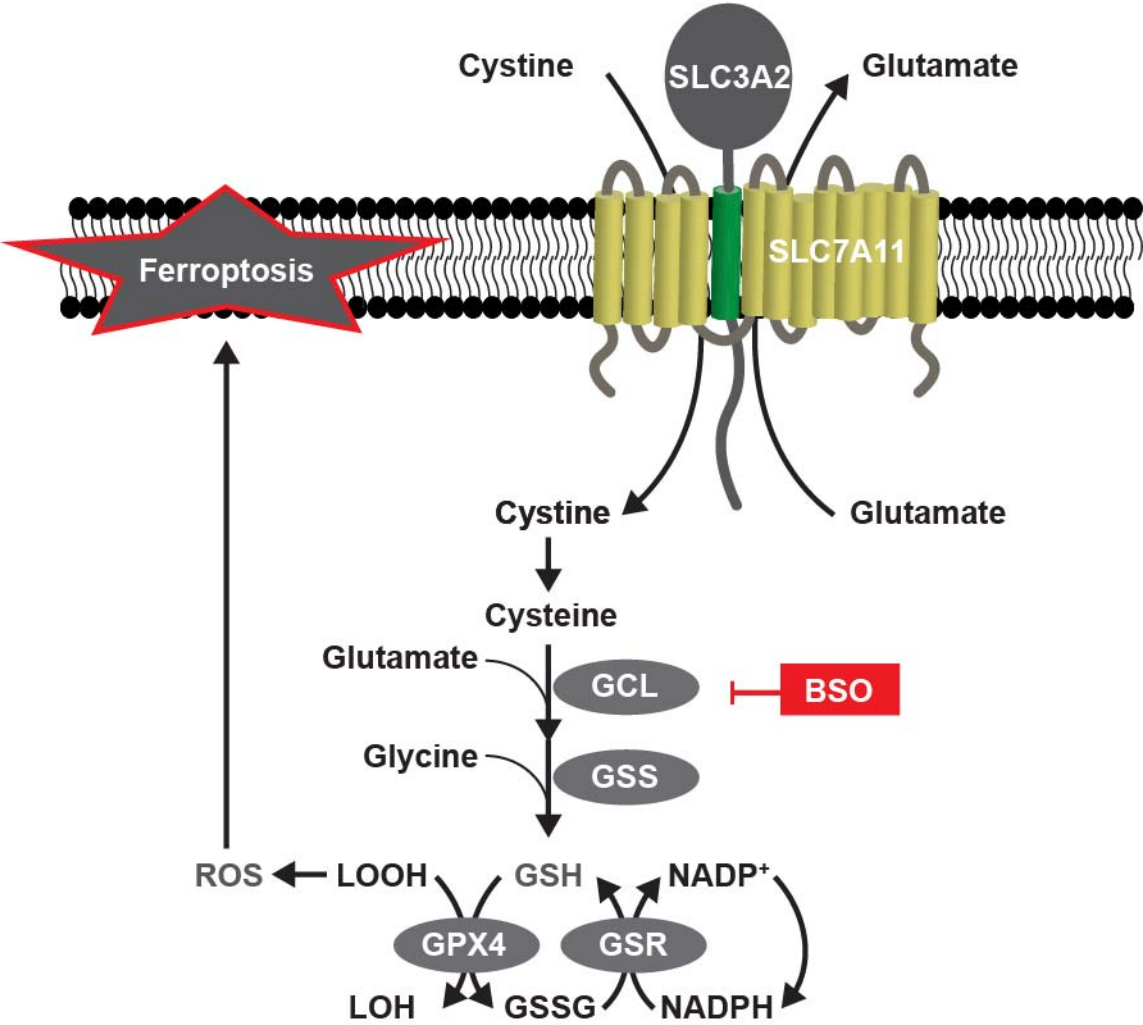
E

Figure 56. Glutamine depletion leads to erastin-induced ferroptosis protection. (A) Simplified scheme of the glutamine metabolism: amino acids (glutamine, leucine or cystine) are transported in the cytoplasm by the SLC transporter machinery (SLC7A11, SLC3A2, SLC1A5 or SLC7A5) regulating glutathione (GSH) synthesis, autophagy and protein synthesis. Thereby, mTORC1 and the mitochondrial respiration (TCA cycle) play crucial roles⁴⁸⁸. (B) Volcano plots comparing p-value and log₂-fold changes of genes and proteins of the in A mentioned SLC transporters significantly enriched between the 3T3 wild-type (WT) and the GCN2 deficient (GCN2^{-/-}) cells stimulated with leucine stress for 8 h (- L 8h). (FDR < 0.05). Data are gained from our transcriptomics and proteomics studies (Section 4.2.). (C) Immunoblot of 3T3 wild-type (WT) cell lysates in the presence of unstarved condition (US), leucine-starvation (- L) or leucine-resupplementation (+ L) for 1 h, 4 h and 8 h. Glutamine (Q; 4 mM) was added during starvation and resupplementation. GRB2 functions as loading control. (D) Quantification of ferroptosis of 3T3 wild-type (WT) and GCN2 deficient (GCN2^{-/-}) cells treated with the ferroptosis inducer erastin (5 µM) in the presence of leucine (- L) or glutamine (- Q) or both starvations by live-cell imaging using CellTox green staining. (E) Microscopic visualization of dead cells (green) after 24 h of erastin and starvation treatments from D in 3T3 wild-type (WT) cells. (C+D) Data are depicted as mean + SEM of three independent experiments or one of two representative gels.

SLC7A11 induction is linked to glutathione (GSH) biosynthesis (Figure 56A). In our transcriptomics and proteomics data, we found that the glutamate-cysteine ligase (GCL) enzyme relevant for GSH synthesis is significantly enriched in wild-type, but not GCN2 deficient cells (Figure 57B). Buthionine sulfoxime (BSO) is a cell-permeable, potent and irreversible inhibitor of GCL that triggers depletion of glutathione levels followed by the induction of ferroptosis⁴⁹⁸ (Figure

57A). To provide evidence that glutathione biosynthesis is affected by the GCN2 absence upon leucine stress, we tracked erastin-induced ferroptosis in combination with BSO treatment. We found that the inhibition of the GCN2 cascade (using a specific GCN2 inhibitor; Section 4.7.) diminished ferroptosis upon leucine stress over time (Figure 57C). This effect was also detected by stimulating the cells on top with erastin (Figure 57C). Combined, we provide a first hint that the GCN2 cascade is relevant for regulating glutathione metabolism upon leucine stress. In summary, we provided evidence that the ISR regulates erastin-induced ferroptosis upon leucine and glutamine stress in a GCN2-dependent manner. We linked this phenomenon to mitochondrial function, the regulation of GSH synthesis and glutamine metabolism. Further studies will follow to provide a clear conclusion how the postulated GCN2-ATF4-SLC axis modulates erastin-induced ferroptosis and which exact role GCN1 plays in this signaling network.

A



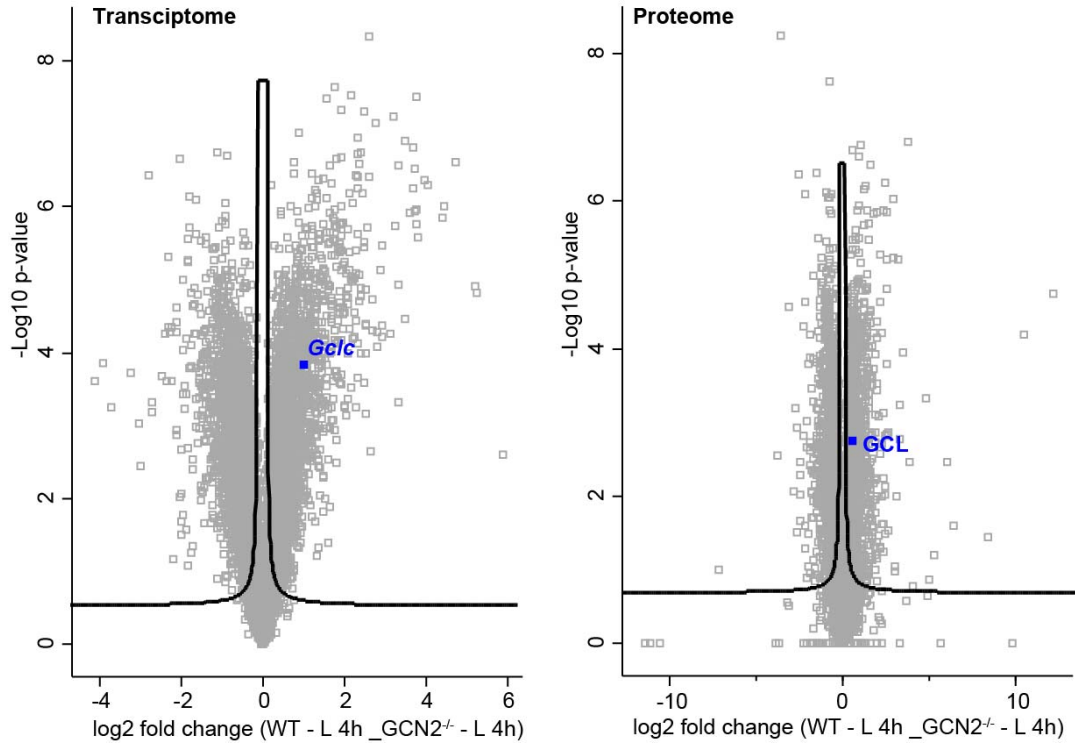
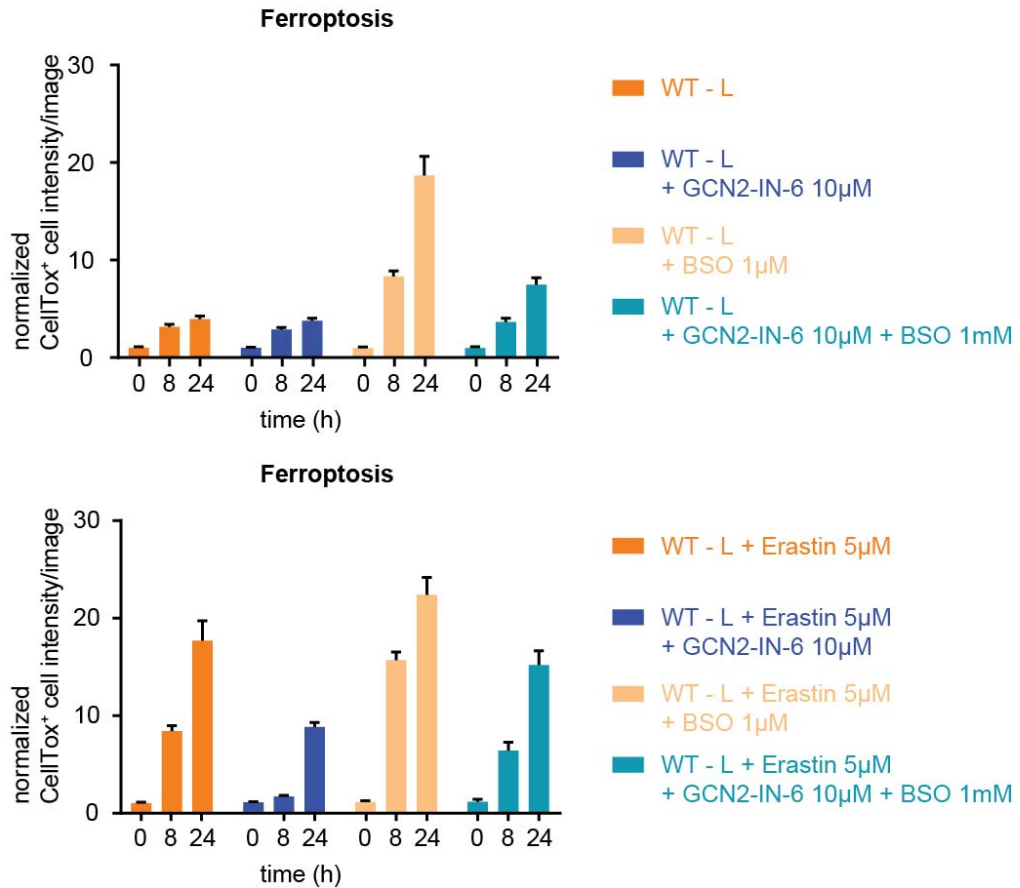
B**C**

Figure 57. Glutathione biosynthesis is affected by GCN2 deficiency upon leucine stress. (A) Simplified scheme of ferroptosis control indicating chemical perturbation of glutathione biosynthesis by BSO treatment. BSO blocks glutamate-cysteine ligase (GCL), the first rate-limiting enzyme of glutathione synthesis. Details are provided in the respective text paragraph. (B) Volcano plots comparing p-value and log₂-fold changes of significantly enriched *Gclc* (glutamate-cysteine ligase catalytic subunit) and GCL between the 3T3 wild-type (WT) and the GCN2 deficient (GCN2^{-/-}) cells at unstarved and leucine-starved (- L 4h) conditions. Data are depicted from the proteomics and transcriptomics studies (Section 4.2.). (C) Quantification of ferroptosis using CellTox green staining in 3T3 wild-type (WT) cells treated with BSO (1 mM) in the presence of leucine starvation for 0 h, 8 h and 24 h in combination with the GCN2 inhibitor GCN2-IN-6 (10 μM). Data are depicted as mean + SEM of three independent experiments.

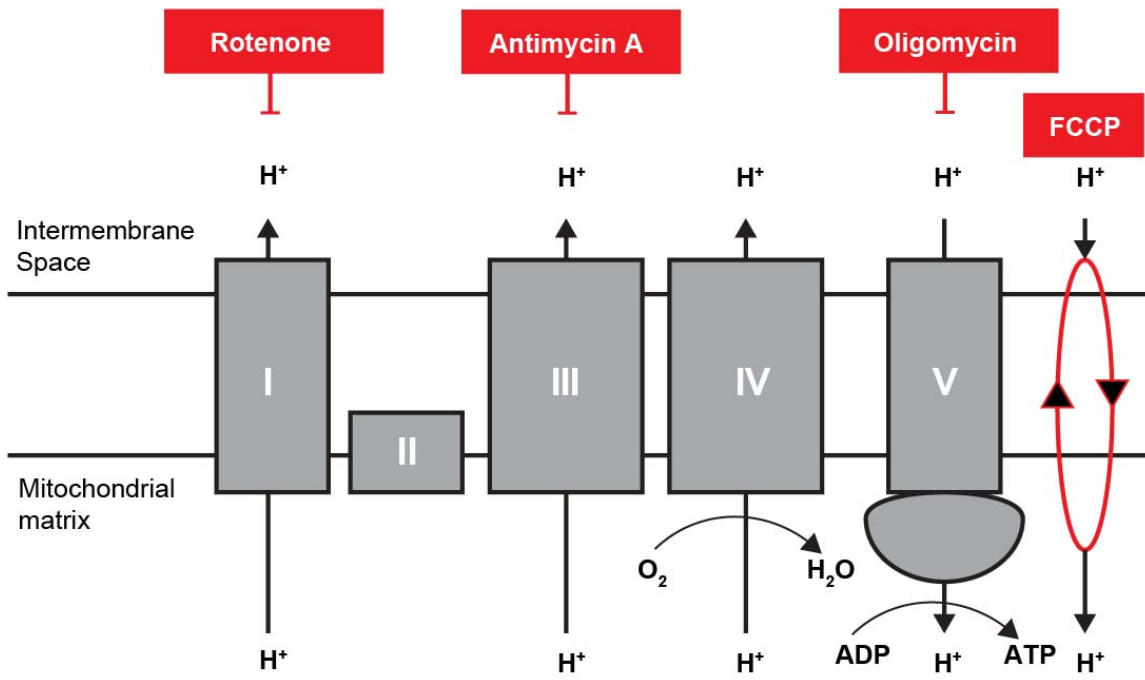
4.3.5. Bioenergetics regulation by GCN1 and GCN2

ATP is generated by two distinct pathways: oxidative phosphorylation (36 mol ATP/mol glucose) and glycolysis (2 mol ATP/mol glucose). Cancer cells boost their progression by reprogramming their metabolism to produce lactate⁴⁹⁹. This metabolic switch is also known as the Warburg effect (or aerobic glycolysis) that is used also by innate immune cells like activated dendritic cells, macrophages and antigen-stimulated T-cells⁵⁰⁰. We highlighted at the transcriptome and proteome level that the bioenergetic profiles of GCN1 and GCN2 deficient cells were already affected under normal growth condition by the loss of both proteins (Section 4.2.; Figures 35 and 41). In this context, we found that both knockout cell lines had a diminished activity to induce gene and proteins relevant in glyconeogenesis and glycolysis as compared to wild-type cells. Moreover, we discovered that GCN1 deficient cells in contrast to wild-type cells showed no significant induction in NADH dehydrogenase, which is the complex I of the electron transport chain (ETC) (Section 4.2.4.; Figure 41). Additionally, we provided evidence that the proficiency of GCN1 and GCN2 upon leucine stress was relevant for processes involved in the regulation of mitochondrial 1C-metabolism, glutaminolysis, serine biosynthesis, amino acid transamination or GSH biosynthesis (Section 4.2.). All these pathways are relevant for the integrity of oxidative phosphorylation and thereby mitochondrial respiration. In addition, we previously described how the GCN2 cascade might regulate glutamine metabolism, which is relevant for mitochondrial respiration and the regulation of ferroptosis⁴⁸⁸ (Section 4.3.4.). Based on these findings, we started to unravel the bioenergetics of GCN1 and GCN2 deficient cells at the cellular level by bioenergetic flux analyses.

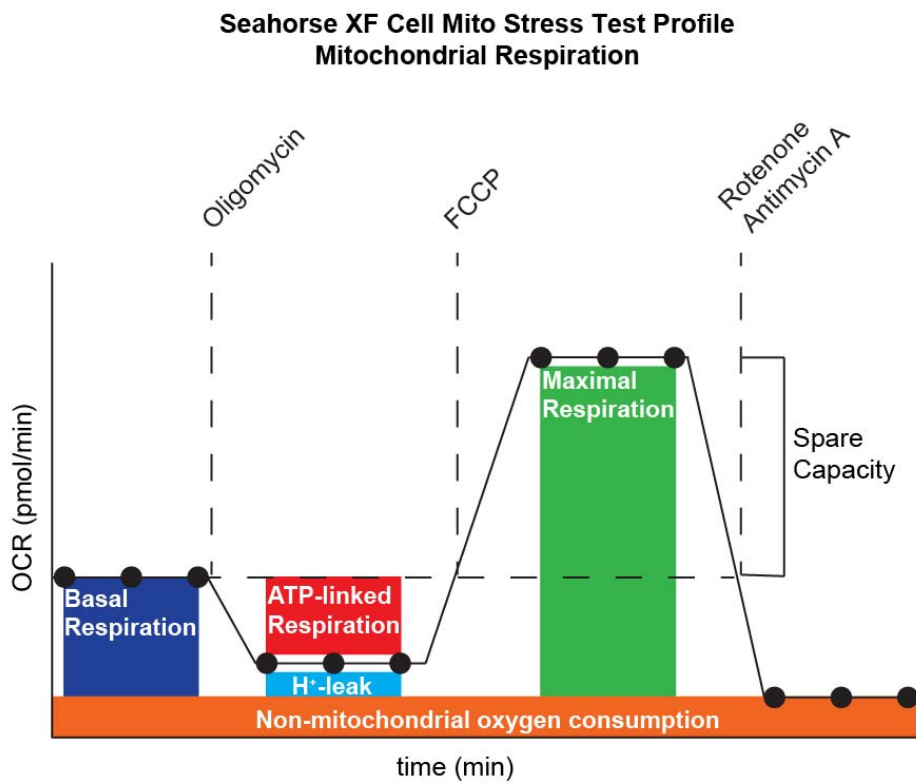
The Seahorse bioenergetic flux system enables the real-time and parallel measurement of the oxygen consumption rate (OCR) and the extracellular acidification rate (ECAR) at the cellular level⁵⁰¹. Both rates are used to determine the overall mitochondrial respiration, which couples oxygen consumption to mitochondrial ATP synthesis. Manipulating this connection via the

sequential injection of specific ETC blocking reagents allows the analysis of the cellular bioenergetic profile (Figure 58A). The Seahorse Mito Stress test (Section 3.4.3.) works as follows (Figure 58B): Basal respiration is the combination of oxygen consumption linked to ATP synthesis and oxygen consumption used to compensate for proton leakage across the inter membrane space. In other words, basal respiration is the OCR measured during cellular homeostasis. This cellular homeostasis is affected by the ATP synthase inhibitor oligomycin, which decreases the OCR and represents ATP-linked respiration. The maximal respiration is determined by a timed injection of the mitochondrial membrane potential uncoupling reagent trifluoromethoxy-carbonylcyanide-phenylhydrazone (FCCP). The spare capacity, defined as the difference between maximal and basal respiration, reflects the mitochondrial capacity to increase ATP synthesis in periods of high energy demand. Finally, the complex I and III inhibitors rotenone and antimycin A are injected to shut down the ECT and yield the non-mitochondrial respiration value. First, we used the described test to determine the OCRs of wild-type compared to *GCN2^{-/-}* and *GCN1^{-/-}* deficient 3T3 cells in an unstarved cellular environment. We found that the maximal and basal respiration levels were equal in *GCN2^{-/-}* deficient and wild-type cells arguing for mitochondrial respiration under normal growth state (Figure 58C). However, the ATP-linked respiration was reduced and the non-mitochondrial oxygen consumption increased in the *GCN2* deficient background. In contrast, the basal respiration level of *GCN1* deficient cells was already lower compared to the other genotypes resulting in a diminished maximal respiratory capacity. This phenomenon can be explained by the dysregulation of complex I as shown in the proteomics study (Section 4.2.4.; Figure 41) and affecting the overall mitochondrial respiration function. Next, we compared the ECARs of all three cell lines (Figure 58D). Both deficient cell lines had lower ECARs than the wild-type counterpart indicating that the glycolysis in the *GCN1* and *GCN2* deficient context was diminished (glycolytic capacity, reserve and basal levels). This finding was consistent with our omics data (Section 4.2.; Figures 35 and 41). In summary, *GCN1* and *GCN2* deficient cells have a distinct energetic phenotype already in normal growth state (Figure 58E). This is mostly relevant for further investigations of stress adaptation. Unfortunately, the experimental design of the flux analyzer cannot tolerate interruption of the supplied assay media, which did not allow us to detect changes resulting from leucine deprivation for now.

A



B



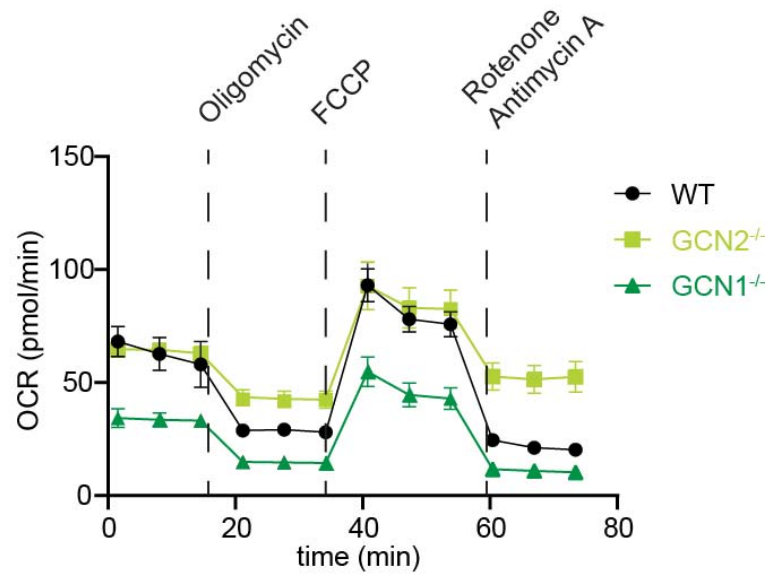
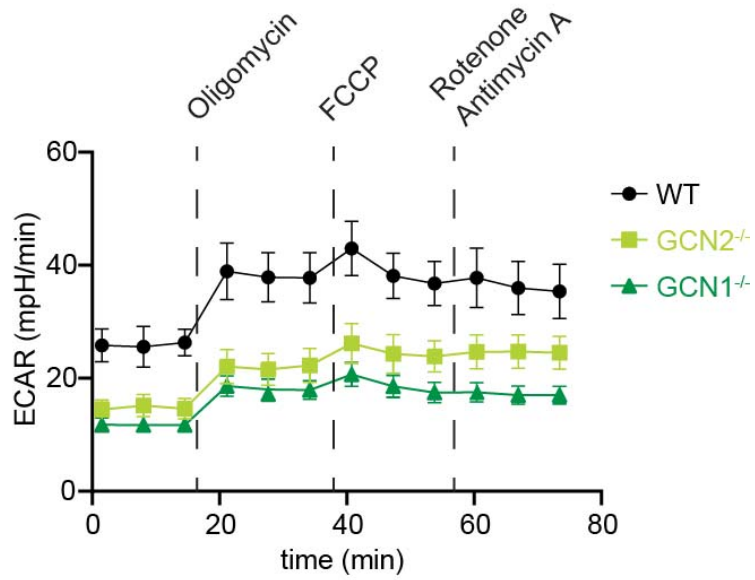
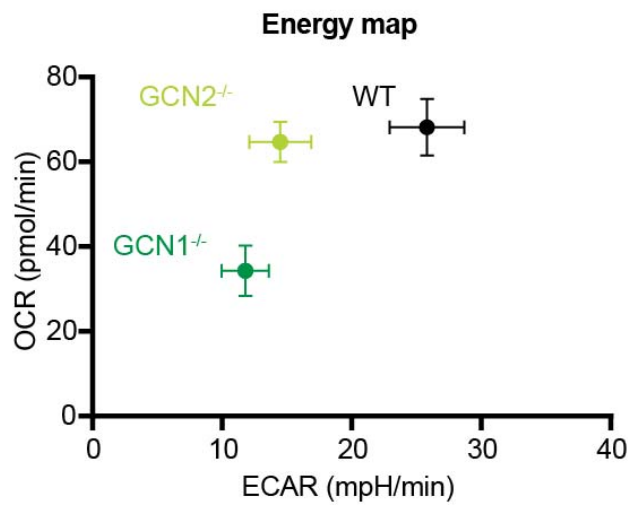
C**D****E**

Figure 58. The cellular bioenergetic profile changes due to the loss of GCN1 or GCN2. (A) Scheme of the electron transport chain chemically perturbed by rotenone (inhibiting complex I; red), antimycin A (inhibiting complex III; red), oligomycin (inhibiting complex V; red) and FCCP (targeting mitochondrial membrane potential; red). (B) Setup of a Seahorse XF Mito Stress test to measure the mitochondrial respiration. Details are explained in the respective text paragraph. (C) Quantification of the oxygen consumption rates (OCRs) of 3T3 wild-type (WT; black), GCN2 (GCN2^{-/-}; light green) and GCN1 (GCN1^{-/-}; dark green) knockout cells treated with the reagents mentioned in A under basal growth condition. (D) Same as C, except: quantification of the extracellular acidification rates (ECARs). (E) Summary of the energetic profile of C+D. (C-E) Data are depicted as mean + SEM of three independent experiments.

To further investigate how the bioenergetics change due to the loss of GCN1 or GCN2, we decided to study the energetic profile in bone marrow derived macrophages (BMDMs). Several studies have highlighted that myeloid cells like macrophages, relevant for innate and adaptive immunity, are modulated by complex metabolic network reprogramming events depending on their inflammatory stimulus: M1 macrophage polarization induces a metabolic shift from OXPHOS to aerobic glycolysis (induced by pro-inflammatory cytokines), while the M2 subtype depends on OXPHOS (induced by anti-inflammatory cytokines)⁵⁰². Together with Dr. Stefanie Dichtl, we stimulated wild-type and GCN2 deficient BMDMs with lipopolysaccharide LPS (pro-inflammatory) or interleukins IL4/13 (anti-inflammatory) for 48 h and compared their OCRs and ECARs to the unstimulated condition. As shown in 3T3 cells, the glycolysis capacity (ECAR) was diminished in GCN2^{-/-} BMDMs compared to the wild-type counterpart (Figure 59C). LPS stimulation triggers the cells towards an increase in ECAR – independent of the genotype (Figure 59B). In contrast, GCN2 deficient BMDMs were unable to shift their metabolic profile towards OXPHOS upon IL4/13 stimulation (Figure 59A). A plausible explanation for the IL4/13-induced M2 polarization suppression in GCN2 knockout cells could be a dysregulation in the glutamine metabolism, because this affects M2, but less M1 polarization^{503,504}. Moreover, Halaby *et al.*²¹⁰ showed that GCN2^{-/-} mice polarized to alternatively activated regulatory macrophages affecting the expression of several genes involved in OXPHOS, but not in glycolysis. To connect the described effect to GCN1, we first needed to differentiate GCN1^{-/-} mouse embryonic stem cells into embryonic bodies and further into macrophages (Section 3.2.2.). After several trials and optimized culture conditions, we were able to generate macrophages in a GCN1 deficient background (Figure 60A), but not in a sufficient viable amount for a bioenergetic flux assay. In contrast to the GCN2^{-/-} and wild-type E14 cells, the GCN1^{-/-} cell line shows a distinct heterogeneously differentiated morphological phenotype and additional growth impairment under normal growth culture condition (Figure 60B). Therefore, we phenotypically characterized the pluripotency of the cells by immunofluorescence microscopy (Section 3.4.5.). GCN1 deficient cells induce the ‘Yamanaka’

factors Oct3/4 and Nanog (Figure 60C). Collectively, we think since *Gcn1* is known to be essential for embryonic development¹¹³, growth defects and differentiation abnormalities could be an explanation for the low macrophage amount.

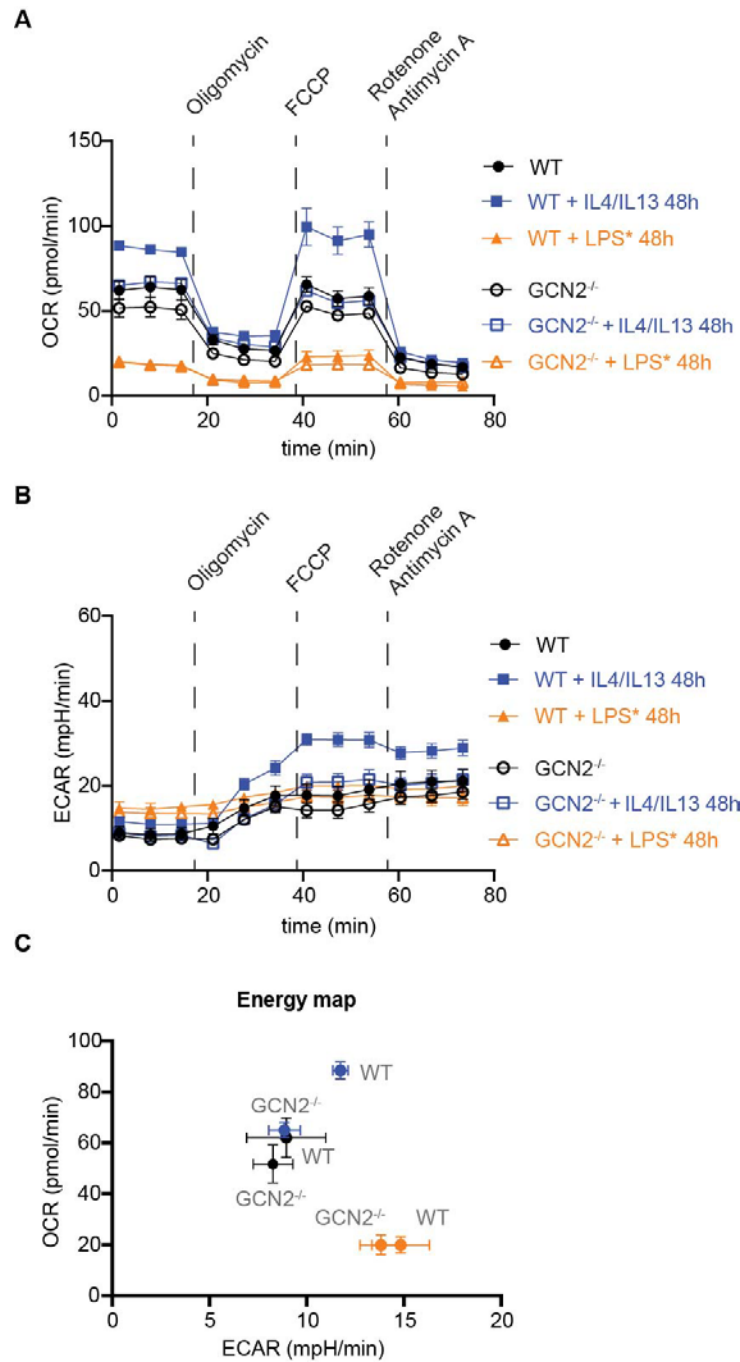
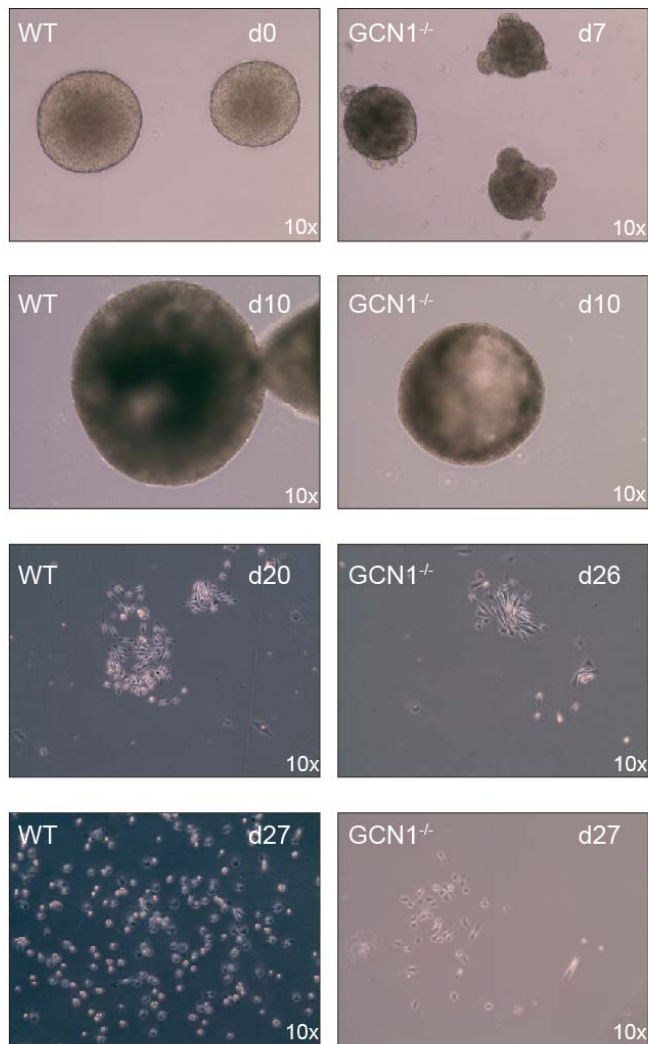


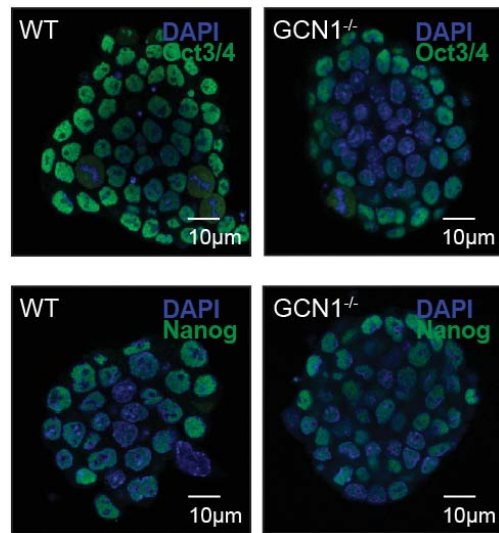
Figure 59. Bone marrow derived GCN2 deficient macrophages are not stimulated towards a polarized M2 phenotype. (A) Quantification of the oxygen consumption rates (OCRs) of bone marrow derived macrophages in wild-type (WT) and GCN2 deficient (GCN2^{-/-}) background treated with IL4/IL13 (10 ng/mL) for 48 h and LPS* (5 ng/mL) for 48 h. Star indicates that the LPS was removed for the Seahorse XF Mito Stress test measurement. (B) Same as A, except: quantification of the extracellular acidification

rates (ECARs). (C) Summary of the energetic profile of A+B. (A-C) Data are depicted as mean + SEM of three independent experiments.

A



C



B

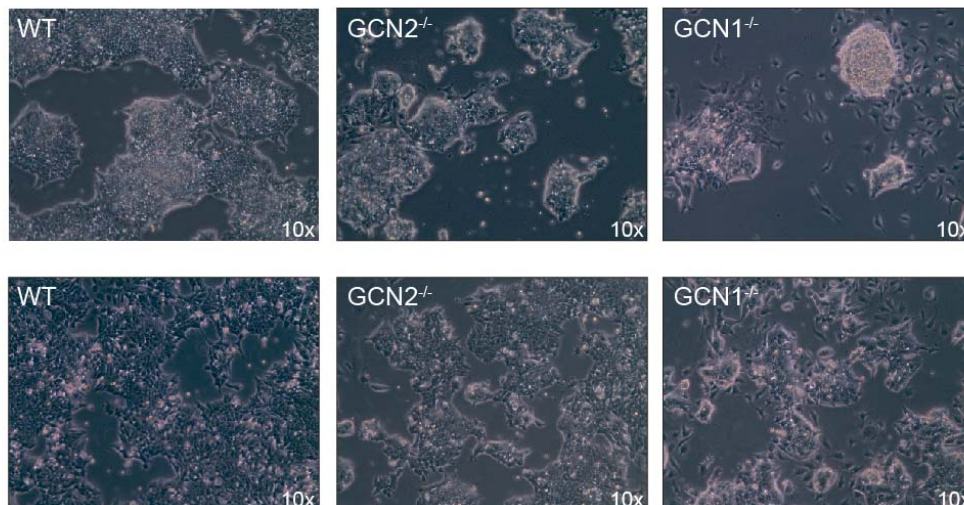


Figure 60. GCN1 deficient mouse embryonic stem cells are phenotypically different to the GCN2 ones. (A) Microscopic images of mouse embryonic stem (ES) cells differentiated into macrophages with wild-type (WT) or GCN1 deficient (GCN1^{-/-}) background. Days (d) indicate the stadium from embryoid body formation to macrophage progenitors to ES-derived macrophages (from top to bottom). (B) Microscopic images of mouse embryonic stem (ES) cells in wild-type (WT), GCN2 deficient (GCN2^{-/-}) or GCN1 deficient (GCN1^{-/-}) background under normal culture conditions. (C) Immunofluorescence images of mouse embryonic stem (ES) cells in wild-type (WT) and GCN1 (GCN1^{-/-}) deficient background. DAPI staining for the nucleus and Alexa Fluor 488 staining for the pluripotency markers Oct3/4 and Nanog. Data are depicted as one or two representative images.

Overall, our data suggest that GCN1 and GCN2 deficient cells demonstrate a complex bioenergetic reprogramming to compensate for the loss of the protein in order to enable cellular homeostasis. We also showed that the loss of both proteins affect the glycolysis and/or OXPHOS. In future studies, we will also introduce amino acid stress to investigate the metabolic rewiring mechanisms in this context.

4.4. Mechanistic analysis of the mammalian amino acid response

4.4.1. Overview

A major aim of this thesis was to investigate the involvement of GCN1 in the mammalian amino acid stress-induced GCN2 pathway. In yeast, GCN1 is considered a crucial factor connecting GCN2, uncharged tRNAs and the ribosomal machinery (with the P-stalk) to enable ISR induction^{114,131}. For several years, the GCN2-regulated ISR was investigated in yeast studies and known up- and down-stream regulators were transferred to the mammalian system⁶⁰. The prevailing dogma of the mammalian amino acid response (Figure 61A) implicates the translation initiation factor eIF2 α and the transcription factor ATF4 as 'rheostats' to regulate and control the protein translation⁷⁴. Thereby, ATF4 mediates the induction of a stress-transcriptional program in which *Ddit3* is expressed (coding for CHOP)⁷¹. However, until 2020, the role and position of GCN1 in the whole cascade was not known^{113,156}. Here, we made use of this extensively studied pathway and present the role of GCN1 in the murine ISR in a chronological order using our set of gene-modified cell lines (Section 4.1.).

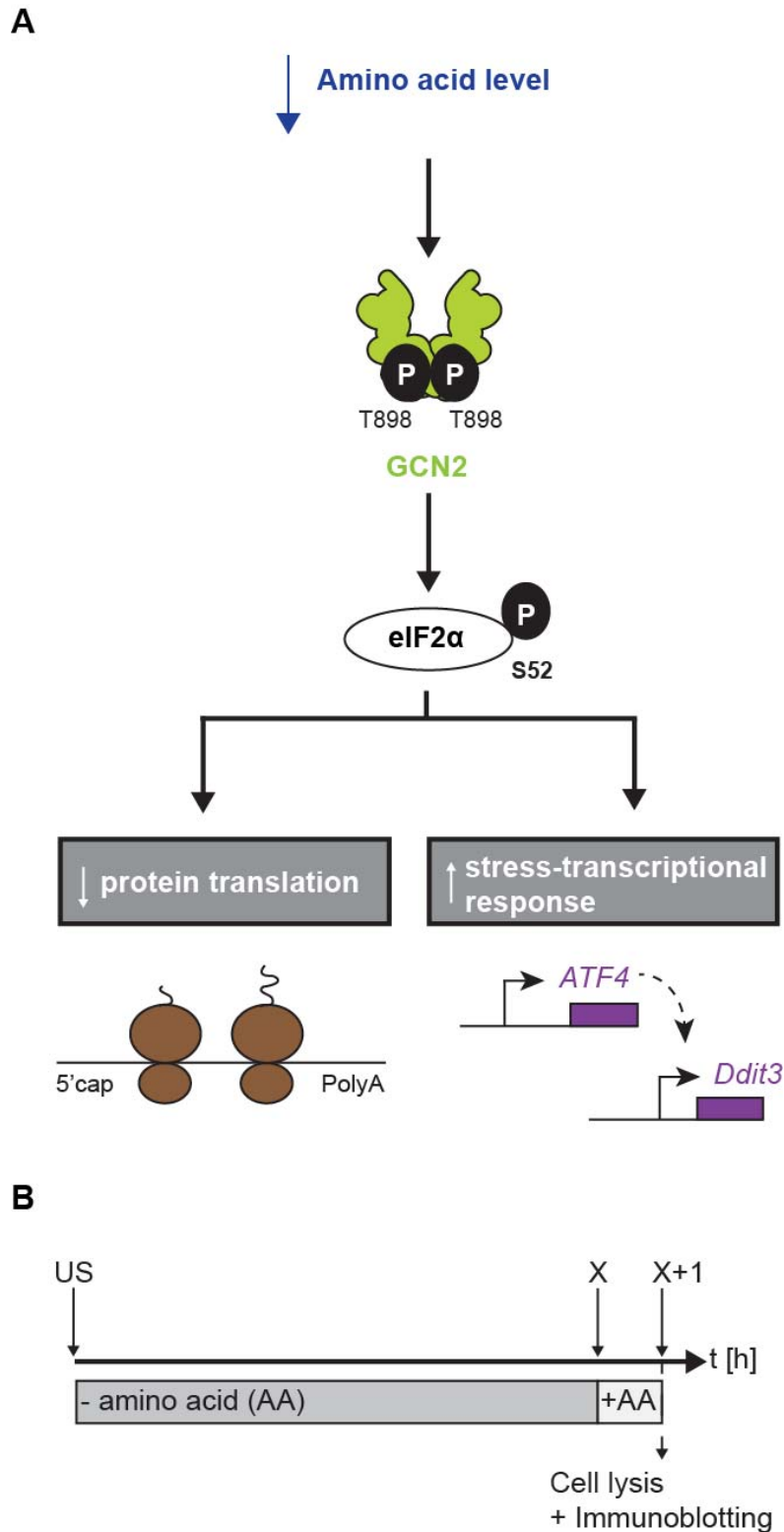


Figure 61. Our working model of the mammalian amino acid response. (A) Our working model of the murine ISR that based on the classical dogma (Section 1.2.3.4.; Figure 9) and will be refined in this thesis⁶¹: amino acid deprivation (blue arrow down) leads to the autophosphorylation of GCN2 (light green) at threonine 898 (T898)⁶⁷. Active GCN2 phosphorylates the translation initiation factor eIF2 α at serine 52 (S52)⁷⁷. This leads to a decrease in protein translation and simultaneously to an increase in the stress

transcriptional response in which transcription factors such as *Atf4* and *Ddit3* (purple) regulate the stress adaptation⁷¹. (B) Our experimental setup for immunoblotting: amino acid starvation (- AA) is applied to cells for an indicated timepoint (X) and a second set of amino acid-starved cells are additionally resupplemented with the depleted amino acid (+ AA) for 1 h prior to cell lysis and immunoblotting. Cells growing for the indicated times in normal culture condition are displayed as unstarved (US).

4.4.2. GCN2 activation is regulated by GCN1

By now, the ribosomal P-stalk and uncharged tRNAs are the proposed activators of GCN2 (Refs. ^{114,166,171}). Activation of GCN2 goes along with its dimerization and autophosphorylation at threonine 898 and 903 (T898 and T903) and threonine 898 is essential for GCN2 activity^{67,72,156,505}. So far, we used our amino acid stress reporter systems to indirectly track active GCN2 by reading out the amino acid stress-mediated induction of CHOP (encoded by *Ddit3*) by fluorescence (*Ddit3::mCherry*) or chemiluminescence (*Ddit3::NanoLuc-PEST*). To obtain a direct readout for the active state of GCN2, we made use of the phosphorylation event at T898, which we measured using a highly specific antibody. This enabled us to mechanistically track GCN2 activation in the context of diverse stimuli and genetic modified backgrounds.

We investigated the GCN2 pathway mainly upon leucine deprivation for 1 h, 4 h and 8 h of stress duration to match the findings of the broad omics analyses using the same setup (Figure 61B). We started by determining the autophosphorylation state of GCN2 at T898 in wild-type 3T3 cells by immunoblotting (Section 3.6.2.). Indicated by a clear band (Figure 62A), the autophosphorylation of GCN2 at T898 was a time-dependent event, which became occupied as soon as leucine was limited (- L). Feeding back leucine to the cells (+ L) reversed the signal towards the same as in the unstarved condition (US), highlighting the plasticity of the connection between amino acid amounts and GCN2 activation. Next, we checked this phosphorylation event in the GCN1 and/or GCN2 deficient cells. As expected, GCN2 was not detected in the GCN2 deficient lines providing a control for antibody specificity (*GCN2^{-/-}* and *GCN2^{-/+} GCN1^{-/-}*) (Figure 62A). Strikingly, we found that in the absence of only GCN1, GCN2 was not autophosphorylated (Figure 62A). In addition, we can confirm these findings as well upon arginine stress (Figure 62B) and in E14 cells (Section 4.6.; Figure 70). Overall, these results conclusively showed that GCN1 is essential for GCN2 activation during amino acid stress in murine cells. Recently, two studies using a knockdown of GCN1 or GCN1 deficient MEFs confirmed this phenomenon^{113,156}.

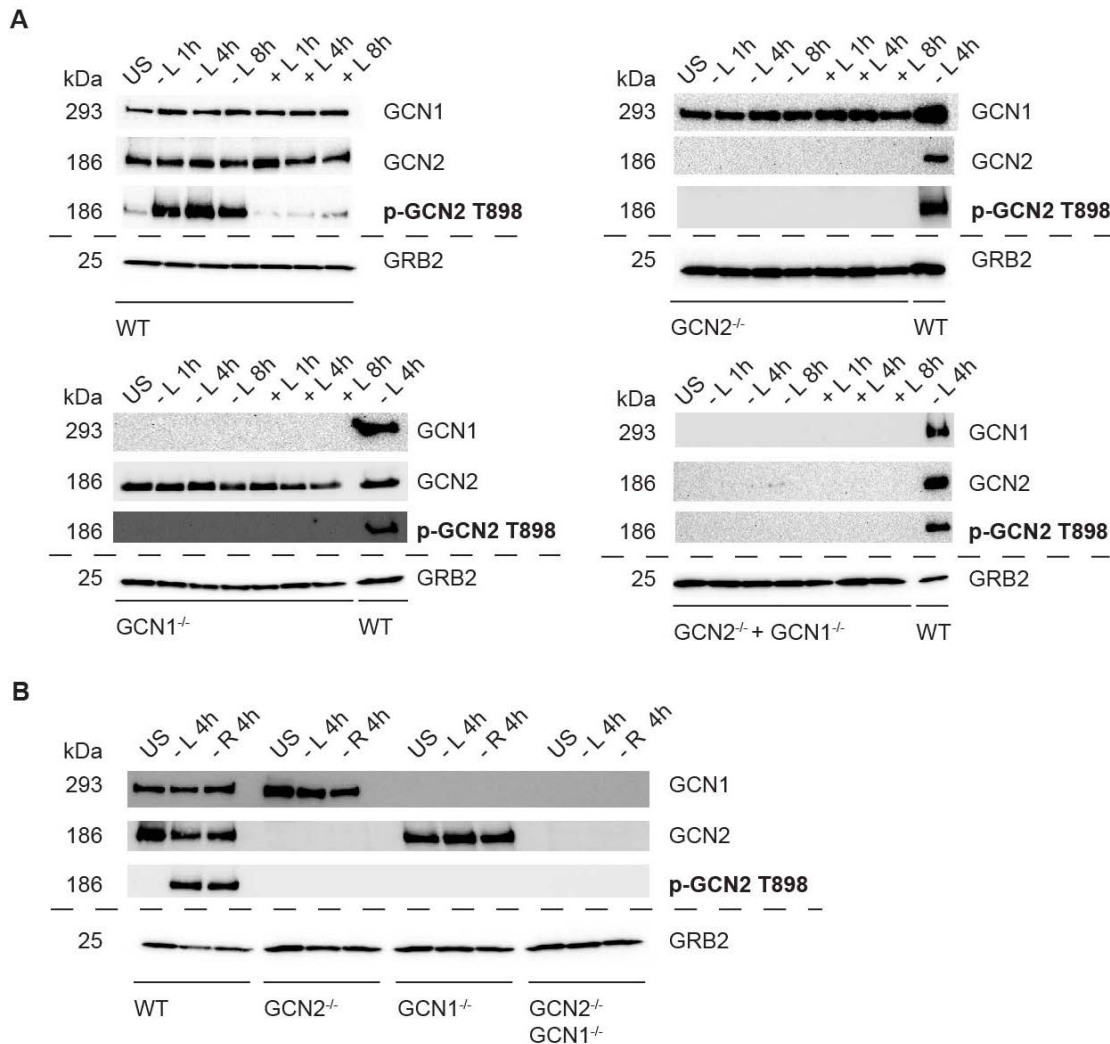


Figure 62. GCN1 acts upstream of GCN2 and regulates its autophosphorylation upon amino acid stress. (A) Immunoblots of 3T3 cell lysates stimulated with unstarved condition (US), leucine-starvation (-L) or leucine-resupplementation (+L) for 1 h, 4 h and 8 h. GRB2 was used as loading control. In bold, the characteristic changes in each analyzed genotype: 3T3 wild-type (WT), GCN2 knockout (GCN2^{-/-}), GCN1 knockout (GCN1^{-/-}) and double knockout (GCN2^{-/-} + GCN1^{-/-}). (B) Same as A, except: arginine (-R) and leucine (-L) starvation for 4 h. (A-B) Data are depicted one of two representative gels.

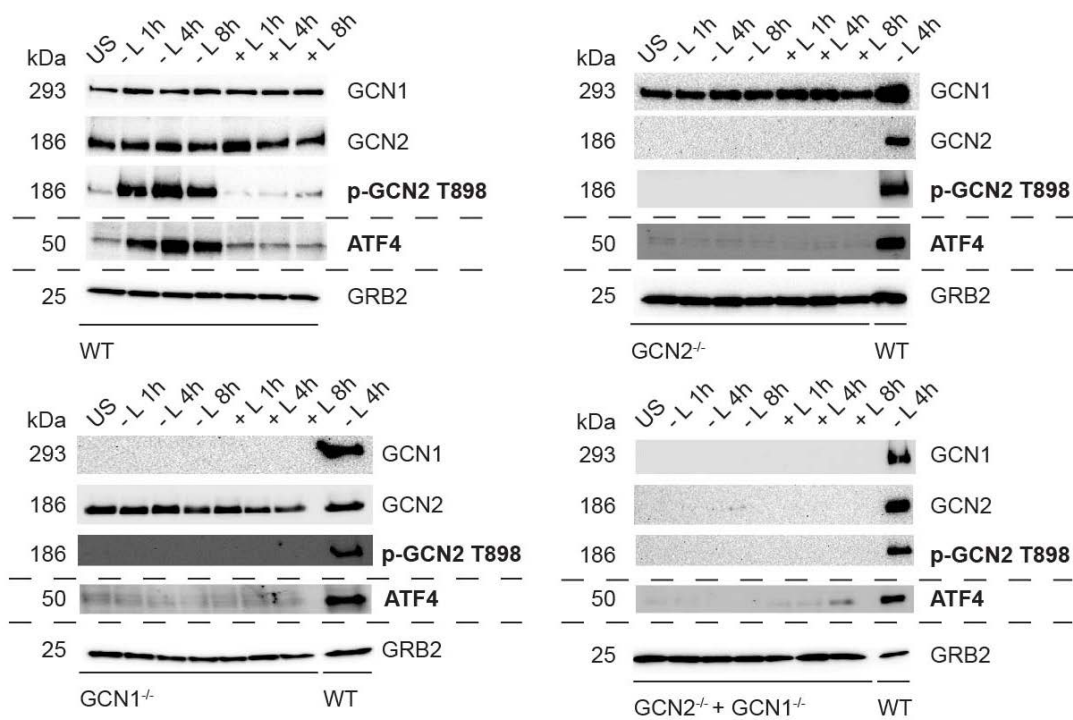
In conclusion, the activation of GCN2 was linked to GCN1 in the cellular surrounding upon amino acid stress. Thereby, GCN1 is an upstream activator of GCN2 involved in the regulation of the ISR upon amino acid stress.

4.4.3. ATF4-dependent transcriptional response is regulated by GCN1

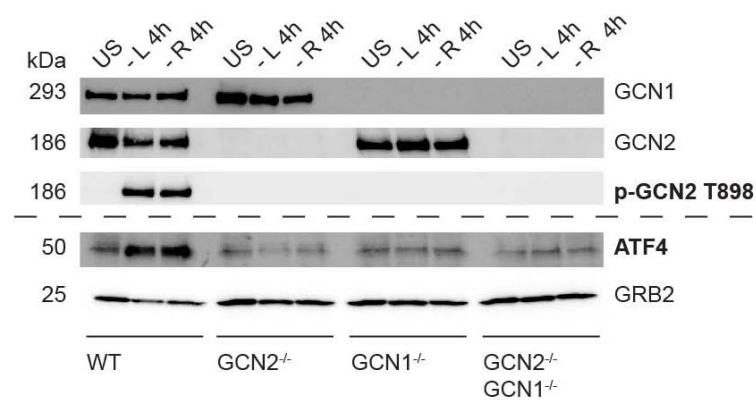
Upon amino acid stress, ATF4 is the main transcription factor that regulates and controls the stress-protective specific induction of proteins relevant for reestablishing cellular homeostasis⁶¹. In our RNASeq analysis (Section 4.2.3.), we highlighted the importance of the stress-

transcriptional response for stress adaptation processes. In this context, we showed as well that ATF4 was regulated at the gene and protein level (Section 4.2.; Figures 26, 30 and 43): In detail, the loss of GCN1 and GCN2 suppresses ATF4 induction upon amino acid starvation. In section 4.4.2., we showed that the activation of GCN2 was absent in a GCN1 deficient background (Figure 62). To address the connection of ATF4 induction with the autophosphorylation of GCN2 in our systems, we read out the key proteins by immunoblotting over time upon amino acid stress. First, we tracked the induction of ATF4 and the autophosphorylation of GCN2 at T898 in wild-type 3T3 cells (Figure 63A). ATF4 induction was activated in a time-dependent fashion under leucine deprivation and reversed by feeding back leucine to the system. This finding manifested the flexibility of the ISR system by sensing amino acid availability followed by signaling stress adaptation. Interestingly, we could not detect any induction of ATF4 over time in either the GCN1 and/or GCN2 deficient context at the protein level, which is in line with our phosphoproteomics data (Section 4.2.4.2.; Figure 43). We also confirmed the aforementioned results upon arginine stress (Figure 63B) and in other murine cells (MEFs and E14 cells) (Section 4.6.; Figure 70). Next, we tracked CHOP (encoded by *Ddit3*) protein expression, which is mediated downstream of ATF4 and is the target of our described stress reporter systems. In line with our phosphoproteomics data (Section 4.2.4.2.; Figure 43), CHOP induction is translationally regulated by ATF4, but shifted in time (Figure 63C). Collectively, these findings indicate that the transcription factors ATF4 and CHOP bypass the translational block caused by amino acid deprivation⁶¹. To answer if the ATF4 induction is directly linked to the autophosphorylation of GCN2, we performed the same experiment in the 'autophospho-dead' mutant cell line, named *Eif2ak4* T898/903A (Section 4.1.; Figure 20). Strikingly, ATF4 was not detected in the mutant cell line arguing that the autophosphorylation of GCN2 was necessary to induce ATF4 upon amino acid stress (Figure 63D). To confirm this axis, we performed the same experiments in an ATF4 deficient cell line (Section 4.1.; Figure 21). As expected, loss of ATF4 did not affect the autophosphorylation event. This means that GCN2 acts upstream of ATF4 (and CHOP) expression.

A



B



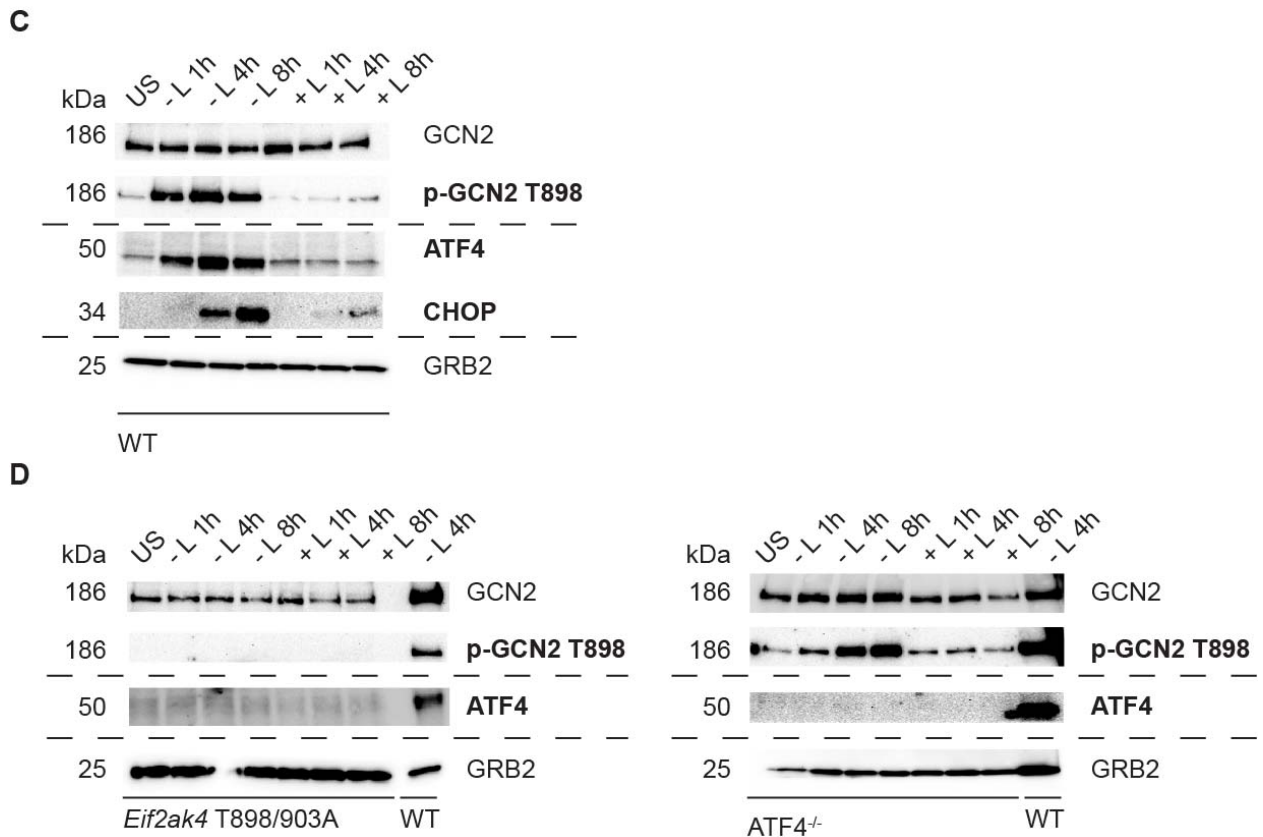


Figure 63. The autophosphorylation of GCN2 triggers the induction of ATF4 upon amino acid stress.

(A) Immunoblots of 3T3 cell lysates stimulated with unstarved condition (US), leucine-starvation (- L) or leucine-resupplementation (+ L) for 1 h, 4 h and 8 h. GRB2 was used as loading control. In bold, the characteristic changes in each analyzed genotype: 3T3 wild-type (WT), GCN2 knockout (GCN2^{-/-}), GCN1 knockout (GCN1^{-/-}) and double knockout (GCN2^{-/-} + GCN1^{-/-}). (B) Same as A, except: arginine (- R) and leucine (- L) starvation for 4 h. (C) Same as A, except: only in wild-type (WT) line. (D) Same as A, except: in ATF4 deficient (ATF4^{-/-}) and ‘autophospho-dead’ GCN2 (*Eif2ak4* T898/903) lines. (A-D) Data are depicted as one of two representative gels.

In conclusion, we showed that the stress-transcriptional response guided by ATF4 was also prevented at the protein level, when solely GCN1 was lost. In addition, we found that the autophosphorylation of GCN2, regulated by GCN1, directly prevented the activation of the stress transcription program controlled by ATF4 and further CHOP. Thus, GCN1 acts upstream of the entire GCN2-ATF4-CHOP pathway in the amino acid response. We therefore conclude that GCN1 is the central ‘sensing event’ necessary to initiate GCN2 activation (most likely in collaboration with ribosomes, uncharged tRNAs or other factors).

4.4.4. eIF2 α phosphorylation is regulated by GCN1

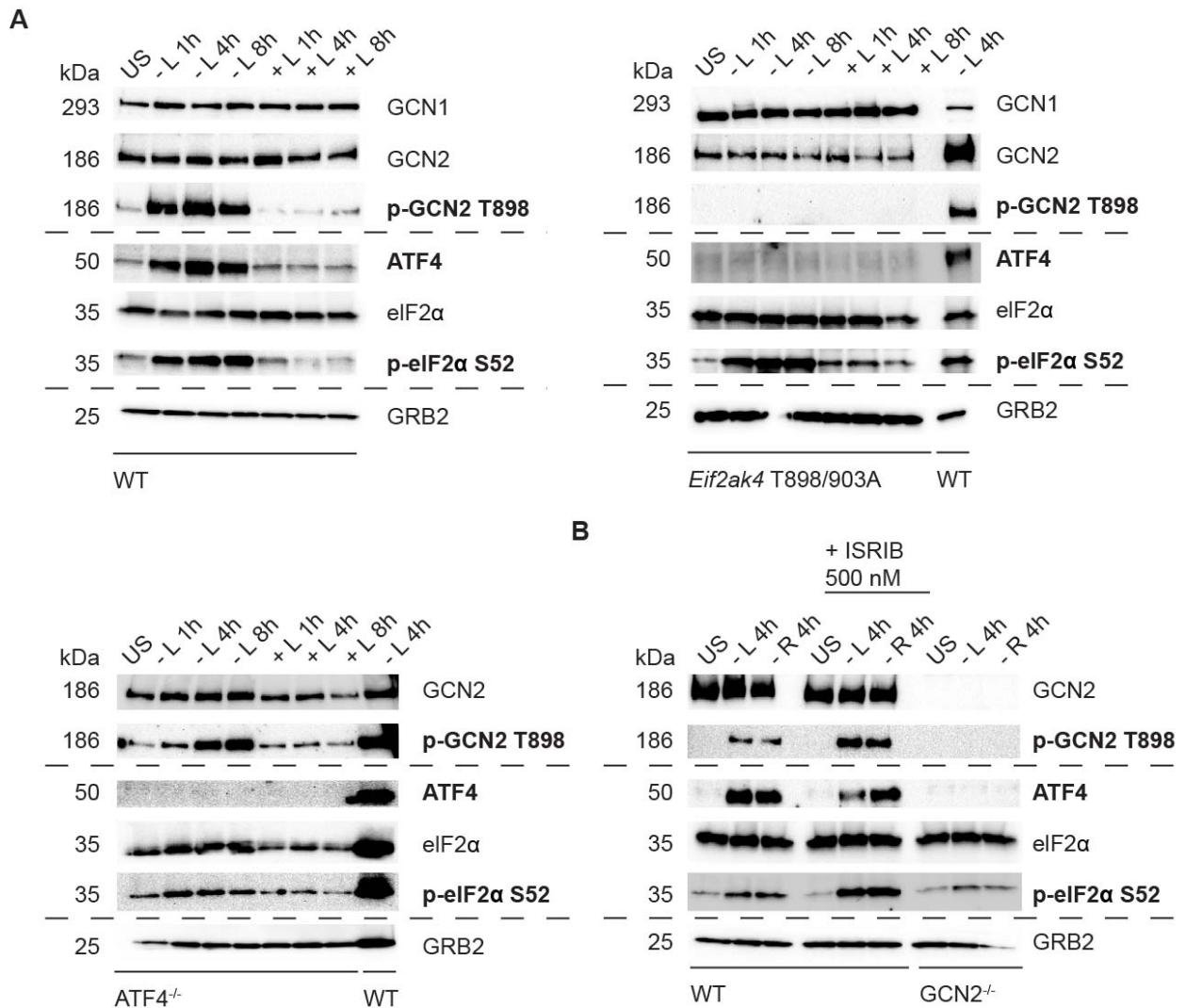
In the classical ISR dogma, the active GCN2 kinase phosphorylates its only known target, the eukaryotic translation initiation factor eIF2, thereby repressing overall cap-dependent translation^{15,75,98,506}. The phosphorylation of the α -subunit of eIF2 inhibits eIF2B, the guanine nucleotide exchange factor, which recycles the condensation reaction: inactive eIF2•GDP to active eIF2•GTP^{76,78,81,82,507}. This arm of the ISR regulation goes hand in hand with the induction of the ATF4-regulated transcriptional program for stress adaptation^{109,439}. We found that the activation of GCN2 and ATF4 is GCN1-dependently regulated (Sections 4.4.2.-4.4.3.). To link the mentioned connection with the phosphorylation of eIF2 α , we performed immunoblotting in the same experimental setup.

First, we tracked the phosphorylation of eIF2 α in the wild-type 3T3 cells at leucine-starved condition (Figure 64A). As expected, the eIF2 α phosphorylation was time-dependent and amino acid-regulated – a finding already shown for the induction of the transcription factors (ATF4 and CHOP) and GCN2 autophosphorylation (phospho-GCN2 T898) (Figures 62 and 63). Next, we checked if the loss of ATF4 or phospho-GCN2 in the respective genetically modified cell lines (ATF4^{-/-} and *Eif2ak4* T898/903A) affected the phosphorylation of eIF2 α . Interestingly, we found that both mutant cell lines were still able to phosphorylate eIF2 α (Figure 64A), showing that the catalytic activity of GCN2 in both cell lines is still intact. Thus, we assumed that the phosphorylation of eIF2 α happens either first, or is uncoupled to the autophosphorylation event of GCN2.

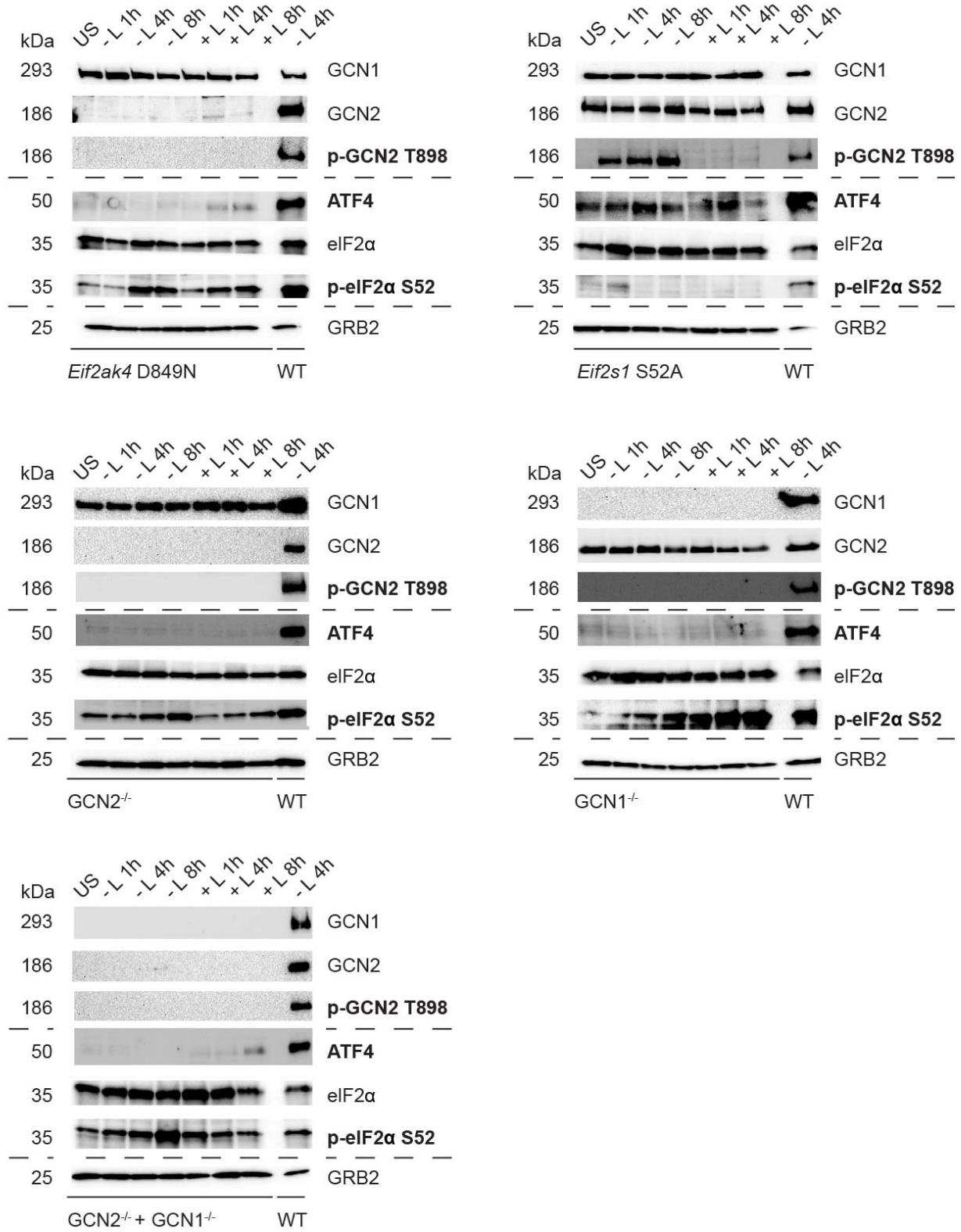
To address if the auto- and substrate phosphorylation events are connected, we used the small-molecule ISR inhibitor (ISRIB) in our experimental setup. This inhibitor works by rescuing the translation in the presence of phospho-eIF2 α by facilitating the assembly of more active eIF2B in an allosteric antagonizing fashion^{85,86,233}. We starved 3T3 cells for leucine or arginine at 4 h and co-treated the cells with ISRIB. We found that the presence of ISRIB reduced ATF4 expression even if the phenomenon was faintly detectable only for leucine starvation (Figure 64B). Recently, ISRIB was shown to work in a defined time frame of ISR activation: ISRIB inhibits low-level ISR activity, but not strong ISR signaling^{85,508}. In addition, cells lacking phosphorylated eIF2 show weak ISR-inhibitory activity of ISRIB^{85,508}.

Consequently, we established a 'catalytic-dead' GCN2 cell line, named *Eif2ak4* D849N (Section 4.1.; Figure 20). Interestingly, in this background, GCN2 was not autophosphorylated and ATF4 was not induced, thereby 'mimicking' the GCN1 and GCN2 deficient lines (Figure 64C+D). Next, we mutated the phosphorylation site of eIF2 α S52 and tracked ATF4 and phospho-GCN2 expression levels. Inactivating the target instead of the catalytic domain of GCN2 showed that the autophosphorylation and ATF4 event was not affected (Figure 64C). These effects were also

observed under arginine deprivation (Figure 64D). Together, this hints that the catalytic activity of GCN2 drives the autophosphorylation event. To test this hypothesis, we extended the timeframe by detecting our key targets at 15 min, 30 min, 60 min and 240 min of stress exposure. We observed that the phosphorylation of eIF2 α correlated with the phosphorylation of GCN2, but ATF4 induction started from 1 h onwards (Figure 64E). This time-dependent difference was already highlighted by Nikonorova *et al.*³⁷⁰.



C



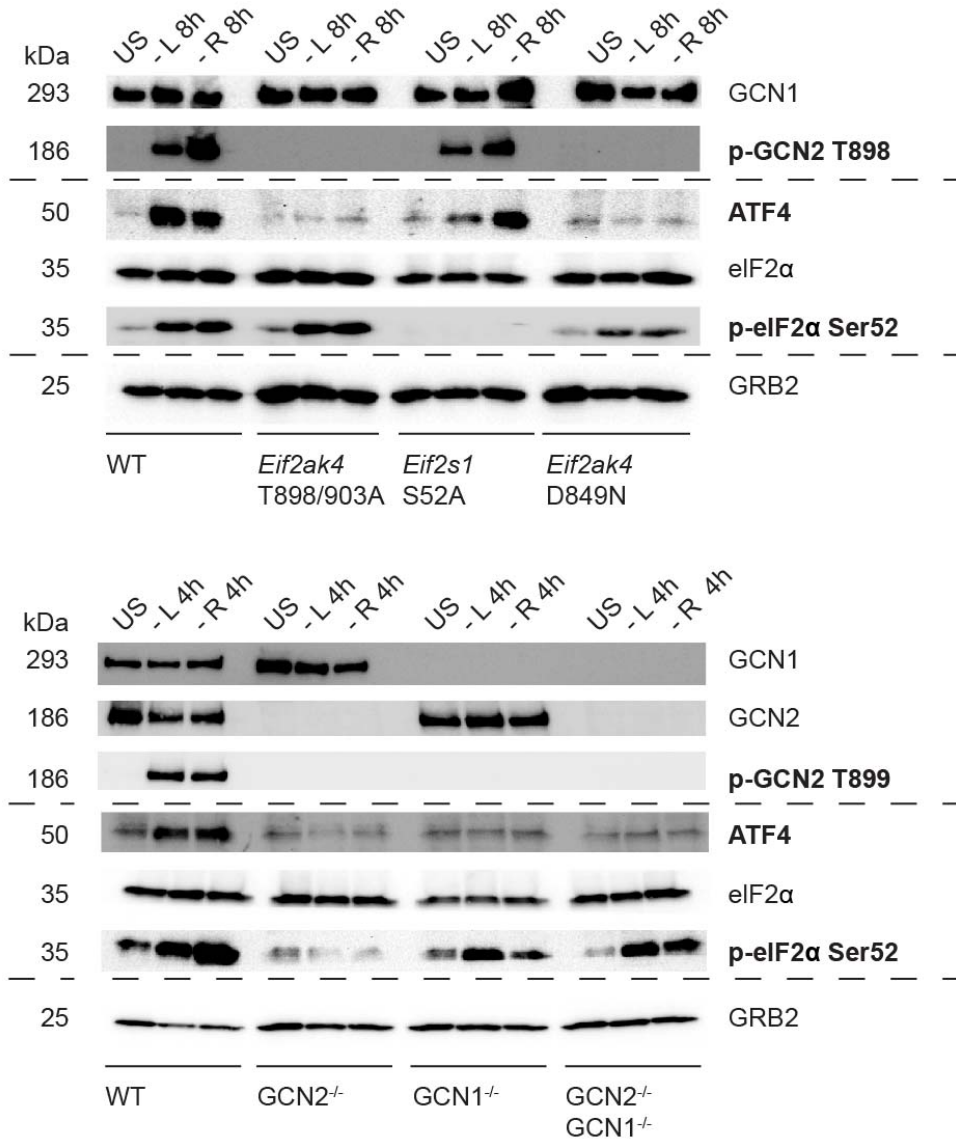
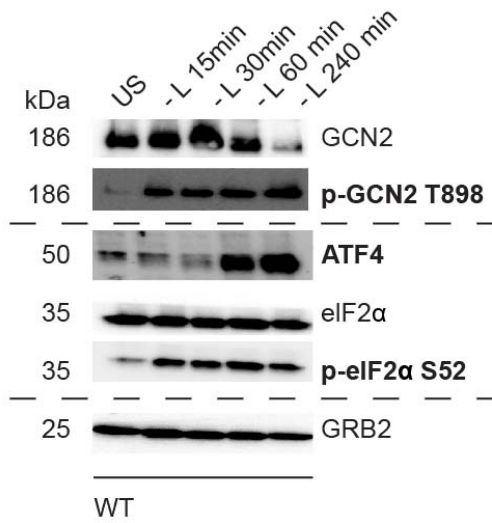
D**E**

Figure 64. GCN2 catalytic activity appears to regulate phosphorylation of eIF2 α and ATF4 induction upon leucine stress in a sequential way. (A) Immunoblots of 3T3 cell lysates stimulated with unstarved condition (US), leucine-starvation (- L) or leucine-resupplementation (+ L) for 1 h, 4 h and 8 h. GRB2 was used as loading control. In bold, the characteristic changes in each analyzed genotype: 3T3 wild-type (WT), ATF4 deficient (ATF4^{-/-}) and ‘autophospho-dead’ GCN2 (*Eif2ak4* T898/903). (B) Same as A, except: arginine (- R) and leucine (- L) starvation for 4 h in wild-type (WT) and GCN2 knockout (GCN2^{-/-}) lines. ISRIB (500 nM) was added at the same time of starvation. (C) Same as A, except: in ‘catalytic-dead’ GCN2 (*Eif2ak4* D849N), ‘target-dead’ eIF2 (*Eif2s1* S52A), GCN1 knockout (GCN1^{-/-}), GCN2 knockout (GCN2^{-/-}) and double knockout (GCN2^{-/-} + GCN1^{-/-}) backgrounds. (D) Same as A, except: arginine (- R) and leucine (- L) starvation for 4 h in 3T3 wild-type (WT), ‘catalytic-dead’ GCN2 (*Eif2ak4* D849N), ‘target-dead’ eIF2 (*Eif2s1* S52A), ‘autophospho-dead’ GCN2 (*Eif2ak4* T898/903), GCN1 knockout (GCN1^{-/-}), GCN2 knockout (GCN2^{-/-}) and double knockout (GCN2^{-/-} + GCN1^{-/-}) backgrounds. (E) Same as A, except: leucine-starvation for 30 min, 60 min, 120 min and 240 min in 3T3 wild-type (WT) background. (A-E) Data are depicted as one of two representative gels.

Based on these results, we extended the prevailing model (Figure 65) in which we link GCN1 to the autophosphorylation of GCN2 and finally to the induction of ATF4. This GCN1-GCN2-ATF4 axis was not affected by the inactivation of the eIF2 α phosphorylation site, but by blocking the catalytic activity of GCN2. We assumed that the catalytic activity of GCN2 is prior and linked to the autophosphorylation of GCN2 and ATF4. As discussed in more detail in section 5.1., our model stands in contrast to the initial findings in yeast, where mutating the substrate site of eIF2 α correlated with the inactivation of GCN4 (yeast ATF4)⁵⁰⁹.

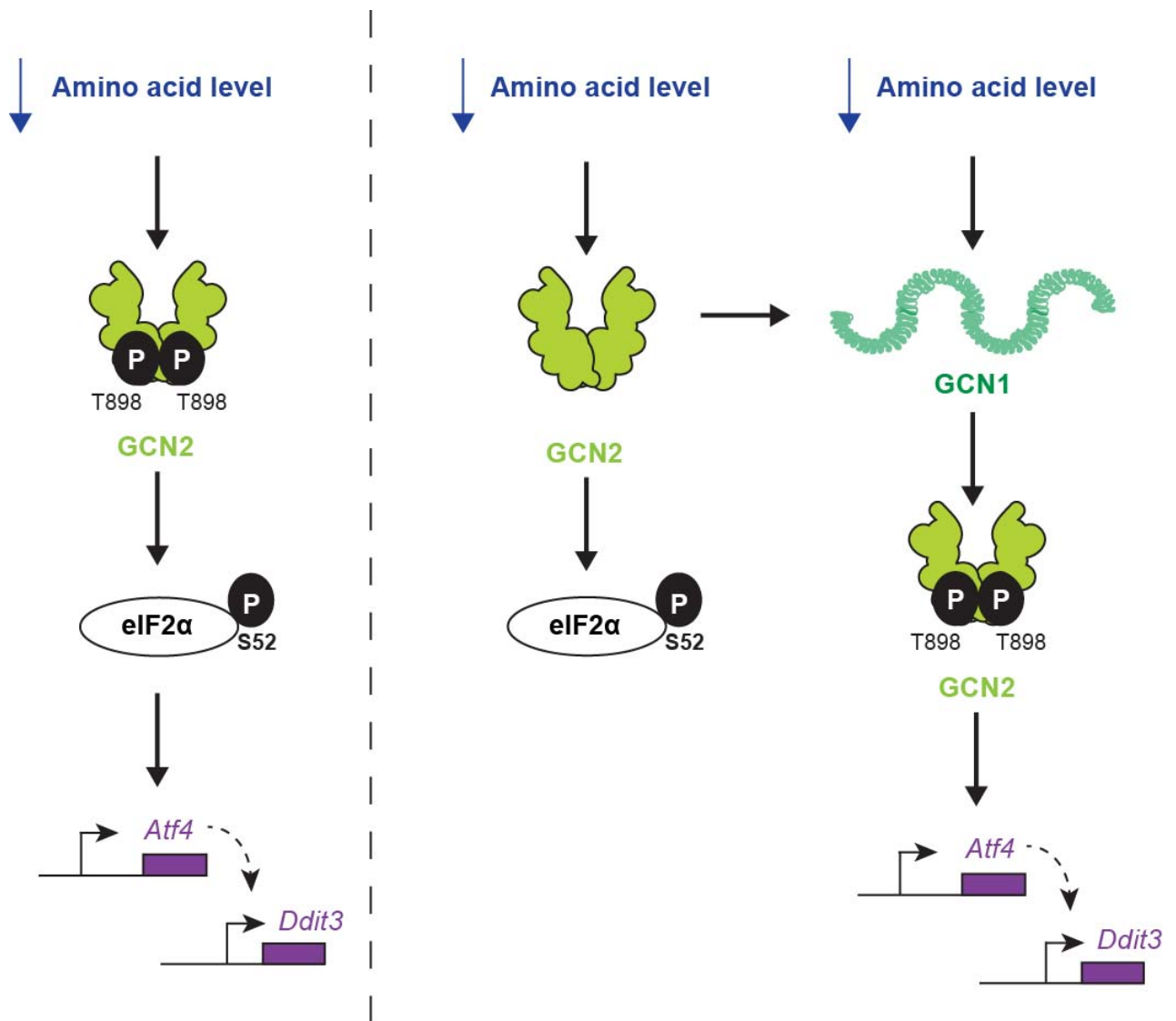


Figure 65. Our refined working model of the mammalian amino acid response. (A) Our refined working model of the murine ISR upon amino acid stress (blue arrow down): we extended the model from the left to the right showing that GCN1 (dark green) is upstream of GCN2 (light green) regulating its autophosphorylation at T898. The autophosphorylation correlates with the induction of the transcription factors ATF4 and CHOP (encoded by *Atf4* and *Ddit3* (purple)) mediating the stress-transcriptional program. This process is separately driven to the phosphorylation of eIF2 α at S52. Most likely, catalytic active GCN2 induces the autophosphorylation of GCN2.

In this context, it is important to mention that we need to refine our model using other techniques than immunoblotting. One cavity of the system was that we only detected a faint band of total GCN2 in the 'autophospho- and catalytic-dead' lines (Figure 63+64). We confirmed by Sanger sequencing that the point mutations of both sites do not change the coding region (Section 7.1.2.). Moreover, the used GCN2 antibody binds to threonine 222 and alanine 223 and consequently

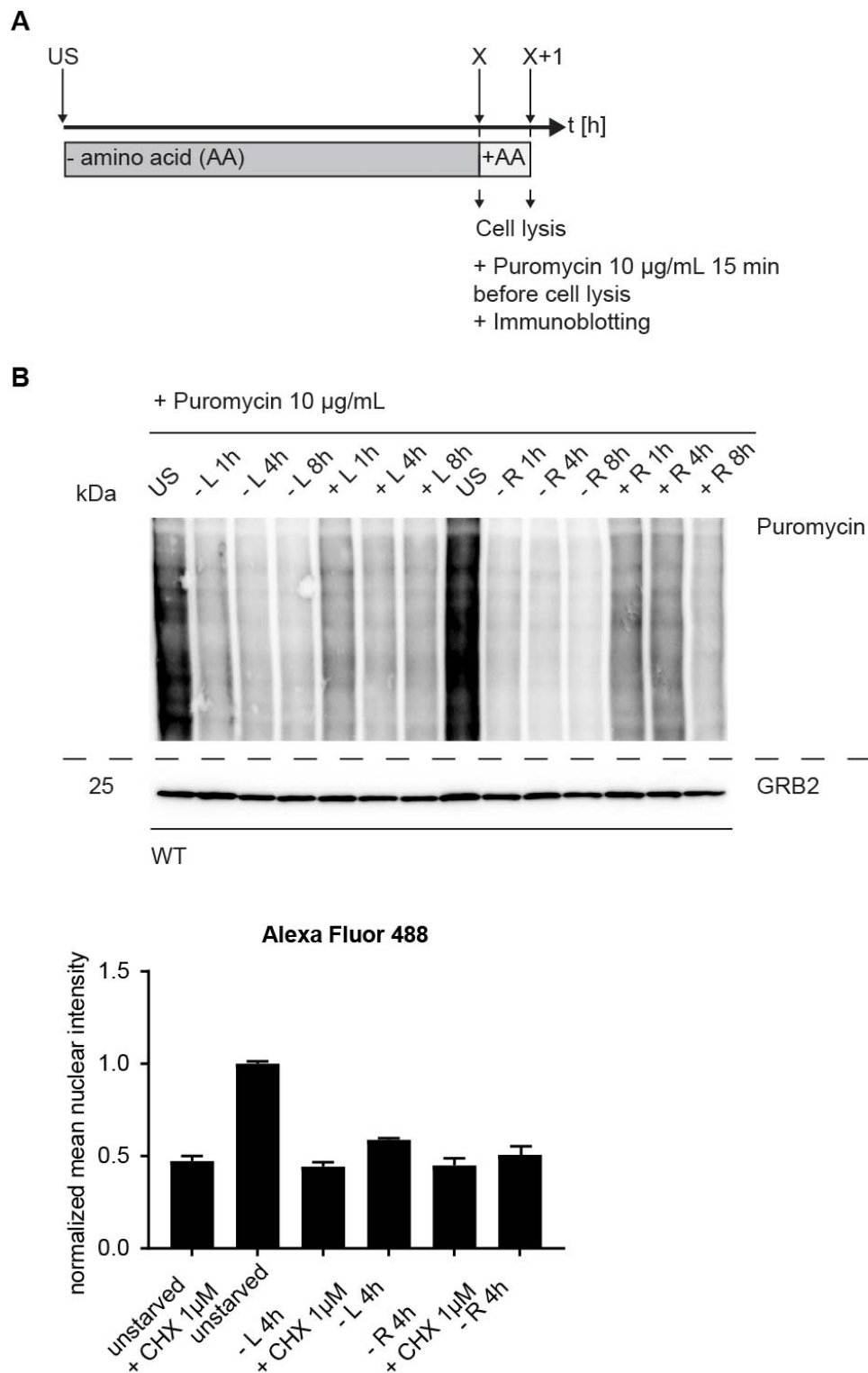
most likely not close to the mutated regions. However, a structural rearrangement would explain the loss of GCN2 detection by immunoblotting, which needs to be tested in the future prospect. A further cavity of the system was the finding that the phosphorylation of eIF2 α was not always absent in the GCN2 deficient or the 'catalytic-dead' cell lines (Figure 64C+D). In theory, the inactivity of the kinase should correlate with no phosphorylation of the key target. From these observations, we draw the following models: (i) eIF2 α can be phosphorylated by the other mammalian stress kinases (PERK, HRI and PKR). However, PERK was not activated by amino acid stress (Section 4.2.2.; Figure 27); (ii) An unknown kinase phosphorylates the target; (iii) The detection of phospho-eIF2 α is influenced by the property of the antibody, which can be crossreactive with the non-phospho form, depending on the cell type and the amount of protein detected. To investigate the effect of eIF2 α in more detail, we tracked the translational response as the next step knowing that eIF2 α phosphorylation correlates with translational shut-down⁷⁷ (Section 4.4.5.).

4.4.5. Translation is regulated by GCN1

The ISR regulates translation initiation by phosphorylating the eukaryotic translation initiation factor eIF2 α at serine 52 upon amino acid stress⁷⁷. To investigate the translational response in a GCN1 and/or GCN2 deficient background upon amino acid stress, the antibiotic puromycin was added additionally to the cultivating cells after the stress duration (Figure 66A), which induces protein termination mimicking the 3' end of an aminoacyl-tRNA⁵¹⁰.

First, we measured translation upon arginine versus leucine deprivation over time in the wild-type 3T3 cells. By now, we did not detect any substantial differences in the regulation of the ISR over time between both stimuli. However, studies from Darnell *et al.*⁵⁹ pointed towards a qualitative difference in translational outcomes based on codon utilization. They concluded that mTORC1 and GCN2 respond insufficiently to arginine deprivation leading to ribosome pausing. This decreases protein production and leads to premature ribosome termination without affecting internal mRNA levels. Indeed, we found that arginine deprivation induced a more potent reduction in translation than leucine does over time (Figure 66B). Adding back the respective amino acid to the cell reversed the translational blockage in a stress- and time-dependent fashion (Figure 66B). To confirm this finding, we read out the protein synthesis by using a fluorimetric OPP-Alexa Fluor 488 assay (Section 3.4.6.). Again, representative for 4 h leucine or arginine starvation, we could show that the decrease in protein translation was more potent upon arginine deprivation (Figure 66B). Next, we checked the translational outcome upon leucine deprivation in the GCN2^{-/-} and GCN1^{-/-} cells. Using both described assays, we found that the deficient cell lines did not block translation as wild-type cells upon leucine deprivation over time (Figure 66C). This finding hints

that eIF2 α is not phosphorylated in the GCN1 and GCN2 deficient cell lines. Therefore, the detection of phospho-eIF2 α by immunoblotting in figure 64 is most likely due to the property of the antibody. Combined, GCN1 and GCN2 loss affected the translation (initiation) upon amino acid stress.



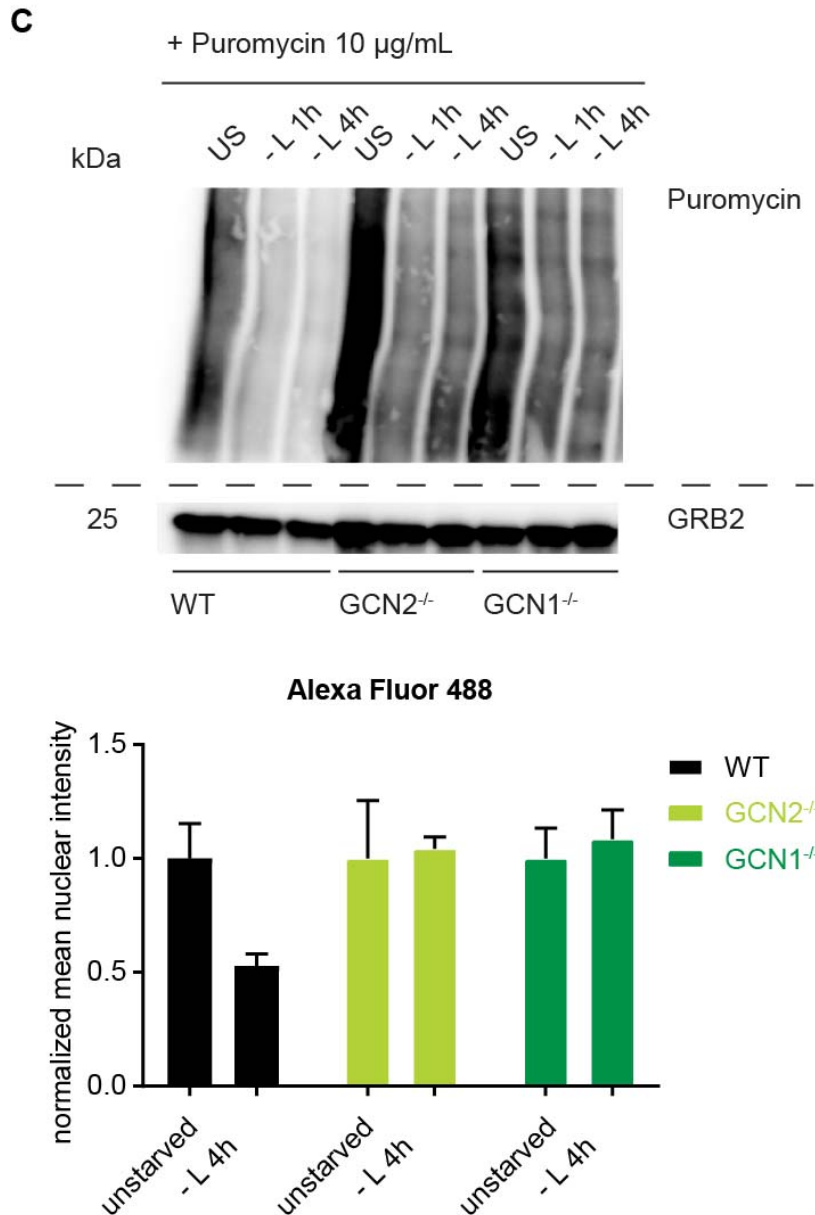


Figure 66. Translational shut-down upon amino acid stress is GCN1 and GCN2 dependent. (A) Our experimental setup for immunoblotting: amino acid starvation (- AA) is applied to cells for an indicated timepoint (X) and a second set of amino acid-starved cells are additionally resupplemented with the depleted amino acid (+ AA) for 1 h prior to cell lysis and immunoblotting. Cells growing for the indicated times in normal culture conditions are displayed as unstarved (US). Puromycin (10 µg/mL) was added 10-15 min before cell lysis. (B) Immunoblot of 3T3 wild-type (WT) lysate treated as described in A for leucine and arginine depletions (- L - R) over time (1h, 4h and 8h). GRB2 was used as loading control. The same setup was applied to OPP-Alexa Fluor 488 quantification, comparing 4 h of stress exposure to unstarved condition. Cycloheximide (CHX, 1 µM) was used as control (translation inhibitor). (C) Same as B, except: leucine starvation for 1 h and 4 h in 3T3 wild-type (WT), GCN2 knockout (GCN2^{-/-}) and GCN1 knockout (GCN1^{-/-}) background. (B+C) Data are depicted as one of three independent experiments.

Overall, arginine and leucine deprivation showed no difference in their time-dependent induction of GCN2 mediated eIF2 α phosphorylation. However, quantitative arginine deprivation induced a more potent translational reduction than leucine deprivation. Moreover, GCN1 and GCN2 presence was necessary for translational shut-down upon amino acid stress.

4.5. Mechanistic analysis of the amino acid stress-regulated mTORC1 signaling

4.5.1. Overview

Amino acid limitation leads to the inactivation of the mTORC1 and the activation of the GCN2 pathways to shutdown protein synthesis in the cellular environment²⁴. Links between the mTORC1 and the GCN2 networks were suggested by Averous *et al.*¹⁷⁹, who postulated in MEFs that GCN2 contributes to the mTORC1 suppression upon leucine stress in an ATF4-independent way. Another key publication was the GCN2-ATF4 dependent regulation of SESTRIN2, the leucine sensor of mTORC1, sustaining suppression of the mTORC1 activity upon prolonged starvation (24 h)³⁴⁴. However, molecular and mechanistic connections of both amino acid signaling pathways are not fully understood. Here, we made use of our genetically modified set of cell lines to provide evidence for a potential interaction of these networks mainly driven by our proposed GCN1-GCN2-ATF4 axis (Section 4.4.).

4.5.2. Interplay of the mTORC1 and the GCN2 amino acid sensing networks

In our multi-omics study (Section 4.2.), we found that the GCN1-GCN2 cascade regulates the same ATF4-mediated processes (e.g. mitochondrial 1C-metabolism or amino acid transport) upon leucine stress as recently reported by insulin-stimulated mTORC1²⁶. In this context, we highlighted that the ATF4 induction is highly dependent on the role of GCN1 in activating GCN2 at its autophosphorylation site (Section 4.4.). A further hint for the connection of the GCN2 and mTORC1 pathways was the time-dependent regulation of mTOR targets for translational control, as identified in our phosphoproteomics data (Section 4.2.4.2.; Figure 44). Despite many remaining questions about these two amino acid response networks, we focused on addressing the interplay with regard to the GCN1 involvement upon leucine depletion. Therefore, we measured active mTORC1 by the phosphorylation of its downstream targets p70S6K at threonine 389 (T389) and 4EBP1 at threonine 37/46 (mouse:T36/45)³⁰⁵.

First, we investigated the phosphorylation of the key mTORC1 targets over time (1 h, 4 h and 8 h) under leucine deprivation in wild-type 3T3 cells by immunoblotting (Figure 67A). In line with the literature¹⁷⁹, we highlighted the inactive status of mTORC1 by no phosphorylation of p70S6K and 4EBP1 at short-term leucine deprivation (1 h) in contrast to normal growth state or

resupplementation of leucine (Figure 67B). In this context, we also underlined the opposite effect having GCN2 active (phospho-GCN2 T898) when mTORC1 is off at 1 h leucine starvation (Figure 67B). Interestingly, and already shown by others^{344,367}, we verified that mTORC1 was reactivated at prolonged leucine starvation (4 h and 8 h) (Figure 67B). To confirm these findings, we performed phospho-Flow analyses for 1 h and 4 h of leucine depletion (Section 3.4.7.). We detected the same outcome, where the intensities for phospho-4EBP1 T36/45 and phospho-S6 S235/S236 (a downstream target of p70S6K) were shifted towards the unstarved control at 4 h leucine stress (Figure 67C). Combined, we could reproduce in our system the findings from literature^{179,344,367} and confirmed our phosphoproteomics data (Section 4.2.4.2.; Figure 44) where mTORC1 is inactive upon short-term and reactivated upon prolonged leucine deprivation.

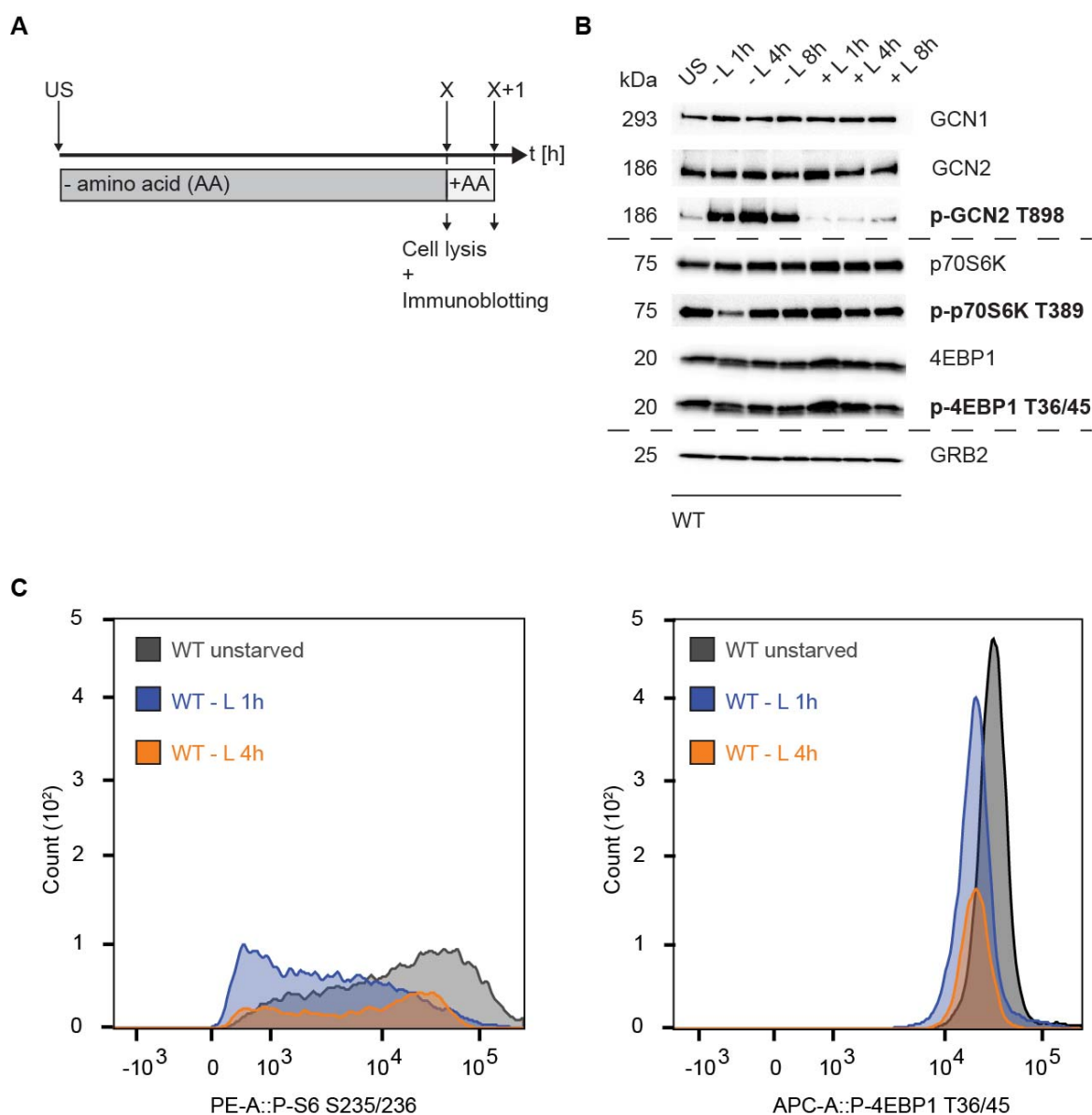


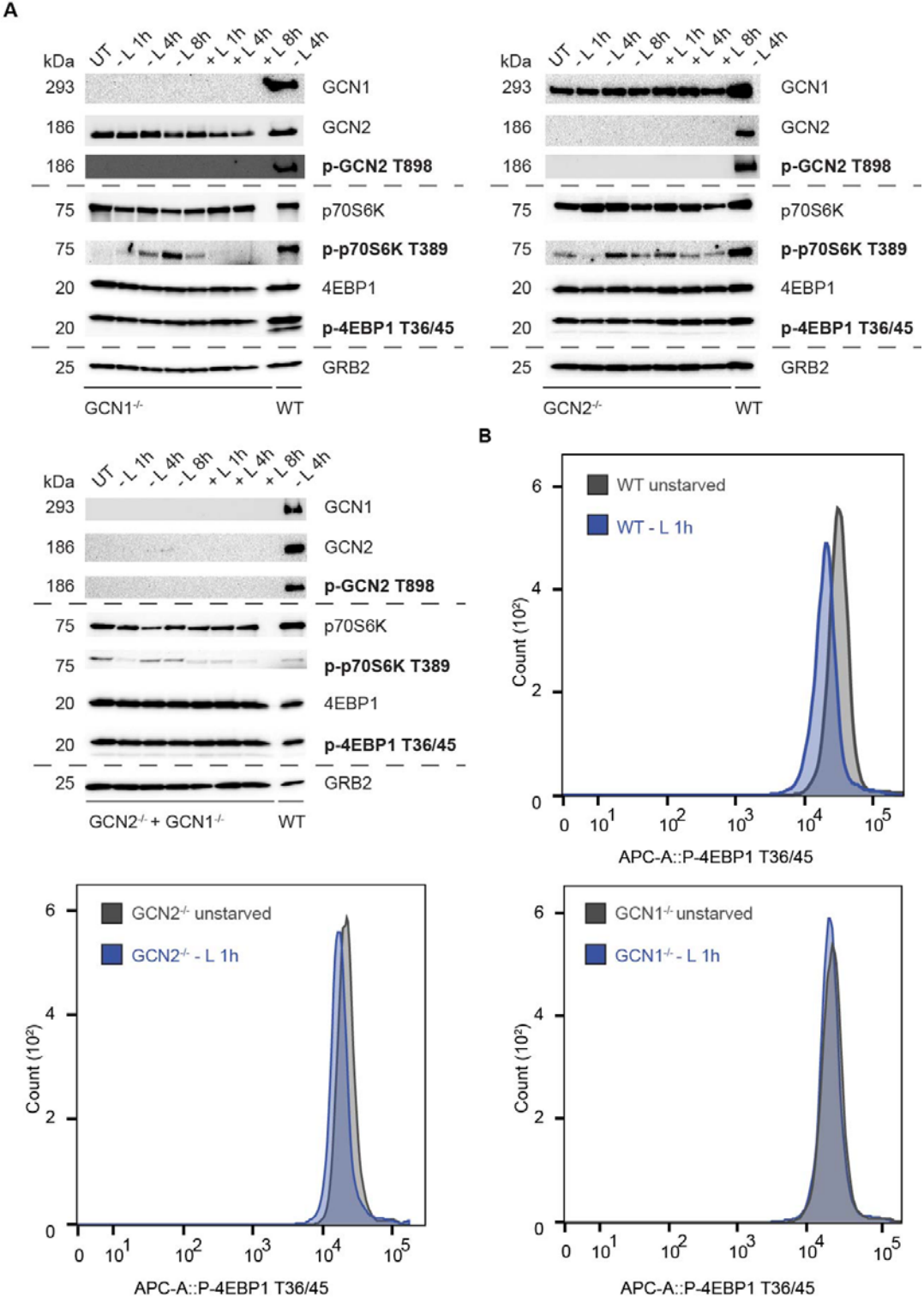
Figure 67. Short-term amino acid stress triggers mTORC1 suppression. (A) Our experimental setup for immunoblotting: amino acid starvation (- AA) is applied to cells for an indicated timepoint (X) and a second set of amino acid-starved cells are additionally resupplemented with the depleted amino acid (+ AA) for 1 h prior to cell lysis and immunoblotting. Cells growing for the indicated times in normal culture conditions are displayed as unstarved (US). (B) Immunoblot of 3T3 wild-type (WT) lysate leucine-starved (- L) for 1h, 4h and 8 h as described in A. GRB2 was used as loading control. In bold, changes of the mTORC1 targets. (C) Same as B, except: Flow analysis of leucine starvation for 1 h and 4 h in 3T3 wild-type (WT) cells measuring p-S6 (S235/236) in the PE channel and p-4EBP1 (T36/45) in the APC channel. (B+C) Data are depicted as one of three independent experiments.

Next, we investigated the involvement of GCN1 and GCN2 in controlling mTORC1 activation upon leucine stress. Interestingly, we found that the phosphorylation events of both mTORC1 targets did not follow the same pattern (Figure 68A). In other words, 4EBP1 was phosphorylated upon leucine stress at 1 h in contrast to p70S6K in the GCN1 and/or GCN2 deficient cells. To verify this finding, we performed phospho-Flow tracking the phosphorylation of 4EBP1 at T36/45 upon leucine stress at 1 h in the GCN1 and GCN2 knockout cell lines. Again, we detected the same phenomenon (Figure 68B). Upon prolonged starvation, the deficient lines regulated both mTORC1 targets as wild-type cells (Figure 68A). Combined, our data point into the direction that GCN1-GCN2 signaling might contribute to mTORC1 suppression at short-term amino acid stress via the regulation of 4EBP1.

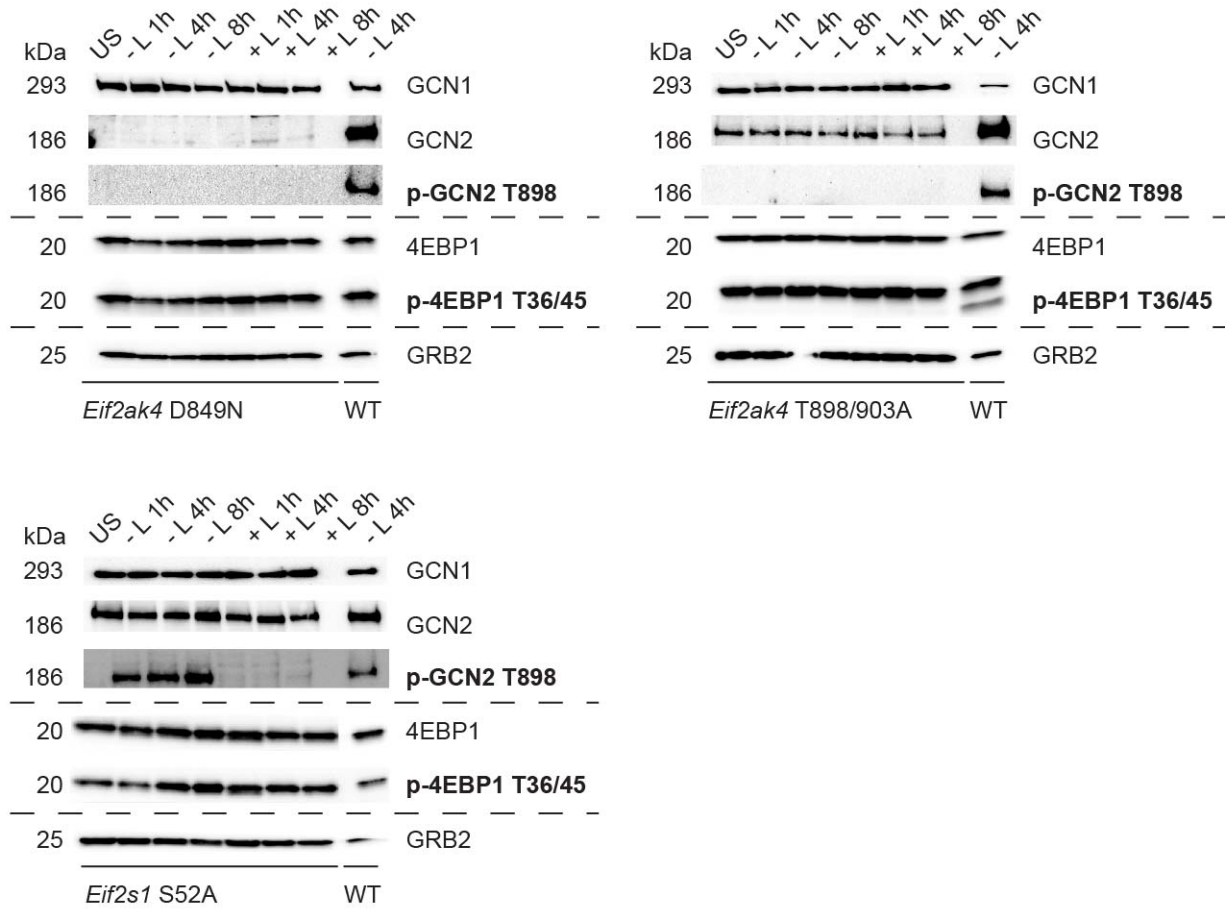
Next, we analyzed the phosphorylation of 4EBP1 in the ‘catalytic-’, ‘autophospho-’ and ‘target-dead’ cell lines by immunoblotting upon leucine stress and across time. Consistent with the GCN1 and/or GCN2 knockout lines, the GCN2 mutated lines (‘catalytic-’ and ‘autophospho-dead’) showed the same results meaning that 4EBP1 was phosphorylated across time (1 h, 4 h and 8 h) (Figure 68C). In contrast, the eIF2 α mutant line ‘mimicked’ the wild-type line showing no 4EBP1 phosphorylation at 1 h leucine stress (Figure 68C). From our perspective, this genotypic difference in regulating 4EBP1 can be explained by the loss of the phospho-GCN2-ATF4 axis in the GCN2 inactive lines, which might be relevant to block 4EBP1 phosphorylation at early amino acid starvation. Recently, 4EBP1 regulation was linked to ATF4 by Vasudevan *et al.*³⁷³, Tameire *et al.*²⁰⁷ and Torrence *et al.*²⁶, who showed that 4EBP1 is a direct transcript of the ATF4-mediated stress program relevant to regulate translation in oncogenic context²⁰⁷ or in response to bacterial infection³⁷³.

Next, we asked if the difference between 4EBP1 versus p70S6K phosphorylation is a leucine stress specific phenomenon. Therefore, we starved the GCN1 and GCN2 pro-/deficient cells for leucine, arginine or lysine at early (1 h) and late (4 h) time points. As shown in figure 68D, arginine deprivation induced the same phenotype that was already described for leucine deprivation. For

the 4EBP1 target, lysine deprivation does not show a difference at given time points across the different genotypes underlining the sensitivity of mTORC1 in sensing amino acids. Together, we could confirm that the mTORC1 targets are regulated in the respective genotypes upon arginine and leucine deprivation in a similar way.



C



D

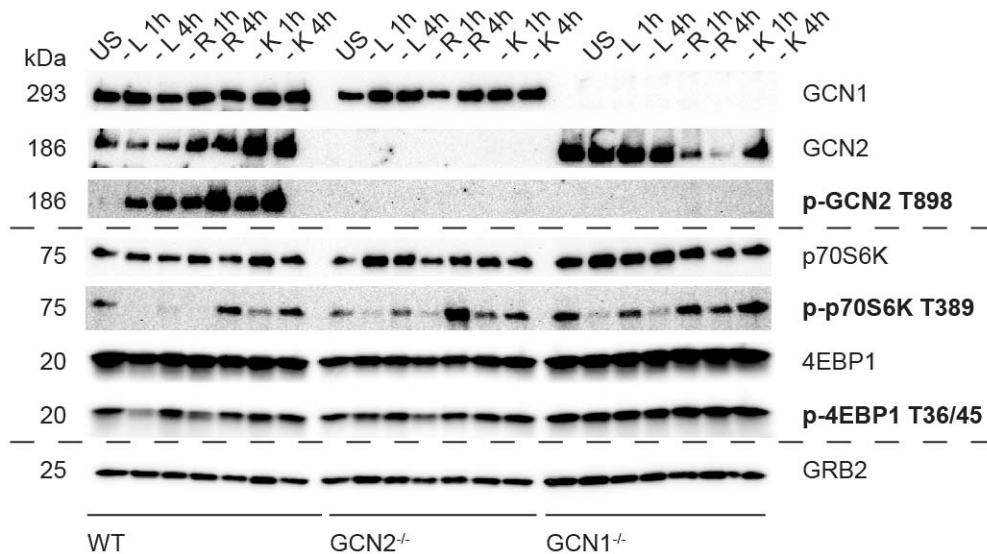


Figure 68. GCN1-GCN2 signaling contributes to mTORC1 suppression upon amino acid stress via 4EBP1 regulation. (A) Immunoblots of 3T3 cell lysates stimulated with unstarved condition (US), leucine-starvation (- L) or leucine-resupplementation (+ L) for 1 h, 4 h and 8 h. GRB2 was used as loading control. In bold, the relevant changes of mTORC1 targets in each analyzed genotype: GCN1 (*GCN1*^{-/-}), GCN2 (*GCN2*^{-/-}) and double (*GCN2*^{-/-} + *GCN1*^{-/-}) knockouts. Wild-type (WT) stimulated cells at 4 h served as

control. (B) Flow analysis of the 4EBP1 phospho-target (T36/45) measured in the APC channel of unstarved and leucine-starved (1 h) 3T3 wild-type (WT), GCN2 (*GCN2*^{-/-}) and GCN1 (*GCN1*^{-/-}) deficient cells. (C) Same as in A, except: lysates of ‘catalytic-dead’ GCN2 (*Eif2ak4* D849N), ‘target-dead’ eIF2 (*Eif2s1* S52A) and ‘autophospho-dead’ GCN2 (*Eif2ak4* T898/903). (D) Same as A, except: arginine (- R), leucine (- L) and lysine (- K) starvations were analyzed in wild-type (WT), GCN1 (*GCN1*^{-/-}) and GCN2 (*GCN2*^{-/-}) knockouts for 1 h and 4 h. (A-D) Data are depicted one of two representative gels or experiments.

Overall, we discovered that the GCN1-GCN2 cascade contributes to mTORC1 suppression at short-term amino acid stress exposure. The loss of the GCN1-GCN2-ATF4 axis solely affected the 4EBP1 and not the p70S6K target of mTORC1 at early leucine or arginine deprivation. Consequently, we designed a model in which we argue that the GCN1-GCN2-ATF4 axis regulates mTORC1 activity upon leucine stress by modulating 4EBP1 and finally translation initiation (Figure 69). This is a process, which is based on a similar principle in which SESTRIN2 inhibits mTORC1 (Section 1.3.6.; Figure 17)³⁴⁴.

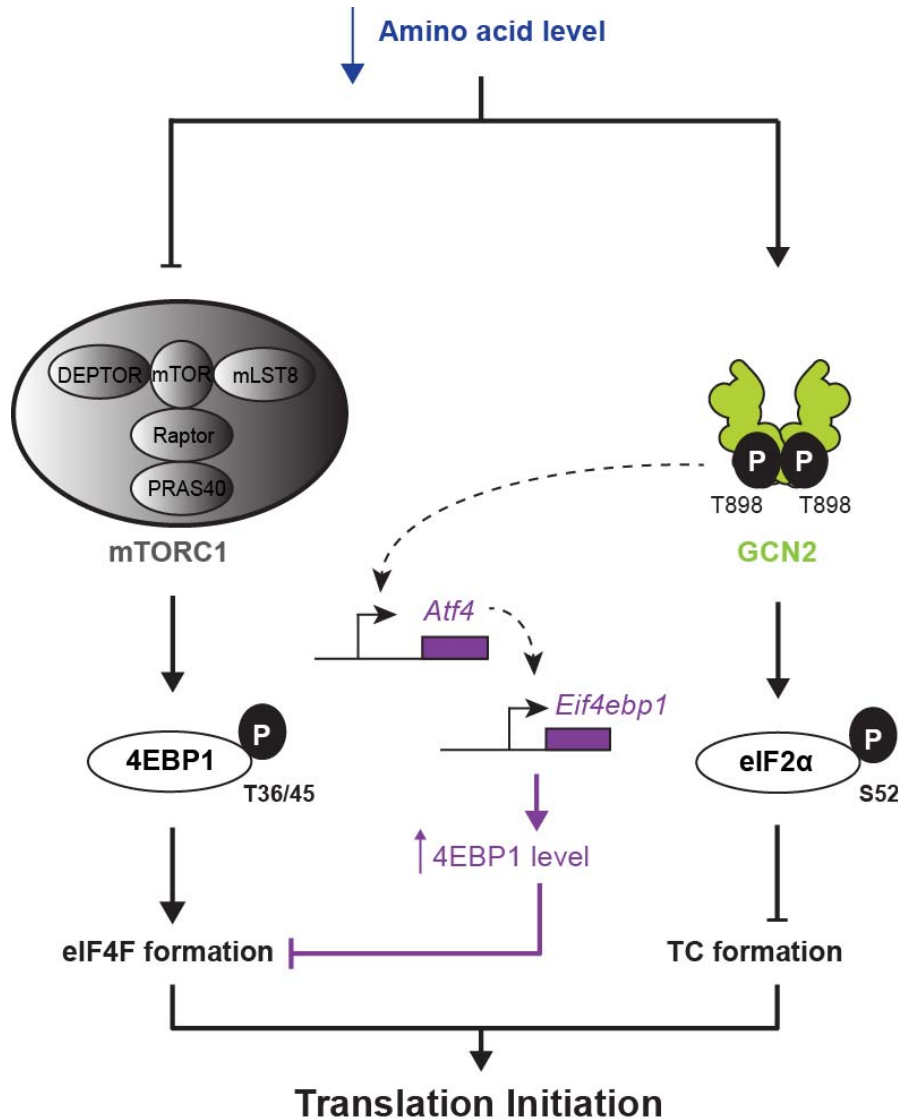


Figure 69. Our refined working model of the mTORC1 and GCN2 interplay upon amino acid stress.

Our refined working model of the mTORC1 and GCN2 interplay upon amino acid stress (blue arrow down): In our perspective GCN2 (light green) contributes to mTORC1 (grey) suppression via the induction of 4EBP1 (encoded by *Eif4ebp1*; purple) mediated by the ATF4-stress transcriptional program upon short-term amino acid stress. 4EBP1 is the downstream target of mTORC1 that is a direct ATF4 transcript (ATF4-4EBP1 axis) and regulates the eIF4F formation at the 5' cap for translation initiation^{26,29,95}. Active GCN2 (autophosphorylated at T898)⁶⁷ phosphorylates eIF2 α and thereby blocks ternary complex formation (TC) crucial for translation initiation as well^{77,94}.

4.6. Molecular verification of genetically modified cell lines in biological context

4.6.1. Overview

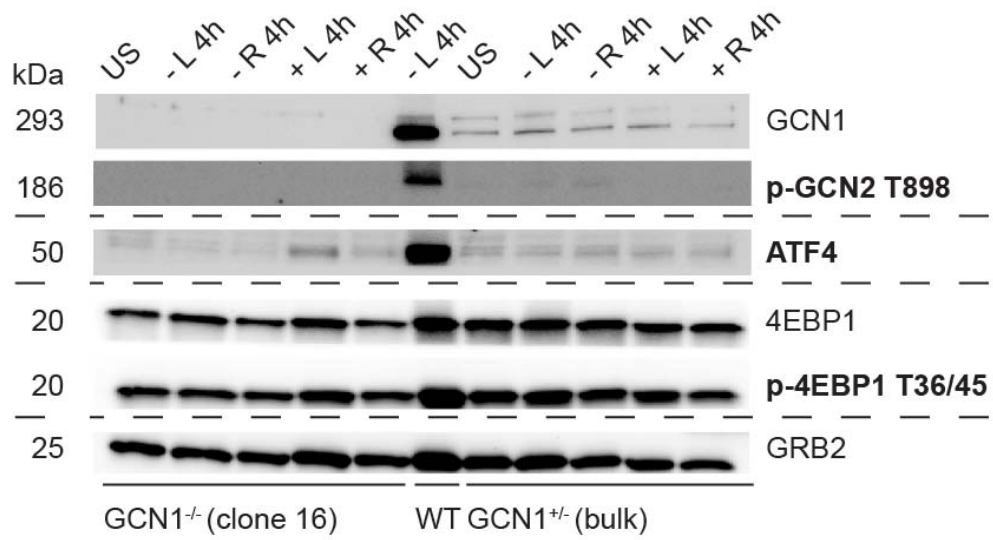
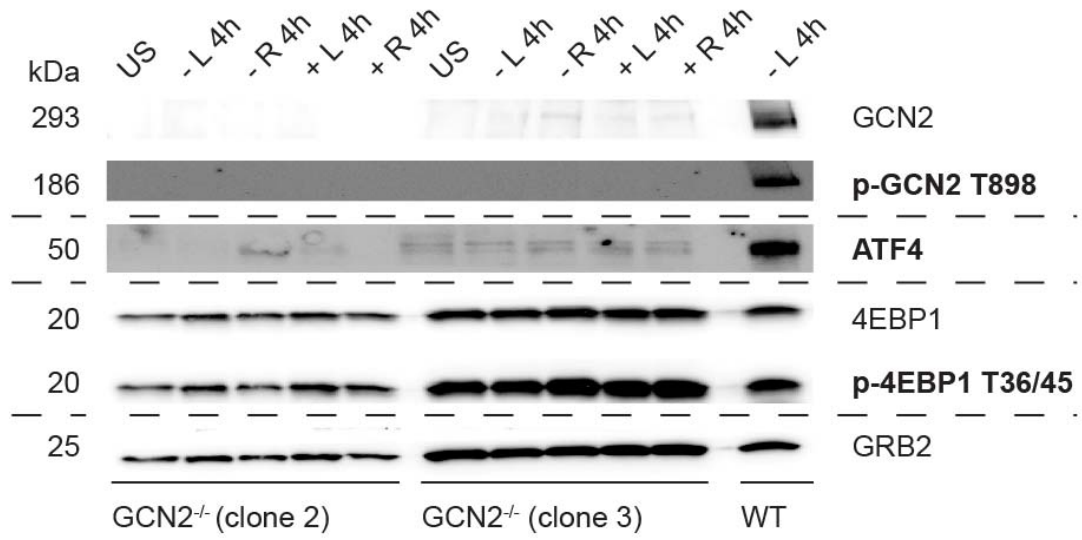
In this thesis, we studied the roles of GCN1 and GCN2 by establishing CRISPR/Cas9-induced single-cell-based knockout clones, which were expanded to cell lines for further functional characterization at the molecular level. However, the single-cell-based technique has some limitations: (i) The procedure is technically challenging coming along with a low positive clonal outcome; (ii) Interclonal heterogeneity could occur; (iii) Multiplexed gene targeting is restrained; (iv) Off-target mutagenesis could be a confounding factor; (v) Technical restrictions in gRNA efficiency and transfection delivery might happen^{511,512}. Therefore, we performed a controlled validation of the GCN1 and GCN2 deficient single-cell clones and their clonal counterparts to ensure no clonal artifacts, which could otherwise result in a disturbed biological interpretation (Section 4.6.2.). In addition, we characterize the ISR-mTOR connection in other murine cell systems (Section 4.6.2.). Moreover, we started to perform rescue experiments in GCN1 and GCN2 deficient cells to regain the wild-type phenotype (Section 4.6.3.).

4.6.2. GCN1 and GCN2 deficiency in different clonal and murine cell systems

The multi-omics approach and further functional studies at the gene, the cell and the protein level (Sections 4.2.-4.5.) were solely conducted from a single-cell derived cell line with a GCN2 or GCN1 deficiency. In addition to that, we established a small number of genetically modified cell clones deficient in both proteins with the CRISPR/Cas9-mediated genome engineering approach (Table 31). Therefore, we aimed to verify our biological findings in further single-cell or bulk derived genetically GCN1 or GCN2 deficient cell lines to ensure biological consistency of our described findings. Moreover, we transferred and compared our data in two further murine cell systems: E14 cells and MEFs. To study the described attempts, we decided to track the autophosphorylation of GCN2, the induction of ATF4 and the phosphorylation of 4EBP1 at T36/45

as a proof of concept upon arginine and leucine starvation for 4 h by immunoblotting. The reason behind this was that we discovered in this thesis: (i) GCN1 regulates the autophosphorylation of GCN2 at T898 upon amino acid stress and consequently activates the ATF4-induced stress transcriptional response (Section 4.4.); (ii) mTORC1 is active over time upon amino acid stress in a GCN1 and/or GCN2 deficient background (Section 4.5.).

We established two GCN2 knockout clones in 3T3 cells from which clone 2 was expanded and used in this thesis (Table 31). Consistent with clone 2, clone 3 showed the same biological pattern in activating the mTORC1 (phospho-4EBP1 T36/45) and suppressing the GCN2 (phospho-GCN2 T898 and ATF4) pathways upon leucine and arginine deprivation at 4 h (Figure 70A). For GCN1, only one single clone (clone 16) was established in 3T3 cells by CRISPR/Cas9 (Table 31). Therefore, we created a GCN1^{+/-} bulk derived cell line with a lentiviral-based CRISPR/Cas9 approach (Section 3.2.3.2.). Importantly, the monoallelic loss of GCN1 was sufficient to prevent the induction of the phospho-GCN2-ATF4 axis and to activate mTORC1 (Figure 70A). Additionally, we screened the same experimental setup in MEFs and E14 cells. Again, the knockout lines show the same described pattern in regulating mTORC1 and GCN2 networks as in the 3T3 counterpart cells (Figure 70B). Combined, the consistent outcome manifested that all three murine cell systems (MEFs, 3T3 and E14 cells) equivalently control the GCN2 and the mTORC1 networks upon amino acid stress. Thus, immortalization of the fibroblasts (3T3 cells) did not affect the overall findings described in sections 4.3.-4.5.

A

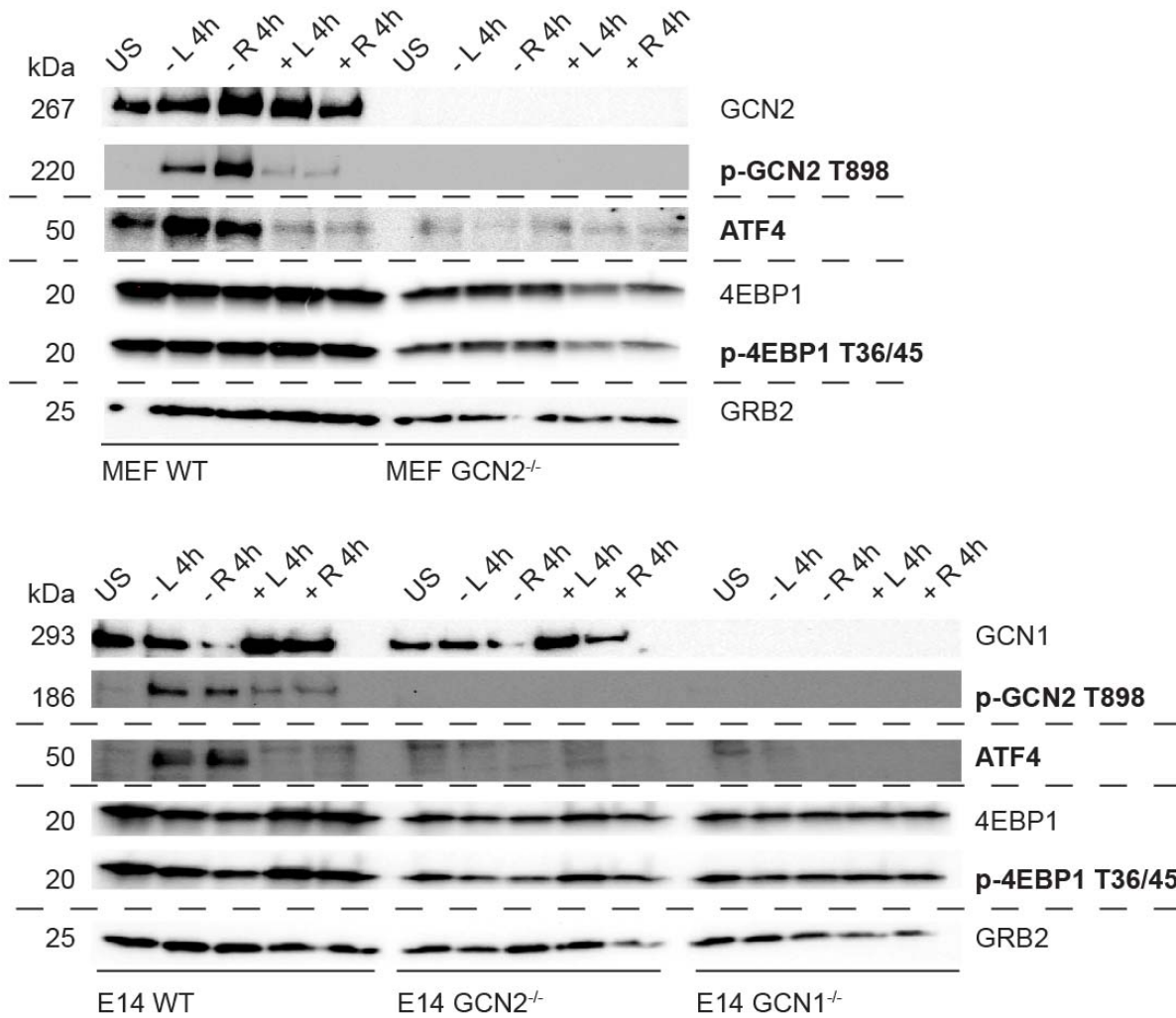
B

Figure 70. Regulation of mTORC1 and GCN2 key targets is not cell- or stress- specific in our studied murine cell systems. (A+B) Immunoblots of leucine (- L) or arginine (- R) starved and leucine (+ L) or arginine (+ R) resupplemented (+ L) lysates of MEFs, 3T3 or E14 cells. Starvation was applied for 4 h and unstarved condition (US) served as internal control. GRB2 was used as loading control. In bold, major changes due to the genetically modification of the GCN1 and GCN2 deficiency (GCN1^{-/-} and GCN2^{-/-}) in contrast to wild-type (WT). Different cell clones as well as single versus bulk derived deficient lines are illustrated. Data are depicted as one of two representative gels. The clones are summarized in table 31.

In conclusion, all genetically engineered or primary GCN1 and GCN2 deficient cell lines in MEFs, E14 or 3T3 cells showed the same functional biological behavior as their genetic counterpart primarily used in this thesis.

4.6.3. Reconstitution of the GCN1 and GCN2 phenotype

We started to reconstitute the GCN1 or GCN2 phenotype in the respective GCN1 or GCN2 deficient cells by rescue experiments. Therefore, we transiently transfected the deficient cells with

Twin-Strep-GCN1 or GCN2-3xFLAG constructs and read out their overexpression by immunoblotting (Figure 71). To verify the activation of the ISR upon amino acid stress in the reconstituted lines, we decided to track the ATF4 induction. Unexpected, we discovered that the reconstituted cell lines induce ATF4 already in normal growth state (Figure 71) arguing for a ‘stress response’ activated during transfection. This result might explain why in our interactomics study the overexpressed GCN1 cells showed a different proteomic signature to the parental wild-type cells (Section 4.2.5.). However, at this stage we do not know if the ATF4 induction is triggered by the GCN2 cascade.

Combined, we found that reconstitution of GCN1 and GCN2 phenotype in the deficient cell lines by transient transfection triggers already in non-starved condition an increase in the ATF4 induction. Thus, in future perspective, we aim to establish stable GCN1 and GCN2 cell lines to apply amino acid stress targeting the GCN2-ISR activation.

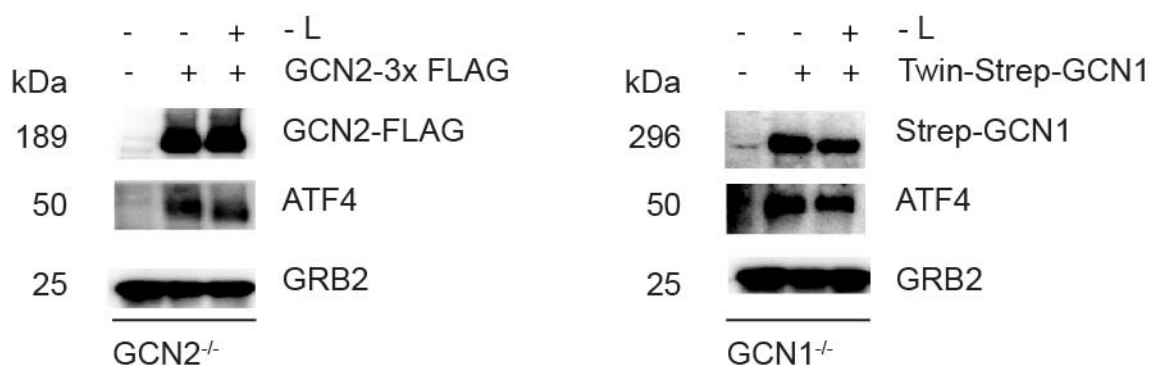


Figure 71. GCN1 and GCN2 reconstituted cells induce ATF4 already at unstarved condition. Immunoblots of 3T3 cell lysates transiently transfected with GCN2-3xFLAG or Twin-Strep-GCN1. GCN2 deficient (GCN2^{-/-}) or GCN1 deficient (GCN1^{-/-}) cells were kept in leucine-starvation or in normal growth medium during transfection. GRB2 was used as loading control.

4.7. Chemical large-scale bioactive kinase compound screen for GCN2 inhibition

4.7.1. Overview

GCN2 has long been considered to be an attractive target for cancer therapeutic development due to the following reasons: (i) The GCN2 pathway is non-essential for either development or normal functions of cells and organisms⁵⁵; (ii) GCN2 is a kinase and can thus be targeted^{513,514}; (iii) Most cancer cells have elevated requirements for amino acids to sustain their growth programs^{49,205,241}. In this case, some cancer cells could become dependent on the GCN2 pathway to negotiate transient amino acid restriction. If GCN2 would be targeted by an inhibitor in

combination with another 'vulnerability', cancer cells would have a synthetically lethal response, which cannot be bypassed. For example, in low-ASNS acute lymphoblastic leukemia, the elimination of the GCN2-ISR in combination with asparagine reduction (asparaginase treatment) induces synthetic lethality²³⁹. By now, two allosteric (GCN2-IN-1 and GCN2-IN-6) and one ATP-competitive (GCN2iB) GCN2 inhibitors are available for research purposes^{239,247,248}. However, their application in clinical therapies remains to be seen.

In collaboration with the Max-Planck-Gesellschaft Lead Discovery Center in Dortmund, we aimed to hunt for novel GCN2 inhibitor candidates. Therefore, we performed a primary GCN2 compound library screen with known and available kinase inhibitors to identify hits, which modulate the GCN2-ISR in a defined way. Our findings as presented in the following, lay the groundwork for a prospective second screen with novel structural compounds.

4.7.2. Primary GCN2 compound library screen: Class-IV-PI3K inhibitors prevent the GCN2-ISR upon leucine stress

In collaboration with Dr. Jan Eickhoff from the Max-Planck-Gesellschaft Lead Discovery Center in Dortmund, we developed a scalable bioactive compound screen to identify specific GCN2 inhibitors. In total, the library contained 3,876 commercially available bioactive reference compounds including many kinase inhibitors, which were screened using our *Ddit3*::mCherry and *Ddit3*::NanoLuc-PEST reporter cell systems (Sections 4.1. and 4.2.). The ISR-regulated transcription factor CHOP (encoded by *Ddit3*) bypasses the translational blockage induced by amino acid stress (Sections 4.2. and 4.4.). Combining this feature with GCN2 deficiency enabled us to perturb and measure the ISR in a GCN2- and amino acid stress-dependent way (Section 4.2). Based on several pre-studies described in the other chapters, we used leucine deprivation as the starvation reagent of choice (Sections 4.2. - 4.6.).

In a first step, 3,876 compounds were screened together with Dr. Jan Eickhoff in the *Ddit3*::mCherry and *Ddit3*::NanoLuc-PEST reporter cell systems upon leucine stress (28 h) to define compounds with a half maximal inhibitory concentration (IC₅₀) lower than 30 µM (Figure 72A). This screen identified 58 active compounds, which can be classified based on their structure and mode of action. This classification in line with literature research, reduced the pool of follow-up 'hits' to 28 compounds (Table 32). One class of the hit-compounds targets class-IV phosphoinositide 3-kinase (PI3K)-related kinase (PIKK) family members, which include along with mechanistic target of rapamycin (mTOR)^{254,260,515-518}, DNA-dependent protein kinase (DNA-PK)⁵¹⁹, ataxia-telangiectasia-mutated (ATM) and ataxia telangiectasia and Rad3-related (ATR) kinases^{520,521}. Interestingly, members of this family (compounds #12, #18 and #23) reduced the mCherry reporter activity in a similar range as the commercially available GCN2 inhibitor GCN2-

IN-1/A-92 (compound #5) (Figure 72B). This information provided us a further hint for the GCN2-mTOR inter-relationship that matched with the described connection of both kinases as referred to many times in this thesis.

Table 32: Compound categorization

Compound	Internal nomenclature	Target	IC₅₀ <i>Ddit3</i> [μM]	Part of the primary screen
R406	#1	Syk/FLT3	unknown	no
Palbociclib	#2	CDK4/6	unknown	no
Sunitinib	#3	VEGFR2/PDGFRβ	unknown	no
WZ4002	#4	EGFR	unknown	no
A-92/GCN2-IN-1	#5	GCN2	unknown	no
Bosutinib	#6	Src/Abl	unknown	no
Vemurafenib	#7	B-RAF	unknown	no
Lestaurtinib	#8	JAK2/FLT3/TrkA	unknown	no
RAF265	#9	RAF/VEGFR2	unknown	no
ML 786	#10	RAF	0.484	yes
PH-797804	#11	p38α/p38β	0.743	yes
Sapanisertib/INK-128	#12	mTOR	0.025	yes
PF 670462	#13	CK1ε and CK1δ	0.485	yes
PIK-75	#14	DNA-PK/p110α	0.0868	yes
GSK2656157	#15	PERK	unknown	no
p38 Inhibitor	#16	P38	0.874	yes
CDK7 Inhibitor	#17	CDK7	0.15	yes
Omipalisib/GSK458	#18	PI3K	0.09	yes
Tropisetron	#19	5-HT3 receptor	0.37	yes
Amcinonide	#20	NO release	< 0.008	yes
Mupirocin	#21	isoleucyl-transfer RNA	0.0943	yes
Skepinone-L	#22	p38	0.182	yes
ETP-46464	#23	mTOR/ATR/ATM	0.779	yes
WYE-125132	#24	mTOR	0.0956	yes
GZD824	#25	pan-Bcr-Abl	0.135	yes
Ralimetinib	#26	p38	0.1	yes
GSK2606414	#27	PERK	unknown	no
GCN2-IN-6	#28	GCN2/PERK	unknown	no

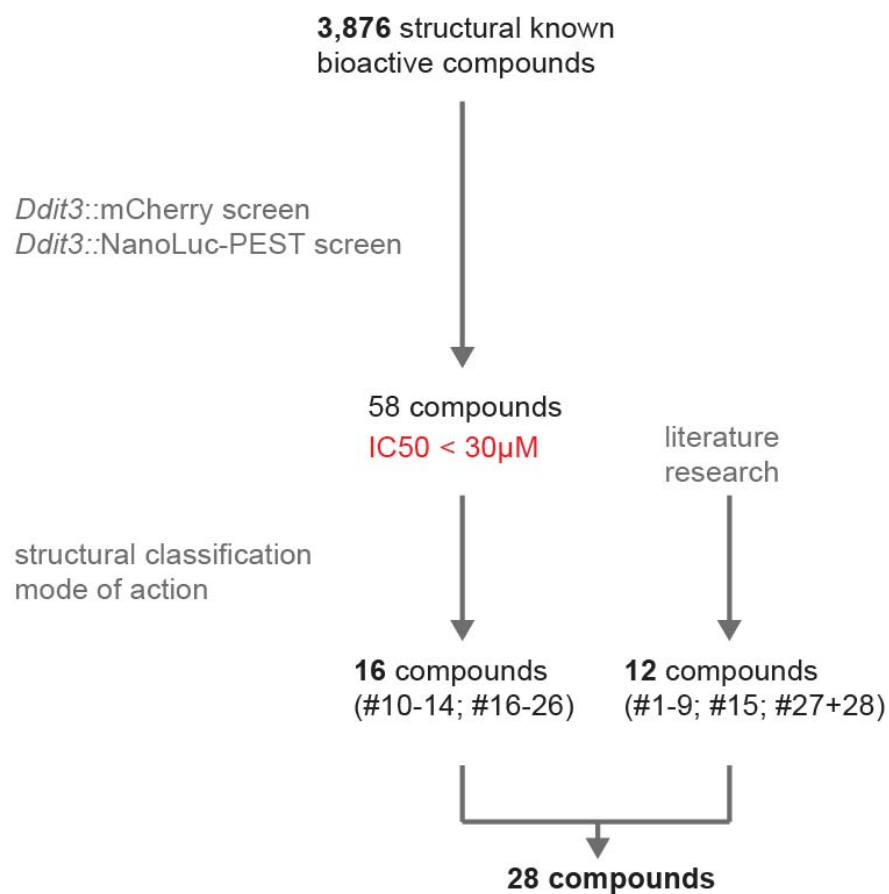
GCN2iB	#29	GCN2	unknown	no
BAY1895344/Elimusertib	#30	ATR	unknown	no

Based on this pre-screening, we used two different techniques (*Ddit3* reporter systems and immunoblotting) to track the chemical perturbation induced by compound treatment to unravel the manipulation of the mammalian ISR upon amino acid stress in cellular context.

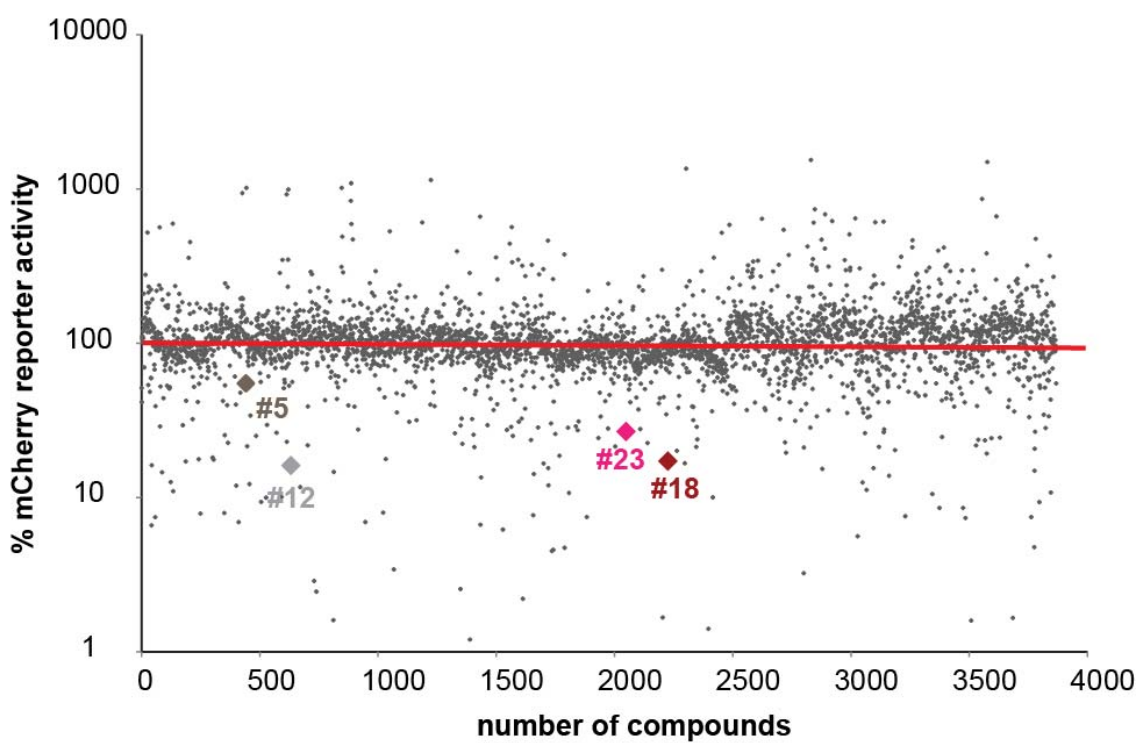
We started with the investigation of the inhibitory potential of our 28 compounds at the protein level by immunoblotting (Section 3.6.2.). Here, we leucine-starved the wild-type 3T3 cells for 8 h. This time point was chosen, because we know from several previous experiments that the ISR is highly activated at 8 h (Section 4.2.; Figure 24). Moreover, we leucine-starved the cells in combination with a high drug concentration of the respective compound (10 μ M), which 'mimicked' the conditions the primary screen was conducted (Figure 72B). At the protein level, we tracked the key players of the ISR (ATF4, phospho-eIF2 α S52A and phospho-GCN2 T898) in addition to mTOR (phospho-mTOR S2448) and PERK (phospho-PERK T980) kinase activities. PERK autophosphorylation at T980 was analyzed to exclude activation of PERK signaling⁷² by leucine stress in combination of compound treatment. mTORC1 activity was read-out by mTOR phosphorylation at S2448, which is induced by PI3K-AKT signaling and is responsive to traditional mTOR inhibitors (rapamycin, Torin-1)^{277,278} (Section 1.3.2.; Figure 11).

Using the ER stress inducing reagent thapsigargin as internal control, we discovered that PERK was not activated either upon leucine stress or in combination with the compound treatments (Figure 72C). This data matched our findings that PERK is not autophosphorylated and consequently not activated upon amino acid stress (Sections 4.2.; Figure 27). However, we found that several compounds affected ATF4 induction (Figure 72C). Latter did not always correlate with a loss of GCN2 autophosphorylation at T898 (e.g. compound #6). Interestingly, we detected rare cases of complete loss of eIF2 α phosphorylation (e.g. compounds #12 and #28). In addition, we found that mTOR phosphorylation was repressed by several inhibitors (e.g. compounds #12 and #18). Also, some inhibitors blocked the phosphorylation of mTOR and GCN2 (e.g. compounds #5 and #12). Most importantly, we provided a further evidence that several class-IV-PI3K inhibitors (compounds #12, #18 and #23) prevented the activation of all ISR targets (ATF4, phospho-eIF2 α S52A and phospho-GCN2 T898) that was consistent to the mCherry pre-screen shown in figure 72B. Moreover, we verified that the reduction of loaded protein for compound #25 (pan-Bcr-Abl inhibitor GZD824) was a result of cellular toxicity induced by this drug, which is used in first-in-human clinical trial for CML^{238,251} (Figure 72D).

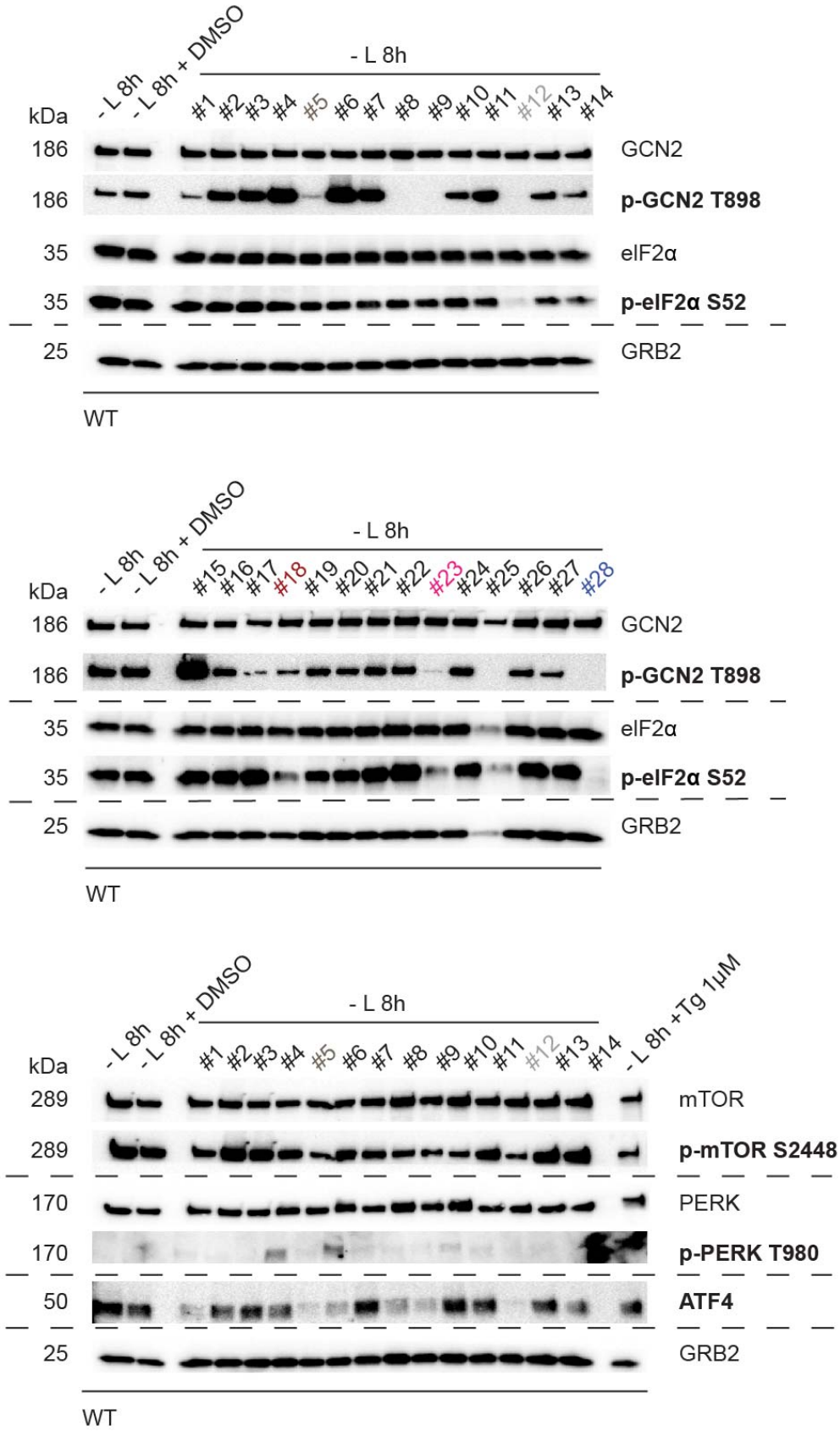
A

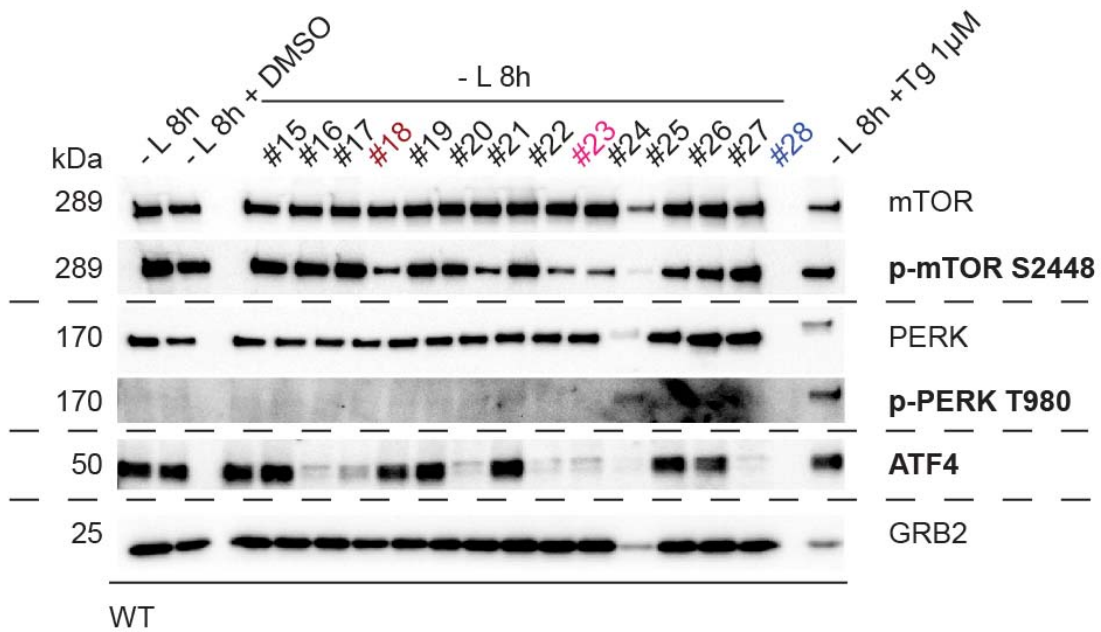


B



C





D

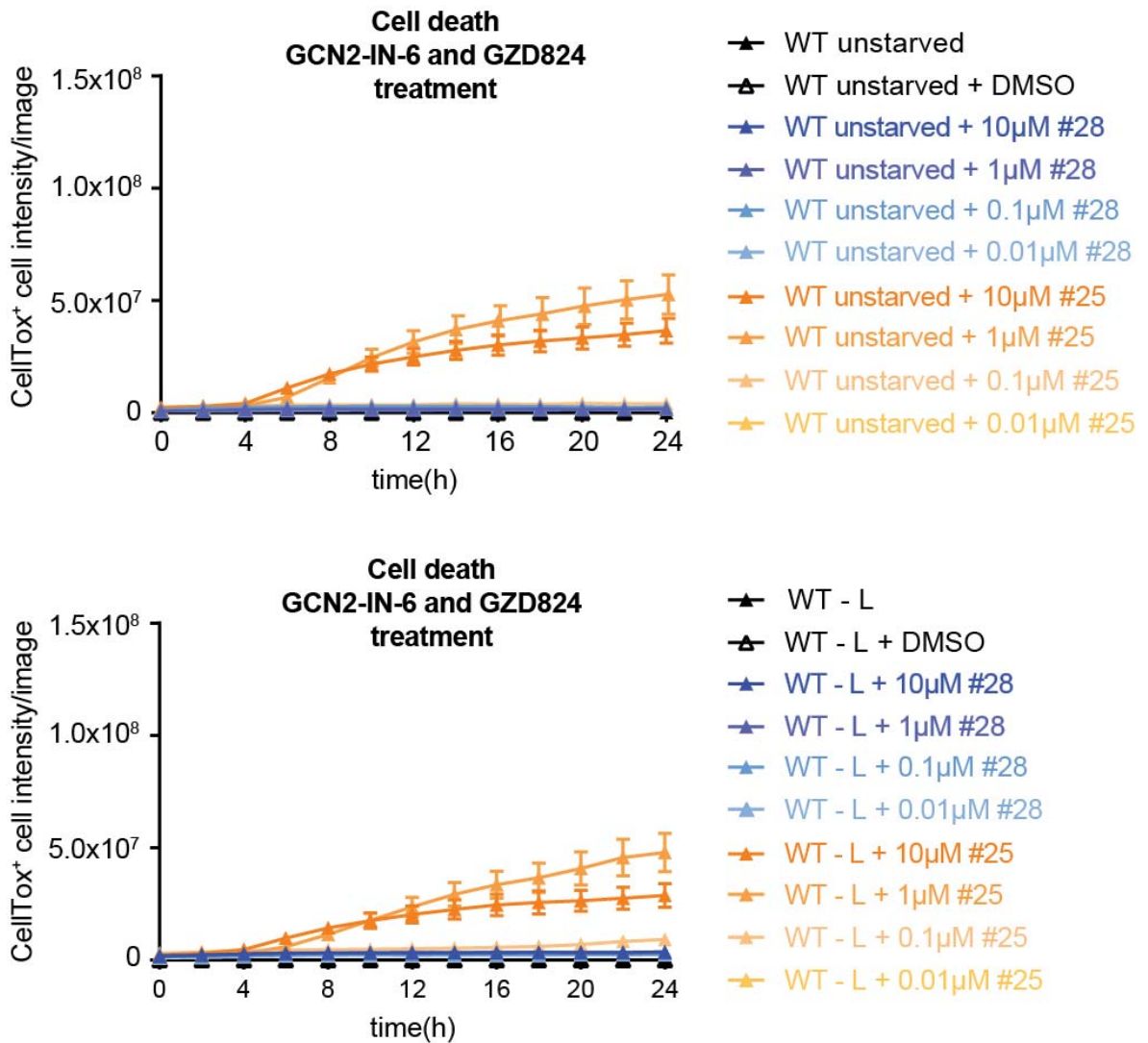


Figure 72. Primary GCN2 compound library screen: class-IV-PI3K inhibitors block the GCN2-ISR upon leucine stress. (A) Scheme of the experimental primary GCN2 compound library: from 3,876 structurally known bioactive compounds, 28 were used for further screening. (B) *Ddit3*:mCherry reporter activity read-out of all 3,876 compounds. Threshold is indicated in red. Some compounds below the threshold are color-coded. (C) Immunoblots of 3T3 wild-type (WT) cell lysates treated with 10 μ M of each compound (#1 - #28) upon leucine starvation (- L 8h). Thapsigargin treatment (Tg; 1 μ M) served as control. DMSO was used as vehicle and GRB2 was used as loading control. Color-coding of B matches to C. Compound classification and IC_{50} values are summarized in table 32. Changes due to the compound treatment are highlighted in bold. Data are depicted as one of two representative gels. (D) Quantification of cell death using CellTox green staining in 3T3 wild-type (WT) cells treated with GCN2-IN-6 (#28) or GZD824 (#25) over time of leucine starvation (- L) or unstarved condition. DMSO was used as vehicle. Data are depicted as mean + SEM of three independent experiments.

Next, we selected all compounds (a total of 12; compounds #1, #5, #6, #8, #9, #12, #17, #18, #21, #23, #24 and #28) suppressing the induction of ATF4 and implemented them in our *Ddit3*:NanoLuc-PEST reporter system. Shown many times in this thesis, ATF4 induction correlates with the CHOP induction at the protein and gene level and is highly regulated by GCN1-GCN2 upon amino acid stress (Sections 4.2. and 4.4.). As internal control, the PERK inhibitor GSK2656157 (compound #15) was used, which showed no block of CHOP induction and consequently a high luciferase signal upon leucine stress at 8 h (Figure 73A). In line with the loss of ATF4 induction (Figure 72C), all 12 compounds reduced the luciferase intensity upon leucine stress at 8 h (Figure 73A). Still, the potency of the signal was very different. For example, the luciferase signal for the treatment with the GCN2 inhibitor GCN2-IN-6 (compounds #28) was higher than for the mTORC1/C2 inhibitor sapanisertib (compounds #12). The same phenomenon was also detected upon arginine deprivation and prolonged stress exposure (Figure 73B+C). Combined, we highlighted that the prevention of ATF4 induction correlates with the block of CHOP induction. Also, the potency of the signal drastically varied between the tested compounds.

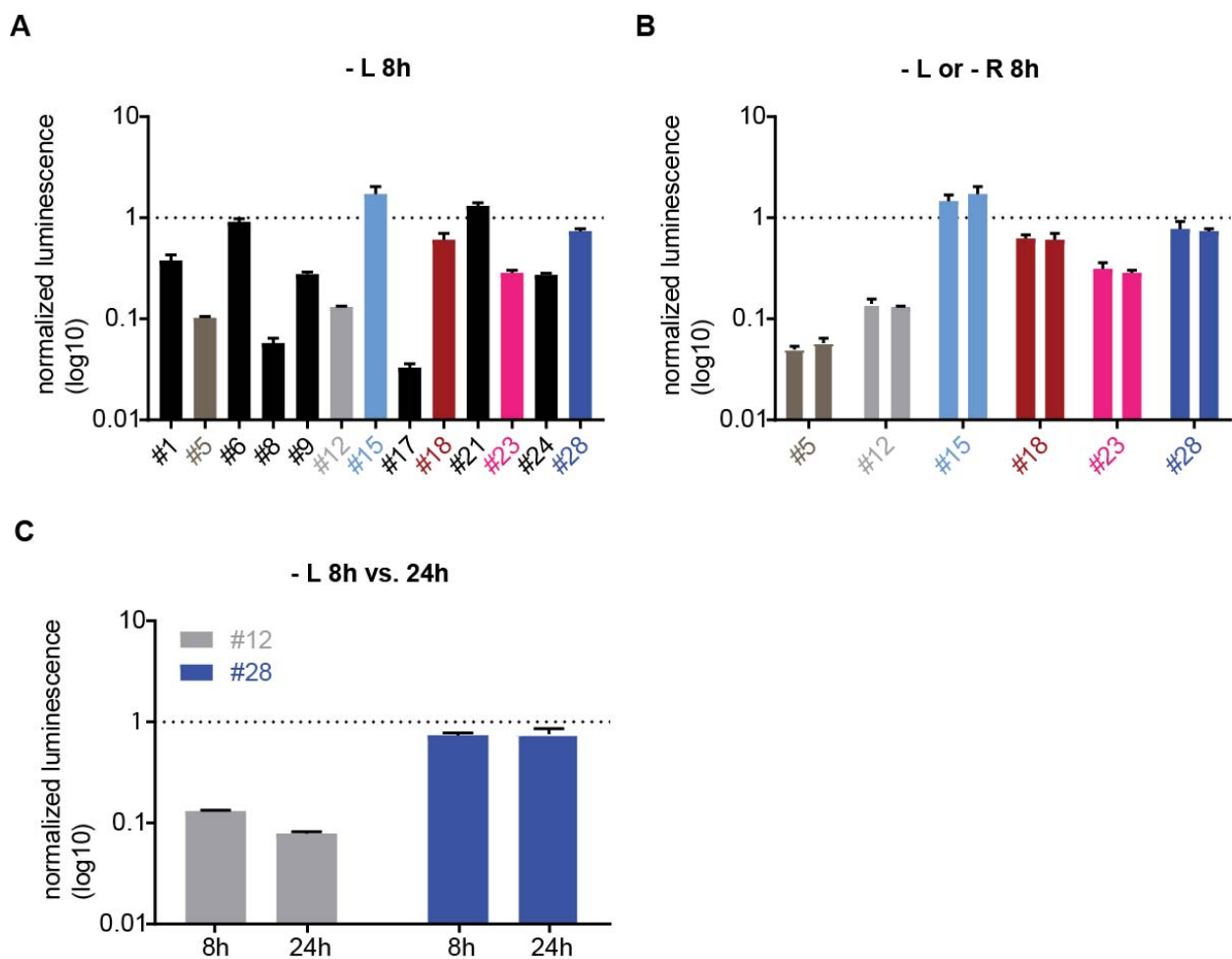


Figure 73. Class-IV-PI3K inhibitors efficiently reduce the *Ddit3* expression upon amino acid stress. (A) Quantification of normalized luminescence of 3T3 *Ddit3*::NanoLuc-PEST cells treated with different compounds (#1, #5, #6, #8, #9, #12, #15, #17, #18, #21, #23, #24 or #28) in combination with leucine-starvation for 8 h. Compound classification summarized in table 32. Color-coding fits to the data in figure 72. Threshold indicated by dashed line. (B) Same as in A, except: cells were leucine- and arginine-starved for 8 h. (C) Same as A, except: cells were leucine-starved for 8 h and 24 h. (A-C) Data are depicted as mean + SEM of three independent experiments.

Combining the information (Figures 72 and 73), we found that the activation of all ISR targets (ATF4, CHOP, phospho-eIF2 α S52 and phospho-GCN2 T898) were efficiently blocked by three compounds (#12, #18 and #23), which belong to the class-IV-PI3K inhibitors. In other words, class-IV-PI3K inhibitors prevent the mammalian amino acid stress-induced ISR like GCN2 inhibitors (GCN2i; compounds #5 and #28) upon amino acid stress.

4.7.3. Class-IV-PI3K inhibitors prevent the GCN2-ISR dose-dependently and GCN2-independently

We previously showed that class-IV-PI3K inhibitors (compounds #12, #18 and #23) prevented the ISR induction upon leucine stress as GCN2i (compounds #5 and #28). To further investigate this phenomenon, we extended our key compound collection by another ATR inhibitor BAY1895344 (compound #30) and the GCN2 inhibitor GCN2iB (compound #29) (Table 32). Follow-up studies on the ISR regulation were separately compared between the two key compound classes: class-IV-PI3K (compounds #12, #18, #23 and #30) and GCN2 (compounds #5, #28 and #29) inhibitors.

GCN2-IN-1/A-92 (compound #5)²⁴⁷ was the first developed allosteric GCN2 inhibitor ($IC_{50} < 0.3 \mu M$) that was optimized to its derivate GCN2-IN-6 (compound #28; $IC_{50} 1.8 nM$)²⁴⁸. The only available ATP-competitive GCN2 inhibitor, GCN2iB (compound #29) was reported in Nakamura *et al.*²³⁹, sensitizing low-ASNS expressing ALL cells to asparaginase treatment inducing apoptosis. Sapanisertib (compound #12) is a potent and selective ATP-competitive mTOR inhibitor with an IC_{50} of 1 nM for both mTOR complexes in cell-free assays, which is already used in clinical trials for solid tumors^{395,396}. PI3K inhibitor Omipalisib (compound #18) and ATR inhibitor ETP-46464 (compound #23) show low IC_{50} values for mTORC1/C2 inhibition as well (Table 32). As ETP-46464 (compound #23), BAY1895344 (compound #30) is an ATR inhibitor used in first-in-human clinical trial for advanced solid tumors^{522,523}.

First, we aimed to address if the mentioned key compounds suppress the ISR upon leucine stress dependent on GCN2. Therefore, we used our GCN2 deficient *Ddit3::mCherry* reporter system (Section 4.2.; Figure 25). As expected, all compounds blocked the mCherry induction and thereby the ISR in a GCN2-independent manner upon leucine stress (Figure 74). This finding ensured that each drug did not induce mCherry expression under conditions where GCN2 was absent. In this context, we also showed that the suppression persisted across time (0 h to 48 h). Next, we tracked the inhibitory potential of the key compounds in broader doses range using the *Ddit3::mCherry* cells. As expected, the compounds blocked mCherry expression in a dose-dependent manner (Figure 75). Interestingly, sapanisertib (compound #12) and omipalisib (compound #18) already efficiently blocked the induction of mCherry at the lowest dose (0.01 μM) in contrast to the ATR inhibitors BAY1895344 (compound #30) and ETP-46464 (compound #23). The GCN2 inhibitor GCN2-IN-1/A-92 (compound #5) was less potent at lower doses than GCN2-IN-6 (compound #28) or GCN2iB (compound #29) (Figure 75). Combined, we showed that all compounds suppressed the ISR dose-dependently, but GCN2-independently upon leucine stress over time.

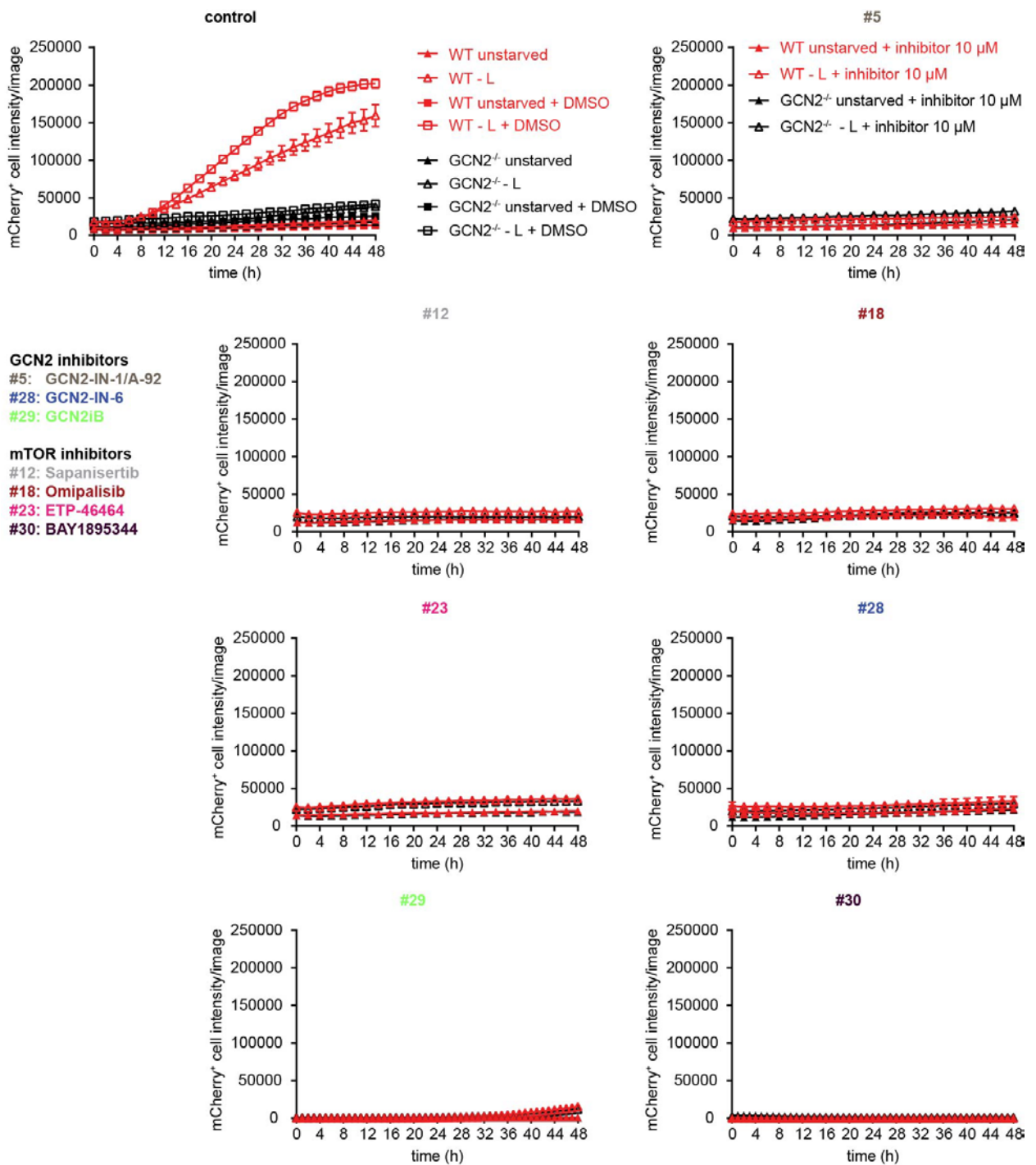


Figure 74. Class-IV-PI3K inhibitors suppress the GCN2-ISR GCN2-independently upon leucine stress. Quantification of mCherry intensity in 3T3 *Ddit3::mCherry* wild-type and GCN2^{-/-} cells treated with 10 μM of the compounds (#5, #12, #18, #23, #28, #29 or #30) upon leucine depletion over time or unstarved condition. DMSO was used as vehicle. Data are depicted as mean + SEM of three independent experiments.

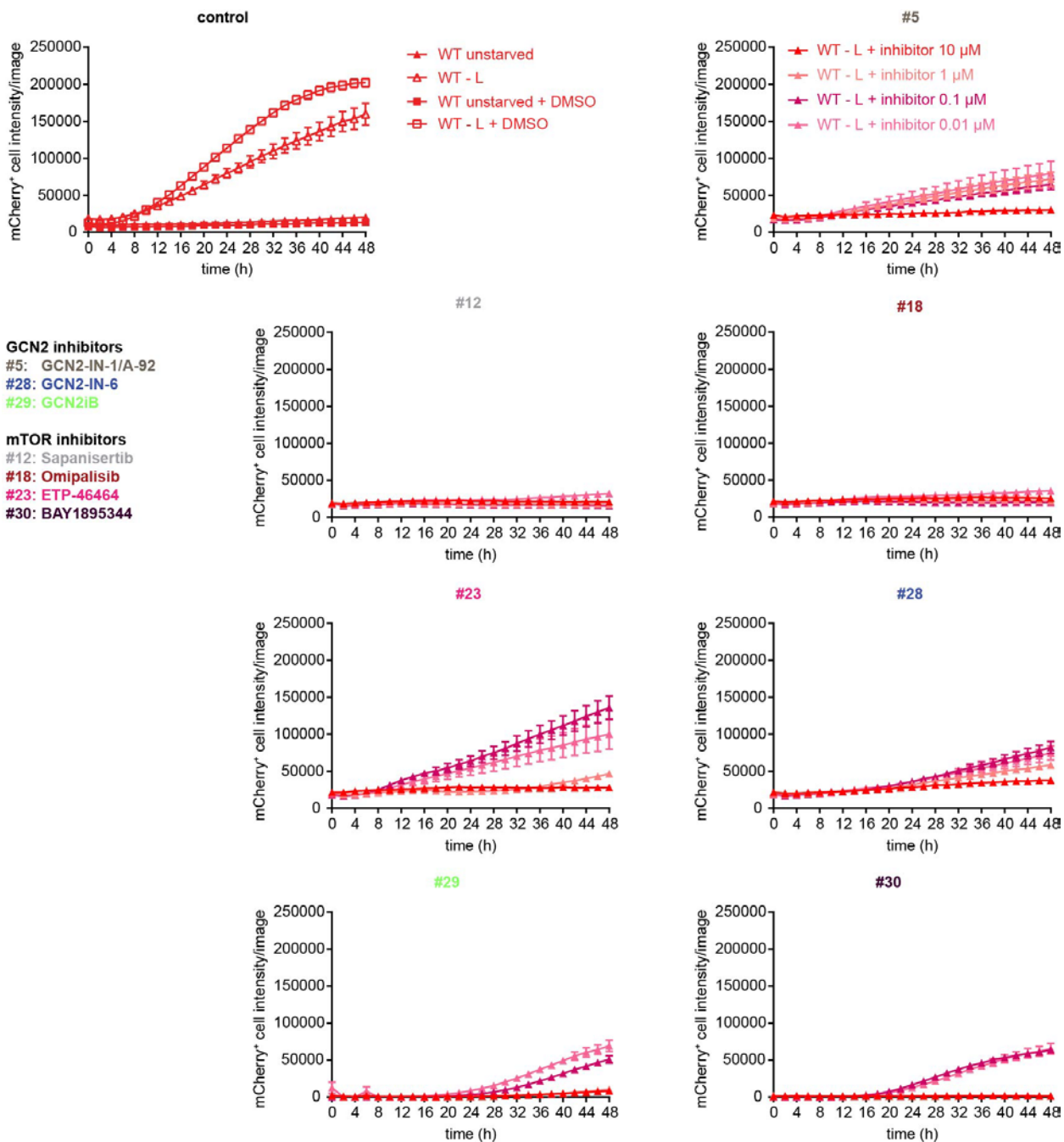
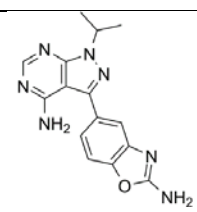
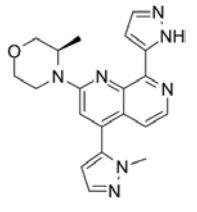
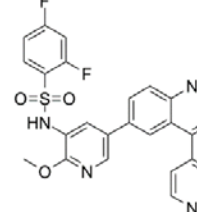
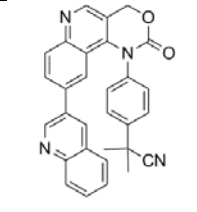
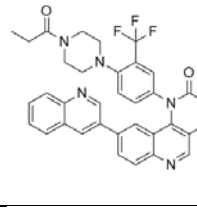
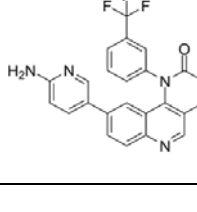


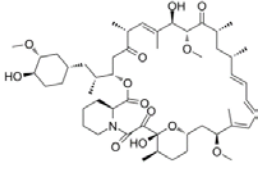
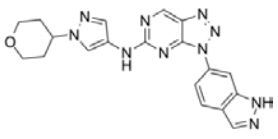
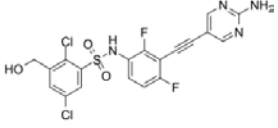
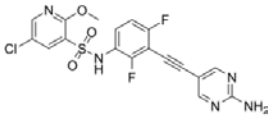
Figure 75. Class-IV-PI3K inhibitors suppress the GCN2-ISR in a dose-dependent manner upon leucine stress. Quantification of mCherry intensity in 3T3 *Ddit3*:mCherry wild-type and *GCN2*^{-/-} cells treated with compounds (#5, #12, #18, #23, #28, #29 or #30) upon leucine depletion over time. DMSO was used as vehicle. Concentration range of the compounds: 0.01, 0.1, 1 and 10 μ M. Data are depicted as mean + SEM of three independent experiments.

Sapanisertib (compound #12) is a small molecule inhibitor belonging to the class of TORKinibs, which selectively blocks both mTOR complexes^{392,395}. Omipalisib (compound #18), ETP-46464 (compound #23) and BAY1895344 (compound #30) also have mTOR inhibitory properties (Table

33). Therefore, we addressed if the inhibitors block in a dose-dependent manner the GCN2 (ATF4 and eIF2 α) and mTORC1 targets (p70S6K and 4EBP1) to benchmark their activities against each other and provide further evidence towards the GCN2-mTORC1 connection.

Table 33: mTOR and GCN2 key compounds

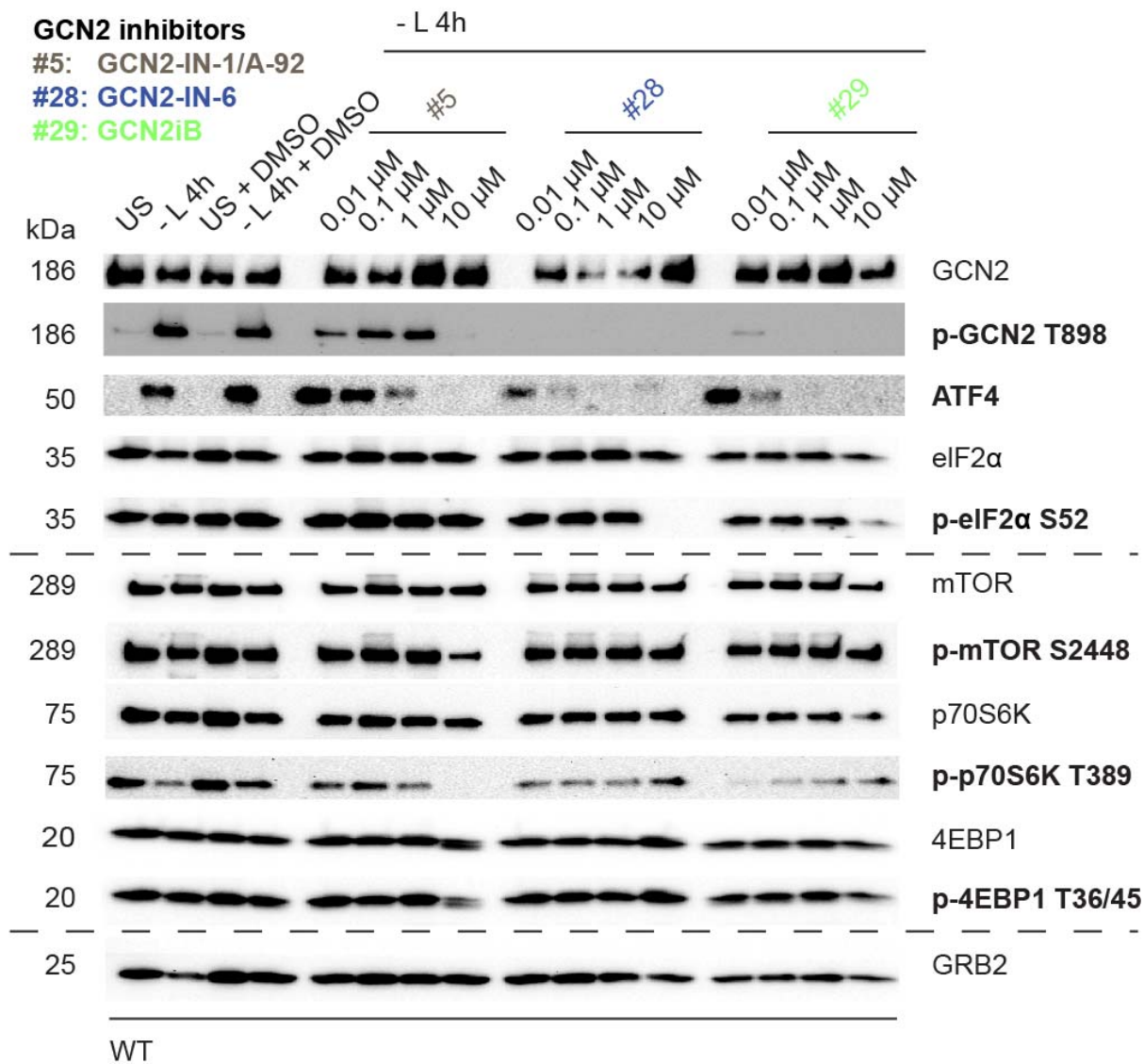
Compound	Sub-class	IC ₅₀ enzymatic	Mode of action	Structure	Reference
Sapanisertib	mTORi	1 nM	ATP-competitive		524
BAY1895344	mTORi	61 nM	ATP-competitive		525
Omipalisib	mTORi	0.18-0.3 nM	ATP-competitive		526
ETP-46464	mTORi	0.6 nM	ATP-competitive		527
Torin-1	mTORi	3 nM	ATP-competitive		390
Torin-2	mTORi	2.81 nM	ATP-competitive		528

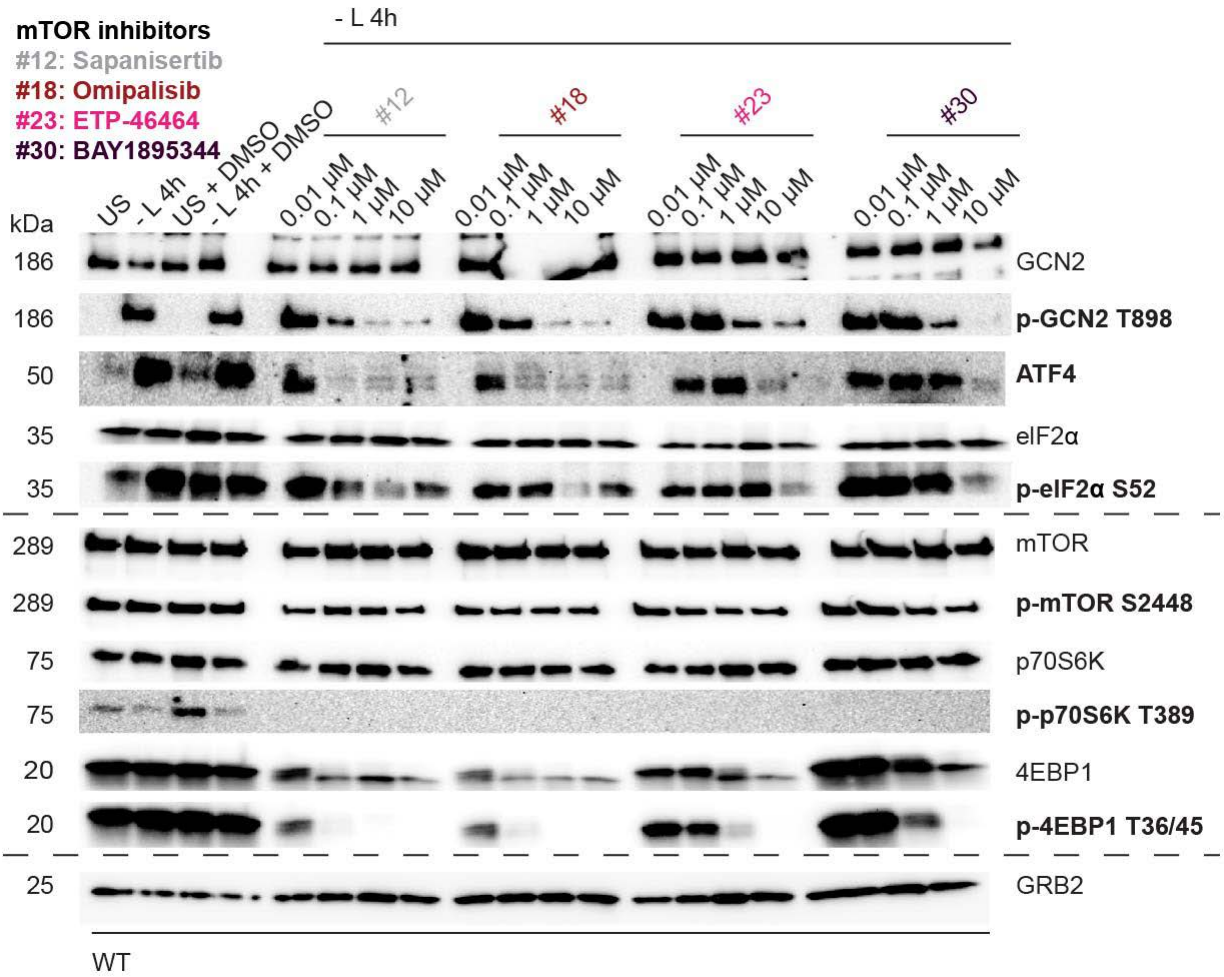
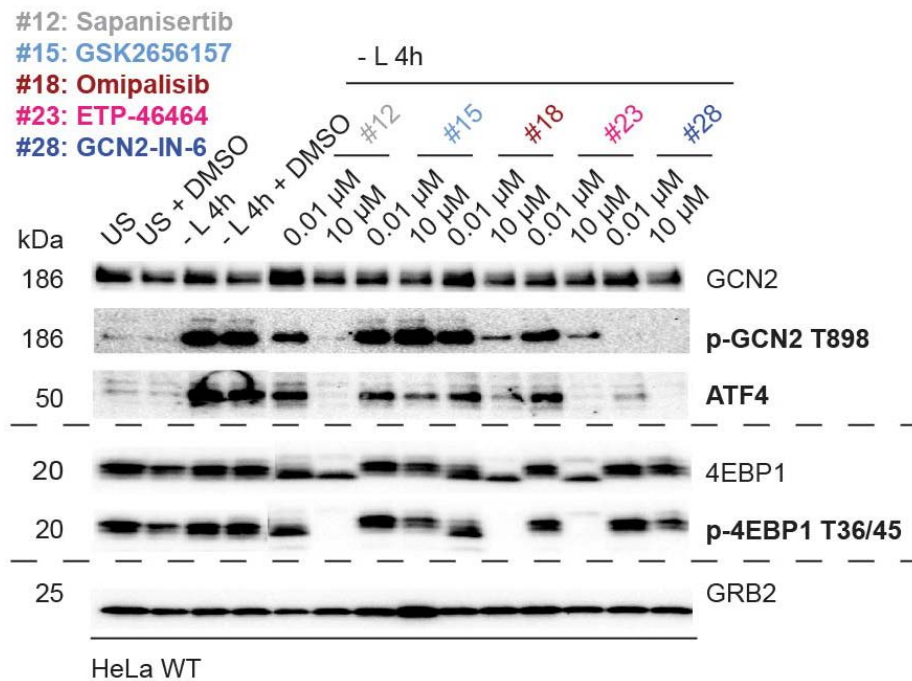
Rapamycin	mTORi	0.1 nM	allosteric		529
GCN2-IN-1/ A-92	GCN2i	< 0.3 μM	allosteric		247
GCN2-IN-6	GCN2i	1.8 nM	allosteric		248
GCN2iB	GCN2i	2.4 nM	ATP- competitive		239

To start, we explored the inhibitory potential of the known GCN2 inhibitors (GCN2-IN-1/A-92, GCN2-IN-6 and GCN2iB). All inhibitors blocked the induction of ATF4 and the autophosphorylation of GCN2 (Figure 76A). However, GCN2-IN-1/A-92 (compound #5) inhibited only at the highest dose, which was consistent with the previously shown mCherry screen data (Figure 75). Most interestingly, the phosphorylation of eIF2α was not affected by GCN2-IN-1/A-92 (compound #5) and the other two GCN2 inhibitors (GCN2-IN-6 and GCN2iB) had minimal inhibitory activity only at the highest concentration (Figure 76A). This was an important finding for the interpretation of the kinase-target interaction and the overall activity of the GCN2 inhibitors on other steps in the GCN2 pathway such as phospho-GCN2 at T898 or ATF4 (Refs.^{239,248}). Moreover, the potency of GCN2iB (compound #29) and GCN2-IN-6 (compound #28) was similar, which manifested the finding in the previous reported mCherry assay (Figure 75). However, GCN2-IN-6 (compound #28) had the lowest IC₅₀ value, as determined by enzymatic and cellular

assays compared to the other two GCN2 inhibitors (Table 33). Therefore, GCN2-IN-6 (compound #28) was used as our internal GCN2i benchmarking control in subsequent assays. Another important finding was that only GCN2-IN-1/A-92 (compound #5) blocked at highest doses (10 μ M) the phosphorylation of the mTORC1 key targets 4EBP1 and p70S6K. This data matched with the potent reduction in luciferase signal comparable to the mTOR inhibitor sapanisertib (compound #12) and the data in the initial screen (Figures 72 C and 73B). Next, we compared the class-IV-PI3K inhibitors in the same setting as previously described. Consistent with the finding reported in figure 75, sapanisertib (compound #12) and omipalisib (compound #18) blocked the ISR cascade already at low doses (ATF4, phospho-GCN2 T898 and phospho-eIF2 α S52) as well as the mTORC1 targets (phospho-4EBP1 T36/45 and phospho-p70S6K T389) (Figure 76B). In contrast, the ATR inhibitors ETP-46464 (compound #23) and BAY1895344 (compound #30) suppressed the mTORC1 targets and GCN2 targets at highest doses in line with the mCherry screen data (Figure 75). Moreover, we checked the inhibitory properties of the GCN2 and class-IV-PI3K inhibitors also in a human cell system upon leucine stress. We found that the compounds prevent the GCN2-ISR and mTORC1 pathways in the same dose-dependency as in the murine cell system (Figure 76C). In this context, we also underlined that the PERK inhibitor (compound #15) did not block either the GCN2 or the mTORC1 cascade that is consistent with the finding in 3T3 cells (Section 4.2; Figure 72). Combined, this argued that all class-IV-PI3K inhibitors suppress in a dose-dependent manner next to the GCN2-ISR also the mTORC1 pathway upon leucine stress (Figure 76D). This finding we verified in murine (3T3) as well as human (HeLa) cells.

A



B**C**

D

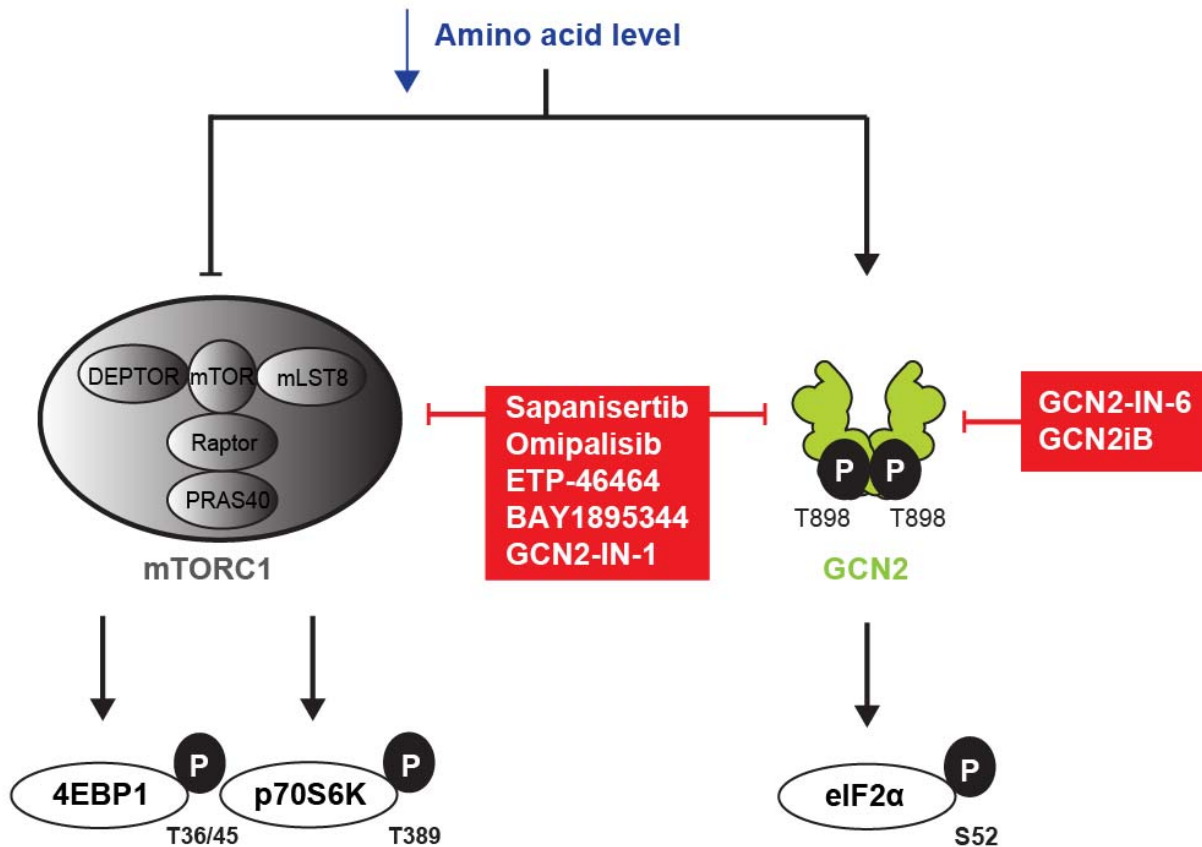


Figure 76. GCN2-IN-1 (A-92) inhibits the mTORC1 pathway only at highest doses upon leucine stress.

(A) Immunoblots of 3T3 wild-type (WT) cell lysates treated with different compounds (#5, #28 and #29) upon leucine depletion for 4 h. DMSO was used as vehicle. Concentration range of compounds: 0.01, 0.1, 1 and 10 μ M. GRB2 was used as loading control. In bold, changes due to the compound treatment. (B) Same as A, except: treatment with compounds (#12, #18, #23 and #30). (C) Same as A, except: treatment with compounds (#12, #15, #18, #23 and #28) in HeLa wild-type (HeLa WT). (D) Schematic representation of GCN2 and mTORC1 suppression upon amino acid depletion by GCN2 inhibitors (GCN2-IN-1, GCN2-IN-6 and GCN2iB) and class-IV-PI3K inhibitors (sapanisertib, omipalisib, ETP-46464 and BAY1895344), respectively. (A-B) Data are depicted as one of two representative gels. In bold, changes due to the compound treatment.

In conclusion, we provided evidence at the protein and cellular level that class-IV-PI3K inhibitors (compounds #12, #18, #23 and #30) can block the GCN2-ISR upon leucine deprivation in a dose-dependent and GCN2-independent manner. All findings could be confirmed in three different read-outs (immunoblotting, *Ddit3*:mCherry and *Ddit3*:NanoLuc-PEST screens). In detail, the GCN2 inhibitor GCN2-IN-1/A-92 (compound #5) prevented mTORC1 signaling at highest doses (10 μ M) in contrast to the other two GCN2 inhibitors (GCN2-IN-6 and GCN2iB). Surprisingly, the phosphorylation of the key target eIF2 α was only prevented by GCN2-IN-6 (compound #28) and

GCN2iB (compound #29) at highest used drug concentration (10 μ M). In addition, all class-IV-PI3K inhibitors (compounds #12, #18, #23 and #30) prevented mTORC1 signaling upon leucine stress. Moreover, we verified the GCN2-ISR and mTORC1 prevention by the class-IV-PI3K inhibitors also in a human cell system. Consequently, we classified the ATR inhibitors (compounds #23 and #30) and the PI3K inhibitor (compound #18) next to sapanisertib (compound #12) as mTOR inhibitors (mTORi) in this thesis (Table 33).

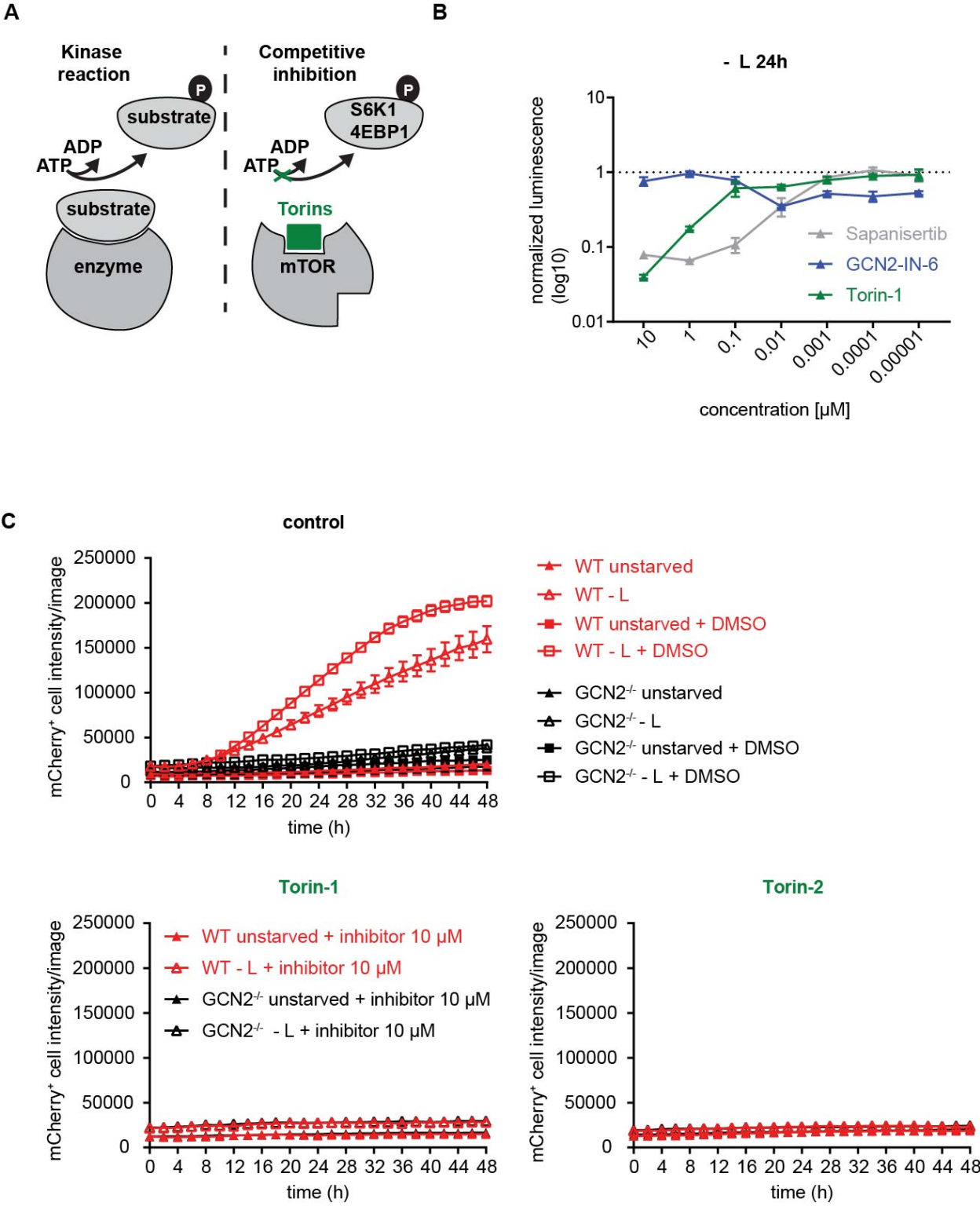
4.7.4. GCN2-ISR is prevented by Torins but not rapamycin

In the previous section, we provided evidence that the class-IV-PI3K inhibitors have mTOR inhibitory property blocking the mTORC1 pathway upon leucine stress. Therefore, we decided to expand our pool of tested drugs by rapamycin and Torins (Table 33) to study the mTOR-GCN2 connection in further detail.

The ATP-competitive inhibitor Torin-1, its derivate Torin-2 and the allosteric inhibitor rapamycin are the most prominent mTOR inhibitors functioning as 'workhorses' to study mTOR-driven cell state changes^{390,524,530,531}. Rapamycin, belonging to the class of rapalogs, targets together with FKBP12 only the mTORC1 complex by allosterically binding the FRB domain of mTOR (Figure 78A)⁵²⁹. In contrast, Torins and other related dual mTORC1/C2 inhibitors (e.g. TORKinibs like sapanisertib) prevent the mTORC1 and mTORC2 activity by blocking the active site of mTOR (Figure 77A)^{390,528}. A further mechanistic difference between rapamycin and ATP-competitive mTOR inhibitors is their sensitivity towards 4EBP1: Rapamycin blocks mTORC1 activity without affecting the phosphorylation of 4EBP1²⁹⁶. This mechanism is still not fully understood, but was recently linked to FKBP12-rapamycin-induced structural occlusion, which is not entirely blocking the kinase site, combined with induced conformational changes, partner protein interaction and structural confinement^{295,296}. In other words, the binding mode of rapamycin-FKBP12 at mTOR specifically inhibits the phosphorylation of the late sites (S65, T70), but not the early sites of 4EBP1 (T37/46)²⁹⁵.

Using our *Ddit3*::NanoLuc-PEST reporter system, we showed that Torin-1 reduced the luciferase signal in a dose-dependent manner upon leucine stress (Figure 77B). This decrease was comparable to the signal gained by sapanisertib (compound #12) in contrast to GCN2-IN-6 (compound #28) treatment. Further, we showed that Torin-1 and Torin-2 blocked the induction of mCherry already at low drug concentration (0.01 μ M) and independent of GCN2 presence (Figure 77C+D). These data matched to the described complementary assays performed with sapanisertib (compound #12) (Figures 74 and 75). In addition, Torin-1 and Torin-2 suppressed the GCN2-ISR and the mTORC1 pathway upon leucine and arginine deprivation (Figure 77E). Strikingly, we discovered that Torins suppress the ISR upon amino acid stress – already at low

drug concentration. In line with the other ATP-competitive mTOR inhibitor sapanisertib (compound #12), we unraveled a by now unknown connection between mTOR and GCN2 upon amino acid stress.



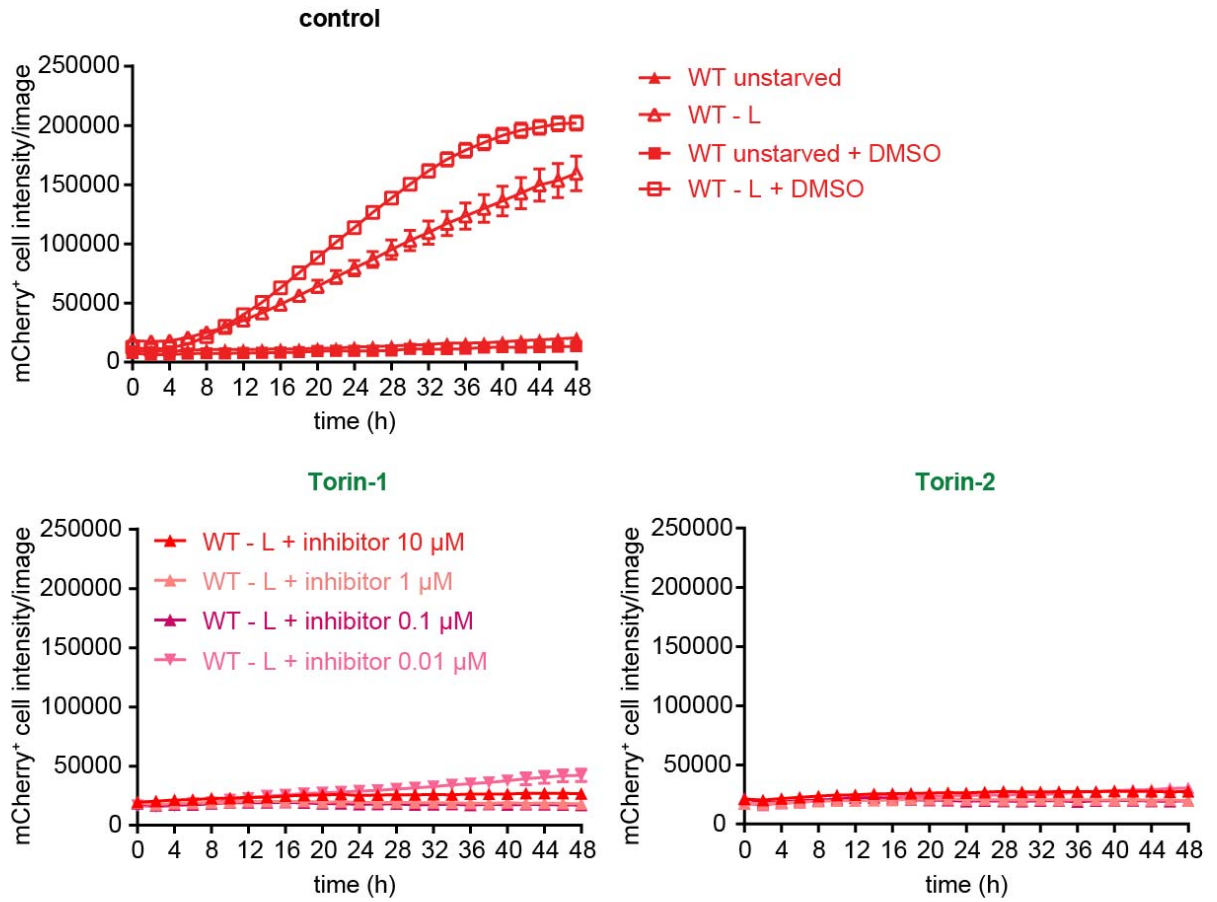
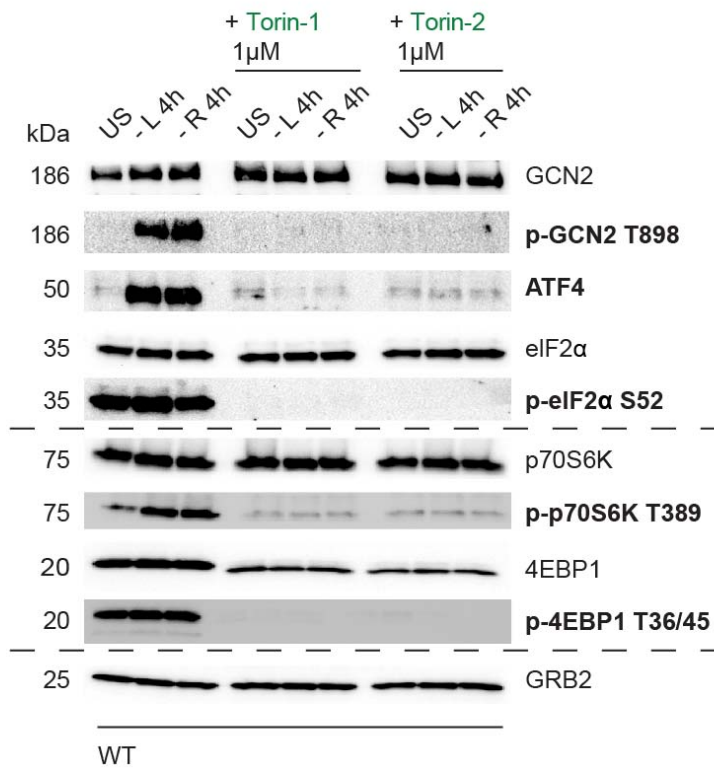
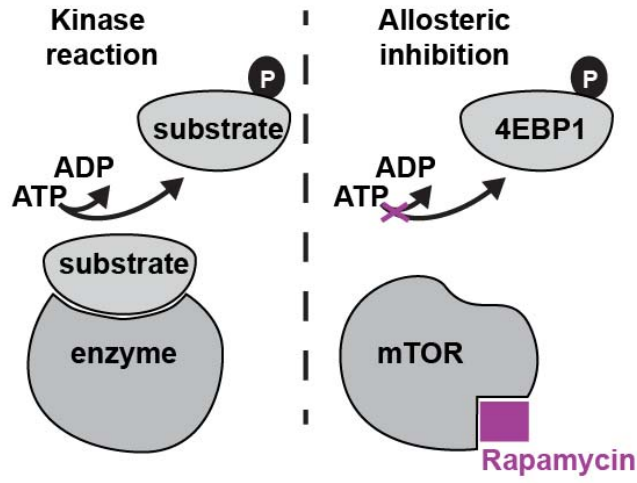
D**E**

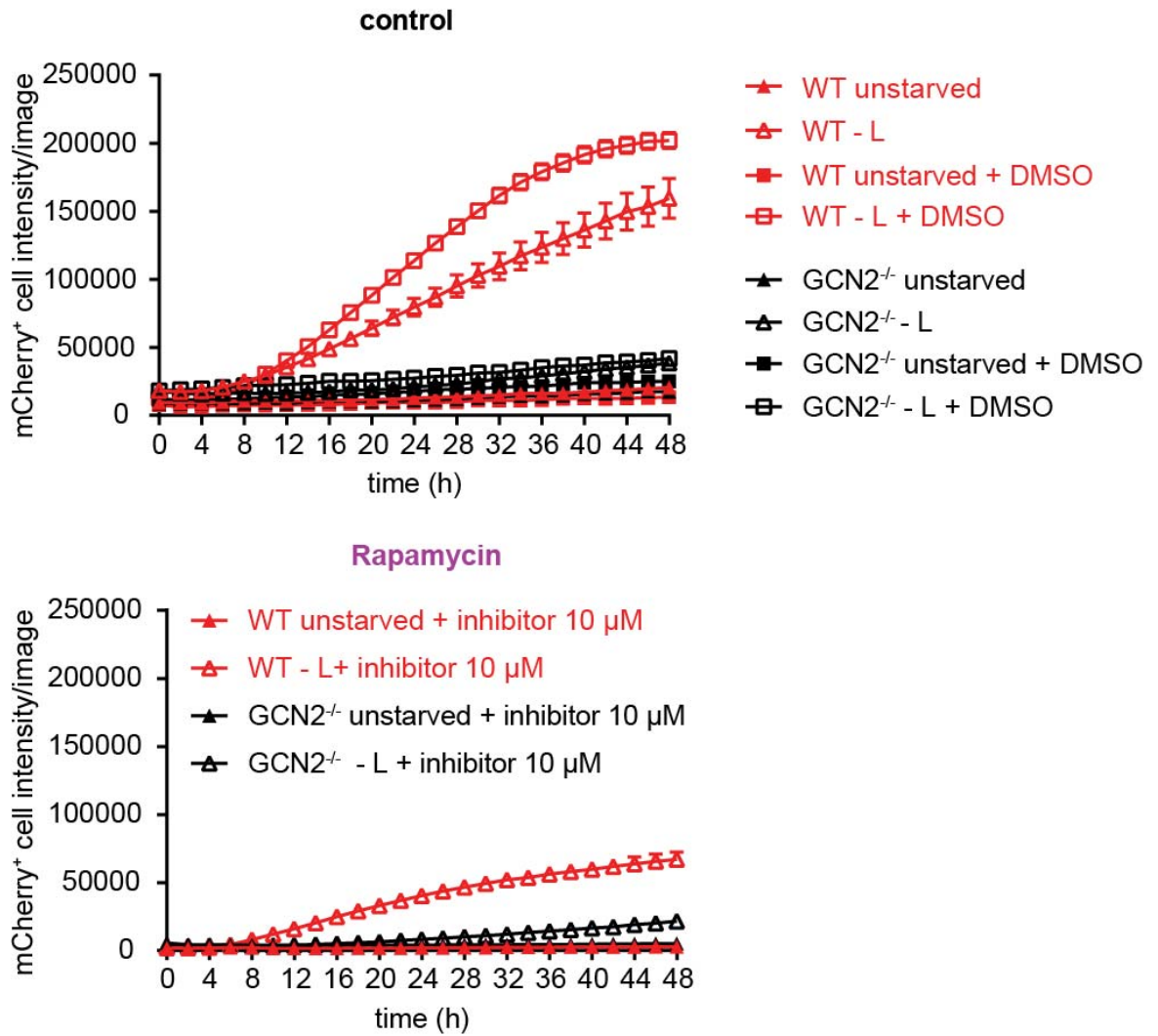
Figure 77. Torins inhibit the GCN2 cascade upon amino acid stress. (A) Simplified scheme of the ATP-competitive mode of inhibition: Torins bind in the active kinase pocket of mTOR preventing its catalytic reaction to phosphorylate S6K1 and 4EBP1. (B) Quantification of normalized luminescence of 3T3 wild-type (WT) cells treated with sapanisertib, Torin-1 and GCN2-IN-6 over a concentration range upon 24 h of leucine stress. (C) Quantification of mCherry intensity in 3T3 *Ddit3::mCherry* wild-type and GCN2^{-/-} cells treated with Torins (Torin-1, Torin-2; 10 μM) upon leucine depletion over time. DMSO was used as vehicle. (D) Quantification of mCherry intensity in 3T3 *Ddit3::mCherry* wild-type and GCN2^{-/-} cells treated with Torins (Torin-1, Torin-2) upon leucine depletion over time. DMSO was used as vehicle. Concentration range of compounds: 0.01, 0.1, 1 and 10 μM. (E) Immunoblot of 3T3 wild-type (WT) cell lysates treated with 1 μM of Torin-1 or Torin-2 upon leucine depletion (- L) or arginine depletion (- R) or unstarved condition (US) for 4 h. DMSO is used as vehicle. GRB2 is used as loading control. In bold, changes due to the compound treatment. (B-E) Data are depicted as mean + SEM of three independent experiments or one of two representative gels.

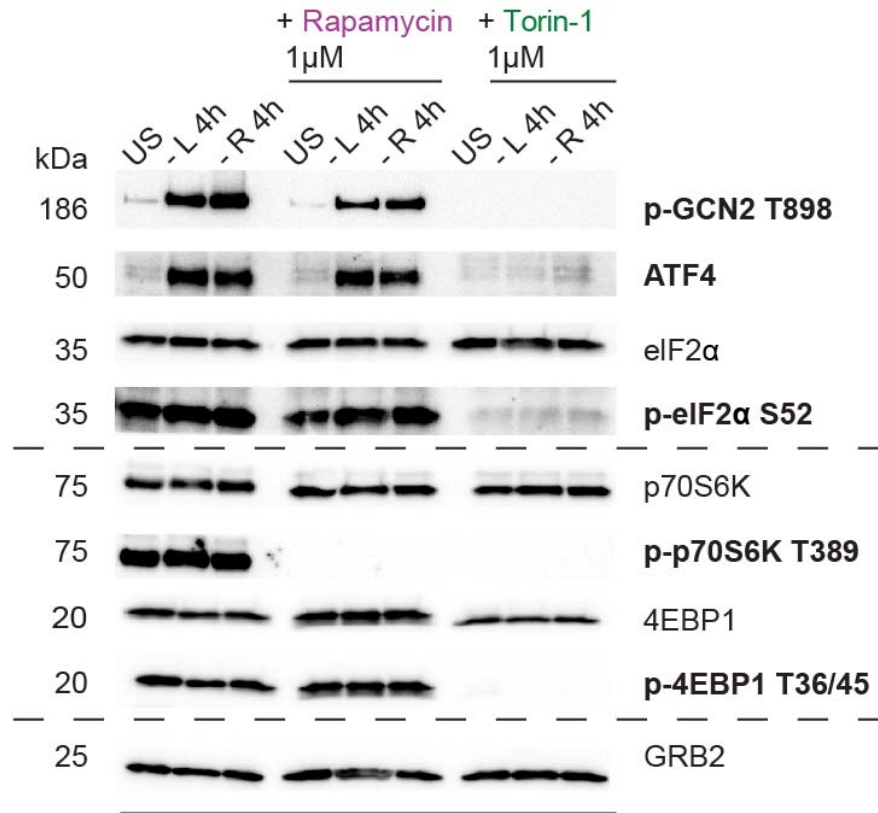
The next step was to compare this finding with rapamycin treatment that solely blocks mTORC1⁵²⁹(Figure 78A). Surprisingly, rapamycin-treated cells still induced the ISR upon leucine treatment over time (Figure 78B). Interestingly, the mCherry⁺ signal was not as strong as for leucine stress alone. However, the cells were still mCherry⁺ after 24 h drug treatment in contrast to GCN2-IN-6 (compound #28) or Torin-1 treatment (Figure 78H). Moreover, we highlighted that rapamycin treatment did not prevent the activation of the key ISR targets (ATF4, phospho-GCN2 T898 and phospho-eIF2α S52) upon arginine and leucine starvation. This effect was independent of GCN2 (Figure 78C) and drug concentration (Figure 78D). In consequence, we performed an experiment by pretreating the cells with rapamycin and inducing stress afterwards. Again, the ISR was not suppressed (Figure 78E). Moreover, we determined if the inhibitors regulate only the ISR upon amino acid depletion. Therefore, we treated RS4;11 cells (human acute leukemia cell line) with asparaginase in combination with the inhibitors. In line with the previous finding, the ISR in RS4;11 cells was prevented upon co-treatment of asparaginase with Torin-1 or GCN2-IN-6 but not rapamycin (Figure 78F). This finding manifests the relevance of GCN2-ISR manipulation for combinational therapeutic cancer strategies²³⁹. In addition, we found that rapamycin treatment in the double GCN1 and GCN2 deficient background activates ATF4 upon leucine stress (Figure 78G). This was not observed when treating with all mTOR inhibitors (Torins and compounds #12, #18, #23 and #30) and GCN2 inhibitors (compounds #5, #28 and #29). This finding underlines the relevance of ATF4 regulation and its transcriptional program upon cellular stress¹⁰². By now, this data assumed that when GCN2 and mTORC1 are inactive, a so far unknown player can still activate ATF4 induction upon amino acid stress. Combined, we found that rapamycin did not inhibit the GCN2-ISR upon amino acid stress or asparaginase treatment, which is in stark contrast to Torins.

A

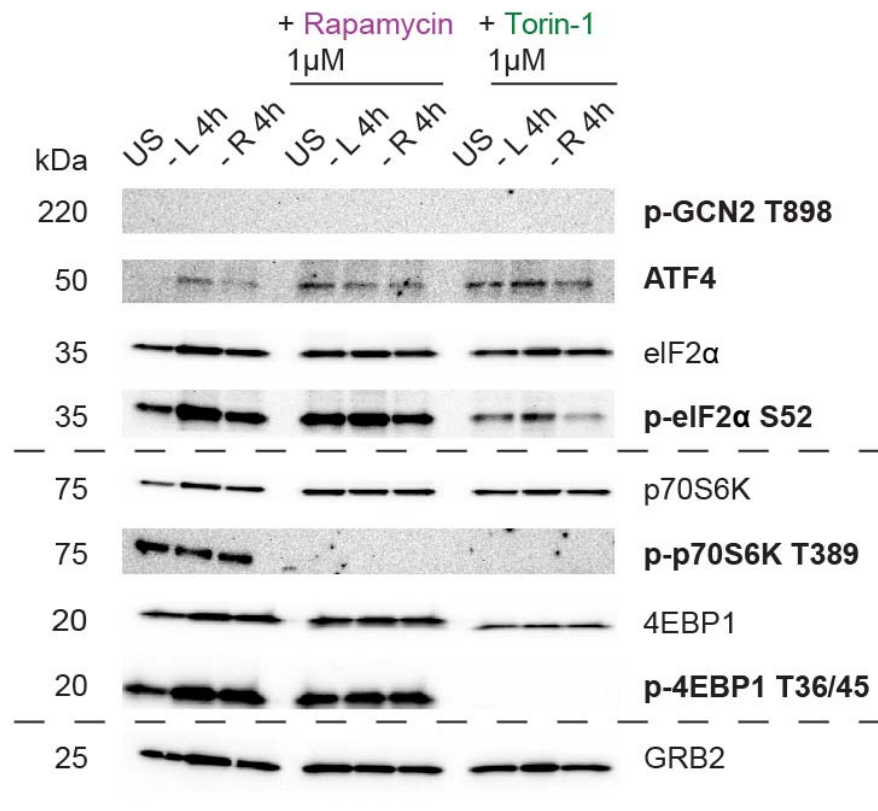


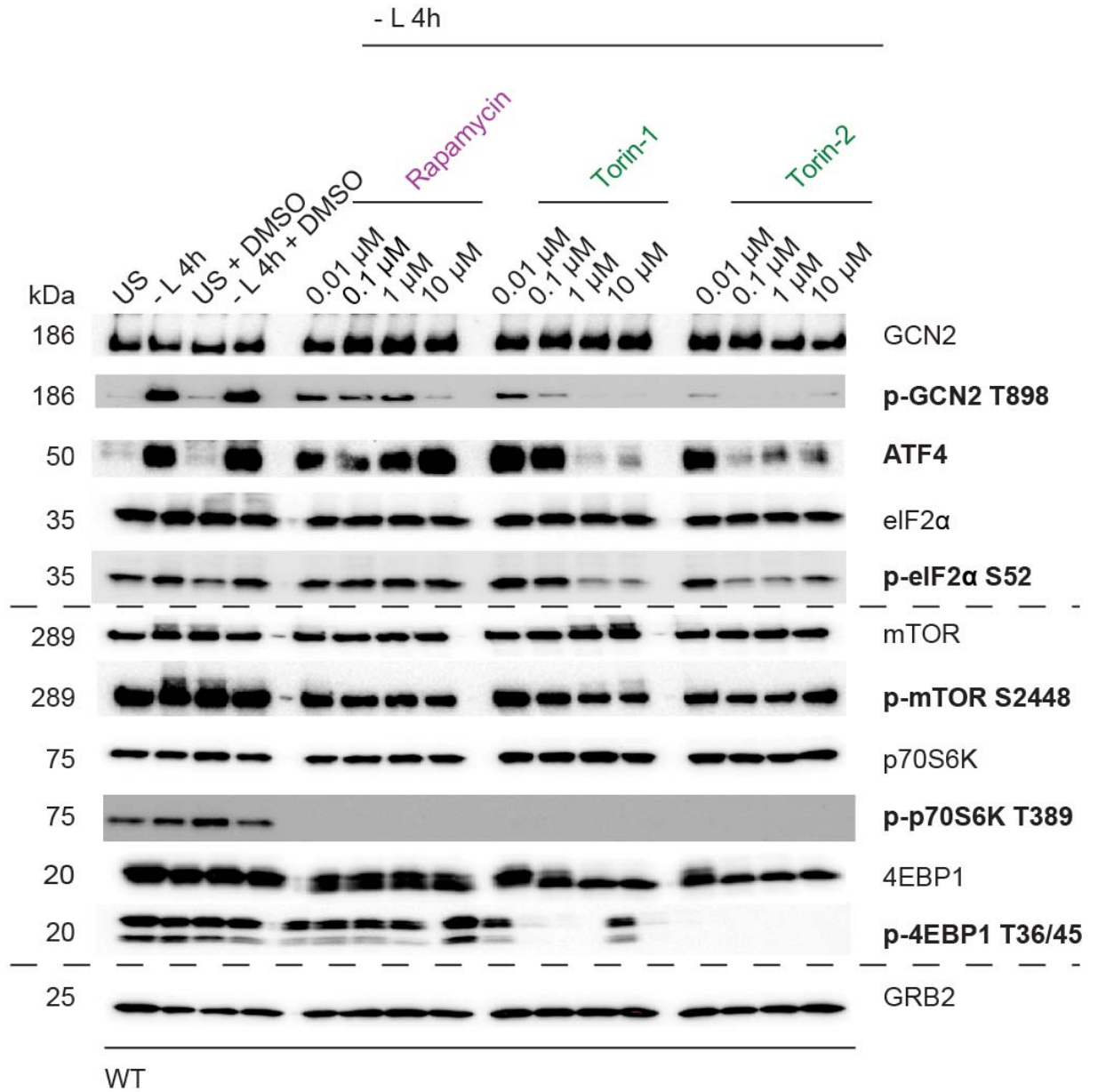
B



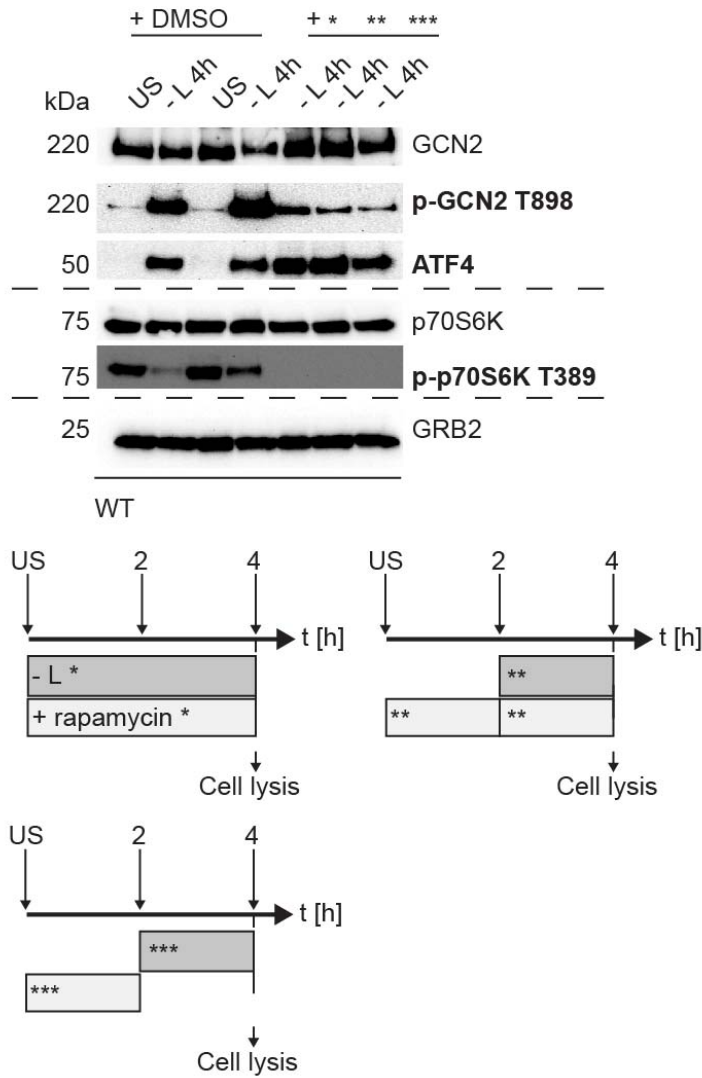
C

WT

*GCN2*^{-/-}

D

E



F



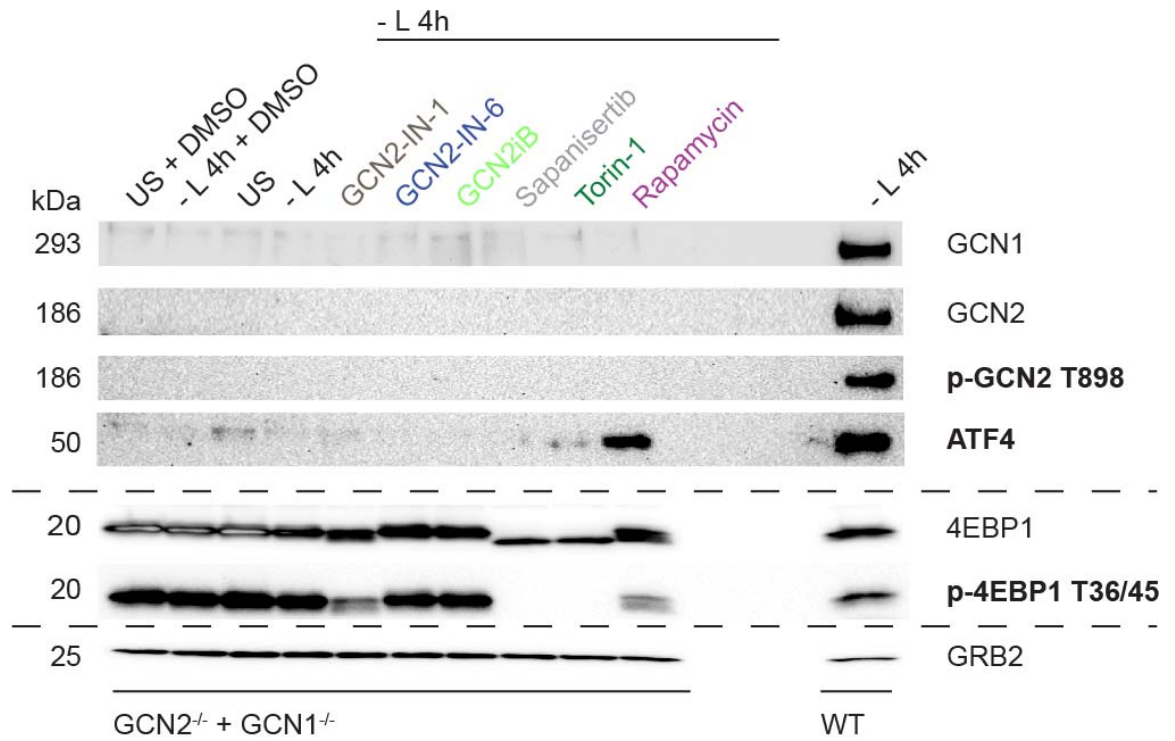
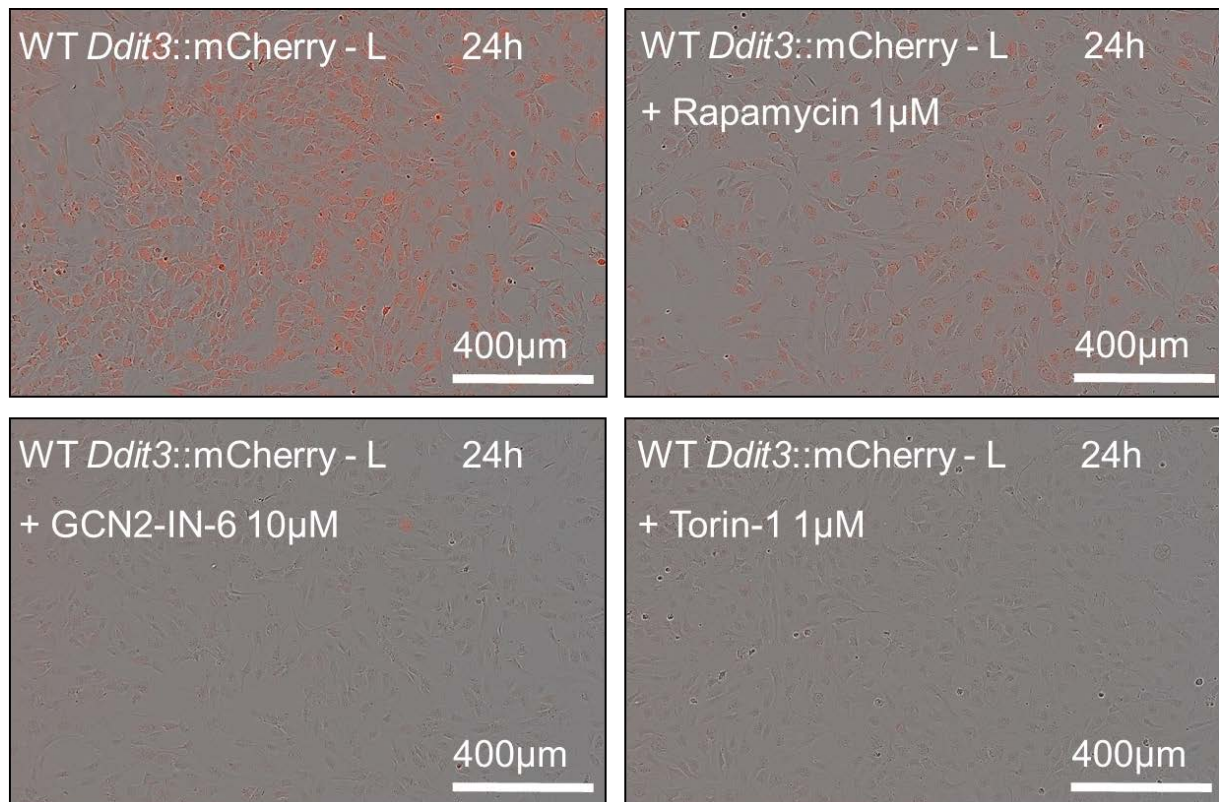
G**H**

Figure 78. Rapamycin does not inhibit the GCN2 cascade upon leucine stress. (A) Simplified scheme of the allosteric mode of inhibition: Rapamycin-FKBP12 binds the FRB domain of mTOR to prevent the phosphorylation of S6K1. (B) Quantification of mCherry intensity in 3T3 *Ddit3::mCherry* wild-type and

GCN2^{-/-} cells treated with rapamycin (10 μM) upon leucine depletion over time. DMSO was used as vehicle. (C) Immunoblots of 3T3 wild-type (WT) and GCN2^{-/-} cell lysates treated with 1 μM of Torin-1 and rapamycin upon leucine depletion (- L) or arginine depletion (- R) or unstarved condition (US) for 4 h. DMSO was used as vehicle. GRB2 is used as loading control. In bold, changes due to the compound treatment. (D) Immunoblot of 3T3 wild-type (WT) cell lysates treated with Torin-1, Torin-2 and rapamycin upon leucine depletion (- L) for 4 h over a concentration range (0.01, 0.1, 1.0 and 10 μM). DMSO was used as vehicle. GRB2 is used as loading control. In bold, changes due to the compound treatment. (E) Same as D, except: treatment of rapamycin (1 μM) at different durations over 2 h and 4 h. Treatment is indicated in the scheme. In bold, changes due to the compound treatment. (F) Immunoblot of asparaginase (1.5 U/mL) plus GCN2-IN-6 (10 μM), sapanisertib (10 μM), Torin-1 (1 μM) or rapamycin (1 μM) treated RS4;11 cell lysates. DMSO served as internal control. (G) Immunoblot of 4 h leucine-starved 3T3 GCN1 and GCN2 (GCN2^{-/-} + GCN1^{-/-}) deficient cell lysates treated with GCN2-IN-1 (10 μM), GCN2-IN-6 (10 μM), GCN2iB (10 μM), sapanisertib (10 μM), Torin-1 (1 μM) or rapamycin (1 μM). GRB2 was used as loading control. DMSO was used as vehicle. (H) Microscopic images of rapamycin (1 μM), Torin-1 (1 μM) and GCN2-IN-6 (10 μM) treated 3T3 *Ddit3::mCherry* wild-type cells at 24 h of leucine stress. (B-G) Data are depicted as mean + SEM of three independent experiments or one of two representative gels.

In conclusion, for the first time, we provided evidence that Torins, in line with the class-IV-PI3K members (compounds #12, #18, #23 and #30), suppressed the GCN2 cascade upon amino acid stress (arginine or leucine deprivation) or asparaginase treatment. Together, the inhibitory effect was only induced by dual mTORC1/C2 inhibitors (further referred as dual mTOR inhibitors or dual mTORi) and not the mTORC1 inhibitor rapamycin. Based on this finding, we constructed a model to dissect how the mTORC1 and the GCN2 pathways are concurrently manipulated by dual mTOR inhibitors upon amino acid stress in a sequential way. In detail, we started to address in the following sections (i) if GCN2 is directly inhibited, (ii) if the inhibition is regulated via the translation initiation factor eIF2 α , (iii) if PERK is involved in this process and (iv) if mTORC2 signaling is relevant for the inhibition.

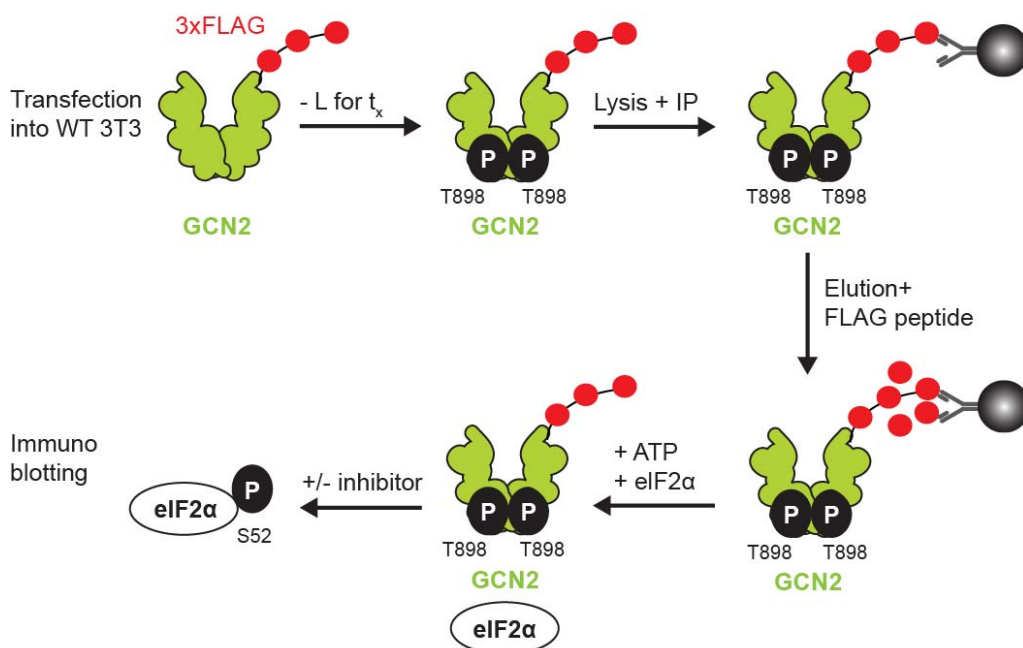
4.7.5. Dual mTORi-mediated GCN2-ISR inhibition is indirect

ATP-competitive dual mTOR inhibitors block the ISR upon amino acid stress. To rule out direct kinase-inhibitor binding, we performed an *in vitro* immunoprecipitation-based GCN2 kinase assay (Section 3.6.4.). The rationale behind this experiment was that GCN2 requires at least three different ligands to turn active (GCN1, the ribosomal P-stalk and/or uncharged tRNAs^{119,131,166,171}). This level of complexity cannot be easily reconstituted *in vitro*, yet. Therefore, we aimed to activate GCN2 inside cells and then recover the activated complex for enzymatic/inhibitor studies.

As illustrated in figure 79, wild-type 3T3 cells were transiently transfected with GCN2-3xFLAG tagged plasmid and leucine-starved prior to lysis and immunoprecipitation using anti-FLAG

beads. The FLAG-tagged GCN2 was eluted with excess FLAG peptide. Afterwards, the eluted GCN2 was mixed with ATP and purified recombinant human eIF2 α . Finally, the inhibitors were added at different doses and the kinase activity read out by tracking its autophosphorylation and the eIF2 α phosphorylation via immunoblots. The same experimental setup was conducted *in-cell*, where the inhibitors were added to the cells prior to the FLAG-tagged GCN2 pulldown.

Ex-cell IP kinase assay



In-cell IP kinase assay

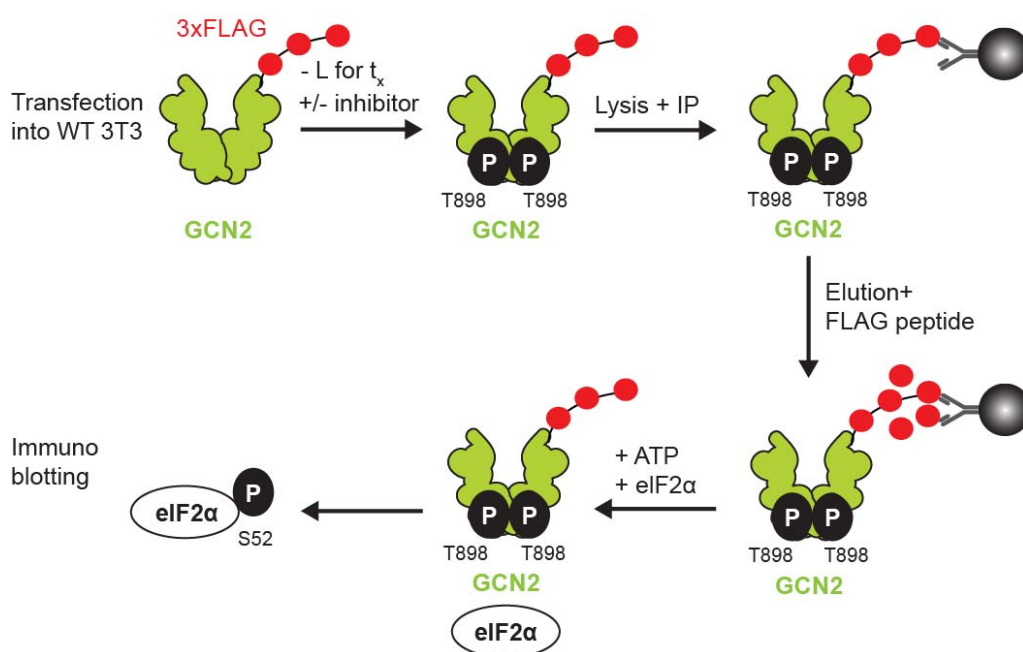
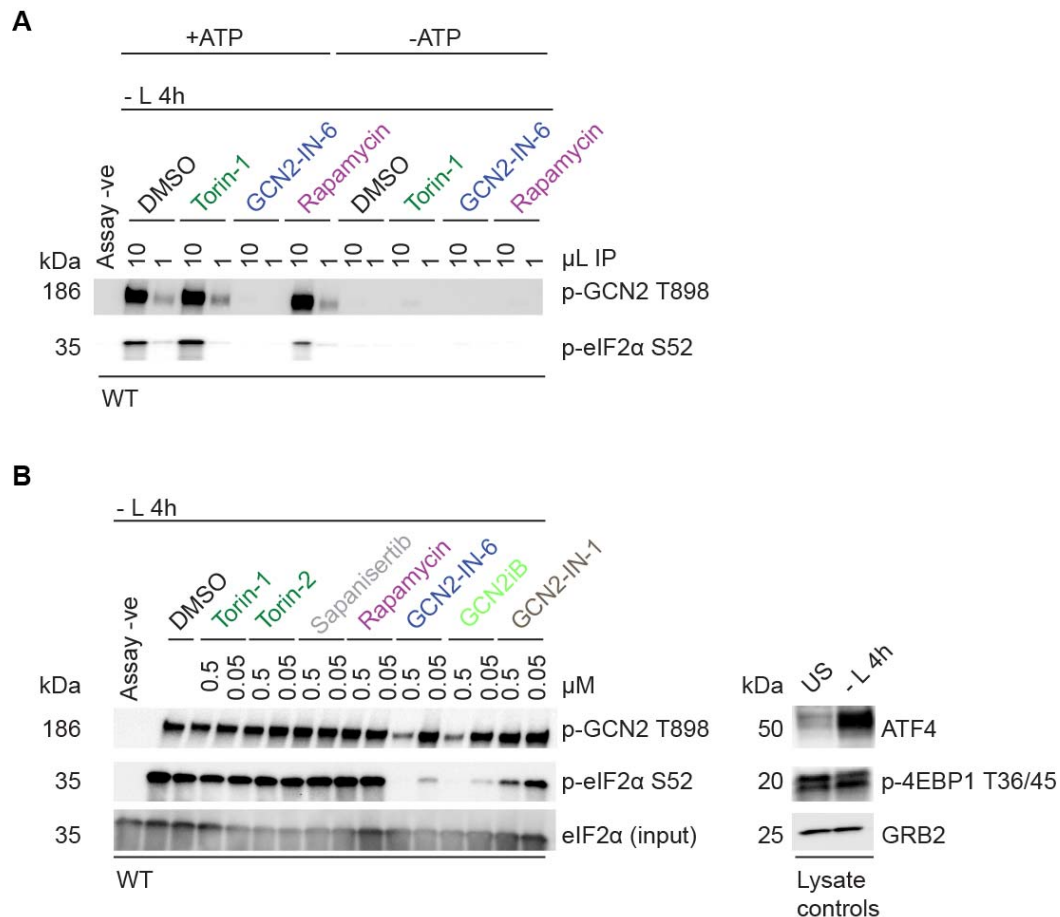
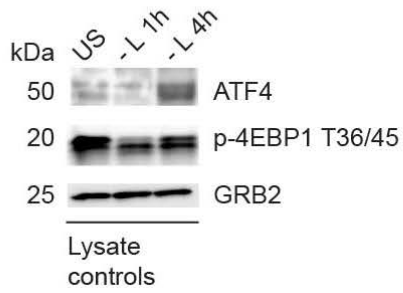
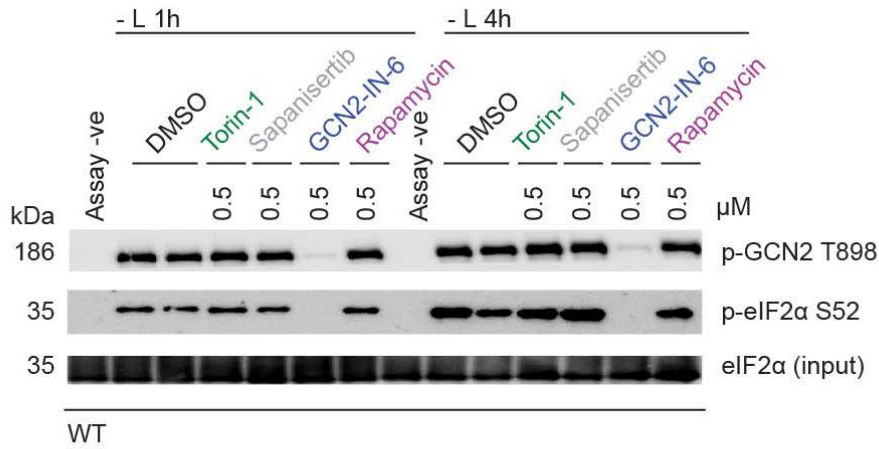
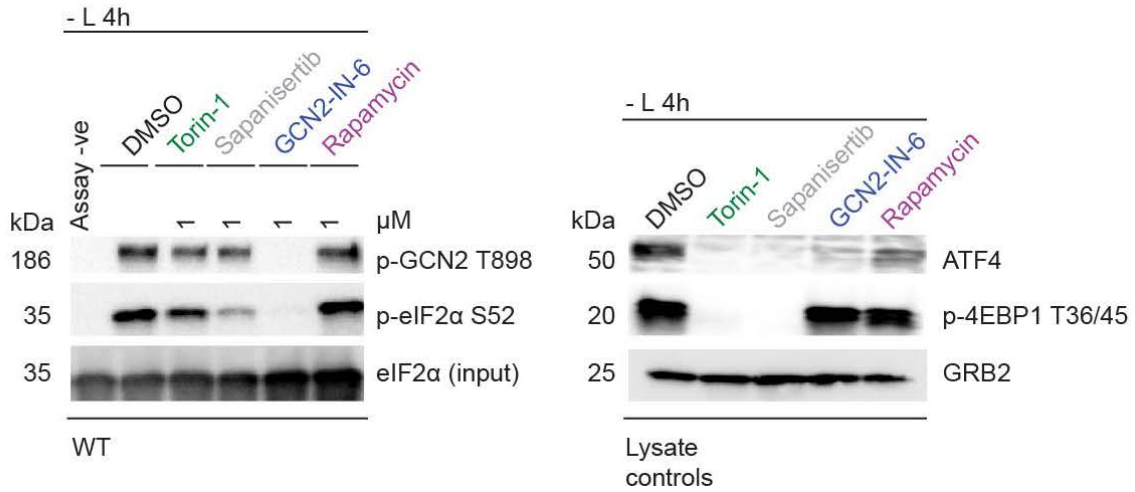


Figure 79. Model of the *in vitro* immunoprecipitation-based GCN2 kinase assay. Scheme of our designed *ex-* and *in-cell* GCN2 kinase assay: 3T3 wild-type (WT) cells were transfected with GCN2-3xFLAG (red) and leucine-starved (- L) for a certain time (t_x) prior to lysis, immunoprecipitation (IP), FLAG-peptide elution and enzymatic reaction (ATP and eIF2 α addition). The difference in the *in-* and *ex-cell* approach is the addition of inhibitors to the cells (*in-cell*) or after the enzymatic reaction (*ex-cell*).

First, we leucine-starved the wild-type cells for 4 h, added rapamycin, Torin-1 and GCN2-IN-6 (compound #28) *ex-cell* and read out phospho-GCN2 T898 and phospho-eIF2 α S52. In this context, we found that only GCN2-IN-6 (compound #28) prevented the kinase and substrate phosphorylations in a dose- and ATP-dependent manner (Figure 80A). Combined, this argues that only GCN2-IN-6 (compound #28) is a direct inhibitor of GCN2. To confirm this, we performed this assay with the other two GCN2 inhibitors (GCN2-IN-1 and GCN2iB) besides rapamycin and Torin-2 treatment. Again, Torin-2 and rapamycin did not show any effect on GCN2 and eIF2 α phosphorylations (Figure 80B). Interestingly, only GCN2iB (compound #29) blocked the phosphorylation of GCN2 and eIF2 α as shown for GCN2-IN-6 (compound #28) in contrast to GCN2-IN-1/A-92 (compound #5). This result could be explained by the high IC₅₀ and further unknown pharmacological properties of GCN2-IN-1/A-92 (compound #5) (Table 33). We also tracked the GCN2 inhibition at different time points (1 h versus 4 h) and performed the assay *in-cell*. As expected, we found the same outcome (Figure 80C+D). Combined, mTORC1/C2 inhibitors (sapanisertib and Torins) and the mTORC1 inhibitor (rapamycin) did not directly prevent the GCN2 kinase activity and its target phosphorylation in contrast to GCN2iB (compound #29) and GCN2-IN-6 (compound #28).



C**D**

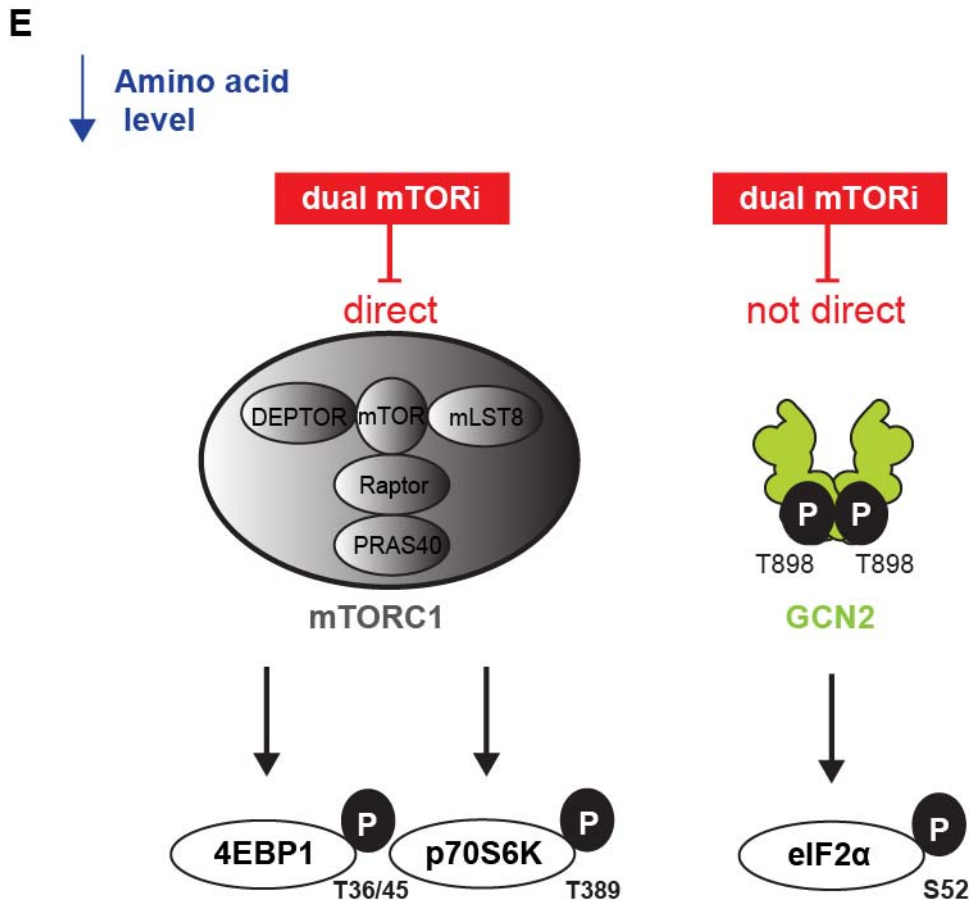


Figure 80. Dual mTOR inhibitors block the GCN2-ISR in an indirect manner upon leucine stress. (A) Immunoblot of pulled GCN2-3xFLAG wild-type (WT) cell lysate treated in *ex-cell in vitro* immunoprecipitation-based GCN2 kinase assay for 4 h of leucine starvation with different amounts of Torin-1, GCN2-IN-6 or rapamycin in the ab- or presence of ATP. (B) Same as A, except: 0.05 and 0.5 μM concentrations of Torin-1, Torin-2, sapanisertib, rapamycin, GCN2-IN-6, GCN2-IN-1 or GCN2iB were used. (C) Same as B, except: different timepoints (1 h versus 4 h) of leucine stress and unstarved condition (US) were applied to Torin-1, sapanisertib, GCN2-IN-6 or rapamycin treated 3T3 wild-type (WT) cells. (D) Same as C, except: *in-cell in vitro* immunoprecipitation-based GCN2 kinase assay for 4 h of leucine stress and treatment of 1 μM of Torin-1, sapanisertib, GCN2-IN-6 and rapamycin. (E) Model showing that dual mTOR inhibitors do not directly block GCN2 upon amino acid depletion. (A-D) Lysate controls were provided by immunoblotting. GRB2 was used as loading control. DMSO served as vehicle. (A-D) Data are depicted as one of two representative gels.

Next, we reversed the setting by determining the mTOR kinase activity in presence of inhibitor treatment (Figure 81). In collaboration with Julian Brötzmann from Prof. Dr. Elena Conti's department, we used a radioactivity-based mTOR kinase activity assay (Section 3.6.5.). Kindly provided by Dr. Yair Gat, the recombinantly expressed and purified mTOR ΔN complex was used, which contains the mTOR kinase (residues 1376-2549) and its binding factor mLST8 (relevant for

mTOR complex formation). In addition, labeled ATP ($[\gamma^{32}\text{P}]\text{-ATP}$) and GST-tagged AKT (residues 450-480; encoded by *Akt1*) enabled the reaction. We found that GCN2-IN-6 (compound #28) did not repress the mTOR activity in a dose-dependent manner (220 nM, 100 nM, 10 nM), which is in stark contrast to Torin-2 and sapanisertib (compound #12) (Figure 81). In line with GCN2-IN-6 (compound #28), rapamycin also did not inhibit mTOR activity as well. This can be explained by the absence of rapamycin binding partner FKBP12 in the reaction to bind the FRB domain and finally inhibit mTOR⁵²⁹ (Figure 81). In summary, the GCN2 inhibitor GCN2-IN-6 did not bind mTOR directly, leading to no repression of its activity.

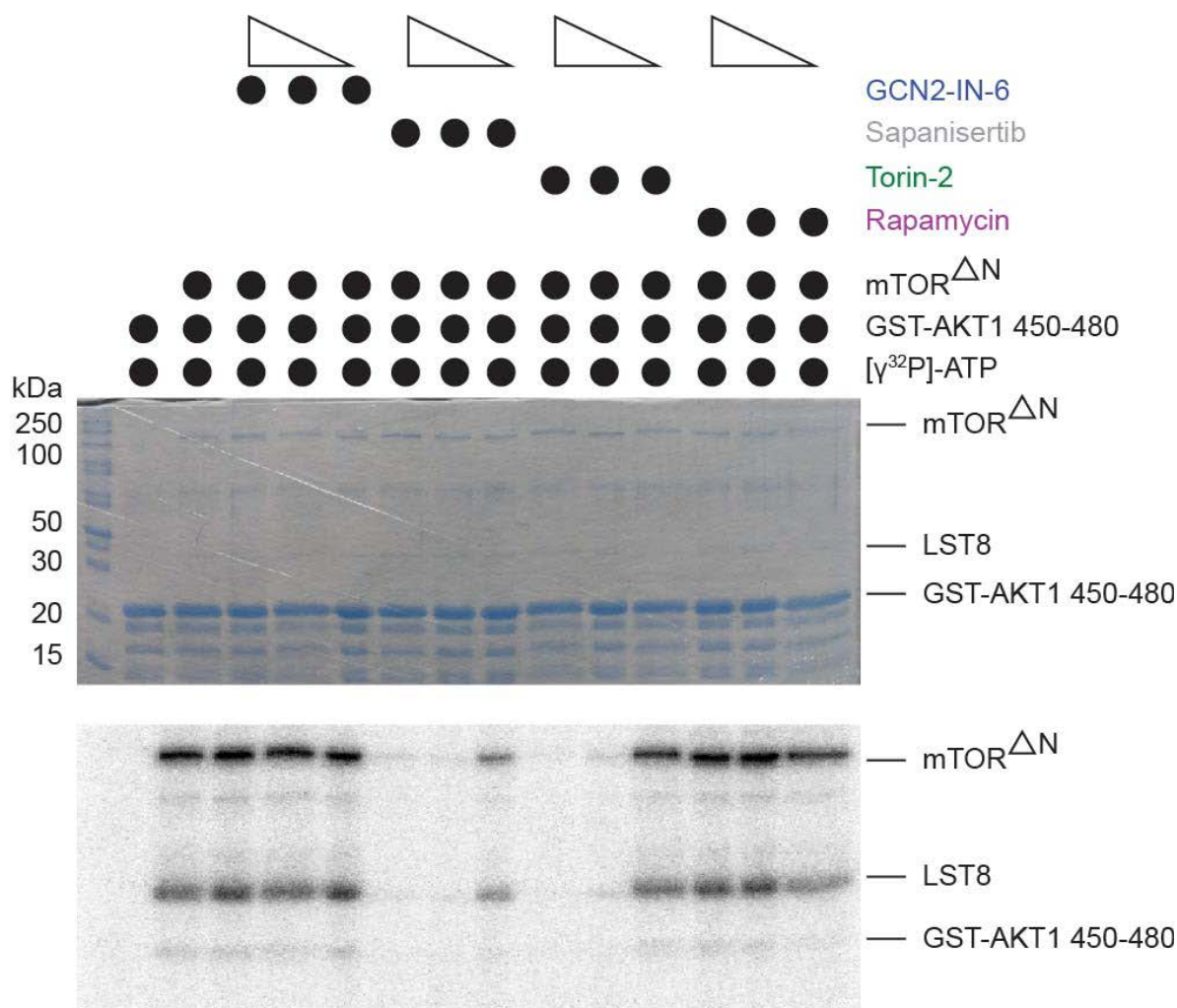


Figure 81. GCN2 inhibitor GCN2-IN-6 does not bind mTOR directly. Radioactivity-based mTOR kinase activity assay: GCN2-IN-6, sapanisertib, rapamycin and Torin-2 were treated at doses from 200 nM to 100 nM to 10 nM (indicated by the rectangle). Reaction without inhibitors and without mTOR ΔN were used as internal controls. Black dot indicates treatment condition. Data are depicted as one of two independent experiments.

In conclusion, we performed two separate *in vitro* kinase assays to track the direct binding of the inhibitors to mTOR and GCN2. In this context, we discovered that only GCN2 inhibitors (GCN2-IN-6 and GCN2iB) directly bind and inhibit GCN2 kinase upon amino acid stress. Dual mTOR inhibitors only directly bind to mTOR kinase. Therefore, our model was refined that dual mTOR inhibitors do not prevent the GCN2-ISR upon amino acid stress in a direct manner (Figure 80E). These data point towards a model where dual mTOR inhibitors indirectly block an upstream step in GCN2 activity.

4.7.6. Dual mTORi-mediated GCN2-ISR inhibition is regulated independently of eIF2 α

We described that the prevention of the GCN2-ISR upon amino acid stress is indirectly executed by dual mTOR inhibitors. In addition, we highlighted that the suppression affected all downstream key targets of GCN2 (ATF4, CHOP and eIF2 α). In section 4.4., we unraveled the connection between the autophosphorylation of GCN2 with eIF2 α and ATF4. In detail, GCN1 regulates the activity of GCN2 and the ATF4 induction upon amino acid stress – independently of eIF2 α . Therefore, we aimed to address if the mTOR inhibitory agents prevent the ISR upon amino acid stress in dependency on eIF2 α .

We treated the wild-type 3T3 and eIF2 α mutant cell lines (*Eif2s1* S52A) with Torin-1, GCN2-IN-6 (compound #28) and rapamycin. Consistent with the wild-type background, Torin-1 and GCN2-IN-6 (compound #28) treatment prevented the induction of the ISR (phospho-GCN2 T898 and ATF4) in cells mutated in the phosphosite of the eIF2 α target (*Eif2s1* S52A) (Figure 82). On top of this, only Torin-1 blocked the mTORC1 targets in *Eif2s1* S52A cells. This finding argues that the prevention of the GCN2-ISR by dual mTOR inhibitors is regulated independent of eIF2 α upon leucine stress. Interestingly, rapamycin treatment in the *Eif2s1* S52A background showed a diminished phosphorylation of 4EBP1 at T36/45, autophosphorylation of GCN2 at T898 and ATF4 induction (Figure 82). In our perspective, the translation initiation regulated by 4EBP1 and eIF2 α might be relevant for the inhibitory process and will be addressed below.

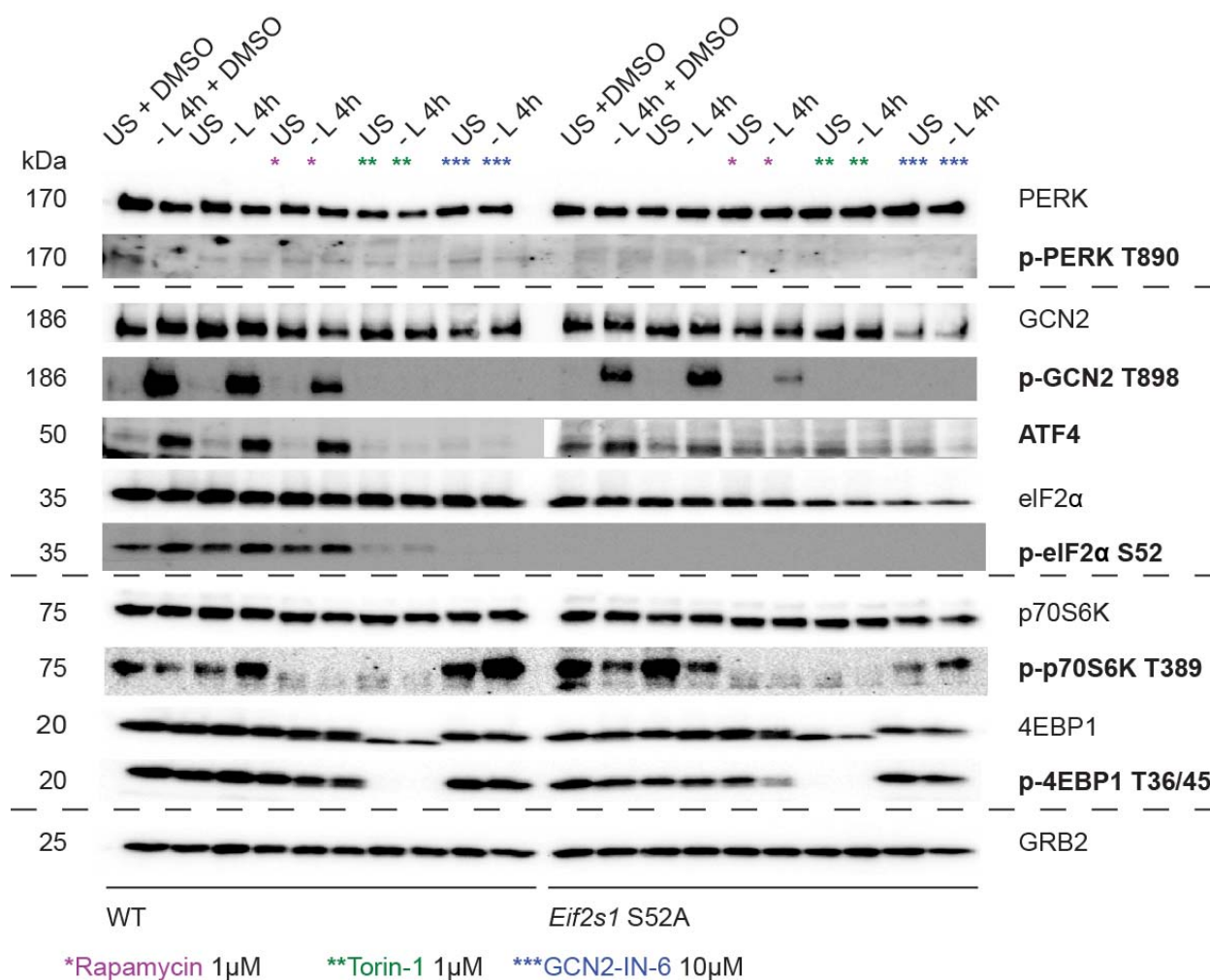


Figure 82. Dual mTOR inhibitors suppress the ISR upon leucine stress in an eIF2α-independent manner. Immunoblot of 4 h leucine-starved (- L) 3T3 wild-type (WT) or *Eif2s1* S52A cell lysates treated with rapamycin (1 μM), Torin-1 (1 μM) or GCN2-IN-6 (10 μM). GRB2 was used as loading control. DMSO was used as vehicle. In bold, changes due to the compound treatment. Data are depicted as one of two representative gels.

In conclusion, dual mTOR inhibitors efficiently blocked the GCN2 cascade upon amino acid stress independently of eIF2α.

4.7.7. Dual mTORi-mediated GCN2-ISR inhibition is regulated independently of PERK

Unfolded proteins and aggregates activate ER stress in the cellular environment, which is sensed and signaled by the eIF2α kinase PERK¹³. Even though PERK and GCN2 show a high genetic conservation in their catalytic as well as autophosphorylation sites, PERK activation is not stimulated by amino acid stress (Section 4.2.; Figure 27). However, the PERK-ISR, the GCN2-ISR and the mTORC1 cascade modulate their transcriptional responses mediated by ATF4

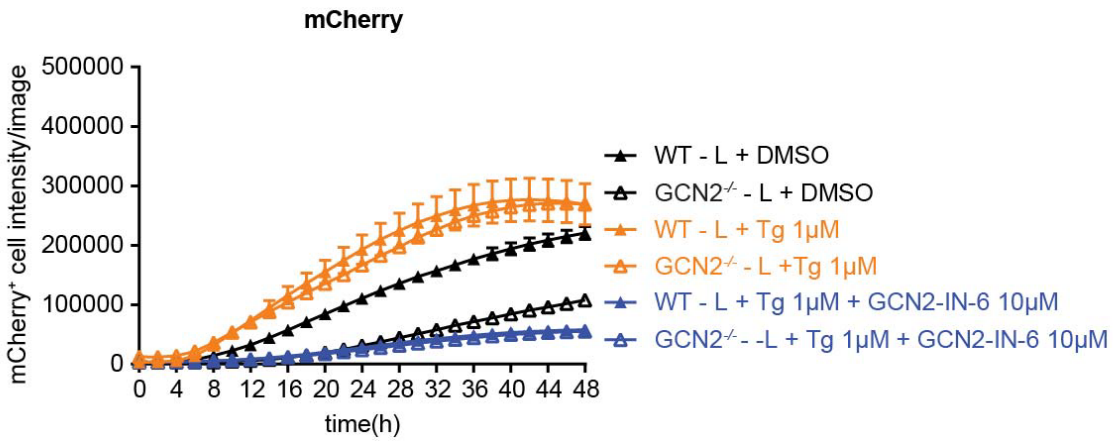
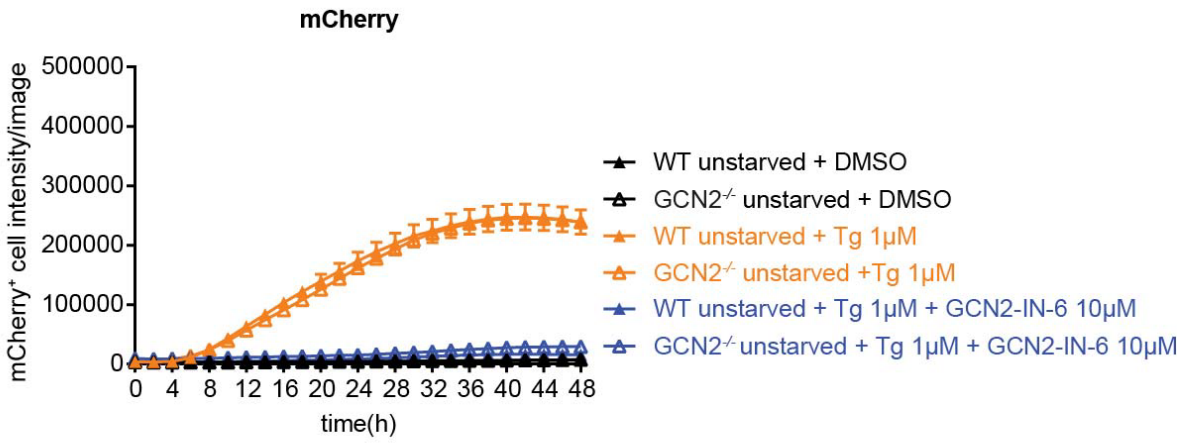
(Ref.²⁶) (Section 4.2.). Therefore, we decided to check if PERK signaling is manipulated by dual mTOR inhibitors assigning the relevance for PERK to the overall specificity of the system.

The GCN2 inhibitor GCN2-IN-6 (compound #28) has an IC₅₀ of 0.26 nM for PERK inhibition²⁴⁸. In this context, we tested if thapsigargin-induced PERK signaling can be blocked by GCN2-IN-6 (compound #28). Using our *Ddit3::mCherry* reporter system, we found that GCN2-IN-6 (compound #28) efficiently blocked the mCherry induction (Figure 83A+E). This process is independent of GCN2 and amino acid stress manifesting our previous finding that PERK is not intrinsically activated by the GCN2-ISR upon amino acid stress (Section 4.2.; Figure 27). Thus, we confirmed with the literature²⁴⁸ that GCN2-IN-6 (compound #28) is a PERK inhibitor.

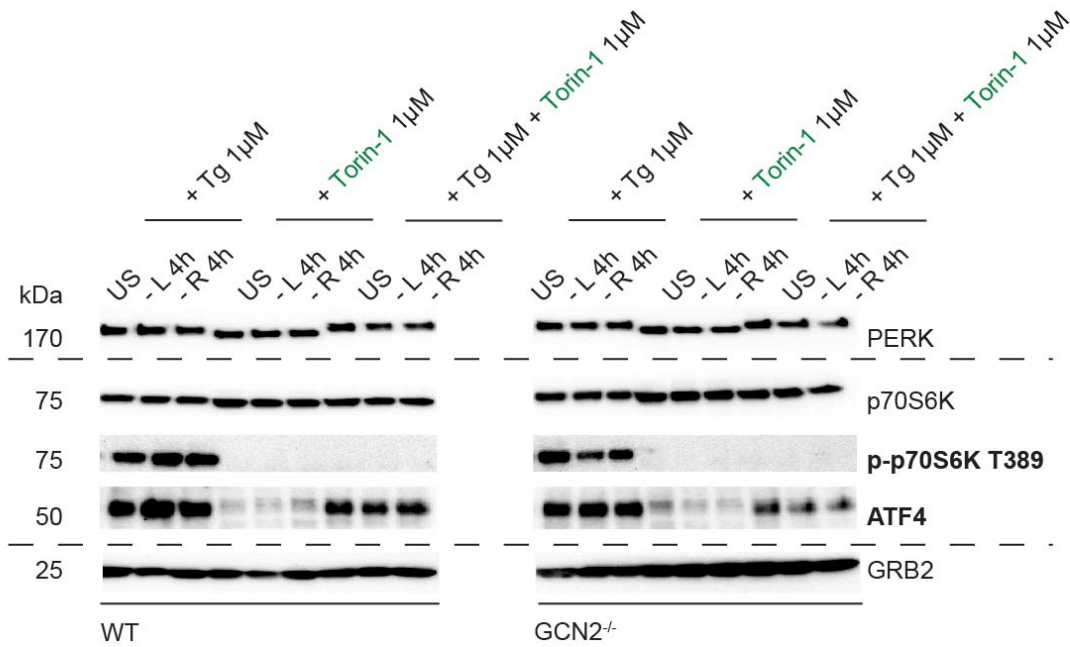
Next, we addressed if Torin-1 also blocks the thapsigargin-induced PERK signaling. Torin-1 did not activate PERK independently of amino acid stress or GCN2 proficiency that is shown by the difference in PERK band height in the immunoblot (Figure 83B). Moreover, Torin-1 prevented ATF4 induction upon amino acid stress that was not shown in combination with thapsigargin-activated PERK signaling independent of GCN2 (Figure 83B). This finding argued that ATF4 induction was still triggered by active PERK while GCN2 was blocked by Torin-1. Therefore, we performed the experiment again tracking the autophosphorylations of PERK and GCN2 besides ATF4 induction. We found that PERK was active (autophosphorylation at T980) and ATF4 as well, but GCN2 not (autophosphorylation T898) upon leucine stress in combination with Torin-1 and thapsigargin treatment (Figure 83C). This data manifested our assumption that the thapsigargin activated PERK-ATF4 axis was not prevented by Torin-1.

GCN2 and PERK share their target eIF2 α ⁶⁰. Therefore, we treated the eIF2 α mutant (*Eif2s1* S52A) with rapamycin, Torin-1 and GCN2-IN-6 (compound #28) in the presence of thapsigargin treatment and leucine stress. The result was the same as described for the wild-type cells (Figure 83C). In both cell lines, we discovered that mTORC1 signaling as indicated by the 4EBP1 or p70S6K phosphorylation was not affected by PERK inhibition induced by GCN2-IN-6 (compound #28). Moreover, Torin-1 did not suppress the PERK signaling in eIF2 α mutant cells. In this context, rapamycin neither suppressed PERK nor GCN2 signaling. Interestingly, the GCN2-ATF4-4EBP1 axis was reduced in the eIF2 α mutant line in the thapsigargin treated condition by rapamycin. This effect did not affect PERK activation and was already shown for the non-thapsigargin treated eIF2 α mutant cells in figure 82.

A



B



E

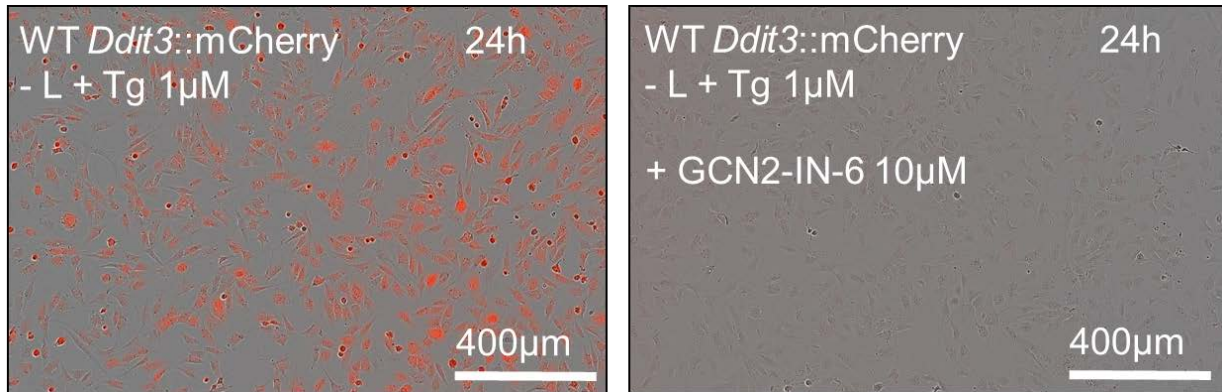


Figure 83. Torin-1 does not suppress PERK signaling independently of GCN2, eIF2 α and amino acid stress. (A) Quantification of mCherry intensity in 3T3 *Ddit3::mCherry* wild-type (WT) and GCN2 knockout (GCN2^{-/-}) cells treated with thapsigargin (Tg; 1 μ M) in the presence of GCN2-IN-6 (10 μ M), over time in unstarved or leucine-starved (- L) medium. DMSO served as vehicle. (B) Immunoblot of 3T3 wild-type (WT) and GCN2 knockout (GCN2^{-/-}) cell lysates treated with Torin-1 (1 μ M) and/or thapsigargin (Tg; 1 μ M) at 4 h in unstarved (US) or leucine (- L) - or arginine-starved (- R) medium. (C) Same as B, except: only unstarved (US) and leucine starved (- L) 3T3 wild-type (WT) and *Eif2s1* S52A cell lysates treated with GCN2-IN-6, rapamycin and Torin-1. (D) Model showing that GCN2-IN-6 but not Torin-1 blocks PERK signaling. (E) Microscopic images of mCherry⁺ cells from B upon leucine stress treated with thapsigargin (Tg; 1 μ M) for 24 h in the presence of GCN2-IN-6 (10 μ M). (B-C) In bold, changes due to the compound treatment. (A-C) Data are depicted as mean + SEM of three independent experiments or one of two representative gels.

In line with the literature²⁴⁸, we confirmed that thapsigargin-induced PERK signaling was inhibited by GCN2-IN-6 (compound #28) independently of amino acid stress or GCN2 presence (Figure 83D). Upon leucine stress, Torin-1 prevents the GCN2 cascade but not the ER stress-induced PERK cascade independently of eIF2 α (Figure 83D). PERK activation (via thapsigargin) or inhibition (via GCN2-IN-6) did not modulate mTORC1 signaling. Rapamycin diminished GCN2 signaling, but not PERK signaling in the phospho-eIF2 α mutant background.

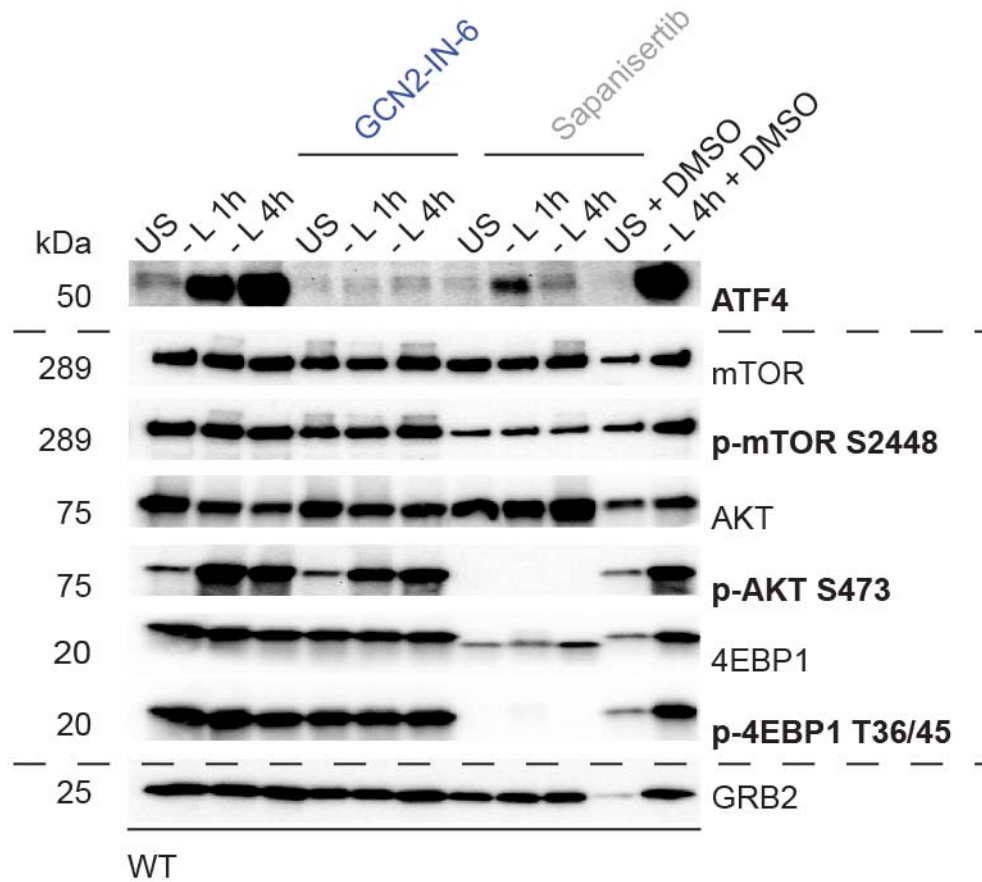
4.7.8. GCN2 inhibition does not affect mTORC2 activity upon leucine stress

One of the most important findings throughout this thesis was that the GCN2-ISR was only suppressed by dual mTORC1/mTORC2 inhibitors and not by the mTORC1 specific inhibitor rapamycin upon amino acid stress (Figure 78). Therefore, the most obvious explanation for this phenomenon would be that mTORC2 is the main driver to regulate GCN2 activation upon amino acid stress.

In a first attempt, we addressed the activity of mTORC2 by tracking the phosphorylation of AKT at serine 473 (S473). This is an indirect readout for active mTORC2 knowing that RICTOR-mTOR complex directly phosphorylates AKT at S473 and facilitates the phosphorylation at threonine 308 in the activation loop by PDK1^{282,532}. Thereby, AKT phosphorylation is not sensitive to acute rapamycin treatment²⁸³ and mSIN1-RICTOR-mTOR function at S473 is required for TORC2 function, but is dispensable for TORC1 function⁵³³.

We treated wild-type 3T3 cells with sapanisertib (compound #12) or GCN2-IN-6 (compound #28) upon leucine depletion. As expected, sapanisertib blocked the phosphorylation of AKT at S473 while GCN2-IN-6 did not (Figure 84A). The same phenomenon was found when performing the experiment in the GCN2 or GCN1 deficient background (Figure 84B). This finding argued that mTORC2 is still active upon amino acid stress and is not regulated by the GCN2 cascade. Next, we tested an available mTORC2 inhibitor JR-AB2-011 (IC₅₀ 0.36 μM) in our murine setting^{533,534}. For now, this inhibitor did not work in our context, which was shown by still phosphorylated AKT – even at high drug doses (Figure 84C).

A



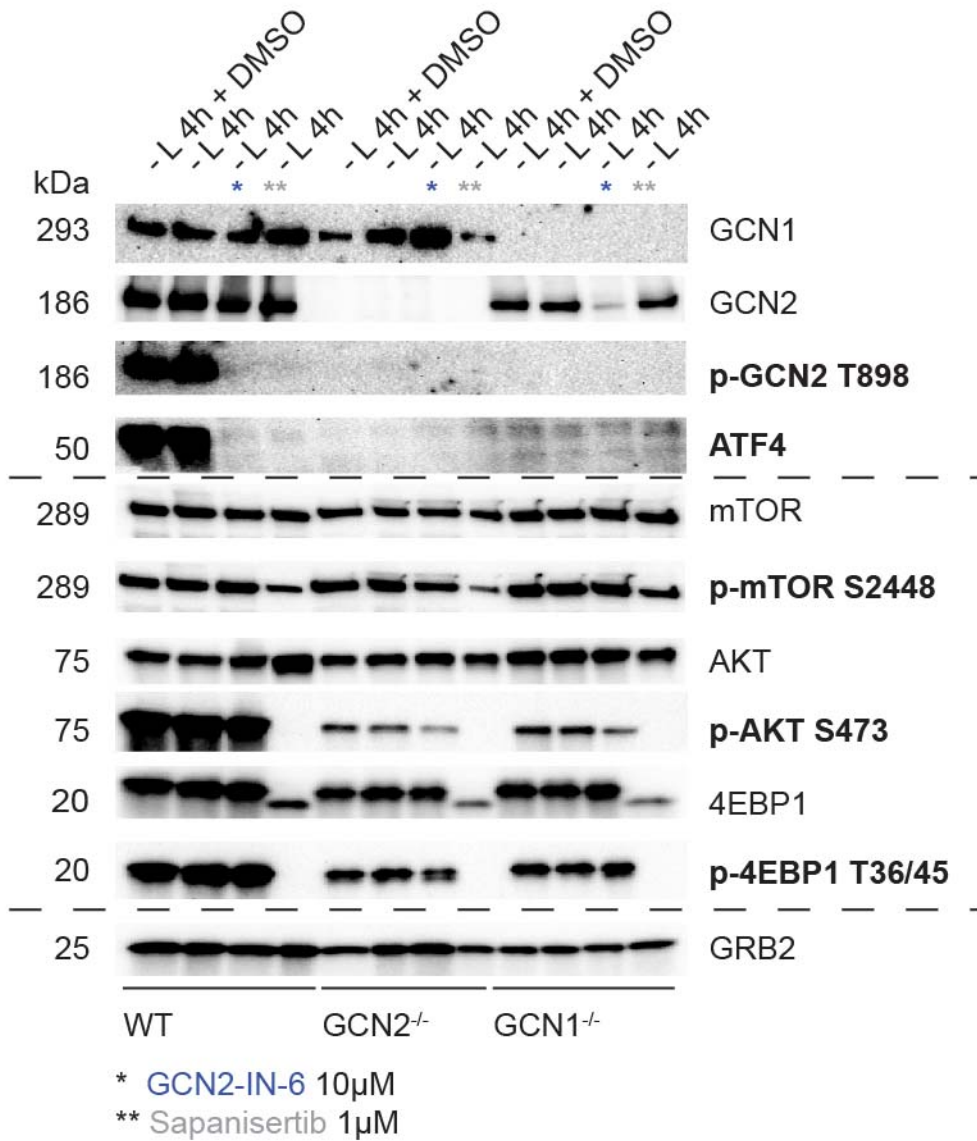
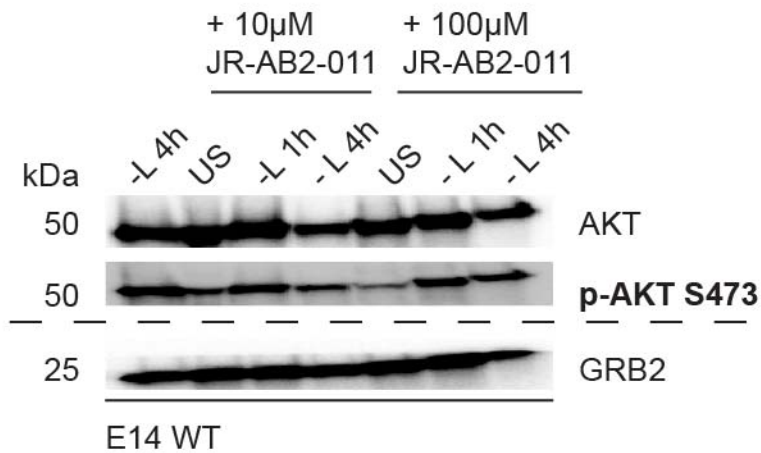
B**C**

Figure 84. GCN2 inhibition did not affect the mTORC2 activity upon leucine stress. (A) Immunoblots of 3T3 wild-type (WT) cell lysates treated with sapanisertib (10 μ M) and GCN2-IN-6 (10 μ M) upon 1 h or 4 h of leucine stress (- L) or unstarved condition (US). DMSO was used as vehicle. GRB2 was used as loading control. (B) Same as A, except: in 3T3 wild-type (WT), GCN2 deficient (GCN2^{-/-}) and GCN1 deficient (GCN1^{-/-}) background only treated for 4h of leucine stress (- L 4h). (C) Same as A, except: treatment with JR-AB2-011 (10 μ M or 100 μ M) in E14 wild-type (E14 WT) cells. (A-C) In bold, changes due to the compound treatment. Data are depicted as one of two representative gels.

Together, we provide a first evidence that specific GCN2-ISR inhibition using GCN2-IN-6 did not affect AKT signaling and thereby indirectly mTORC2 activity. Further studies will follow to directly manipulate mTORC2 and mTORC1 side-by-side using siRNA-based depletion of the specific regulatory proteins RICTOR and RAPTOR, respectively. This approach will finally underline the role of mTORC2 in the manipulation of the GCN2-ISR upon amino acid stress by dual mTOR inhibitors (Section 5.6.).

4.7.9. Dual mTORi-mediated GCN2-ISR inhibition is time-dependent

The mTORC1 activity is time-dependently regulated upon amino acid stress³⁶⁰. For example, we postulated in section 4.5. that the GCN1-GCN2 signaling prevents the mTORC1 activation upon short-term amino acid stress exposure via the ATF4-4EBP1 axis. To address this time-dependency also in the context of manipulating the GCN2-ISR mediated by dual mTOR inhibitors, we tracked the ISR induction for short-term (1 h) and prolonged (4 h) amino acid stress in combination with inhibitor treatment.

Surprisingly, we discovered that ATP-competitive mTOR inhibitors blocked GCN2 activity only after long-term stress exposure (4 h) (Figure 85A). In contrast, GCN2-IN-6 suppressed GCN2 already at 1 h and rapamycin had no effect on GCN2 autophosphorylation over time of leucine stress (1 h and 4 h). Therefore, we performed a 'spike-in' experiment starving the wild-type 3T3 cells first for 2 h before adding the respective inhibitor and then incubating the cells for another 1 h prior to lysis. Under these conditions, the ISR was blocked by the dual mTOR inhibitors (Figure 85B). Next, we addressed a broader time-range by adding Torin-1 to the pre-starved cells for 1 h, 2 h, 3 h and 4 h. Torin-1 suppressed the ISR not at 1 h, but at 2 h, 3 h and 4 h (Figure 85C). This finding led to the assumption that the suppression of the ISR by dual mTOR inhibitors might be dependent on the duration of amino acid stress exposure. However, this time-dependency is still under investigation. In this context, we will also address the different pharmacokinetic properties of the GCN2 inhibitors, because only GCN2-IN-6 blocked the autophosphorylation of GCN2 at 1 h leucine stress (Figure 85A).

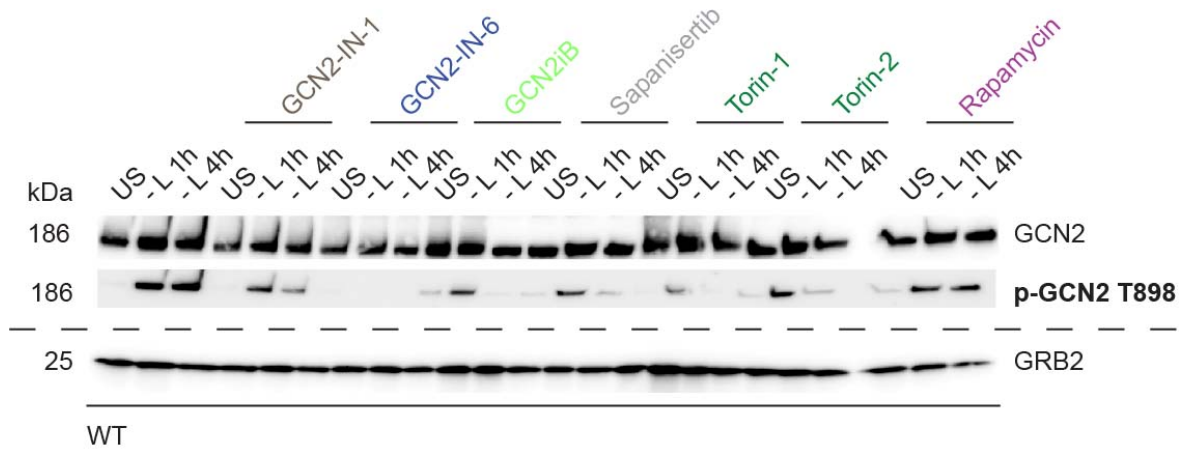
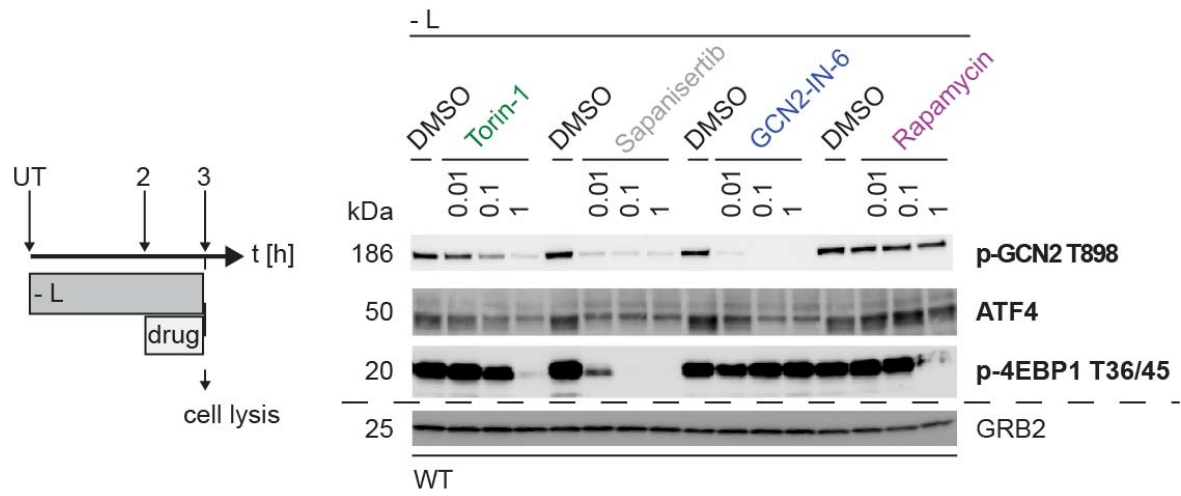
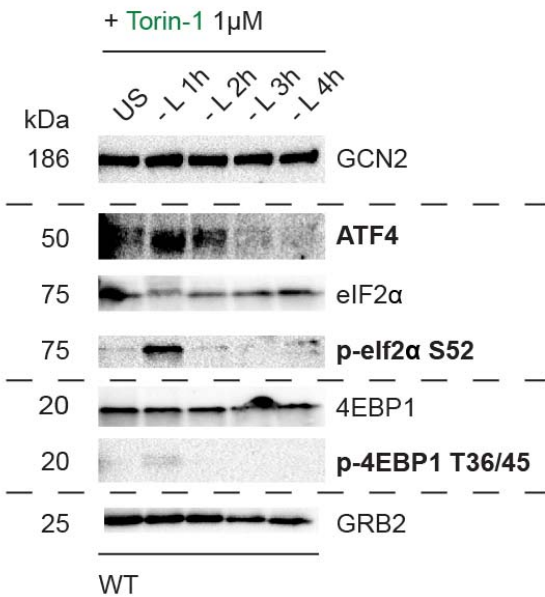
A**B****C**

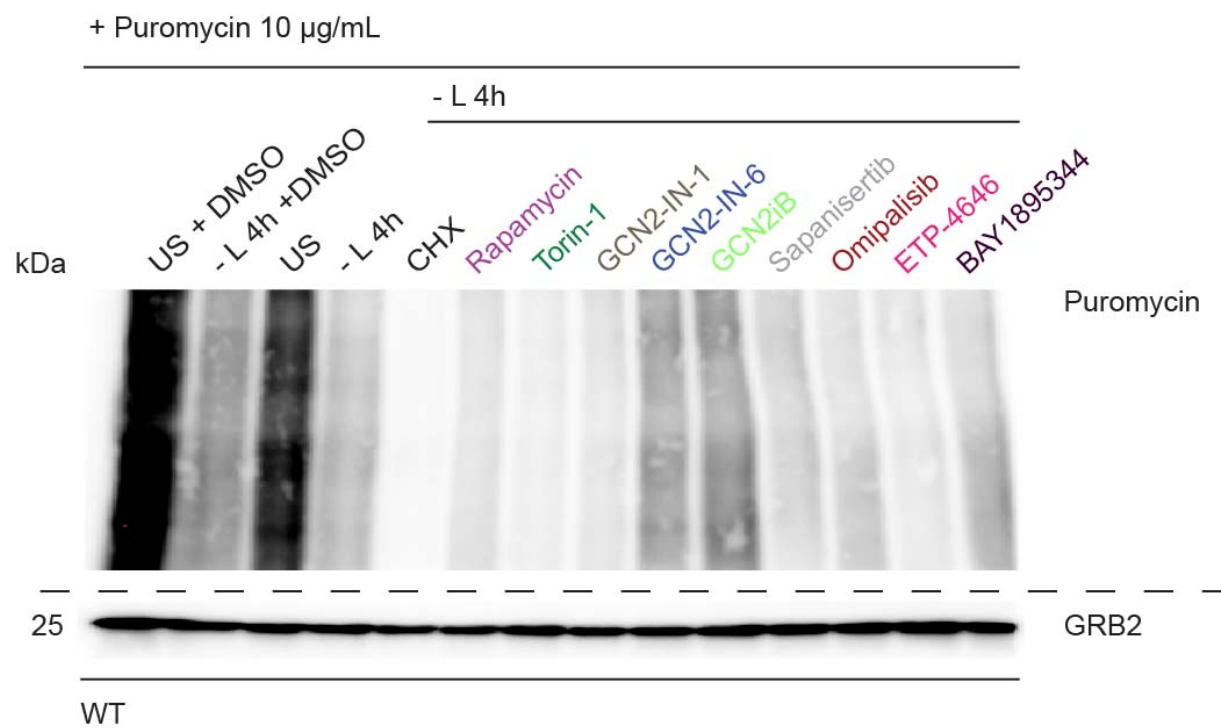
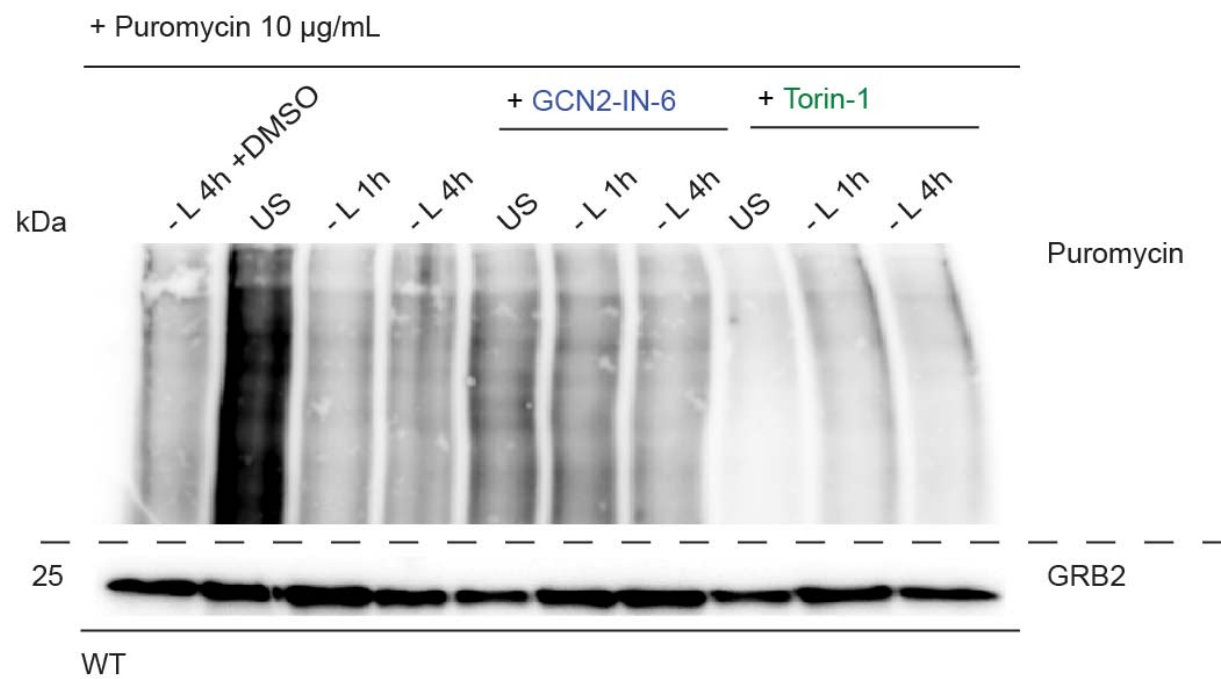
Figure 85. Dual mTOR inhibitors suppress the GCN2 cascade in a time-dependent manner upon leucine stress. (A) Immunoblot of 3T3 wild-type (WT) cell lysates treated with Torin-1 (1 μ M), Torin-2 (1 μ M), rapamycin (1 μ M), sapanisertib (10 μ M), GCN2-IN-1 (10 μ M), GCN2-IN-6 (10 μ M) or GCN2iB (10 μ M) upon unstarved condition (US) or leucine depletion (- L) for 1 h and 4 h. GRB2 is used as loading control. (B) Immunoblot of 3T3 wild-type (WT) cell lysates treated with Torin-1 (0.01-1 μ M), rapamycin (0.01-1 μ M), sapanisertib (0.01-1 μ M) or GCN2-IN-6 (0.01-1 μ M) for 1 h after 2 h of leucine depletion (- L). DMSO is used as vehicle. GRB2 is used as loading control. (C) Immunoblot of 3T3 wild-type (WT) cell lysates treated with Torin-1 (1 μ M) upon unstarved condition (US) or leucine depletion (- L) for 1 h, 2 h, 3 h and 4 h. GRB2 is used as loading control. (A-C) In bold, changes due to the compound treatment. (A-C) Data are depicted as one of two representative gels.

In conclusion, we provided a first hint that the manipulation of the ISR by dual mTOR inhibitors is most likely regulated by the duration of amino acid stress.

4.7.10. Translation is regulated by GCN2 and mTOR inhibition

Torin-1 efficiently blocks translation, which is only substantially achieved by rapamycin treatment in normal growth state and does not affect phosphorylation of eIF2 α ³⁹⁰. A plausible explanation was drawn by this finding towards the rapamycin-insensitivity of blocking phospho-4EBP1 at T36/45 (Refs.^{295,305,311,390,535}). Therefore, we used translation as a readout strategy to explore the downstream effect of mTOR versus GCN2 inhibition upon amino acid stress. We treated our wild-type 3T3 cells with mTORi and GCN2i, and tracked the translational profile using puromycin treatment after 4 h of leucine stress.

In line with Thoreen *et al.*³⁹⁰, we showed that rapamycin did also not induce a strong translational shut-down compared to Torin-1 upon leucine stress (Figure 86A). In addition, all inhibitors known to block both mTOR complexes (sapanisertib, omipalisib, Torin-1, ETP-46464 and BAY1895344) induced a strong translational shut-down. Interestingly, GCN2-IN-1/A-92 (compound #5) showed a comparable profile as Torin-1. This makes sense, because we showed before that GCN2-IN-1 efficiently blocked mTORC1 besides GCN2 upon amino acid stress (Section 4.7.3.; Figure 77A). All inhibitors only affecting the GCN2 cascade (GCN2-IN-6 and GCN2iB) did not induce a strong translational shut-down as compared to the other illustrated inhibitors. The difference in translational shut-down dependent on compound treatment was also verified by a time-dependent analysis of translation in GCN1 and GCN2 deficient cells (Figure 86B-D). In this context, Torin-1 decreased translation equally efficient in wild-type, GCN1 and GCN2 knockout background in contrast to GCN2-IN-6.

A**B**

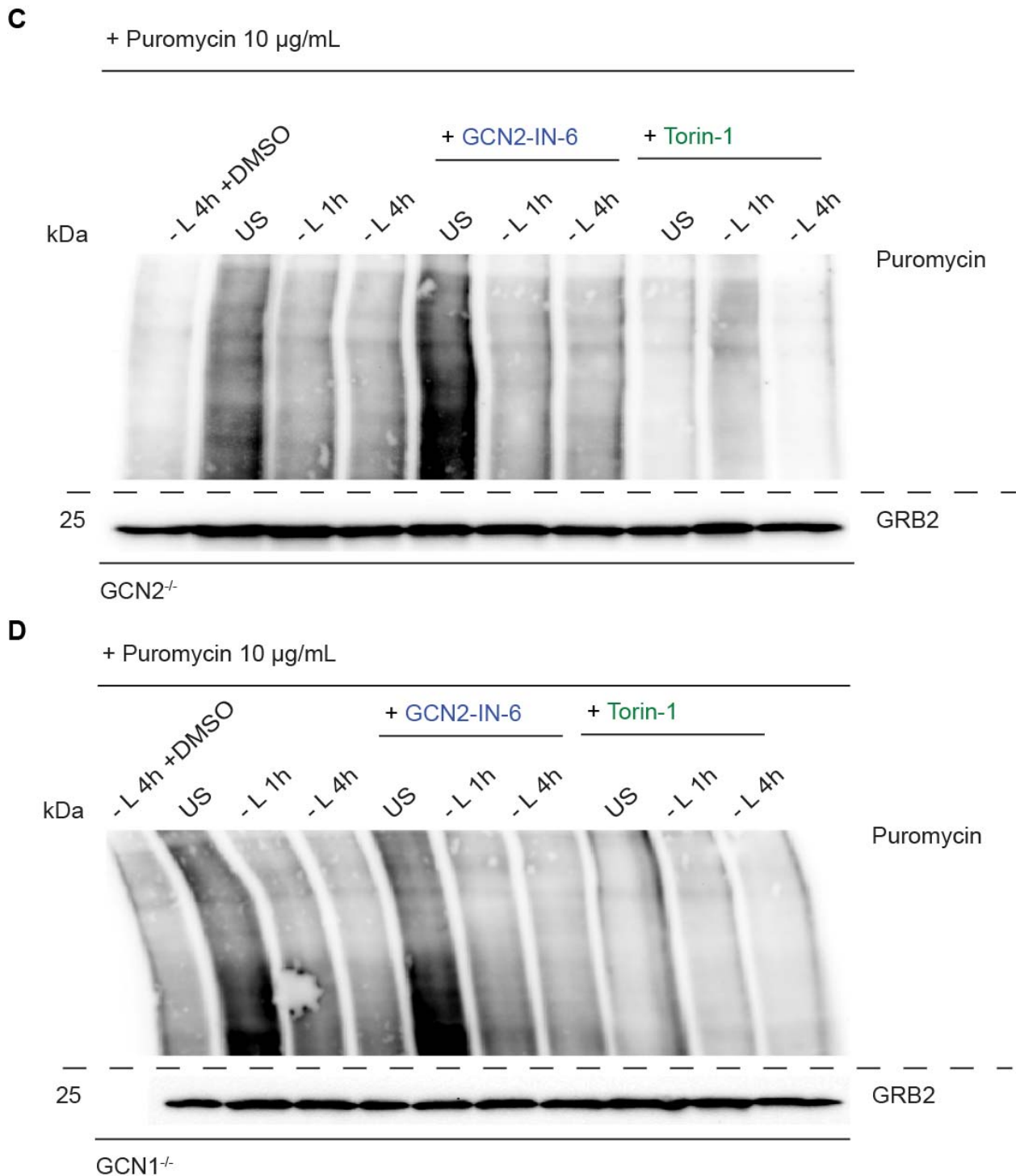


Figure 86. Dual mTOR inhibitors induce a more potent translational shut-down upon amino acid stress than rapamycin or GCN2 inhibitors. (A) Immunoblot of 4 h leucine-starved (- L) 3T3 wild-type (WT) cell lysates treated with rapamycin, Torin-1, GCN2-IN-1, GCN2-IN-6, GCN2iB, sapanisertib, omipalisib, ETP-46464 or BAY-1895344 prior to puromycin addition (10 $\mu\text{g/mL}$). GRB2 was used as loading control. DMSO was used as vehicle. Concentration of all inhibitors was 10 μM . Cycloheximide (CHX 1 μM) was used as control. (B-D) Same as A, except: GCN2-IN-6 and Torin-1 treatment in 3T3 wild-type (WT),

GCN2 deficient (GCN2^{-/-}) or GCN1 deficient (GCN1^{-/-}) background upon leucine starvation (- L 1h or 4h) and unstarved condition (US). (A-D) Data are depicted one of two representative gels.

In conclusion, we tracked translation to understand how single or combined inhibition of GCN2 and mTOR activity is regulated. We showed that the dual block of mTOR and GCN2 was most efficient in shutting down translation. Collectively, we currently consider a model in which translational shut-down is only potentially achieved when preventing 4EBP1 phosphorylation at T36/45 that is discussed in more detail in section 5.6.

4.7.11. Energy sensing is regulated by GCN2 and mTOR inhibition

In response to stress, cellular ATP is depleted, which activates AMP-activated protein kinase (AMPK), the key regulator of cellular energy, which can be measured by its phosphorylation at threonine 172 (T172)⁵³⁶⁻⁵³⁸. Thereby, phosphorylated AMPK inactivates mTORC1 triggering the inhibition of protein synthesis and the activation of autophagy³³⁴. Disruption of mitochondrial function correlated with AMPK and HRI-ATF4 induction, sensitizing mTORC1 signaling inhibition⁵³⁹. Furthermore, Kaspar *et al.*⁵⁴⁰ showed that CHOP-ATF4 interaction is needed to prevent early respiratory chain deficiency and energy crisis upon mitochondrial dysfunction⁵⁴⁰. To start addressing the role of the amino acid ISR in sensing mitochondrial integrity and its connection to the mTORC1 pathway, we checked AMPK activity upon GCN2 (GCN2-IN-6; compound #28) and mTOR inhibition (sapanisertib; compound #12) in combination with leucine deprivation in wild-type 3T3 cells.

Therefore, early (1 h) versus late (4 h) leucine stress was applied to the wild-type cells. In line with the literature³³⁴, we confirmed that AMPK activation negatively regulated mTORC1 activity. In detail, we could match mTORC1 reactivation at 4 h to the inactivation of AMPK (Figure 87B). The reversed phenomenon was seen at 1 h. Interestingly, the disruption of the ISR by GCN2-IN-6 (compound #28) treatment inactivated the ISR cascade (phospho-GCN2 T898 and ATF4) at 1 h triggering no activation of AMPK (phospho-AMPK T172). In other words, when the GCN2 cascade and phospho-AMPK were blocked mTORC1 was active (phosphorylated 4EBP1 T36/45). In contrast, when mTORC1 was suppressed by sapanisertib (compound #12), AMPK was active. Combined, we concluded that the manipulation of the GCN2 cascade affects mitochondrial function and the internal ATP levels by controlling the AMPK activation status to transfer this information to mTORC1 at early leucine stress exposure (Figure 87A). However, this model still needs to be dissected in further perspective.

The next step was to connect these findings to mitochondrial function (Figure 87C). As reported by Condon *et al.*⁵³⁹, the dysregulation of mitochondrial function is sensed through AMPK and HRI-

ATF4. This was investigated using oligomycin treatment, which disrupts the ATP synthase function inducing mitochondrial stress⁵³⁹. Therefore, we analyzed the amino acid response upon oligomycin treatment. We found that the GCN2-ISR was not activated by oligomycin treatment over time, which is shown in the immunoblot by no autophosphorylated GCN2 (Figure 87C). However, oligomycin activated ATF4. At this stage, we assumed that HRI would trigger the induction of ATF4, even if we miss the control in this context^{65,66,539}. Combined, this argued that the GCN2-ISR was not activated by mitochondrial stress in the experimental setting from Condon *et al.*⁵³⁹. Next, we treated the wild-type cells with oligomycin and leucine stress. Thereby, the GCN2 cascade was activated that was shown by the autophosphorylation of GCN2 and more potent ATF4 (Figure 87C). Mitochondrial stress in addition to leucine stress triggered the induction of AMPK, but its activation did not correlate with the inhibition of mTORC1. To investigate the regulating of mTORC1 upon leucine and mitochondrial stress, we will apply GCN2 and mTOR inhibition in future perspective.

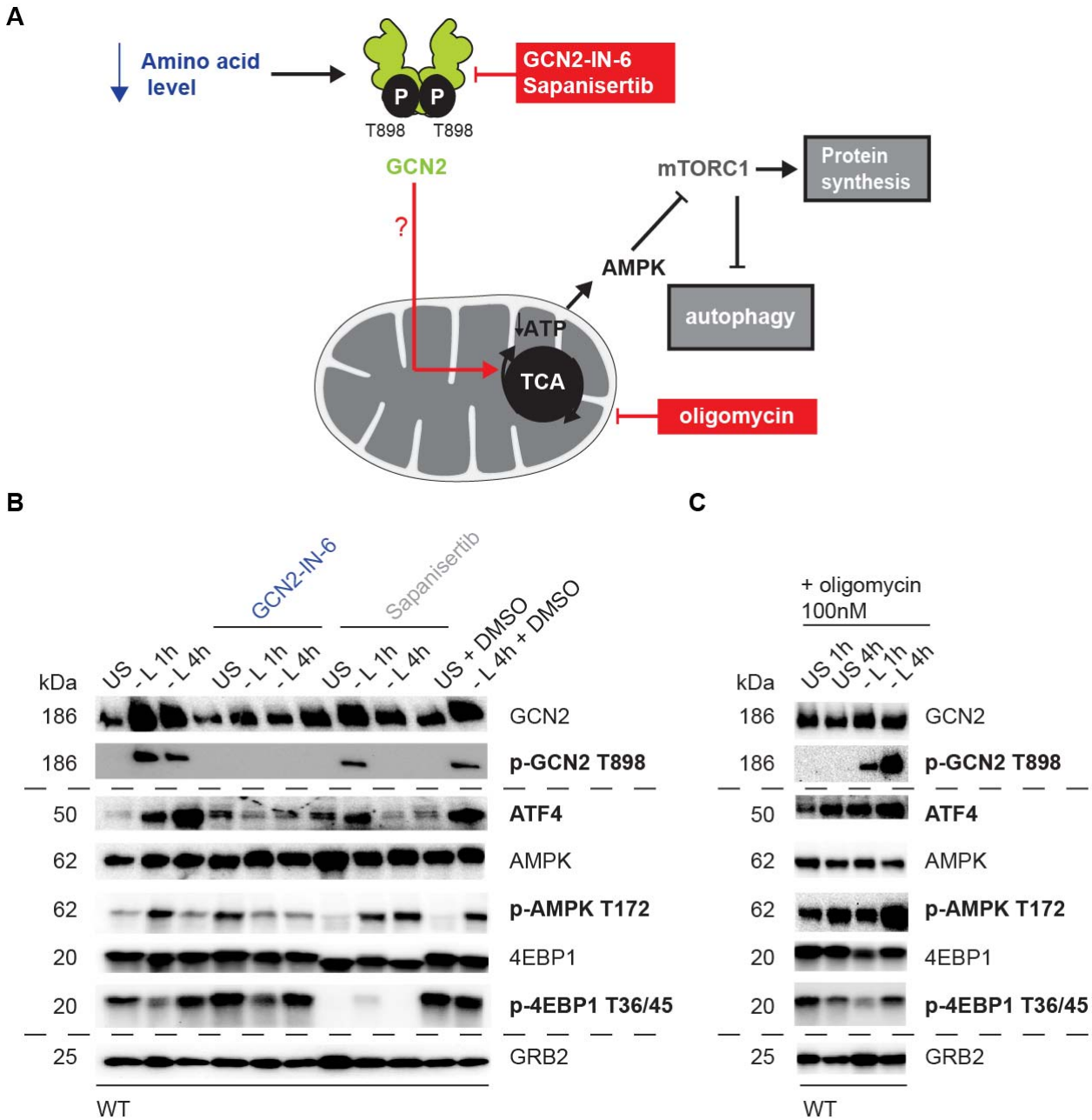


Figure 87. Energy sensing via AMPK is affected by GCN2 inhibition upon leucine stress. (A) Model how GCN2, mTORC1 and AMPK might be connected upon amino acid stress. (B) Immunoblot of 3T3 wild-type (WT) cell lysates treated with sapanisertib (10 μ M) or GCN2-IN-6 (10 μ M) upon unstarved condition (US) or leucine depletion (- L) for 1 h and 4 h. GRB2 is used as loading control. DMSO is used as vehicle. (B) Immunoblot of 3T3 wild-type (WT) cell lysates treated with oligomycin (100 nM) for 1 h or 4 h upon unstarved (US) or leucine-starved (- L) conditions. GRB2 is used as loading control. Data are depicted as mean + SEM of one of two representative gels.

Overall, we showed that the amino acid stress-induced GCN2 cascade affected energy sensing by AMPK and following mTORC1 regulation. Mitochondrial stress, induced by manipulating the

ATP synthase via oligomycin treatment, did not activate the GCN2 cascade, but activates ATF4 induction.

4.7.12. Ferroptosis is regulated by GCN2 and mTOR inhibition

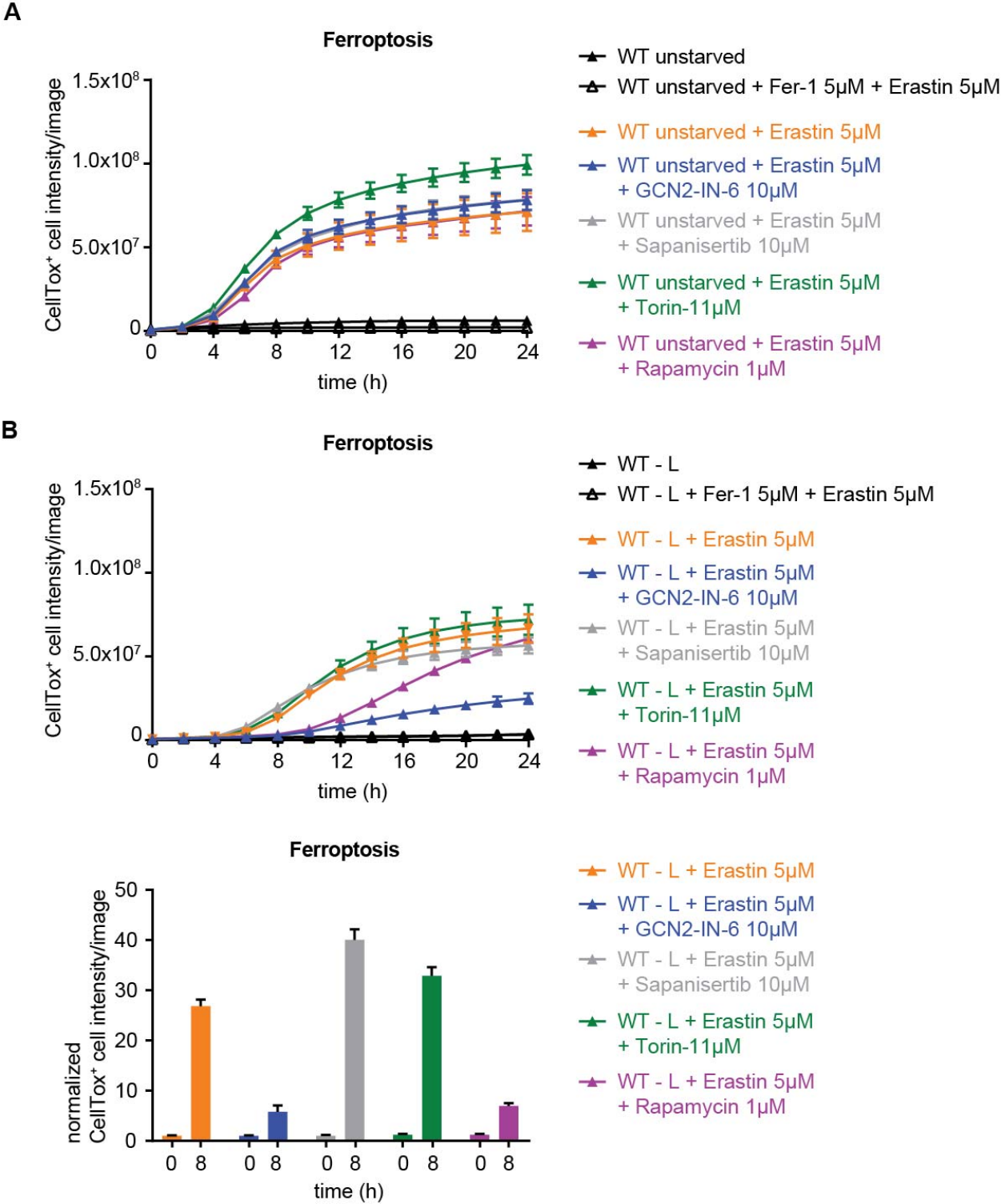
We observed that GCN2 deficient cells were protected from erastin-induced ferroptosis while wild-type cells were ferroptosis-sensitive upon leucine deprivation for 24 h (Section 4.3.; Figure 54). To confirm this finding, we tracked erastin-stimulated ferroptosis upon leucine stress across time in combination with GCN2 inhibition. Moreover, we started to address the connection of ferroptosis to mTOR signaling. Recently, Colon *et al.*⁴⁰ showed in U2OS cells (human bone osteosarcoma epithelial cells) that mTOR inhibition (by sapanisertib) can suppress erastin-induced ferroptosis.

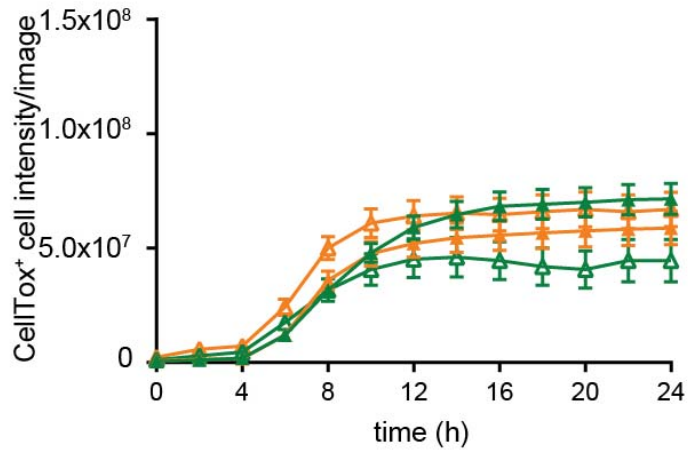
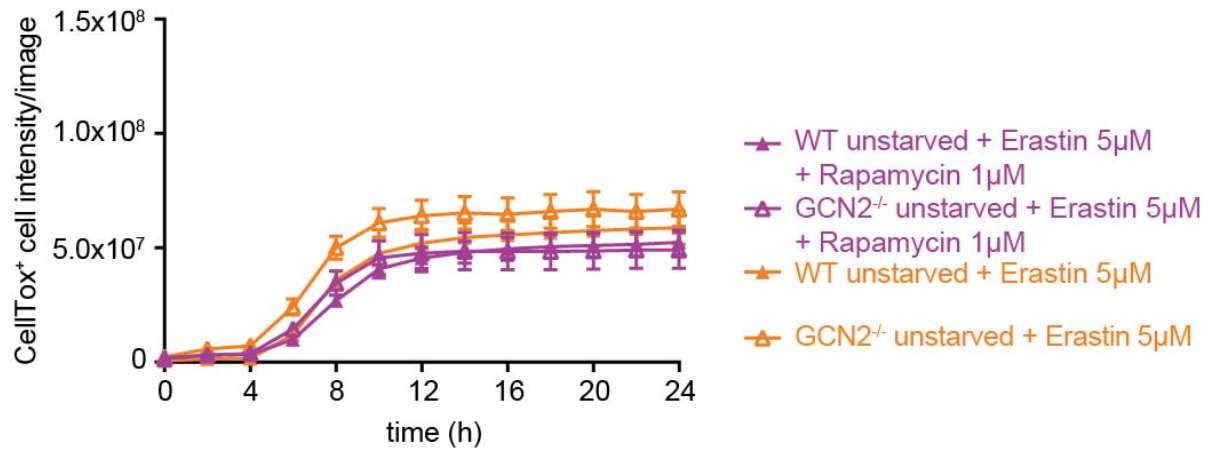
In contrast to the finding from Conlon *et al.*⁴⁰, we showed that 3T3 wild-type cells died by erastin-induced ferroptosis independently of mTOR or GCN2 inhibitor treatment (sapanisertib, GCN2-IN-6, rapamycin and Torin-1) upon unstarved condition (Figure 88A). At this stage, this finding argues that ferroptosis is highly cell-specific modulated. Upon leucine stress, GCN2-IN-6-stimulated cells showed no severe induction of erastin-induced ferroptosis (Figure 88B). In contrast, erastin-stimulated ferroptosis was induced by Torin-1 and sapanisertib (compound #12). Rapamycin-stimulated cells started to die after 12 h.

This finding manifested that erastin-induced ferroptosis is modulated upon leucine stress. Blocking of the GCN2-ISR renders the cells resistant to erastin-stimulated ferroptosis induction upon leucine deprivation. In other words, we confirmed our previous data in section 4.3. (Figure 54) showing that the genetically deficient GCN2 cells and the GCN2 inhibitor treated wild-type cells are ferroptosis-protected upon erastin treatment. However, the dual inhibition of the mTOR and the GCN2 pathways by Torin-1 and sapanisertib (compound #12) promoted ferroptosis independently of leucine stress exposure.

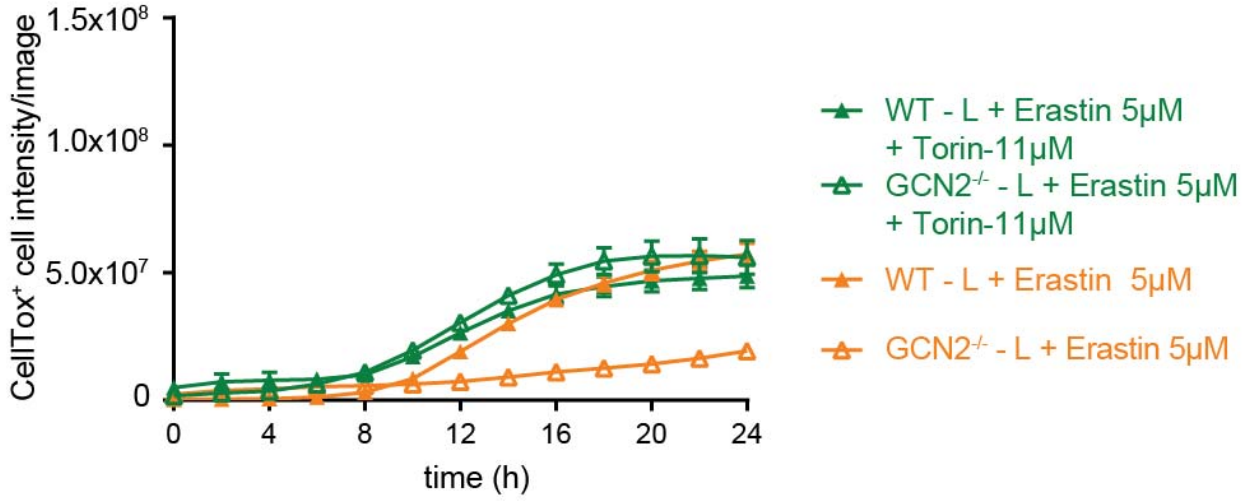
Therefore, we checked Torin-1 treatment in a GCN2 deficient cellular context stimulated with erastin. As expected, the erastin-stimulated wild-type and GCN2 deficient cells died by ferroptosis over time at normal growth state (Figure 88C). Most interestingly, upon leucine stress and erastin treatment, the GCN2 deficient cells started to die when treated with Torin-1. In contrast, rapamycin treatment did not prevent the ferroptosis protection of GCN2 deficient cells upon leucine stress. Combined, this hinted that erastin-treated ferroptosis is regulated by the ISR upon leucine stress – independent of mTORC1 function. In addition, Torin-1 induces ferroptosis independent of leucine stress and GCN2 presence. In this context, Gu *et al.*⁴⁶⁴ showed at oncogenic background that mTORC2 mediates the phosphorylation of SLC7A11 at S26 and thereby the inactivation of SLC7A11, which can be reversed by Torin-1. Erastin and Torin-1

stimulation resulted in ferroptosis⁴⁶⁴. However, this study was not conducted upon amino acid stress. At this stage, we concluded that the described Torin-1-mediated ferroptotic effect is not triggered by amino acid stress and solely a consequence of the phosphorylation status of SLC7A11 regulated by mTORC2 activity.

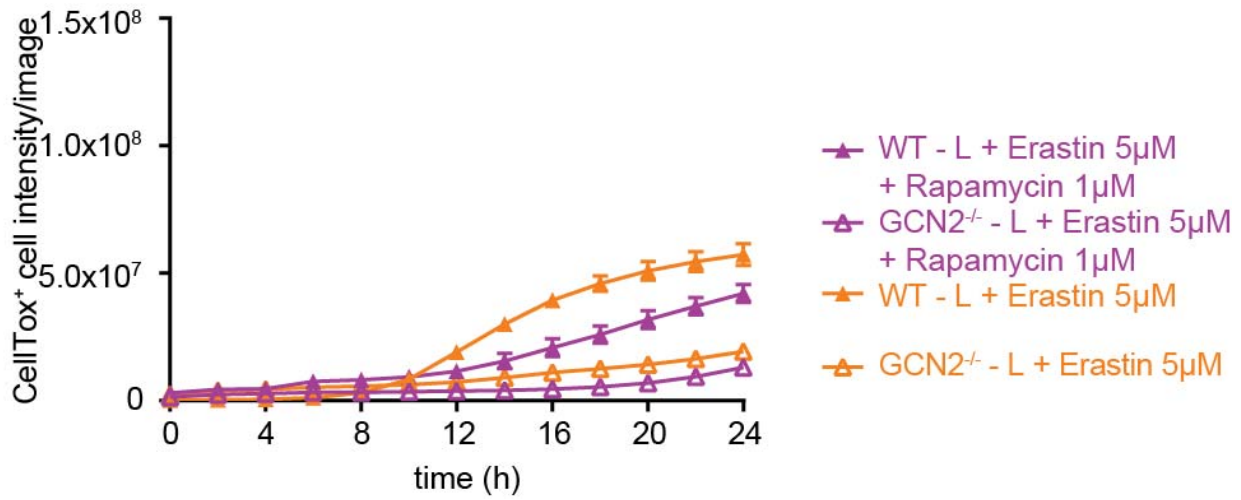


C**Ferroptosis****Ferroptosis**

Ferroptosis



Ferroptosis



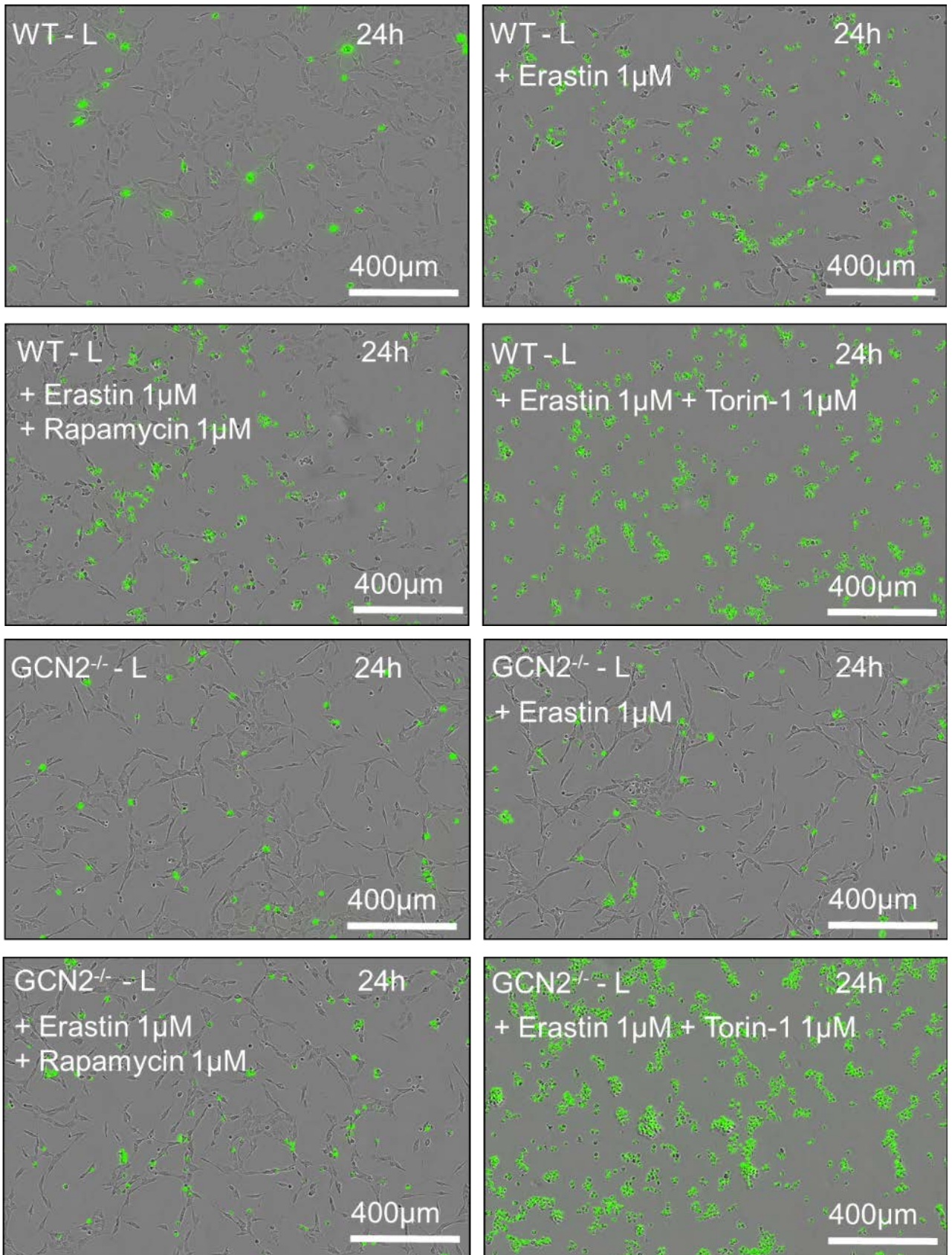


Figure 88. Torin-1 induces ferroptosis in contrast to GCN2-IN-6 and rapamycin upon leucine stress independent of GCN2 proficiency. (A) Quantification of ferroptosis using CellTox green staining in 3T3

wild-type (WT) cells treated with erastin (5 μ M) in the presence of GCN2-IN-6 (10 μ M), rapamycin (1 μ M), Torin-1 (1 μ M) or sapanisertib (10 μ M) over time in unstarved condition. Ferrostatin-1 (Fer-1; 5 μ M) was added as control to block erastin-induced death. (B) Same as A, except: upon leucine stress. (C) Same as A, except: only Torin-1 (1 μ M) and rapamycin (1 μ M) treatment upon leucine stress in 3T3 wild-type (WT) and GCN2 deficient (GCN2^{-/-}) background. Microscopic images illustrate cell death (green) at 24 h of leucine stress. (A-C) Data are depicted as mean + SEM of three independent experiments.

In conclusion, we provided a further evidence that the loss of GCN2 upon leucine stress renders the cells 'resistant' towards erastin-stimulated ferroptosis induction. Moreover, we strengthened that this protection is reverted only by dual mTOR inhibition. Further studies will follow to address the connection of mTOR, GCN2 and ferroptosis by genetically targeting SLC7A11. In addition, we aim to track ferroptosis in combination with mTOR and GCN2 inhibition in oncogenic context.

5. Discussion

The GCN2 kinase is non-essential, but highly conserved in all eukaryotic species fulfilling its role as the amino acid sensor of the integrated stress response (ISR)⁶⁰. From yeast to humans, this ancient pro-survival cell- and stress-type specific protection pathway is fundamental for cell state to cope with amino acid stress⁶¹. Especially cancer cells rely on this metabolic defense signaling network to reprogram their metabolism for pro-survival and high fitness in a nutrient-limited environment^{199,541}. GCN2 is of increasing interest for therapeutic purposes due to its involvement in a large array of physiological (e.g. immune system regulation) and pathophysiological (e.g. acute lymphoblastic leukemia) processes^{23,239}. Most of the molecular genetic studies on GCN2 have been conducted in *Saccharomyces cerevisiae* (budding yeast), where its overall mode of action was revealed: amino acid stress leads to an accumulation of uncharged tRNAs activating GCN2 (dimerization and autophosphorylation), which phosphorylates the eukaryotic translation initiation factor eIF2 α ²⁵. This process is accompanied by the large HEAT-repeat protein GCN1 and triggers the blockage of global protein synthesis at the ribosomal machinery⁵⁴². Simultaneously, translation of a specific set of transcripts increases, which is induced by the transcription factor ATF4 for stress adaptation^{71,72,439}. This stress-protective program is also used by the PERK (ER stress-induced ISR) and the mTORC1 (other amino acid sensing hub for cell growth) pathways to control translation in terms of cellular stress^{15,26,29,95}.

In this PhD thesis, I aimed to unravel how the mammalian GCN2 driven amino acid signaling network controls cell state adaptation upon amino acid stress. A key part of my approach was to integrate the regulation of amino acid sensing and ISR activation via GCN1 and mTORC1. Therefore, I used a diverse set of techniques including genetic mutagenesis, chemical perturbation and multi-omics studies. Specifically, I aimed to address (i) how the mammalian GCN2-ISR can be compared to the prevailing budding yeast-based dogma of GCN2 activation, (ii) the global transcriptome and proteome changes the GCN1-GCN2 signaling network induces to regulate cell state upon amino acid starvation, (iii) which role GCN1 plays in the overall context and its function beyond the ISR regulation, (iv) how the GCN2 and the mTORC1 amino acid sensing pathways interact and (v) how the GCN2 driven ISR can be chemically perturbed for long-term therapeutic purposes. Collectively, the outcome of this work revealed new insights into how the GCN1-GCN2 and mTORC1 amino acid sensing pathways function and connect at the molecular and mechanistic level in mammals.

My key findings towards the mentioned objectives (i-v) are the following ones:

1. GCN1 acts upstream of GCN2 to regulate GCN2 autophosphorylation and consequently its activation to trigger the ATF4-mediated transcriptional response for stress adaptation.
2. Upon leucine stress, GCN1 and GCN2 regulate not only protein translation, but also purine biosynthesis and antioxidative response in an isogenic and time-dependent manner, which is reflected by clear systematic changes at the transcriptome and the proteome level.
3. The GCN2-ISR modulates the SLC7A11/SLC3A2 transporter system upon specific amino acid stress stimuli and consequently regulates erastin-induced ferroptosis.
4. GCN1 has ISR - and consequently GCN2- and amino acid stress- independent functions. First evidence is provided that GCN1 is most likely involved in ribosome quality control, DNA-dependent processes such as DNA damage response and bioenergetics.
5. Upon amino acid stress, the GCN2 and mTORC1 pathways connect most likely via the ATF4-4EBP1 axis in a time-dependent way to regulate translation.
6. Dual ATP-competitive mTOR inhibitors (e.g. Torins) and class-IV-PI3K inhibitors (e.g. ATR inhibitors) concurrently block the mTORC1 and the GCN2 branches of cellular amino acid sensing upon long-term amino acid stress in a PERK and eIF2 α -independent manner.

5.1. Our model of the mammalian amino acid response

Using our CRISPR/Cas9 genetically modified cell lines derived from diverse murine cell systems (MEFs, 3T3 and E14 cells), we constructed a model of how the mammalian GCN2-ISR works at the mechanistic and molecular level in the context of the prevailing yeast dogma. In addition to reports in budding yeast and MEFs^{15,67,505}, we highlight that amino acid stress (leucine or arginine depletion) triggers the autophosphorylation and thereby activation of GCN2 at threonine 898 in a reversible and time-dependent manner. Strikingly, we found that the autophosphorylation of GCN2 is dependent on GCN1, which was also recently published by two other groups^{113,156}. In addition, we discovered that the autophosphorylation of GCN2 is essential to directly activate the transcription factor ATF4 at the gene and the protein level. Consequently, this process controls the ATF4-dependent stress transcriptional program, such as the expression of the pro-apoptotic transcription factor CHOP. Interestingly, in this context, the GCN2 target, which is the eukaryotic translation initiation factor eIF2 α , was still phosphorylated in an ATF4 deficient or GCN2 'autophospho-dead' background upon amino acid stress. This finding is consistent with the data reported by Harding *et al.*¹⁵ in ATF4 deficient MEFs. Furthermore, we dissected the interplay of phospho-GCN2-ATF4 versus phospho-eIF2 α using genetically modified cell lines mutated in the GCN2 kinase and in the eIF2 α phosphorylation target loci. We provide evidence that the catalytic function of GCN2 is crucial for the autophosphorylation and the induction of ATF4. In a time-dependent comparison, we found that the time-dependent phosphorylation of eIF2 α and the autophosphorylation of GCN2 correlate well, while ATF4 is induced at later time points. This time-difference matches to the report in Nikonorova *et al.*³⁷⁰ and framed our model in a way that the catalytic activity of GCN2 most likely triggers the autophosphorylation of GCN2. This assumption still needs to be confirmed by structural studies. Paradoxically, we discovered that the inhibitory phospho-eIF2 α target mutation does not prevent the autophosphorylation of GCN2 and the ATF4 induction. This finding stands in contrast to the data from Dever *et al.*⁵⁰⁹ reported in budding yeast experiments, who showed that the inhibitory S52A mutation of eIF2 α is sufficient to suppress GCN4 induction (GCN4 is the yeast homologue of ATF4). These data led to the prevailing dogma how GCN4 (same for ATF4) controls translation by the 'uORF reinitiation delay model' in an eIF2-GTP dependent manner^{71,97}. However, in mammals regulated reinitiation downstream of the positive regulatory uORF1 accounts for most, but not all eIF2 α phosphorylation-mediated translation of ATF4 arguing for an alternative way to regulate ATF4 induction⁹⁷. This suggest other effectors to modulate ATF4 induction. For example, it is known that mTORC1 regulates ATF4 induction in an eIF2 α -independent manner²⁶. Combined, we linked the ATF4 triggered induction of the transcriptional stress program to the autophosphorylation (and GCN1 involvement) instead to the action of the eIF2 α target. In addition, we highlighted in the double (GCN1 and GCN2) to

single knockout comparison that GCN1 and GCN2 deficient cells were isogenic in regulating ATF4 and eIF2 α . This regulatory process of activating GCN2 matched to all three studied murine cell lines.

Overall, we discovered a critical step in the activation of GCN2: GCN1 acts upstream of GCN2 to regulate its autophosphorylation and consequently the downstream ATF4 induction, which is independent of eIF2 α phosphorylation.

5.2. Global transcriptome and proteome changes upon leucine stress

Using a multi-omics approach, we found that the leucine stress-induced ISR activates for instance processes involved in mitochondrial 1C-metabolism, amino acid transport and tRNA aminoacylation for protein synthesis over time. In this context, we discovered at the transcriptome and proteome level that these processes are GCN1- and GCN2-dependently regulated suggesting an isogenic signature of GCN1 and GCN2 in modulating the amino acid response. Recently, Torrence *et al.*, Park *et al.* and Ben-Sahra *et al.*^{26,29,95} detected the mentioned processes in their RNASeq analyses. In detail, Torrence *et al.*²⁶ demonstrated that insulin-stimulated and consequently active mTORC1 mediates in an ATF4, but eIF2 α -independent manner 61 transcripts, which were shared with the ER stress-stimulated PERK-ISR^{15,26}. In our transcriptomics data, these 61 transcripts were also significantly enriched in a GCN1 and GCN2 dependent way upon leucine stress. Another connection between the ISR and the mTORC1 pathway was highlighted by Klann *et al.*²⁷ who showed in a proteomics study that the PERK-ISR and the mTORC1 network regulate the same precise set of proteins. Due to these parallels across studies, we verified that insulin treatment (mTORC1 activation) and tunicamycin treatment (PERK activation)²⁶ do not stimulate the GCN2-ISR in our setup. Importantly, we added the novel finding that the amino acid stress-induced ISR regulates the same stress-protection program, on both transcriptome and proteome level, as the PERK-ISR and the mTORC1 pathway. From our point of view, this regulation is also triggered in an ATF4-dependent and eIF2 α -independent way. This assumption was emphasized by our previously described finding that GCN1 is essential for the regulation of ATF4 induction in an eIF2 α -independent fashion. However, the limitation of our study persists that this conclusion needs to be confirmed by omics studies in an ATF4 deficient and phospho-eIF2 α mutated context.

Overall, we discovered that the GCN1-GCN2-ISR activates upon leucine stress the same transcriptional program that was reported for the insulin-stimulated mTORC1 pathway and the ER stress-induced PERK-ISR²⁶. Consequently, we found that GCN1-GCN2 signaling modulates purine biosynthesis and antioxidative response next to protein translation upon amino acid stress at the transcriptome and proteome level.

5.3. Cell state adaptation upon amino acid stress

We discovered that GCN1 mediates the autophosphorylation of GCN2 triggering its activation and consequently the induction of ATF4 upon amino acid stress. In our multi-omics study, we highlighted that amino acid transporters (SLC transporters) are modulated upon leucine starvation over time in a GCN1- and GCN2-dependent manner. In this context, we found that the heterodimeric SLC7A11/SLC3A2 transporter complex (system x_c^-) is significantly upregulated upon leucine stress over time only in the GCN1 and GCN2 proficient background at the transcriptome and the proteome level. This antiporter system is relevant for transporting the anionic form of cysteine in exchange for glutamate into the cytoplasm^{365,481} controlling glutathione biosynthesis and thereby preventing ROS-induced non-apoptotic iron-dependent cell death, termed ferroptosis^{480,490–492}. Cancer cells modulate the system x_c^- to buffer cellular redox stress to be protected against ferroptosis^{483,484}. The activity of SLC7A11 was reported to be tracked by its mTORC2-mediated phosphorylation at serine 26 (Ref.⁴⁶⁴). In our phosphoproteomics study, we detected this phosphosite to be significantly enriched upon leucine stress in the GCN1 and GCN2 proficient background. Moreover, Torrence *et al.*²⁶ reported that the system x_c^- regulates glutathione biosynthesis in an ATF4-dependent way downstream of growth signals. At proteome level, we found that glutathione metabolism was also affected by the loss of GCN2. Collectively, we decided to investigate our proposed GCN1-GCN2-ATF4 axis by the regulation of SLC7A11 using ferroptosis as a readout. We discovered that the ISR can modulate ferroptosis induction upon leucine and glutamine stress, however only by erastin treatment (SLC7A11 blockade) and not RSL3 treatment (GPX4 blockade). Strikingly, we found that GCN2 deficient cells were protected from ferroptosis for 24 h upon leucine and glutamine deprivation. Interestingly, glutamine deprivation but not leucine deprivation induced ferroptosis protection in wild-type cells. By now, the difference in amino acid depletion affecting ferroptosis is still unsolved and might be affected by oncogenic background. For example, Conlon *et al.*⁴⁰ reported that U2OS cells can suppress erastin-induced ferroptosis only upon arginine stress that was independently regulated by the GCN2-ISR or mTOR pathway. Furthermore, Gao *et al.*⁴⁸⁸ linked erastin-induced ferroptosis induction to the role of mitochondria. Thereby, glutaminolysis and the TCA cycle are essential for ferroptosis-associated mitochondrial membrane potential hyperpolarization and lipid peroxide accumulation. First evidence that GCN1 and GCN2 have a dysregulated mitochondrial and glycolytic capacity already at normal growth state was shown by the proteomics study followed by Seahorse analysis. Moreover, we found in our omics studies that glutamine metabolizing enzymes (*Gclc*, *Gpt2*) as well as glutamine-associated transporters (*SLC7A1*, *SLC7A5*) are downregulated in the GCN1 and GCN2 deficient background upon leucine stress. We also showed that the BSO blocked glutathione synthesis leads to reduced ferroptosis induction when

GCN2 is inhibited upon leucine depletion. Mitochondrial stress alone does not activate the GCN2 driven ISR, but we found hints that the AMPK energy sensor, relevant for mitochondrial regulation is affected by the loss of GCN2 (Ref.⁵⁴³). Based on these data, we reasoned that the amino acid stress-induced GCN1-GCN2-ATF4-SLC7A11 axis is relevant for the regulation of glutamine metabolism and mitochondrial respiration and finally the sensitivity to erastin-induced ferroptosis. However, one limitation of our model is that GCN1 deficient cells die by ferroptosis after 12 h and GCN2 inhibitor-treated cells show the same kinetics in contrast to the 24 h protection in GCN2 knockout cells. We know from simple cultivation experiments and our omics data that these deficient cell lines have an intrinsic adaptive signature affecting cellular growth. Therefore, we aim for a further ferroptosis readout to better compare the different genotypes. In addition, we will transfer the omics findings to a cellular context and dissect the differences between amino acid depletion towards ferroptosis. Moreover, we aim to determine the ATP and GSH levels in the different genotypes upon stress exposure to investigate the role of mitochondria in further context. Overall, we discovered that the GCN2-ISR modulates the SLC7A11/SLC3A2 transporter system upon different amino acid stress stimuli and can thereby regulate erastin-induced ferroptosis induction.

5.4. Unexpected functions of murine GCN1

Initially found in yeast, GCN1 directly interacts with GCN2 at its C-terminus and is associated with the ribosomal machinery^{131,150}. Recently, the Cryo-EM structure of GCN1 was published highlighting that GCN1 is bound to a collided and stalled disome, which was found under steady-state condition and not amino acid starvation¹¹⁴. In line with these data, we provided evidence by interaction proteomics that GCN1 is associated (but not directly) with the uL10 component of the ribosomal P-stalk. However, we detected an enrichment for this component only under normal growth state and we could not observe co-sedimentation of GCN1 on a disome or polysome fraction. In addition, a direct interaction of GCN1 with GCN2 could also not be verified by several different approaches independently of amino acid stress. By now, only Wu *et al.*¹⁴⁰ showed in a non-starved condition about 10 % interaction of GCN1 with a disome, but no interaction with GCN2. Combined, our data contrast the yeast model, which argues for a transient interaction of GCN1, GCN2 and the ribosomal machinery. First evidence that GCN1 has functions beyond its involvement in the GCN2-ISR was uncovered in this thesis: GCN1 controlled the normal expression (without amino acid stress) of complex I activity of the electron transport chain and caused a distinct bioenergetic profile compared to the GCN2^{-/-} and wild-type cells. Future studies will strengthen this finding by setting it also into the context of amino acid stress. For example, we aim to compare ASNase treatment (asparagine depletion)²³⁹ and halofuginone treatment

(glutamyl-prolyl-tRNA synthetase inhibition)¹⁵⁶ in comparison to leucine stress to investigate the stress specificity in more detail. Moreover, we will address the role of GCN1 in the ETC in further context by manipulating the complex I activity. First evidence that GCN1 is involved in DNA-regulated processes was stated by the interaction proteomics and proteomics studies highlighting a transient interaction of GCN1 with the MRN complex, which is relevant for DNA double-strand break repair⁴⁷⁰. In this context, Yamazaki *et al.*¹¹³ recently highlighted that GCN1 regulates cell cycle and cell proliferation and Clementi *et al.*⁴⁵⁴ and Choo *et al.*⁴⁵⁵ even connected DNA synthesis to stress response.

Overall, GCN1 controls GCN2 but also has other functions in controlling cellular homeostasis despite the ISR. Perhaps GCN1 has a constitutive role in homeostasis and ribosome quality control, which is accentuated or enhanced when amino acid stress causes increased translational stress, which regulates GCN2 activation at a collided and stalled disome. In the future, we will address, if translational stress and ribosome collision are coactivators of GCN1, as it was recently found for the cytosolic DNA sensor cGAS (cyclic GMP-AMP synthase)⁵⁴⁴. We will also address the interplay of replication and amino acid stress to manifest the role of GCN1 in DNA damage response and DNA replication linked processes. In addition, we are also interested in dissecting the relevance of GCN1 in regulating the electron transport chain integrity and linking this to the role of mitochondria in ferroptosis.

5.5. Time-dependency of the mTORC1-GCN2 interplay upon amino acid stress

Amino acid demand regulates the following two amino acid sensing pathways in a diametrically opposite way: amino acid stress inhibits mTORC1 signaling and activates the GCN2 cascade to shut down translation²⁴. However, this process is affected in a time-dependent manner, which means that prolonged amino acid stress leads to a reactivation of mTORC1 while GCN2 is constantly active. By now, the reactivation of mTORC1 is not fully understood, but a link to the glutamine metabolism was reported³⁶⁰. As consequence of the known time-dependent activation status of mTORC1, we decided to dissect the connection between the GCN2 and the mTORC1 pathways at short- (1 h) and long-term (4 h or 8 h) amino acid stress exposure. Consistent with the data from Tan *et al.*⁵⁰, we found that mTORC1 is reactivated after prolonged stress duration independently of the GCN2-ISR and that the addition of glutamine leads to mTORC1 reactivation. Moreover, we discovered that the GCN2-ISR regulates mTORC1 activation upon short-term amino acid stress. This was detected in all three murine cell lines and analyzed by immunoblotting and phosphoproteomics. In other words, when the GCN1-GCN2-ATF4 axis was blocked at short-term amino acid stress, mTORC1 was active and translation was not prevented. This finding is in

line with Averous *et al.*¹⁷⁹ and Nikonorova *et al.*³⁷⁰, who showed that GCN2 contributes to mTORC1 suppression upon leucine and arginine depletion, and also asparaginase treatment. In this context, both groups proposed that this process is mediated ATF4-independently. However, we could not strengthen this finding of ATF4-independency in our setting at this stage. To find a direct correlation with their data, we aim to repeat their experimental setup in our system (e.g. different amino acid stress inducers, timeframes and cell lines). Apart from that, we showed that only the regulation of the 4EBP1 phospho-target (at T36/45; relevant for translation initiation) and not the p70S6K phospho-target (at T389; relevant for ribosome biogenesis) of mTORC1 was modulated by the GCN2-ISR upon early arginine or leucine stress exposure. In other words, 4EBP1 was phosphorylated already at short-term amino acid stress when the GCN1-GCN2-ATF4 axis was suppressed upon amino acid stress. This finding might be relevant, because both mTORC1 targets are generally used side-by-side for reading out mTORC1 activity since the discovery of their role in amino acid sufficiency control by Hara *et al.*⁴¹. For example, Averous *et al.*¹⁷⁹ and Nikonorova *et al.*³⁷⁰, manifested their data by reading out only the p70S6K target phosphorylation levels. At this stage, we concluded that the GCN2-ISR could regulate mTORC1 via 4EBP1 induction at early stress exposure and finally translation initiation. Recently, 4EBP1 regulation was linked to ATF4. A so-called ATF4-4EBP1 axis was postulated by Vasudevan *et al.*³⁷³ and Tameire *et al.*²⁰⁷, who showed that 4EBP1 is a direct transcript, which is highly expressed upon induction of ATF4. In line with these data, Torrence *et al.*²⁶ found that insulin-stimulated mTORC1 also induces the ATF4-mediated transcription of 4EBP1. In our multi-omics study, we discovered that 4EBP1 is also transcriptionally regulated dependent on the presence of GCN1 and GCN2, and that its activation-phosphosite (mouse: T36/45) is controlled time-dependently upon leucine stress. Moreover, we also detected other translation factors, such as eIF4B and eIF3c, whose phosphosite occupancy or expression is upregulated in a GCN2-GCN1- and time-dependent fashion upon leucine stress. Additionally, we discovered that the energy sensor AMPK also regulates mTORC1 activation in a time-dependent manner upon amino acid stress. In other words, GCN2 inhibition prevented the induction of AMPK and consequently the suppression of mTORC1 upon short-term amino acid stress. Thus, we propose a connection between the GCN2-ISR and the mTORC1 pathways in a starved cellular environment, which can in part be controlled by the ATF4-mediated-stress transcriptional program. In detail, we think that the GCN2-ATF4-4EBP1 axis could modulate mTORC1 activation and thereby translation in a similar mode of action as it is described for the GCN2-ATF4 mediated expression of the mTORC1 leucine sensor SESTRIN2 (GCN2-ATF4-SESTRIN2 axis)³⁴⁴. However, at this stage, this assumption still needs further investigation, especially with regards to the kinetics following this 'potential' mechanism in more detail. Recently, Böhm *et al.*²⁹⁵ showed the dynamic mechanism of 4EBP1 recognition by NMR: A stepwise phosphorylation of early and late phosphosites of 4EBP1

by mTOR and the structural switches necessary to release eIF4E for the initiation of cap-dependent translation.

Overall, we highlighted that the mTORC1 and the GCN2 pathways are connected upon arginine and leucine deprivation. Most likely, at short-term stress exposure, GCN2 suppresses mTORC1 via 4EBP1 induction and ultimately translation regulation. However, further studies are needed to investigate this specific interaction in more detail, where we especially focus on the link between the translation repressor 4EBP1 and the translation initiator eIF2 α . A major obstacle is that most studies dissect the mTORC1 and GCN2 axis using different timeframes, cell lines or treatments. Therefore, it is still equally unclear how amino acid requirements might diverge in cell types or organisms with different metabolic needs lacking mechanistic explanation for how known metabolic inputs such as leucine and arginine impinge on both pathways.

5.6. Concurrent suppression of the mTOR and the GCN2 pathways upon amino acid stress

GCN2 is an appealing drug target for tumorigenic malignancies, because (i) GCN2 regulates a pro-survival cellular stress protection pathway²³, (ii) GCN2 is non-essential⁵⁴⁵ and (iii) GCN2 is highly modulated by environmental cues like oxidative or nutrient stress⁶⁰. Recent studies, in which the GCN2 cascade modulates MYC-driven cancer progression^{207,240,252,366} or AML therapeutic interventions^{239,546}, highlighted the importance to hunt for novel GCN2 inhibitors. By now, only three commercially available GCN2 inhibitors (GCN2-IN-1, GCN2-IN-6 and GCN2iB) exist^{239,247,248}. To expand the toolbox for GCN2 cascade inhibition, we performed a 3,876 large kinase compound screen to detect potentially novel GCN2 inhibitory candidates. Strikingly, we found that class-IV-PI3K inhibitors such as ATR inhibitors (ETP-4646 and BAY1895344) concurrently suppress the mTOR and the GCN2 pathways upon amino acid stress. ATR inhibition turned out to be a novel and promising cancer treatment strategy for tumors with DNA damage response (DDR) defects and strong replication stress^{522,523}. Several hints from our multi-omics analysis point towards DDR and DNA replication, which is affected by the GCN1-GCN2 signaling and opens new avenues for further amino acid and replication stress response studies. In addition, we discovered that other dual ATP-competitive mTORC1/mTORC2 inhibitors such as Torins and sapanisertib (TORKinibs) suppress the GCN2-ISR at already low drug concentration (0.1 μ M) in a GCN2-independent manner. In detail, these inhibitory agents prevent the amino acid ISR not by direct binding to GCN2 and independently of eIF2 α and PERK. Based on these findings, we concluded that the effect is (i) amino acid stress driven (not PERK affected), (ii) targeting the activation of GCN2 (not eIF2 α dependent) and (iii) is most likely controlled by mTOR. Interestingly, the inability of dual mTOR inhibitors to block PERK signaling was highly relevant for

presenting an effect, which is distinct between the PERK-ISR and GCN2-ISR, that are overall quite similar with regards to their molecular function as reported by several studies^{15,26,345,370}. However, most importantly, the specific mTORC1 inhibitor rapamycin^{388,529} was not able to suppress the GCN2-ISR. This was also highlighted in response to different stress stimuli (asparaginase treatment or amino acid depletion). Consequently, we targeted translational shut-down and discovered that only the inhibition of both mTOR complexes (no phosphorylation of 4EBP1, p70S6K and eIF2 α) leads to a potent shut down of protein synthesis upon leucine stress in contrast to rapamycin (no phosphorylation of p70S6K) and GCN2 inhibition (no phosphorylation of eIF2 α) alone. The mentioned difference in translational outcome by rapamycin treatment versus dual mTOR inhibitors was already reported by Thoreen *et al.*³⁹⁰. In future perspective, we aim to investigate, if dual mTOR inhibitors in contrast to rapamycin (and most likely all rapalogs) suppress the GCN2-ISR upon amino acid stress due to the action of mTORC2 or due to the relevance of 4EBP1 regulation. This assumption is based on the notion that rapamycin is insensitive to modulate 4EBP1 phosphorylation at T36/45^{295,296} and its mTORC2 blockage is highly cell type- and stress-specific^{279,390–392}. Since mTOR is essential and the only available specific mTORC2 inhibitor did not work in our setting to address the relevance of mTORC2 in manipulating the GCN2-ISR, we aim for the dissection of the interplay between mTORC1, mTORC2 and GCN2 using a siRNA-based knockdown of the Raptor (regulatory protein of mTORC1) and Rictor (regulatory protein of mTORC2) proteins in context of inhibitor and amino acid stress treatment. This still unsolved interplay would provide us essential information to elucidate other differences between dual mTOR inhibitors and rapamycin detected in this thesis: (i) Rapamycin did not induce potent erastin-stimulated ferroptosis upon leucine stress; (ii) Rapamycin treatment in a GCN1-GCN2 deficient context can stimulate ATF4 induction upon leucine stress. Another way to address this complex interplay will be by mutating the TSC complex, which is the key node of transferring information from the PI3K-AKT, the mTORC2 and the RAS-RAF-MEK-ERK networks⁵⁴⁷. The RAS-RAF-MEK-ERK signaling in regulating the ISR will be addressed in detail as well, since we provide first evidence that the RAF/VEGFR2 inhibitor (RAF265)^{548,549} potentially blocks the phospho-GCN2-ATF4 axis upon leucine stress. Another interesting finding was the time-dependent inhibition of the GCN2-ISR: ISR suppression by dual mTOR inhibitors was so far only detected at prolonged stress (4 h) and not short-term stress exposure (1 h) arguing for a role of mTOR in modulating the activation of GCN2 depending on the amino acid stress duration. Moreover, we detected that the three GCN2 inhibitors (GCN2-IN-1, GCN2-IN-6 and GCN2iB) had distinct pharmacokinetic signatures in blocking the GCN2 cascade and regulating mTORC1 activation upon amino acid stress. For example, GCN2-IN-1 was able to block mTORC1 signaling upon amino acid stress. Based on our extensive data sets, we conclude that both pathways interplay in a time-dependent and interchangeable way.

In summary, we discovered a concurrent blockage of both major amino acid sensing pathways upon amino acid stress mediated by dual ATP-competitive mTOR inhibitors and other class-IV-PI3K inhibitors such as ATR inhibitors. This prevention of both amino acid sensing pathways was verified in murine and human cell systems. In a biochemical context, this finding could be relevant for studies in which TORKinibs were used to answer mTOR specific functions upon amino acid stress. For therapeutic implications this finding would be useful for targeting of cellular vulnerabilities modulated by translational control such as pro-invasion of metastases⁵⁵⁰ or addressing drug resistance of cancer cells⁴⁰⁹.

5.7. Outlook

The field of amino acid stress sensing and signaling is now being investigated with much greater success and more in-depth than before. In our view, and as a result of the work herein, three major outstanding issues are at the forefront of this research area: (i) We lack structural information about the GCN1-ribosome-GCN2-uncharged tRNA interplay. Essentially, structural information about how GCN2 is activated remains elusive. While parts of the process are known superficially (e.g. the yeast GCN1-ribosome Cryo-EM structure¹¹⁴ and the GCN2 kinase domain¹³⁸), the entire picture that links a low amino acid environment to GCN2-dependent ISR activation will be essential to fully understand this extraordinarily complex pathway; (ii) Our findings argue that mTORC1 and GCN2 are linked by a more complex mechanism of action than previously thought. Our data suggest that mTORC1 licenses GCN2 activity - how this occurs in detail remains unclear, especially in light of the kinetics and sub-cellular location of the key players. A conceivable possibility is that mTORC1 and GCN2 co-evolved to integrate cellular information about amino acid amounts and are dependent on each other. To progress in this field, an essential step will be the temporal identification of the key phosphosites on both kinases along with site-specific mutagenesis of them and their reconstitution to understand the phosphorylation crosstalk between these pathways; (iii) A key finding of this thesis concerned the differences in cellular transcriptome and proteome states in the absence of GCN1 or GCN2. Conventionally, these proteins are grouped within the same pathway and considered isogenic to each other. Indeed, we showed that GCN1 has an obligatory role in GCN2 activation. However, the fact that the omics data between the GCN1 and GCN2 knockouts are substantially different argues that a more detailed molecular genetic approach will be required to understand GCN1 and how GCN1 regulates ribosome collision sensing, and finally how this function translates to GCN2 activation. We will use chemical and biological manipulation to investigate the GCN2-ISR and the mTORC1 connection over time upon different amino acid depletion and amino acid stress mimicking drugs in murine and human systems. In detail, we will focus on the regulation of translation, autophagy

and the pharmacokinetic properties of rapalogs versus GCN2 inhibitors, TORKinibs and ATR inhibitors. Moreover, we will perform a second inhibitor screen with the Max-Planck-Gesellschaft Lead Discovery Center to hunt for novel GCN2 inhibitor candidates. In addition, the described findings from the omics studies will be applied at the molecular and the mechanistic level to understand how the ATF4-transcriptional program can regulate the mitochondrial function in terms of the TCA cycle, the 1C-metabolism, the glutaminolysis and the glutathione synthesis. This will allow us to understand how the GCN2-ATF4-SLC axis modulates ferroptosis induction upon amino acid stress. Furthermore, we will work on understanding the bioenergetic profiles of GCN1 versus GCN2 and investigate the function of GCN1 in ribosomal collision. Moreover, we will address the reconstitution of our genetically modified cell lines and the role of the other eIF2 α kinases upon amino acid stress. Finally, we apply our system to a MYC-driven oncogenic context, which aims for the induction of tumor cell death by manipulating the GCN1-GCN2-mTORC1 network.

6. References

1. Moughan, P. J. Protein: Digestion, Absorption and Metabolism. in *Encyclopedia of Food and Health* 524–529 (Elsevier Inc., 2015). doi:10.1016/B978-0-12-384947-2.00572-9.
2. Rose, A. J. *et al.* Amino Acid Nutrition and Metabolism in Health and Disease. *Nutrients* 11, (2019).
3. Liu, Z. & Barrett, E. J. Human protein metabolism: Its measurement and regulation. *Am. J. Physiol. - Endocrinol. Metab.* 283, 1105–1112 (2002).
4. Cahill, G. F. Fuel Metabolism In Starvation. *Annu. Rev. Nutr* 26, 1–22 (2006).
5. Hipp, M. S. *et al.* The proteostasis network and its decline in ageing. (2019) doi:10.1038/s41580-019-0101-y.
6. Wu, G. *et al.* Amino acids: metabolism, functions, and nutrition. (2009) doi:10.1007/s00726-009-0269-0.
7. Berg J, Tymoczko J, S. L. *Protein Turnover and Amino Acid Catabolism.* (2015).
8. Martínez-Reyes, I. & Chandel, N. S. Mitochondrial TCA cycle metabolites control physiology and disease. *Nat. Commun.* 11, 1–11 (2020).
9. Murray, P. J. Amino acid auxotrophy as a system of immunological control nodes. *Nat. Immunol.* (2016).
10. Marc, J., Ae, R. & Wu, G. Glutamine, arginine, and leucine signaling in the intestine. (2009) doi:10.1007/s00726-008-0225-4.
11. Wang, W. & Zou, W. Amino Acids and Their Transporters in T Cell Immunity and Cancer Therapy. *Mol. Cell* 80, 384–395 (2020).
12. Labbadia, J. & Morimoto, R. I. The Biology of Proteostasis in Aging and Disease. (2015) doi:10.1146/annurev-biochem-060614-033955.
13. Walter, P. & Ron, D. The unfolded protein response: From stress pathway to homeostatic regulation. *Science* (80-.). 334, 1081–1086 (2011).
14. Velichko, A. K. *et al.* Mechanisms of heat shock response in mammals. *Cell. Mol. Life Sci.* 70, 4229–4241 (2013).
15. Harding, H. P. *et al.* An integrated stress response regulates amino acid metabolism and resistance to oxidative stress. *Mol. Cell* 11, 619–633 (2003).
16. Scheper, G. C. *et al.* Inactivation of eIF2B and Phosphorylation of PHAS-I in Heat-shocked Rat Hepatoma Cells*. *J. Biol. Chem.* (1997) doi:10.1074/jbc.272.43.26850.
17. Harding, H. P., Zhang, Y. & Ron, D. Protein translation and folding are coupled by an endoplasmic-reticulum-resident kinase. *Nature* (1999).
18. Heldens, L. *et al.* An Atypical Unfolded Protein Response in Heat Shocked Cells. (2011) doi:10.1371/journal.pone.0023512.
19. Korennykh, A. V. *et al.* Cofactor-mediated conformational control in the bifunctional kinase/RNase Ire1. *BMC Biol.* 9, 1–16 (2011).
20. Rubio, C. *et al.* Homeostatic adaptation to endoplasmic reticulum stress depends on Ire1 kinase activity. *J. Cell Biol.* 193, 171–184 (2011).
21. Lin, W. *et al.* The integrated stress response prevents demyelination by protecting oligodendrocytes against immune-mediated damage. *J. Clin. Invest.* 117, 448–456 (2007).
22. Hetz, C. *et al.* Pharmacological targeting of the unfolded protein response for disease intervention. *Nat. Chem. Biol.* 15, 764–775 (2019).
23. Costa-Mattioli, M. & Walter, P. The integrated stress response: From mechanism to disease. *Science* 368, (2020).
24. Liu, G. Y. & Sabatini, D. M. mTOR at the nexus of nutrition, growth, ageing and disease. *Nat. Rev. Mol. Cell Biol.* 21, 183–203 (2020).

25. Castilho, B. A. *et al.* Keeping the eIF2 alpha kinase Gcn2 in check. *Biochim. Biophys. Acta - Mol. Cell Res.* 1843, 1948–1968 (2014).
26. Torrence, M. *et al.* The mTORC1-mediated activation of ATF4 promotes protein and glutathione synthesis downstream of growth signals. *Elife* 10, (2021).
27. Klann, K., Tascher, G. & Münch, C. Functional Translatome Proteomics Reveal Converging and Dose-Dependent Regulation by mTORC1 and eIF2 α . *Mol. Cell* 77, 1–13 (2019).
28. Misra, J. *et al.* Discordant regulation of eIF2 kinase GCN2 and mTORC1 during nutrient stress. *Nucleic Acids Res.* 1–17 (2021) doi:10.1093/nar/gkab362.
29. Ben-Sahra, I. *et al.* mTORC1 induces purine synthesis through control of the mitochondrial tetrahydrofolate cycle. (2016).
30. Li, Y. *et al.* Termination of autophagy and reformation of lysosomes regulated by mTOR. *Nature* (2010) doi:10.1038/nature09076.
31. Dikic, I. & Elazar, Z. Mechanism and medical implications of mammalian autophagy. (2018) doi:10.1038/s41580-018-0003-4.
32. Scott, S. V. & Klionsky, D. J. Delivery of proteins and organelles to the vacuole from the cytoplasm. *Curr. Opin. Cell Biol.* 10, 523–529 (1998).
33. Hopfner, K.-P. & Hornung, V. Cell intrinsic recognition and defence systems against foreign genetic material encompass. (2020) doi:10.1038/s41580-020-0244-x.
34. Onodera, J. & Ohsumi, Y. Autophagy Is Required for Maintenance of Amino Acid Levels and Protein Synthesis under Nitrogen Starvation* S. *J. Biol. Chem.* 280, 31582–31586 (2005).
35. Lin, T.-C. *et al.* Autophagy Resetting glutamine-dependent metabolism and oxygen consumption. *Autophagy* 8, 1477–1493 (2012).
36. Elmore, S. *et al.* Apoptosis: A Review of Programmed Cell Death. *Toxicol. Pathol.* 35, 495–516 (2007).
37. Castedo, M., Ferri, K. F. & Kroemer, G. News and Commentary Mammalian Target of Rapamycin (mTOR): Pro-and Anti-Apoptotic. (2002) doi:10.1038/sj/cdd/4400978.
38. Singh, R. *et al.* Regulation of apoptosis in health and disease: the balancing act of BCL-2 family proteins. (2019) doi:10.1038/s41580-018-0089-8.
39. Schmidt, S. *et al.* A MYC/GCN2/eIF2 α negative feedback loop limits protein synthesis to prevent MYC-dependent apoptosis in colorectal cancer. *Nat Cell Biol* 21, 1413–1424 (2019).
40. Conlon, M. *et al.* A Compendium of Kinetic Cell Death Modulatory Profiles Identifies Ferroptosis Regulators. *bioRxiv Syst. Biol.* (2019) doi:10.1101/826925.
41. Hara, K. *et al.* Amino acid sufficiency and mTOR regulate p70 S6 kinase and eIF-4E BP1 through a common effector mechanism. *J. Biol. Chem.* 273, 14484–14494 (1998).
42. Dibble, C. C. & Manning, B. D. Signal integration by mTORC1 coordinates nutrient input with biosynthetic output. *Nat. Cell Biol.* 15, 555–564 (2013).
43. Ban, H. *et al.* Arginine and Leucine regulate p70 S6 kinase and 4E-BP1 in intestinal epithelial cells. *Int. J. Mol. Med.* 13, 537–543 (2004).
44. Efeyan, A., Zoncu, R. & Sabatini, D. M. Amino acids and mTORC1: From lysosomes to disease. *Trends Mol. Med.* 18, 524–533 (2012).
45. Fox, H. L. *et al.* Amino acid effects on translational repressor 4E-BP1 are mediated primarily by L-leucine in isolated adipocytes. *Am. J. Physiol. - Cell Physiol.* 275, (1998).
46. Lynch, C. J. *et al.* Regulation of amino acid-sensitive TOR signaling by leucine analogues in adipocytes. *J. Cell. Biochem.* 77, 234–251 (2000).

47. Durán, R. V. *et al.* Glutaminolysis Activates Rag-mTORC1 Signaling. *Mol. Cell* 47, 349–358 (2012).
48. Smith, R. J. & Wilmore, D. W. *Glutamine Nutrition and Requirements; Glutamine Nutrition and Requirements.* (1990) doi:10.1177/014860719001400412.
49. Wise, D. R. & Thompson, C. B. Glutamine addiction: a new therapeutic target in cancer. *Trends Biochem. Sci.* 35, 427–433 (2010).
50. Tan, H. W. S., Sim, A. Y. L. & Long, Y. C. Glutamine metabolism regulates autophagy-dependent mTORC1 reactivation during amino acid starvation. *Nat. Commun.* 8, (2017).
51. Krane, S. M. *et al.* The importance of proline residues in the structure, stability and susceptibility to proteolytic degradation of collagens. (2008) doi:10.1007/s00726-008-0073-2.
52. Singal, S. A. *et al.* The production of fatty livers in rats on threonine-and lysine-deficient diets. *J. Biol. Chem.* 200, 867–874 (1953).
53. Noguchi, Y. *et al.* Ketogenic Essential Amino Acids Modulate Lipid Synthetic Pathways and Prevent Hepatic Steatosis in Mice. (2010) doi:10.1371/journal.pone.0012057.
54. Tremblay, F. *et al.* Role of dietary proteins and amino acids in the pathogenesis of insulin resistance. *Annu. Rev. Nutr.* 27, 293–310 (2007).
55. Zhang, P. *et al.* The GCN2 eIF2 α Kinase Is Required for Adaptation to Amino Acid Deprivation in Mice. *Mol. Cell. Biol.* 22, 6681–6688 (2002).
56. Chantranupong, L. *et al.* The CASTOR Proteins Are Arginine Sensors for the mTORC1 Pathway. *Cell* 165, 153–164 (2016).
57. Wolfson, R. L. *et al.* Sestrin2 is a leucine sensor for the mTORC1 pathway. *Science* (80-.). 351, 43–48 (2016).
58. Wang, S. *et al.* Lysosomal amino acid transporter SLC38A9 signals arginine sufficiency to mTORC1. *Science* (80-.). 347, 188–194 (2015).
59. Darnell, A. M. *et al.* Translational Control through Differential Ribosome Pausing during Amino Acid Limitation in Mammalian Cells. *Mol. Cell* 71, 229–243.e11 (2018).
60. Taniuchi, S., Miyake, M., Tsugawa, K., Oyadomari, M. & Oyadomari, S. Integrated stress response of vertebrates is regulated by four eIF2 α kinases. *Sci. Rep.* 6, 1–11 (2016).
61. Hinnebusch, A. G. Translational regulation of GCN4 and the general amino acid control of yeast. *Annu. Rev. Microbiol.* 59, 407–450 (2005).
62. Cambiaghi, T. D. *et al.* Evolutionarily conserved IMPACT impairs various stress responses that require GCN1 for activating the eIF2 kinase GCN2. *Biochem. Biophys. Res. Commun.* 443, 592–597 (2014).
63. Lavoie, H. *et al.* Dimerization-induced allostery in protein kinase regulation. *Trends Biochem. Sci.* 39, 475–486 (2014).
64. Chen, J.-J. *et al.* Translational Control by Heme-Regulated eIF2 α Kinase during Erythropoiesis. (2014) doi:10.1097/MOH.0000000000000030.
65. Guo, X. *et al.* Mitochondrial dysfunction is signaled to the integrated stress response by OMA1, DELE1 and HRI. *bioRxiv* (2019) doi:10.1101/715896.
66. Fessler, E. *et al.* A pathway coordinated by DELE1 relays mitochondrial stress to the cytosol. *Nature* 579, 433 (2020).
67. Romano, P. R. *et al.* Autophosphorylation in the Activation Loop Is Required for Full Kinase Activity In Vivo of Human and Yeast Eukaryotic Initiation Factor 2 α Kinases PKR and GCN2. *Mol. Cell. Biol.* 18, 2282–2297 (1998).
68. Hinnebusch, A. G. & Fink, G. R. Positive regulation in the general amino acid control of *Saccharomyces*

- cerevisiae. *Proc. Natl. Acad. Sci. U. S. A.* 80, 5374–5378 (1983).
69. Morris, D. R. *et al.* Upstream Open Reading Frames as Regulators of mRNA Translation. *Mol. Cell* 20, 8635–8642 (2000).
 70. Shatsky, I. N. *et al.* Cap-Independent Translation: What's in a Name? *Trends Biochem. Sci.* 43, 882–895 (2018).
 71. Vattem, K. M. & Wek, R. C. Reinitiation involving upstream ORFs regulates ATF4 mRNA translation in mammalian cells. *Proc. Natl. Acad. Sci. U. S. A.* 101, 11269–11274 (2004).
 72. Harding, H. P. *et al.* Stress-Induced Gene Expression in Mammalian Cells. *Mol. Cell* 6, 1099–1108 (2000).
 73. Newman, J. R. S. & Keating, A. E. Comprehensive identification of human bZIP interactions with coiled-coil arrays. *Science (80-.)*. 300, 2097–2101 (2003).
 74. Hinnebusch, A. G. & Lorsch, J. R. The mechanism of eukaryotic translation initiation: New insights and challenges. *Cold Spring Harb. Perspect. Biol.* 4, 1–26 (2012).
 75. Adomavicius, T. *et al.* The structural basis of translational control by eIF2 phosphorylation. (2019) doi:10.1038/s41467-019-10167-3.
 76. Bogorad, A. M. *et al.* Novel mechanisms of eIF2B action and regulation by eIF2 phosphorylation. *Nucleic Acids Res.* 45, 11962–11979 (2017).
 77. Gordiyenko, Y. *et al.* Structural basis for the inhibition of translation through eIF2 α phosphorylation. (2019) doi:10.1038/s41467-019-10606-1.
 78. Anand, A. A. *et al.* Structural basis of eIF2B-catalyzed GDP exchange and phosphoregulation by the integrated stress response. *bioRxiv* 495, 504654 (2018).
 79. Kashiwagi, K. *et al.* Structural basis for eIF2B inhibition in integrated stress response. <http://science.sciencemag.org/> (2019).
 80. Tsai, J. C. *et al.* Structure of the nucleotide exchange factor eIF2B reveals mechanism of memory-enhancing molecule. (2018) doi:10.1126/science.aag0939.
 81. Sidrauski, C. *et al.* Pharmacological dimerization and activation of the exchange factor eIF2B antagonizes the integrated stress response. *Elife* 2015, 1–27 (2015).
 82. Schoof, M. *et al.* eIF2B conformation and assembly state regulates the integrated stress response. *Elife* 10, (2021).
 83. Kenner, L. R. *et al.* STRUCTURAL BIOLOGY eIF2B-catalyzed nucleotide exchange and phosphoregulation by the integrated stress response. <http://science.sciencemag.org/> (2019).
 84. Zyryanova, A. F. *et al.* ISRIB Blunts the Integrated Stress Response by Allosterically Antagonising the Inhibitory Effect of Phosphorylated eIF2 on eIF2B. *Mol. Cell* 81, 88-103.e6 (2021).
 85. Rabouw, H. H. *et al.* Small molecule ISRIB suppresses the integrated stress response within a defined window of activation. *Proc. Natl. Acad. Sci. U. S. A.* 116, 2097–2102 (2019).
 86. Anand, A. A. & Walter, P. Structural insights into ISRIB, a memory-enhancing inhibitor of the integrated stress response. *FEBS J.* 287, 239–245 (2020).
 87. Bugallo, R. *et al.* Fine tuning of the unfolded protein response by ISRIB improves neuronal survival in a model of amyotrophic lateral sclerosis. *Cell Death Dis.* 11, (2020).
 88. Halliday, M. *et al.* Partial restoration of protein synthesis rates by the small molecule ISRIB prevents neurodegeneration without pancreatic toxicity. (2015) doi:10.1038/cddis.2015.49.
 89. Sekine, Y. *et al.* Mutations in a translation initiation factor identify the target of a memory-enhancing compound. *Science (80-.)*. 348, 1027–1030 (2015).
 90. Sidrauski, C. *et al.* Pharmacological brake-release of mRNA translation enhances cognitive memory. *Elife*

- 2013, 1–22 (2013).
91. Jousse, C. *et al.* Inhibition of a constitutive translation initiation factor 2 α phosphatase, CReP, promotes survival of stressed cells. *J. Cell Biol.* 163, 767–775 (2003).
 92. Novoa, I., Zeng, H., Harding, H. P. & Ron, D. Feedback inhibition of the unfolded protein response by GADD34-mediated dephosphorylation of eIF2 α . *J. Cell Biol.* 153, 1011–1021 (2001).
 93. Andreev, D. E. *et al.* TASEP modelling provides a parsimonious explanation for the ability of a single uorf to derepress translation during the integrated stress response. *Elife* 7, 1–20 (2018).
 94. Baird, T. D. & Wek, R. C. Thematic Review Series: Nutrient Control of Metabolism and Cell Signaling Eukaryotic Initiation Factor 2 Phosphorylation and Translational Control in Metabolism 1,2. *Adv. Nutr* 3, 307–321 (2012).
 95. Park, Y., Reyna-Neyra, A., Philippe, L. & Thoreen, C. C. mTORC1 Balances Cellular Amino Acid Supply with Demand for Protein Synthesis through Post-transcriptional Control of ATF4. *Cell Rep.* 19, 1083–1090 (2017).
 96. Harding, H. P. *et al.* Regulated Translation Initiation Controls Stress-Induced Gene Expression in Mammalian Cells Heather. *Aviat. Week Sp. Technol. (New York)* 161, 32 (2004).
 97. Lu, P. D., Harding, H. P. & Ron, D. Translation reinitiation at alternative open reading frames regulates gene expression in an integrated stress response. *J. Cell Biol.* 167, 27–33 (2004).
 98. Palam, L. R., Baird, T. D. & Wek, R. C. Phosphorylation of eIF2 Facilitates Ribosomal Bypass of an Inhibitory Upstream ORF to Enhance CHOP Translation * □ *S. J. Biol. Chem.* 286, 10939–10949 (2011).
 99. Lee, Y.-Y. *et al.* An Upstream Open Reading Frame Regulates Translation of GADD34 during Cellular Stresses That Induce eIF2 Phosphorylation * □ *S. J. Biol. Chem.* 284, 6661–6673 (2009).
 100. Zhou, D. *et al.* Phosphorylation of eIF2 Directs ATF5 Translational Control in Response to Diverse Stress Conditions *. *J. Biol. Chem.* 283, 7064–7073 (2008).
 101. Baird, T. D. & Wek, R. C. Eukaryotic initiation factor 2 phosphorylation and translational control in metabolism. *Adv. Nutr.* 3, 307–321 (2012).
 102. Wortel *et al.* Surviving Stress: Modulation of ATF4-Mediated Stress Responses in Normal and Malignant Cells. *Trends Endocrinol MEdab.* 176, 139–148 (2017).
 103. Chaveroux, C. *et al.* Molecular mechanisms involved in the adaptation to amino acid limitation in mammals. *Biochimie* 92, 736–745 (2010).
 104. Penn, M. D., Galgoci, B. & Greer, H. Identification of AAS genes and their regulatory role in general control of amino acid biosynthesis in yeast. *Proc. Natl. Acad. Sci. U. S. A.* 80, 2704–2708 (1983).
 105. Marton, T. J., Crouch, D. & Hinnebusch, A. G. *GCN1, a Translational Activator of GCN4 in Saccharomyces cerevisiae, Is Required for Phosphorylation of Eukaryotic Translation Initiation Factor 2 by Protein Kinase GCN2. Molecular and Cellular Biology* <http://mcb.asm.org/> (1993).
 106. Schurch, A., Miozzari, J. & Hutter, R. Regulation of tryptophan biosynthesis in *Saccharomyces cerevisiae*: mode of action of 5 methyl tryptophan and 5 methyl tryptophan sensitive mutants. *J. Bacteriol.* 117, 1131–1140 (1974).
 107. Vazquez De Aldana, C. R., Maiton, M. J. & Hinnebusch, A. G. GCN20, a novel ATP binding cassette protein, and GCN1 reside in a complex that mediates activation of the eIF-2 α kinase GCN2 in amino acid-starved cells. *EMBO J.* 14, 3184–3199 (1995).
 108. Vazquez de Aldana, C. R., Wek, R. C., Segundo, P. S., Truesdell, A. G. & Hinnebusch, A. G. Multicopy tRNA genes functionally suppress mutations in yeast eIF-2 alpha kinase GCN2: evidence for separate pathways coupling GCN4 expression to unchanged tRNA. *Mol. Cell. Biol.* 14, 7920–7932 (1994).
 109. Marton, M. J., Vazquez de Aldana, C. R., Qiu, H., Chakraborty, K. & Hinnebusch, A. G. Evidence that GCN1

- and GCN20, translational regulators of GCN4, function on elongating ribosomes in activation of eIF2 α kinase GCN2. *Mol. Cell. Biol.* 17, 4474–4489 (1997).
110. Lee, E. C. & Strange, K. GCN-2 dependent inhibition of protein synthesis activates osmosensitive gene transcription via WNK and Ste20 kinase signaling. 1269–1277 (2012) doi:10.1152/ajpcell.00294.2012.
 111. Rousakis, A. *et al.* The general control nonderepressible-2 kinase mediates stress response and longevity induced by target of rapamycin inactivation in *Caenorhabditis elegans*. *Aging Cell* 2, 742–751 (2013).
 112. Hirose, T. & Robert Horvitz, H. The Translational Regulators GCN-1 and ABCF-3 Act Together to Promote Apoptosis in *C. elegans*. (2014) doi:10.1371/journal.pgen.1004512.
 113. Yamazaki, H. *et al.* Ribosome binding protein GCN1 regulates the cell cycle and cell proliferation and is essential for the embryonic development of mice. *PLoS Genet.* 16, 1–23 (2020).
 114. Pochopien, A. A. *et al.* Structure of Gcn1 bound to stalled and colliding 80S ribosomes. (2021) doi:10.1073/pnas.2022756118/-DCSupplemental.
 115. Sood, R., Porter, A. C., Olsen, D., Cavener, D. R. & Wek, R. C. *A Mammalian Homologue of GCN2 Protein Kinase Important for Translational Control by Phosphorylation of Eukaryotic Initiation Factor-2*. (2000).
 116. Doerks, T., Copley, R. R., Schultz, J., Ponting, C. P. & Bork, P. Systematic identification of novel protein domain families associated with nuclear functions. *Genome Res.* 12, 47–56 (2002).
 117. Zhu, S., Sobolev, A. Y. & Wek, R. C. Histidyl-tRNA synthetase-related sequences in GCN2 protein kinase regulate in vitro phosphorylation of eIF-2. *J. Biol. Chem.* 271, 24989–24994 (1996).
 118. Wek, S. A., Zhu, S. & Wek, R. C. The histidyl-tRNA synthetase-related sequence in the eIF-2 alpha protein kinase GCN2 interacts with tRNA and is required for activation in response to starvation for different amino acids. *Mol. Cell. Biol.* 15, 4497–4506 (1995).
 119. Qiu, H., Dong, J., Hu, C., Francklyn, C. S. & Hinnebusch, A. G. The tRNA-binding moiety in GCN2 contains a dimerization domain that interacts with the kinase domain and is required for tRNA binding and kinase activation. *EMBO J.* 20, 1425–1438 (2001).
 120. Arnez, J. G. *et al.* Crystal structure of histidyl-tRNA synthetase from *Escherichia coli* complexed with histidyl-adenylate. *EMBO J.* 14, 4143–4155 (1995).
 121. Dong, J., Qiu, H., Garcia-Barrio, M., Anderson, J. & Hinnebusch, A. G. Uncharged tRNA activates GCN2 by displacing the protein kinase moiety from a bipartite tRNA-binding domain. *Mol. Cell* 6, 269–279 (2000).
 122. Narasimhan, J., Staschke, K. A. & Wek, R. C. Dimerization Is Required for Activation of eIF2 Kinase Gcn2 in Response to Diverse Environmental Stress Conditions*. *J. Biol. Chem.* 279, 22820–22832 (2004).
 123. He, H. *et al.* Crystal structures of GCN2 protein kinase C-terminal domains suggest regulatory differences in yeast and mammals. *J. Biol. Chem.* 289, 15023–15034 (2014).
 124. Kubota, H. *et al.* Budding Yeast GCN1 Binds the GI Domain to Activate the eIF2 α Kinase GCN2. *J. Biol. Chem.* 276, 17591–17596 (2001).
 125. Donzé, O. & Picard, D. Hsp90 Binds and Regulates Gcn2, the Ligand-Inducible Kinase of the α Subunit of Eukaryotic Translation Initiation Factor 2. *Mol. Cell. Biol.* 20, 1897–1897 (2000).
 126. Visweswaraiyah, J. *et al.* Evidence that eukaryotic translation elongation factor 1A (eEF1A) binds the Gcn2 protein C terminus and inhibits Gcn2 activity. *J. Biol. Chem.* 286, 36568–36579 (2011).
 127. Zhu, S. & Wek, R. C. Ribosome-binding domain of eukaryotic initiation factor-2 kinase GCN2 facilitates translation control. *J. Biol. Chem.* 273, 1808–1814 (1998).
 128. Cherkasova, V. A. & Hinnebusch, A. G. Translational control by TOR and TAP42 through dephosphorylation of eIF2 α kinase GCN2. *Genes Dev.* 17, 859–872 (2003).
 129. Garcia-Barrio, M. *et al.* Serine 577 is phosphorylated and negatively affects the tRNA binding and eIF2 α

- kinase activities of GCN2. *J. Biol. Chem.* 277, 30675–30683 (2002).
130. Sattlegger, E. & Hinnebusch, A. G. Separate domains in GCN1 for binding protein kinase GCN2 and ribosomes are required for GCN2 activation in amino acid-starved cells. *EMBO J.* 19, 6622–6633 (2000).
 131. Marton, M. J. *et al.* Evidence that GCN1 and GCN20, translational regulators of GCN4, function on elongating ribosomes in activation of eIF2 α kinase GCN2. *Mol. Cell. Biol.* 17, 4474–4489 (1997).
 132. Dar, A. C., Dever, T. E. & Sicheri, F. Higher-order substrate recognition of eIF2 α by the RNA-dependent protein kinase PKR. *Cell* 122, 887–900 (2005).
 133. Axten, J. M. *et al.* Discovery of 7-methyl-5-(1-([3-(trifluoromethyl)phenyl]acetyl)-2,3-dihydro-1H-indol-5-yl)-7H-pyrrolo[2,3-d]pyrimidin-4-amine (GSK2606414), a Potent and Selective First-in-Class Inhibitor of PKR-like Endoplasmic Reticulum Kinase (PERK). *J. Med. Chem.* 2, 1–5 (1997).
 134. Padyana, A. K., Qiu, H., Roll-Mecak, A., Hinnebusch, A. G. & Burley, S. K. Structural basis for autoinhibition and mutational activation of eukaryotic initiation factor 2 α protein kinase GCN2. *J. Biol. Chem.* 280, 29289–29299 (2005).
 135. Hinnebusch, A. G. eIF2 α kinases provide a new solution to the puzzle of substrate specificity. *Nat. Struct. Mol. Biol.* (2005).
 136. Dey, M. *et al.* Requirement for kinase-induced conformational change in eukaryotic initiation factor 2 α (eIF2 α) restricts phosphorylation of Ser51. (2010) doi:10.1073/pnas.1014872108/-DCSupplemental.
 137. Cole, J. L. *et al.* Activation of PKR: An open and shut case? James. *Trends Biochem Sci.* 32, 57–62 (2009).
 138. De Oliveira, T. M. *et al.* The structure of human GCN2 reveals a parallel, back-to-back kinase dimer with a plastic DFG activation loop motif. *Biochem. J.* 477, 275–284 (2020).
 139. Visweswaraiyah, J., Lee, S. J., Hinnebusch, A. G. & Sattlegger, E. Overexpression of eukaryotic translation elongation factor 3 impairs Gcn2 protein activation. *J. Biol. Chem.* 287, 37757–37768 (2012).
 140. Wu, C. C. C. *et al.* Ribosome Collisions Trigger General Stress Responses to Regulate Cell Fate. *Cell* 182, 404-416.e14 (2020).
 141. Wout, P. K. *et al.* *Saccharomyces cerevisiae* Rbg1 protein and its binding partner gir2 interact on polyribosomes with Gcn1. *Eukaryot. Cell* 8, 1061–1071 (2009).
 142. Wang, A., Luan, H. H. & Medzhitov, R. An evolutionary perspective on immunometabolism. *Science* (80-.). 363, (2019).
 143. Kerr, I. D. *et al.* Sequence analysis of twin ATP binding cassette proteins involved in translational control, antibiotic resistance, and ribonuclease L inhibition. *Biochem. Biophys. Res. Commun.* 315, 166–173 (2004).
 144. Gavin, A.-C. *et al.* Functional organization of the yeast proteome by systematic analysis of protein complexes. *NATURE* vol. 415 (2002).
 145. Uetz, P. *et al.* A comprehensive analysis of protein-protein interactions in *Saccharomyces cerevisiae*. *NATURE* vol. 403 (2000).
 146. Tyzack, J. K. *et al.* ABC50 interacts with eukaryotic initiation factor 2 and associates with the ribosome in an ATP-dependent manner. *J. Biol. Chem.* 275, 34131–34139 (2000).
 147. Anda, S. *et al.* Activation of Gcn2 in response to different stresses. *PLoS One* 12, 1–13 (2017).
 148. Roffé, M., Hajj, G. N. M., Azevedo, H. F., Alves, V. S. & Castilho, B. A. IMPACT Is a Developmentally Regulated Protein in Neurons That Opposes the Eukaryotic Initiation Factor 2 Kinase GCN2 in the modulation of Neurite Outgrowth. (2013) doi:10.1074/jbc.M113.461970.
 149. Pereira, C. M. *et al.* IMPACT, a protein preferentially expressed in the mouse brain, binds GCN1 and inhibits GCN2 activation. *J. Biol. Chem.* 280, 28316–28323 (2005).
 150. Kubota, H. *et al.* GI domain-mediated association of the eukaryotic initiation factor 2 α kinase GCN2 with its

- activator GCN1 is required for general amino acid control in budding yeast. *J. Biol. Chem.* 275, 20243–20246 (2000).
151. Waller, T., Lee, S. J. & Sattlegger, E. Evidence that Yih1 resides in a complex with ribosomes. *FEBS J.* 279, 1761–1776 (2012).
 152. Sattlegger, E. *et al.* Gcn1 and actin binding to Yih1: Implications for activation of the eIF2 kinase GCN2. *J. Biol. Chem.* 286, 10341–10355 (2011).
 153. Wout, P. K., Sattlegger, E., Sullivan, S. M. & Maddock, J. R. *Saccharomyces cerevisiae* Rbg1 protein and its binding partner gir2 interact on polyribosomes with Gcn1. *Eukaryot. Cell* 8, 1061–1071 (2009).
 154. Sattlegger, E. *et al.* YIH1 is an actin-binding protein that inhibits protein kinase GCN2 and impairs general amino acid control when overexpressed. *J. Biol. Chem.* 279, 29952–29962 (2004).
 155. Ishikawa, K. *et al.* Cell growth control by stable Rbg2/Gir2 complex formation under amino acid starvation. *Genes to Cells* 18, 859–872 (2013).
 156. Kim, Y. *et al.* Aminoacyl-tRNA synthetase inhibition activates a pathway that branches from the canonical amino acid response in mammalian cells. *Proc. Natl. Acad. Sci. U. S. A.* 117, 8900–8911 (2020).
 157. Izquierdo, Y. *et al.* Arabidopsis nonresponding to oxylipins locus NOXY7 encodes a yeast GCN1 homolog that mediates noncanonical translation regulation and stress adaptation. *Plant Cell Environ.* 41, 1438–1452 (2018).
 158. Rolland, T. *et al.* A proteome-scale map of the human interactome network. *Cell* 159, 1212–1226 (2014).
 159. Luck, K. *et al.* A reference map of the human binary protein interactome. *Nature* 580, 402–408 (2020).
 160. Cook-Mills, J. M. *et al.* VCAM-1 signals during lymphocyte migration: Role of reactive oxygen species. *Mol. Immunol.* 39, 499–508 (2002).
 161. Baluapuri, A., Wolf, E. & Eilers, M. Target gene-independent functions of MYC oncoproteins. *Nat. Rev. Mol. Cell Biol.* 21, 255–267 (2020).
 162. Cho, N. H. *et al.* OpenCell: proteome-scale endogenous tagging enables the cartography of human cellular organization. *bioRxiv* 2021.03.29.437450 (2021).
 163. Götz, C. & Montenarh, M. Protein kinase CK2 in development and differentiation. *Biomed. Reports* 6, 127–133 (2017).
 164. Channavajhala, P. & Seldin, D. C. Functional interaction of protein kinase CK2 and c-Myc in lymphomagenesis. *Oncogene* 21, 5280–5288 (2002).
 165. Ramirez, M., Wek, R. C. & Hinnebusch, A. G. *Ribosome Association of GCN2 Protein Kinase, a Translational Activator of the GCN4 Gene of Saccharomyces cerevisiae.* *Molecular and Cellular Biology* vol. 11 <http://mcb.asm.org/> (1991).
 166. Inglis, A. J. *et al.* Activation of GCN2 by the ribosomal P-stalk. *Proc. Natl. Acad. Sci.* 201813352 (2019) doi:10.1073/pnas.1813352116.
 167. Peschek, J., Acosta-Alvear, D., Mendez, A. S. & Walter, P. A conformational RNA zipper promotes intron ejection during non-conventional XBP1 mRNA splicing. *EMBO Rep.* 16, 1688–1698 (2015).
 168. González, A. & Hall, M. N. Nutrient sensing and TOR signaling in yeast and mammals. *EMBO J.* 36, 397–408 (2017).
 169. Jiménez-Díaz, A., Remacha, M., Ballesta, J. P. G. & Berlanga, J. J. Phosphorylation of Initiation Factor eIF2 in Response to Stress Conditions Is Mediated by Acidic Ribosomal P1/P2 Proteins in *Saccharomyces cerevisiae*. (2013).
 170. Ishimura, R. *et al.* Activation of GCN2 kinase by ribosome stalling links translation elongation with translation initiation. (2016) doi:10.7554/eLife.14295.001.

171. Harding, H. P. *et al.* The ribosomal P-stalk couples amino acid starvation to GCN2 2 activation in mammalian cells. *Elife* 8, 1–19 (2019).
172. Wek, R. C., Jackson, B. M. & Hinnebusch, A. G. *Juxtaposition of domains homologous to protein kinases and histidyl-tRNA synthetases in GCN2 protein suggests a mechanism for coupling GCN4 expression to amino acid availability (translational control/aminoacyl-tRNA synthetase)*. *Proc. Natl. Acad. Sci. USA* vol. 86 (1989).
173. Wek, R. C., Ramirez, M., Jackson, B. M. & Hinnebusch, A. G. Identification of positive-acting domains in GCN2 protein kinase required for translational activation of GCN4 expression. *Mol. Cell. Biol.* 10, 2820–2831 (1990).
174. Helgstrand, M. *et al.* The Ribosomal Stalk Binds to Translation Factors IF2, EF-Tu, EF-G and RF3 via a Conserved Region of the L12 C-terminal Domain. *J. Mol. Biol.* 365, 468–479 (2007).
175. Mohr, D. *et al.* GTPase activation of elongation factors Tu and G on the ribosome. *Biochemistry* 41, 12520–12528 (2002).
176. Nomura, N. *et al.* Archaeal ribosomal stalk protein interacts with translation factors in a nucleotide-independent manner via its conserved C terminus. *Proc. Natl. Acad. Sci. U. S. A.* 109, 3748–3753 (2012).
177. Buck, M. D., Sowell, R. T., Kaech, S. M. & Pearce, E. L. Metabolic Instruction of Immunity. *Cell* 169, 570–586 (2017).
178. Bessede, A. *et al.* Aryl hydrocarbon receptor control of a disease tolerance defence pathway. *Nature* 511, 184–190 (2014).
179. Averous, J. *et al.* GCN2 contributes to mTORC1 inhibition by leucine deprivation through an ATF4 independent mechanism. *Sci. Rep.* 6, 1–10 (2016).
180. Costa-Mattioli, M. *et al.* Translational control of hippocampal synaptic plasticity and memory by the eIF2a kinase GCN2. (2005) doi:10.1038/nature03897.
181. Ball, H. J. *et al.* Tryptophan-catabolizing enzymes – party of three. (2014) doi:10.3389/fimmu.2014.00485.
182. Cobbold, S. P. *et al.* Infectious tolerance via the consumption of essential amino acids and mTOR signaling. *PNAS* (2009).
183. Munn, D. H. & Mellor, A. L. Indoleamine 2,3 dioxygenase and metabolic control of immune responses. *Trends Immunol.* 34, 137–143 (2013).
184. Xue, Q. *et al.* Regulation of iNOS on immune cells and its role in diseases. *Int. J. Mol. Sci.* 19, (2018).
185. Tripathi, P. *et al.* Nitric oxide and immune response. *Indian J. Biochem. Biophys.* 44, 310–319 (2007).
186. Schindler, H. & Bogdan, C. NO as a signaling molecule: Effects on kinases. *Int. Immunopharmacol.* 1, 1443–1455 (2001).
187. Gobert, A. P. *et al.* *Helicobacter pylori* arginase inhibits nitric oxide production by eukaryotic cells: A strategy for bacterial survival. www.pnas.org/cgi/doi/10.1073/pnas.241443798 (2001).
188. Rodriguez, P. C. *et al.* Arginase I production in the tumor microenvironment by mature myeloid cells inhibits T-cell receptor expression and antigen-specific T-cell responses. *Cancer Res.* 64, 5839–5849 (2004).
189. Pesce, J. T. *et al.* Arginase-1-expressing macrophages suppress Th2 cytokine-driven inflammation and fibrosis. *PLoS Pathog.* 5, (2009).
190. Pearce, E. J. *et al.* Priming of the immune response by schistosome eggs. *Parasite Immunol.* 27, 265–270 (2005).
191. Trottein, F. *et al.* A Type I IFN-Dependent Pathway Induced by *Schistosoma mansoni* Eggs in Mouse Myeloid Dendritic Cells Generates an Inflammatory Signature. *J. Immunol.* 172, 3011–3017 (2004).
192. Van de Velde, L. A. *et al.* Stress Kinase GCN2 Controls the Proliferative Fitness and Trafficking of Cytotoxic T Cells Independent of Environmental Amino Acid Sensing. *Cell Rep.* 17, 2247–2258 (2016).

193. Munn, D. H. *et al.* GCN2 kinase in T cells mediates proliferative arrest and anergy induction in response to indoleamine 2,3-dioxygenase. *Immunity* 22, 633–642 (2005).
194. Van De Velde, L. A. *et al.* T Cells encountering myeloid cells programmed for amino acid-dependent Immunosuppression Use Rictor/mTORC2 Protein for proliferative checkpoint decisions. *J. Biol. Chem.* 292, 15–30 (2017).
195. Liu, K. *et al.* Diversity in (p)ppGpp metabolism and effectors Kuanqing. *Curr Opin Microbiol* 63, 1–18 (2015).
196. Ravindran, R. *et al.* Vaccine activation of the nutrient sensor GCN2 in dendritic cells enhances antigen presentation. *Science (80-)*. 343, 313–317 (2014).
197. Chu, J. *et al.* Translation Initiation Factors: Reprogramming Protein Synthesis in Cancer. *Trends Cell Biol.* 26, 918–933 (2016).
198. Robichaud, N., Sonenberg, N., Ruggero, D. & Schneider, R. J. Translational control in cancer. *Cold Spring Harb. Perspect. Biol.* 11, (2019).
199. Ye, J. *et al.* The GCN2-ATF4 pathway is critical for tumour cell survival and proliferation in response to nutrient deprivation. *EMBO J.* 29, 2082–2096 (2010).
200. Wang, Y. *et al.* Amino acid deprivation promotes tumor angiogenesis through the GCN2/ATF4 pathway. *Neoplasia (United States)* 15, 989–997 (2013).
201. Tameire, F. *et al.* Cell Intrinsic and Extrinsic Activators of the Unfolded Protein Response in Cancer: Mechanisms and Targets for Therapy. *Semin Cancer Biol.* 176, 139–148 (2015).
202. Ozcan, U. *et al.* Loss of the Tuberous Sclerosis Complex Tumor Suppressors Triggers the Unfolded Protein Response to Regulate Insulin Signaling and Apoptosis. *Mol. Cell* 29, 541–551 (2008).
203. Hart, L. S. *et al.* ER stress-mediated autophagy promotes Myc-dependent transformation and tumor growth. *J. Clin. Invest.* 122, 4621–4634 (2012).
204. Beroukhi, R. *et al.* The landscape of somatic copy-number alteration across human cancers. *Nature* 463, 899–905 (2010).
205. Stine, Z. E. *et al.* MYC, Metabolism, and Cancer MYC function. *Cancer discovery* vol. 5 (2015).
206. Wang, R. *et al.* The transcription factor Myc controls metabolic reprogramming upon T lymphocyte activation Ruoning. 148, 825–832 (2008).
207. Tameire, F. *et al.* ATF4 couples MYC-dependent translational activity to bioenergetic demands during tumour progression. *Nat. Cell Biol.* 21, 889–899 (2019).
208. Gatell, J. M. *et al.* Tumor-Associated Macrophages and Survival in Classic Hodgkin's Lymphoma. *N. Engl. J. Med.* 362, 339–354 (2008).
209. Fridman, W. H. *et al.* The immune contexture in human tumours: Impact on clinical outcome. *Nat. Rev. Cancer* 12, 298–306 (2012).
210. Halaby, M. J. *et al.* GCN2 drives macrophage and MDSC function and immunosuppression in the tumor microenvironment. *Sci. Immunol.* 4, 1–18 (2019).
211. Gabrilovich, D. I. *et al.* Coordinated regulation of myeloid cells by tumours Dmitry. *Nat Rev Immunol* 23, 1–7 (2011).
212. Bronte, V. *et al.* Recommendations for myeloid-derived suppressor cell nomenclature and characterization standards. *Nat. Commun.* 7, 1–10 (2016).
213. Corzo, C. A. *et al.* HIF-1 α regulates function and differentiation of myeloid-derived suppressor cells in the tumor microenvironment. *J. Exp. Med.* 207, 2439–2453 (2010).
214. Franklin, R. *et al.* Ontogeny of Tumor-associated Macrophages and Its Implication in Cancer Regulation. *Trends Cancer* 2, 20–34 (2016).

215. Milyavsky, M. *et al.* A Distinctive DNA damage response in human hematopoietic stem cells reveals an apoptosis-independent role for p53 in self-renewal. *Cell Stem Cell* 7, 186–197 (2010).
216. Miharada, K. *et al.* Dppa5 improves hematopoietic stem cell activity by reducing endoplasmic reticulum stress. *Cell Rep.* 7, 1381–1392 (2014).
217. Han, J. *et al.* ER-stress-induced transcriptional regulation increases protein synthesis leading to cell death. *Nat. Cell Biol.* 15, 481–490 (2013).
218. Rutkowski, D. T. *et al.* Adaptation to ER stress is mediated by differential stabilities of pro-survival and pro-apoptotic mRNAs and proteins. *PLoS Biol.* 4, 2024–2041 (2006).
219. Pakos-Zebrucka, K. *et al.* The integrated stress response. *EMBO Rep.* 17, 1374–1395 (2016).
220. Van Galen, P. *et al.* Integrated Stress Response Activity Marks Stem Cells in Normal Hematopoiesis and Leukemia. *CellReports* 25, 1109-1117.e5 (2018).
221. Heydt, Q. *et al.* Oncogenic FLT3-ITD supports autophagy via ATF4 in acute myeloid leukemia. *Oncogene* 37, 787–797 (2018).
222. Jacque, N. *et al.* Targeting glutaminolysis has antileukemic activity in acute myeloid leukemia and synergizes with BCL-2 inhibition. *Blood* 126, 1346–1356 (2015).
223. Miraki-Moud, F. *et al.* Arginine deprivation using pegylated arginine deiminase has activity against primary acute myeloid leukemia cells in vivo. *Blood* 125, 4060–4068 (2015).
224. Willems, L. *et al.* Inhibiting Glutamine uptake represents an attractive new strategy for treating acute myeloid leukemia. *Blood* 122, 3521–3532 (2013).
225. Hu, G. *et al.* The Amino Acid Sensor Eif2ak4/GCN2 Is Required for Proliferation of Osteoblast Progenitors in Mice. *J Bone Min. Res.* 176, 139–148 (2020).
226. Sundrud, M. S. *et al.* 10-Halofuginone Inhibits TH17 Cell Differentiation by Activating the.pdf. *Science (80-.).* 324, 1334–1338 (2010).
227. Keller, T. L. *et al.* Halofuginone and other febrifugine derivatives inhibit prolyl- tRNA synthetase. *Nat Cell Biol* 176, 139–148 (2017).
228. Lühder, F. *et al.* Autoimmune Inflammation. *J. Neuroimmunol.* 192, 2167–2176 (2009).
229. Xavier, S. *et al.* Amelioration of radiation-induced fibrosis. Inhibition of transforming growth factor- β signaling by halofuginone. *J. Biol. Chem.* 279, 15167–15176 (2004).
230. Oishi, H. *et al.* Halofuginone treatment reduces interleukin-17A and ameliorates features of chronic lung allograft dysfunction in a mouse orthotopic lung transplant model. *J. Hear. Lung Transplant.* 35, 518–527 (2016).
231. Loscalzo, D. *et al.* Duality of fibroblast-like synoviocytes in RA. *Nat Rev Rheumatol* 23, 1–7 (2013).
232. Bottini, N. & Firestein, G. S. Duality of fibroblast-like synoviocytes in RA: Passive responders and imprinted aggressors. *Nat. Rev. Rheumatol.* 9, 24–33 (2013).
233. Sidrauski, C., McGeachy, A. M., Ingolia, N. T. & Walter, P. The small molecule ISRIB reverses the effects of eIF2 α phosphorylation on translation and stress granule assembly. *Elife* 2015, 1–16 (2015).
234. Van Der Knaap, M. S. *et al.* Mutations in each of the five subunits of translation initiation factor eIF2B can cause leukoencephalopathy with vanishing white matter. *Ann. Neurol.* 51, 264–270 (2002).
235. Devi, L. & Ohno, M. Deletion of the eIF2 α Kinase GCN2 Fails to Rescue the Memory Decline Associated with Alzheimer's Disease. *PLoS One* 8, 1–8 (2013).
236. Ma, T. *et al.* Plasticity and Spatial Memory Deficits. *Nat. Neurosci.* 16, 1299–1305 (2013).
237. Helseth, A. R. *et al.* Cholinergic neurons constitutively engage the ISR for dopamine modulation and skill learning in mice. *Science* 372, (2021).

238. Kato, Y. *et al.* GZD824 inhibits GCN2 and sensitizes cancer cells to amino acid starvation stress. *Mol. Pharmacol.* 98, 669–676 (2020).
239. Nakamura, A. *et al.* Inhibition of GCN2 sensitizes ASNS-low cancer cells to asparaginase by disrupting the amino acid response. *Proc. Natl. Acad. Sci. U. S. A.* 115, E7776–E7785 (2018).
240. Schmidt, S. *et al.* A MYC–GCN2–eIF2 α negative feedback loop limits protein synthesis to prevent MYC-dependent apoptosis in colorectal cancer. *Nat. Cell Biol.* 21, 1413–1424 (2019).
241. Torrence, M. E. & Manning, B. D. Nutrient Sensing in Cancer. *Annu. Rev. Cancer Biol.* 2, 251–269 (2018).
242. Dash, P. K. *et al.* Inhibition of eukaryotic initiation factor 2 alpha phosphatase reduces tissue damage and improves learning and memory after experimental traumatic brain injury. *J. Neurotrauma* 32, 1608–1620 (2015).
243. Tsaytler, P., Harding, H. P., Ron, D. & Bertolotti, A. Selective inhibition of a regulatory subunit of protein phosphatase 1 restores proteostasis. *Science (80-)*. 332, 91–94 (2011).
244. Krzyzosiak, A. *et al.* Target-Based Discovery of an Inhibitor of the Regulatory Phosphatase PPP1R15B. *Cell* 174, 1216–1228.e19 (2018).
245. Crespillo-Casado, A., Chambers, J. E., Fischer, P. M., Marciniak, S. J. & Ron, D. PPP1R15A-mediated dephosphorylation of eIF2 α is unaffected by Sephin1 or Guanabenz. (2017) doi:10.7554/eLife.26109.001.
246. Dedigama-Arachchige, P. M. *et al.* Identification of PP1-Gadd34 substrates involved in the unfolded protein response using K-BIPS, a method for phosphatase substrate identification †. 14, 121 (2018).
247. Dorsch, D. Triazolo Inhibitors of GCN2 Patent. 2012, (2013).
248. Fujimoto, J. *et al.* Identification of Novel, Potent, and Orally Available GCN2 Inhibitors with Type i Half Binding Mode. *ACS Med. Chem. Lett.* 10, 1498–1503 (2019).
249. Phase II Study of Clinical Activity of Pegaspargase in Women With Relapsed or Refractory Epithelial Ovarian Cancer, Fallopian Tube Cancer, and/or Primary Peritoneal Cancer. <https://clinicaltrials.gov/ct2/show/NCT01313078> (2010).
250. Gao, L. *et al.* Microcystin-LR inhibits testosterone synthesis via reactive oxygen species-mediated GCN2/eIF2 α pathway in mouse testes. *Sci. Total Environ.* 781, 146730 (2021).
251. Ren, X. *et al.* Identification of GZD824 as an orally bioavailable inhibitor that targets phosphorylated and nonphosphorylated breakpoint cluster region-Abelson (Bcr-Abl) kinase and overcomes clinically acquired mutation-induced resistance against imatinib. *J. Med. Chem.* 56, 879–894 (2013).
252. Yue, M. *et al.* Oncogenic MYC Activates a Feedforward Regulatory Loop Promoting Essential Amino Acid Metabolism and Tumorigenesis. *Cell Rep.* 21, 3819–3832 (2017).
253. Keith, C. T. & Schreiber, S. L. PIK-related kinases: DNA repair, recombination, and cell cycle checkpoints. *Science (80-)*. 270, 50–51 (1995).
254. Sabatini, D. M., Erdjument-Bromage, H., Lui, M., Tempst, P. & Snyder, S. H. RAFT1: A mammalian protein that binds to FKBP12 in a rapamycin-dependent fashion and is homologous to yeast TORs. *Cell* 78, 35–43 (1994).
255. Yang, H. *et al.* Structural Mechanisms of mTORC1 activation by RHEB and inhibition by PRAS40. *Nature* 176, 139–148 (2017).
256. Yang, H. *et al.* MTOR kinase structure, mechanism and regulation. *Nature* 497, 217–223 (2013).
257. Immun, J. & Maeda, K. A mammalian protein targeted by Gl-arresting rapamycin-receptor complex. 18. *Lebrun. P. & Spiegelberg. H. I. J. Immun* vol. 21 (1991).
258. Bierer, B. E. *et al.* Two distinct signal transmission pathways in T lymphocytes are inhibited by complexes formed between an immunophilin and either FK506 or rapamycin. *Proc. Natl. Acad. Sci. USA* vol. 87 (1990).

259. Chung, J., Kuo, C. J., Crabtree, G. R. & Blenis, J. Rapamycin-FKBP specifically blocks growth-dependent activation of and signaling by the 70 kd S6 protein kinases. *Cell* 69, 1227–1236 (1992).
260. Kunz, J. *et al.* Target of rapamycin in yeast, TOR2, is an essential phosphatidylinositol kinase homolog required for G1 progression. *Cell* 73, 585–596 (1993).
261. Eng, C. P. *et al.* Activity Of Rapamycin (AY-22,989) Against Transplanted Tumors. *The Journal Of Antibiotics* (1984).
262. Vézina, C. & Kudelski, A. Rapamycin (AY-22,989), a new antifungal antibiotic. I. taxonomy of the producing streptomycete and isolation of the active principle. *J. Antibiot. (Tokyo)*. 28, 721–726 (1975).
263. Martel, R. R. *et al.* Inhibition of the immune response by rapamycin, a new fungal antibiotic. *J. Physiol. Pharmacol.* (1977).
264. Houchens, D. P. *et al.* Human brain tumor xenografts in nude mice as a chemotherapy model. *Eur. J. Cancer Clin. Oncol.* 19, 799–805 (1983).
265. Heitman, J., Movva, N. R. & Hall, M. N. Targets for cell cycle arrest by the immunosuppressant rapamycin in yeast. *Science (80-)*. 253, 905–909 (1991).
266. Kim, D. *et al.* GβL, a Positive Regulator of the Rapamycin- Sensitive Pathway Required for the Nutrient-Sensitive Interaction between Raptor and mTOR. *Mol. Cell* 11, 895–904 (2003).
267. Kim, D. H. *et al.* mTOR interacts with raptor to form a nutrient-sensitive complex that signals to the cell growth machinery. *Cell* 110, 163–175 (2002).
268. Hara, K. *et al.* Raptor, a binding partner of target of rapamycin (TOR), mediates TOR action. *Cell* 110, 177–189 (2002).
269. Peterson, T. R. *et al.* DEPTOR Is an mTOR Inhibitor Frequently Overexpressed in Multiple Myeloma Cells and Required for Their Survival. *Cell* 137, 873–886 (2009).
270. Sancak, Y. *et al.* PRAS40 Is an Insulin-Regulated Inhibitor of the mTORC1 Protein Kinase. *Mol. Cell* 25, 903–915 (2007).
271. Haar, E. *et al.* Insulin signalling to mTOR mediated by the Akt/PKB substrate PRAS40. *Nat. Cell Biol.* 9, 316–323 (2007).
272. Murase, K. *et al.* EF-Tu Binding Peptides Identified, Dissected, and Affinity Optimized by Phage Display GDP conformation of EF-Tu. Because EF-Tu is abundant in the cell, other functions have been suggested, particularly during periods of cellular stress when protein syn-g. *Chem. Biol.* 10, 161–168 (2003).
273. Nojima, H. *et al.* The Mammalian Target of Rapamycin (mTOR) Partner, Raptor, Binds the mTOR Substrates p70 S6 Kinase and 4E-BP1 through Their TOR Signaling (TOS) Motif*. *J. Biol. Chem.* 278, 15461–15464 (2003).
274. Guertin, D. A. *et al.* Ablation in Mice of the mTORC Components raptor, rictor, or mLST8 Reveals that mTORC2 Is Required for Signaling to Akt-FOXO and PKCα, but Not S6K1. *Dev. Cell* 11, 859–871 (2006).
275. Aylett, C. H. S. *et al.* Architecture of human mTOR complex 1. *Science (80-)*. 351, 48–52 (2016).
276. Yip, C. K., Murata, K., Walz, T., Sabatini, D. M. & Kang, S. A. Structure of the Human mTOR Complex I and Its Implications for Rapamycin Inhibition. *Mol. Cell* 38, 768–774 (2010).
277. Navé, B. T. *et al.* Mammalian target of rapamycin is a direct target for protein kinase B: Identification of a convergence point for opposing effects of insulin and amino-acid deficiency on protein translation. *Biochem. J.* 344, 427–431 (1999).
278. Peterson, R. T., Beal, P. A., Comb, M. J. & Schreiber, S. L. FKBP12-rapamycin-associated protein (FRAP) autophosphorylates at serine 2481 under translationally repressive conditions. *J. Biol. Chem.* 275, 7416–7423 (2000).

279. Sarbassov, D. D. *et al.* Prolonged Rapamycin Treatment Inhibits mTORC2 Assembly and Akt/PKB. *Mol. Cell* 22, 159–168 (2006).
280. Sarbassov, D. D. *et al.* Rictor, a Novel Binding Partner of mTOR, Defines a Rapamycin-Insensitive and Raptor-Independent Pathway that Regulates the Cytoskeleton. *Curr. Biol.* 14, ARTMED1118 (2004).
281. Frias, M. A. *et al.* mSin1 Is Necessary for Akt/PKB Phosphorylation, and Its Isoforms Define Three Distinct mTORC2s. *Curr. Biol.* 16, 1865–1870 (2006).
282. Jacinto, E. *et al.* SIN1/MIP1 Maintains rictor-mTOR Complex Integrity and Regulates Akt Phosphorylation and Substrate Specificity. *Cell* 127, 125–137 (2006).
283. Yang, Q. *et al.* Identification of Sin1 as an essential TORC2 component required for complex formation and kinase activity. *Genes Dev.* 20, 2820–2832 (2006).
284. Pearce, L. R. *et al.* Identification of Protor as a novel Rictor-binding component of mTOR complex-2. *Biochem. J.* 405, 513–522 (2007).
285. Woo, S. Y. *et al.* PRR5, a novel component of mTOR complex 2, regulates platelet-derived growth factor receptor β expression and signaling. *J. Biol. Chem.* 282, 25604–25612 (2007).
286. Kim, E. *et al.* Regulation of TORC1 by Rag GTPases in nutrient response. *Nat Cell Biol* 63, 1–18 (2014).
287. Chen, X. *et al.* Cryo-EM structure of human mTOR complex 2. *Cell Res.* 28, 518–528 (2018).
288. Stutfeld, E. *et al.* Architecture of the human mTORC2 core complex. *Elife* 7, 1–12 (2018).
289. Liu, L. *et al.* mTORC2 Regulates Neutrophil Chemotaxis In A cAMP- And RhoA-Dependent Fashion. *Dev Cell.* 23, 1–7 (2010).
290. Schmidt, K. M. *et al.* Inhibition of mTORC2/RICTOR Impairs Melanoma Hepatic Metastasis. *Neoplasia (United States)* 20, 1198–1208 (2018).
291. Morrison Joly, M. *et al.* Two distinct mTORC2-dependent pathways converge on Rac1 to drive breast cancer metastasis. *Breast Cancer Res.* 19, 1–15 (2017).
292. Jacinto, E. *et al.* Mammalian TOR complex 2 controls the actin cytoskeleton and is rapamycin insensitive. *Nat. Cell Biol.* 6, 1122–1128 (2004).
293. Lamming, D. W. *et al.* Rapamycin-induced insulin resistance is mediated by mTORC2 loss and uncoupled from longevity. *Science (80-.)*. 23, 1–7 (2012).
294. Gaubitz, C. *et al.* Molecular Basis of the Rapamycin Insensitivity of Target Of Rapamycin Complex 2. *Mol. Cell* 58, 977–988 (2015).
295. Bö, R. *et al.* The dynamic mechanism of 4E-BP1 recognition and phosphorylation by mTORC1. *Mol. Cell* 81, 1–14 (2021).
296. Choo, A. Y., Yoon, S. O., Sang, G. K., Roux, P. P. & Blenis, J. Rapamycin differentially inhibits S6Ks and 4E-BP1 to mediate cell-type-specific repression of mRNA translation. *Proc. Natl. Acad. Sci. U. S. A.* 105, 17414–17419 (2008).
297. Sonenberg, N. & Hinnebusch, A. G. Regulation of Translation Initiation in Eukaryotes: Mechanisms and Biological Targets. *Cell* 136, 731–745 (2009).
298. Sonenberg, N. & Dever, T. E. Eukaryotic translation initiation factors and regulators. *Curr. Opin. Struct. Biol.* 13, 56–63 (2003).
299. Tsukiyama-Kohara, K. *et al.* Tissue distribution, genomic structure, and chromosome mapping of mouse and human eukaryotic initiation factor 4E-binding proteins 1 and 2. *Genomics* 38, 353–363 (1996).
300. Tsukiyama-Kohara, K. *et al.* Adipose tissue reduction in mice lacking the translational inhibitor 4E-BP1. *Nat. Med.* 7, 1128–1132 (2001).
301. Paku, K. S. *et al.* A conserved motif within the flexible C-terminus of the translational regulator 4E-BP is

- required for tight binding to the mRNA cap-binding protein eIF4E. *Biochem. J.* 441, 237–245 (2012).
302. Gingras, A. C. *et al.* Regulation of 4E-BP1 phosphorylation: A novel two step mechanism. *Genes Dev.* 13, 1422–1437 (1999).
303. Reinhard, C., Thomas, G. & Kozma, S. C. A single gene encodes two isoforms of the p70 S6 kinase: Activation upon mitogenic stimulation. *Proc. Natl. Acad. Sci. U. S. A.* 89, 4052–4056 (1992).
304. Saitoh, M. *et al.* Regulation of an activated S6 kinase 1 variant reveals a novel mammalian target of rapamycin phosphorylation site. *J. Biol. Chem.* 277, 20104–20112 (2002).
305. Fingar, D. C. *et al.* mTOR Controls Cell Cycle Progression through Its Cell Growth Effectors S6K1 and 4E-BP1/Eukaryotic Translation Initiation Factor 4E. *Mol. Cell. Biol.* 24, 200–216 (2004).
306. Dorrello, N. V. *et al.* S6K1- and bTRCP-Mediated Degradation of PDCD4 Promotes Protein Translation and Cell Growth. 314, 467–472 (2006).
307. Holz, M. K., Ballif, B. A., Gygi, S. P. & Blenis, J. mTOR and S6K1 mediate assembly of the translation preinitiation complex through dynamic protein interchange and ordered phosphorylation events. *Cell* 123, 569–580 (2005).
308. Gingras, A. C. *et al.* Raught, B. & Sonenberg, N. Regulation of translation initiation by FRAP/mTOR. *Genes Dev.* 15, 807–826 (2001).
309. Meyuhas, O. & Drazhen, A. *et al.* Ribosomal Protein S6 Kinase. From TOP mRNAs to Cell Size. *Progress in Molecular Biology and Translational Science* vol. 90 109–153 (2009).
310. Fonseca, B. D. *et al.* LARP1 is a major phosphorylation substrate of mTORC1. *bioRxiv* (2018) doi:10.1101/491274.
311. Burnett, P. E., Barrow, R. K., Cohen, N. A., Snyder, S. H. & Sabatini, D. M. RAFT1 phosphorylation of the translational regulators p70 S6 kinase and 4E-BP1. *Proc. Natl. Acad. Sci. U. S. A.* 95, 1432–1437 (1998).
312. Pullen, N. *et al.* Phosphorylation and activation of p70(s6k) by PDK1. *Science (80-.).* 279, 707–710 (1998).
313. Porstmann, T. *et al.* SREBP Activity Is Regulated by mTORC1 and Contributes to Akt-Dependent Cell Growth. *Cell Metab.* 8, 224–236 (2008).
314. Robitaille, A. M. *et al.* Quantitative phosphoproteomics reveal mTORC1 activates de novo pyrimidine synthesis. *Science (80-.).* 339, 1320–1323 (2013).
315. Ben-Sahra, I. *et al.* Stimulation of de novo pyrimidine synthesis by growth signaling through mTOR and S6K1. *Science (80-.).* 23, 1–7 (2013).
316. Ganley, I. G. *et al.* ULK1·ATG13·FIP200 complex mediates mTOR signaling and is essential for autophagy. *J. Biol. Chem.* 284, 12297–12305 (2009).
317. Sophie Mokas, J. R. M. *et al.* Uncoupling Stress Granule Assembly and Translation Initiation Inhibition. *Mol. Biol. Cell* 20, 2673–2683 (2009).
318. Kim, J. *et al.* AMPK and mTOR regulate autophagy through direct phosphorylation of Ulk1. *Nat. Cell Biol.* 13, 132–141 (2011).
319. Kim, Y. M. *et al.* MTORC1 phosphorylates UVRAG to negatively regulate autophagosome and endosome maturation. *Mol. Cell* 57, 207–218 (2015).
320. Düvel, K. *et al.* Activation of a metabolic gene regulatory network downstream of mTOR complex 1. *Mol Cell* 39, 171–183 (2010).
321. Cunningham, J. T. *et al.* mTOR controls mitochondrial oxidative function through a YY1-PGC-1 α transcriptional complex. *Nature* 450, 736–740 (2007).
322. Zid, B. M. *et al.* 4E-BP Extends Lifespan upon Dietary Restriction by Enhancing Mitochondrial Activity in *Drosophila*. *Cell* 139, 149–160 (2009).

323. Inoki, K. *et al.* Rheb GTPase is a direct target of TSC2 GAP activity and regulates mTOR signaling. *Genes Dev.* 17, 1829–1834 (2003).
324. Long, X., Lin, Y., Ortiz-Vega, S., Yonezawa, K. & Avruch, J. Rheb binds and regulates the mTOR kinase. *Curr. Biol.* 15, 702–713 (2005).
325. Sancak, Y. *et al.* The rag GTPases bind raptor and mediate amino acid signaling to mTORC1. *Science (80-.)*. 320, 1496–1501 (2008).
326. Valvezan, A. J. & Manning, B. D. Molecular logic of mTORC1 signalling as a metabolic rheostat. *Nat. Metab.* 1, 321–333 (2019).
327. Demetriades, C., Doumpas, N. & Teleman, A. A. Regulation of TORC1 in response to amino acid starvation via lysosomal recruitment of TSC2. *Cell* 156, 786–799 (2014).
328. Menon, S. *et al.* Spatial control of the TSC complex integrates insulin and nutrient regulation of mTORC1 at the lysosome. *Cell* 156, 771–785 (2014).
329. Manning, B. D., Tee, A. R., Logsdon, M. N., Blenis, J. & Cantley, L. C. Identification of the tuberous sclerosis complex-2 tumor suppressor gene product tuberlin as a target of the phosphoinositide 3-kinase/Akt pathway. *Mol. Cell* 10, 151–162 (2002).
330. Garami, A. *et al.* Insulin activation of Rheb, a mediator of mTOR/S6K/4E-BP signaling, is inhibited by TSC1 and 2. *Mol. Cell* 11, 1457–1466 (2003).
331. Harrington, L. S. *et al.* The TSC1-2 tumor suppressor controls insulin-PI3K signaling via regulation of IRS proteins. *J. Cell Biol.* 166, 213–223 (2004).
332. Shan, O. *et al.* Inappropriate Activation of the TSC/Rheb/mTOR/S6K Cassette Induces IRS1/2 Depletion, Insulin Resistance, and Cell Survival Deficiencies. *Curr. Biol. B* 14, ARTMED1118 (2010).
333. Shaw, R. J. *et al.* The LKB1 tumor suppressor negatively regulates mTOR signaling. *Cancer Cell* 6, 91–99 (2004).
334. Gwinn, D. M. *et al.* AMPK phosphorylation of raptor mediates a metabolic checkpoint. *Mol. Cell* 30, 214–226 (2008).
335. Su, M.-Y. *et al.* Hybrid Structure of the RagA/C-Ragulator mTORC1 Activation Complex. *Mol Cell* 66, 693–698 (2017).
336. Bar-Peled, L., Schweitzer, L. D., Zoncu, R. & Sabatini, D. M. Ragulator is a GEF for the rag GTPases that signal amino acid levels to mTORC1. *Cell* 150, 1196–1208 (2012).
337. Rogala, K. *et al.* Structural basis for the docking of mTORC1 on the lysosomal surface. *Science (80-.)*. 176, 139–148 (2019).
338. Shen, K., Valenstein, M. L., Gu, X. & Sabatini, D. M. Arg-78 of Nprl2 catalyzes GATOR1-stimulated GTP hydrolysis by the Rag GTPases. *J. Biol. Chem.* 294, 2970–2975 (2019).
339. Wolfson, R. L. *et al.* KICSTOR recruits GATOR1 to the lysosome and is necessary for nutrients to regulate mTORC1. *Nature* 176, 139–148 (2017).
340. Bar-Peled, L. *et al.* A tumor suppressor complex with GAP activity for the Rag GTPases that signal amino acid sufficiency to mTORC1. *Science (80-.)*. 340, 1100–1106 (2013).
341. Petit, C. S., Rocznik-Ferguson, A. & Ferguson, S. M. Recruitment of folliculin to lysosomes supports the amino acid-dependent activation of rag gtpases. *J. Cell Biol.* 202, 1107–1122 (2013).
342. Tsun, Z. Y. *et al.* The Folliculin tumor suppressor is a GAP for RagC/D GTPases that signal amino acid levels to mTORC1. *Mol Cell* 52, 1–140 (2013).
343. Saxton, R. A. *et al.* Structural basis for leucine sensing by the Sestrin2-mTORC1 pathway. *Science (80-.)*. 351, 53–58 (2016).

344. Ye, J. *et al.* GCN2 sustains mTORC1 suppression upon amino acid deprivation by inducing Sestrin2. *Genes Dev.* 29, 2331–2336 (2015).
345. Saveljeva, S. *et al.* Endoplasmic reticulum stress-mediated induction of SESTRIN 2 potentiates cell survival. *Oncotarget* 7, 12254–12266 (2016).
346. Parmigiani, A. *et al.* Sestrins Inhibit mTORC1 Kinase Activation Through the GATOR Complex. *Cell Rep* 9, 1281–1291 (2014).
347. Chantranupong, L. *et al.* The Sestrins interact with GATOR2 to negatively regulate the amino acid sensing pathway upstream of mTORC1. *Cell Rep.* 23, 1–7 (2014).
348. Saxton, R. A., Chantranupong, L., Knockenhauer, K. E., Schwartz, T. U. & Sabatini, D. M. Mechanism of arginine sensing by CASTOR1 upstream of mTORC1. *Nature* 536, (2016).
349. Rebsamen, M. *et al.* SLC38A9 is a component of the lysosomal amino acid sensing machinery that controls mTORC1. *Nature* 519, 477–481 (2015).
350. Wyant, G. A. *et al.* mTORC1 Activator SLC38A9 Is Required to Efflux Essential Amino Acids from Lysosomes and Use Protein as a Nutrient. *Cell* 171, 642-654.e12 (2017).
351. Gu, X. *et al.* SAMTOR is an S-adenosylmethionine sensor for the mTORC1 pathway. *Science* (80-.). 358, 813–818 (2017).
352. Yuan, H.-X., *et al.* The Sin1 PH domain connects mTORC2 to PI3K Hai-Xin. *Cancer Discov.* 63, 1–18 (2015).
353. Gan, X. *et al.* Evidence for direct activation of mTORC2 kinase activity by phosphatidylinositol 3,4,5-trisphosphate. *J. Biol. Chem.* 286, 10998–11002 (2011).
354. Ebner, M. *et al.* Localization of mTORC2 activity inside cells. *J. Cell Biol.* 216, 343–353 (2017).
355. Kazyken, D. *et al.* AMPK directly activates mTORC2 to promote cell survival during acute energetic stress. *Sci Signal.* 12, 1–37 (2019).
356. Yu, L. *et al.* Autophagy termination and lysosome reformation regulated by mTOR. *Nature* 465, 942–946 (2010).
357. Kim. *et al.* AMPK and mTOR regulate autophagy through direct phosphorylation of Ulk1. *Genetics* 201, 1615 (2015).
358. Napolitano, G. *et al.* mTOR-dependent phosphorylation controls TFEB nuclear export. *Nat. Commun.* 9, (2018).
359. Martina, J. A. *et al.* TFEB and TFE3 are novel components of the integrated stress response. *EMBO J.* 35, 479–495 (2016).
360. Tan, H. W. S. *et al.* Glutamine metabolism regulates autophagy-dependent mTORC1 reactivation during amino acid starvation. *Nat. Commun.* 8, (2017).
361. Wyant, G. A. *et al.* Nufip1 is a ribosome receptor for starvation-induced ribophagy. *Science* (80-.). 360, 751–758 (2018).
362. Kraft, C. *et al.* Mature ribosomes are selectively degraded upon starvation by an autophagy pathway requiring the Ubp3p/Bre5p ubiquitin protease. *Nat. Cell Biol.* 10, 602–610 (2008).
363. Guo, J. Y. *et al.* Autophagy provides metabolic substrates to maintain energy charge and nucleotide pools in Ras-driven lung cancer cells. *Genes Dev.* 30, 1704–1717 (2016).
364. An, H. *et al.* Systematic Analysis of Ribophagy in Human Cells Reveals By-stander Flux During Selective Autophagy Heeseon. *Nat Cell Biol.* 176, 139–148 (2018).
365. Palacin, M. *et al.* The genetics of heteromeric amino acid transporters. *Physiology* 20, 112–124 (2005).
366. Wise, D. R. *et al.* Myc regulates a transcriptional program that stimulates mitochondrial glutaminolysis and leads to glutamine addiction. *Proc. Natl. Acad. Sci. U. S. A.* 105, 18782–18787 (2008).

367. Weng Siong Tan, H. *et al.* Glutamine metabolism regulates autophagy-dependent mTORC1 reactivation during amino acid starvation. (2016) doi:10.1038/s41467-017-00369-y.
368. Pavlova, N. N. *et al.* Translation in amino-acid-poor environments is limited by tRNAGln charging. *Elife* 9, 1–27 (2020).
369. Yuan, W. *et al.* General control nonderepressible 2 (GCN2) kinase inhibits target of rapamycin complex 1 in response to amino acid starvation in *Saccharomyces cerevisiae*. *J. Biol. Chem.* 292, 2660–2669 (2017).
370. Nikonorova, I. A. *et al.* Time-resolved analysis of amino acid stress identifies eIF2 phosphorylation as necessary to inhibit mTORC1 activity in liver. *J. Biol. Chem.* 293, 5005–5015 (2018).
371. Wengrod, J. *et al.* Phosphorylation of eIF2 α triggered by mTORC1 inhibition and PP6C activation is required for autophagy and is aberrant in PP6C-mutated melanoma. *Sci. Signal.* 8, 1–12 (2015).
372. Byun, J. K. *et al.* A Positive Feedback Loop between Sestrin2 and mTORC2 Is Required for the Survival of Glutamine-Depleted Lung Cancer Cells. *Cell Rep.* 20, 586–599 (2017).
373. Vasudevan, D. *et al.* The GCN2-ATF4 Signaling Pathway Induces 4E-BP to Bias Translation and Boost Antimicrobial Peptide Synthesis in Response to Bacterial Infection. *Cell Rep.* 21, 2039–2047 (2017).
374. Kuma, A. *et al.* The role of autophagy during the early neonatal starvation period. *Nature* 432, 1032–1036 (2004).
375. Peng, M. *et al.* Sestrins Function as Guanine Nucleotide Dissociation Inhibitors for Rag GTPases to Control mTORC1 Signaling. *Cell.* 23, 1–7 (2014).
376. Yuan, M. *et al.* Identification of Akt-independent regulation of hepatic lipogenesis by mammalian target of rapamycin (mTOR) complex 2. *J. Biol. Chem.* 287, 29579–29588 (2012).
377. Peterson, T. *et al.* mTOR complex 1 regulates lipin 1 localization to control the SREBP pathway. *Cell* 23, 1–7 (2011).
378. Hagiwara, A. *et al.* Hepatic mTORC2 activates glycolysis and lipogenesis through Akt, glucokinase, and SREBP1c. *Cell Metab.* 15, 725–738 (2012).
379. Cloëtta, D. *et al.* Inactivation of mTORC1 in the developing brain causes microcephaly and affects gliogenesis. *J. Neurosci.* 33, 7799–7810 (2013).
380. Thomanetz, V. *et al.* Ablation of the mTORC2 component rictor in brain or Purkinje cells affects size and neuron morphology. *J. Cell Biol.* 201, 293–308 (2013).
381. Curatolo, P. *et al.* Tuberous sclerosis. *Lancet* 372, 657–668 (2008).
382. Takei, N. *et al.* Brain-derived neurotrophic factor induces mammalian target of rapamycin-dependent local activation of translation machinery and protein synthesis in neuronal dendrites. *J. Neurosci.* 24, 9760–9769 (2004).
383. Lamming, D. W., Ye, L., Sabatini, D. M. & Baur, J. A. Rapalogs and mTOR inhibitors as anti-aging therapeutics. *J. Clin. Invest.* 123, 980–989 (2013).
384. Bitto, A. *et al.* Transient rapamycin treatment can increase lifespan and healthspan in middle-aged mice. *Elife* 5, 1–17 (2016).
385. Herranz, N. *et al.* mTOR regulates MAPKAPK2 translation to control the senescence-associated secretory phenotype. *Nat. Cell Biol.* 17, 1205–1217 (2015).
386. Laberge, R. *et al.* mTOR regulates the pro-tumorigenic senescence-associated secretory phenotype by promoting IL1A translation. *Nat Cell Biol.* 17, 1049–1061 (2015).
387. Menon, S. *et al.* Common corruption of the mTOR signaling network in human tumors. *Oncogene* 23, 1–7 (2008).
388. Napoli, K. L. & Taylor, P. J. From beach to bedside: History of the development of sirolimus. *Ther. Drug*

- Monit.* 23, 559–586 (2001).
389. Guertin, D. A. & Sabatini, D. M. The pharmacology of mTOR inhibition. *Sci. Signal.* 2, 1–7 (2009).
390. Thoreen, C. C. *et al.* An ATP-competitive mammalian target of rapamycin inhibitor reveals rapamycin-resistant functions of mTORC1. *J. Biol. Chem.* 284, 8023–8032 (2009).
391. García-Martínez, J. M. *et al.* Ku-0063794 is a specific inhibitor of the mammalian target of rapamycin (mTOR). *Biochem. J.* 421, 29–42 (2009).
392. Feldman, M. E. *et al.* Active-site inhibitors of mTOR target rapamycin-resistant outputs of mTORC1 and mTORC2. *PLoS Biol.* 7, 0371–0383 (2009).
393. Hietakangas, V. & Cohen, S. M. Re-evaluating AKT regulation: Role of TOR complex 2 in tissue growth. *Genes Dev.* 21, 632–637 (2007).
394. Hayakawa, M. *et al.* Synthesis and biological evaluation of pyrido[3',2':4,5]furo[3,2-d]pyrimidine derivatives as novel PI3 kinase p110 α inhibitors. *Bioorganic Med. Chem. Lett.* 17, 2438–2442 (2007).
395. Voss, M. H. *et al.* Phase 1 study of mTORC1/2 inhibitor sapanisertib (TAK-228) in advanced solid tumours, with an expansion phase in renal, endometrial or bladder cancer. *Br. J. Cancer* 123, 1590–1598 (2020).
396. Hsieh, A. C. *et al.* The translational landscape of mTOR signalling steers cancer initiation and metastasis. *Nature* 485, 55–61 (2012).
397. Testing of the Anti Cancer Drugs CB-839 HCl (Telaglenastat) and MLN0128 (Sapanisertib) in Advanced Stage Non-small Cell Lung Cancer. <https://clinicaltrials.gov/ct2/show/NCT04250545> (2020).
398. Pinelli, D. *et al.* Rapamycin ameliorates the CTLA4-Ig-mediated defect in CD8+ T cell immunity during gammaherpesvirus infection. *Am J Transplant.* 17, 139–148 (2015).
399. Fernando, M., Peake, P. W. & Endre, Z. H. Biomarkers of calcineurin inhibitor nephrotoxicity in transplantation. *Biomark. Med.* 8, 1247–1262 (2014).
400. Zhang, L. *et al.* Mammalian Target of Rapamycin Complex 1 Orchestrates Invariant NKT Cell Differentiation and Effector Function. *J. Immunol.* 193, 1759–1765 (2014).
401. Shiao, S. L. *et al.* Human Effector Memory CD4 + T Cells Directly Recognize Allogeneic Endothelial Cells In Vitro and In Vivo. *J. Immunol.* 179, 4397–4404 (2007).
402. Canaud, G. *et al.* Inhibition of the mTORC Pathway in the Antiphospholipid Syndrome. *N. Engl. J. Med.* 371, 303–312 (2014).
403. Kim, K. W. *et al.* The effect of mammalian target of rapamycin inhibition on T helper type 17 and regulatory T cell differentiation in vitro and in vivo in kidney transplant recipients. *Immunology* 144, 68–78 (2015).
404. Bestard, O. *et al.* Costimulatory blockade with mTor inhibition abrogates effector T-cell responses allowing regulatory T-cell survival in renal transplantation. *Transpl. Int.* 24, 451–460 (2011).
405. Sadler, T. M. *et al.* Combination therapy for treating breast cancer using antiestrogen, ERA-923, and the mammalian target of rapamycin inhibitor, temsirolimus. *Endocr. Relat. Cancer* 13, 863–873 (2006).
406. Mondesire, W. H. *et al.* Targeting mammalian target of rapamycin synergistically enhances chemotherapy-induced cytotoxicity in breast cancer cells. *Clin. Cancer Res.* 10, 7031–7042 (2004).
407. Meric-Bernstam, F. & Gonzalez-Angulo, A. M. Targeting the mTOR signaling network for cancer therapy. *J. Clin. Oncol.* 27, 2278–2287 (2009).
408. Rodrik-Outmezguine, V. S. *et al.* mTOR kinase inhibition causes feedback-dependent biphasic regulation of AKT signaling. *Cancer Discov.* 1, 248–259 (2011).
409. Rodrik-Outmezguine, V. S. *et al.* Overcoming mTOR Resistance Mutations with a New Generation mTOR Inhibitor. *Nature* 176, 139–148 (2018).
410. Fan, Q. W. *et al.* A Kinase Inhibitor Targeted to mTORC1 Drives Regression in Glioblastoma. *Cancer Cell* 31,

- 424–435 (2017).
411. Waldner, M. *et al.* New perspectives on mTOR inhibitors (rapamycin, rapalogs and TORKinibs) in transplantation. *Br. J. Clin. Pharmacol.* 1158–1170 (2016) doi:10.1111/bcp.12893.
412. Shi, Z. *et al.* Activation of the PERK-ATF4 pathway promotes chemo-resistance in colon cancer cells. *Sci. Rep.* 9, 1–8 (2019).
413. Hinnebusch, A. G. Evidence for translational regulation of the activator of general amino acid control in yeast. *Proc. Natl. Acad. Sci. U. S. A.* 81, 6442–6446 (1984).
414. Zeitler, L. *et al.* Anti-ferroptotic mechanism of il4i1-mediated amino acid metabolism. *Elife* 10, 1–22 (2021).
415. Zhuang, L. *et al.* Pure populations of murine macrophages from cultured embryonic stem cells. Application to studies of chemotaxis and apoptotic cell clearance | Elsevier Enhanced Reader. *Journal of Immunological Methods* (2012).
416. Scheuner, D. *et al.* Translational control is required for the unfolded protein response and in vivo glucose homeostasis. *Mol. Cell* 7, 1165–1176 (2001).
417. Yusa, K. *et al.* A hyperactive piggyBac transposase for mammalian applications. *Proc. Natl. Acad. Sci. U. S. A.* 108, 1531–1536 (2011).
418. Li, Z. *et al.* Simple piggyBac transposon-based mammalian cell expression system for inducible protein production. *Proc. Natl. Acad. Sci. U. S. A.* 110, 5004–5009 (2013).
419. Bustin, S. A. *et al.* Quantification of mRNA using real-time reverse transcription PCR (RT-PCR): Trends and problems. *J. Mol. Endocrinol.* 29, 23–39 (2002).
420. Dobin, A. *et al.* STAR: Ultrafast universal RNA-seq aligner. *Bioinformatics* 29, 15–21 (2013).
421. Liao, Y. *et al.* FeatureCounts: An efficient general purpose program for assigning sequence reads to genomic features. *Bioinformatics* 30, 923–930 (2014).
422. CoreTeam, R. *R: A Language and Environment for Statistical Computing.* vol. 2 (2017).
423. Nadler, S. G. *et al.* Differential expression and sequence-specific interaction of karyopherin α with nuclear localization sequences. *J. Biol. Chem.* 272, 4310–4315 (1997).
424. Tyanova, S. *et al.* The Perseus computational platform for comprehensive analysis of (prote)omics data. *Nat. Methods* 13, 731–740 (2016).
425. Humphrey, S. J., Azimifar, S. B. & Mann, M. High-throughput phosphoproteomics reveals in vivo insulin signaling dynamics. *Nat. Biotechnol.* 33, 990–995 (2015).
426. Humphrey, S. J., Karayel, O., James, D. E. & Mann, M. High-throughput and high-sensitivity phosphoproteomics with the EasyPhos platform. *Nat. Protoc.* 13, 1897–1916 (2018).
427. Cox, J. & Mann, M. MaxQuant enables high peptide identification rates, individualized p.p.b.-range mass accuracies and proteome-wide protein quantification. *Nat. Biotechnol.* 26, 1367–1372 (2008).
428. Bruderer, A. G., Kyle Danielson, D., Kandhadai, P. & Werker, J. F. Sensorimotor influences on speech perception in infancy. *Proc. Natl. Acad. Sci. U. S. A.* 112, 13531–13536 (2015).
429. Bekker-Jensen, D. B. *et al.* Rapid and site-specific deep phosphoproteome profiling by data-independent acquisition without the need for spectral libraries. *Nat. Commun.* 11, 1–12 (2020).
430. Mehravar, M., Shirazi, A., Mehrazar, M. M., Nazari, M. & Banan, M. CRISPR/Cas9 System for Efficient Genome Editing and Targeting in the Mouse NIH/3T3 Cells. *Avicenna J. Med. Biotechnol.* 11, 149–155 (2019).
431. Hartman, M. E. *et al.* An optimized and simplified system of mouse embryonic stem cell cardiac differentiation for the assessment of differentiation modifiers. *PLoS One* 9, (2014).
432. Belov, A. A. & Mohammadi, M. Grb2, a double-edged sword of receptor tyrosine kinase signaling. *Sci. Signal.*

- 5, 1–7 (2012).
433. Wiśniewski, J. R., Hein, M. Y., Cox, J. & Mann, M. A 'proteomic ruler' for protein copy number and concentration estimation without spike-in standards. *Mol. Cell. Proteomics* 13, 3497–3506 (2014).
 434. Knott, G. J. & Doudna, J. A. CRISPR-Cas guides the future of genetic engineering. *Science (80-.)*. 361, 866–869 (2018).
 435. England, C. *et al.* NanoLuc: A Small Luciferase is Brightening up the Field of Bioluminescence. *Bioconjug Chem.* 176, 139–148 (2016).
 436. Berry, S. L. *et al.* Development of NanoLuc-PEST expressing *Leishmania mexicana* as a new drug discovery tool for axenic- and intramacrophage-based assays. *PLoS Negl. Trop. Dis.* 12, 1–20 (2018).
 437. Protter, D. S. W. & Parker, R. Principles and Properties of Stress Granules. *Trends Cell Biol.* 26, 668–679 (2016).
 438. Stark, R., Grzelak, M. & Hadfield, J. RNA sequencing: the teenage years. *Nat. Rev. Genet.* 20, 631–656 (2019).
 439. Dey, S. *et al.* Both transcriptional regulation and translational control of ATF4 are central to the integrated stress response. *J. Biol. Chem.* 285, 33165–33174 (2010).
 440. Nakazawa, M. *et al.* Oxygen Availability and Metabolic Adaptations. *Nat Rev Cancer* 176, 139–148 (2016).
 441. Koyanagi, M. *et al.* Ablation of TSC2 enhances insulin secretion by increasing the number of mitochondria through activation of mTORC1. *PLoS One* 6, (2011).
 442. Ducker, G. *et al.* One-Carbon Metabolism in Health and Disease Gregory. *Cell Metab.* 29, 1–10 (2017).
 443. Locasale, J. W. *et al.* Serine, Glycine and the one-carbon cycle. *Nat. Rev Cancer* 13, 572–583 (2013).
 444. Reich, S. *et al.* A multi-omics analysis reveals the unfolded protein response regulon and stress-induced resistance to folate-based antimetabolites. *Nat. Commun.* 11, 1–15 (2020).
 445. Di Marcantonio, D. *et al.* ATF3 Coordinates Serine and Nucleotide Metabolism to Drive Cell Cycle Progression in Acute Myeloid Leukemia. *Mol Cell.* 1–13 (2021) doi:10.2139/ssrn.3832368.
 446. Pyronnet, S. *et al.* Human eukaryotic translation initiation factor 4G (eIF4G) recruits Mnk1 to phosphorylate eIF4E. *EMBO J.* 18, 270–279 (1999).
 447. Méndez-Lucas, A. *et al.* Mitochondrial phosphoenolpyruvate carboxykinase (PEPCK-M) is a pro-survival, endoplasmic reticulum (ER) stress response gene involved in tumor cell adaptation to nutrient availability. *J. Biol. Chem.* 289, 22090–22102 (2014).
 448. Thomas, G. V. *et al.* Hypoxia-inducible factor determines sensitivity to inhibitors of mTOR in kidney cancer. *Nat. Med.* 12, 122–127 (2006).
 449. Laughner, E. *et al.* HER2 (neu) signaling increases the rate of synthesis : Novel mechanism for HIF-1-mediated vascular endothelial growth factor expression. *Am. Soc. Microbiol.* 21, 3995–4004 (2001).
 450. Hudson, C. C. *et al.* Regulation of Hypoxia-Inducible Factor 1 α Expression and Function by the Mammalian Target of Rapamycin. *Mol. Cell. Biol.* 22, 7004–7014 (2002).
 451. Brugarolas, J. B. *et al.* TSC2 regulates VEGF through mTOR-dependent and -independent pathways. *Cancer Cell* 4, 147–158 (2003).
 452. Zhong, H. *et al.* Modulation of hypoxia-inducible factor 1 α expression by the epidermal growth factor/phosphatidylinositol 3-kinase/PTEN/AKT/FRAP pathway in human prostate cancer cells: Implications for tumor angiogenesis and therapeutics. *Cancer Res.* 60, 1541–1545 (2000).
 453. Martire, S. & Banaszynski, L. A. The roles of histone variants in fine-tuning chromatin organization and function. *Nat. Rev. Mol. Cell Biol.* 21, 522–541 (2020).
 454. Clementi, E. *et al.* Persistent DNA damage triggers activation of the integrated stress response to promote

- cell survival under nutrient restriction. *BMC Biol.* 18, 1–15 (2020).
455. Choo, J. A. M. Y., Schlösser, D., Manzini, V., Magerhans, A. & Dobbstein, M. The integrated stress response induces R-loops and hinders replication fork progression. *Cell Death Dis.* 11, (2020).
456. Klann, K. & Münch, C. Unbiased translation proteomics upon cell stress. *Mol. Cell. Oncol.* 7, (2020).
457. Chen, K. *et al.* The Overlooked Fact: Fundamental Need for Spike-In Control for Virtually All Genome-Wide Analyses. *Mol. Cell. Biol.* 36, 662–667 (2016).
458. Bagert, J. D. *et al.* Quantitative, time-resolved proteomic analysis by combining bioorthogonal noncanonical amino acid tagging and pulsed stable isotope labeling by amino acids in cell culture. *Mol. Cell. Proteomics* 13, 1352–1358 (2014).
459. Tanzer, M. *et al.* Phosphoproteome profiling uncovers a key role for CDKs in TNF signaling. *bioRxiv Prepr.* 1–13 (2020).
460. Hansen, F. M. *et al.* Data-independent acquisition method for ubiquitinome analysis reveals regulation of circadian biology. *Nat. Commun.* 12, (2021).
461. Cohen, A. & Hall, M. N. An Amino Acid Shuffle Activates mTORC1. *Cell* 136, 399–400 (2009).
462. Grasmann, G. *et al.* PCK2 opposes mitochondrial respiration and maintains the redox balance in starved lung cancer cells. *bioRxiv* (2020).
463. Leithner, K. *et al.* PCK2 activation mediates an adaptive response to glucose depletion in lung cancer. *Oncogene* 1044–1050 (2015) doi:10.1038/onc.2014.47.
464. Gu, Y. *et al.* mTORC2 regulates amino acid metabolism in cancer by phosphorylation of the cystine-glutamate antiporter xCT. *Mol. Cell.* 176, 139–148 (2017).
465. Pullen, N. & Thomas, G. The modular phosphorylation and activation of p70(s6k). *FEBS Lett.* 410, 78–82 (1997).
466. Han, J. W. *et al.* Rapamycin, wortmannin, and the methylxanthine SQ20006 inactivate p70s6k by inducing dephosphorylation of the same subset of sites. *J. Biol. Chem.* 270, 21396–21403 (1995).
467. Dufner, A. & Thomas, G. Ribosomal S6 kinase signaling and the control of translation. *Exp. Cell Res.* 109, 100–109 (1999).
468. Cox, J. & Mann, M. Quantitative, high-resolution proteomics for data-driven systems biology. *Annu. Rev. Biochem.* 80, 273–299 (2011).
469. Keilhauer, E. C., Hein, M. Y. & Mann, M. Accurate protein complex retrieval by affinity enrichment mass spectrometry (AE-MS) rather than affinity purification mass spectrometry (AP-MS). *Mol. Cell. Proteomics* 14, 120–135 (2015).
470. Hopfner, K. P. *et al.* The Rad50 zinc-hook is a structure joining Mre11 complexes in DNA recombination and repair. *Nature* 418, 562–566 (2002).
471. Lamarche, B. J., Orazio, N. I. & Weitzman, M. D. The MRN complex in double-strand break repair and telomere maintenance. *FEBS Lett.* 584, 3682–3695 (2010).
472. Drané, P. *et al.* TIRR regulates 53BP1 by masking its histone methyl-lysine binding function. *Nature* 543, 211–216 (2017).
473. Eliezer, Y. *et al.* Interplay between the DNA damage proteins MDC1 and ATM in the regulation of the spindle assembly checkpoint. *J. Biol. Chem.* 289, 8182–8193 (2014).
474. Loscalzo, D. *et al.* USP10 Regulates p53 Localization and Stability by Deubiquitinating p53. *Cell* 23, 1–7 (2010).
475. Hein, M. Y. *et al.* A Human Interactome in Three Quantitative Dimensions Organized by Stoichiometries and Abundances. *Cell* 163, 712–723 (2015).

476. Chen, X. *et al.* Cellular degradation systems in ferroptosis. *Cell Death and Differentiation* (2021) doi:10.1038/s41418-020-00728-1.
477. Thul, P. J. & Lindskog, C. The human protein atlas: A spatial map of the human proteome. *Protein Sci.* 27, 233–244 (2018).
478. Van Vliet, A. R. *et al.* The ER Stress Sensor PERK Coordinates ER-Plasma Membrane Contact Site Formation through Interaction with Filamin-A and F-Actin Remodeling. *Mol. Cell* 65, 885-899.e6 (2017).
479. Buchan, J. R. & Parker, R. Eukaryotic Stress Granules : The Ins and Out of Translation. *Mol. Cell* 36, 932 (2009).
480. Yang, W. S. *et al.* Regulation of ferroptotic cancer cell death by GPX4. *Cell* 156, 317–331 (2014).
481. Koppula, P., Zhuang, L. & Gan, B. Cystine transporter SLC7A11/xCT in cancer: ferroptosis, nutrient dependency, and cancer therapy. *Protein Cell* (2020) doi:10.1007/s13238-020-00789-5.
482. Mou, Y. *et al.* Ferroptosis, a new form of cell death: Opportunities and challenges in cancer. *J. Hematol. Oncol.* 12, 1–16 (2019).
483. Song, X. & Long, D. Nrf2 and Ferroptosis: A New Research Direction for Neurodegenerative Diseases. *Front. Neurosci.* 14, 1–15 (2020).
484. Sun, X. *et al.* Activation of the p62-Keap1-NRF2 pathway protects against ferroptosis in hepatocellular carcinoma cells. *Hepatology* 63, 173–184 (2016).
485. Poltorack, C. D. & Dixon, S. J. Understanding the Role of Cysteine in Ferroptosis: Progress & Paradoxes. *FEBS J.* (2021) doi:10.1111/febs.15842.
486. Wang, W. *et al.* CD8+ T cells regulate tumour ferroptosis during cancer immunotherapy. *Nature* 569, 270–274 (2019).
487. Zhang, Y. *et al.* mTORC1 couples cyst(e)ine availability with GPX4 protein synthesis and ferroptosis regulation. (2021) doi:10.1038/s41467-021-21841-w.
488. Gao, M. *et al.* Role of Mitochondria in Ferroptosis. *Mol. Cell* 73, 354-363.e3 (2019).
489. Yang, W. S. & Stockwell, B. R. Ferroptosis: Death by Lipid Peroxidation. *Trends Cell Biol.* 26, 165–176 (2016).
490. Dixon, S. J. *et al.* Ferroptosis: An iron-dependent form of nonapoptotic cell death. *Cell* 149, 1060–1072 (2012).
491. Tang, D., Chen, X., Kang, R. & Kroemer, G. Ferroptosis: molecular mechanisms and health implications. *Cell Research* vol. 31 107–125 (2021).
492. Zheng, J. & Conrad, M. The Metabolic Underpinnings of Ferroptosis. *Cell Metabolism* vol. 32 920–937 (2020).
493. Dixon, S. J. *et al.* Pharmacological inhibition of cystine-glutamate exchange induces endoplasmic reticulum stress and ferroptosis. *Elife* 2014, 1–25 (2014).
494. Pedro, J. *et al.* Renal Failure in Mice. *Nat Cell Biol.* 16, 1180–1191 (2016).
495. Shintoku, R. *et al.* Lipoxygenase-mediated generation of lipid peroxides enhances ferroptosis induced by erastin and RSL3. *Cancer Sci.* 108, 2187–2194 (2017).
496. Skouta, R. *et al.* Ferrostatins inhibit oxidative lipid damage and cell death in diverse disease models. *J. Am. Chem. Soc.* 136, 4551–4556 (2014).
497. Anthonymuthu, T. S. *et al.* Resolving the paradox of ferroptotic cell death: Ferrostatin-1 binds to 15LOX/PEBP1 complex, suppresses generation of peroxidized ETE-PE, and protects against ferroptosis. *Redox Biol.* 38, 101744 (2021).
498. Griffith, O. W. & Meister, A. Potent and specific inhibition of glutathione synthesis by buthionine sulfoximine

- (S-n-butyl homocysteine sulfoximine). *J. Biol. Chem.* 254, 7558–7560 (1979).
499. Parks, S. K., Mueller-Klieser, W. & Pouyssegur, J. Lactate and Acidity in the Cancer Microenvironment. *Annu. Rev. Cancer Biol.* 4, 141–158 (2020).
500. Kelly, B. & O'Neill, L. A. J. Metabolic reprogramming in macrophages and dendritic cells in innate immunity. *Cell Res.* 25, 771–784 (2015).
501. Gu, X., Ma, Y., Liu, Y. & Wan, Q. Measurement of mitochondrial respiration in adherent cells by Seahorse XF96 Cell Mito Stress Test. *STAR Protoc.* 2, 100245 (2021).
502. Murray, P. J. Macrophage Polarization. *Annu. Rev. Physiol.* 79, 541–566 (2017).
503. Liu, P. S. *et al.* A-Ketoglutarate Orchestrates Macrophage Activation Through Metabolic and Epigenetic Reprogramming. *Nat. Immunol.* 18, 985–994 (2017).
504. Jha, A. K. *et al.* Network integration of parallel metabolic and transcriptional data reveals metabolic modules that regulate macrophage polarization. *Immunity* 42, 419–430 (2015).
505. Deng, J. *et al.* Activation of *gcn2* in uv-irradiated cells inhibits translation. *Curr. Biol.* 12, 1279–1286 (2002).
506. Jiang, H. Y. & Wek, R. C. Phosphorylation of the α -subunit of the eukaryotic initiation factor-2 (eIF2 α) reduces protein synthesis and enhances apoptosis in response to proteasome inhibition. *J. Biol. Chem.* 280, 14189–14202 (2005).
507. Zyryanova, A. F. *et al.* Binding of ISRIB reveals a regulatory site in the nucleotide exchange factor eIF2B. *Science* (80-.). (2018).
508. Zyryanova, A. F. *et al.* ISRIB Blunts the Integrated Stress Response by Allosterically Antagonising the Inhibitory Effect of Phosphorylated eIF2 on eIF2B. *Mol. Cell* 1–16 (2020) doi:10.1016/j.molcel.2020.10.031.
509. Dever, T. E. *et al.* Phosphorylation of Initiation Factor 2 α by Protein Kinase GCN2 Mediates Gene-Specific Translational Control of GCN4 in Yeast. 66, (1992).
510. Aviner, R. *et al.* The science of puromycin: From studies of ribosome function to applications in biotechnology. *Comput. Struct. Biotechnol. J.* 18, 1074–1083 (2020).
511. Giuliano, C. J., Lin, A., Girish, V. & Sheltzer, J. M. Generating Single Cell-Derived Knockout Clones in Mammalian Cells with CRISPR/Cas9. *Curr. Protoc. Mol. Biol.* 128, 1–25 (2019).
512. Ye, M., Wilhelm, M., Gentschev, I. & Szalay, A. A modified limiting dilution method for monoclonal stable cell line selection using a real-time fluorescence imaging system: A practical workflow and advanced applications. *Methods Protoc.* 4, 1–14 (2021).
513. Cohen, P. *et al.* Protein kinases - The major drug targets of the twenty-first century? *Nat. Rev. Drug Discov.* 1, 309–315 (2002).
514. Bhullar, K. S. *et al.* Kinase-targeted cancer therapies: Progress, challenges and future directions. *Mol. Cancer* 17, 1–20 (2018).
515. Helliwell, S. B. *et al.* TOR1 and TOR2 are structurally and functionally similar but not identical phosphatidylinositol kinase homologues in yeast. *Mol. Biol. Cell* 5, 105–118 (1994).
516. Brown, E. J. *et al.* A mammalian protein targeted by G1-arresting rapamycin-receptor complex. *Nature* 369, 756–758 (1994).
517. Chiu, M. I. *et al.* RAPT1, a mammalian homolog of yeast Tor, interacts with the FKBP12/rapamycin complex. *Proc. Natl. Acad. Sci. U. S. A.* 91, 12574–12578 (1994).
518. Schmelzle, T. *et al.* TOR, a central controller of cell growth. *Cell* 103, 253–262 (2000).
519. Hartley, K. O. *et al.* DNA-dependent protein kinase catalytic subunit: A relative of phosphatidylinositol 3-kinase and the ataxia telangiectasia gene product. *Cell* 82, 849–856 (1995).
520. Savitsky, K. *et al.* A single ataxia telangiectasia gene with a product similar to PI-3 kinase. *Science* (80-.).

- 268, 1749–1753 (1995).
521. Zhang, N. *et al.* Isolation of full-length ATM cDNA and correction of the ataxia-telangiectasia cellular phenotype. *Proc. Natl. Acad. Sci. U. S. A.* 94, 8021–8026 (1997).
522. Yap, T. A. *et al.* First-in-Human Trial of the Oral Ataxia Telangiectasia and RAD3-Related (ATR) Inhibitor BAY 1895344 in Patients with Advanced Solid Tumors. *Cancer Discov.* (2020) doi:10.1158/2159-8290.cd-20-0868.
523. Thomas, A. *et al.* Therapeutic targeting of ATR yields durable regressions in small cell lung cancers with high replication stress. *Cancer Cell* 39, 566-579.e7 (2021).
524. Liu, Q. *et al.* mTOR Mediated Anti-Cancer Drug Discovery. *Drug Discov* 23, 1–7 (2008).
525. Lücking, U. *et al.* Damage Incorporated: Discovery of the Potent, Highly Selective, Orally Available ATR Inhibitor BAY 1895344 with Favorable Pharmacokinetic Properties and Promising Efficacy in Monotherapy and in Combination Treatments in Preclinical Tumor Models. *J. Med. Chem.* 63, 7293–7325 (2020).
526. Knight, S. D. *et al.* Discovery of GSK2126458, a highly potent inhibitor of PI3K and the mammalian target of rapamycin. *ACS Med. Chem. Lett.* 1, 39–43 (2010).
527. Toledo, L. I. *et al.* A cell-based screen identifies ATR inhibitors with synthetic lethal properties for cancer-associated mutations. *Nat Struct Mol Biol.* 18, 721–727 (2011).
528. Liu, Q. *et al.* Discovery of 9-(6-aminopyridin-3-yl)-1-(3-(trifluoromethyl)phenyl)benzo[h][1,6]naphthyridin-2(1H)-one (Torin2) as a potent, selective and orally available mTOR inhibitor for treatment of cancer. *J Med Chem.* 54, 1473–1480 (2011).
529. Edwards, S. R. and T. J. W. The Rapamycin-Binding Domain of the Protein Kinase mTOR is a Destabilizing Domain*. *Biol. Chem.* 282, 13395–13401 (2013).
530. Sun, S.-Y. mTOR kinase inhibitors as potential cancer therapeutic drugs. *Cancer Lett.* 23, 1–7 (2013).
531. Liu, Q. *et al.* Kinome-wide selectivity profiling of ATP-competitive mammalian target of rapamycin (mTOR) inhibitors and characterization of their binding kinetics. *J. Biol. Chem.* 287, 9742–9752 (2012).
532. Sarbassov, D. D., Guertin, D. A., Ali, S. M. & Sabatini, D. M. Phosphorylation and regulation of Akt/PKB by the rictor-mTOR complex. *Science* (80-.). 307, 1098–1101 (2005).
533. Benavides-Serrato, A. *et al.* Correction: Specific blockade of Rictor-mTOR association inhibits mTORC2 activity and is cytotoxic in glioblastoma (PLoS One (2017) 12:4 (e0176599) DOI: 10.1371/journal.pone.0176599). *PLoS One* 14, 4–7 (2019).
534. Guo, Y. *et al.* CC-223, NSC781406, and BGT226 Exerts a Cytotoxic Effect Against Pancreatic Cancer Cells via mTOR Signaling. *Front. Pharmacol.* 11, (2020).
535. Wang, X. *et al.* Distinct Signaling Events Downstream of mTOR Cooperate To Mediate the Effects of Amino Acids and Insulin on Initiation Factor 4E-Binding Proteins. *Mol. Cell. Biol.* 25, 2558–2572 (2005).
536. Hardie, D. G. *et al.* The AMP-activated protein kinase pathway - New players upstream and downstream. *J. Cell Sci.* 117, 5479–5487 (2004).
537. Carling, D. *et al.* The AMP-activated protein kinase cascade - A unifying system for energy control. *Trends Biochem. Sci.* 29, 18–24 (2004).
538. Hawley, S. A. *et al.* Characterization of the AMP-activated protein kinase kinase from rat liver and identification of threonine 172 as the major site at which it phosphorylates AMP-activated protein kinase. *J. Biol. Chem.* 271, 27879–27887 (1996).
539. Condon, K. J. *et al.* Genome-wide CRISPR screens reveal multitiered mechanisms through which mTORC1 senses mitochondrial dysfunction. *Proc. Natl. Acad. Sci. U. S. A.* 118, (2021).
540. Kaspar, S. *et al.* Adaptation to mitochondrial stress requires CHOP-directed tuning of ISR. *Sci. Adv.* (2021).

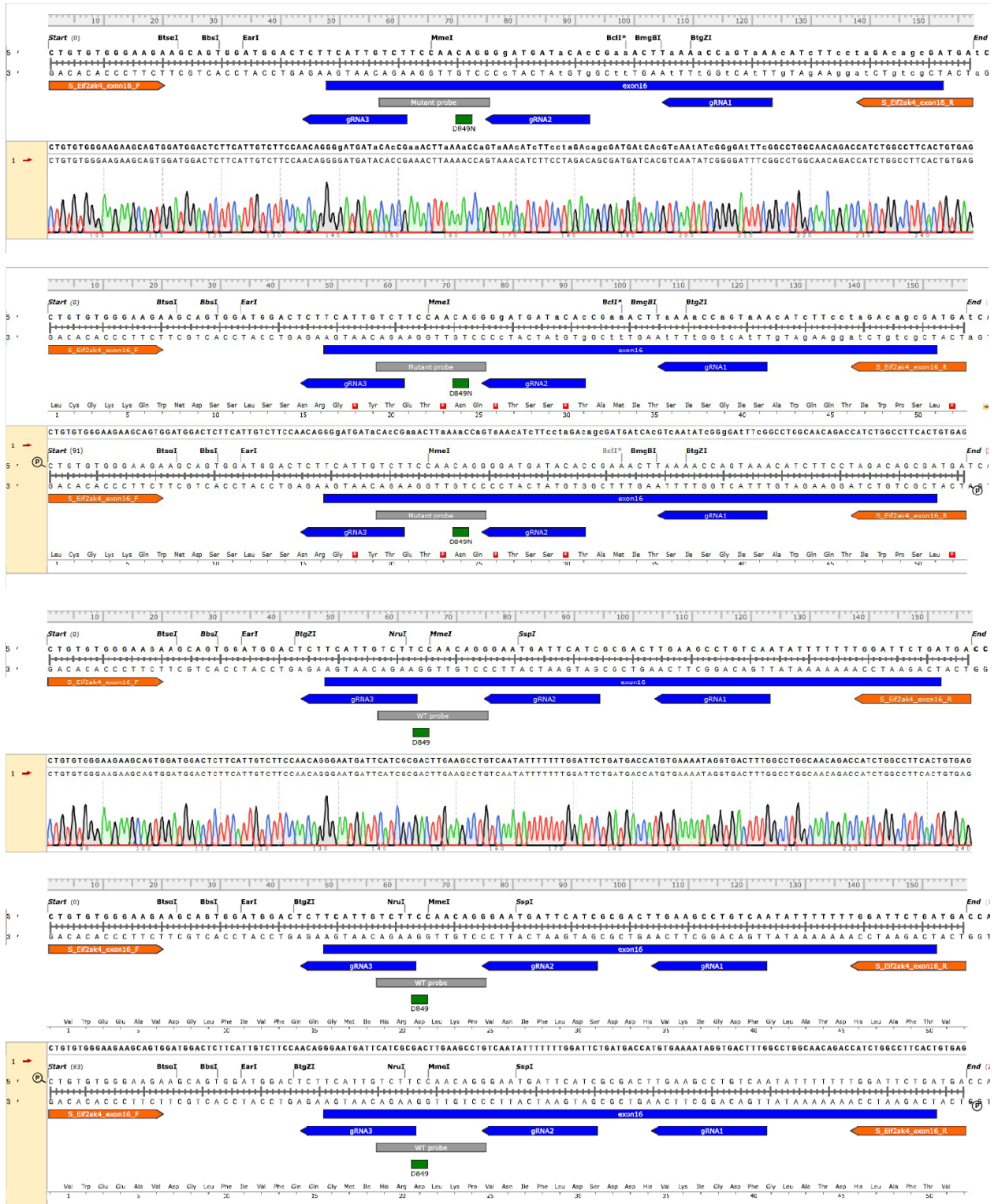
541. Yang, X. *et al.* ATF4 Regulates CD4+T Cell Immune Responses through Metabolic Reprogramming. *Cell Rep.* 23, 1754–1766 (2018).
542. Garcia-Barrio, M. *et al.* Association of GCN1-GCN20 regulatory complex with the N-terminus of eIF2alpha kinase GCN2 is required for GCN2 activation. *EMBO J.* 19, 1887–1899 (2000).
543. Martínez-Reyes, I. *et al.* AMPK and GCN2-ATF4 signal the repression of mitochondria in colon cancer cells. *Biochem. J.* 444, 249–259 (2012).
544. Wan, L. *et al.* Translation stress and collided ribosomes are co-activators of cGAS. *Mol. Cell* 1–15 (2021) doi:10.1016/j.molcel.2021.05.018.
545. Anthony, T. G. *et al.* Preservation of Liver Protein Synthesis during Dietary Leucine Deprivation Occurs at the Expense of Skeletal Muscle Mass in Mice Deleted for eIF2 Kinase GCN2*. *J. Biol. Chem.* 279, 36553–36561 (2004).
546. Wilson, G. J. *et al.* The eukaryotic initiation factor 2 kinase GCN2 protects against hepatotoxicity during asparaginase treatment. *Am. J. Physiol. - Endocrinol. Metab.* 305, (2013).
547. Henske, E. P. *et al.* Tuberous sclerosis complex. *Nat. Rev. Dis. Prim.* 2, (2016).
548. Mordant, P. *et al.* Dependence on phosphoinositide 3-kinase and RAS-RAF pathways drive the activity of RAF265, a novel RAF/VEGFR2 inhibitor, and RAD001 (everolimus) in combination. *Mol. Cancer Ther.* 9, 358–368 (2010).
549. Asati, V. *et al.* PI3K/Akt/mTOR and Ras/Raf/MEK/ERK signaling pathways inhibitors as anticancer agents: Structural and pharmacological perspectives. *Eur. J. Med. Chem.* 109, 314–341 (2016).
550. Graff, J. R. *et al.* Translational control and metastatic progression: Enhanced activity of the mRNA cap-binding protein eIF-4E selectively enhances translation of metastasis-related mRNAs. *Clinical & Experimental Metastasis* vol. 20 (2003).

Sequence alignment (mutation indicated by red box) of wild-type and *Gcn1^{-/-}* in 3T3 (lentiviral)

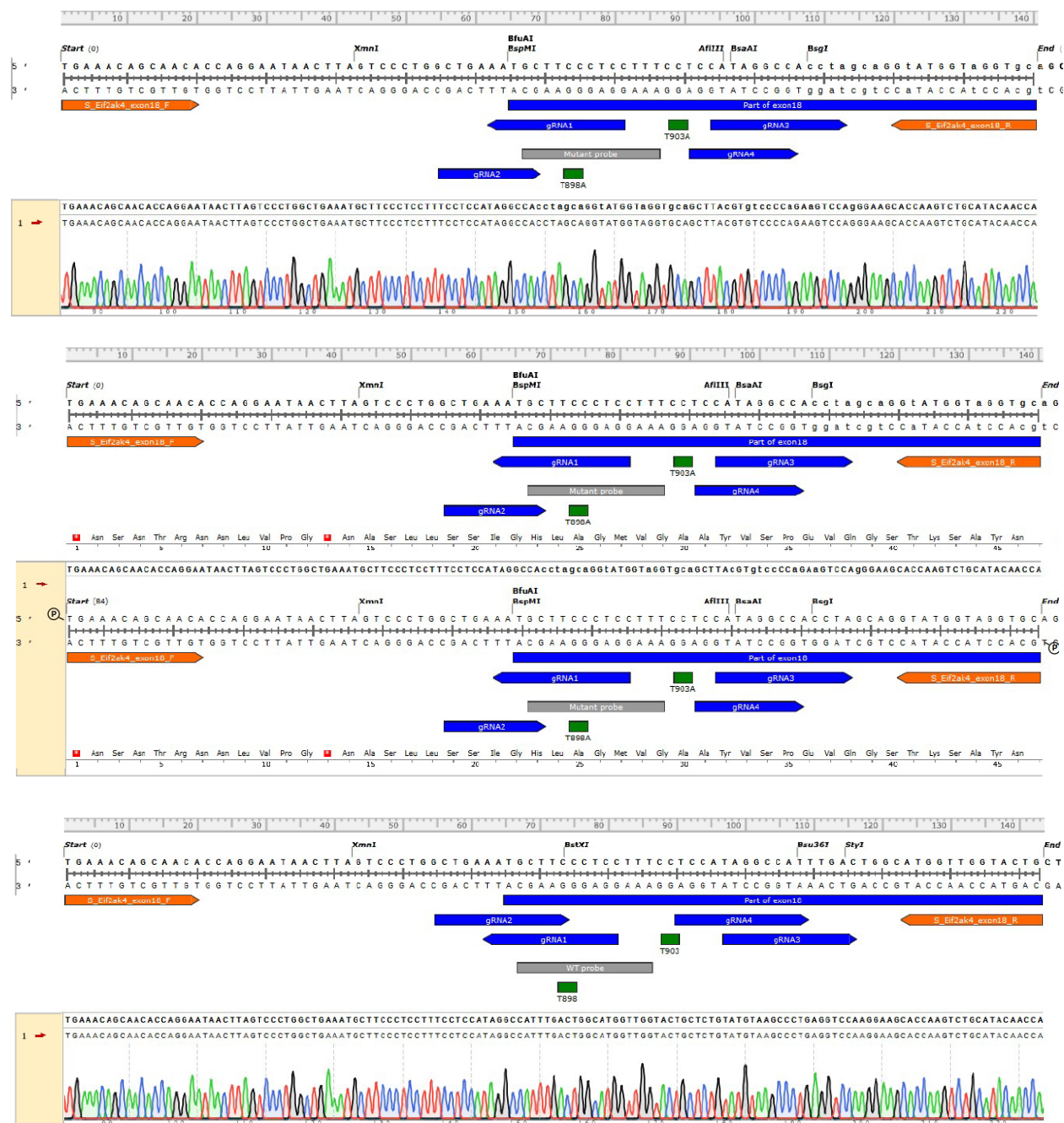


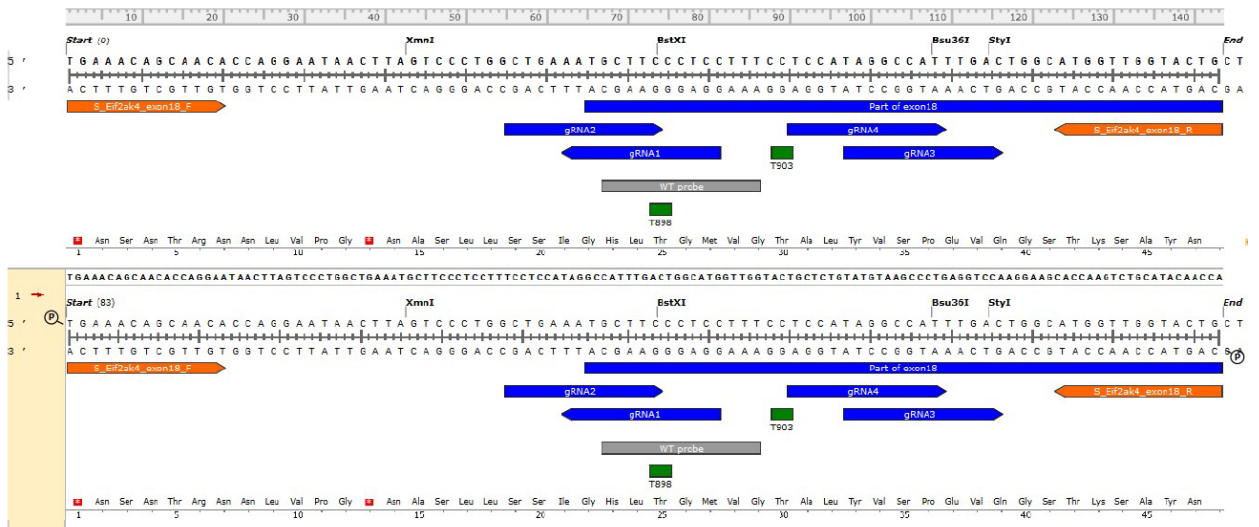
7.1.2. Sequence alignments of *Eif2ak4* and *Eif2s1* point mutations

Sequence alignment (mutation indicated by green box) of wild-type and *Eif2ak4* D849N in 3T3

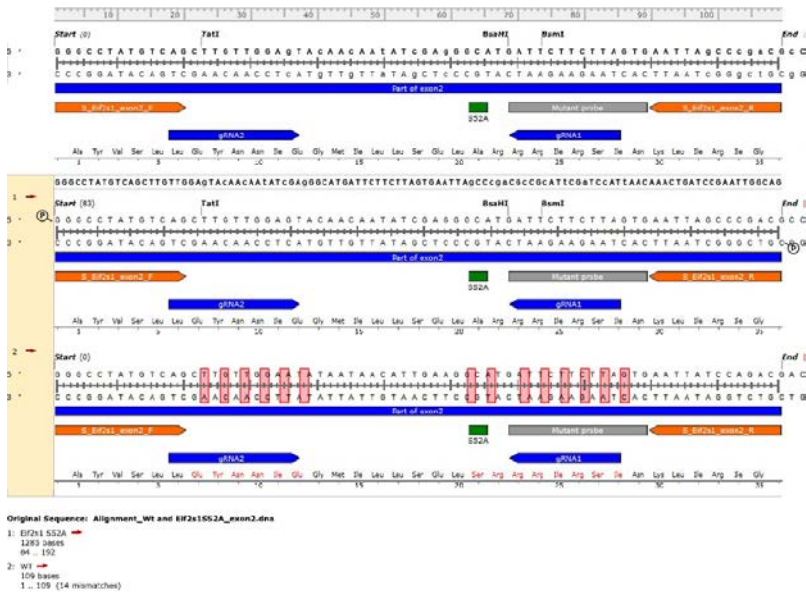
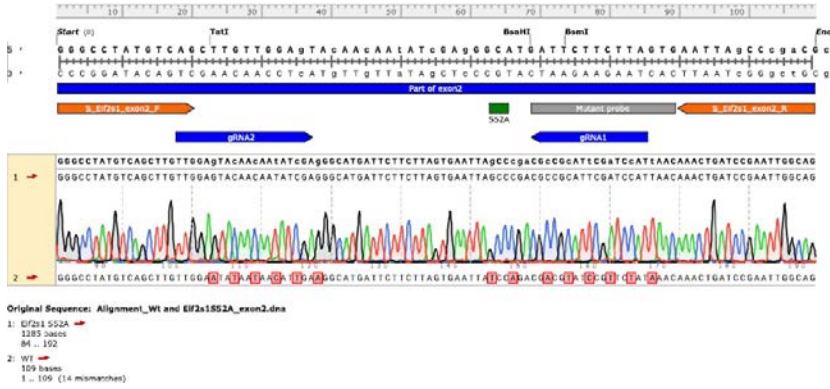


Sequence alignment (mutation indicated by green box) of wild-type and *Eif2ak4* T898/903 in 3T3





Sequence alignment (mutation indicated by green box) of wild-type and *Eif2s1* S52A in 3T3



7.1.4. Sequence alignments of the GCN2-dependent amino acid stress reporter cell systems

Sequence alignment (insertion indicated by light blue bar) of wild-type and *Ddit3::NanoLuc-PEST* in 3T3



Sequence alignment (insertion indicated by red bar) of wild-type and *Ddit3:mCherry* in 3T3





Original sequence: Alignment: WT and Ptd1b/WT, contig 10

1. 100% identity

2. 100% identity

3. 100% identity

4. 100% identity

Sequence alignment (insertion indicated by red bar) of wild-type and *Ddit3:mCherry* in E14

